USGS
science for a changing world

Studies by the U.S. Geological Survey in Alaska, 2001

Professional Paper 1678

U.S. Department of the Interior
U.S. Geological Survey

Cover photograph: Falling Mountain and Mount Cerberus dacite domes, from the River Lethe on floor of the Valley of Ten Thousand Smokes.

Studies by the U.S. Geological Survey in Alaska, 2001

John P. Galloway, Editor

Professional Paper 1678

U.S. Department of the Interior
U.S. Geological Survey

U.S. Department of the Interior
Gale A. Norton, Secretary

U.S. Geological Survey
Charles G. Groat, Director

U.S. Geological Survey, Reston, Virginia: 2003

For sale by U.S. Geological Survey Information Services
Box 25286, Denver Federal Center
Denver, CO 80225

This report and any updates to it are available online at:
http://geopubs.wr.usgs.gov/prof-paper/p1678/

Additional USGS publications can be found at:
http://geology.usgs.gov/products.html

For more information about the USGS and its products:
Telephone: 1–888–ASK–USGS (1–888–275–8747)
World Wide Web: http://www.usgs.gov/

Cataloging-in-publication data are on file with the Library of Congress (URL http://www.loc.gov/).

Published in the Western Region, Menlo Park, California
Manuscript approved for publication, April 3, 2003
Text edited by George A. Havach
Production and design by Sara Boore and Susan Mayfield

Contents

ENVIRONMENT AND CLIMATE

HAZARDS

BIBLIOGRAPHIES

Contributors

Anchorage

Gamble, Bruce M.
Karl, Susan M.
Miller, Thomas P.
Schmidt, Jeanine M.
Waythomas, Christopher F.
U.S. Geological Survey
4200 University Dr.
Anchorage, AK 99508–4667

Denver

O'Neill, J. Michael, Mail Stop 905
Siems, David F., Mail Stop 973
U.S. Geological Survey
P.O. Box 25046, Mail Stop __
Denver Federal Center
Denver, CO 80225

Fairbanks

Layer, Paul W.
Department of Geology and Geophysics
University of Alaska
Fairbanks, Fairbanks, AK 99775
McGuire, Anthony D.
USGS Alaska Cooperative Fish and Wildlife Research Unit
University of Alaska
Fairbanks, AK 99775
Meier, Rose
Silapaswan, Cherie
Spatial Ecology Lab
Institute of Arctic Biology
University of Alaska
Fairbanks, AK 99775–7000
Nye, Christopher J.
Alaska Division of Geological and Geophysical Surveys and Alaska Volcano Observatory
Fairbanks, AK 99755
Swanson, David
Natural Resource Conservation Service
Fairbanks, AK 99775
Yoshikawa, Kenji
University of Alaska
Water & Environmental Research Center
Fairbanks, AK 99775

Menlo Park

Dusel-Bacon, Cynthia, Mail Stop 901
Fierstein, Judy, Mail Stop 937
Galloway, John P., Mail Stop 901
Harden, Jennifer W., Mail Stop 962
Hildreth, Wes, Mail Stop 937
Lanphere, Marvin A., Mail Stop 937
Manies, Kristen L., Mail Stop 962
U.S. Geological Survey
345 Middlefield Rd., Mail Stop __
Menlo Park, CA 94025

Fort Collins

Steltzer, Heidi
Department of Forest Sciences
Colorado State University
Fort Collins, CO 80523
Stottlemyer, Robert
U.S. Geological Survey
240 W. Prospect Rd.
Fort Collins, CO 80526

Palo Alto

Wooden, Joseph L.
USGS–SUMAC
Ion Probe Lab
Green Building, Room 89
367 Panama St.
Stanford University
Stanford, CA 94305–2220

Others

Amos, Katie E.

Cole, Ronald B.
Department of Geology
Allegheny College
Meadville, PA 16335

Baichtal, James F.
U.S. Forest Service
P.O. Box 19515
Thorne Bay, AK 99919

Blodgett, Robert
Department of Zoology
Oregon State University
Corvallis, OR 97331

Eastham, Kevin R.
Department of Earth and Atmospheric Sciences
Purdue University
West Lafayette, IN 47907–1397

Fredricksen, Rick
WGM Inc.
P.O. Box 100059
Anchorage, AK 99510

Harris, Anita G.
1523 E. Hillsboro Blvd. #1031
Deerfield Beach, FL 33441

Mortensen, James K.
Pacific Centre for Isotopic and Geochemical Research
Department of Earth & Ocean Sciences
University of British Columbia
6339 Stores Rd.
Vancouver, B.C., Canada V6T 1Z4

Oliver, Douglas H.
Department of Geological Sciences
Southern Methodist University
Dallas, TX 75275–0395

Randerson, Jim
Division of Engineering and Applied Science and Geological and Planetary Sciences
California Institute of Technology
Pasadena, CA 91125

Rhoades, Charles.
Department of Forestry
University of Kentucky
Lexington, KY 40546

Ridgway, Kenneth D.
Department of Earth and Atmospheric Sciences
Purdue University
West Lafayette, IN 47907–1397

Rohr, David M.
Department of Geology
Sul Ross State University
Alpine TX 79832

Swanson, Donald K.
U.S. Forest Service
P.O. Box 907
Baker City, OR 97814

Studies by the U.S Geological Survey in Alaska, 2001

John P. Galloway, Editor

Introduction

By John P. Galloway

The collection of 14 studies that follow continues the series[1] of U.S. Geological Survey (USGS) investigative reports in Alaska under the broad umbrella of the geologic sciences. This series presents new and sometimes-preliminary findings that are of interest to Earth scientists in academia, government, and industry; to land and resource managers; and to the general public. The reports presented in *Studies by the U.S. Geological Survey in Alaska* cover a broad spectrum of topics from various parts of the State (fig. 1), serving to emphasize the diversity of USGS efforts to meet the Nation's needs for Earth-science information in Alaska.

The chapters in this volume are organized under the topics Geologic Framework, Environment and Climate, and Hazards. This organization is intended to reflect the scope and objectives of current USGS programs in Alaska.

Geologic Framework studies provide background information that is the scientific basis for present and future Earth-science investigations. Dusel-Bacon and Harris report the discovery of several new fossil occurrences of late Paleozoic conodonts and radiolarians in the Seventymile and Yukon-Tanana terranes, and of Late Triassic conodonts in the Seventymile terrane in east-central Alaska. The Seventymile terrane in Alaska is equivalent to the Slide Mountain terrane in Canada; both are oceanic assemblages composed of fault-bounded slices of serpentinized periodotite, weakly metamorphosed mafic volcanic rocks, and Mississippian to Upper Triassic sedimentary rocks. Dusel-Bacon and Harris discuss the Upper Triassic rocks and both oceanic rocks of the Seventymile and Slide Mountain terranes and continental-margin rocks of the Yukon-Tanana terrane and ancestral North America.

In their first study, Dusel-Bacon and others present evidence that the mineralization at the Lead Creek Pb-Zn-Ag prospect, located in east-central Alaska, comprises an epigenetic vein and manto-style replacement deposit and that previous correlation with syngenetic, middle Paleozoic mineralization in the Finlayson Lake area of the Yukon Territory, Canada, is unwarranted.

In their second study, Dusel-Bacon and others report a new ion-microprobe U-Pb zircon age of 111±2 Ma for the Orthogneiss unit of the West Point Complex. They conclude that a previously determined age based on conventional U-Pb zircon analysis of a sample from the West Point orthogeneiss which gave an upper intercept of 671±34 Ma averaged several distinct isotopic populations and thus is geologically meaningless. If their interpretation of the mid-Cretaceous samples and the U-Pb zircon ages is correct, the maximum igneous crystallization age of the West Point orthogneiss and the minimum igneous crystallization age of the posttectonic Salcha intrusion imply that the mid-Cretaceous (synmetamorphic?) and posttectonic intrusion occurred during a narrow timespan between 113 and 111 Ma.

Oliver and Dusel-Bacon discuss a new structural analysis that has helped define a polyphase deformation history in ductilely deformed tectonites between the Chena and Salcha

[1] From 1975 through 1988, *Geologic Studies in Alaska* was published as a series of USGS Circulars, which were titled *The United States Geological Survey in Alaska: Accomplishments During 19xx*. From 1989 to 1994, the series was published as more formal USGS Bulletins. As a result of a reorganization in 1995 of USGS publications, the series is now being published as USGS Professional Papers.

Rivers in the Yukon-Tanana Upland of east-central Alaska. Kinematic analysis has identified widespread top-to-the-northwest and top-to-the-southeast shear senses and, in the structurally low Nasina assemblage, more local top-to-the-northwest fabrics. The top-to-the-northwest fabrics are interpreted to have resulted from Early Jurassic thrusting of allochthonous tectonites over the North American continental margin, and the top-to-the-southeast fabrics are attributed to mid-Cretaceous crustal extension that exhumed structurally lower rocks. The particularly well developed top-to-the-southeast fabrics around the West Point Complex may have formed during tectonic exhumation of the igneous and metamorphic complex, similar to the exhumation that is proposed for the Salcha River gneiss dome.

Amos and Cole's study of Tertiary volcanic rocks of the central Talkeetna Mountains provides new insight into the tectonomagmatic history of south-central Alaska. Although the timing and extent of subduction-related magmatism is poorly defined for the early Tertiary of south-central Alaska, geochemical analysis of volcanic rocks of the central Talkeetna Mountains indicates that subduction-related magmatic processes were important in the evolution of these rocks but that these rocks also lack some "typical" arc volcanic geochemical affinities. This trend is consistent with the interpretation that in western Alaska, from about 56 to 50 Ma, a transition occurred from subduction-related magmatism to postsubduction, possibly intraplate magmatism during which rocks typical of both environments were erupted. The mixed geochemical affinity of the volcanic rocks indicates that a similar transition occurred in south-central Alaska during Eocene time. Geochemical data suggest that a depleted mantle reservoir existed beneath south-central Alaska during the early Tertiary. This depleted mantle reservoir could represent the original composition of the upper mantle beneath the Wrangellia composite terrane, or it could have formed as a slab window beneath south-central Alaska after passage of a trench-spreading ridge-trench triple junction.

Sedimentologic and structural investigations by O'Neill and others along the trace of the Talkeetna thrust fault reveal the following relations: (1) the Kahiltna assemblage in the footwall of the Talkeetna thrust fault represents proximal submarine-fan deposits that were derived from strata exposed in the adjacent hanging wall of the fault; (2) the structure along the fault trace is that of minor thrust slices in the juxtaposed upper and lower plates, is nonpenetrative, and is restricted to within 20 to 50 m of the thrust fault. Lower-plate rocks containing rounded pebble to boulder clasts and macrofossils adjacent to the fault are undeformed. The proximal sedimentary relation between the footwall and hanging-wall rocks, along with the absence of well-developed penetrative-deformation fabrics, suggests that the Talkeetna Fault is not a major nappelike structure with tens of kilometers of tectonic transport, and so this individual fault zone does not mark a major tectonic-terrane boundary in south-central Alaska.

Regional mapping by Schmidt and Gamble, along with lithogeochemistry, suggests that many of the Tertiary plutonic rocks exposed in the northern Talkeetna Mountains belong to a "specialized" granite or granophile suite with high SiO_2 content. Major-, minor-, and trace-element geochemical analyses of fresh plutonic host rocks, altered rocks, and stream sediment suggest that the Clark Bar prospect has a potential to host granitoid Sn-Mo-Ag mineralization. Strongly altered rocks at Clark Bar are rich in Ag, Be, Ce, La, Li, Mo, Sn, and Zn, and some rocks are rich in Bi, Hg, and Sb. Associated Paleocene granitic rocks are SiO_2 rich and have a trace-element chemistry consistent with granophile or "specialized," S-type granites. Both the Clark Bar prospect and the regionally extensive Paleocene plutons have a moderate potential to host Sn-Ag-Mo and (or) W and rare-earth-element deposits.

Blodgett and others present evidence that Early Middle Devonian (Eifelian) gastropods from the Wadleigh Limestone in the Alexander terrane of southeastern Alaska demonstrate biogeographic affinities with those of central Alaska and Eurasia. They describe six species from a locality of the Wadleigh Limestone, most of which are conspecific or closely allied with coeval gastropod faunas from the Nixon Fork subterrane of the Farewell terrane of west-central Alaska and from the Livengood terrane of east-central Alaska. None of the species described is known from contemporaneous, miogeoclinal strata of western Canada, and none is recognized within coeval rocks of nonaccreted western North America. These close affinities suggest that the Alexander terrane, like the related Farewell and Livengood terranes, is of Eurasian origin.

Rohr and Blodgett describe a new Silurian gastropod, *Kirkospira glacialis* n.gen., n.sp., from the Upper Silurian part of the Willoughby Limestone of Glacier Bay, southeastern Alaska

(Rohr and Boldgett). The material examined, which was collected by the USGS in 1906 and 1917 from one of the two small islands immediately northeast of Willoughby Island, is part of a large-shelled molluscan facies that is observed on both Willoughby and Drake Islands. This Alexander terrane fauna is biogeographically most closely allied to other Late Silurian faunas from the Ural Mountains of Russian and the Farewell terrane of southwestern Alaska.

Stottlemyer and others discuss treeline biogeochemistry and dynamics in Noatak National Preserve. Their previous studies have focused on quantifying the sensitivity of the terrestrial ecosystem to global change, especially climate—in particular, soil temperature, moisture, and nitrogen availability—on ecosystem processes within an 800-ha-area watershed in a boreal biome. This study continues their previous work and updates their results from an intensive study conducted during 1997–98 on below-ground processes in taiga, tundra, and the taiga-tundra transition zone. They present data that in high-latitude ecosystems, changes in the carbon and nitrogen budgets are closely linked. The potential effects of seasonal changes on above-ground temperature and moisture may be partly offset by significant increases in below-ground moisture from thawing.

In two related studies, Harden and others and Manies and others discuss the effects of fire on soil temperature and vegetative regrowth for different soil-drainage classes in east-central Alaska. About 40 to 60 percent of the land surface in Alaska consists of poorly drained soils. Both studies present data on how fire affects the carbon storage of boreal forest and how this response varies with drainage types. Drainage type affects such factors as fire frequency and severity, vegetation recovery, and rates of decomposition. They suggest that large-scale patterns of fire are partly controlled by soil drainage and that ice-rich soil (zones of discontinuous permafrost) may be particularly "elastic" in their ability to store, release, and sequester carbon. Understanding variations in soil temperature, soil drainage, and fire history will give us a better understanding of the sensitivity of boreal regions to climate change.

Hildreth and others discuss Trident Volcano, which consists of four contiguous stratovolcanoes and several peripheral lava domes. Construction of the four principle edifices proceeded stepwise from northeast to southwest. The oldest stratovolcano, East Trident, had a brief eruptive lifetime around 143±8 ka. Trident I ended its activity by about 101±12 ka. The eruptive volume of 3 to 4 km^3 for the third stratovolcano, West Trident, was largely completed by 44±12 ka. After glacial dissection of the three Pleistocene cones, a fourth edifice, Southwest Trident, was constructed between 1953 and 1974. Reconstruction of the eroded edifices yields an estimated eruptive volume for the whole Trident group of 21±4 km^3. Averaged over 143±8 k. k.y., this output yields a long-term eruption rate of 0.11 to 0.18 km^3/k.y., far smaller than the rates calculated for neighboring Mageik and Katmai Volcanoes.

Waythomas and others present recent studies of the geology and eruptive history of Kanaga Volcano in the western Aleutian Islands of Alaska that have yielded new information about the timing of Holocene eruptions and an improved understanding of the evolution of the volcano. Their studies indicate that a major topographic feature on northern Kanga Island, a rim of a collapsed caldera, likely formed as the result of a northward-directed flank collapse which was not necessarily associated with a major eruption. Dacitic lapilli tephra deposits began accumulating on Kanaga Island about 11 ka, suggesting that most of the modern volcanic cone formed during Holocene time. At least 11 major tephra-producing eruptions of Kanaga Volcano have been documented. Tephra deposits on nearby Adak Island were believed to have been erupted from Kanaga Volcano throughout the Holocene. Tephrostratigraphic and chronologic data, however, indicate that only a few of the Adak tephra deposits are directly correlatable with eruptions of Kanaga Volcano, and so the source of the major pumiceous tephra deposits on Adak is uncertain.

Two bibliographies at the end of the volume list reports covering Alaska Earth-science topics in USGS publications during 2001 and reports about Alaska by USGS authors in non-USGS publications during the same period.

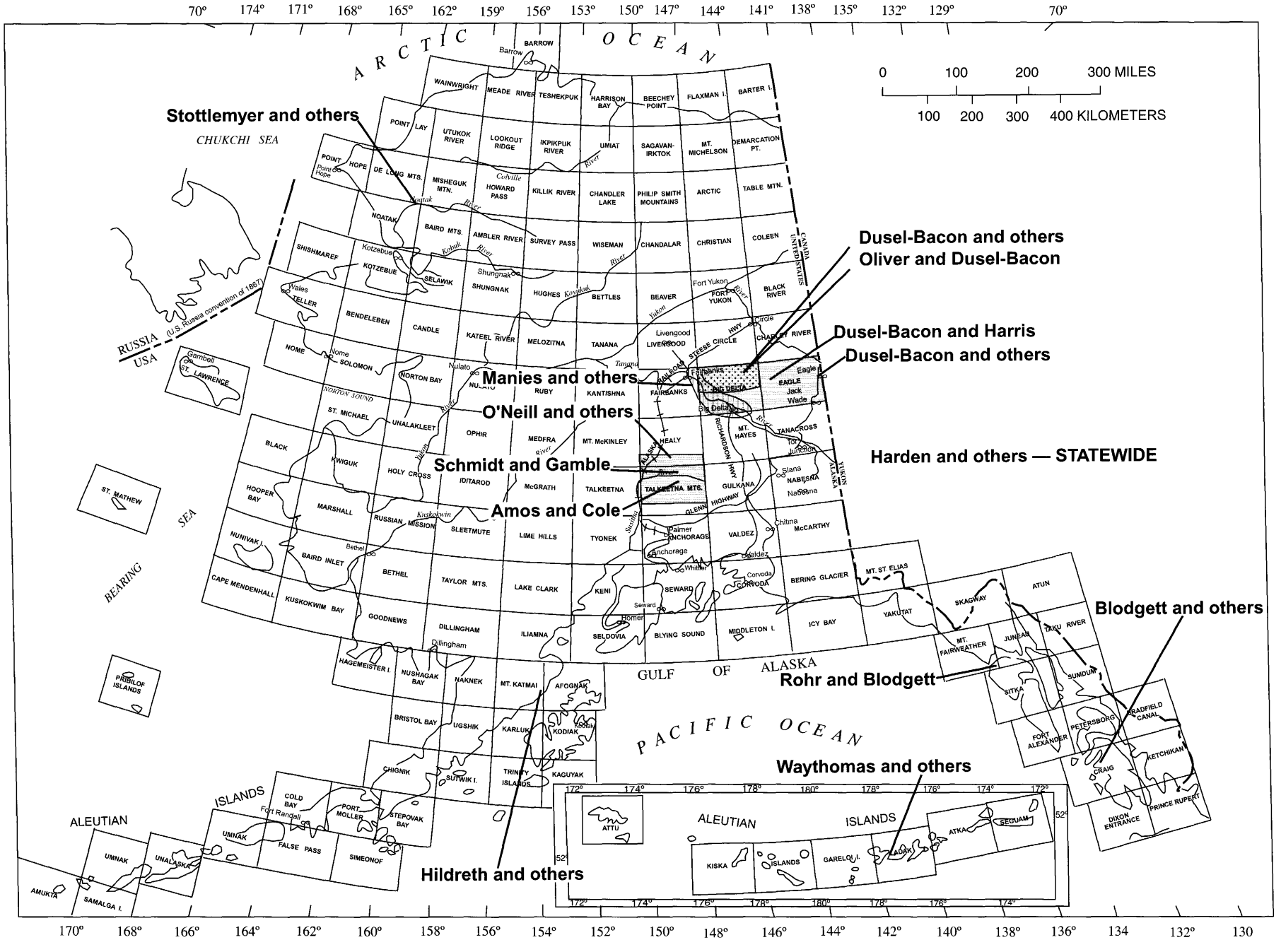

Figure 1. Index map of Alaska, showing 1:250,000-scale quadrangles and locations of study areas discussed in this volume.

Studies by the U.S. Geological Survey in Alaska, 2001
U.S. Geological Survey Professional Paper 1678

New Occurrences of Late Paleozoic and Triassic Fossils from the Seventymile and Yukon-Tanana Terranes, East-Central Alaska, with Comments on Previously Published Occurrences in the Same Area

By Cynthia Dusel-Bacon and Anita G. Harris

Abstract

The discovery of several new fossil occurrences of late Paleozoic conodonts and radiolarians in the Seventymile and Yukon-Tanana terranes, and of Late Triassic conodonts in the Seventymile terrane in east-central Alaska, has prompted a reevaluation of other late Paleozoic and Triassic fossils reported from the same areas. The report, in 1995, of giant parafusulinids in the Seventymile terrane within the same stratigraphic interval that more than 20 years before produced poorly preserved Permian brachiopods helped to place these beds in the middle Guadalupian and to position the terrane at tropical to subtropical latitudes near ancestral North America during the Middle Permian. The Seventymile terrane in Alaska is equivalent to the Slide Mountain terrane in Canada; both terranes are oceanic assemblages composed of fault-bounded slices of serpentinized peridotite, weakly metamorphosed mafic volcanic rocks, and Mississippian to Upper Triassic sedimentary rocks. A more southerly Permian paleolatitude for the Slide Mountain terrane also is suggested by faunal data and by paleomagnetic data from the Sylvester Allochthon in northern and central British Columbia. Although general agreement exists that the Seventymile-Slide Mountain terrane represents a basin floored by oceanic crust off the western margin of ancestral North America, the original width of the ocean basin is disputed. Our Permian faunal data are consistent with formation of the basin in either a narrow ocean that was depositionally tied to ancestral North America, or a wider Paleozoic Pacific ocean adjacent to a rifted continental fragment. Late Carnian and early Norian (Late Triassic) conodonts occur in weakly metamorphosed sedimentary rocks of the Seventymile terrane in the Fortymile River area of east-central Alaska and are widespread in the Canadian Cordillera and in central and southeastern Alaska. It was previously proposed that Middle(?) and Upper Triassic siliciclastic-carbonate strata of the Sylvester Allochthon represent an overlap sequence which loosely links North America and the Slide Mountain terrane. Considerable uncertainty exists, however, regarding the original contact between the Upper Triassic rocks and both oceanic rocks of the Seventymile and Slide Mountain terranes and continental-margin rocks of the Yukon-Tanana terrane and ancestral North America. Therefore, we interpret the wide distribution of Late Triassic conodonts in the various allochthonous terranes and in the North American continental margin as indicating that these areas shared approximately similar warm, normal-marine conditions along the Late Triassic continental margin but not that they represent an overlap assemblage, in the sense of draping across contacts between outboard allochthonous pericratonic and arc fragments and the ancient Pacific margin.

Introduction

The Yukon-Tanana Upland of east-central Alaska is composed of fault-bounded assemblages of ductilely deformed Proterozoic(?) and Paleozoic metasedimentary and middle Paleozoic metaigneous rocks that are intruded by synkinematic to postkinematic Late Triassic and Early Jurassic granitoids and postkinematic Cretaceous and Tertiary granitoids (figs. 1–3). The ductilely deformed rocks are tectonically overlain by weakly metamorphosed oceanic igneous rocks and associated Paleozoic and Triassic sedimentary rocks of the Seventymile terrane and are stratigraphically overlain by Cretaceous and Tertiary volcanic rocks (Foster, 1992; Foster and others, 1994). The ages and origins of the various fault-bounded assemblages of metamorphic rocks, and their relation to each other and to the western continental margin of North America, are uncertain, largely owing to inadequate paleontologic age control. Fossil occurrences are few and far between in the weakly metamorphosed late Paleozoic and Triassic rocks of the Seventymile terrane and even more unusual in the underlying, more recrystallized and ductilely deformed assemblages.

Some of the fossil localities we describe below have not been reported previously because the fossils, chiefly microfossils, are too poorly preserved to provide more than a generalized age assignment. In large areas of metamorphosed bedrock, however, such as those that make up much

of east-central Alaska, the announcement of any fossil find could encourage other workers to sample for microfossils that might, in turn, produce more biostratigraphically useful data. Since the late 1990s, late Paleozoic and Triassic conodonts have been reported from several new localities south of the Tintina Fault system in the Charley River, Eagle, and Big Delta quadrangles. We present these data here for the first time. In addition, we summarize information on previously published fossils of the same or similar age, terrane, and broad geographic area as our new occurrences, so that all the data are presented together.

Regional Geologic Setting

The ductilely deformed assemblages of the Yukon-Tanana Upland, together with the granitoids that intrude them and the structurally juxtaposed oceanic rocks of the Seventymile terrane, occupy a suspect position in the northern Cordillera: the assemblages are fault bounded along most of their length and lie between autochthonous or slightly displaced North American strata and outboard allochthonous terranes (fig. 1). The ductilely deformed rocks were originally grouped as a single terrane, the Yukon-Tanana terrane, by Jones and others (1987) and Monger and Berg (1987) but were subsequently subdivided on the basis of differences in the composition and origin of protoliths and in the structural and metamorphic histories of their components (for example, Foster and others, 1985; Nokleberg and others, 1989; Hansen and others, 1991; Dusel-Bacon and others, 1995; Hansen and Dusel-Bacon, 1998; Dusel-Bacon and Cooper, 1999). In this chapter, we use the subdivision (assemblage) terminology of Dusel-Bacon and others (2002). Part of the Yukon-Tanana terrane, as originally defined, has been dextrally offset approximately 450 km by the Tintina Fault system (fig. 1), during Late Cretaceous through Eocene time (Roddick, 1967; Tempelman-Kluit, 1979).

The structurally lowest rocks exposed in the Alaskan part of the Yukon-Tanana Upland are the Lake George assemblage of Dusel-Bacon and Cooper (1999) and the undivided Fairbanks schist of Robinson and others (1990) and Chena River sequence of Smith and others (1994) (fig. 2); both of these units consist of amphibolite-facies orthogneiss (including bodies of augen gneiss), felsic and mafic schist and gneiss, and lesser amounts of pelitic schist, quartzite, and marble. Although no fossils have been found in the units, U-Pb dating of zircons from the metaigneous rocks indicate Middle and Late Devonian crystallization ages for their igneous protoliths (Dusel-Bacon and Aleinikoff, 1996; Dusel-Bacon and others, 2001). Depositional ages for the metasedimentary rocks that are assumed to be intruded by the protoliths of these metaigneous rocks are therefore Devonian or earlier.

Overlying the above-described amphibolite-facies assemblage is a sequence of greenschist-facies, quartz-rich clastic metasedimentary rocks, mafic and felsic metavolcanic rocks, and marble that we assign to the Nisutlin assemblage of Hansen and Dusel-Bacon (1998) (figs. 1, 2). The Nisutlin assemblage consists of a lower sequence of rocks characterized by carbonaceous quartzite and calc-phyllite (equivalent to the Nasina assemblage of Wheeler and McFeely, 1991); an upper sequence characterized by quartz-eye semischist, white-mica phyllite, quartzite, marble, and bimodal metavolcanic rocks (Foster and others, 1994); and, locally, Permian metavolcanic rocks. Devonian and Mississippian U-Pb zircon protolith ages have been determined for felsic metavolcanic rocks in both the upper (semischist) sequence and the lower (carbonaceous) sequence in east-central Alaska (Foster, 1992; Dusel-Bacon and others, 1993, 1998; Smith and others, 1994) and the Yukon Territory, Canada (Mortensen, 1992). Permian felsic metavolcanic rocks occur in association with carbonaceous rocks north of the Fortymile River, just west of the Alaska-Yukon Territory border (fig. 3; Dusel-Bacon and others, 1998). These Permian rocks presumably are equivalent to the Klondike Schist of Mortensen (1988) that crops out along the Top-of-the-World Highway to the south (fig. 3).

In most areas, the contact between the greenschist-facies Nisutlin assemblage and adjacent amphibolite-facies assemblages has been interpreted as a low-angle fault (for example, Pavlis and others, 1993; Foster and others, 1994; Hansen and Dusel-Bacon, 1998), but given the limited bedrock exposure in the region, a gradational stratigraphic contact, as proposed by Smith and others (1994) for the upper Chena River area (near lat 65° N., long 145° W., fig. 2), cannot be ruled out for at least some localities.

In the eastern part of the Yukon-Tanana Upland (fig. 3), the Nisutlin assemblage is overlain by amphibolite-facies garnet amphibolite, biotite±hornblende±garnet gneiss and schist, marble, quartzite, metachert, and pelitic schist (Foster, 1976; Hansen and others, 1991), as well as by small bodies of tonalitic orthogneiss (Day and others, 2000; Szumigala and others, 2000). The rocks were previously referred to as the Taylor Mountain assemblage (Hansen and others, 1991; Dusel-Bacon and others, 1995) but are now referred to as the Fortymile River assemblage (figs. 2, 3; see Dusel-Bacon and others, 2002, and for an explanation of this terminologic change). A Paleozoic protolith age for at least part of the layered metamorphic sequence was proposed by Foster (1976) on the basis of a few poorly preserved crinoid columnals in marble. An Early Mississippian or older age for at least some of the Fortymile River assemblage is indicated by a U-Pb zircon crystallization age of 343±4 Ma determined for tonalitic orthogneiss that presumably intrudes the adjacent schist and gneiss (Day and others, 2002).

The structurally highest rocks that crop out in the central and eastern parts of the Yukon-Tanana Upland (figs. 2, 3) are part of a belt of fault-bounded slices of varyingly serpentinized peridotite; weakly metamorphosed mafic volcanic rocks, including pillowed greenstone; and Mississippian to Upper Triassic sedimentary rocks. This assemblage is partly interpreted as a dismembered ophiolite (Foster and others, 1994). These oceanic rocks, which are included in the Seventymile terrane in Alaska, are generally considered to be equivalent to the Slide Mountain terrane in Canada, as proposed by Harms

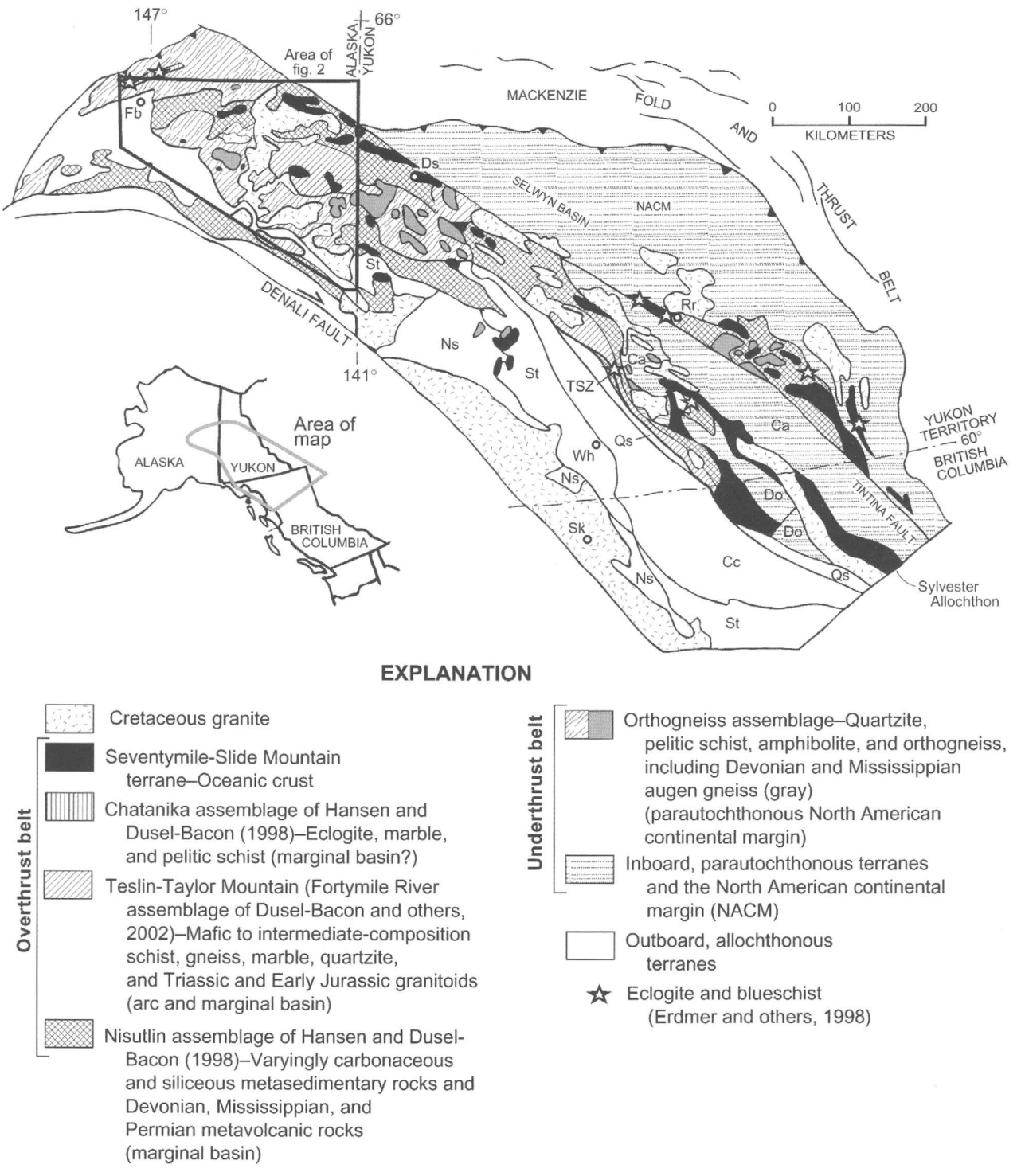

Figure 1. Simplified terrane and tectonic assemblage map of northern Canadian and Alaskan Cordillera (modified from Hansen and others, 1991, and Dusel-Bacon and Cooper, 1999). Abbreviations in terrane map: Towns: Ds, Dawson; Fb, Fairbanks; Rr, Ross River; Sk, Skagway; Wh, Whitehorse. Terranes: Ca, Cassiar; Cc, Cache Creek; Do, Dorsey; Ns, Nisling; Qs, Quenellia; St, Stikinia; TSZ, Teslin suture zone. Unlabeled area surrounding Fairbanks is alluvium of the Tanana River Valley; unlabeled area adjacent to north side of the Denali Fault in Alaska comprises various terranes not discussed in this chapter. Tertiary granitoids not shown. The Yukon-Tanana Upland physiographic province in Alaska includes all the area north of the Tanana River Valley; units above that are included in the broadly defined Yukon-Tanana terrane are the Chatinika assemblage of Hansen and Dusel-Bacon (1998) (equivalent to unit ec of Foster and others, 1994), the Fortymile River assemblage of Dusel-Bacon and others (2002), the Nisutlin assemblage of Hansen and Dusel-Bacon (1998), and the orthogneiss assemblage of Hansen and Dusel-Bacon (1998).

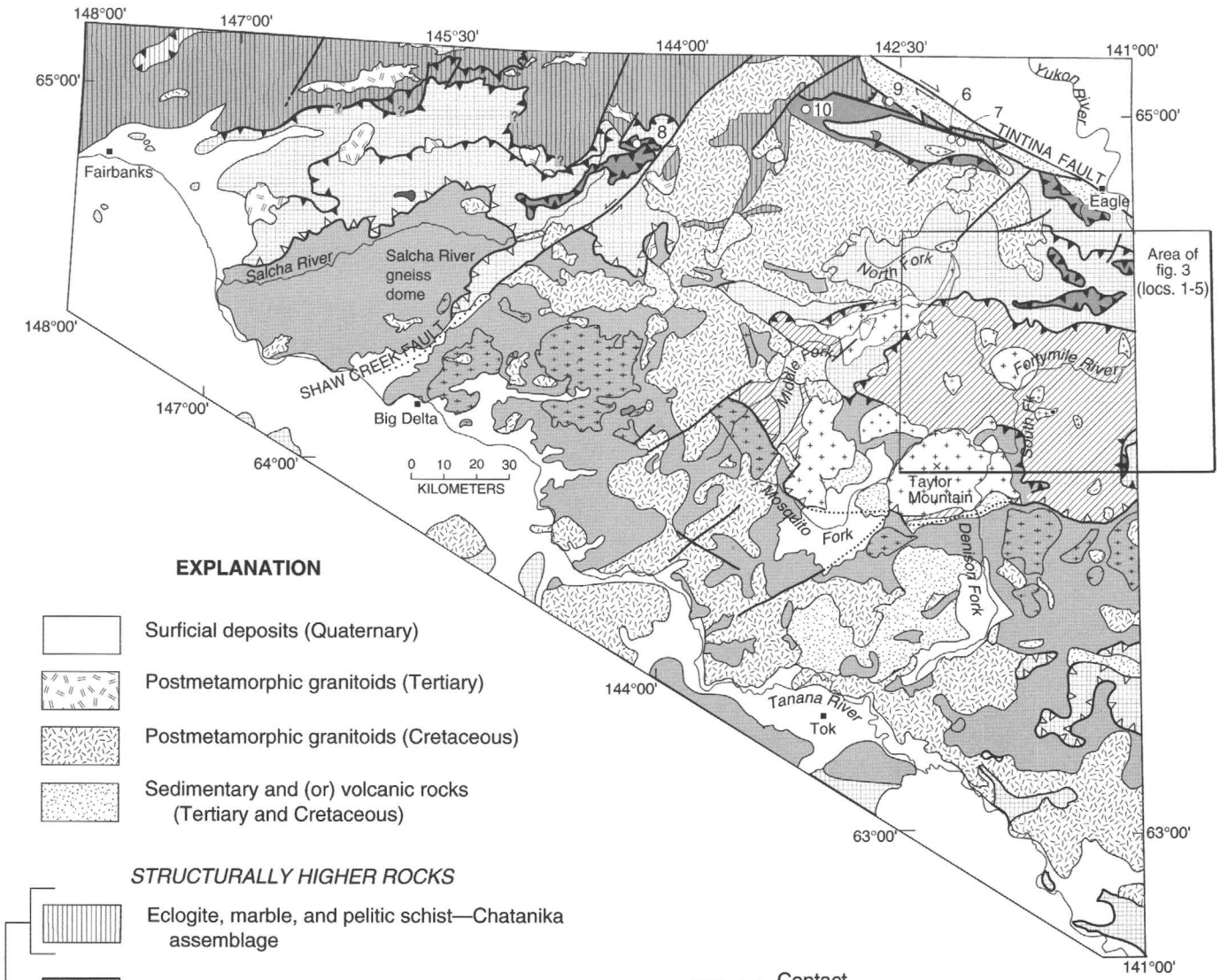

Figure 2. Generalized geologic map of east-central Alaska, showing fossil localities in the Seventymile and Yukon-Tanana terranes. Geology from Foster (1992) and Dusel-Bacon and others (1993, 2002). Unpatterned areas are Late Proterozoic to Cambrian and Devonian sedimentary rocks north of the Tintina Fault, and Quaternary surficial deposits elsewhere.

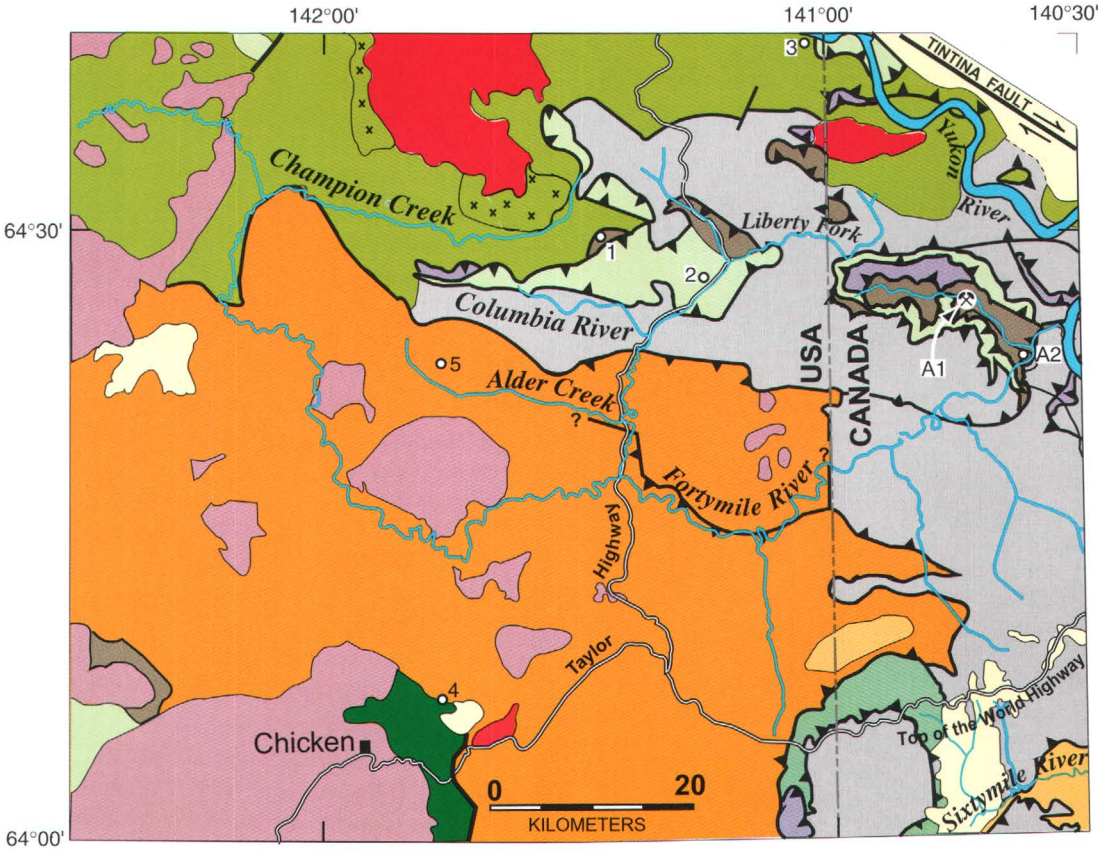

EXPLANATION

- Unmetamorphosed volcanic and sedimentary rocks (Tertiary and Cretaceous)
- Postmetamorphic granitoids (Cretaceous)
- Synmetamorphic to postmetamorphic granitoids (Early Jurassic and Late Triassic)

SEVENTYMILE TERRANE

- Serpentinized peridotite
- Greenstone, diabase, metalimestone (Triassic, Permian, and Mississippian), and metachert
- Argillite and metasandstone

FORTYMILE RIVER ASSEMBLAGE

- Amphibolite-facies biotite-hornblende gneiss, amphibolite, marble (Mississippian?- Late Permian?), and metachert
- Granodioritic orthogneiss (Early Mississippian)

NISUTLIN ASSEMBLAGE

- Quartz-muscovite±chlorite±feldspar schist (Permian)–Klondike Schist of Mortensen (1988)
- Quartz-chlorite-muscovite±calcite schist, micaceous quartzite, and marble (Mississippian)
- Carbonaceous quartzite, muscovite-chlorite schist, and marble (Mississippian and Devonian)–Nasina assemblage of Wheeler and McFeely (1991)
- Greenschist-facies metasedimentary and metaigneous rocks (Mesozoic and Paleozoic)–Chicken Metamorphic Complex of Werdon and others (2001)
- Thrust fault, sawteeth on upper plate, queried where uncertain
- Strike-slip fault, right-lateral offset
- Hornfels
- Clinton Creek Mine
- o5 Conodont sample locality

Figure 3. Generalized geologic map of eastern Alaska, showing fossil localities in the Fortymile River area (modified from Foster, 1976, 1992, and Mortensen, 1988). Units included in the broadly defined Yukon-Tanana terrane are the Fortymile River assemblage of Dusel-Bacon and others (2002), the Nisutlin assemblage of Hansen and Dusel-Bacon (1998), and the Chicken Metamorphic Complex of Werdon and others (2001).

and others (1984). Rocks of the Seventymile terrane are low grade, not penetratively deformed, and structurally overlie (in east-central Alaska; Foster, 1992) or are imbricated with (in the Yukon Territory, Canada; Mortensen, 1990) rocks of the Nisutlin or Fortymile River assemblage (fig. 3).

In the northwestern part of the Yukon-Tanana Upland, klippen of continental-margin metamorphic rocks, including marble and pelitic schist, locally contain occurrences of high-pressure and high-temperature eclogite (Dusel-Bacon and others, 1989). These klippen, referred to as the Chatanika assemblage (terminology of Hansen and Dusel-Bacon, 1998; equivalent to unit ec of Foster and others, 1994), were thrust over rocks of the undivided Fairbanks schist-Chena River sequence (figs. 1, 2).

Microfossils

Conodonts

Conodonts are one of the major biostratigraphic indices for marine rocks of latest Cambrian through Triassic age. They can be mechanically and chemically concentrated from various unmetamorphosed clastic and carbonate rock types (Harris and Sweet, 1989). Their extraction from low- to medium-grade metamorphic rocks is mostly limited to metalimestone, metadolostone, marble, and metachert (Rejebian and others, 1987). Conodonts, which can be freed from chert by using the same technique as for radiolarian extraction (Harris and Sweet, 1989), are commonly a paleontologic bonus in radiolarian chert residues. Conodonts are also the microfossils of choice in metamorphosed carbonate areas where other fossil groups are unlikely to be preserved well enough for other than generalized age assignment. The conodont localities discussed below are mainly from very low grade to low-grade metamorphosed carbonate and unmetamorphosed biosiliceous rocks.

Late Triassic Conodonts in East-Central Alaska

Locality 1

Relatively abundant conodonts were recovered from an approximately 10-ft-thick core interval (731.6–741.1-ft interval of diamond-drill hole LC–7, fig. 4) of locally recrystallized, slightly pyritic, gray-and-black carbonaceous quartzose limestone of the Seventymile terrane that was drilled by WGM, Inc., on the Lead Creek property of Doyon Ltd. (see Dusel-Bacon, Mortensen, and Fredericksen, this volume) in the southwestern part of the Eagle C–1 quadrangle (loc. 1, fig. 3; table 1). The only other acid-resistant mineralized fossils from the core are phosphatized sponge fragments. All conodonts in the collection are Pa elements (platform elements that in metapolygnathids and epigondolellids function as food shredders and grinders; pl. 1) except for one M element (pick-shaped elements that likely grasped, pierced, and may also have shredded food). The conodonts are mostly incomplete and poorly preserved juveniles and subadults that probably represent post-mortem sorting during hydraulic transport. In this depositional setting, most of the adult Pa elements were probably left in lag concentrates in slightly higher energy environments, while the more delicate, lighter ramiform elements (serrated single-bladed to multibladed shredding elements) were likely carried into lower-energy environments as winnows. Some diagnostic features of the few relatively complete adult specimens in the collection (pl. 1) are partly to mostly obscured by annealed sand- to silt-size quartz grains and pyrite. Nearly all specimens are incomplete because of post-mortem transport from or within a relatively shallow water, high-energy, quartz-rich regime, a probable second interval of transport during redeposition of some or all of the conodonts, and later tectonic fracturing and minor attenuation. The conodonts have a color-alteration index (CAI; Epstein and others, 1977) of 5, indicating that they were subjected to a thermal regime that reached a temperature of at least 300°C. Although a mid-Cretaceous (96 Ma) felsic dike or sill that cuts low-grade metacarbonate and metasedimentary rocks of the Seventymile terrane 53 ft higher up in drill hole LC–7 (see Dusel-Bacon, Mortensen, and Fredericksen, this volume) likely supplied the latest heat to affect the conodonts, regional thrusting and emplacement of rocks of the Seventymile terrane during the early Mesozoic (Hansen and Dusel-Bacon, 1998; Dusel-Bacon and others, 2002) may also have been responsible for the elevated CAI value.

Four conodont species were identified in the Lead Creek collection: 1) *Epigondolella quadrata* Orchard (pl. 1, figs. 1–15), (2) *Metapolygnathus nodosus* (Hayashi), (3) *M. primitius* (Mosher) (pl. 1, figs. 16, 17), and (4) *M. samueli* Orchard (identified by M.J. Orchard, Geological Survey of Canada). Specimens of *E. quadrata* overwhelmingly dominate the collection; *Metapolygnathus* spp. It is represented by only one to a few specimens each (loc. 1, fig. 3; table 1). The Pa elements of most metapolygnathids and epigondolellids have a relatively coarsely ornate platform and a free blade that joins the platform in a central position. Similar Pa elements in Devonian and younger Paleozoic conodont faunas (for example, polygnathids and pseudopolygnathids of the Devonian and Early Mississippian) occupied warm, relatively shallow water, normal-marine environments. The Lead Creek metapolygnathid and epigondolellid species and their taphonomy suggest derivation from a similar habitat.

Although all the conodont species from the Lead Creek core probably originated in similar environments, not all have overlapping ranges (fig. 4). *Metapolygnathus nodosus* is the most common and widespread late Carnian to very earliest Norian conodont, occurring in the Tethyan region in the western part of the North American Cordillera, and elsewhere (Orchard, 1991c). *M. nodosus* completely overlaps the range of *M. samueli*, as well as the early part of the range of *M. primitius* (fig. 4). *M. primitius* is restricted to its zone, which straddles the Carnian-Norian boundary (fig. 4). *M. primitius*

is widespread in the northern part of the western Cordillera (Orchard, 1983, 1991b, c; B.R. Wardlaw and A.G. Harris, U.S. Geological Survey unpub. collns.) and the Tethyan region; the holotype is from western Nevada (Mosher, 1970). *M. samueli* and *E. quadrata* also are known from the northwestern part of the Canadian Cordillera (Orchard, 1991b, c). *E. quadrata* is not known to cooccur with any of the three conodont species with which it cooccurs in the Lead Creek drill core.

The occurrence of *Metapolygnathus nodosus*, *M. samueli*, *M. primitius*, and *Epigondolella quadrata* in the Lead Creek drill core is explainable in several ways (fig. 4): (1) The cored interval is a condensed section (that is, sediment was very slowly and (or) intermittently deposited) that includes part or all of the overlapping range of *M. nodosus* with *M. samueli* and *M. primitius*, as well as part or all of the range of *E. quadrata*; (2) Upper *M. nodosus* Zone and Lower and (or) lower Upper *M. primitius* Zone conodont-bearing deposits were redeposited during the *E. quadrata* Zone, in which case the cored interval would be of *E. quadrata* Zone age; or (3) all the conodont species were redeposited after the *E. quadrata* Zone, and so the cored interval could be considered only no older than the *E. quadrata* Zone (no older than very early Norian). Given the dominance of specimens of *E. quadrata*, the older species were more likely redeposited during the *E. quadrata* Zone.

Locality 2

Another late Carnian or early Norian conodont locality lies 11 km southeast of the Lead Creek site (loc. 2, fig. 3; table 1; Foster and others, 1994, p. 231) and within the greenstone unit of the Seventymile terrane. This locality yielded *Metapolygnathus primitius* (T.R. Carr, written commun. to H.L. Foster, U.S. Geological Survey, 1985), a latest Carnian and earliest Norian species that is only slightly older than the youngest conodont (*Epigondolella quadrata*) from the Lead Creek core (fig. 4).

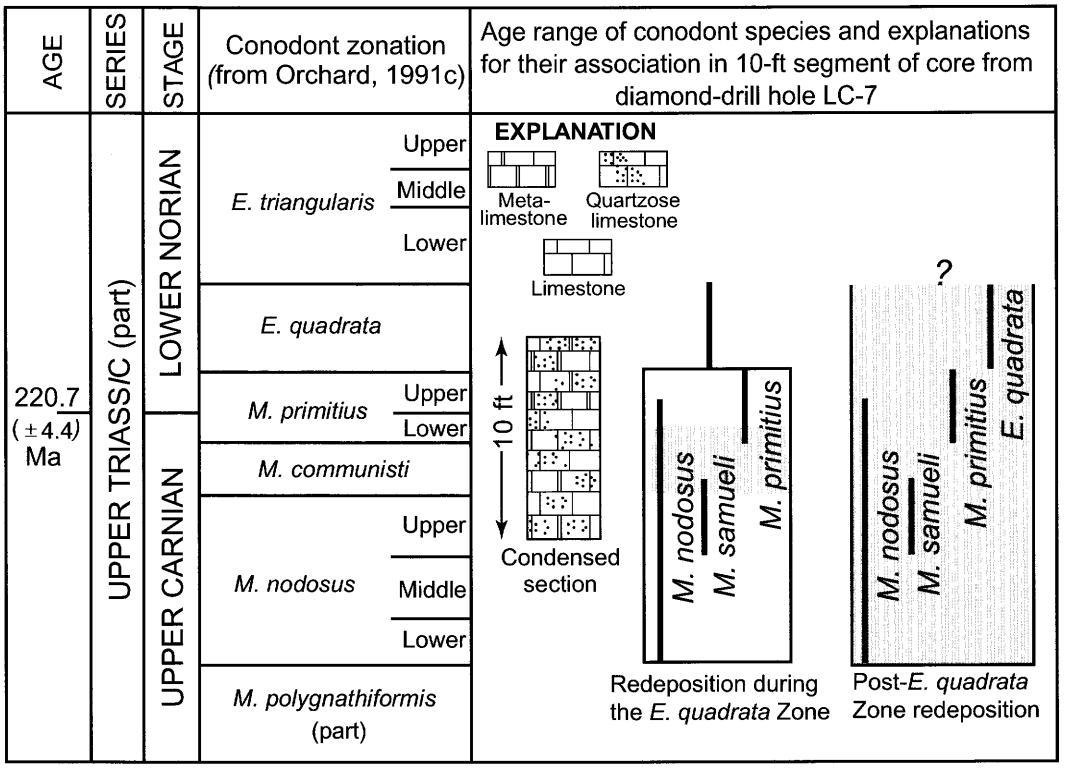

Figure 4. Age range of conodonts from core drilled by WGM, Inc., on the Lead Creek property of Doyon Ltd. (loc. 1, fig. 3; table 1). Conodont data are explainable in several ways; three interpretations are shown here. Condensed section: Very slow to intermittent deposition from the Upper *Metapolygnathus nodosus* Zone into the *Epigondolella quadrata* Zone so that at least part of the range of all four species is represented. Redeposition during the *E. quadrata* Zone: Conodonts from deposits of at least *M. communisti* Zone into Lower *M. primitius* Zone age are redeposited during the *E. quadrata* Zone (gray band shows minimum interval of overlap of *M. nodosus, M. samueli,* and *M. primitius*). Post-*E. quadrata* Zone redeposition: All species are redeposited so that age of core interval can be no older than the *E. quadrata* Zone. Several other interpretations are possible, including a structural discontinuity. Isotopic age for Carnian-Norian boundary from Gradstein and others (1995).

Table 1. Data for fossil localities shown in figures 2 and 3.

[CAI, color-alteration index of Epstein and others (1977) and Rejebian and others (1987)]

Fossil locality	Terrane assignment, map unit, and sample lithology	Fauna	Age	Remarks
1 (fig. 3), Eagle C–1 quadrangle, lat 64°31′09″ N., long 141°25′42″ W.	Seventymile terrane. Unit Pq of Foster (1976); quartzite and argillite that includes unmetamorphosed to slightly metamorphosed phyllite, metaconglomerate, chert, limestone and (or) marble, and graywacke to metagraywacke. Core consists of gray and black carbonaceous, quartzose limestone that is locally recrystallized and has poorly developed stylolites, as well as minor white calcite veins, rare quartz veins as much as 1.3 cm in diameter, and scattered pyrite. From WGM, Inc.'s, drilling of Doyon Ltd.'s Lead Creek property, diamond-drill hole LC–7; core split vertically from 731.6 to 741.1 ft below the surface.	Conodonts: 75 chiefly juvenile, subadult, and a few adult Pa elements *Epigondolella quadrata* Orchard (pl. 1, figs. 1–15) Indigenous and (or) redeposited conodonts: 73 epigondolellid and (or) metapolygnathid Pa element fragments 1 xaniognathiform Pb element Redeposited(?) conodonts of late Carnian and very earliest Norian age (see pl. 1 for age range of redeposited? species): 1 Pa element *Metapolygnathus nodosus* (Hayashi) 2 Pa elements *M. primitius* (Mosher) (pl, 1, figs. 16, 17) 1 Pa element *M. samueli* Orchard CAI=5, indicating that host rock reached at least 300°C. Collected by WGM, Inc., geologists and submitted by C. Dusel-Bacon; identified by A.G. Harris. USGS colln. Mes. 35008	No older than *E. quadrata* Zone (no older than early early Norian, exclusive of Upper *M. primitius* Zone); see figure 4 for late Carnian and early Norian conodont zonation.	9.8 kg of rock was processed; 3.42 kg did not break down. Heavy-mineral concentrate: chiefly rhombohedral dolomite, euhedral pyrite, carbonaceous flakes, quartz, minor composite ferruginous flakes, conodonts, phosphatized sponge fragments, and rare well-rounded zircons.
2 (fig. 3), Eagle B–1 quadrangle, lat 64°28′40″ N., long 141°14′35″ W. Outcrop at mile 130.5 along the Taylor Highway.	Seventymile terrane. Unit PzPq of Foster (1976); mainly greenstone but includes chert, phyllite, and quartzite. Conodonts are from carbonate within unit.	Conodonts: *Metapolygnathus primitius* (Mosher) Collected by Arco Oil and Gas Co. geologists and identified by T.R. Carr (written commun., 1985).	*M. primitius* Zone (latest Carnian and earliest Norian); see figure 4 for conodont zonation and age range of *M. primitius*.	---
3, Eagle C–1 quadrangle, lat 64°40′30″ N., long 141°02′30″ W.	Quartz-chlorite-muscovite schist unit of the Yukon-Tanana terrane (Nisutlin assemblage of Hansen and Dusel-Bacon, 1998). Unit PzPq of Foster (1976); quartz-mica schist and greenschist but also includes quartzite, marble, quartz phyllite, and greenstone.	Poorly preserved conodonts of late Paleozoic age Collected by Arco Oil and Gas Co. geologists and identified by T.R. Carr (oral commun., 1985).	Late Paleozoic, possibly Mississippian.	---
4, Eagle A–2 quadrangle, lat 64°07′00″ N., long 141°46′15″ W.	Chicken Metamorphic Complex (Werdon and others, 2001) of uncertain origin. Collected near confluence of Napoleon Creek and the South Fork of the Fortymile River. Sample is from metalimestone interlayered with greenstone.	Poorly preserved conodonts of late Paleozoic age Collected by Arco Oil and Gas Co. geologists and identified by T.R. Carr (oral commun., USGS,1985).	Late Paleozoic, possibly Mississippian.	---
5, Eagle B–2 quadrangle, lat 64°24′52″ N., long 141°46′59″ W.	Fortymile River assemblage of the Yukon-Tanana terrane (Dusel-Bacon and others, 2002). Outcrop of alternating quartzose and metacarbonate layers; collection from several metacarbonate layers through 1 m of section. Sample is from a large marble body within amphibolite-facies unit characterized by biotite gneiss and amphibolite.	Conodonts: 8 incomplete recrystallized Pa elements of *Cavusgnathus* sp. or *Adetognathus* sp. (1 specimen retains a small remnant of a right-margin free blade) 14 indeterminate fragments CAI=6.5–8, indicating that host rock reached at least 450°C. Collected by C. Dusel-Bacon and identified by A.G. Harris. Field No. 96ADb60b; USGS colln. 33342–PC	Late Meramecian to early Sakmarian (Late Mississippian to early Early Permian).	The predominance of representatives of the family Cavusgnathidae suggests a warm, possibly intermittently restricted, shallow-water depositional setting. 7.4 kg of rock was processed; 0.8 kg did not break down. Heavy-mineral concentrate: chiefly ferruginous composite partly carbonaceous muscovite grains.

Table 1. Data for fossil localities shown on figures 2 and 3—Continued

Fossil locality	Terrane assignment, map unit, and sample lithology	Fauna	Age	Remarks
6, Eagle D–3 quadrangle, lat 64°56′20″ N., long 142°09′ W.	Seventymile terrane. Unit Pq of Foster (1976); outcrop and subcrop of unmetamorphosed calcareous siltstone associated with brachiopod-bearing calcareous siltstone; in fault slice between amphibolite-facies metamorphic rocks on the north and an igneous dike on the south.	Fusulinids: *Parafusulina*? sp. A of Stevens, 1995 Collected by F. Cole and R. Flanders and identified by C.H. Stevens (San Jose State University). Field No. 82AFr103 San Jose State Museum of Paleontology Nos. 4, 5, and 8	Wordian (middle Guadalupian; middle Middle Permian).	According to Stevens (1995), the closest known occurrence of giant fusulinids in western North America, is in the Slide Mountain terrane, northern British Columbia, Canada, and is on strike with the Alaskan locality, suggesting that the two terranes are closely related.
7a, Eagle D–3 quadrangle, lat 64°55′45″ N., long 142°04′33″ W.	Seventymile terrane. Unit Pq of Foster (1976); outcrops of unmetamorphosed brachiopod-bearing calcareous, fine-grained quartzitic sandstone and siltstone in fault slice between amphibolite-facies metamorphic rocks on the north and an igneous dike on the south.	Brachiopods: *Anemonaria* sp. *Megousia* sp. *Neospirifer* sp. *Spiriferella* sp. *Tityrophora*? sp. *Yakovlevia* sp. Punctate spiriferoid, indeterminate Collected by H.L. Foster in 1972 and identified by J.T. Dutro, Jr. Field No. 72AFr445; USGS colln. 24951–PC	Permian----------	J.T. Dutro, Jr., USGS (written commun. 1973), suggested correlation of these beds with the basal sandstone unit of the Tahkandit Limestone at the type section. We believe that the brachiopods are likely the same age as the fusulinids (middle Guadalupian), as the beds can be walked into the fusulinid locality and share the same lithology (see Stevens, 1995).
7b, Eagle D–3 quadrangle, lat 64°55′45″ N., long 142°04′31″ W.	Seventymile terrane(?). Unit Pq of Foster (1976); rubble interval of unmetamorphosed gray, fine-grained quartzite, about 60 m wide; in fault slice between amphibolite-facies metamorphic rocks on the north and an igneous dike on the south.	Brachiopods and one pelecypod: *Anemonaria*? sp. *Megousia* sp. *Neospirifer* sp. *Spiriferella* sp. *Thamnosia*? sp. *Waagenoconcha*? sp. Orthotetid indeterminate Pectinid pelecypod fragment Collected by H.L. Foster in 1973 and identified by J.T. Dutro, Jr. Field No. 73AFr112; USGS colln. 23598–PC	Permian----------	See remarks, loc. 7a.
7c, Eagle D–3 quadrangle, lat 64°55′46″ N., long 142°06′40″ W.	Seventymile terrane. Unit Pq of Foster (1976); about 1.5 km west of locality 7a and likely the same bed.	Brachiopods: *Chonetinella*? sp. *Neospirifer*? sp. *Spiriferella* sp. *Yakovlevia* sp. Productoid, indeterminate Punctate spiriferoid, indeterminate Collected by H.L Foster in 1973 and identified by J.T. Dutro, Jr. Field No. 73AFr122B; USGS colln. 23599–PC	Permian----------	See remarks for locality 7a.
8a, Big Delta D–1 quadrangle, lat 64°54′28″ N., long 144°15′10″ W.	Seventymile terrane. From red chert associated with green and gray chert. Chert is interlayered with basaltic greenstone that, in turn, is associated with serpentized ultramafic rocks (Foster and others, 1978). Sedimentary rocks are associated with the peridotite of Salcha River (Foster and others, 1994).	Conodonts: juvenile Pa elements *Mesogondolella* sp. of Sakmarian–Guadalupian morphotype *Streptognathodus* sp. xaniognathiform element Collected by T.E.C. Keith in 1975 and identified by B.R. Wardlaw (Foster and others, 1978) Radiolarians: *Paronaella* sp. forms with complete outer margins connecting the three primary arms unnamed morphotypes related to late stages of the family Albaillellidea unnamed elongate ladderlike specimens with large reticulate pores Collected by T.E.C. Keith in 1975 and identified by D.L. Jones, USGS (Foster and others, 1978) Field No. 75AFr3295	Radiolarians indicate a Late Pennsylvanian to Middle Permian age; the conodonts restrict the age to Sakmarian–early Artinskian (middle Early Permian; see fig. 6).	---

Table 1. Data for fossil localities shown on figures 2 and 3—Continued

Fossil locality	Terrane assignment, map unit, and sample lithology	Fauna	Age	Remarks
8b, Big Delta D–1 quadrangle, lat 64°54′29″ N., long 144°15′08″ W.	Seventymile terrane. Same description as for locality 8a.	Conodonts: 1 juvenile Pa element *Mesogondolella* sp. Collected by T.E.C. Keith, USGS, in 1975 and identified by B.R. Wardlaw (oral commun., 2002). Field No. 77AFr3189; USGS colln. 33657–PC Radiolarians: *Paronaella*? cf. *P.*? sp. A of Murchey, 1990 (rare) *Pseudoalbaillella* u-forma Holdsworth and Jones, 1980 [type specimens—this sample], morphotype 1 of Ishiga (abundant) *Pseudoalbaillella levitoflexa* (Nazarov) Isakova and Nazarov, 1986 (few) *Pseudoalbaillella* sp. aff. *P. levitoflexa* (shorter abdomen) (abundant) *Pseudoalbaillella* sp. aff. *P. bulbosa* Ishiga (few) *Pseudoalbaillella* sp. aff. *P. scalprata* Holdsworth and Jones, 1980 (rare) *Triactofenestrella* sp., morphotype group 2 of Murchey (abundant) Collected by T.E.C. Keith in 1977 and identified by B.L. Murchey (written commun., 2002) Field No. 77AFr3189; MR0349	Radiolarians indicate a Late Pennsylvanian or early Early Permian (Asselian or Sakmarian) age; the single conodont indicates a Permian age, thereby restricting the age of the collection to the Asselian or Sakmarian.	The conodonts from nearby locality 8a occur with similar radiolarians, suggesting that the two collections may be of the same age (Sakmarian or early Artinskian).
9, Charley River A–4 quadrangle, lat 65°02′21″ N., long 142°33′20″ W.	Seventymile terrane(?). Greenstone unit gs of Brabb and Churkin (1969); Foster and Keith (1987) remapped the area near this sample and placed it in a greenstone unit that they include in the Seventymile terrane. Sample from metalimestone layers in 2-m-thick interval of interbedded metalimestone and metasandstone in 15-m-high cliff.	Conodonts: 4 robust bar fragments 4 possible conodont bar fragments CAI=5, indicating that host rock reached at least 300°C Collected by C. Dusel-Bacon and identified by A.G. Harris Field No. 96ADb58a	Silurian to Early Triassic, possibly late Paleozoic, given the local geologic framework.	Four of these poorly preserved apatitic fragments are conodonts; the other four fragments may also be conodonts. 7.9 kg of rock was processed; 3.5 kg did not break down. Heavy-mineral concentrate: chiefly weathered pyrite and carbonaceous flakes with finely disseminated pyrite.
10, Charley River A–5 quadrangle, lat 65°02′04″ N., long 143°10′45″ W.	Seventymile terrane. Northwest part of peridotite of Mount Sorenson of Foster and others (1994); red-and-gray chert overlain by massive greenstone (gabbro and serpentine crop out to south) (Foster and others, 1994).	Radiolarians: *Albaillella* sp. cf. *A. undulata* Deflandre *Albaillella* sp. cf. *A. uncus* Won *Albaillella* spp. 1 pylentonemiid, possibly *Pylentonema* sp. poorly preserved spheroidal spumellarians poorly preserved sponge spicules Collected by H.L. Foster and identified by B.L. Murchey; re-examined by Murchey in 2002 (written commun., 2002) 85AFr82–103 USGS colln. MR 3553	Osagean or younger Mississippian, probably Osagean or Meramecian (late Early–early Late Mississippian).	Albaillellas are common and fairly diverse, though quite poorly preserved.

Late Triassic Conodonts from Other Areas in the Canadian Cordillera and Alaska

Late Carnian and early Norian conodonts are widespread in the Canadian Cordillera (Orchard, 1983, 1991b, c; Poulton and others, 1999) and in Alaska (fig. 5). In Canada, well-exposed, continuous sections of Upper Triassic rocks have been systematically sampled during integrated stratigraphic, sedimentologic, and conodont and ammonoid biostratigraphic studies by specialists (Orchard, 1983, 1991a–c), but not in southeastern and south-central Alaska, where most late Carnian and early Norian conodont samples were collected during regional-scale geologic mapping, resource exploration, and tectonic studies and to date and assess the paleogeographic affinities of terranes and subterranes. Further complicating a geologic interpretation of the samples from southeastern and south-central Alaska is the fact that many of them were collected within and adjacent to the Denali Fault system.

Foster and others (1994) noted that some of the weakly metamorphosed sedimentary rocks at the *Metapolygnathus primitius* locality (loc. 2, fig. 3; table 1) are similar to those described by Abbott (1982) at the Clinton Creek open-pit asbestos mine 25 km east-southeast in the Yukon Territory, Canada (fig. 3). A conodont collection from beds above the ore body in the main pit at Clinton Creek yielded *Metapolygnathus*? sp. indicating a Carnian to very earliest Norian age (loc. A1, fig. 3; table 2). Another collection about 5 km farther southeast yielded Late Triassic *Neogondolella* sp. (loc. A2, fig. 3; table 2).

Farther southeast in the Yukon Territory, Canada (area B, fig. 5; table 2), in rocks northeast of the Tintina Fault that are part of ancestral North America, at least three conodont collections in the vicinity of Chert Mountain contain *Metapolygnathus* sp. of late Carnian to very earliest Norian age. Farther south near the Alaska Highway bridge over the White River (area C, fig. 5; table 2), and south of the Denali Fault, several conodont samples from the Wrangellia terrane yielded *Epigondolella triangularis* of late early Norian age.

In south-central Alaska, at least 20 conodont collections have been dated as late Carnian, early Norian, and Norian from the Healy, Mount McKinley, and Talkeetna quadrangles (area D, fig. 5; table 2). Of these collections, 14 are restricted to the *Metapolygnathus communisti* and (or) *M. primitius* Zones, and the rest are long ranging within the late Carnian or Norian. *M. communisti*, *M. primitius*, and *Neogondolella* spp. are the most common conodonts in the collections, although metapolygnathids generally do not cooccur with neogondolellids; most of the collections are restricted to the very late Carnian and (or) earliest Norian (*M. communisti* through *M. primitius* Zones). At least 15 of the collections are from an intensely deformed, thick (>1,000 m) sequence of generally thin bedded, carbonaceous and calcareous marine sedimentary rocks of Late Triassic age (unit Trcs of Csejtey and others, 1992) exposed in a series of fault slices of the Denali Fault system for at least 300 km along the Alaska Range. Csejtey and others considered this unit to be part of the Yukon-Tanana terrane. Most of the conodonts are from carbonate to silty carbonate lenses or layers interpreted as

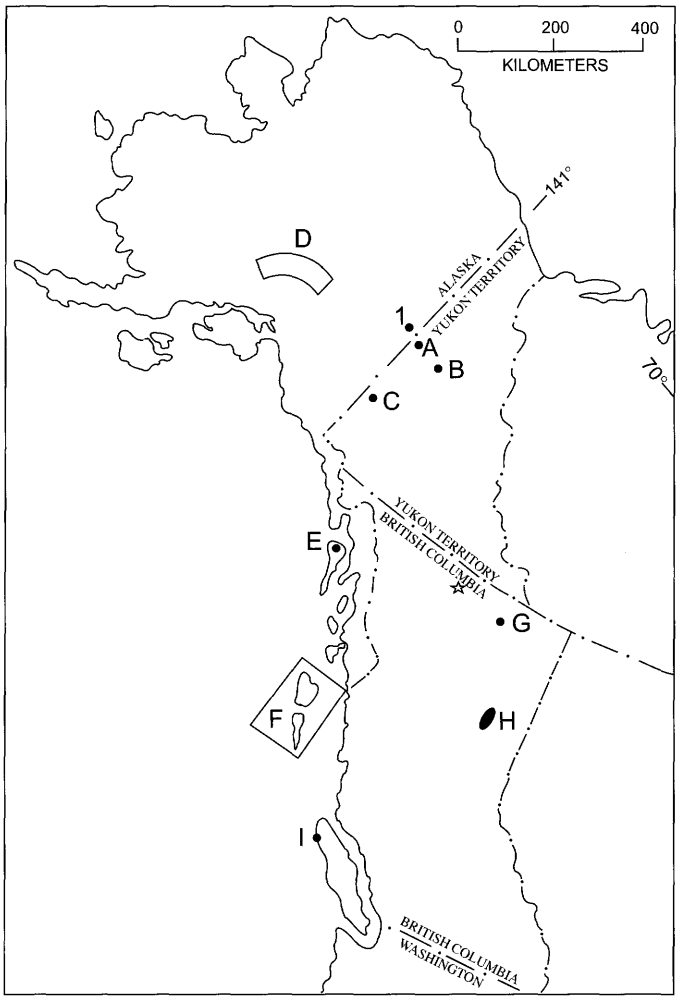

Figure 5. Sketch map of the Pacific Northwest, showing areas of selected sample localities for late Carnian and (or) early Norian conodont faunas (Lower *nodosus* through *triangularis* Zones) in the Canadian Cordillera (from Orchard, 1991c) and southeastern, south-central (table 2), and east-central (table 1) Alaska. Canadian terrane assignments from Orchard (1991a, fig. 1). 1, Seventymile terrane, east-central Alaska (loc. 1, fig. 3; table 1); A, Seventymile terrane, western Yukon Territory, Canada (locs. A1, A2, fig. 3; table 2); B, ancestral North America, western Yukon Territory (area B, table 2); C, Wrangellia terrane, western Yukon Territory (area C, table 2); D, Yukon-Tanana terrane, south-central Alaska, along the Denali Fault system, (area D; table 2); E, Alexander terrane, southeastern Alaska, northern Admiralty Island (area E, table 2); F, Wrangellia terrane, Queen Charlotte Islands; G, ancestral North America, northeastern British Columbia, sections at Mount McLearn and about 25 km farther south along the Alaska Highway (Orchard, 1991c); H, ancestral North America, northeastern British Columbia, mainly sections along Peace River, 100 to 150 km west of Fort St. John and a few sections north of the Peace River along a tributary of the Halfway River (Orchard, 1991c); I, Wrangellia terrane, Klaskino Inlet, Vancouver Island. Star, Middle Permian giant parafusulinid sample locality from the Sylvester Allochthon in northern British Columbia, which is the nearest giant parafusulinid sample locality to that in the Seventymile terrane (loc. 6, fig. 2; table 1).

Table 2. Data for Triassic conodont localities A through E referred to in text but not listed in table 1.

[See figure 5 for locations. Most collections in area D from Csejtey and others (1992) were reexamined in 1995 and, where necessary, revised by A.G. Harris and B.R. Wardlaw. Conodont zonation for the late Carnian and early Norian is shown in figure 4]

Sample locality or area	Terrane assignment, lithologic unit, and age	Source
Area A		
Locality A1 (also shown in fig. 3) lat 64°26′41″ N., long 140°43′38″ W. Above ore body, southwest end of main pit, Clinton Creek deposit.	Seventymile terrane Late Triassic, probably Carnian	Poulton and others (1999) GSC loc. C–102345, M.J. Orchard (written commun., 2002).
Locality A2 (also shown in fig. 3) Yukon Territory lat 64°24′59″ N., long 140°38′08″ W. On road to the Clinton Creek open-pit asbestos mine, 1 km northwest of Township turnoff.	Seventymile terrane Late Triassic	Poulton and others (1999) GSC loc. C–102265, M.J. Orchard (written commun., 2002).
Area B Yukon Territory lat 64°23′45″ N., long 138°52′00″ W. About 1,500 m northeast of Chert Mountain.	Ancestral North America Late Carnian to earliest Norian	Poulton and others (1999) GSC locs. C–150066, C–150068, and C–150069.
Area C Yukon Territory All in vicinity of the Alaska Highway bridge over the White River	Wrangellia terrane	Poulton and others (1999).
lat 61°59′24″ N., long 140°36′54″ W.	*Epigondolella triangularis* Zone, late early Norian; Nikolai Greenstone	GSC loc. C–210045.
lat 61°57′57″ N., long 140°45′18″ W.	*E. triangularis* Zone, late early Norian; Chitistone Limestone	GSC loc. C–210048.
lat 61°58′16″ N., long 140°38′56″ W.	*E. triangularis* Zone, late early Norian; Chitistone Limestone	GSC loc. C–210056.
Area D South-central Alaska	All from the Yukon-Tanana terrane and unit Ꝛcs of Csejtey and others (1992) unless otherwise noted.	
Mount McKinley D–1 quadrangle lat 63°57′50″ N., long 150°17′20″ W.	Late Carnian	Collected by A.B. Till, USGS; identified by A.G. Harris; USGS colln. Mes. 33374.
Talkeetna C–6 quadrangle lat 62°44′12″ N., long 152°58′ W.	Lower part Upper *Metapolygnathus primitius* Zone, very earliest Norian	Collected by N.J. Silberling, identified by A.G. Harris; USGS colln. Mes. 33378.
Talkeetna C–6 quadrangle lat 62°44′58″ N., long 152°51′24″ W.	Late Carnian	Collected by N.J. Silberling, identified by A.G. Harris; USGS colln. Mes. 33379.
Talkeetna D–4 quadrangle lat 62°59′42″ N., long 151°56′40″ W.	Lower part Upper *M. primitius* Zone, very earliest Norian	Collected by N.J. Silberling, identified by A.G. Harris; USGS colln. Mes. 33381.
Healy C–6 quadrangle lat 63°40′07″ N., long 149°36′25″ W.	*M. communisti* Zone into lower part of Upper *M. primitius* Zone, very late Carnian–very earliest Norian	Fossil loc. 73, Csejtey and others (1992).
Healy C–5 quadrangle lat 63°40′12″ N., long 149°08′12″ W.	*M. primitius* Zone, latest Carnian–earliest Norian	Fossil loc. 74, Csejtey and others (1992).
Healy C–5 quadrangle lat 63°37′45″ N., long 149°06′55″ W.	*M. communisti* Zone into lower part of Upper *M. primitius* Zone, very late Carnian–very earliest Norian	Fossil loc. 75, Csejtey and others (1992); USGS colln. Mes. 33382.
Healy C–2 quadrangle lat 63°44′14″ N., long 147°49′14″ W.	*M. primitius* Zone, latest Carnian–earliest Norian	Fossil loc. 82, Csejtey and others (1992).
Healy C–2 quadrangle lat 63°44′46″ N., long 147°38′55″ W.	*M. primitius* Zone, latest Carnian–earliest Norian	Fossil loc. 83, Csejtey and others (1992)
Healy C–2 quadrangle lat 63°44′57″ N., long 147°37′12″ W.	*M. primitius* Zone, latest Carnian–earliest Norian	Fossil loc. 84, Csejtey and others (1992).

Table 2. Data for Triassic conodont localities A through E referred to in text but not listed in table 1—Continued

Sample locality or area	Terrane assignment, lithologic unit, and age	Source
Area D (continued) South-central Alaska	All from the Yukon-Tanana terrane and unit Ŧcs of Csejtey and others (1992) unless otherwise noted.	
Healy C–2 quadrangle lat 63°43′47″ N., long 147°36′05″ W.	*M. primitius* Zone, latest Carnian–earliest Norian	Fossil loc. 87, Csejtey and others (1992).
Healy C–3 quadrangle lat 63°32′58″ N., long 148°05′05″ W.	*M. communisti* Zone into lower part Upper *M. primitius* Zone, very late Carnian–very earliest Norian	Fossil loc. 90, Csejtey and others (1992).
Healy C–2 quadrangle lat 63°32′50″ N., long 147°59′10″ W.	*M. primitius* Zone, latest Carnian–earliest Norian	Fossil loc. 91, Csejtey and others (1992).
Healy B–3 quadrangle lat 63°25′07″ N., long 148°06′14″ W.	*M. primitius* Zone, latest Carnian–earliest Norian	Fossil loc. 93, Csejtey and others (1992).
Healy B–3 quadrangle lat 63°25′58″ N., long 148°05′42″ W.	*M. communisti* Zone into lower part of Upper *M. primitius* Zone, very late Carnian–very earliest Norian	Fossil loc. 94, Csejtey and others (1992).
Healy A–6 quadrangle lat 63°00′16″ N., long 149°57′18″ W.	Chulitna terrane (Silberling and others, 1994) *M. primitius* Zone, latest Carnian–earliest Norian; unit JŦrs of Csejtey and others (1992)	Fossil loc. 154, Blodgett and Clautice (2000).
Area E Southeastern Alaska Northern Admiralty Island; all in the Juneau A–2 quadrangle	All collections from the Admiralty subterrane of the Alexander terrane (Monger and Berg, 1987); all collections from the Hyd Formation.	
lat 58°03′35″ N., long 134°34′03″ W.	*M. nodosus* Zone through Upper *M. primitius* Zone, late Carnian–earliest Norian	Collected by C.D. Taylor, identified by A.G. Harris; USGS colln. Mes. 35023.
lat 58°04′47″ N., long 134°36′53″ W.	Upper *M. primitius* Zone, earliest Norian	Collected by J.M. Proffett, identified by A.G. Harris; USGS colln. Mes. 35018.
lat 58°05′23″ N., long 134°42′04″ W.	*M. nodosus* Zone into lower part of Upper *M. primitius* Zone, late Carnian–very earliest Norian	Collected by N.A. Duke, identified by A.G. Harris; USGS colln. Mes. 35050.
lat 58°07′56″ N., long 134°41′26″ W.	*M. nodosus* Zone through Upper *M. primitius* Zone, late Carnian–earliest Norian	Same as previous sample; USGS colln. Mes. 35051.

distal calciturbidites that are intercalated with hemipelagic and pelagic layers. The metamorphic grade and deformational history of these rocks vary from slice to slice.

On northern Admiralty Island, southeastern Alaska (area E, fig. 5; table 2), samples of slightly to moderately metamorphosed black calcareous argillite and carbonate rocks of the Hyd Formation, included in the Admiralty subterrane of the Alexander terrane, yielded conodont collections containing *Metapolygnathus primitius* with and without *M. nodosus*. These collections position part of the Hyd Formation in the Lower *M. primitius* Zone to the lower part of the Upper *M. primitius* Zone, or in the Lower and Upper *M. primitius* Zones (see fig. 4 for conodont zonation). Another collection from the same area yielded abundant *Neogondolella navicula* (Huckriede) and a few specimens of *M. primitius*, indicating the Upper *M. primitius* Zone of very earliest Norian age. Farther south, in the Queen Charlotte Islands, British Columbia, Canada (area F, fig. 5; table 2), conodonts from the Kunga Group of Cameron and Tipper (1985) have produced a relatively complete late Carnian and early Norian record from 11 key sections stretching the length of the islands (Orchard, 1991c) that have enabled refinement of late Carnian and early Norian conodont biostratigraphy. The biostratigraphy and taxonomy applied to conodonts from rocks of late Carnian and early Norian age across Alaska are derived from the conodont successions of the Queen Charlotte Islands, northeastern British Columbia, and northern Vancouver Island (areas F–I, fig. 5; Orchard, 1991b, c).

Late Paleozoic Conodonts in East-Central Alaska

Localities 3 and 4

Conodonts of late Paleozoic age were recovered from marble in unit Pzq of Foster (1976) in the Eagle quadrangle: at one locality from the quartz-chlorite-muscovite±calcite schist, micaceous quartzite, and marble unit of the Nisutlin assemblage, Yukon-Tanana terrane (loc. 3, fig. 3; table 1), and at the other locality from the greenschist-facies Chicken Metamorphic Complex of Werdon and others (2001) of uncertain origin (loc. 4, fig. 3; table 1). Both collections contain poorly preserved late Paleozoic, possibly Mississippian conodonts (T.R. Carr, formerly ARCO Oil and Gas Co., oral commun. to H.L. Foster, 1985).

Locality 5

An outcrop of interlayered metacarbonate and quartzose rocks, about 1 m thick, in the Eagle B–2 quadrangle (loc. 5, fig. 3; table 1) yielded poorly preserved recrystallized conodonts. The collection is from a large (8 by 15 km) marble body within an amphibolite-facies unit characterized by biotite gneiss and amphibolite that was included in the Y4 subterrane of the Yukon-Tanana terrane by Foster and others (1994); this unit is here considered part of the Fortymile River assemblage of the Yukon-Tanana terrane. Although all the conodonts in this collection are incomplete, enough features are preserved to identify some as *Cavusgnathus* sp. or *Adetognathus* sp., of combined late Meramecian to Sakmarian age (early Late Mississippian to early Early Permian). These and other genera of the family Cavusgnathidae are characteristic of warm, shallow-water environments, particularly when they are the only conodonts in a collection. Cavusgnathids and adetognathids are a major component of the shallow-water facies of the Mississippian and Pennsylvanian part of the Lisburne Group of the Brooks Range and subsurface North Slope (for example, Krumhardt and others, 1996; Harris and others, 1997).

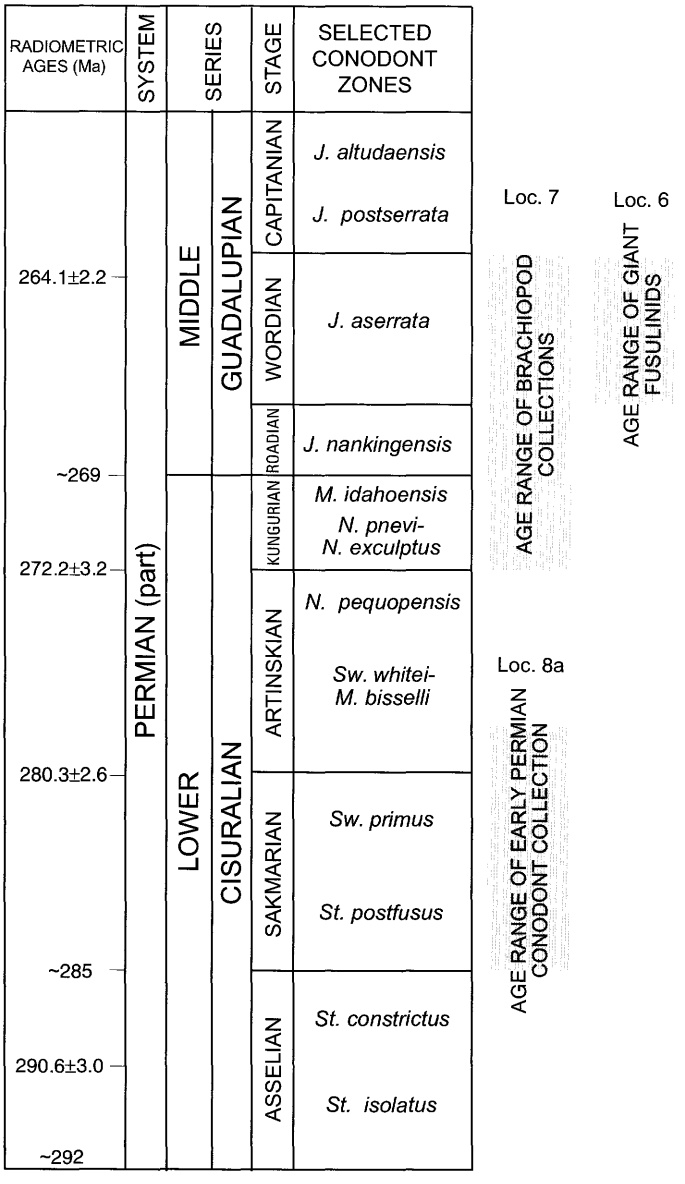

Figure 6. Selected conodont zones for the Early and Middle Permian, showing age ranges of Permian collections from sample localities 6 through 8 (fig. 2; table 1). Radiometric ages and selected conodont zones from Jin and others (1997). Conodont genera: *J., Jinogondolella; M., Mesogondolella; N., Neostreptognathodus; St., Streptognathodus; Sw., Sweetognathus.*

Localities 8a and 8b

Two conodont samples from the Seventymile terrane in the Big Delta D–1 quadrangle (loc. 8, fig. 2; locs. 8a, 8b, table 1) yielded conodonts of Permian age. Red chert from locality 8a was collected for radiolarians but also yielded a few conodonts. The radiolarians are Late Pennsylvanian to Middle Permian; the conodonts restrict the age to middle Early Permian (Sakmarian and early Artinskian; fig. 6). A re-collection of red chert in the same vicinity (loc. 8b) yielded only one poorly preserved *Mesogondolella* sp. of Permian age. Radiolarians from this sample indicate a Late Pennsylvanian or early Early Permian (Asselian and Sakmarian) age (loc. 8b, table 1). Thus, taken together, the collection is restricted to the Asselian and Sakmarian. On the basis of conodonts from locality 8a and radiolarians from locality 8b, both samples could be of the same or nearly the same age—Sakmarian and early Artinskian (fig. 6).

Locality 9

An outcrop of interlayered slightly metamorphosed carbonate and clastic rocks within a greenstone unit (loc. 9, fig. 2; table 1) included in the Seventymile terrane by Foster and Keith (1987) yielded several conodont fragments that merely provide a generalized age of Silurian to Early Triassic. The sample was collected from the northern margin of the peridotite of Mount Sorensen (Foster and others, 1994). The local geologic framework favors a late Paleozoic age.

Fusulinids (Loc. 6)

Giant parafusulinid foraminifers (loc. 6, fig. 2; table 1) were discovered in a sliver of unmetamorphosed(?) to slightly metamorphosed quartzose sedimentary rocks (unit Pq of Foster, 1976) that occur as a fault slice adjacent to a southern splay of the Tintina Fault in the northernmost-central part of the Eagle quadrangle (Stevens, 1995). The fault slice (too small to be shown in fig. 2) lies between amphibolite-facies rocks on the north and a felsic dike on the south (Foster, 1976). Foster (1992) assigned these rocks to the Seventymile terrane. In his report on giant parafusulinid foraminifers from the Seventymile terrane in the Eagle quadrangle, Stevens took the opportunity to summarize all occurrences and illustrate

together many of the species of this western North American group. Giant parafusulinids (species >2 cm long) are restricted to middle Guadalupian (Wordian; middle Middle Permian) rocks of western North America, where they are known from eight areas that extend from Mexico to Alaska: three southern areas in Coahuila and Sonora Provinces, northern Mexico, and West Texas; three central areas that have been referred to the McCloud belt arc in northern California, Washington, and southern British Columbia, Canada; and two northernmost areas within the Sylvester Allochthon in northern British Columbia and in the Seventymile terrane of east-central Alaska. Stevens divided the 15 North American species of giant fusulinids into two major groups on the basis of internal features that appear to be geographically limited. He retained one group in the genus *Parafusulina*, species of which occur only in Coahuila Province, Mexico, and in West Texas, and conditionally designated the other group *Parafusulina*?, which occurs in all eight areas except Coahuila Province. *Parafusulina*? is virtually restricted to the allochthonous tectonostratigraphic terranes of the western Cordillera, except West Texas, which was part of ancestral North America. The occurrence of giant parafusulinids representative of both geographic groups in West Texas is evidence of some faunal exchange between ancestral North America and more outboard areas during the Middle Permian.

According to C.H. Stevens (oral commun., 2002), parafusulinids occur mostly in limestone, silty sandy limestone, and limy siltstone (their host in the Seventymile terrane); some localities have associated brachiopods. The host rock, associated biota, and local and regional stratigraphic relations indicate that the giant parafusulinids lived in the shallow waters of tropical to at least subtropical North America and relatively nearby outboard islands and near-surface submarine edifices. The outboard-island occurrences were subsequently dislocated to higher latitudes along the margins of western North America. The giant parafusulinids of the Seventymile terrane appear to be the farthest traveled. The giant-parafusulinid locality in the Sylvester Allochthon of northern British Columbia, Canada, lies about 500 km southeast of that in the Seventymile terrane (star, fig. 5; compare with loc. 6, fig. 2).

Radiolarians

Three radiolarian collections of late Paleozoic age are known from the Seventymile terrane. Two of these collections are from red chert associated with green-and-gray chert interlayered with basaltic greenstone that, in turn, occurs with the peridotite of Salcha River (Foster and others, 1994) in the northeastern part of the Big Delta quadrangle (Foster and others, 1978). The two samples were collected near one another at different times (loc. 8, fig. 2; locs. 8a, 8b, table 1). Both samples yielded radiolarians, as well as a few conodonts. The sample collected in 1975 (loc. 8a, table 1) was described by Foster and others (1978) in generalized taxonomic terms. The other sample (loc. 8b), collected in 1977, contains much the same radiolarians (B.L. Murchey, written commun., 2002), including several specimens of *Pseudoalbaillella* sp., subordinate *Triactofenestrella* sp., and rare *Paronaella*? cf. *P.*? sp. A of Murchey (1990), indicating a Late Pennsylvanian or early Early Permian age. The associated conodonts in both collections restrict that age to Sakmarian to early Artinskian (middle Early Permian, fig. 6). According to B.L. Murchey (written commun., 2002), the radiolarians in these two collections are generally found in argillaceous and cherty facies that were deposited along the margin (outer slope) of late Paleozoic North America. Because the faunas are fairly diverse, the radiolarian-bearing chert might have formed between very proximal facies dominated by such forms as *Triactofenestrella* and *Paronaella*? cf. *P.*? sp. A of Murchey (1990) (wagonwheel or discoidal forms, possibly with photosynthetic symbionts) and typical distal ribbon-chert faunas dominated by such elongate forms as *Pseudoalbaillella*. The radiolarian faunas from the Big Delta quadrangle are similar to those of the Havallah Formation in Nevada, which likely formed in a backarc basin.

The third radiolarian collection is from red-and-gray chert overlain by massive greenstone in the Seventymile terrane, southeastern Charley River quadrangle (loc. 10, fig. 2; table 1). The fauna is poorly preserved, consisting mainly of *Albaillella*, spheroidal spumellarians, and sponge spicules. B.L. Murchey, who reexamined the collection in 2002, agreed with her original faunal list and age assignment to the Osagean or younger Mississippian, probably Osagean or Meramecian (late early or early late Mississippian).

Megafossils

Brachiopods (Locs. 7a–7c)

Exposures of unmetamorphosed brachiopod-bearing calcareous siltstone and fine-grained quartzite were discovered in a fault slice just south of the main part of the Tintina Fault system during geologic mapping of the Eagle quadrangle (Foster, 1976) (loc. 7, fig. 2; locs. 7a–7c, table 1), in the same fault slice from which the giant fusulinids were subsequently collected. Three brachiopod collections were made in 1972 and 1973, two of which were nearby and the third 2 km to the west. The brachiopods are preserved as casts and molds. According to J.T. Dutro, Jr. (written communs., 1972, 1973), *Spiriferella* sp. and *Neospirifer* sp. occur in all collections, *Anemonaria* sp., *Megousia* sp. and *Yakovlevia* sp. in two collections, and *Chonetinella*? sp., *Thamnosia*? sp., *Tityrophora*? sp., and *Waagenoconcha*? sp. in one collection each. J.T. Dutro, Jr. (written commun., 1973), identified the collections as Permian and suggested a correlation with the lower sandstone unit of the Tahkandit Limestone north of the Tintina Fault in the southeastern Charley River quadrangle, about 30 km north of locality 7. At the type section of the Tahkandit in the southeastern Charley River quadrangle, species of six of the brachiopod genera identified in the Eagle quadrangle rocks—*Megousia*, *Neospirifer*, *Spiriferella*, *Thamnosia*, *Waagenoconcha*, and *Yakovlevia*—occur in the lower sandstone unit and (or) overlying limestone (Brabb and Grant, 1971);

the sandstone unit has not been recognized beyond the type area. Brabb and Grant, who noted that the Permian brachiopod faunas of the Tahkandit show affinities to those in the Canadian Arctic Archipelago and east-central Greenland, suggested a late Leonardian age (Kungurian) for the sandstone unit and an age of late Leonardian to early Guadalupian (Kungurian-early Wordian) for the entire formation (latest Early and early Middle Permian). The suggestion that the brachiopod beds of the Seventymile terrane that lie south of the Tintina Fault system in the Eagle quadrangle are correlative with the lower beds of the Tahkandit on the north side of the Tintina Fault in ancestral North American strata is based on lithologic similarity and generic-level correlation. Most of the brachiopod genera in collections from the Eagle quadrangle are relatively long ranging in the Early and Middle Permian. Some genera were widespread paleogeographically, and some were more common in some areas than elsewhere. For example, *Megousia* has a relatively worldwide distribution, and *Waagenoconcha* is a common Arctic form but also occurs in the Salt Range of Pakistan (B.R. Wardlaw, oral commun., 2002). *Yakovlevia*, *Chonetinella*, and *Thamnosia* are more common in cool- than in warm-water faunas but occur in both (Bamber and Barss, 1969).

Although the correlation of brachiopod faunas from the fault sliver in the northern part of the Eagle quadrangle (locs. 7a–7c, table 1) with those of the Tahkandit Limestone north of the Tintina Fault, as suggested by Brabb and Grant (1971), does explain the similarity of the faunas at a generic level and their geographic proximity, it does not take into account the separation of the localities by a major, long-lived transform fault and the association of the Tahkandit with continental-margin rocks only, whereas the low-grade sedimentary rocks of the fault sliver in the Seventymile terrane are associated with serpentinite (Foster, 1976).

We believe that because of the nearby discovery of giant parafusulinids (Stevens, 1995) in the same belt of rocks which contains the brachiopod localities, the age of the brachiopod beds in the Seventymile terrane is now updated and well constrained. The fusulinid locality is 2.5 km northwest of the westernmost brachiopod collection (locs. 6, 7, fig. 2; locs. 6, 7c, table 1) and could well be within the same stratigraphic interval. The fusulinids were discovered while field-mapping the brachiopod-bearing beds for several kilometers along strike, in blocks and boulders of brachiopod-bearing calcareous siltstone that were dug from beneath a thin layer of tundra (Stevens, 1995). Proximity, lithology, and both geologic and apparent stratigraphic position provide compelling evidence that, like the giant fusulinids, the brachiopod faunas first collected in the early 1970s are of middle Guadalupian (Wordian) age.

Discussion

Our most biostratigraphically diagnostic fossils are from Middle Permian and Late Triassic (late Carnian and early Norian) weakly metamorphosed strata of the Seventymile terrane. The rocks most analogous to ours are those from the Sylvester Allochthon, one of the largest klippen assigned to the Slide Mountain terrane (Gabrielse, 1991), which rests directly on the Cassiar terrane, a displaced sliver of ancestral North America (Harms, 1986; Nelson, 1993) in northern British Columbia, Canada (fig. 1). Both the Seventymile and Slide Mountain terranes contain supracrustal thrust slices of basalt and interbedded black argillite, chert, calcarenite, and quartz/chert sandstone that are structurally interleaved with serpentinized peridotite; the Sylvester Allochthon also contains a slice of igneous rocks of island-arc affinity.

Division I, the structurally lowest fault-bounded slice of the Sylvester Allochthon, consists of deep-water sedimentary rocks and minor basalt-diabase sills and flows; division II contains deep-water sedimentary rocks that are structurally interleaved with panels of ultramafic rocks, gabbro, and amphibolite (Nelson, 1993). Both divisions I and II have yielded conodonts of Early Mississippian to Permian age (Nelson, 1993). The presence of quartz-bearing sedimentary rocks and the continuity of sedimentation associated with basaltic volcanism during the Mississippian, Pennsylvanian, and Permian led Nelson to conclude that division II is an ophiolite characterized by slow spreading and a sedimentation rate higher than that of normal pelagic sequences, owing to the deposition of terrigenous sedimentary rocks. For this reason, Nelson concluded that division II more likely represents a backarc or marginal basin rather than typical midocean floor. Triassic sedimentary rocks occur at the highest level in division II (Nelson, 1993). Division III, the uppermost structural package within the allochthon, contains the Permian giant-fusulinid-bearing limestone (star, fig. 5; Ross, 1969), together with slices of Pennsylvanian and Permian calc-alkaline volcanic and plutonic rocks, chert, and tuff assigned to the Harper Ranch subterrane of Quesnellia. One thrust panel of division III, assigned to the Yukon-Tanana terrane, consists of an Early Mississippian granitoid that intrudes volcanogenic and siliciclastic sedimentary rocks (Nelson, 1993). Nelson proposed a pre-Mesozoic reconstruction of the elements in the Sylvester Allochthon in which a late Paleozoic arc (Harper Ranch subterrane) is built partly on the pericratonic Yukon-Tanana terrane and partly on primitive oceanic basement (division III), which is separated from North America by the Slide Mountain marginal basin (divisions I, II).

A more southerly paleolatitude for the Seventymile and Slide Mountain terranes is suggested not only by the Permian faunas from these related terranes but also by paleomagnetic data from the Sylvester Allochthon in northern and central British Columbia, Canada: an Early Permian paleomagnetic pole from a unit correlative with Pennsylvanian and Permian volcanic rocks of division II restores to the approximate latitude of northern California (Richards and others, 1993). A paleogeographic affinity of division III of the Sylvester Allochthon with lower-latitude North America is also suggested by the presence of a diverse brachiopod and coralline fauna of North American-Uralian affinity in that division, and by the similarity of the giant fusulinids in division III to those in Texas (Nelson, 1993).

Although general agreement exists that the Seventymile-Slide Mountain terrane represents a basin floored by oceanic crust off the western margin of ancestral North America, the original width of the ocean basin is disputed. For example, Nelson (1993) depicted the Slide Mountain ocean as a narrow ocean that is depositionally tied to ancestral North America, whereas other workers have modeled it as a vast Paleozoic Pacific Ocean (Harms and Murchey, 1992; Monger and others, 1991). If the rocks that host the Permian fusulinids and brachiopods in the north-central part of the Eagle quadrangle (loc. 6, fig. 2) are truly quartzites (as opposed to biosiliceous sedimentary rocks, as described by Foster, 1976), proximity to a continental source terrane would be required. That continental source, however, could be either the ancestral continental margin of North America or the rifted continental fragment proposed to have been derived from it (Tempelman-Kluit, 1979); thus, the presence of quartzite does not indicate whether the siliceous sedimentary rocks formed in a marginal sea or at the margin of a major open ocean. In discussing the Klamath terrane farther to the south in northern California, Stevens and others (1990) proposed that the degree of dissimilarity of faunas of the McCloud belt with autochthonous forms requires an extensive deep-water barrier, several thousand kilometers wide, between the eastern Klamath Mountains and ancestral North America, whereas regional geologic considerations led Miller (1987) to suggest a fairly close Permian connection between the McCloud belt and North America.

The dip direction of the subduction zone beneath the oceans represented by the Seventymile and Slide Mountain terranes is also disputed. The Slide Mountain ocean is proposed to have been bordered on the west by an east-dipping subduction zone and related arc (Gabrielse, 1991; Nelson, 1993), whereas the Anvil ocean of Tempelman-Kluit (1979), a likely northern extension of the Slide Mountain ocean, is thought to have been consumed along its western margin by a west-dipping subduction zone (Tempelman-Kluit, 1979; Hansen, 1990; Hansen and Dusel-Bacon, 1998).

Division II of the Sylvester Allochthon is partly overlain by a Triassic siliciclastic sedimentary sequence referred to as the Table Mountain sediments by Nelson (1993). Conodonts from the Table Mountain sediments have yielded Middle(?) and Late Triassic ages (Nelson, 1993). Nelson stated that Table Mountain sediments in the Sylvester Allochthon have parallels with units of similar age and composition in the allochthonous Quesnel terrane to the south, but also within the parautochthonous Cassiar terrane and the continental margin of North America exposed in the Selwyn Basin and the Canadian Rockies. She further concluded that the relatively thin Upper Triassic Table Mountain sediments are the distal, southwesterly end of the clastic wedge of ancestral North America, present in the Rocky Mountains. Thus, according to this hypothesis, the Upper Triassic siliciclastic carbonate strata of Table Mountain represent an overlap sequence that loosely linked North America and the Slide Mountain terrane before imbrication and emplacement of the Sylvester Allochthon onto the continental margin (Nelson, 1993).

Central to the interpretation of the Upper Triassic sedimentary rocks as an overlap assemblage is the assumption that they were originally deposited on the ophiolitic rocks of Slide Mountain and on the ancient North American continental margin. Although both the upper and lower contacts of the Table Mountain sediments are sheared, Nelson (1993) interpreted their original relation to the underlying ophiolitic rocks of division II to be a sheared depositional contact because of the absence of evidence for older-over-younger strata that would indicate a thrust relation. Nelson cited two other areas where the contacts between Triassic units that are lithologically equivalent to the Table Mountain sediments (Slocan Group of Klepacki and Wheeler, 1985, and the Takla Group of Monger and others, 1992) and the underlying Slide Mountain terrane are either an unconformity (Slocan Group) or a remobilized unconformity (Takla Group). Harms (1986, 1989), however, interpreted the sheared contacts between the Table Mountain sediments (her unit 8P) and underlying volcanic and ultramafic rocks of the Slide Mountain terrane as thrust faults. Faults have also been mapped between the Triassic sedimentary rocks, the greenstone and peridotite components of the Seventymile terrane (equivalent to the Slide Mountain terrane), and the continental-margin Nasina assemblage of the Yukon-Tanana terrane near the Clinton Creek mine in the Yukon Territory, just east of the United States-Canadian border (fig. 3; Mortensen, 1988). In the Lead Creek drill hole from which our Late Triassic conodonts were recovered (loc. 1, fig. 3; table 1), a thrust fault separates low-grade metasedimentary rocks of the Seventymile terrane from overlying greenstone of the Seventymile terrane (see Dusel-Bacon, Mortensen, and Fredericksen, this volume), and the surface contact of these two units is also interpreted to be a thrust fault (Foster, 1992). In Alaska, faults are also inferred to separate Triassic low-grade metasedimentary rocks from underlying assemblages of the Yukon-Tanana terrane, although actual contacts cannot be traced with any certainty (Foster, 1992). Foster (1992) inferred a depositional contact between fine-grained Triassic sedimentary rocks and adjacent greenstone where they are exposed along the Taylor Highway (fig. 3) in east-central Alaska.

The uncertainty associated with the original contact between the Upper Triassic rocks and both oceanic rocks of the Seventymile and Slide Mountain terranes and continental-margin rocks of the Yukon-Tanana terrane and ancestral North America also holds for the widely distributed Upper Triassic rocks associated with allochthonous terranes in other areas of the western Cordillera shown in figure 5 (all localities except B, G, and H). Therefore, we view the wide distribution of Late Triassic conodonts in the various allochthonous terranes and in the North American continental margin as an indication that all the various areas shared approximately similar warm, normal-marine conditions along the Late Triassic continental margin, but not that they represent an overlap assemblage in the sense of draping across contacts between outboard allochthonous pericratonic and arc fragments and the ancient Pacific margin.

Although an unambiguous tectonic model of the evolution of oceanic and adjacent crustal elements of the western

Cordillera likely may never be achieved, the discovery of new fossil occurrences plays an important role in identifying elements of the continental margin and placing additional constraints on the tectonic models that will continue to evolve.

Acknowledgments

Melanie Hopkins of the U.S. Geological Survey (USGS) provided invaluable assistance in the office, particularly with illustrations. Charlie Bacon (USGS), Jim Mortensen (University of British Columbia), and Vicki Hansen (Southern Methodist University) participated in east-central Alaskan fieldwork. Discussions with C.M. Henderson (University of Calgary), M.J. Orchard (Geological Survey of Canada), C.H. Stevens (San Jose State University, Calif.), B.R. Wardlaw (USGS), Tekla Harms (Amherst College), and JoAnne Nelson (British Columbia Ministry of Energy, Mines and Petroleum Resources) helped put our data into context. We thank WGM, Inc., geologists Bob Rogers, Holly Morris, and Tom Corbett for providing the first author with the Lead Creek drill core that was to contain such biostratigraphically interesting conodonts, and Greg Sheardown and C.G. ("Riz") Bigelow of Ventures Resource Corp. for permission to publish the conodont data. Careful reviews by Julie Dumoulin (USGS) and Dwight Bradley (USGS) improved the manuscript.

References Cited

Abbott, Grant, 1982, Origin of the Clinton Creek asbestos deposit, *in* Yukon exploration and geology: Whitehorse, Yukon Territory, Canada, Department of Indian and Northern Affairs, Exploration and Geological Services Division, p. 18–25.

Bamber, E.W., and Barss, M.S., 1969, Stratigraphy and palynology of a Permian section, Tahkandik River, Yukon Territory: Geological Survey of Canada Paper 68–18, 39 p.

Blodgett, R.B., and Clautice, K.B., 2000, Fossil locality map for the Healy A–6 quadrangle, south-central Alaska: Alaska Division of Geological and Geophysical Surveys Report of Investigations 2000–5, 42 p., scale 1:63,360.

Brabb, E.E., and Churkin, Michael, Jr., 1969, Geologic map of the Charley River quadrangle, east-central Alaska: U.S. Geological Survey Miscellaneous Geologic Investigations Map I–573, scale 1:250,000.

Brabb, E.E., and Grant, R.E., 1971, Stratigraphy and paleontology of the revised type section for the Tahkandit Limestone (Permian) in east-central Alaska: U.S. Geological Survey Professional Paper 703, 26 p.

Cameron, B.E.B., and Tipper, H.W., 1985, Jurassic stratigraphy of the Queen Charlotte Islands, British Columbia: Geological Survey of Canada, Bulletin 365, 49 p.

Csejtey, Béla, Jr., Mullen, M.W., Cox, D.P., and Stricker, G.D., 1992, Geology and geochronology of the Healy quadrangle, south-central Alaska: U.S. Geological Survey Miscellaneous Investigations Map I–1961, 63 p., 2 sheets, scale 1:250,000.

Day, W.C., Aleinikoff, J.N., and Gamble, Bruce, 2002, Geochemistry and age constraints on metamorphism and deformation in the Fortymile River area, eastern Yukon-Tanana Upland, Alaska, *in* Wilson, F.H., and Galloway, J.P., eds., Studies by the U.S. Geological Survey in Alaska, 2000: U.S. Geological Survey Professional Paper 1662, p. 5–18.

Day, W.C., Gamble, B.M., Henning, M.W., and Smith, B.D, 2000, Geologic setting of the Fortymile River area—polyphase deformational history within part of the eastern Yukon-Tanana uplands of Alaska, *in* Kelly, K.D., and Gough, L.P., eds., Geologic studies in Alaska by the U.S. Geological Survey, 1998: U.S. Geological Survey Professional Paper 1615, p. 65–82.

Dusel-Bacon, Cynthia, and Aleinikoff, J.N., 1996, U-Pb zircon and titanite ages for augen gneiss from the Divide Mountain area, eastern Yukon-Tanana upland, Alaska, and evidence for the composite nature of the Fiftymile Batholith, *in* Moore, T.E., and Dumoulin, J.A., eds., Geologic studies in Alaska by the U.S. Geological Survey during 1994: U.S. Geological Survey Bulletin 2152, p. 131–141.

Dusel-Bacon, Cynthia, Bressler, J.R., Takaoka, H., Mortensen, J.K., Oliver, D.H., Leventhal, J.S., Newberry, R.J., and Bundtzen, T.K., 1998, Stratiform zinc-lead mineralization in Nasina assemblage rocks of the Yukon-Tanana Upland in east-central Alaska: U.S. Geological Survey Open-File Report 98–340 [URL http://geopubs.wr.usgs.gov/open-file/of98-340/].

Dusel-Bacon, Cynthia, Brosgé, W.P., Till, A.B., Doyle, E.O., Mayfield, C.F., Reiser, H.N., and Miller, T.P., 1989, Distribution, facies, ages, and proposed tectonic associations of regionally metamorphosed rocks in northern Alaska: U.S. Geological Survey Professional Paper 1497–A, 44 p.

Dusel-Bacon, Cynthia, and Cooper, K.M., 1999, Trace-element geochemistry of metabasaltic rocks from the Yukon-Tanana Upland and implications for the origin of tectonic assemblages in east-central Alaska: Canadian Journal of Earth Sciences, v. 36, no. 10, p. 1671–1695.

Dusel-Bacon, Cynthia, Csejtey, Béla, Jr., Foster, H.L., Doyle, E.O., Nokleberg, W.J., and Plafker, George, 1993, Distribution, facies, ages, and proposed tectonic associations of regionally metamorphosed rocks in east and south-central Alaska: U.S. Geological Survey Professional Paper 1497–C, 73 p.

Dusel-Bacon, Cynthia, Hansen, V.L., and Scala, J.A., 1995, High-pressure amphibolite facies dynamic metamorphism and the Mesozoic tectonic evolution of an ancient continental margin, east-central Alaska: Journal of Metamorphic Geology, v. 13, no. 1, p. 9–24.

Dusel-Bacon, Cynthia, Lanphere, M.A., Sharp, W.D., Layer, P.W., and Hansen, V.L., 2002, Mesozoic thermal history and timing of structural events for the Yukon-Tanana Upland, east-central Alaska—$^{40}Ar/^{39}Ar$ data from metamorphic and plutonic rocks: Canadian Journal of Earth Sciences, v. 39, no. 6, p. 1013–1051.

Dusel-Bacon, Cynthia, Wooden, J.L., and Bressler, J.R., 2001, New U-Pb zircon and geochemical evidence for bimodal mid-Paleozoic magmatism and syngenetic base metal mineralization in the Yukon-Tanana terrane, Alaska [abs.]: Geological Society of America Abstracts with Programs, v. 33, no. 6, p. A–185.

Epstein, A.G., Epstein, J.B., and Harris, L.D., 1977, Conodont color alteration—an index to organic metamorphism: U.S. Geological Survey Professional Paper 995, 27 p.

Erdmer, Philippe, Ghent, E.D., Archibald, D.A., and Stout, M.Z., 1998, Paleozoic and Mesozoic high-pressure metamorphism at the margin of ancestral North America in central Yukon: Geological Society of America Bulletin, v. 110, no. 5, p. 615–629.

Foster, H.L., 1976, Geologic map of the Eagle quadrangle, Alaska: U.S. Geological Survey Miscellaneous Investigations Series Map I–922, scale 1:250,000.

——1992, Geologic map of the eastern Yukon-Tanana region, Alaska: U.S. Geological Survey Open-File Report 92–313, scale 1:500,000.

Foster, H.L., Cushing, G.W., Keith, T.E.C., and Laird, Jo, 1985, Early Mesozoic tectonic history of the Boundary area, east-central Alaska: Geophysical Research Letters, v. 12, no. 9, p. 553–556.

Foster, H.L., Jones, D.L., Keith, T.E.C., Wardlaw, B.R., and Weber, F.R., 1978, Late Paleozoic radiolarians and conodonts found in chert of Big Delta quadrangle, *in* Johnson, K.M., *ed.*, United States Geological Survey in Alaska—accomplishments during 1977: U.S. Geological Survey Circular 772–B, p. B34–B36.

Foster, H.L., and Keith, T.E.C., 1987, Preliminary geology, including the Tintina fault system of part of the southwestern Charley River quadrangle, Alaska, *in* Hamilton, T.D., and Galloway, J.P., eds., Geological studies in Alaska by the U.S. Geological Survey during 1986: U.S. Geological Survey Circular 998, p. 59–61.

Foster, H.L., Keith, T.E.C., and Menzie, W.D., 1994, Geology of the Yukon-Tanana area of east-central Alaska, *in* Plafker, George, and Berg, H.C., eds., The geology of Alaska, v. G–1 *of* The geology of North America: Boulder, Colo., Geological Society of America, p. 205–240.

Gabrielse, Hubert, 1991, Late Paleozoic and Mesozoic terrane interactions in north-central British Columbia: Canadian Journal of Earth Sciences, v. 28, no. 6, p. 947–957.

Gradstein, F.M., Agterberg, F.P., Ogg, J.G., Hardenbol, Jan, van Veen, Paul, Thierry, Jacques, and Huang, Zehui, 1995, A Triassic, Jurassic, and Cretaceous time scale, *in* Time scales and global stratigraphic correlation: Society of Economic Paleontologists and Mineralologists Special Publication 54, p. 95–126.

Hansen, V.L., 1990, Yukon-Tanana terrane—a partial acquittal: Geology, v. 18, no. 4, p. 365–369.

Hansen, V.L., and Dusel-Bacon, Cynthia, 1998, Structural and kinematic evolution of the Yukon-Tanana upland tectonites, east-central Alaska—a record of late Paleozoic to Mesozoic crustal assembly: Geological Society of America Bulletin, v. 110, no. 2, p. 211–230.

Hansen, V.L., Heizler, M.T., and Harrison, T.M., 1991, Mesozoic thermal evolution of the Yukon-Tanana composite terrane—new evidence from $^{40}Ar/^{39}Ar$ data: Tectonics, v. 10, no. 1, p. 51–76.

Harms, T.A., 1986, Structural and tectonic analysis of the Sylvester allochthon, northern British Columbia: Implications for Paleozoic geography and accretion: Tucson, University of Arizona, Ph.D. thesis, 80 p.

——1989, Geology of the northeast Needlepoint Mountain and Erickson mine areas, northern British Columbia: British Columbia Ministry of Energy, Mines and Petroleum Resources Geological Fieldwork 1988, Paper 1989–1, p. 339–345.

Harms, T.A., Coney, P.J., and Jones, D.L., 1984, The Sylvester allochthon, Slide Mountain terrane, British Columbia—a correlative of oceanic terranes of northern Alaska [abs]: Geological Society of America Abstracts with Programs, v. 16, no. 5, p. 288.

Harms, T.A., and Murchey, B.L., 1992, Setting and occurrence of Late Paleozoic radiolarians in the Sylvester allochthon, part of a proto-Pacific ocean floor terrane in the Canadian Cordillera: Palaeogeography, Palaeoclimatology, Palaeoecology, v. 96, no. 1–2, p. 127–139.

Harris, A.G., Brenckle, P.L., Baesemann, J.F., Krumhardt, A.P., and Gruzlovic, P.D., 1997, Comparison of conodont and calcareous microfossil biostratigraphy and lithostratigraphy of the Lisburne Group (Carboniferous), Sadlerochit Mountains, northeast Brooks Range, Alaska, *in* Dumoulin, J.A., and Gray, J.E., eds., Geologic studies in Alaska by the U.S. Geological Survey, 1995: U.S. Geological Survey Professional Paper 1574, p. 195–291.

Harris, A.G., and Sweet, W.C., 1989, Mechanical and chemical techniques for separating microfossils from rock, sediment, and residue matrix, *in* Feldmann, R.M., Chapman, R.E., and Hannibal, J.T., eds., Paleotechniques: Paleontological Society Special Publication 4, p. 70–86.

Holdsworth, B.K., and Jones, D.L., 1980, Preliminary radiolarian zonation for Late Devonian through Permian time: Geology, v. 8, no. 6, p. 281–285.

Isakova, T.N., and Nazarov, B.B., 1986, Stratigraphy and microfauna of the Late Carboniferous-Early Permian of the Southern Urals: Moscow Nauka, Trudy IN AN SSSR, v. 402, 213 p. [in Russian].

Jin, Yugan, Wardlaw, B.R., Glenister, B.F., and Kotlyar, G.V., 1997, Permian chronostratigraphic subdivisions: Episodes, v. 20, no. 1, p. 10–15.

Jones, D.L., Silberling, N.J., Coney, P.J., and Plafker, George, 1987, Lithotectonic terrane map of Alaska (west of the 141st Meridian): U.S. Geological Survey Miscellaneous Field Studies Map MF–1874–A, scale 1:2,500,000.

Klepacki, D.W., and Wheeler, J.O., 1985, Stratigraphic and structural relations of the Milford, Kaslo and Slocan Groups, Goat Range, Lardeau and Nelson map areas, British Columbia, *in* Current research, part A: Geological Survey of Canada Paper 1985–1A, p. 277–286.

Krumhardt, A.P., Harris, A.G., and Watts, K.F., 1996, Lithostratigraphy, microlithofacies, and conodont biostra-

tigraphy and biofacies of the Wahoo Limestone (Carboniferous), eastern Sadlerochit Mountains, northeast Brooks Range, Alaska: U.S. Geological Survey Professional Paper 1568, 70 p.

Miller, M.M., 1987, Disbursed remnants of a northeast Pacific fringing arc: Upper Paleozoic terranes of Permian McCloud affinity, western U.S.: Tectonics, v. 6, no. 6, p. 807–830.

Monger, J.W.H., and Berg, H.C., 1987, Lithotectonic terrane map of western Canada and southeastern Alaska: U.S. Geological Survey Miscellaneous Field Studies Map MF–1874–B, scale 1:2,500,000.

Monger, J.W.H., Wheeler, J.O., Tipper, H.W., Gabrielse, Hubert, Harms, Tekla, Struik, L.C., Campbell, R.B., Dodds, C.J., Gehrels, G.E., and O'Brien, J.A., 1991, Upper Devonian to Middle Jurassic assemblages, part B, Cordilleran terranes, *in* Gabrielse, Hubert, and Yorath, C.J. eds., Geology of the Cordilleran orogen in Canada, v.G–2 *of* The geology of North America: Boulder, Colo., Geological Society of America, p. 281–328.

Mortensen, J.K., 1988, Geology of southwestern Dawson map area: Geological Survey of Canada Open-File 1927, scale 1: 250,000.

——1990, Geology and U-Pb geochronology of the Klondike District, west-central Yukon Territory: Canadian Journal of Earth Sciences, v. 27, no. 7, p. 903–914.

——1992, Pre-mid-Mesozoic tectonic evolution of the Yukon-Tanana terrane, Yukon and Alaska: Tectonics, v. 11, no. 4, p. 836–853.

Mosher, L.C., 1970, New conodont species as Triassic guide fossils: Journal of Paleontology, v. 44, no. 4, p. 895–946.

Murchey, B.L., 1990, Age and depositional setting of siliceous sediments in the upper Paleozoic Havallah sequence near Battle Mountain, Nevada; implications for the paleogeography and structural evolution of the western margin of North America, *in* Harwood, D.S., and Miller, M.M., eds., Paleozoic and early Mesozoic paleogeographic relations: Sierra Nevada, Klamath Mountains, and related terranes: Boulder, Colo., Geological Society of America Special Paper 255, p. 137–155.

Nelson, J.L., 1993, The Sylvester Allochthon; upper Paleozoic marginal-based and island-arc terranes in northern British Columbia: Canadian Journal of Earth Sciences, v. 30, no. 3, p. 631–643.

Nokleberg, W.J., Foster, H.L., and Aleinikoff, J.N., 1989, Geology of the northern Copper River Basin, eastern Alaska Range, and southern Yukon-Tanana Basin, southern and east-central Alaska, *in* Nokleberg, W.J., and Fisher, M.A., eds., Alaskan geological and geophysical transect: American Geophysical Union Field Trip Guidebook T104, p. 34–63.

Orchard, M.J., 1983, *Epigondolella* populations and their phylogeny and zonation in the Upper Triassic: Fossils and Strata, no. 15, p. 177–192.

——1991a, Conodonts, time, and terranes—an overview of the biostratigraphic record in the western Canadian Cordillera, *in* Orchard, M.J., and McCracken, A.D., eds., Ordovician and Triassic conodont paleontology of the Canadian Cordillera: Geological Survey of Canada Bulletin 417, p. 1–25.

——1991b, Late Triassic conodont biochronology and biostratigraphy of the Kunga Group, Queen Charlotte Islands, British Columbia, *in* Woodworth, G.J., ed., Evolution and hydrocarbon potential of the Queen Charlotte basin, British Columbia: Geological Survey of Canada Paper 90–10, p. 173–193.

——1991c, Upper Triassic conodont biochronology and new index species from the Canadian Cordillera, *in* Orchard, M.J., and McCracken, A.D., eds., Ordovician and Triassic conodont paleontology of the Canadian Cordillera: Geological Survey of Canada Bulletin 417, p. 299–335.

Pavlis, T.L., Sisson, V.B., Foster, H.L., Nokleberg, W.J., and Plafker, George, 1993, Mid-Cretaceous extensional tectonics of the Yukon-Tanana terrane, Trans-Alaskan Crustal Transect (TACT), east-central Alaska: Tectonics, v. 12, no. 1, p. 103–122.

Poulton, T.P., Orchard, M.J., Gordey, S.P., and Davenport, P., compilers, 1999, Selected Yukon fossil determinations, *in* Gordey, S.P., and Makepeace, A.J., compilers, Yukon digital geology: Geological Survey of Canada Open File D 3826 and Department of Indian and Northern Affairs, Exploration and Geological Services Division Open File 1999–1(D).

Rejebian, V.A., Harris, A.G., and Huebner, J.S., 1987, Conodont color alteration; an index to regional metamorphism, contact metamorphism, and hydrothermal alteration: Geological Society of America Bulletin, v. 99, no. 4, p. 471–479.

Richards, D.R., Butler, R.F., and Harms, T.A., 1993, Paleomagnetism of the late Paleozoic Slide Mountain terrane, northern and central British Columbia: Canadian Journal of Earth Sciences, v. 30, no. 9, p. 1898–1913.

Robinson, M.S., Smith, T.E., and Metz, P.A., 1990, Bedrock geology of the Fairbanks Mining District: Alaska Division of Geological and Geophysical Surveys Professional Report 106, 2 sheets, scale 1:63,360.

Roddick, J.A., 1967, Tintina trench: Journal of Geology, v. 75, no. 1, p. 23–33.

Ross, C.A., 1969, Upper Paleozoic Fusulinacea—*Eowaeringella* and *Wedekindellina* from Yukon Territory and giant *Parafusulina* from British Columbia, *in* Contributions to Canadian paleontology: Geological Survey of Canada Bulletin 182, p. 129–134.

Silberling, N.J., Jones, D.L., Monger, J.W.H., Coney, P.J., Berg, H.C., and Plafker, George, 1994, Lithotectonic terrane map of Alaska and adjacent parts of Canada, pl. 3 *of* Plafker, George, and Berg, H.C., eds., The geology of Alaska, v. G–1 *of* The Geology of North America: Boulder, Colo., Geological Society of America, scale 1:2,500,000.

Smith, T.E., Robinson, M.S., Weber, F.R., Waythomas, C.W., and Reifenstuhl, R.R., 1994, Geologic map of the upper Chena River area, eastern Interior Alaska: Alaska Division of Geological and Geophysical Surveys Professional Report 115, scale 1:63,360, 19 p.

Stevens, C.H., 1995, A giant Permian fusulinid from east-central Alaska with comparisons to all giant fusulinids in

western North America: Journal of Paleontology, v. 69, no. 5, p. 802–812.

Stevens, C.H., Yancey, T.E., and Hanger, R.A., 1990, Significance of the provincial signature of Early Permian faunas of the eastern Klamath terrane, *in* Harwood, D.S., and Miller, M.M., eds., Paleozoic and early Mesozoic paleogeographic relations; Sierra Nevada, Klamath Mountains, and related terranes: Geological Society of America Special Paper 255, p. 201–218.

Szumigala, D.J., Newberry, R.J., Werdon, M.B., Finseth, B.A., and Pinney, D.S., 2000, Preliminary bedrock geologic map of a portion of the Fortymile Mining District, Alaska: Alaska Division of Geological and Geophysical Surveys Preliminary Interpretive Report 2000–6, scale 1:63,360.

Tempelman-Kluit, D.J., 1979, Transported cataclasite, ophiolite and granodiorite in Yukon: evidence of arc-continent collision: Geological Survey of Canada Paper 79–14, 27 p.

Werdon, M.B., Newberry, R.J., Szumigala, D.J., and Pinney, D.S., 2001, Geologic map of the Eagle A–2 quadrangle, Fortymile Mining District, Alaska: Alaska Division of Geological and Geophysical Surveys Preliminary Interpretive Report 2001–3a, scale 1:63,360.

Wheeler, J.O., and McFeely, Patricia, 1991, Tectonic assemblage map of the Canadian Cordillera and adjacent parts of the United States of America: Geological Survey of Canada Map 1712A, scale 1:2,000,000.

PLATE 1

Plate 1. Late Triassic conodonts from metalimestone in core from the WGM, Inc., diamond-drill hole on Doyon Ltd.'s Lead Creek property, Seventymile terrane, southwesternmost Eagle C–1 quadrangle, east-central Alaska (loc. 1, fig. 3). Scanning-electron micrographs of carbon-coated specimens (USGS colln. Mes. 35008); illustrated specimens reposited in the U.S. National Museum (USMN), Washington, D.C. See table 1 for lithologic description of samples and analysis and age assignment of faunules.

Figures 1–15. *Epigondolella quadrata* Orchard. Pa elements. Magnification: upper and lower views, ×75; enlarged lower views, ×150.

1, 2. USNM No. 519496, incomplete rectangular subadult with bifurcate scar. Marginal and carinal nodes equal in number to, but smaller than, those on specimen in figure 3.

3–5. USNM No. 519497, quadrate subadult, showing pit in center of platform.

6–8. USNM No. 519498, quadrate subadult. Posteriormost carinal node smaller than preceding node, centrally located pit, and square termination of scar.

9–11. USNM No. 519499, quadrate juvenile, showing microreticulation restricted to posterior half of platform margin, centrally constricted longitudinal margin, and bifurcate scar.

12–14. USMN No. 519500, quadrate juvenile, showing subdued central-platform constriction and square termination of scar.

15. USNM No. 519501, nearly complete, though somewhat deformed, rectangular subadult, showing equal length of platform and blade and high spikelike marginal nodes.

16, 17. *Metapolygnathus primitius* (Mosher). USNM No. 519502, ovate juvenile Pa element. Keel and basal scar mostly obscured by adventitious mineral matter; pit in center of platform beneath largest carinal node. Microreticulation restricted to posterior half of platform margin. Magnification, ×75.

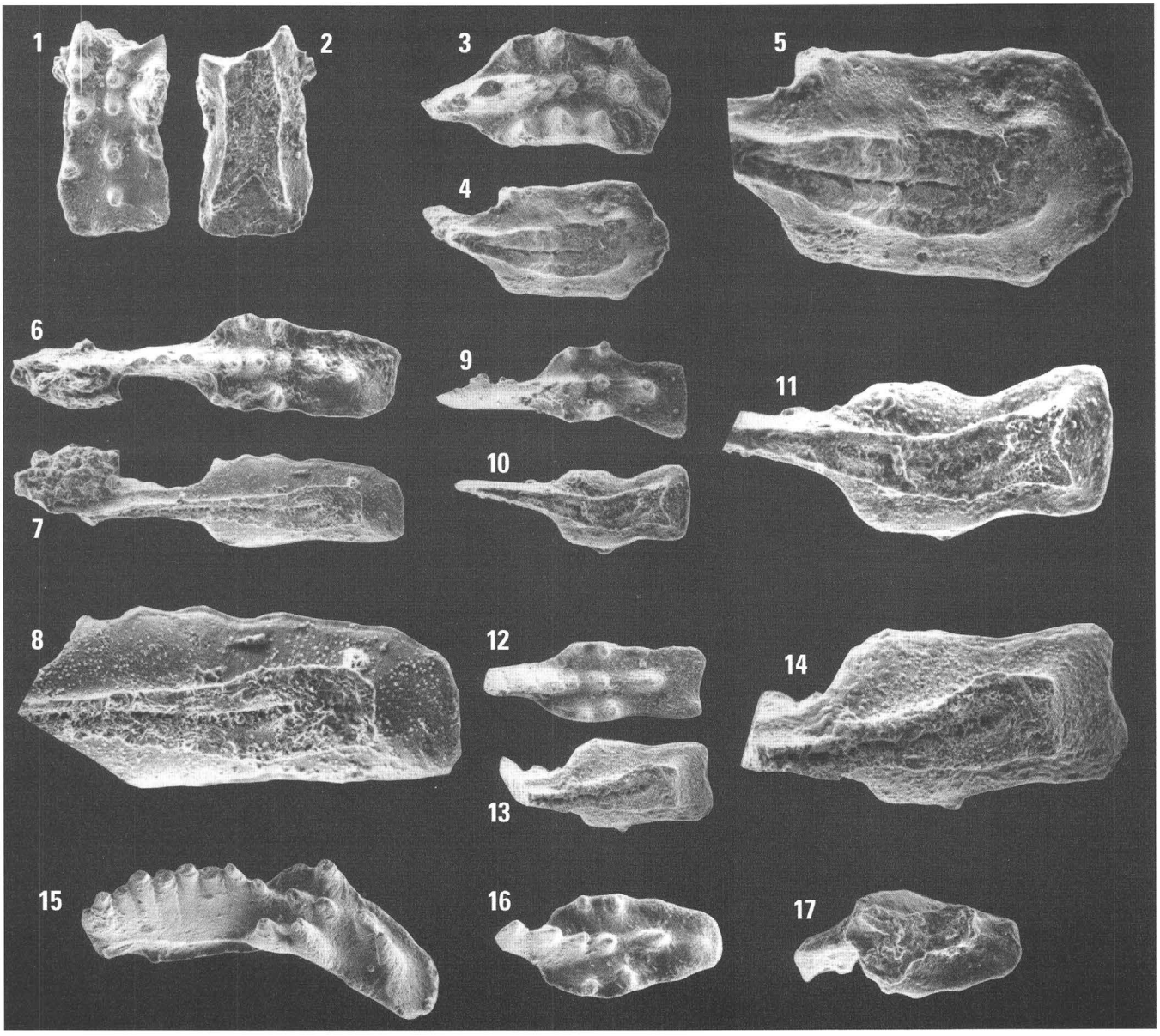
1
2
3
4
5
6
7
8
9
10
11
12
13
14
15
16
17

Studies by the U.S. Geological Survey in Alaska, 2001
U.S. Geological Survey Professional Paper 1678

Cretaceous Epigenetic Base-Metal Mineralization at the Lead Creek Prospect, Eastern Yukon-Tanana Upland, Alaska: Constraints from U-Pb Zircon Dating and Pb-Isotopic Analyses of Sulfides

By Cynthia Dusel-Bacon, James K. Mortensen, and Rick S. Fredericksen

Abstract

The Lead Creek Pb-Zn-Ag prospect, located 8 km west of the Taylor Highway in the Eagle C–1 quadrangle, eastern Alaska, occurs in very weakly metamorphosed sedimentary and volcanic rocks of the Seventymile terrane. The Seventymile terrane forms a belt of fault-bounded slices of varyingly serpentinized peridotite, weakly metamorphosed mafic volcanic rocks (including pillowed greenstone), and Mississippian to Upper Triassic sedimentary rocks. Lead Creek diamond-drill hole LC–7 penetrated 783 ft of weakly metamorphosed sedimentary and volcanic rocks, as well as altered felsic hypabyssal rocks that we interpret to be dikes or sills. Pyrite, galena, sphalerite, and minor chalcopyrite mineralization in the Lead Creek core occurs in crosscutting veins and veinlets, silicified breccia, and, less commonly, stratiform replacement zones. Zircons separated from a felsic dike or sill rock gave a concordant $^{206}Pb/^{238}U$ age of 96.2±1.0 Ma, which we interpret to be the crystallization age of the sample. About 13 km northwest of the Lead Creek property, a Cretaceous(?) pluton that intrudes a chlorite-muscovite-quartz schist unit of the Yukon-Tanana terrane caused the formation of base- and precious-metal-bearing skarns (Champion I and II prospects). Pb-isotopic compositions determined for galena samples from the Lead Creek prospect and one sample from the Champion II prospect all fall within the field defined by igneous feldspars from Early Cretaceous and mid-Cretaceous intrusions and are far removed from the sulfide Pb-isotopic compositions that would be expected for middle Paleozoic syngenetic mineralization. The compositional similarity of the galena samples from the Lead Creek and Champion II prospects clearly indicates that mineralization in the two occurrences was nearly contemporaneous and that the lead in the Lead Creek prospect was also likely derived from Cretaceous intrusions. We propose that the mineralization at Lead Creek comprises an epigenetic vein and manto-style replacement deposit and that previous correlation with syngenetic, middle Paleozoic mineralization in the Finlayson Lake area, central Yukon Territory, Canada, is unwarranted. The base- and precious-metal mineralization at Lead Creek likely represents a more distal equivalent to the epigenetic, pluton-related skarn mineralization at the Champion I and II prospects.

Introduction

The vicinity of the Lead Creek prospect (fig. 1) has been a focus of mineral exploration since the 1970s. In summer 1968, the U.S. Geological Survey conducted a geochemical and geologic reconnaissance of parts of the Fortymile River drainage area in the eastern part of the Eagle quadrangle (Foster and Clark, 1970). During this reconnaissance, galena was discovered in float on a ridge just west of the recent Lead Creek drilling. Rock and stream-sediment samples in the Champion Creek area showed anomalous Ag, Pb, Zn, Cr, Cu, and Mo contents (Foster and Clark, 1970). In the middle and late 1970s, stream-sediment sampling by the Alaska Division of Geological and Geophysical Surveys and WGM, Inc., showed anomalous Pb, Ag, and Zn contents in an 8-km-long tributary to Columbia Creek, subsequently given the informal name "Lead Creek" (WGM, Inc., 1979). Stream-sediment and soil analyses from the upper part of the creek showed highly anomalous Pb and Ag contents, and siliceous nodules containing 2 weight percent Pb and 2 troy oz Ag/ton were observed weathering from black pelitic schist (WGM, Inc., 1979). Trenching in an area underlain by graphitic schist resulted in the discovery of Pb-Ag mineralization within what was interpreted to be siliceous exhalites that were interbedded in the schist; the graphitic schist was enriched in Pb and Ag as well. Exploratory drilling, managed by WGM, Inc., was conducted on the Lead Creek property in 1978 and subsequently in 1997, 2000, and 2001.

The U.S. Bureau of Mines evaluated the mineral resources of the Fortymile River area, including the Lead Creek area, during 1993 and 1994. Siliceous nodules within graphitic schist generally contained as much as 2 weight percent Pb and 29 ppm Ag; a select sample of the siliceous nodules contained 10.7 weight percent Pb, 112.5 ppm Ag and 1,174 ppm Sb (U.S. Bureau of Mines, 1995). Galena was identified in crosscutting quartz veins,

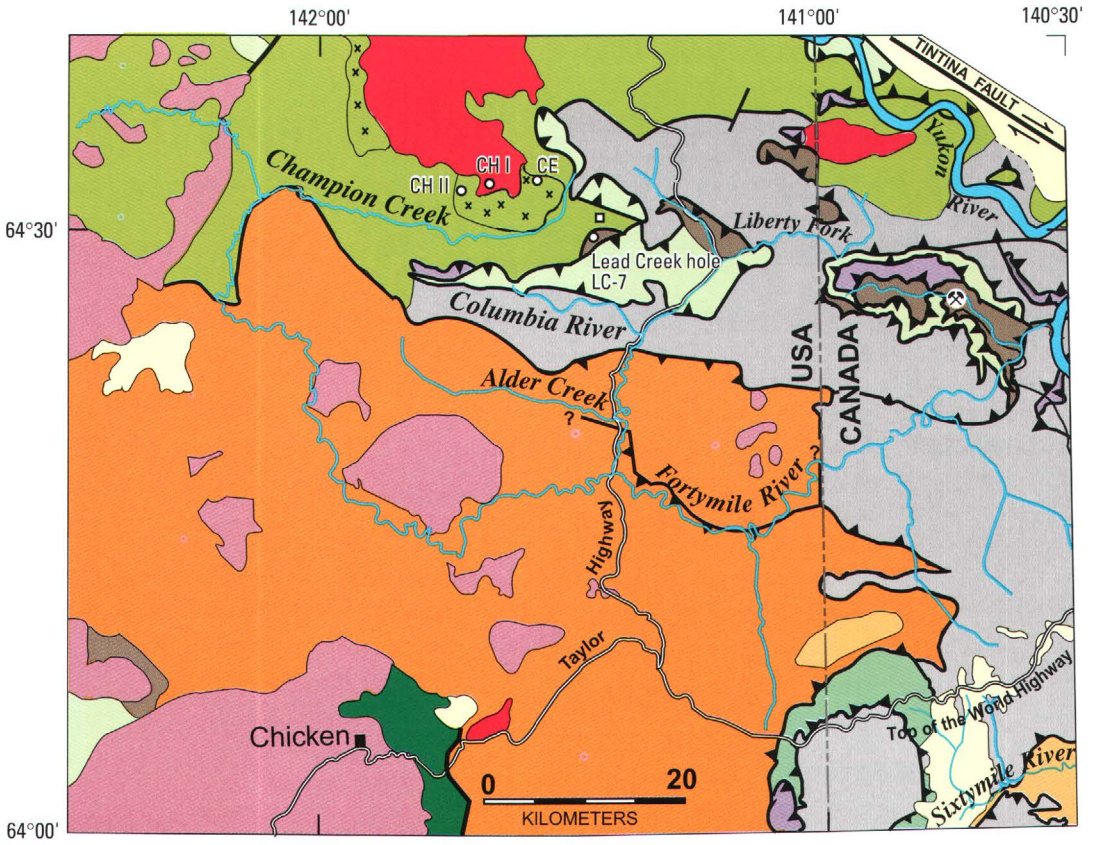

EXPLANATION

- Unmetamorphosed volcanic and sedimentary rocks (Tertiary and Cretaceous)
- Postmetamorphic granitoids (Cretaceous)
- Synmetamorphic to postmetamorphic granitoids (Early Jurassic and Late Triassic)

SEVENTYMILE TERRANE

- Serpentinized peridotite
- Greenstone, diabase, metalimestone (Triassic, Permian, and Mississippian), and metachert
- Argillite and metasandstone

FORTYMILE RIVER ASSEMBLAGE

- Amphibolite-facies biotite-hornblende gneiss, amphibolite, marble (Mississippian?- Late Permian?), and metachert
- Granodioritic orthogneiss (Early Mississippian)
- Quartz-muscovite±chlorite±feldspar schist (Permian)–Klondike Schist of Mortensen (1988)
- Quartz-chlorite-muscovite±calcite schist, micaceous quartzite, and marble (Mississippian)
- Carbonaceous quartzite, muscovite-chlorite schist, and marble (Mississippian and Devonian)–Nasina assemblage of Wheeler and McFeely (1991)
- Greenschist-facies metasedimentary and metaigneous rocks (Mesozoic and Paleozoic)–Chicken Metamorphic Complex of Werdon and others (2001)
- Thrust fault; sawteeth on upper plate, queried where uncertain
- Strike-slip fault, right-lateral offset
- Hornfels
- Clinton Creek Mine
- Drill hole localities discussed in text
- Siliceous nodules locality

Figure 1. Generalized geologic map of the Fortymile River area, eastern Alaska, showing location of Lead Creek diamond-drill hole LC–7 within the Seventymile terrane (modified from Foster, 1976, 1992, and Mortensen, 1988). Localities CH I, CH II, and CE, U.S. Bureau of Mines (1995) skarn prospects Champion I, Champion II, and Champion East, respectively. Location of hornfels from Foster (1976) and U.S. Bureau of Mines (1995); area of siliceous nodules from U.S. Bureau of Mines (1995).

and a sample from a feldspar porphyry dike contained 1,309 ppm Pb and 2,450 ppm As (U.S. Bureau of Mines, 1995).

Sampling by Dusel-Bacon and others (1998) in the vicinity of the siliceous nodules yielded a sample of pyrite-bearing carbonaceous quartzite containing >10,000 ppm As and 170 ppb Au, and a grab sample of highly mineralized and oxidized gray-and-yellow-banded weathered rock contained 2,330 ppb Au, 2,126 ppm Ag, >10,000 ppm As, >100 ppm Cd, 1,420 ppm Cu, 10.8 weight percent Pb, and >10,000 ppm Sb.

In the late 1970s and continuing into the mid-1990s, the origin of the base and precious metals was uncertain but was thought to be primarily stratabound, syngenetic sedimentary exhalative mineralization (WGM, Inc., 1979, 2001), or of less process specific, shale-hosted origin (Schmidt, 1997). The discovery of numerous large volcanic-hosted deposits within carbonaceous assemblages in the Finlayson Lake area, central Yukon Territory, Canada, in the mid-1990s (Hunt, 1997) increased interest in the mineral-resource potential of the Lead Creek area. The Finlayson Lake deposits occur in middle Paleozoic rocks just east of the right-lateral Tintina Fault zone in rocks of the Yukon-Tanana terrane, comparable to those in the greater Fortymile River area. Restoration of 450 km of right-lateral offset along the fault zone brings these two areas relatively close together.

Dusel-Bacon and others (1998) concluded that the variety of metals and host rocks at the Lead Creek prospect may indicate the presence of multiple ages and styles of mineralization. Pb- and Ag-enriched siliceous nodules in carbonaceous schist and metachert suggest a possible diagenetic origin. However, the presence of a relatively young feldspar porphyry dike in the vicinity that showed anomalous Pb and As contents, as well as the high levels of Pb, Sb, and As in oxidized material, along with the presence of quartz-galena veins, evidence for local contact-metamorphic effects, and the presence of sulfide-bearing intrusions in the immediate area, suggests that some metals may have been remobilized or introduced during a later magmatic hydrothermal event (Dusel-Bacon and others, 1998). Our isotopic investigations of the Lead Creek core were undertaken to date the mineralization and to test the proposed correlation between mineralization in the Lead Creek and Finlayson Lake areas.

Local Geologic Setting of Lead Creek

The Lead Creek property occurs near the contacts of several geologic units (fig. 1; Foster, 1976, 1992). Most of the drilling at Lead Creek penetrated very weakly metamorphosed sedimentary and volcanic rocks of the Seventymile terrane, which forms a belt of fault-bounded slices of varyingly serpentinized peridotite, weakly metamorphosed mafic volcanic rocks (including pillowed greenstone), and Mississippian to Upper Triassic sedimentary rocks. The terrane is interpreted, in part, as a dismembered ophiolite (Foster and others, 1994). Rocks of the Seventymile terrane are not penetratively deformed and structurally overlie (in east-central Alaska; Foster, 1992) or are imbricated with (in the Yukon; Mortensen, 1990) continental-margin rocks of the Nasina assemblage (Wheeler and McFeely, 1991), the Klondike Schist (Mortensen, 1988; Dusel-Bacon and others, 1998), and the Fortymile River assemblage (fig. 1; Dusel-Bacon and others, 2002) of the Yukon-Tanana terrane. Northeast-trending high-angle faults further complicate the structural relation between the poorly exposed bedrock units in the region (for example, Werdon and others, 2001).

At Lead Creek, low-grade sedimentary rocks of the Seventymile terrane are bordered to the north by greenschist-facies carbonaceous rocks of the Nasina assemblage and an unnamed unit of chlorite-muscovite-quartz schist of uncertain age. A Cretaceous(?) pluton that intrudes the chlorite-muscovite-quartz schist north of Champion Creek caused local hornfelsing of the chlorite schist to biotite metamorphic grade (Foster, 1976) and formation of base- and precious-metal-bearing skarns (Champion I and II prospects; U.S. Bureau of Mines, 1995), 13 km northwest of the Lead Creek property (fig. 1). The U.S. Bureau of Mines concluded that the Cu-Pb-Zn-Ag-Au mineralization at these prospects constitutes pyroxene skarn within a roof pendant of Paleozoic biotite schist (Champion I property) and a stratabound lens of garnet-pyroxene skarn that formed in intercalated marble units within a Paleozoic quartz-mica schist proximal to Cretaceous or Tertiary dacite to granodiorite intrusive rocks (Champion II property). The north contact of the low-grade sedimentary rocks that contain the Lead Creek prospect was interpreted by WGM, Inc. (2001), to be a high-angle normal fault, downdropped to the north; and the south contact with greenstone and minor diabase, limestone, and metachert of the Seventymile terrane was interpreted by Foster (1992) as a thrust fault. About 9 km to the east, along the Taylor Highway, weakly metamorphosed argillite, shale, limestone, and sandstone (unit Pzs of Foster and Keith, 1969) and silicified tuff(?) (unit MzPzt of Foster, 1976), comparable to the rocks drilled at Lead Creek, was interpreted by Foster (1976) to be in depositional contact with greenstone of the Seventymile terrane.

Lead Creek Base- and Precious-Metal Target

The Lead Creek Pb-Zn-Ag prospect is 9 km west of the Taylor Highway in the Eagle C–1 quadrangle (fig. 1) on Doyon Ltd.'s Native selection lands that are currently held (as of April 2002) under option by Ventures Resource Corp. as part of its 609,000-acre Champion property. The most productive diamond-drill holes on the property are located in an area referred to as "Pebble Dike Hill," 1.3 km south of the small area in which metalliferous siliceous nodules were discovered. Diamond drilling in the Pebble Dike Hill area (drill hole LC–01–15) in 2001 intersected 50.6 ft of rock containing 5.1 weight percent Pb and 11.9 troy oz Ag/ton. A hole (LC–00–14) drilled the previous year, 400 ft to the north, yielded rock containing 6.4 weight percent Pb and 23.3 troy oz Ag/ton over an interval of 31.5 ft (Ventures Resource Corp., 2001). These two drill holes were collared approximately 370 m south of drill hole LC–7 (fig. 1), drilled in 1997, from which we selected the various core samples for our analyses. Higher-grade drill-core intervals for drill hole LC–7 are listed in table 1.

Table 1. Assay results for higher-grade intervals in diamond-drill hole LC–7 (fig. 1).

[Data from Venture Resources Corp. (2001)]

Drill-hole interval					
From (ft)	To (ft)	Length (ft)	Ag (oz/ton)	Pb (wt pct)	Zn (wt pct)
496.0	504.0	8.0	2.8	3.5	0.3
552.0	566.0	14.0	2.2	3.1	1.0
593.0	599.5	6.5	2.6	3.7	2.6
721.5	725.0	3.5	8.8	14.2	.3

The Lead Creek property is underlain by at least three thrust panels (WGM, Inc., 2001). The upper thrust panel, which is preserved as klippen on ridgetops, consists of graphitic and micaceous schist (Nasina assemblage and the quartz-muscovite schist units; fig. 1) that has been thrust over a middle panel composed of interbedded mafic to intermediate-composition metavolcanic rocks, siltstone, and limestone (greenstone unit of the Seventymile terrane) that, in turn, have been thrust over a lower panel of predominantly Triassic limestone (see Dusel-Bacon and Harris, this volume), siltstone, shale, and sandstone (low-grade sedimentary rocks of the Seventymile terrane). Rocks of the upper panel crop out on a hill that contains the high-grade polymetallic mineralization occurring as siliceous cerussite(?)-bearing nodules which are believed to occur in structural zones cutting rocks of the upper panel (WGM, Inc., 2001). Rocks of the middle and lower panels underlie Pebble Dike Hill. All structural units are cut by dikes and plugs of dacite porphyry, granodiorite, and diabase (WGM, Inc., 2001).

Lead Creek diamond-drill hole LC–7 (fig. 1) penetrated 783 ft of weakly metamorphosed sedimentary rocks that dip ~40° E., as well as weakly metamorphosed volcanic rocks and altered felsic hypabyssal rocks (fig. 2). The first ~250 ft consists of the middle-panel assemblage of calcareous rocks and interlayered siltstone underlain by metabasalt and minor siltstone. This assemblage is separated from a lower-panel assemblage by an ~100-ft-thick mylonite zone. The lower panel is composed primarily of limestone and carbonaceous siltstone, with several thin intervals of silicified felsic rocks that were initially interpreted as either felsic tuff or dikes. Late Carnian to early Norian (Late Triassic) conodonts were recovered from an ~10-ft-thick interval of locally recrystallized, slightly pyritic, carbonaceous quartzose limestone (see Dusel-Bacon and Harris, this volume) within the lower panel (fig. 2). Core from one of the felsic intervals (sample LC7–678, figs. 2, 3*D*) was sampled for U-Pb zircon dating. This interval is described in the drill log as "pale tan-green massive tuffaceous limestone with scattered lapilli; vaguely bedded perpendicular to core axis; pervasively bleached; with numerous blebs of talc, few calcite veins, and traces of very fine grained pyrite." This description was probably based primarily on the apparent fabric, which was interpreted to be depositional. In thin section, however, no preferred orientation of minerals is evident. Sample LC7–678 has a porphyritic texture and contains a few volume percent of 1- to 1.5-mm-diameter relict phenocrysts that were probably feldspar and mafic silicates, set in a fine-grained groundmass of polygonal quartz and intergranular calcite and white mica. We conclude that the fabric visible in the core (fig. 3*D*) is formed by parallel fractures and is not evidence of a tuffaceous origin for the felsic rock; instead, we infer that the dated sample is a felsic dike or sill rock.

Pyrite, galena, sphalerite, and minor chalcopyrite occur in carbonaceous shale, argillite, graywacke, and limestone within the lower-panel assemblage. Mineralization occurs in crosscutting veins and veinlets (fig. 3*A*), silicified breccias (fig. 3*B*), and, less commonly, stratiform replacement zones (fig. 3*C*). The relation between the mineralization and the high-grade polymetallic mineralization in siliceous cerussite(?)-bearing nodules in structural zones cutting rocks of the upper panel is uncertain (WGM, Inc., 2001).

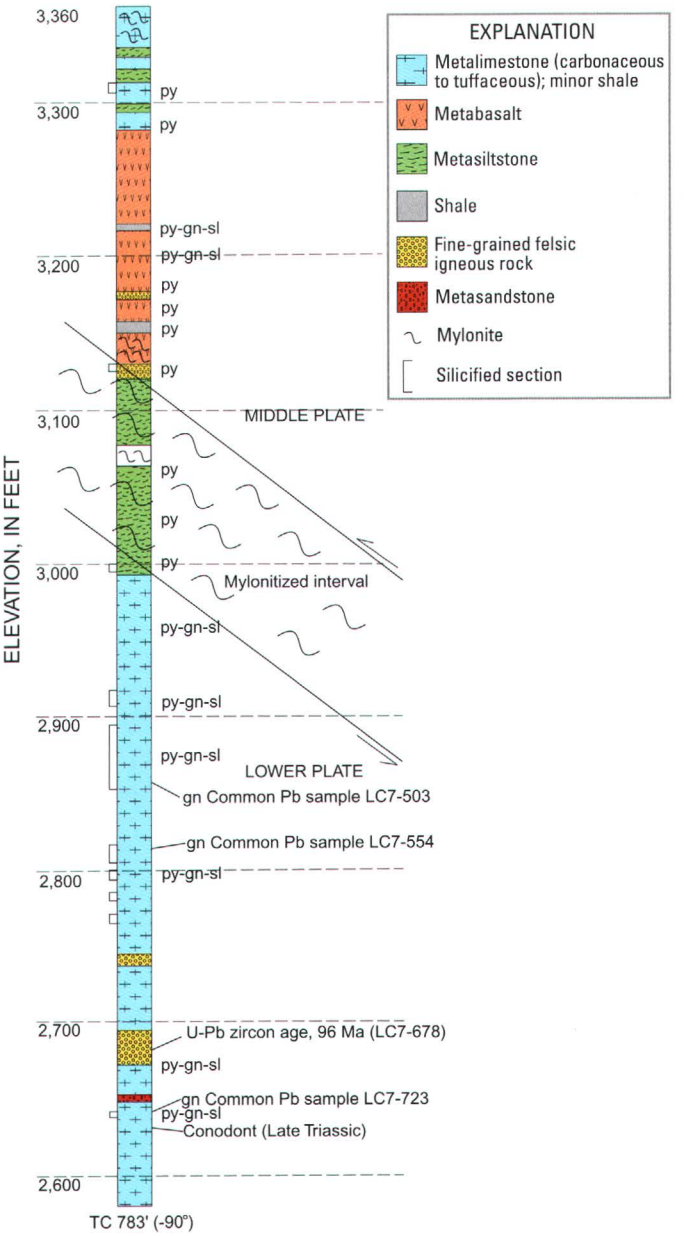

Figure 2. Generalized core log for diamond-drill hole LC–7 (WGM, Inc., 2001) (see fig. 1 for location). Collar of drill hole is located at lat 64°31′09″ N., long 141°25′42″ W. All contacts are shown schematically as horizontal.

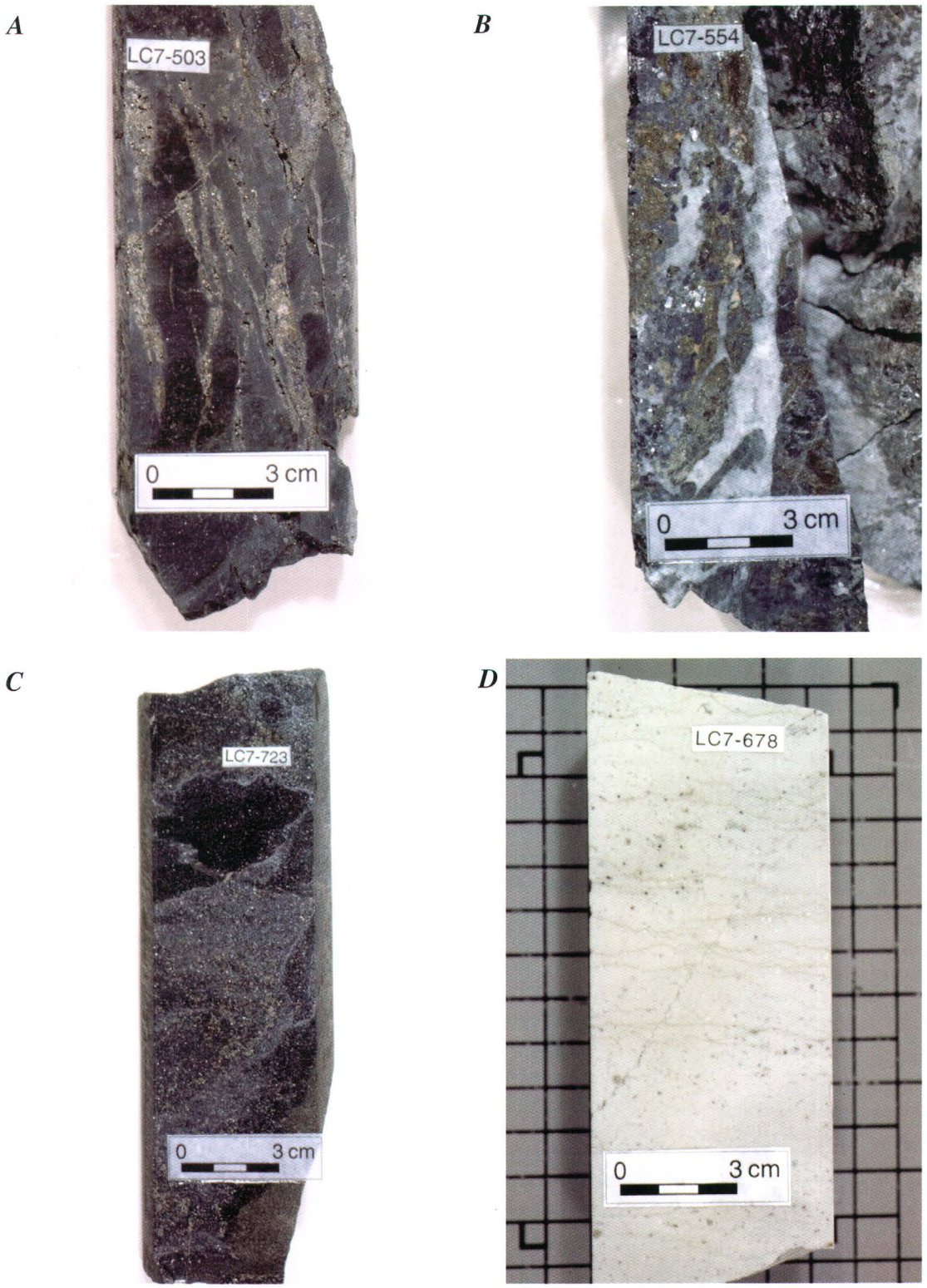

Figure 3. Core samples from Lead Creek diamond-drill hole LC–7 (fig. 1) for which Pb-isotopic data were determined. Last three numbers in label give depth (in feet) from collar of drill hole. Sample locations are shown in fig. 2. *A*, Carbonaceous and calcareous fine-grained quartz arenite with veins or fracture fillings of pyrite and galena. *B*, Fracture and breccia matrix fillings of pyrite (brassy-metallic color), galena (silver-metallic color), sphalerite (pinkish-metallic color), calcite (bright white), and quartz (grayer white) from within a 4-ft interval of brecciated and silicified limestone. *C*, Semimassive, fine- to medium-grained pyrite and galena disseminated in a laminated carbonaceous quartz siltstone/sandstone, with scattered traces of sphalerite. *D*, U-Pb zircon sample of fine-grained porphyritic felsic igneous rock. Photographs by Mike Diggles.

U-Pb Geochronology

Zircons were separated from an ~3-kg sample of felsic igneous rock (split-core interval 670–678.5 ft in diamond-drill hole LC–7, fig. 1; see fig. 3*D*), using conventional crushing, grinding, Wilfley table, heavy liquids, and Frantz magnetic-separator techniques. U-Pb analyses were done in the Geochronology Laboratory of the University of British Columbia, using the methodology for zircon grain selection, abrasion, dissolution, geochemical preparation, and mass spectrometry of Mortensen and others (1995). Procedural blanks for Pb and U were 2 and 1 pg, respectively. The U-Pb data are plotted on a conventional U-Pb concordia diagram in figure 4. Errors attached to individual analyses were calculated by using the numerical error-propagation method of Roddick (1987). Decay constants used are those recommended by Steiger and Jäger (1975). Compositions for initial common Pb were from the model of Stacey and Kramer (1975). All errors are listed at the 2σ level.

A moderate amount of euhedral, pale-yellow zircon was recovered from the sample. A range of grain morphologies was present in the concentrate, which mainly consisted of stubby to elongate prisms with simple to multifaceted terminations. Rounded cloudy cores were present within many of the grains. Six single and multigrain fractions were analyzed (table 2). Most fractions were air abraded (Krogh, 1982) before dissolution to minimize the effects of postcrystallization Pb loss. Considerable scatter is present in the data, reflecting both inheritance in some grains and postcrystallization Pb loss that has affected two of the fractions. Fraction A, consisting of four tips broken off of grains with obvious cloudy cores, and fraction D, consisting of a single stubby multifaceted prism with no visible core, yield overlapping concordant analyses, with a total range in $^{206}Pb/^{238}U$ age of 96.2±1.0 Ma, which is interpreted as the crystallization age of the sample. Fractions B (unabraded elongate prisms) and E (a single stubby multifaceted prism) have evidently lost a significant amount of Pb, indicating a previously unrecognized post-Cretaceous thermal/structural event. Fractions C (elongate square prism) and F (stubby multifaceted prism) did not contain visible cores but yielded much older Pb/Pb ages, indicating that at least some grains in each of these fractions contained inherited "cryptic" cores which could not be distinguished visually.

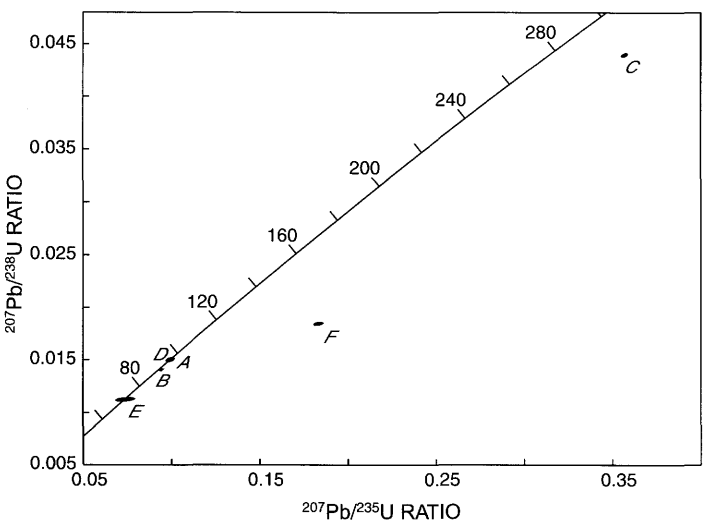

Figure 4. Conventional concordia U-Pb plot for zircons from sample LC7–678. Position of sample in drill core is shown in figure 2; photograph of core from which zircons were separated is shown in figure 3*D*.

Pb-Isotopic Analyses

Small clean cubes of galena were handpicked, washed, and dissolved in dilute HCl. Approximately 10 to 25 ng of Pb as chloride was loaded on a rhenium filament, and isotopic compositions were determined by using a modified VG54R thermal-ionization mass spectrometer. The measured ratios were corrected for instrumental mass fractionation of 0.12 percent per mass unit, based on repeated measurements of the National Bureau of Standards SRM 981 Standard Isotopic Reference Material. Errors reported in table 3 were determined by propagating all mass-fractionation and analytical errors through the calculation.

Pb-isotopic compositions were determined for galena samples from three different drill-core intervals of hole LC–7 (fig. 5; table 3). In addition, Pb-isotopic analyses of galena from a surface sample of mineralization at the Lead Creek property (U.S. Bureau of Mines, 1995), and of galena from a sulfide sample from the Champion II prospect (Venture Resources Corp., 2001), are plotted in figure 5.

The Pb-isotopic data plotted in figure 5, are shown with reference to the "shale curve" of Godwin and Sinclair (1982), which closely approximates the evolution of upper-crustal Pb in the North American miogeocline and the Yukon-Tanana terrane of the northern Cordillera. Also shown is the field defined by the Pb-isotopic compositions of feldspars from Early Cretaceous and mid-Cretaceous intrusions, and from various closely associated mineral occurrences, in the Yukon-Tanana terrane of western Yukon and east-central Alaska (data from Aleinikoff and others, 2000; Joyce, 2002). Although the ultimate origin of the Early Cretaceous and mid-Cretaceous magmatism in interior Alaska is still uncertain, the fact that the Pb-isotopic compositions of igneous feldspar fall on or close to the shale curve clearly indicates that the magmas either are entirely crustal in origin or represent mantle-derived melts that have been extensively contaminated with upper-crustal rocks. Pb-isotopic analyses of galena from the Lead Creek samples, as well as of galena from the Champion II sample, all fall within the field defined by igneous feldspars and are far removed from the sulfide Pb-isotopic compositions that would be expected for middle Paleozoic syngenetic mineralization (fig. 5).

Table 2. Zircon U-Pb analytical data for sample LC7–678 (fig. 2).

Sample description[1]	Weight (mg)	U content (ppm)	Pb^2 content (ppm)	$^{206}Pb/^{204}Pb$ ratio[3]	Total common Pb content (pg)	$^{208}Pb^2$ content (atomic percent)	$^{206}Pb/^{238}U$[4] ratio (±1σ)	$^{207}Pb/^{235}U$[4] ratio (±1σ)	$^{207}Pb/^{206}Pb$[4] ratio (±1σ)	$^{206}Pb/^{238}U$ age ratio (Ma; ±2σ)	$^{207}Pb/^{206}Pb$ age ratio (Ma; ±2σ)
A: N2,+149,tips,4	0.020	162	2.4	449	7	8.9	0.01510 (0.19)	0.09989 (0.52)	0.04799 (0.42)	96.6 (0.4)	98.6 (20.1)
B: N2,62-92,e,u,10	.070	709	10.4	800	56	13.6	.01410 (0.14)	.09419 (0.34)	.04861 (0.24)	90.0 (0.3)	128.9 (11.3)
C: N2,134-149,e,1	.020	207	9.6	2,264	5	13.8	.04399 (0.15)	.35686 (0.21)	.05884 (0.15)	277.5 (0.8)	561.3 (6.7)
D: N2,+149,s,1	.020	276	4.1	740	7	9.8	.01504 (0.54)	.09937 (1.01)	.04793 (0.82)	96.2 (1.0)	95.6 (38.8)
E: M2,+149,s,1	.020	252	2.8	149	27	7.5	.01126 (0.53)	.07388 (3.26)	.04769 (3.03)	72.0 (0.8)	83.9 (143.0)
F: N2,+149,s,1	.020	322	6.2	876	9	11.1	.01843 (0.28)	.18324 (0.60)	.07212 (0.50)	117.7 (0.7)	989.3 (20.2)

[1] N2, M2 = nonmagnetic, magnetic at given degrees of side slope on Frantz isodynamic magnetic separator. Grain size in micrometers; u, unabraded; e, elongate; s, stubby. Number refers to number of grains analyzed.

[2] Radiogenic Pb; corrected for blank, initial common Pb, and spike.

[3] Corrected for spike and fractionation.

[4] Corrected for blank Pb and U, and common Pb.

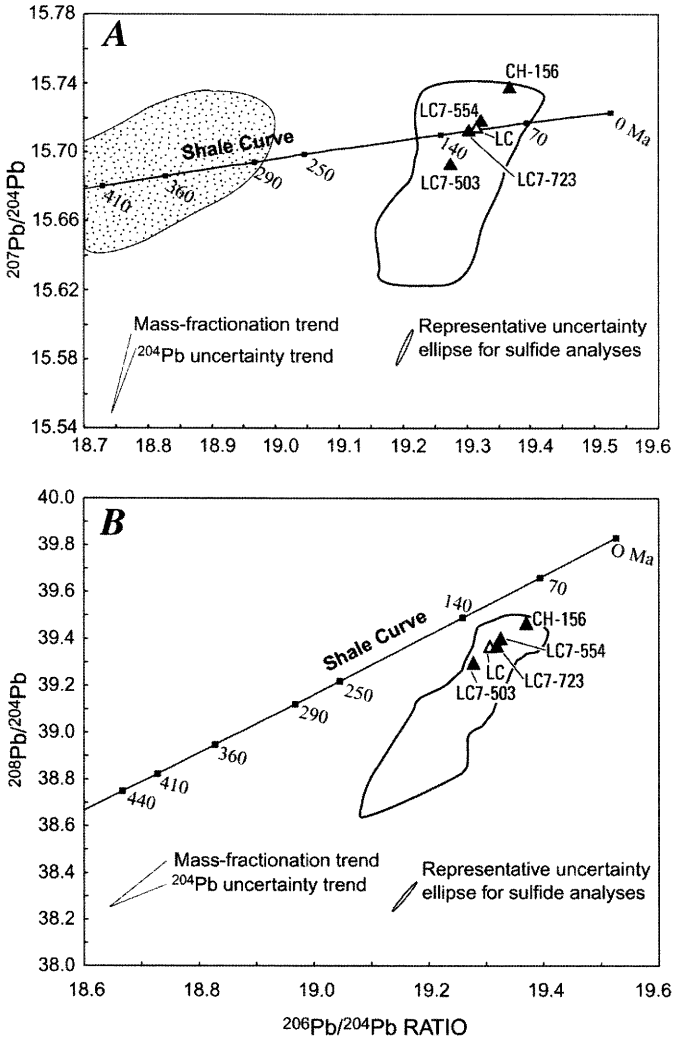

Table 3. Common Pb data for Lead Creek and Champion II prospects.

[Positions of galena samples in core from diamond-drill hole LC–7 are shown in figure 2; photographs of core from which galena was sampled at Lead Creek are shown in figures 3*A* through 3*C*. Sample LC, galena from a Lead Creek sample collected by the U.S. Bureau of Mines (1995). Numbers in parenthesis, 2σ error]

Sample	$^{206}Pb/^{204}Pb$ ratio	$^{207}Pb/^{204}Pb$ ratio	$^{208}Pb/^{204}Pb$ ratio
LC7-723	19.304 (0.01)	15.713 (0.01)	39.365 (0.01)
LC7-554	19.323 (0.01)	15.719 (0.01)	39.398 (0.01)
LC7-503	19.275 (0.01)	15.694 (0.01)	39.294 (0.01)
CH-156	19.368 (0.01)	15.738 (0.01)	39.463 (0.01)
LC	19.316 (0.01)	15.715 (0.01)	39.368 (0.01)

Figure 5. ^{207}Pb-isotopic (*A*) and ^{208}Pb-isotopic (*B*) compositions of galena samples from the Lead Creek and Champion II prospects, eastern Alaska (fig. 1). Shale curve of Godwin and Sinclair (1982) is shown for reference, as well as fields for Pb-isotopic compositions of galena from Devonian and Mississippian stratiform syngenetic occurrences from interior Alaska (stippling; Dusel-Bacon and others, 1998) and for igneous feldspars from Early and mid-Cretaceous intrusions and closely associated mineral occurrences from the western Yukon Territory, Canada, and east-central Alaska (black outline; Aleinikoff and others, 2000; Joyce, 2002). Positions of galena samples in core from diamond-drill hole LC–7 are shown in figure 2; photographs of core from which galena was sampled at Lead Creek are shown in figures 3*A* through 3*C*. Solid triangles, galena data from our samples from Lead Creek and one sample we analyzed from Champion II drill core (from 156-ft interval in drill hole CH–1). Open triangle LC, galena data from a Lead Creek sample previously collected by the U.S. Bureau of Mines (1995). Representative uncertainty ellipses extend from center of triangle symbols.

The Champion II occurrence, which is clearly a skarn, is presumed to be genetically associated with the Cretaceous intrusion that lies immediately north of this occurrence. The compositional similarity of the galena samples from the Lead Creek and Champion II prospects clearly indicates that mineralization in the two occurrences was nearly contemporaneous and that Pb in the Lead Creek prospect also was likely derived from Cretaceous intrusions.

Discussion

The mid-Cretaceous (96.2±1.0 Ma) U-Pb zircon crystallization age determined for the felsic igneous rock that was penetrated in diamond drilling at the Lead Creek prospect (presumed to be a dike or sill rock), and the Cretaceous common Pb signatures from galena samples, suggest that the mineralization at both Lead and Champion Creeks is related to felsic magmatism. The mineralization at Lead Creek is therefore interpreted to comprise an epigenetic vein and manto-style replacement deposit (WGM, Inc., 2001), and correlation with syngenetic, middle Paleozoic mineralization in the Finlayson Lake area is thus unwarranted. The base- and precious-metal mineralization at Lead Creek likely represents a more distal equivalent to the epigenetic, pluton-related skarn mineralization at the Champion I and II prospects.

Acknowledgments

We thank former WGM, Inc., geologists Bob Rogers and Holly Morris for providing the first author with the Lead Creek diamond-drill core, and C.G. ("Riz") Bigelow of Ventures Resource Corp. for permission to publish their data. Tom Corbett provided a brief but helpful tour of the Lead Creek property in 1996. We appreciate the insight provided by Rainer Newberry during examination of the core regarding the likely replacement origin of the mineralization. We also thank the staff of the Geochronology Laboratory of the University of British Columbia for their assistance with the analyses reported here. Melanie Hopkins contributed invaluable help with illustrations. Careful reviews by Rainer Newberry and Jeanine Schmidt improved the manuscript.

References Cited

Aleinikoff, J.N., Farmer, G.L., Rye, R.O., and Nokleberg, W.J., 2000, Isotopic evidence for the sources of Cretaceous and Tertiary granitic rocks, east-central Alaska—implications for the tectonic evolution of the Yukon-Tanana terrane: Canadian Journal of Earth Sciences, v. 37, no. 6, p. 945–956.

Dusel-Bacon, Cynthia, Bressler, J.R., Takaoka, Hidetoshi, Mortensen, J.K., Oliver, D.H., Leventhal, J.S., Newberry, R.J., and Bundtzen, T.K., 1998, Stratiform zinc-lead mineralization in Nasina assemblage rocks of the Yukon-Tanana Upland in east-central Alaska: U.S. Geological Survey Open-File Report 98–340 [URL http://geopubs.wr.usgs.gov/open-file/of98-340/].

Dusel-Bacon, Cynthia, Lanphere, M.A., Sharp, W.D., Layer, P.W., and Hansen, V.L., 2002, Mesozoic thermal history and timing of structural events for the Yukon-Tanana Upland, east-central Alaska—$^{40}Ar/^{39}Ar$ data from metamorphic and plutonic rocks: Canadian Journal of Earth Sciences, v. 39, no. 6, p. 1013–1051.

Foster, H.L., 1976, Geologic map of the Eagle quadrangle, Alaska: U.S. Geological Survey Miscellaneous Investigations Series Map I–922, scale 1:250,000.

———1992, Geologic map of the eastern Yukon-Tanana Region, Alaska: USGS Open-File Report 92–313, 26 p., scale 1:500,000.

Foster, H.L., and Clark, S.H.B., 1970, Geochemical and geologic reconnaissance of a part of the Fortymile area, Alaska: U.S. Geological Survey Bulletin 1312–M, 29 p.

Foster, H.L., and Keith, T.E.C., 1969, Geology along the Taylor Highway, Alaska: U.S. Geological Survey Bulletin 1281, 36 p., scale 1:25,000.

Foster, H.L., Keith, T.E.C., and Menzie, W.D., 1994, Geology of the Yukon-Tanana area of east-central Alaska, *in* Plafker, George, and Berg, H.C., eds., The geology of Alaska, v. G–1 *of* The geology of North America: Boulder, Colo., Geological Society of America, p. 205–240.

Godwin, C.I., and Sinclair, A.J., 1982, Average lead isotope growth curves for shale-hosted zinc-lead deposits, Canadian Cordillera: Economic Geology, v. 77, no. 3, p. 675–690.

Hunt, J.A., 1997, Massive sulphide deposits in the Yukon-Tanana and adjacent terranes, *in* Yukon exploration and geology, 1996: Whitehorse, Yukon Territory, Canada, Department of Indian and Northern Affairs, Exploration and Geological Services Division, p. 35–45.

Joyce, N.L., 2002, Geologic setting, nature and structural evolution of intrusion-hosted Au-bearing veins at the Longline occurrence, Moosehorn Range area, west-central Yukon Territory: Vancouver, University of British Columbia, M.Sc. thesis, 196 p.

Krogh, T.E., 1982, Improved accuracy of U-Pb zircon ages by the creation of more concordant systems using an air abrasion technique: Geochimica et Cosmochimica Acta, v. 46, no. 4, p. 637–649.

Mortensen, J.K., 1988, Geology of southwestern Dawson map area: Geological Survey of Canada Open-File 1927, scale 1: 250,000.

——1990, Geology and U-Pb geochronology of the Klondike District, west-central Yukon Territory: Canadian Journal of Earth Sciences, v. 27, no. 7, p. 903–914.

Mortensen, J.K., Ghosh, D., and Ferri, F., 1995, U-Pb age constraints of intrusive rocks associated with copper-gold porphyry deposits in the Canadian Cordillera, *in* Schroeter, T.G., ed., Porphyry deposits of the northwestern Cordillera of North America: Canadian Institute of Mining and Metallurgy Special Volume 46, p. 142–158.

Roddick, J.C., 1987, Generalized numerical error analysis with application to geochronology and thermodynamics: Geochimica et Cosmochimica Acta, v. 51, no. 8, p. 2129-2135.

Schmidt, J.M., 1997, Shale-hosted Zn-Pb-Ag and barite deposits of Alaska, *in* Goldfarb, R.J., and Miller, L.D., eds., Mineral deposits of Alaska: Economic Geology Monograph 9, p. 35–65.

Stacey, J.S., and Kramer, J.D., 1975, Approximation of terrestrial lead isotope evolution by a two-stage model: Earth and Planetary Science Letters, v. 26, no. 2, p. 207–221.

Steiger, R.H. and Jäger, Emilie, 1977, Subcommission on geochronology convention on the use of decay constants in geo- and cosmochronology: Earth and Planetary Science Letters, v. 36, no. 3, p. 359–362.

U.S. Bureau of Mines, 1995, Final report of the mineral resource evaluation of the Bureau of Land Management Black River and Fortymile River subunits: U.S. Bureau of Mines Open File Report 79–95, 226 p.

Ventures Resource Corp., 2001, Quarterly Report, September 30th, 2001: URL http://www.venturesresource.com/quarterly_reports/Q3-01.pdf.

Werdon, M.B., Newberry, R.J., Szumigala, D.J., and Pinney, D.S., 2001, Geologic map of the Eagle A–2 quadrangle, Fortymile Mining District, Alaska: Alaska Division of Geological and Geophysical Surveys Preliminary Interpretive Report 2001–3a, scale 1:63,360.

WGM, Inc., 1979, 1978 Annual progress report on the Lead Creek prospect: Anchorage, Alaska, prepared for Doyon Ltd., 25 p.

——2001, 2000 Annual progress report on the Champion property, Alaska: Anchorage, Alaska, prepared for Doyon Ltd. on behalf of Ventures Resource Corp., 46 p.

Wheeler, J.O., and McFeely, Patricia, 1991, Tectonic assemblage map of the Canadian Cordillera and adjacent parts of the United States of America: Geological Survey of Canada Map 1712A, scale 1:2,000,000.

Studies by the U.S. Geological Survey in Alaska, 2001
U.S. Geological Survey Professional Paper 1678

A Cretaceous Ion-Microprobe U-Pb Zircon Age for the West Point Orthogneiss: Evidence for Another Gneiss Dome in the Yukon-Tanana Upland

By Cynthia Dusel-Bacon, Joseph L. Wooden, and Paul W. Layer

Abstract

We report a new ion-microprobe U-Pb zircon age of 111±2 Ma for the Orthogneiss unit of the West Point Complex (informally referred to as the West Point orthogneiss), which we interpret as the time of its igneous crystallization. Our age was determined by spot analyses of clear euhedral rims on individual zircon crystals whose faceted habit and, in some crystals, oscillatory zoning are consistent with a magmatic origin. Spot analyses of darker cores within individual zircons yielded a large population with ages of approximately 375±8 Ma and smaller populations with ages of approximately 1.1, 1.4, 1.8, and 2.6 Ga. We interpret these older cores as zircons entrained in melt derived from typical Paleozoic basement of the Yukon-Tanana Upland, which contains middle Paleozoic metaigneous rocks and abundant Precambrian inheritance in both the metaigneous and metasedimentary rocks. Our data indicate that a previously determined conventional U-Pb zircon analysis of a sample from the West Point orthogneiss that gave an upper-intercept age of 671±34 Ma actually averaged several distinct isotopic populations and thus gave a geologically meaningless age. We also determined an ion-microprobe U-Pb zircon age of 355±4 Ma for augen gneiss from the margin of the West Point Complex; this sample represents an intrusive event that probably is the source of some of the middle Paleozoic inherited zircon cores in the sample of West Point orthogneiss.

An undeformed granitic rock that crosscuts the metamorphic fabric of the sillimanite gneiss dome of the Salcha River, 30 km to the southwest, gives a preferred ion-microprobe U-Pb zircon age of 113±2 Ma. Similarities between this dome and the West Point Complex, in terms of protoliths, map scale, and proposed structural contact of the high-grade rocks with overlying greenschist-facies rocks, suggest that the West Point area is also a gneiss dome. Our new U-Pb zircon ages, together with other U-Pb and $^{40}Ar/^{39}Ar$ studies in the Yukon-Tanana Upland, indicate that mid-Cretaceous (synmetamorphic?) intrusion, metamorphism, and posttectonic intrusion all occurred within a narrow timespan. If our interpretations of mid-Cretaceous samples and their U-Pb zircon ages are correct, the maximum igneous-crystallization age of the West Point orthogneiss and the minimum igneous-crystallization age of the posttectonic Salcha River intrusion together imply that the mid-Cretaceous metamorphic episode occurred between 113 and 111 Ma.

Introduction

Amphibolite-facies metasedimentary and metaigneous rocks of continental affinity compose much of the Yukon-Tanana terrane in east-central Alaska (fig. 1). In the northern part of the Big Delta quadrangle, a 600-km^2 circular area of sillimanite gneiss, with subordinate felsic dikes, quartzite, marble, and amphibolite, forms the sillimanite gneiss dome of the Salcha River (figs. 1, 2; Dusel-Bacon and Foster, 1983). This gneissic body was subsequently referred to as the Salcha River Dome by Pavlis and others (1993) and as the Salcha River gneiss dome by Dusel-Bacon and others (2002), whose terminology we hereinafter adopt. Pavlis and others postulated that the Salcha River gneiss dome was exhumed during late Early Cretaceous regional extension. Another nearly circular, ~150-km^2 area of high-grade gneiss and metasedimentary rocks, the main subject of this chapter, crops out approximately 75 km northeast of the center of the Salcha River gneiss dome, in a topographically high area that includes 5,865-ft-high West Point peak (figs. 1, 2). This complex, referred to as the West Point Complex by Smith and others (1994), consists of peraluminous granitic orthogneiss, sillimanite gneiss, quartzite, and marble. The peraluminous orthogneiss (Orthogneiss unit of the West Point Complex of Smith and others, 1994; hereinafter referred to as the West Point orthogneiss) lies in the core of a metaigneous and high-grade metamorphic complex in the northeastern part of the Big Delta quadrangle that forms the core of an east-west-trending antiform (Smith and others, 1994).

Medium-grained biotite-muscovite granitic orthogneiss from the core of the West Point Complex was previously sampled for U-Pb zircon dating in 1983 during an Alaska Division of Geological and Geophysical Surveys mapping project in the upper Chena River area (Smith and others, 1994). Ther-

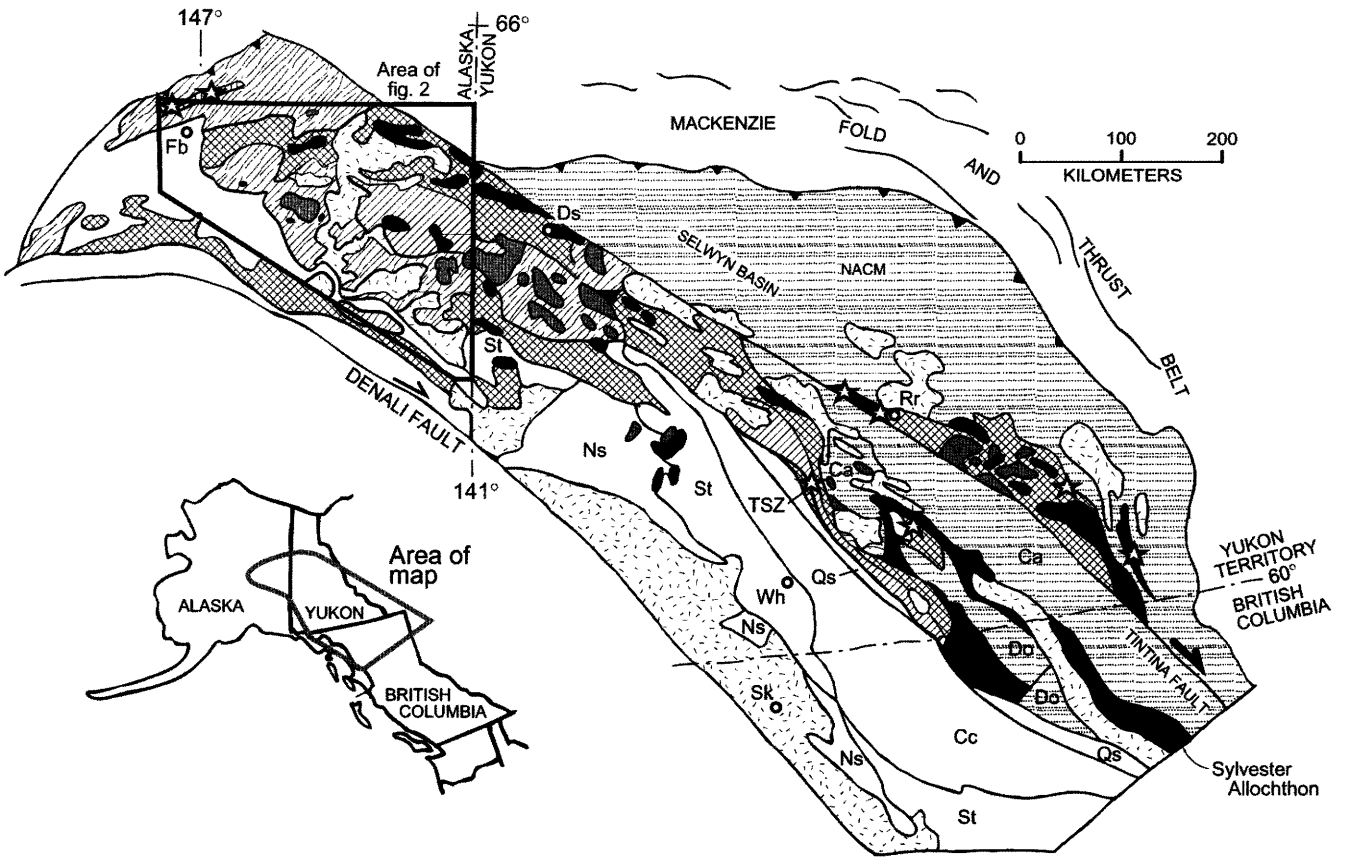

EXPLANATION

Overthrust belt

- Cretaceous granite
- Seventymile-Slide Mountain terrane–Oceanic crust
- Chatanika assemblage of Hansen and Dusel-Bacon (1998)–Eclogite, marble, and pelitic schist (marginal basin?)
- Teslin-Taylor Mountain (Fortymile River assemblage of Dusel-Bacon and others, 2002)–Mafic to intermediate-composition schist, gneiss, marble, quartzite, and Triassic and Early Jurassic granitoids (arc and marginal basin)
- Nisutlin assemblage of Hansen and Dusel-Bacon (1998)–Varyingly carbonaceous and siliceous metasedimentary rocks and Devonian, Mississippian, and Permian metavolcanic rocks (marginal basin)

Underthrust belt

- Orthogneiss assemblage–Quartzite, pelitic schist, amphibolite, and orthogneiss, including Devonian and Mississippian augen gneiss (gray) (parautochthonous North American continental margin)
- Inboard, parautochthonous terranes and the North American continental margin (NACM)
- Outboard, allochthonous terranes
- ☆ Eclogite and blueschist (Erdmer and others, 1998)

Figure 1. Simplified terrane and tectonic assemblage map of northern Canadian and the Alaskan Cordillera (modified from Hansen and others, 1991, and Dusel-Bacon and Cooper, 1999). Towns (circles): Ds, Dawson; Fb, Fairbanks; Rr, Ross River; Sk, Skagway; Wh, Whitehorse. Terranes: Ca, Cassiar; Cc, Cache Creek; Do, Dorsey; Ns, Nisling; Qs, Quenellia; St, Stikinia. Unlabeled area surrounding Fairbanks is alluvium of the Tanana River Valley; unlabeled area adjacent to north side of the Denali Fault in Alaska comprises various terranes not discussed in this chapter. Tertiary granitoids not shown. The Yukon-Tanana Upland physiographic province in Alaska includes all the area north of the Tanana River Valley; units above that are included in the broadly defined "Yukon-Tanana terrane" are the Chatinika assemblage of Hansen and Dusel-Bacon (1998; equivalent to unit ec of Foster and others, 1994), the Fortymile River assemblage of Dusel-Bacon and others (2002), the Nisutlin assemblage of Hansen and Dusel-Bacon (1998), and the orthogneiss assemblage of Hansen and Dusel-Bacon (1998).

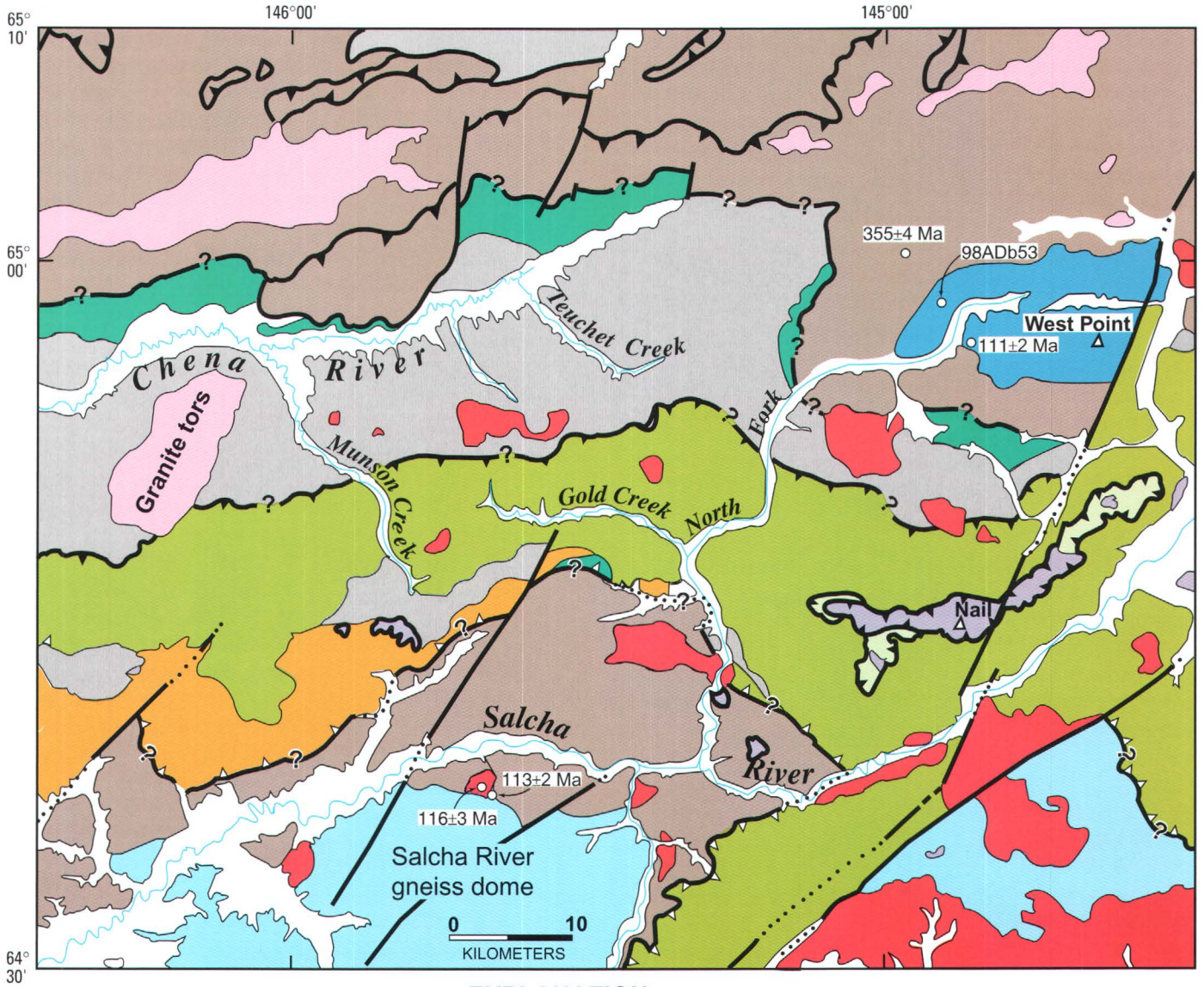

EXPLANATION

- Surficial deposits (Quaternary)
- Postmetamorphic granitoids (Tertiary and Cretaceous)

STRUCTURALLY HIGHER ROCKS

- Peridotite (purple), greenstone, metalimestone, metachert, and metasedimentary rocks (Triassic, Permian, and Mississippian–Seventymile terrane)
- Greenschist-facies semischist, phyllite, quartzite, marble, and greenstone (Mississippian and Devonian)–Butte subterrane of the Yukon-Tanana terrane of Pavlis and others (1993)
- Greenschist-facies quartzofeldspathic mylonite schist and gneiss (Mississippian and Devonian)

STRUCTURALLY LOWER ROCKS

- Greenschist-facies carbonaceous quartzite and phyllite and felsic and mafic metavolcanic rocks (Mississippian and Devonian)–Nasina assemblage of Wheeler and McFeely (1991)
- Amphibolite-facies calcareous phyllite and marble
- Amphibolite-facies peltic schist, quartzite, marble, and amphibolite
- Amphibolite-facies sillimanite gneiss, quartzite, and marble
- Amphibolite-facies quartzite, marble, pelitic schist, and orthogneiss–West Point Complex of Smith and others (1994)

- Contact
- Fault; dotted where concealed
- Thrust fault; sawteeth on upper plate, queried where uncertain
- Low-angle normal fault; sawteeth on upper plate, dotted where concealed, queried where uncertain
- ○ Sample site
- △ Named Peak

Figure 2. Geologic map of the northern part of the Big Delta quadrangle (south of lat 65° N.) and the southern Circle quadrangle (north of lat 65° N.) (modified from Weber and others, 1978, and Foster, 1992, respectively), showing locations of sample sites discussed in text.

mal-ionization mass-spectrometric (TIMS) analyses of five multigrain zircon fractions yielded a highly discordant array. A discordia chord plotted through the array gave an upper-intercept age of 671±34 Ma (Late Proterozoic) that Smith and others interpreted as the time of igneous crystallization of the orthogneiss; they concluded that the metapelitic and metapsammitic wallrocks, which they correlated with the Fairbanks schist unit of Robinson and others (1990), had a Late Proterozoic minimum depositional age. Monazite separated from the orthogneiss that yielded the Late Proterozoic upper-intercept age gave a concordant U-Pb age of 115 Ma (Smith and others, 1994).

Owing to the importance of the Late Proterozoic crystallization age proposed for the granitic orthogneiss (which led Smith and others, 1994, to designate the entire West Point Complex and adjacent quartzite-dominant basement rocks as Precambrian) and the high degree of Pb loss reflected in the extreme discordance of the U-Pb zircon data, we resampled the orthogneiss at the same locality as the previously collected sample. Because of the possible presence of inherited, xenocrystic cores within igneous zircons, this second collection of zircons was dated by using the sensitive high-resolution ion microprobe (SHRIMP) that analyzes ~30-μm-diameter areas, resulting in ages for both inherited cores and magmatic rims. In addition to redating the orthogneiss, we carried out SHRIMP U-Pb geochronology on a sample of augen gneiss that intrudes the pelitic schist unit flanking the orthogneiss core of the West Point Complex, as well as on a granitic sample from a postkinematic granitoid body that intrudes the Salcha River gneiss dome to the southwest. To address the cooling history of the West Point orthogneiss, we also determined $^{40}Ar/^{39}Ar$ ages for biotite and white mica from the same sample as that used for U-Pb geochronology.

Regional Tectonic Framework

The Yukon-Tanana Upland of east-central Alaska and the Yukon Territory, Canada (fig. 1), consists of thrust sheets of ductilely deformed metasedimentary and metaigneous assemblages of uncertain age and origin that are overlain by klippen of weakly metamorphosed oceanic rocks of the Seventymile-Slide Mountain terrane and are intruded by postkinematic Early Jurassic, Cretaceous, and Tertiary granitoids (Foster and others, 1994). The ductilely deformed metamorphic assemblages have commonly been referred to as the Yukon-Tanana terrane (for example, Coney and others, 1980; Mortensen, 1992), a term used to collectively describe the broad band of heterogeneous metamorphic assemblages that lies between the right-lateral Denali and Tintina Fault zones in east-central Alaska and the Yukon Territory (fig. 1). A flap of this heterogeneous province has been dextrally offset by approximately 450 km along the Tintina Fault and now lies northeast of the fault. Several studies (for example, Churkin and others, 1982; Foster and others, 1985; Aleinikoff and others, 1987; Hansen, 1990) have shown that these assemblages have different geologic histories.

On the basis of protolith assemblages and pluton distribution, structural and kinematic data, metamorphic pressure-temperature data, and metamorphic-cooling ages, the following tectonic history has been proposed (Hansen and others, 1991; Dusel-Bacon and others, 1995, 2002; Hansen and Dusel-Bacon, 1998). Upper-plate assemblages—peridotite, greenstone, and Mississippian to Triassic metasedimentary rocks of the Seventymile terrane; eclogitic rocks of the Chatinika assemblage (terminology of Hansen and Dusel-Bacon, 1998; equivalent to unit ec of Foster and others, 1994) of the Yukon-Tanana terrane; and amphibolite-facies gneiss, amphibolite, marble, and metachert of the Fortymile River assemblage of Dusel-Bacon and others (2002)—were affected by pre-Jurassic, northeastward-directed, apparent margin-normal crustal contraction, interpreted to have occurred during west-dipping subduction before their emplacement onto lower-plate continental-margin rocks (including Paleozoic protoliths of the West Point Complex). Greenschist-facies siliciclastic and volcanic rocks (Nisutlin terrane, fig. 1) occur at intermediate structural levels. The association of rocks of the Nisutlin terrane with oceanic rocks of the Seventymile terrane, and the fact that Late Triassic and Early Jurassic granitoids intrude both the Fortymile River assemblage and the Nisutlin terrane in the eastern Yukon-Tanana Upland but are absent in lower-plate assemblages, suggest an allochthonous origin for the Nisutlin terrane as well. Amphibolite-facies marginal-basin schist, gneiss, and quartzite of continental affinity and peraluminous to metaluminous Devonian and Mississippian orthogneiss, commonly augen gneiss, that occur at the lowest structural level—the Lake George assemblage of Dusel-Bacon and Cooper (1999), the Chena River sequence of Smith and others (1994), and the Fairbanks schist unit—are interpreted to be parautochthonous to the early to middle Paleozoic continental margin of North America. Early and Middle Jurassic (>188–185 Ma) northwestward-directed, apparent margin-parallel crustal contraction and imbrication resulted in crustal thickening and tectonic burial of lower-plate assemblages and a northwestward-vergent penetrative fabric shared by both upper- and lower-plate assemblages. Subsequent Early Cretaceous (135–110 Ma) tectonism was widespread throughout the Yukon-Tanana Upland. In some areas, particularly in the eastern part of the upland and bordering the Salcha River gneiss dome, Early Cretaceous cooling appears to have accompanied southeastward-directed crustal extension that resulted in exposure of the structurally deepest parautochthonous continental rocks (Hansen and others, 1991; Pavlis and others, 1993; Hansen and Dusel-Bacon, 1998). In other areas, however, such as in the southeastern part of the Big Delta quadrangle, Early Cretaceous metamorphic cooling ages are not associated with southeastward-vergent deformation, and so the Early Cretaceous tectonism in those areas may have resulted from crustal contraction rather than extension (Day and others, 2002; Dusel-Bacon and others, 2002).

Local Geology

The gneiss, quartzite, and marble in the core of the West Point Complex are successively overlain by (1) a unit of amphibolite-facies pelitic schist, quartzite, marble, amphibolite, and small bodies and sills (3-m-thick concordant layers) of augen gneiss; (2) calcareous phyllite and marble; and (3) varyingly carbonaceous, siliceous, and calcareous quartzite and phyllite and minor felsic and mafic greenschist-facies metavolcanic rocks (fig. 2; Weber and others, 1978; Smith and others, 1994). Metamorphic grade in the amphibolite-facies rocks ranges from the staurolite zone to the sillimanite zone (Dusel-Bacon and others, 1989, 1993). In the southeastern part of the Circle quadrangle, the maximum metamorphic grade appears to be close to the muscovite+quartz=sillimanite+K-feldspar+water isograd (Foster and others, 1983), indicating peak temperatures of about 600–650°C (Chatterjee and Johannes, 1974). A sample of augen gneiss from a small body that intrudes the northern margin of the pelitic schist unit north of the headwaters of the Salcha River along the north flank of the West Point Complex yielded a conventional (TIMS) U-Pb zircon age of approximately 340 Ma (Foster and others, 1987). This age, interpreted as the approximate igneous-crystallization age of the augen gneiss, is the upper-intercept age of a discordia line drawn through two fine-grained zircon fractions and slightly above a third fine-grained fraction. This stratigraphic sequence in the greater West Point area is nearly the same as that overlying the sillimanite gneiss unit of the Salcha River gneiss dome. A greenschist-facies semischist unit (noncarbonaceous part of the Nisutlin assemblage of Hansen and Dusel-Bacon, 1998; referred to as the Butte subterrane of the Yukon-Tanana terrane by Pavlis and others, 1993, and hereinafter as the Butte assemblage) overlies both high-grade areas along a poorly exposed contact interpreted as a low-angle fault, but the sense of motion along the fault is open to speculation (Dusel-Bacon and others, 1993; Pavlis and others, 1993; Foster and others, 1994; Smith and others, 1994).

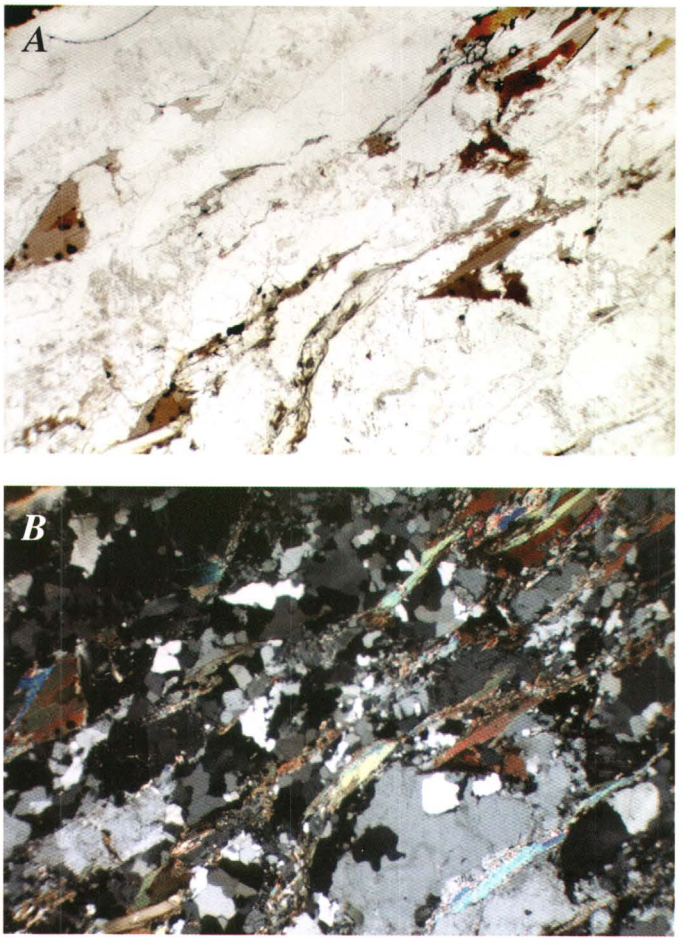

Figure 3. Photomicrograph of sample 96ADb10A of West Point orthogneiss (tables 1-4) taken with transmitted light (*A*) and crossed polars (*B*). Note alignment of thin biotite and muscovite grains; in figure 3*B*, muscovite is yellow, green, and pink, biotite is brown, K-feldspar is light gray, and quartz is black or white, depending on orientation of quartz grains.

Geochronology

Description of Geochronology Samples

Sample 96ADb10A (tables 1–4) is a quartz–K-feldspar–plagioclase–muscovite–biotite orthogneiss. The moderately well developed foliation is defined by aligned micas and elongate feldspar grains (fig. 3). Quartz grains are primarily annealed, with only weak undulatory extinction and lattice preferred orientation, suggesting that recrystallization of quartz outlasted most of the deformation. No evidence of retrograde metamorphism was observed. Trace amounts of apatite, chlorite, zircon, titanite, and Fe-Ti oxides are present. The sample was collected from one of the large blocks of homogeneous orthogneiss rubble that make up one of the steep peaks, along a glaciated ridge west of West Point (fig. 2). To ensure that we sampled the same rock which had previously yielded the highly discordant TIMS U-Pb zircon upper-intercept age of 671±34 Ma, the first author obtained a hand specimen from the exact site of the previously sampled rock.

Sample 98ADb55B (tables 1, 4) is a quartz-biotite-microcline-plagioclase augen gneiss. Although the gneiss has a well-developed foliation, petrographic examination reveals that the quartz forms sub-millimeter-thick layers (parallel to foliation) and exhibits straight grain boundaries and uniform extinction, indicating annealing. The sample was collected from a large block below an outcrop of augen gneiss within the pelitic schist unit (fig. 2; Chena River sequence of Smith and others, 1994).

Sample 98ADb66B (tables 1, 4) is a hypidiomorphic-granular, medium-grained granite. K-feldspar is approximately equal in abundance to plagioclase; the rock contains minor biotite, some of which has been altered to chlorite, and trace amounts of Fe-Ti oxides. No alignment of mica or feldspars was observed to suggest foliation. The only evidence of deformation is quartz straining, manifested as patchy to undulose extinction. The sample was collected from an ~70-cm-thick granitic dike that crosscuts the foliation of sillimanite gneiss at the northern

Table 1. U-Pb geochronologic data for (meta)igneous rocks of the West Point Complex and Salcha River gneiss dome.

[All ages in millions of years. Spot analyses are listed in order of increasing $^{206}Pb/^{238}U$ age. cr, correction for common Pb by either ^{204}Pb or ^{207}Pb method, as indicated; err corr, error correction; r (after isotope number), radiogenic]

Spot name	Spot position	U (ppm)	Th (ppm)	$^{232}Th/^{238}U$ ratio	^{207}Pb-cr $^{206}Pb/^{238}U$ age	1σ age	^{204}Pb-cr $^{206}Pb/^{238}U$ age	1σ age	^{204}Pb-cr $^{207}Pb/^{235}U$ age	1σ age	^{204}Pb-cr $^{207}Pb/^{206}Pb$ age	1σ age	^{207}Pb-cr ^{206}Pb-r/^{238}U ratio	1σ	Total $^{238}U/^{206}Pb$ ratio	1σ	Total $^{207}Pb/^{206}Pb$ ratio	Error (pct)	^{204}Pb-cr $^{238}U/^{206}Pb$-r	Error (pct)	^{204}Pb-cr ^{207}Pb-r/^{206}Pb-r	Error (pct)	^{204}Pb-cr ^{207}Pb-r/^{235}U	Error (pct)	^{204}Pb-cr ^{206}Pb-r/^{238}U	Error (pct)	err corr
Sample 96ADb10A																											
10—7.1	r	759	703	0.96	101.5	1.6	100.1	1.7	77.6	14.0	——	——	0.0159	0.0002	62.28	1.5	0.0570	2.6	63.88	1.7	0.0368	18.8	0.079	18.9	0.0157	1.7	0.092
10—9.1	r	775	68	.09	104.8	1.6	105.2	1.6	111.8	2.9	——	——	.0164	.0003	60.79	1.5	.0513	2.3	60.79	1.5	.0513	2.3	.116	2.8	.0165	1.5	.552
10—1.1	r	1,448	211	.15	110.0	1.6	109.8	1.6	106.8	2.7	——	——	.0172	.0002	57.98	1.4	.0496	1.6	58.19	1.4	.0468	2.2	.111	2.6	.0172	1.4	.543
10—4.1	r	1,278	102	.08	110.5	1.6	109.9	1.6	100.0	4.9	——	——	.0173	.0003	57.73	1.5	.0497	1.7	58.17	1.5	.0437	5.0	.104	5.2	.0172	1.5	.284
10—5.1	r	1,434	153	.11	110.0	1.6	110.2	1.6	112.7	3.5	——	——	.0172	.0002	58.16	1.4	.0475	1.7	58.02	1.5	.0494	3.0	.117	3.3	.0172	1.5	.438
10—2.1	r	1,322	246	.19	112.2	1.6	111.2	1.6	96.4	2.6	——	——	.0176	.0003	57.13	1.4	.0461	2.2	57.46	1.4	.0415	2.5	.100	2.9	.0174	1.4	.501
10—8.1	r	1,114	68	.06	111.5	1.8	111.4	1.8	111.0	5.4	——	——	.0174	.0003	57.22	1.6	.0498	1.9	57.35	1.6	.0480	4.9	.116	5.1	.0174	1.6	.312
10—3.1	r	5,387	67	.01	114.1	1.6	113.8	1.5	109.1	2.1	——	——	.0179	.0002	56.02	1.4	.0480	.8	56.15	1.4	.0462	1.6	.113	2.1	.0178	1.4	.661
10—26.1	r	3,019	651	.22	115.1	1.6	114.9	1.6	112.6	2.0	——	——	.0180	.0002	55.55	1.4	.0478	.8	55.58	1.4	.0473	1.2	.117	1.8	.0180	1.4	.749
10—33.1	r	7,064	235	.03	121.4	1.6	121.3	1.6	120.1	2.1	——	——	.0190	.0003	52.59	1.4	.0485	1.1	52.63	1.4	.0479	1.3	.126	1.9	.0190	1.4	.727
10—10.1	r	5,339	176	.03	121.7	1.7	121.5	1.7	118.8	2.0	——	——	.0191	.0003	52.49	1.4	.0480	.8	52.54	1.4	.0473	1.2	.124	1.8	.0190	1.4	.755
10—31.1	r	7,771	132	.02	125.9	1.7	125.9	1.7	124.7	1.8	——	——	.0197	.0003	50.70	1.4	.0485	.5	50.72	1.4	.0481	.7	.131	1.5	.0197	1.4	.891
10—6.1	r	5,721	532	.10	128.8	1.7	128.7	1.7	126.4	2.0	——	——	.0202	.0003	49.51	1.4	.0492	.7	49.61	1.4	.0477	.9	.133	1.6	.0202	1.4	.829
10—5.2	c	1,317	75	.06	219.1	3.1	222.3	3.1	266.5	5.1	——	——	.0346	.0005	28.46	1.4	.0633	1.2	28.51	1.4	.0620	1.6	.300	2.2	.0351	1.4	.655
10—30.1	c	1,722	591	.35	267.3	3.7	267.7	3.6	272.7	4.1	——	——	.0423	.0006	23.57	1.4	.0530	.7	23.58	1.4	.0527	1.0	.308	1.7	.0424	1.4	.800
10—8.2	c	729	161	.23	304.6	4.8	304.4	4.7	301.5	7.8	——	——	.0484	.0008	20.63	1.6	.0540	1.4	20.68	1.6	.0519	2.5	.346	3.0	.0484	1.6	.531
10—1.2	c	719	269	.39	327.0	4.6	326.3	4.5	317.2	5.7	——	——	.0520	.0008	19.18	1.4	.0545	1.2	19.26	1.4	.0512	1.5	.367	2.1	.0519	1.4	.679
10—23.2	r	445	116	.27	338.7	5.3	339.0	5.2	343.3	7.6	——	——	.0539	.0009	18.52	1.6	.0542	2.1	18.52	1.6	.0540	2.1	.402	2.6	.0540	1.6	.600
10—25.1	c	218	102	.48	353.6	5.4	353.8	5.5	355.8	15.8	——	——	.0564	.0009	17.68	1.6	.0559	1.8	17.73	1.6	.0540	5.1	.420	5.3	.0564	1.6	.300
10—32.1	r	947	344	.38	354.8	4.9	355.1	4.8	359.2	4.8	——	——	.0566	.0008	17.66	1.4	.0541	.8	17.66	1.4	.0543	.8	.424	1.6	.0566	1.4	.868
10—28.1	c	1,586	476	.31	361.3	4.9	361.1	4.8	358.6	4.8	——	——	.0577	.0008	17.33	1.4	.0543	.6	17.35	1.4	.0533	.8	.424	1.6	.0576	1.4	.863
10—24.1	c	590	230	.40	362.4	5.1	362.3	5.0	360.7	7.7	——	——	.0578	.0008	17.26	1.4	.0551	1.0	17.30	1.4	.0535	2.1	.427	2.6	.0578	1.4	.559
10—34.1	r	1,729	547	.33	370.5	5.0	370.5	5.0	370.4	7.0	——	——	.0592	.0008	16.88	1.4	.0552	1.5	16.90	1.4	.0540	1.8	.440	2.3	.0592	1.4	.611
10—29.1	c	227	167	.76	371.9	5.7	371.4	5.6	364.8	8.3	——	——	.0594	.0009	16.81	1.5	.0555	1.6	16.86	1.5	.0529	2.3	.432	2.7	.0593	1.5	.566
10—12.1	c	650	259	.41	374.1	5.6	372.1	5.5	346.9	7.1	——	——	.0597	.0009	16.76	1.5	.0529	1.7	16.83	1.5	.0497	1.9	.407	2.4	.0594	1.5	.626
10—6.2	c	529	300	.59	378.2	5.4	377.3	5.4	365.4	10.3	——	——	.0604	.0009	16.55	1.5	.0540	1.4	16.59	1.5	.0521	3.0	.433	3.4	.0603	1.5	.435
10—21.1	c	148	67	.47	383.6	7.3	382.5	7.2	368.8	18.2	——	——	.0613	.0012	16.27	1.9	.0562	3.4	16.36	1.9	.0520	5.6	.438	5.9	.0611	1.9	.326
10—22.1	c	1,517	475	.32	387.8	5.4	387.0	5.3	376.5	5.7	——	——	.0620	.0009	16.12	1.4	.0548	1.1	16.16	1.4	.0526	1.1	.449	1.8	.0619	1.4	.785
10—23.1	c	896	496	.57	391.7	5.6	390.9	5.6	380.5	11.8	——	——	.0626	.0009	15.95	1.5	.0551	1.3	16.00	1.5	.0528	3.4	.455	3.7	.0625	1.5	.392
10—16.1	c	791	862	1.13	401.5	6.1	401.3	6.0	399.1	7.5	——	——	.0643	.0010	15.55	1.5	.0552	1.5	15.57	1.5	.0544	1.7	.481	2.3	.0642	1.5	.675
10—2.2	c	1,236	779	.65	402.5	5.6	407.5	5.6	467.0	7.9	771	33.4	.0644	.0009	15.30	1.4	.0660	.8	15.33	1.4	.0649	1.6	.584	2.1	.0653	1.4	.663
10—27.1	c	493	77	.16	450.9	6.4	488.4	6.8	849.1	9.8	1,964	16.4	.0725	.0011	12.68	1.4	.1221	.8	12.71	1.4	.1205	.9	1.308	1.7	.0787	1.4	.843
10—20.1	c	526	265	.52	469.8	7.3	487.9	8.1	678.5	30.4	1,376	115.2	.0756	.0012	12.35	1.6	.1102	1.2	12.72	1.7	.0877	6.0	.951	6.2	.0786	1.7	.275
10—15.1	c	530	148	.29	743.5	10.8	845.9	11.7	1,481.1	12.7	2,564	12.0	.1223	.0019	7.13	1.5	.1713	.7	7.13	1.5	.1707	.7	3.300	1.6	.1402	1.5	.900
10—14.1	c	33	13	.41	825.3	22.7	872.1	22.9	1,206.1	30.3	1,866	60.4	.1366	.0040	6.90	2.8	.1141	3.3	6.90	2.8	.1141	3.3	2.280	4.4	.1449	2.8	.642
10—17.1	c	306	79	.27	1,088.7	19.3	1,067.8	15.5	905.7	87.3	——	——	.1840	.0035	5.52	1.6	.0629	13.4	5.55	1.6	.0580	15.1	1.440	15.2	.1802	1.6	.103
10—3.2	c	80	59	.76	1,179.8	20.1	1,178.8	19.1	1,172.8	18.9	1,162	41.6	.2008	.0038	4.97	1.8	.0806	1.7	4.98	1.8	.0786	2.1	2.174	2.7	.2007	1.8	.645
10—11.1	c	245	122	.52	1,691.4	25.9	1,704.6	23.6	1,757.7	16.5	1,821	22.0	.3000	.0052	3.30	1.6	.1128	.9	3.30	1.6	.1113	1.2	4.646	2.0	.3027	1.6	.792
10—13.1	c	65	39	.62	1,877.2	38.6	1,875.7	33.9	1,870.0	24.6	1,864	36.9	.3380	.0080	2.96	2.1	.1142	1.6	2.96	2.1	.1140	2.0	5.307	2.9	.3377	2.1	.714
10—4.2	c	65	17	.27	1,917.1	34.3	1,909.3	30.0	1,882.2	22.0	1,852	33.5	.3464	.0072	2.89	1.8	.1161	1.2	2.90	1.8	.1133	1.9	5.384	2.6	.3447	1.8	.700
10—19.1	c	189	131	.71	2,186.1	39.2	2,263.9	33.3	2,437.7	20.4	2,586	23.1	.4037	.0085	2.37	1.7	.1742	1.4	2.38	1.7	.1729	1.4	10.031	2.2	.4208	1.7	.784
10—18.1	c	92	88	.98	2,578.8	58.8	2,601.6	44.5	2,639.2	21.1	2,668	15.1	.4919	.0136	2.01	2.1	.1817	.9	2.01	2.1	.1817	.9	12.453	2.3	.4972	2.1	.916
Sample 98ADb55B																											
55B—6.1	—	708	70	0.10	173.1	2.4	173.5	2.4	178.4	4.1	——	——	0.0272	0.0004	36.59	1.4	0.0527	1.8	36.66	1.4	0.0511	2.1	0.192	2.5	0.0273	1.4	0.555
55B—9.1	—	4,776	963	.21	297.3	3.5	297.6	3.5	302.3	3.4	——	——	.0472	.0006	21.16	1.2	.0534	.5	21.16	1.2	.0532	.5	0.347	1.3	.0472	1.2	.917
55B—15.1	—	3,269	711	.22	302.9	3.6	303.1	3.6	306.0	3.6	——	——	.0481	.0006	20.75	1.2	.0537	.6	20.77	1.2	.0530	.6	0.352	1.4	.0481	1.2	.882
55B—19.1	—	2,308	470	.21	302.2	3.7	303.2	3.6	316.1	4.8	——	——	.0480	.0006	20.72	1.2	.0568	.7	20.77	1.2	.0550	1.3	0.365	1.8	.0482	1.2	.687
55B—14.1	—	1,411	307	.23	307.0	4.0	307.0	4.0	306.1	4.7	——	——	.0488	.0006	20.47	1.3	.0535	.8	20.50	1.3	.0523	1.2	0.352	1.8	.0488	1.3	.740

Table 1. U-Pb geochronologic data for (meta)igneous rocks of the West Point Complex and Salcha River gneiss dome—Continued

Spot name	Spot position	U (ppm)	Th (ppm)	$^{232}Th/^{238}U$ ratio	^{207}Pb-cr $^{206}Pb/^{238}U$ age	1σ	^{204}Pb-cr $^{206}Pb/^{238}U$ age	1σ	^{204}Pb-cr $^{207}Pb/^{235}U$ age	1σ	^{204}Pb-cr $^{207}Pb/^{206}Pb$ age	1σ	^{207}Pb-cr ^{206}Pb-r/^{238}U ratio	1σ	Total $^{238}U/^{206}Pb$ ratio	1σ	Total $^{207}Pb/^{206}Pb$ ratio	Error (pct)	^{204}Pb-cr $^{238}U/^{206}Pb$-r	Error (pct)	^{204}Pb-cr ^{207}Pb-r/^{206}Pb-r	Error (pct)	^{204}Pb-cr ^{207}Pb-r/^{235}U	Error (pct)	^{204}Pb-cr ^{206}Pb-r/^{238}U	Error (pct)	err corr
Sample 98ADb55B																											
55B—5.1	—	935	203	.22	312.6	3.9	313.0	3.8	318.1	5.9	——	——	.0497	.0006	20.04	1.3	.0561	1.0	20.10	1.3	.0536	1.8	0.368	2.2	.0498	1.3	.576
55B—12.1	—	2,307	651	.29	321.9	3.9	322.3	3.9	327.3	4.1	——	——	.0512	.0006	19.50	1.2	.0538	.8	19.50	1.2	.0538	.8	0.380	1.5	.0513	1.2	.838
55B—13.1	—	1,779	333	.19	328.1	4.1	328.3	4.1	330.8	4.1	——	——	.0522	.0007	19.13	1.3	.0538	.6	19.14	1.3	.0535	.7	0.385	1.5	.0522	1.3	.874
55B—16.1	—	2,900	550	.20	331.0	4.3	331.1	4.3	333.1	4.5	——	——	.0527	.0007	18.96	1.3	.0538	.8	18.97	1.3	.0534	.9	0.388	1.6	.0527	1.3	.821
55B—11.1	—	1,451	347	.25	333.8	4.1	333.6	4.0	331.7	4.9	——	——	.0531	.0007	18.80	1.2	.0540	.9	18.83	1.2	.0528	1.2	0.386	1.7	.0531	1.2	.712
55B—8.1	—	1,161	346	.31	338.1	4.2	337.9	4.1	335.5	4.8	——	——	.0539	.0007	18.57	1.2	.0533	1.0	18.58	1.2	.0528	1.1	0.392	1.7	.0538	1.2	.747
55B—17.1	—	770	111	.15	339.4	4.2	339.1	4.1	334.9	5.0	——	——	.0541	.0007	18.50	1.3	.0533	1.0	18.52	1.3	.0525	1.2	0.391	1.8	.0540	1.3	.713
55B—18.1	—	2,269	612	.28	344.1	4.1	344.1	4.1	344.4	4.0	——	——	.0548	.0007	18.24	1.2	.0534	.6	18.24	1.2	.0534	.6	0.404	1.4	.0548	1.2	.886
55B—7.1	—	706	254	.37	350.2	4.4	350.5	4.4	353.7	5.3	——	——	.0558	.0007	17.90	1.3	.0541	1.2	17.90	1.3	.0541	1.2	0.417	1.8	.0559	1.3	.717
55B—1.1	—	453	96	.22	353.4	4.6	352.7	4.5	343.8	9.5	——	——	.0563	.0007	17.72	1.3	.0546	1.5	17.78	1.3	.0520	3.0	0.403	3.3	.0562	1.3	.405
55B—20.1	—	206	221	1.11	353.4	5.1	354.1	5.0	363.2	8.3	——	——	.0563	.0008	17.72	1.5	.0546	2.2	17.71	1.5	.0552	2.3	0.430	2.7	.0565	1.5	.534
55B—3.1	—	586	218	.38	355.1	4.5	355.2	4.5	355.9	5.6	——	——	.0566	.0007	17.65	1.3	.0538	1.4	17.65	1.3	.0538	1.4	0.420	1.9	.0566	1.3	.690
55B—10.1	—	1,224	423	.36	357.2	4.3	356.9	4.3	352.9	4.4	——	——	.0570	.0007	17.55	1.2	.0538	.8	17.57	1.2	.0530	.8	0.416	1.5	.0569	1.2	.823
55B—4.1	—	385	213	.57	363.1	4.8	362.5	4.7	354.5	7.2	——	——	.0579	.0008	17.25	1.3	.0539	1.6	17.29	1.3	.0524	2.0	0.418	2.4	.0578	1.3	.556
55B—2.1	—	2,740	732	.28	369.9	4.4	369.7	4.4	367.5	4.2	——	——	.0591	.0007	16.94	1.2	.0538	.6	16.94	1.2	.0536	.6	0.436	1.4	.0590	1.2	.897
Sample 98ADb66B																											
66B–26.1	c	919	94	0.11	78.8	1.6	78.8	1.6	79.7	3.8	--	--	0.0123	0.0003	80.95	2.0	0.0514	3.0	81.29	2.0	0.0482	4.6	0.082	5.0	0.0123	2.0	0.409
66B–12.2	r	1,402	171	.13	95.6	1.8	95.6	1.8	94.6	3.3	--	--	.0149	.0003	66.71	1.9	.0505	1.8	66.97	1.9	.0474	3.2	.098	3.7	.0149	1.9	.517
66B–30.1	r	757	76	.10	95.2	1.9	95.7	1.9	103.8	3.5	--	--	.0149	.0003	66.73	2.0	.0539	2.4	66.87	2.0	.0522	2.9	.108	3.5	.0150	2.0	.568
66B–8.2	r	5,043	172	.04	99.9	1.8	99.8	1.8	97.9	2.0	--	--	.0156	.0003	64.03	1.8	.0479	.9	64.10	1.8	.0470	1.1	.101	2.1	.0156	1.8	.854
66B–12.1	c	1,307	58	.05	100.5	1.9	100.6	1.9	103.0	2.6	--	--	.0157	.0003	63.56	1.9	.0492	1.9	63.56	1.9	.0492	1.9	.107	2.7	.0157	1.9	.712
66B–16.1	r	588	20	.04	101.9	2.1	101.8	2.1	100.6	3.2	--	--	.0159	.0003	62.82	2.0	.0474	2.7	62.82	2.0	.0474	2.7	.104	3.4	.0159	2.0	.600
66B–22.1	c	495	47	.10	107.0	2.2	106.6	2.1	99.9	6.0	--	--	.0167	.0003	59.62	2.0	.0500	4.9	60.00	2.0	.0450	6.0	.103	6.3	.0167	2.0	.318
66B–13.1	c	465	46	.10	108.7	2.2	108.3	2.2	102.7	4.5	--	--	.0170	.0003	58.83	2.0	.0482	3.0	59.03	2.0	.0456	4.2	.106	4.6	.0169	2.0	.438
66B–17.1	r	3,926	158	.04	112.2	2.0	112.2	2.0	112.1	2.2	--	--	.0176	.0003	56.94	1.8	.0482	1.0	56.94	1.8	.0482	1.0	.117	2.1	.0176	1.8	.880
66B–2.1	r	2,418	96	.04	112.4	2.1	112.5	2.0	114.3	2.5	--	--	.0176	.0003	56.74	1.8	.0500	1.2	56.80	1.8	.0491	1.4	.119	2.3	.0176	1.8	.786
66B–15.1	c	755	95	.13	112.7	2.2	112.5	2.2	109.7	3.9	--	--	.0176	.0003	56.79	1.9	.0470	3.2	56.79	1.9	.0470	3.2	.114	3.8	.0176	1.9	.517
66B–18.1	c	314	49	.16	113.4	2.4	113.4	2.4	112.7	6.4	--	--	.0178	.0004	55.97	2.1	.0533	3.3	56.35	2.1	.0480	5.6	.117	6.0	.0177	2.1	.352
66B–20.1	c	811	89	.11	114.4	2.2	114.6	2.2	118.5	3.2	--	--	.0179	.0003	55.74	1.9	.0500	2.2	55.74	1.9	.0500	2.2	.124	2.9	.0179	1.9	.663
66B–22.2	r	3,274	124	.04	114.8	2.1	114.7	2.1	112.5	3.6	--	--	.0180	.0003	55.36	1.8	.0523	1.4	55.70	1.8	.0473	2.8	.117	3.4	.0180	1.8	.545
66B–5.1	r	508	50	.10	115.5	2.3	115.5	2.3	116.4	3.6	--	--	.0181	.0004	55.30	2.0	.0487	2.7	55.30	2.0	.0487	2.7	.122	3.3	.0181	2.0	.600
66B–7.1	r	3,528	121	.04	118.9	2.2	118.8	2.2	117.3	3.7	--	--	.0186	.0003	53.36	1.8	.0534	1.5	53.75	1.8	.0477	2.7	.122	3.3	.0186	1.8	.556
66B–23.1	c	631	38	.06	119.0	2.3	119.1	2.3	121.4	5.0	--	--	.0186	.0004	53.43	2.0	.0521	2.4	53.61	2.0	.0494	3.9	.127	4.4	.0187	2.0	.447
66B–20.2	r	992	125	.13	119.2	2.3	119.5	2.3	123.6	3.2	--	--	.0187	.0004	53.47	1.9	.0502	1.9	53.47	1.9	.0502	1.9	.129	2.7	.0187	1.9	.701
66B–24.2	r	1,910	37	.02	120.1	2.3	120.2	2.3	121.7	9.2	--	--	.0188	.0004	52.05	1.9	.0653	2.2	53.13	1.9	.0491	7.8	.127	8.0	.0188	1.9	.241
66B–11B	r	1,141	153	.14	120.0	2.6	120.4	2.8	126.7	29.9	--	--	.0188	.0004	48.53	1.9	.1184	5.9	53.03	2.3	.0511	25.4	.133	25.5	.0189	2.3	.092
66B–1.1	r	6,867	166	.03	122.2	2.2	122.2	2.2	120.9	3.1	--	--	.0191	--	51.83	1.8	.0546	1.1	52.28	1.8	.0479	2.1	.126	2.8	.0191	1.8	.656
66B–11	r	1,175	157	.14	120.9	6.9	119.9	8.1	--	--	--	--	.0189	.0011	39.27	2.9	.2525	11.5	53.27	6.8	--	--	--	--	.0188	6.8	--
66B–10.1	r	613	75	.13	125.6	2.5	125.1	2.4	117.1	4.3	--	--	.0197	.0004	50.92	2.0	.0472	2.6	51.04	2.0	.0453	3.3	.122	3.9	.0196	2.0	.507
66B–3.1	c	88	1	.01	120.2	6.5	106.5	23.7	--	--	--	--	.0188	.0010	14.50	2.1	.6271	1.3	60.02	22.5	--	--	--	--	.0167	22.5	--
66B–9.1	r	1,372	110	.08	138.9	2.6	139.6	2.6	150.3	3.8	--	--	.0218	.0004	45.60	1.9	.0541	1.7	45.67	1.9	.0529	1.9	.160	2.7	.0219	1.9	.701
66B–19.2	r	20,048	579	.03	170.6	3.0	170.9	3.0	174.8	3.0	--	--	.0268	.0005	37.20	1.8	.0513	.3	37.23	1.8	.0507	.4	.188	1.8	.0269	1.8	.976
66B–29.2	r	8,264	2,948	.37	223.7	4.3	223.8	5.9	224.4	63.2	--	--	.0353	.0007	19.94	1.8	.2874	.7	28.31	2.7	.0508	32.3	.247	32.4	.0353	2.7	.082
66B–6.1	c	358	312	.90	307.2	6.1	303.6	6.3	254.9	41.7	--	--	.0488	.0010	19.65	1.9	.0853	4.8	20.73	2.1	.0429	18.8	.285	18.9	.0482	2.1	.112
66B–28.1	c	4,875	1,234	.26	306.0	5.8	306.2	5.8	309.3	5.4	--	--	.0486	.0009	20.54	1.9	.0537	.5	20.56	1.9	.0531	0.6	.356	2.0	.0486	1.9	.950
66B–29.1	c	917	192	.22	357.4	6.8	357.0	6.7	352.1	12.2	--	--	.0570	.0011	17.40	1.9	.0601	1.8	17.56	1.9	.0528	3.7	.415	4.1	.0569	1.9	.467
66B–14.1	c	612	173	.29	601.9	11.4	627.1	13.4	858.9	63.2	--	--	.0979	.0019	9.19	1.9	.1423	2.5	9.79	2.2	.0944	11.0	1.330	11.2	.1022	2.2	.200
66B–24.1	c	236	30	.13	651.4	12.5	659.4	12.4	737.4	14.8	982	41.9	.1063	.0021	9.27	2.0	.0730	1.9	9.28	2.0	.0719	2.1	1.067	2.8	.1077	2.0	.692
66B–4.1	c	96	25	.26	827.5	16.3	829.2	15.8	844.1	15.8	884	39.1	.1370	.0029	7.29	2.0	.0685	1.9	7.29	2.0	.0685	1.9	1.296	2.8	.1373	2.0	.732
66B–8.1	c	686	191	.29	936.1	16.5	949.9	16.1	1,054.0	12.6	1,276	12.6	.1563	.0030	6.30	1.8	.0837	.6	6.30	1.8	.0833	.6	1.824	1.9	.1588	1.8	.943
66B–7.2	c	96	63	.69	1,057.5	20.5	1,059.4	19.6	1,073.3	17.9	1,102	36.7	.1783	.0038	5.59	2.0	.0779	1.6	5.60	2.0	.0762	1.8	1.878	2.7	.1786	2.0	.739
66B–9.1	c	50	26	.55	1,323.0	28.3	1,315.7	26.3	1,272.2	24.3	1,199	50.5	.2278	.0054	4.40	2.2	.0823	2.1	4.42	2.2	.0801	2.6	2.501	3.4	.2264	2.2	.653
66B–19.1	c	208	134	.66	1,598.6	29.3	1,643.3	27.3	1,822.0	17.4	2,033	15.6	.2814	.0058	3.44	1.9	.1253	.9	3.44	1.9	.1253	.9	5.016	2.1	.2904	1.9	.906
66B–25.1	c	292	137	.48	2,149.6	43.5	2,124.8	36.2	2,053.6	18.3	1,983	11.1	.3958	.0094	2.56	2.0	.1218	.6	2.56	2.0	.1218	.6	6.557	2.1	.3904	2.0	.955
66B–21.1	c	260	267	1.06	2,295.7	44.5	2,313.0	36.5	2,352.2	17.9	2,386	10.1	.4278	.0099	2.32	1.9	.1536	.6	2.32	1.9	.1536	.6	9.141	2.0	.4316	1.9	.953
66B–27.1	c	40	32	.84	2,662.9	65.7	2,661.7	47.9	2,659.8	23.2	2,658	19.5	.5115	.0154	1.95	2.2	.1825	1.1	1.96	2.2	.1806	1.2	12.729	2.5	.5112	2.2	.882

Table 2. $^{40}Ar/^{39}Ar$ single-grain laser step-heating data for biotite and white mica from sample 96ADb10A of West Point orthogneiss (see fig. 7).

[Weighted average of J (irradiation parameter) from standards: biotite, 0.009587±0.000038; white mica, 0.009205±0.000056]

Laser power (mW)	Cumulative ^{39}Ar	$^{40}Ar/^{39}Ar$ ratio	1σ	$^{37}Ar/^{39}Ar$ ratio	1σ	$^{36}Ar/^{39}Ar$ ratio	1σ	Atm. ^{40}Ar (pct)	Ca/K ratio	1σ	Cl/K ratio	1σ	Radiogenic $^{40}Ar/^{39}K$ ratio	1σ	Age (Ma)	1σ (Ma)
96ADb10A (biotite)																
100	0.012	6.415	0.029	0.0340	0.0051	0.01089	0.00085	50.4	0.0624	0.0094	0.00290	0.00017	3.170	0.253	54.0	4.2
150	.059	5.891	.012	.0098	.0011	.00228	.00022	11.5	.0180	.0021	.00356	.00005	5.189	.065	87.6	1.1
200	.174	5.437	.011	.0012	.0004	.00056	.00008	3.0	.0021	.0008	.00365	.00003	5.244	.025	88.5	.4
300	.331	5.288	.016	.0017	.0004	—.00004	.00005	—.2	.0032	.0007	.00362	.00006	5.270	.022	88.9	.4
450	.506	5.287	.021	.0032	.0003	—.00014	.00004	—.8	.0059	.0005	.00350	.00006	5.299	.024	89.4	.4
600	.711	5.307	.017	.0021	.0003	.00002	.00003	.1	.0039	.0005	.00377	.00006	5.273	.020	89.0	.3
750	.850	5.228	.022	.0021	.0006	—.00020	.00005	—1.2	.0039	.0010	.00383	.00006	5.260	.027	88.8	.5
900	.920	5.273	.023	.0079	.0009	—.00027	.00010	—1.5	.0145	.0017	.00376	.00006	5.325	.038	89.8	.6
1,100	.933	5.166	.055	.0483	.0051	—.00078	.00064	—4.6	.0886	.0094	.00349	.00020	5.373	.198	90.6	3.3
1,300	.945	5.108	.048	.0955	.0055	—.00138	.00050	—8.2	.1752	.0102	.00371	.00027	5.495	.155	92.6	2.6
1,500	.955	5.008	.073	.0226	.0054	—.00169	.00087	—10.1	.0415	.0100	.00400	.00032	5.480	.267	92.4	4.4
1,750	.965	4.984	.057	.1308	.0055	—.00299	.00046	—18.1	.2401	.0101	.00390	.00033	5.851	.149	98.5	2.4
2,000	.982	5.189	.057	.0471	.0038	—.00103	.00032	—6.0	.0863	.0070	.00370	.00015	5.469	.113	92.2	1.9
3,000	.995	4.997	.042	—.0019	.0041	—.00292	.00043	—17.4	—.0036	.0076	.00326	.00018	5.831	.135	98.1	2.2
8,000	1.000	4.663	.053	.0004	.0116	—.00473	.00088	—30.2	.0007	.0214	.00411	.00053	6.032	.268	101.4	4.4
Integrated----------		5.323	.007	.0072	.0002	.00007	.00003	.4	.0132	.0004	.00367	.00002	5.273	.011	89.0	.4
96ADb10A (white mica)																
300	0.006	6.143	0.022	0.0101	0.0023	0.00151	0.00045	7.3	0.0186	0.0042	0.00026	0.00020	5.669	0.135	91.8	2.1
400	.008	6.988	.081	.0143	.0095	.00189	.00131	8.0	.0263	.0175	.00083	.00049	6.401	.394	103.3	6.2
600	.020	6.100	.022	.0109	.0012	.00171	.00019	8.3	.0200	.0021	.00056	.00010	5.567	.061	90.2	1.0
800	.047	6.284	.006	.0044	.0006	.00121	.00012	5.7	.0081	.0011	.00041	.00003	5.898	.035	95.4	.6
1,000	.089	6.432	.009	.0012	.0003	.00190	.00008	8.8	.0022	.0005	.00046	.00006	5.842	.025	94.5	.4
1,200	.148	6.340	.012	.0017	.0003	.00103	.00007	4.8	.0031	.0006	.00038	.00002	6.008	.024	97.1	.4
1,400	.258	6.272	.010	.0018	.0002	.00111	.00003	5.2	.0033	.0004	.00040	.00002	5.916	.013	95.7	.2
1,700	.372	6.298	.011	.0013	.0002	.00110	.00005	5.2	.0023	.0004	.00036	.00002	5.944	.019	96.1	.3
2,000	.511	6.217	.024	.0023	.0001	.00081	.00003	3.9	.0042	.0003	.00046	.00002	5.948	.025	96.2	.4
3,000	.725	6.153	.022	.0027	.0001	.00095	.00002	4.6	.0050	.0002	.00041	.00003	5.844	.023	94.5	.4
4,000	.810	6.228	.011	.0007	.0002	.00057	.00007	2.7	.0013	.0003	.00040	.00003	6.031	.023	97.5	.4
7,000	.982	6.295	.021	.0010	.0001	.00078	.00001	3.7	.0018	.0002	.00038	.00002	6.037	.021	97.6	.3
8,000	1.000	6.311	.022	.1388	.0015	.00124	.00014	5.7	.2547	.0028	.00054	.00008	5.927	.047	95.8	.7
Integrated----------		6.252	.007	.0044	.0001	.00097	.00001	4.6	.0081	.0001	.00041	.00001	5.936	.008	96.0	.6

margin of the Salcha River gneiss dome (fig. 2); we interpret this dike to be part of an undeformed stock that intrudes the dome. A conventional U-Pb zircon age of 116±3 Ma was previously determined for a granitoid sample from that stock (fig. 2; Aleinikoff and others, 1984a).

U-Pb Zircon Data

Analytical Techniques

U-Pb zircon analyses were conducted on the SHRIMP–RG (reverse geometry) ion microprobe co-operated by the U.S. Geological Survey (USGS) and Stanford University. Zircons, concentrated by standard heavy-mineral-separation processes, were mounted in epoxy, polished, and imaged with transmitted light, reflected light, and cathodoluminescence to identify internal structures and defects. The mounted zircons were washed with 1 *N* HCl and distilled water, dried, and coated with approximately 10 nm of Au. The primary O_2^- ion beam (~8–15 nA) typically produces a spot with a diameter of 30 to 40 µm and a depth of 1 to 2 µm for an analysis time of 9–12 minutes. Concentration data were standardized against zircon standard SL–13 (238 ppm U) and are accurate to about 10 to 20 percent, and age data were standardized against zircons AS3 and AS57 (1,098 Ma from the anorthositic gabbro, Duluth Complex; Paces and Miller, 1993), which were analyzed repeatedly throughout the duration of the session. Data reduction followed the method of Williams (1998), using the PRAWN and LEAD program of T.R. Ireland (unpub. program routine) and the Squid and Isoplot/Ex program of Ludwig (2001).

U-Pb data are generally plotted on either a Tera-Wasserburg or a Wetherill concordia diagram. Tera-Wasserburg concordia diagrams are plotted with data uncorrected for common Pb because only these data allow the determination of age trends that may result from mixing of zircons of different ages or from loss of radiogenic Pb, whereas a Wetherill concordia diagram is plotted with data corrected for the measured ^{204}Pb content in each spot. Because most Phanerozoic zircons contain only traces of ^{207}Pb and ion-microprobe analyses consume only 1 to 2 ng of material, counting statistics for ^{207}Pb are poor, and atomic ratios involving ^{207}Pb, especially the $^{207}Pb/^{235}U$ ratio needed for Wetherill concordia diagrams, have relatively high analytical uncertainties. $^{207}Pb/^{206}Pb$ ratios, however, can be measured much more precisely than $^{204}Pb/^{206}Pb$ ratios, and so $^{206}Pb/^{238}U$ ages corrected by using measured $^{207}Pb/^{206}Pb$ ratios are most reliable for ion-microprobe data from Phanerozoic samples, whereas a Tera-Wasserburg concordia diagram is preferred for evaluating and displaying these data.

Results

Sample 96ADb10A

Ion-microprobe spot analyses of sample 96ADb10A (table 1) were made for 33 zircon grains separated from the West Point orthogneiss. In transmitted light, the zircons are mostly subhedral, elongate, doubly terminated prisms, with lesser amounts of anhedral crystals and broken grains (fig. 4). In scanning-electron-microscope cathodoluminescence (SEM–CL) images (fig. 4*C*, 4*D*, and 4*E*), grain interiors are generally dark (that is, U rich) and exhibit euhedral oscillatory zoning, commonly surrounded by a light (that is, U poor) outer margin that, in turn, is overgrown by a medium-gray rim, which in some zircons contains concentrically arranged oscillatory zoning. Ion-microprobe spot analyses of zircon cores, homogeneous grains, and rims clearly indicate that the previous multigrain TIMS age for this sample (671±34 Ma; Smith and others, 1994), which Smith and others interpreted as the time of igneous crystallization of the granitic orthogneiss, actually averaged several distinct isotopic populations. U-Pb ion-microprobe spot analyses within most cores, such as in grains 1 and 2 (figs. 4*C*, 4*D*), yield Devonian ages, but several other cores yielded Archean or Proterozoic ages of ~2.6, 1.8, 1.4, and 1.1 Ga (fig. 5*A*; table 1). In contrast, zircon rims on 13 out of 15 grains (such as those shown for grains 1 and 2) and one partial fragment of what might be a complete grain (grain 26, fig. 4*E*) yielded Early Cretaceous ages (table 1). A plot of $^{206}Pb/^{238}U$ age versus Th/U ratio for individual zircon spot analyses (fig. 6*A*) shows that the Th/U ratios are very low (<0.2) for the spots that yielded Early Cretaceous ages. These very low Th/U ratios generally indicate zircons grown under fluid-rich, oxidizing conditions—either in a metamorphic or a fluid-rich magmatic environment. In contrast, the variation in the Th/U ratio of Devonian (~375 Ma) zircon cores is typical of that of magmatic zircons.

The Tera-Wasserburg concordia diagram for this sample (fig. 5*A*) illustrates the systematics of the spots that yielded Phanerozoic ages. Four discordia lines (dashed lines, fig. 5*A*) are drawn through the data points to indicate possible interpretations of these data. Two of the chords (red ovals on left, fig. 5*A*) connect a large population of Devonian (~375±8 Ma) cores with older data for other zircon cores from this sample. The upper-intercept ages of these two discordia should not be taken specifically but only as an indication of Late Archean and Protoproterozoic ages that we interpret as the general inheritance ages from crustal materials. These ages (~2.6 and 1.8 Ga, respectively) are commonly observed as inheritance ages in felsic magmatic rocks (Aleinikoff and others, 1986; Heslop and others, 1995; Dusel-Bacon and Aleinikoff, 1996) and as detrital ages in metasedimentary rocks of the Yukon-Tanana Upland (Aleinikoff and others, 1984b, 1995; Foster and others, 1987). The other two discordia lines pass through the Early Cretaceous zircon population, one of which (green ovals, fig. 5*A*) connects the Early Cretaceous zircon population with the Devonian core ages, illustrating a possible mixing trend between the two populations and (or) an episodic Pb-loss trend for Devonian grains affected by Cretaceous events. A mixing trend would most likely result from placement of the ion-microprobe spot on the boundary between two ages of zircons. The ages for this discordia, particularly the younger age, are not meant to indicate the actual ages of specific geologic events. The other discordia line is defined by the seven grains (red ovals on right, fig. 5*A*) with the youngest Early

Cretaceous ages. The steep trend of this discordia line and its rightward slant indicate that these grains have undergone Pb loss. The lower-intercept age of this discordia line is the same, within error, as the weighted-mean-average age of 112±2 Ma for seven of the most concordant spots from zircon rims (spots 10–1.1 through 10–26.1, table 1). Eliminating from this group two grains with very high U contents, which may cause calibration problems (Williams and Hergt, 2000), gives an age of 111±2 Ma. Four spots (10–33.1 through 10–6.1, table 1) on rims with very high U contents (5,000–8,000 ppm) yielded ages of 121 to 129 Ma, which also may be unreliable because of calibration problems. The U-Pb systematics in this sample are clearly complex. Although the effects of the metamorphic event on this rock have not been accounted for in this interpretation, this event must have occurred 111 Ma or later if the crystallization age has been correctly identified.

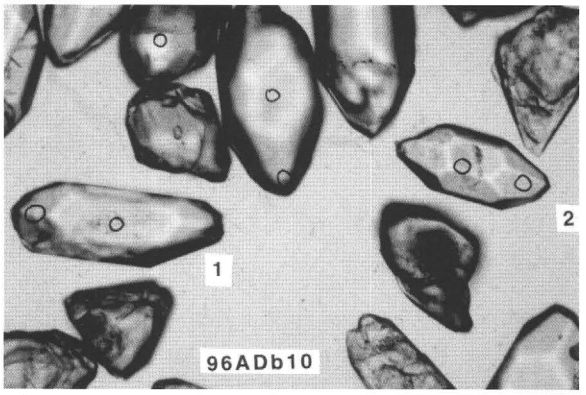

A

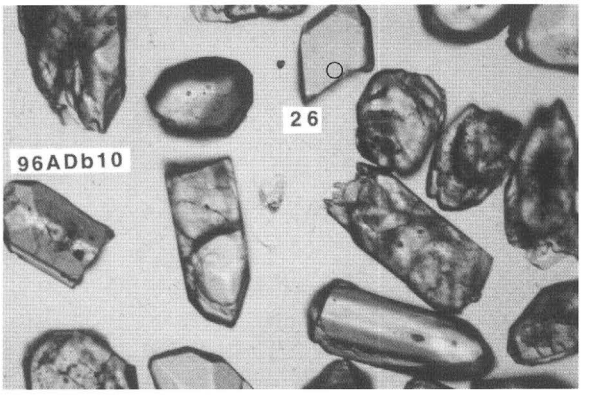

B

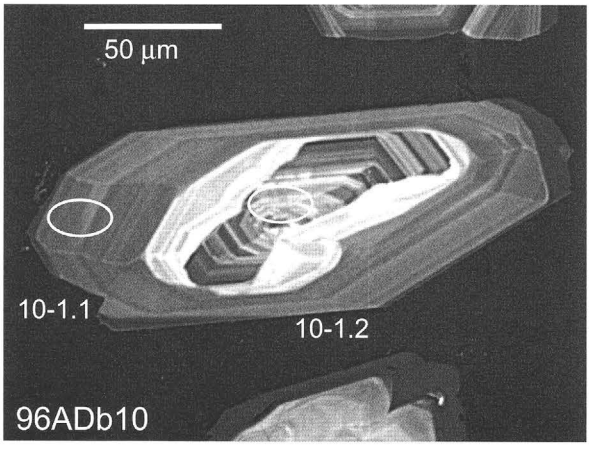

C

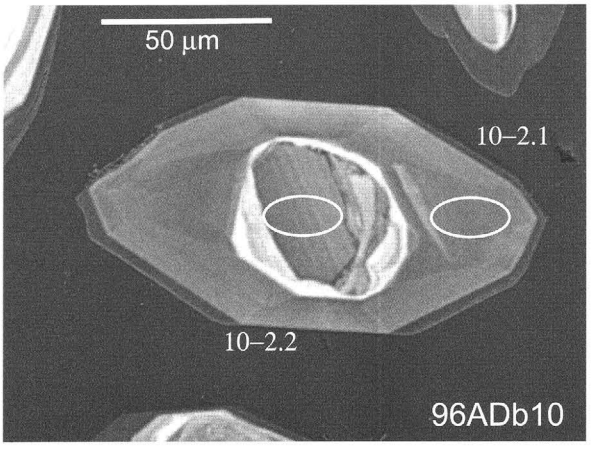

D

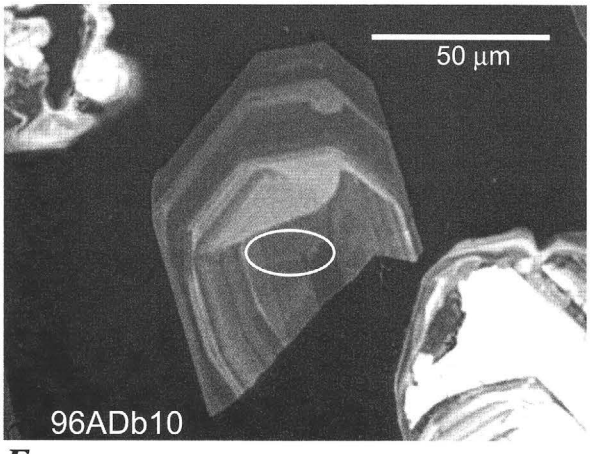

E

Figure 4. Photomicrographs of selected zircons separated from sample 96ADb10A of West Point orthogneiss (table 1). Numbers, analyzed grains; circles in figures 4*A*, 4*B*, locations of ion-microprobe spot analyses. Figures 4*A* and 4*B* were taken in transmitted light; figures 4*C* through 4*E* are scanning-electron-microscope cathodoluminescence images, in which ellipses show outlines of ion-microprobe analytical spots, approximately 20 µm in diameter and 2 µm deep.

Sample 98ADb55B

Zircons from sample 98ADb55B (tables 1, 4) are blocky, 100 to 200 µm long, with regular to irregular compositional zoning. Rim and core structures are not as obvious as in samples 96ADb10A (fig. 4; table 1) and 98ADb66B (table 1), although cores may be present. We made no attempt to find cores with the ion microprobe, because our primary objective was to determine the crystallization age. However, augen gneiss samples containing zircons without obvious inheritance is unusual for the Lake George assemblage. The 20 analyses on this sample concentrated on the edges of grains and provided an age range from 173 to 370 Ma (fig. 5*B*; table 1). Although most of the older ages plot on or near concordia, a clear trend away from concordia defines a discordia line with an upper-intercept age of 360±13 Ma and a lower-intercept age of 44±69 Ma. U contents range from 200 to almost 5,000 ppm in these spots, and the younger ages are approximately associated with higher U contents. This correlation supports the interpretation of this discordia line as reflecting Pb loss. Although the lower-intercept age is too imprecise to be meaningful, the upper-intercept age provides a general estimate of the crystallization age. Six spots (55B–7.1 through 55B–4.1, table 1), all with lower U contents, yielded a weighted-mean-average age of 355±4 Ma, which is probably the best estimate of the crystallization age of this sample. We interpret these data to indicate a crystallization age of about 355 Ma for the protolith of the augen gneiss and to suggest an episodic event(s) during the mid-Cretaceous and (or) Tertiary that disturbed the U-Pb systematics of these zircons. Possible causes of Pb loss include mid-Cretaceous plutonism (that we interpret to have formed the West Point orthogneiss), mid-Cretaceous crustal extension (Pavlis and others, 1993), latest Cretaceous and early Tertiary plutonism (Wilson and others, 1985; Smith and others, 1994), and Eocene uplift, as suggested by apatite fission-track ages (Dusel-Bacon and Murphy, 2001).

Sample 98ADb66B

Sample 98ADb66B (tables 1, 4) is an undeformed granitoid that we interpret to be a dike. The zircons generally range in length from 100 to 200 µm, are subhedral to euhedral with double terminations, and many grains have conspicuous high-U rims and lower-U cores. U-Pb ages range from 79 to 2,600 Ma; all ages older than 300 Ma were found in cores (fig. 5*C*; table 1). Older core ages are mostly Precambrian, but even these ages range from about 827 to 2,700 Ma, with no age grouping. Zircons with ages of 96 to 126 Ma dominate the analyzed population. These ages were measured on both zircon rims and cores that have U contents ranging from 300 to almost 7,000 ppm. Th/U ratios for these younger zircons are all less than 0.2 and, as discussed for sample 96ADb10A (table 1), indicate a fluid-rich, oxidizing system. Unlike the West Point orthogneiss, however, this granitoid has no planar fabric and is clearly postkinematic;

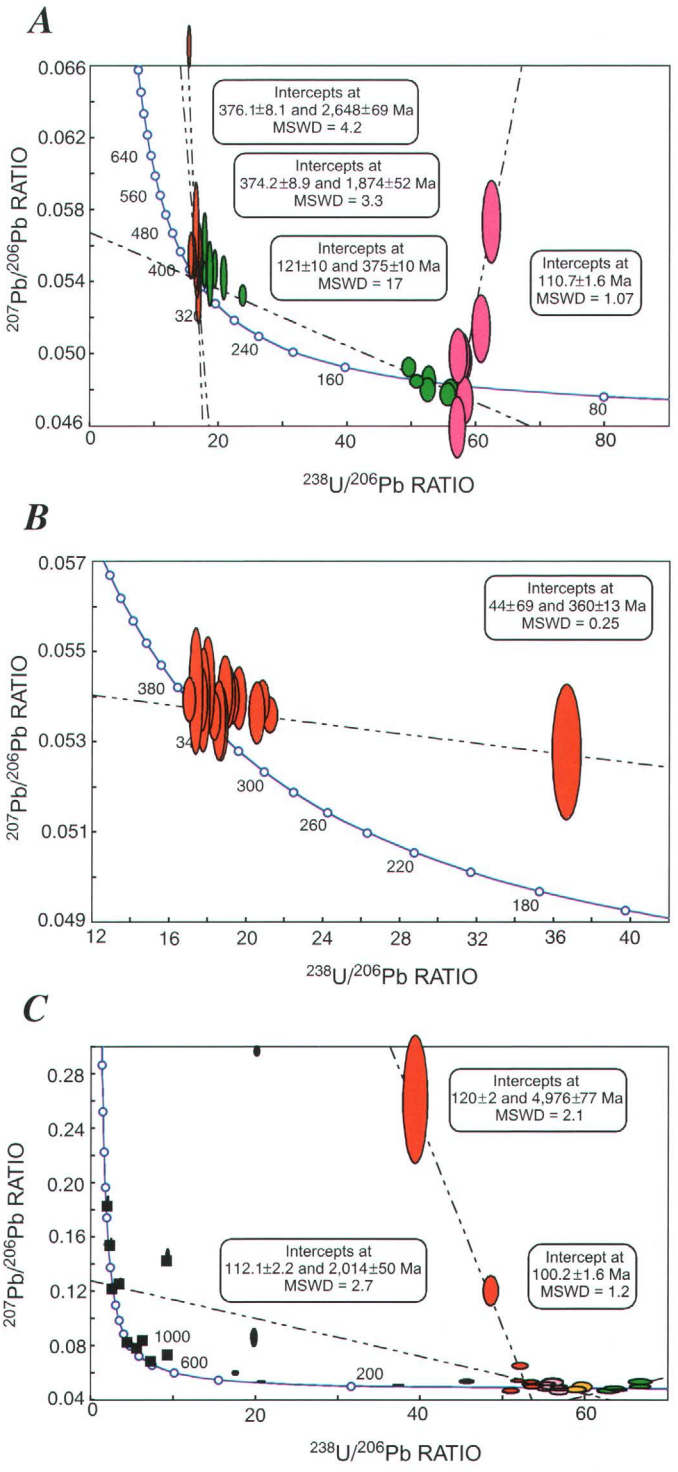

Figure 5. Tera-Wasserburg concordia plot for ion-microprobe U-Pb zircon samples 96ADb10A (*A*), 98ADb55B (*B*), and 98ADb66B (*C*) (table 1). See text for explanation of colored error ellipses. In figure 5*C*, black error ellipses and squares (substituted for error ellipses that are too small to be easily distinguished on plot) show data points that were omitted from interpretation of Cretaceous crystallization age for this sample. MSWD, mean standard of weighted deviates.

thus, its Early Cretaceous crystallization was magmatic, not metamorphic. Although the sample must have an Early Cretaceous age of 100 to 120 Ma, the U-Pb systematics of these younger spot analyses are highly complex, and an unambiguous age cannot easily be determined for the igneous-crystallization event. In the following discussion, we ignore any possible calibration problems that might have resulted from high U contents because no obvious pattern of U contents is apparent in this data set.

Three discordia lines are used to illustrate possible age trends in the Cretaceous grains. Nine spots (66B–7.1 through 66B–3.1, table 1) on seven rims and two cores (red ellipses, fig. 5*C*) define a discordia line with a lower-intercept age of 120±2 Ma and an upper-intercept age of 4,976±77 Ma. This age trend clearly results from some grains (four with strongly discordant data) incorporating significant amounts of common Pb during their formation. Although the upper-intercept age of this trend is not geologically significant, the lower-intercept age provides a good estimate of the maximum crystallization age. The second discordia line, with lower- and upper-intercept ages of 112±2 and 2,014±50 Ma, respectively, is provided only as an example of a mixing trend between Cretaceous and older inherited cores and (or) of Cretaceous episodic Pb loss from older cores. The mixing and (or) episodic Pb loss do not seem to have been important factors in our interpretation of the Cretaceous U-Pb data. The third discordia line, defined by five spots (66B–12.2 through 66B–16.1, table 1) on four rims and one core (green ellipses, fig. 5*C*), intersects the concordia at 100.2±1.6 Ma, suggesting a recent Pb-loss trend nearly identical to that observed in sample 96ADb10A. This intercept, which is clearly a minimum crystallization age, more likely represents a group of grains strongly affected by Pb loss. Some analyses (yellow ellipses, fig. 5*C*) were excluded from age calculations because they probably represent partial Pb loss. Seven concordant spots (66B–17.1 through 66B–51, table 1) on three cores and five rims (pink ellipses, fig. 5*C*) provide a weighted-mean-average age of 113±2 Ma that could represent the crystallization age, because these grains appear to be unaffected by Pb loss. Although the weighted-mean-average age of 14 spots with ages ranging from 107 to 122 Ma is 114±3 Ma, this suite clearly seems to include spots from at least two groups with average ages of about 113 and 120 Ma. We are unable to decide whether 113 or 120 Ma is the best estimate of the crystallization age, but we prefer the 113±2-Ma age because it is not complicated by any significant common-Pb component or by evidence of Pb loss.

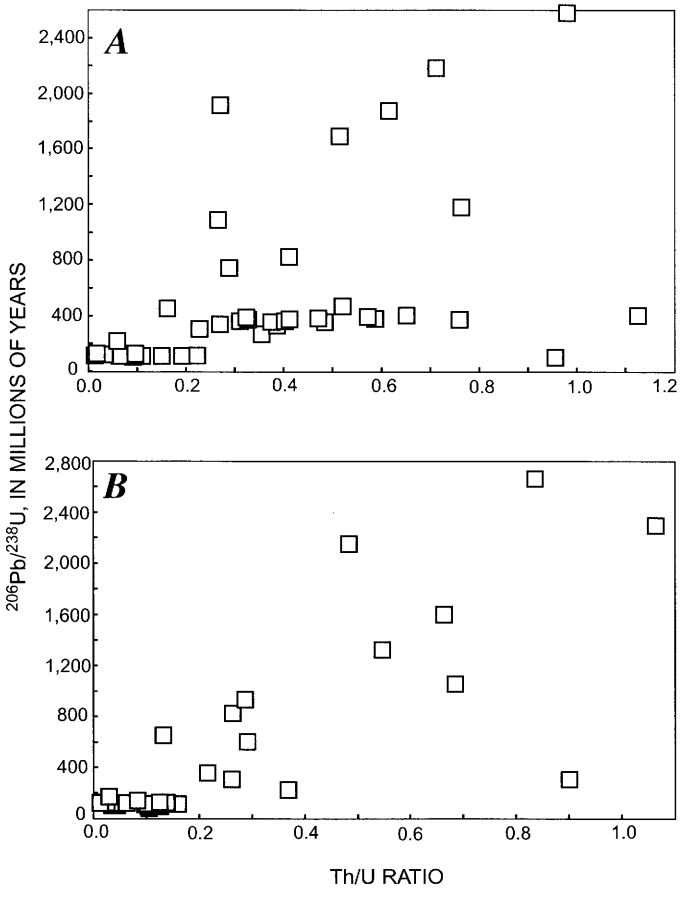

Figure 6. $^{206}Pb/^{238}U$ age versus Th/U ratio for spot analyses of individual zircons in samples 96ADb10A (*A*) and 98ADb66B (*B*) (table 1).

Interpretation of U-Pb data

As mentioned above, the Early Cretaceous (111±2 Ma) U-Pb ages for zircon rims from the West Point orthogneiss could represent either magmatic or metamorphic crystallization of new zircon. In magmatic crystallization, Early Cretaceous zircon rims (and one newly formed zircon) would have formed during a Cretaceous magmatic event in which wall-rocks that included quartzite, pelitic schist, and Devonian augen gneiss were remobilized (anatectically melting); metamorphism of the gneiss would have followed shortly thereafter but not have resulted in the formation of new zircon rims. In metamorphic crystallization, the Early Cretaceous zircon rims would have formed during amphibolite-facies metamorphism of a Devonian intrusion. The morphology of zircons in the West Point orthogneiss and the conditions necessary to form metamorphic zircon are important factors that bear on our evaluation of these two possible events.

Accessory zircon typically forms as a liquidus phase in magmas of granitic to tonalitic composition (Poldervaart, 1956). Bipyramidal prisms with euhedral internal zoning and long needlelike inclusions are characteristic of unimpeded growth in a liquid (Silver, 1969). Metamorphic zircons grown in mafic igneous rocks under amphibolite-, granulite-, and eclogite-facies conditions are generally rounded to elongate, with small crystal faces, rounded edges, and patchy and irregular growth zones (see Creaser and others, 1997). Metamorphic mantles and rims around igneous zircons have been observed in pyroxene-bearing intrusions metamorphosed under both granulite-facies (van Breemen and others, 1986, 1987) and upper-amphibolite-facies (Barr and others, 1987) conditions. Metamorphic reactions involving breakdown of the high-Zr

phases orthopyroxene, clinopyroxene, and amphibole are the most likely sources for the zirconium in the metamorphic rims. The metamorphic zircon mantles observed by van Breemen and others (1986, 1987) and Barr and others (1987) generally do not conform to the inner morphology of the magmatic zircon cores.

The formation of metamorphic zircons and metamorphic rims on preexisting igneous zircon cores in granitic rocks devoid of pyroxene or amphibole is not so well established. A phenomenon called Ostwald ripening, in which large crystals tend to grow at the expense of smaller crystals so as to minimize their surface energy, appears to be a factor in the coarsening of grain size in high-grade, granulite-facies rocks (Spear, 1993). This same principle could apply to the formation of zircon rims derived from the redistribution of zircon from smaller crystals during high-grade metamorphism.

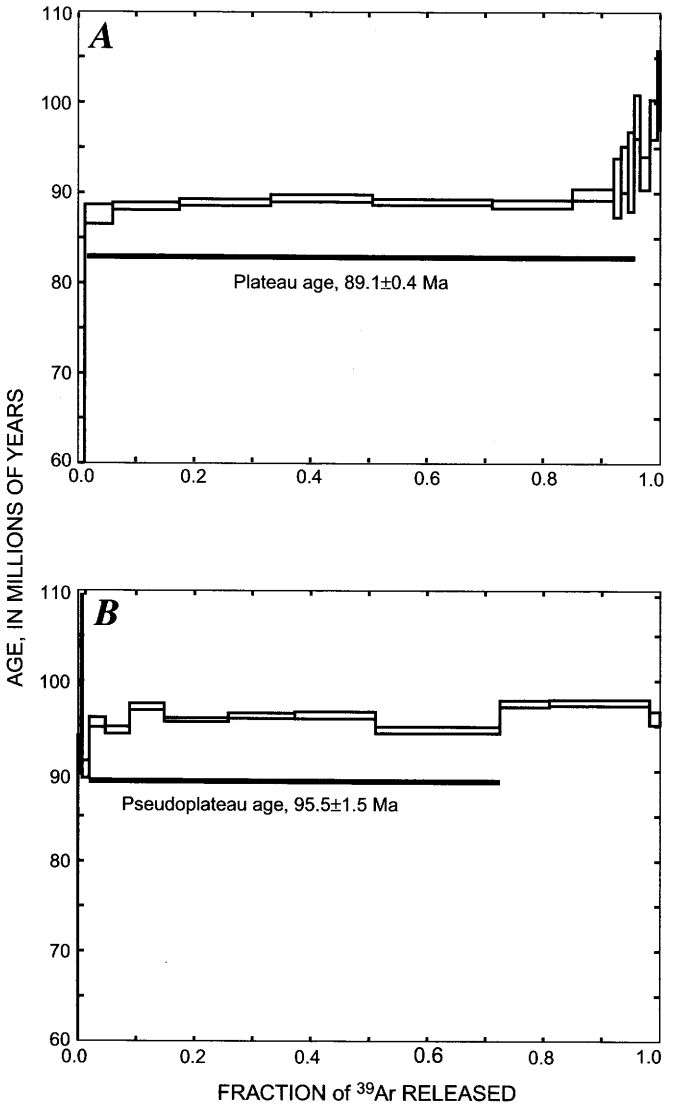

Figure 7. Ar-release spectra for biotite (*A*) and white mica (*B*) from sample 96ADb10A of West Point orthogneiss (tables 2, 3). Box heights of each rectangle are ±1σ.

Given the paucity of definitive studies involving the interpretation of mantles and rims on igneous zircons in granitic rocks that are devoid of pyroxene or amphibole, we conclude that it is impossible to unequivocally determine whether the zircon rims in the West Point orthogneiss formed under magmatic or metamorphic conditions. Nevertheless, we favor a magmatic origin for the zircon rims in the West Point orthogneiss for the following reasons. (1) Many zircon rims show features indicative of magmatic crystallization, including oscillatory growth zoning (clearly displayed at the margin of grain 1, fig. 4*C*, which yielded a 109.8-Ma age), the presence of needlelike inclusions (observed in the outer rims of a few zircon grains), and elongate and well-faceted terminations. (2) A previous U-Pb SHRIMP study of zircons from four different samples of augen gneiss from the Lake George assemblage in the eastern Yukon-Tanana Upland revealed no evidence for metamorphic rims on Devonian (~360 Ma) zircons (Heslop and others, 1995), in spite of the fact that wallrocks to the augen gneiss underwent high-pressure (7–12 kbars) and moderate- to high-temperature (500–700°C) metamorphism (Dusel-Bacon and others, 1995). We consider it unlikely that the metamorphic grade in the vicinity of the West Point orthogneiss (believed to be <650°C, as stated above) was high enough to cause any precipitation of new zircon. The mineralogy of the samples of granitoid orthogneiss in these two studies is similar.

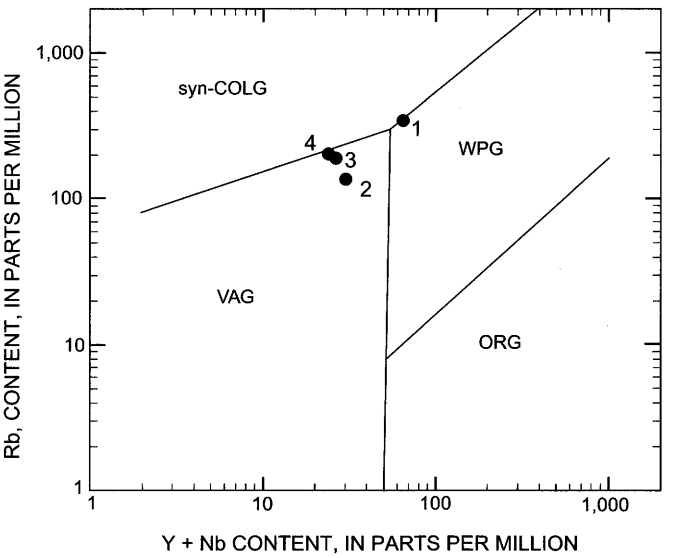

Figure 8. Rb–Y+Nb tectonic discrimination diagram (Pearce and others, 1984) for granitic samples from areas of West Point orthogneiss and Salcha River gneiss dome. Samples: 1, 98ADb55B, Devonian augen gneiss sample; 2, 98ADb53B, undated granitic orthogneiss from the West Point Complex; 3, 96ADb10A, Cretaceous granitic orthogneiss from the West Point Complex; 4, 98ADb66B, Cretaceous granitic dike that intrudes the Salcha River gneiss dome. See table 4 for complete geochemical analyses. ORG, orogenic granite; syn-COLG, syncollisional granite; VAG, volcanic-arc granite; WPG, within-plate granite.

Table 3. Summary of $^{40}Ar/^{39}Ar$ ages for biotite and white mica from sample 96ADb10A of West Point orthogneiss.

[Samples were run against standard Mmhb–1 (513.9 Ma) and processed by using the constants of Steiger and Jäger (1977). Bold ages, interpreted; error limits, 1σ. MSWD, mean standard of weighted deviates]

Mineral	Integrated age (Ma)	Plateau age (Ma)	Comments
Biotite--------	89.0±0.4	89.1±0.4	10-fraction plateau, 94-percent gas release; MSWD=1.0.
White mica---	96.0±0.6	95.5±1.5	7-fraction pseudoplateau, 71-percent gas release; MSWD=6.5.

In spite of our preferred crystallization age of 111±2 Ma for the West Point orthogneiss, we recognize that this interpretation is equivocal and still leaves open the exact temporal relation between intrusion of the gneiss protolith and subsequent metamorphism. A TIMS U-Pb age on monazite from the previously dated sample of West Point orthogneiss is 116±4 Ma (J.N. Aleinikoff, written commun., 2002). Thus, the monazite age and the zircon age agree within analytical uncertainty. The monazite could have crystallized either during intrusion of the granitoid or during subsequent regional metamorphism. Independent geologic evidence, discussed in the section below entitled "Tectonic Implications," indicates the near-contemporaneity of mid-Cretaceous metamorphism and posttectonic plutonism, and so ascribing either a metamorphic or an igneous origin to the zircon rims in the West Point orthogneiss is a somewhat academic question.

$^{40}Ar/^{39}Ar$ Data

Analytical Techniques

A sample of West Point orthogneiss (96ADb10A, tables 1–4) from the same locality at which the U-Pb sample was collected was submitted to the Geochronology Laboratory of the University of Alaska, Fairbanks, for $^{40}Ar/^{39}Ar$ analysis of the biotite and white mica. The mica separates were wrapped in aluminum foil and arranged in one of two levels, labeled top or bottom, within aluminum cans, 2.5 cm in diameter and 4.5 cm high. Samples were run against standard MMhb–1 (Samson and Alexander, 1987), dated at 513.9 Ma (Lanphere and others, 1990). The samples were irradiated at 35 MW-h in position 5C of the uranium-enriched research reactor of McMaster University in Hamilton, Ontario, Canada.

Upon their return from the reactor, the sample and monitors were loaded into 2-mm-diameter holes in a copper tray, which was then loaded in an ultra-high-vacuum extraction line. The monitors were fused, and the sample was step-heated, using a 6-W Ar-ion laser, according to the method of York and others (1981) and Layer and others (1987). Ar was purified by using a liquid nitrogen cold trap and an SAES Zr-Al getter at 400°C. The samples were then analyzed on a VG–3600 mass spectrometer at the Geophysical Institute of the University of Alaska, Fairbanks. The measured Ar isotopes were corrected for system blank and mass discrimination, as well as for Ca-, K-, and Cl-interference reactions, according to the method of McDougall and Harrison (1988).

$^{40}Ar/^{39}Ar$ Results

Detailed analyses are listed in table 2, and the $^{40}Ar/^{39}Ar$ results are summarized in table 3. The biotite analysis yields a flat age spectrum, with a plateau age of 89.0±0.4 Ma and an indication of a slight Ar loss at ~54 Ma. The spectra steps up to an older age of 101.4±4.4 Ma in the last 10 percent of gas release. This sample may have been originally older than the plateau age.

The sample of white mica was irradiated separately from the biotite above, and two splits of the separate were run. In the first run, the raw data were lost because of a hard-drive failure. Both spectra from this sample show a shallow U-shaped plateau and some Ar loss, with hints of excess Ar. The white mica is significantly older than the biotite. In the second run, the white mica yielded a pseudoplateau age of 95.5±1.5 Ma, consistent with visual inspection of the data from the first run and a calculated plateau age of 95.6±0.6 Ma based on the summary output data.

Interpretation of $^{40}Ar/^{39}Ar$ Data

The $^{40}Ar/^{39}Ar$ plateau age of 89 Ma for biotite from our sample of West Point orthogneiss overlaps a K-Ar age of 89.8±2.7 Ma that was determined for biotite from the previously dated U-Pb zircon sample whose upper-intercept age was interpreted by Smith and others (1994) to indicate a Late Proterozoic crystallization age for the orthogneiss. K-Ar ages for biotite and hornblende pairs from three different undeformed plutons in the study area to the southeast of West Point (fig. 1) fall in the range 92–96 Ma. In the study area north of West Point, a K-Ar age of 85 Ma was determined for biotite from the southernmost small pluton, and biotite and muscovite pairs gave K-Ar ages in the range 68–77 Ma for plutons farther to the north (Smith and others, 1994). In agreement with Smith and others, we interpret our biotite age as a thermal overprint from the numerous unmetamorphosed Cretaceous and Tertiary age plutons in the study area.

Table 4. Geochemical analyses of samples of granite and orthogneiss discussed in text.

[Quadrangles: BD, Big Delta; CI, Circle. Major- and minor-element-oxide contents in weight percent; trace-element contents in parts per million. Analyzed at the GeoAnalytical laboratory, Washington State University, Pullman. Trace-element contents of V, Cr, Ni, Cu, Zn, Ga, and Zr determined by wavelength-dispersive X-ray-fluorescence analysis and of other elements by inductively coupled plasma mass-spectrometric analysis. LOI, weight loss on ignition]

Sample	98ADb55B	98ADb53B	96ADb10A	98ADb66B
No. (fig. 8)	1	2	3	4
Rock type	Augen gneiss	Granite orthogneiss	Granite orthogneiss	Granitic dike intruding sillimanite gneiss
Lat, long	65°00′47″ N., 144°56′15″ W.	64°58′45″ N., 144°53′38″ W.	64°55′30″ N., 144°49′30″ W.	64°37′50″ N., 145°40′22″ W.
Quadrangle	CI A–2	BD D–2	BD D–2	BD C–4
Major- and minor-element oxides				
SiO_2	73.51	73.51	74.49	72.67
Al_2O_3	13.80	14.21	14.06	14.91
FeO	1.53	1.76	1.36	.59
MgO	.32	.36	.34	.19
CaO	.94	1.82	1.29	1.36
Na_2O	3.01	2.88	2.40	2.40
K_2O	6.14	4.17	5.50	7.14
TiO_2	.22	.14	.18	.07
P_2O_5	.06	.11	.07	.10
MnO	.03	.05	.02	.02
Total	99.56	99.00	99.71	99.44
LOI	.49	.91	.53	.40
Trace elements				
Sc	6.20	9.20	4.20	3.90
V	19	19	12	5
Cr	4	2	9	0
Ni	7	6	9	3
Cu	7	3	13	2
Zn	50	34	37	15
Ga	20	14	17	18
Rb	341	135	187	200
Cs	5.13	2.90	2.69	6.43
Sr	101	190	180	171
Ba	735	796	642	487
Pb	26.00	19.40	41.30	57.50
La	44.85	33.68	39.05	10.10
Ce	81.07	65.37	73.42	21.23
Pr	8.75	7.39	7.93	2.56
Nd	30.76	28.23	29.46	9.66
Sm	7.10	6.00	7.25	2.71
Eu	.57	1.22	1.02	.73
Gd	6.44	3.93	5.70	2.58
Tb	1.22	.58	.76	.49
Dy	7.52	3.42	3.49	2.81
Ho	1.49	.73	.56	.49
Er	4.06	2.10	1.22	1.20
Tm	.61	.33	.16	.17
Yb	3.83	2.12	.91	1.00
Lu	.54	.33	.14	.14
Y	41.69	20.23	15.74	13.54
Zr	142	105	103	46
Hf	4.41	3.09	3.59	1.73
Nb	22.54	9.93	10.76	10.36
Ta	2.48	.60	.73	1.92
Th	29.68	13.42	22.54	7.51
U	3.33	1.50	4.38	3.38

Geochemistry of (Meta)Granitic Rocks of the West Point Complex and Salcha River Gneiss Dome Areas

Major-, minor-, and trace-element data for the three U-Pb samples and for an undated sample of granitic orthogneiss from the core of the West Point Complex are listed in table 4. The undated sample (98ADb53B, fig. 2) is a weakly foliated, strongly altered, medium-grained, biotite-bearing granitic rock composed of approximately 80 volume percent perthitic K-feldspar with microcline twinning, subordinate plagioclase, quartz, biotite, white mica, and trace amounts of scattered, tiny (approx 0.1 mm diam) garnets, titanite, and Fe-Ti oxides. The rock has a weakly developed fabric defined by a preferred orientation of K-feldspar grains, quartz aggregates, and interstitial, scattered, medium-brown biotite crystals. Much of the biotite is altered to chlorite, and some of the smaller K-feldspar grains are altered to white mica. Quartz in the rock has been annealed, as evidenced by its uniform extinction and straight grain boundaries. Texturally, this rock is similar to the dated granitic orthogneiss, but the abundance of microcline twinning in sample 98ADb53B is similar to that of the dated sample of Devonian augen gneiss (sample 98ADb55B, tables 1, 4).

All four granitic samples have evolved, aluminous and potassic major-element compositions. Unlike the other samples, however, the sample of the granitic dike that intrudes the Salcha River gneiss dome is depleted in all rare-earth elements (La through Lu), as well as in Th, Zr, and Hf (table 4). This relative depletion is likely due to partitioning into accessory minerals, such as allanite and zircon, that remained in the crystal mush from which the melt was segregated. On an Rb-versus-Y+Nb discrimination diagram based on the empirical assignment of granitoids to various tectonic settings, the two samples of West Point orthogneiss and the granitic dike from the Salcha River gneiss dome plot close to one another at the margin of the volcanic-arc field where it adjoins the syncollisional field. The sample of augen gneiss plots along the syncollisional/within-plate boundary but near the apex between these two fields and the volcanic-arc field. All other samples of augen gneiss of known or likely Devonian age in the Lake George assemblage of the Yukon-Tanana Upland similarly plot near the apex of all three fields.

Sample 79AFr2010 of Aleinikoff and others (1984a), from an undeformed granitic stock that intrudes the Salcha River gneiss dome, was previously dated by them at 116±3 Ma. The sample has a major-element composition similar to that of sample 98ADb66B (table 4) but a higher Y content (26 versus 13.54 ppm) and a slightly higher Rb content (216 versus 200 ppm) (Aleinikoff and others, 2000). The Nb content of sample 79AFr2010 is known to be only <10 ppm but probably is similar to that of sample 98ADb66B (10.36 ppm). On this basis, the granitic stock would also plot along the boundary of the syncollisional and volcanic-arc fields, close to sample 98ADb66B. More valuable information, in terms of magma genesis, for the undeformed granitoid is provided by the Pb-, Sr-, O-, and Nd-isotopic data on sample 79AFr2010 determined by Aleinikoff and others (2000, who reported a high $^{207}Pb/^{204}Pb$ ratio (15.72 in K-feldspar), initial $^{87}Sr/^{86}Sr$ ratio (0.74132±0.00009), $\delta^{18}O$ value (11.1 permil), and Σ_{Nd} value (−21.4). These isotopic compositions overlap those expected for intermediate-composition to felsic Paleozoic crust and are consistent with derivation of the granitoid by anatexis of preexisting Yukon-Tanana crust (Aleinikoff and others, 2000), as well as with the abundance of Early Proterozoic inheritance in the igneous zircons, including sample 79AFr2010 and the samples of granitoid orthogneiss and granitic dikes in our study.

Tectonic Implications

The SHRIMP U-Pb zircon data and whole-rock compositional data indicate that the samples of mid-Cretaceous orthogneiss and undeformed granite from the West Point and Salcha River gneiss dome areas, respectively, were largely derived from preexisting continental basement, although the exact tectonic setting in which this magmatism occurred remains uncertain. Blum (1985) proposed that the mid-Cretaceous granitoids in the Fairbanks area were derived from subduction beneath the Yukon-Tanana terrane, whereas Newberry (2000) proposed that the mid-Cretaceous (116–110 Ma) intrusions in interior Alaska represent collisional magmatism. Hansen and Dusel-Bacon (1998) and Dusel-Bacon and others (2002) suggested that the oldest (~115 Ma) mid-Cretaceous plutons may have been emplaced during regional exhumation of higher-grade, lower-plate assemblages after burial by obducted thrust sheets. Evidence that the Salcha River gneiss dome was exposed during this postulated decompression event consists of the presence of andalusite-bearing quartz veins and partial melts within the core of the dome and the permissible closeness of the 113±2-Ma SHRIMP zircon crystallization ages for our granitoid dike sample, the 116±3-Ma TIMS U-Pb zircon age for the adjacent small undeformed intrusion within the dome, and a 113.6±2.8-Ma hornblende $^{40}Ar/^{39}Ar$ cooling age of hornblende-biotite-plagioclase schist from near the proposed detachment between the amphibolite-facies rocks and the overlying greenschist-facies Butte assemblage (see Dusel-Bacon and others, 2002). This geochronologic data set provides a narrow range of Early Cretaceous time during which the metamorphic rocks cooled and, in regard to the West Point orthogneiss, were emplaced and metamorphosed, before intrusion by crosscutting, undeformed granitoids. Ascribing either a metamorphic or igneous origin to the zircon rims in the West Point orthogneiss is compatible with this model because independent evidence suggests a near-contemporaneity for the two events. If our interpretations of the mid-Cretaceous samples and their U-Pb zircon ages are correct, the maximum igneous-crystallization age of the

West Point orthogneiss and the minimum igneous-crystallization age of the posttectonic Salcha intrusion imply that the mid-Cretaceous metamorphic episode occurred between 113 and 111 Ma.

Additional constraints on the timing of metamorphism and posttectonic plutonism in the southeastern part of the Big Delta quadrangle, which may be applicable to the timing of events in the study area (fig. 1), are currently being generated by a comparable SHRIMP U-Pb zircon analysis of amphibolite-grade rocks 75 km to the south, in the Central Creek area, where Day and others (2002) have reported U-Pb ages of 116±4 and 116±2 Ma for what they interpret as metamorphic overgrowths on zircons from a biotite quartzofeldspathic gneiss and a biotite-sillimanite paragneiss, respectively. If correctly interpreted, these ages would appear to date the timing of Cretaceous metamorphism in that area. Day and others have also proposed that this metamorphic event closely preceded the emplacement of undeformed granitic dikes which yielded a SHRIMP U-Pb zircon age of 111±4 Ma.

Whereas the timing of metamorphism and postkinematic plutonism in the West Point and Salcha River gneiss dome areas appears to be similar to that in the Central Creek area in the southeastern part of the Big Delta quadrangle, the sense of shear and the deformational history during the mid-Cretaceous event appear to have differed in these two areas. Day and others (2002) equated this mid-Cretaceous metamorphic episode in their study area with westward-vergent thrusting and observed no evidence of top-to-the-southeast extension. Dusel-Bacon and others' (2002) kinematic study in the Central Creek area also indicated top-to-the-west and top-to-the-northwest structural vergence, with no evidence of the top-to-the-southeast deformation that was equated with crustal extension in the Salcha River gneiss dome area (Pavlis and others, 1993) and in the northeastern Tanacross area, near the Alaska-Yukon Territory border (Hansen and Dusel-Bacon, 1998). Kinematic measurements in the vicinity of the West Point Complex, though sparse, locally indicate top-to-the-southeast vergence (see Oliver and Dusel-Bacon, this volume), which is permissive evidence for the regional extensional event proposed for other parts of the Yukon-Tanana Upland.

Acknowledgments

Charlie Bacon (USGS) played a key role in fieldwork and sample collection. Melanie Hopkins (USGS) provided graphical and office support. Chuck Holdsworth (USGS) expertly separated the zircons from our samples. Brad Ito (USGS) kept the SHRIMP–RG working, and Harold Persing (USGS) provided able all-around assistance with the SHRIMP. Jeff Drake of the University of Alaska, Fairbanks, assisted in the preparation and analysis of mica samples for $^{40}Ar/^{39}Ar$ dating. We thank USGS geologists John Aleinikoff and Dwight Bradley for their helpful reviews of the manuscript.

References Cited

Aleinikoff, J.N., Dusel-Bacon, Cynthia, and Foster, H.L., 1984a, Uranium-lead isotopic ages of zircon from sillimanite gneiss, east-central Alaska, and implications for Paleozoic metamorphism, Big Delta quadrangle, *in* Coonrad, W.L. and Elliott, R.L., eds., The United States Geological Survey in Alaska—accomplishments during 1981: U.S. Geological Survey Circular 868, p. 45–48.

———1986, Geochronology of augen gneiss and related rocks, Yukon-Tanana terrane, east-central Alaska: Geological Society of America Bulletin, v. 97, no. 5, p. 626–637.

Aleinikoff, J.N., Dusel-Bacon, Cynthia, Foster, H.L., and Nokleberg, W.J., 1987, Lead isotopic fingerprinting of tectono-stratigraphic terranes, east-central Alaska: Canadian Journal of Earth Sciences, v. 24, no. 10, p. 2089–2098.

Aleinikoff, J.N., Farmer, G.L., Rye, R.O., and Nokleberg, W.J., 2000, Isotopic evidence for the sources of Cretaceous and Tertiary granitic rocks, east-central Alaska—implications for the tectonic evolution of the Yukon-Tanana terrane: Canadian Journal of Earth Sciences, v. 37, no. 6, p. 945–956.

Aleinikoff, J.N., Foster, H.L., Nokleberg, W.J., and Dusel-Bacon, Cynthia, 1984b, Isotopic evidence from detrital zircons for Early Proterozoic crustal material, east-central Alaska, *in* Coonrad, W.L., and Elliott, R.L., eds., The United States Geological Survey in Alaska—accomplishments during 1981: U.S. Geological Survey Circular 868, p. 43–45.

Aleinikoff, J.N., Moore, T.E., Nokleberg, W.J., and Koch, R.D., 1995, Preliminary U-Pb ages from detrital zircons from the Arctic Alaska and Yukon-Tanana terranes, Alaska [abs.]: Geological Society of America Abstracts with Programs, v. 27, no. 5, p. 2.

Barr, S.M., Raeside, R.P., and van Breemen, Otto, 1987, Grenvillian basement in the northern Cape Breton Highlands, Nova Scotia: Canadian Journal of Earth Sciences, v. 24, no. 5, p. 992–997.

Blum, J.D., 1985, A petrologic and Rb-Sr isotopic study of intrusive rocks near Fairbanks, Alaska: Canadian Journal of Earth Sciences, v. 22, no. 9, p. 1314–1321.

Chatterjee, N.D., and Johannes, Wilhelm, 1974, Thermal stability and standard thermodynamic properties of synthetic $2M_1$-muscovite, $KAl_2(AlSi_3O_{10}(OH)_2)$: Contributions to Mineralogy and Petrology, v. 48, p. 89–114.

Churkin, Michael, Jr., Foster, H.L., Chapman, R.M., and Weber, F.R., 1982, Terranes and suture zones in east-central Alaska: Journal of Geophysical Research, v. 87, no. 5, p. 3718–3730.

Coney, P.J., Jones, D.L., and Monger, W.H., 1980, Cordilleran suspect terranes: Nature, v. 288, no. 5789, p. 329–333.

Creaser, R.A., Heaman, L.M., and Erdmer, Philippe, 1997, Timing of high-pressure metamorphism in the Yukon-Tanana terrane, Canadian Cordillera—constraints from U-Pb zircon dating of eclogite from the Teslin tectonic zone: Canadian Journal of Earth Sciences, v. 34, no. 5, p. 709–715.

Day, W.C., Aleinikoff, J.N., Henning, M.H., Gamble, B.M., and Gough, L.P., 2002, Overview of the bedrock geologic setting of the Big Delta B–2 quadrangle, Alaska [abs.]: Alaska Miners Association Biennial Conference, 18th, Fairbanks, 2002, Abstracts, p. 10–11.

Dusel-Bacon, Cynthia, and Aleinikoff, J.N., 1996, U-Pb zircon and titanite ages for augen gneiss from the Divide Mountain area, eastern Yukon-Tanana upland, Alaska, and evidence for the composite nature of the Fiftymile Batholith, *in* Moore, T.E., and Dumoulin, J.A., eds., Geologic studies in Alaska by the U.S. Geological Survey during 1994: U.S. Geological Survey Bulletin 2152, p. 131–141.

Dusel-Bacon, Cynthia, Brosgé, W.P., Till, A.B., Doyle, E.O., Mayfield, C.F., Reiser, H.N., and Miller, T.P., 1989, Distribution, facies, ages, and proposed tectonic associations of regionally metamorphosed rocks in northern Alaska: U.S. Geological Survey Professional Paper 1497–A, 44 p., 2 sheets, scale 1:1,000,000.

Dusel-Bacon, Cynthia, and Cooper, K.M., 1999, Trace-element geochemistry of metabasaltic rocks from the Yukon-Tanana Upland and implications for the origin of tectonic assemblages in east-central Alaska: Canadian Journal of Earth Sciences, v. 36, no. 10, p. 1671–1695.

Dusel-Bacon, Cynthia, Csejtey, Béla, Jr., Foster, H.L., Doyle, E.O., Nokleberg, W.J., and Plafker, George, 1993, Distribution, facies, ages, and proposed tectonic associations of regionally metamorphosed rocks in east- and south-central Alaska: U.S. Geological Survey Professional Paper 1497–C, 73 p., 2 sheets, scale 1:1,000,000.

Dusel-Bacon, Cynthia, and Foster, H.L., 1983, A sillimanite gneiss dome in the Yukon crystalline terrane, east-central Alaska—petrography and garnet-biotite geothermometry: U.S. Geological Survey Professional Paper 1170–E, 25 p.

Dusel-Bacon, Cynthia, Hansen, V.L., and Scala, J.A., 1995, High-pressure amphibolite facies dynamic metamorphism and the Mesozoic tectonic evolution of an ancient continental margin, east-central Alaska: Journal of Metamorphic Geology, v. 13, no. 1, p. 9–24.

Dusel-Bacon, Cynthia, Lanphere, M.A., Sharp, W.D., Layer, P.W., and Hansen, V.L., 2002, Mesozoic thermal history and timing of structural events for the Yukon-Tanana Upland, east-central Alaska—$^{40}Ar/^{39}Ar$ data from metamorphic and plutonic rocks: Canadian Journal of Earth Sciences, v. 39, no. 6, p. 1013–1051.

Dusel-Bacon, Cynthia, and Murphy, J.M., 2001, Apatite fission-track evidence of widespread Eocene heating and exhumation in the Yukon-Tanana Upland, interior Alaska: Canadian Journal of Earth Sciences, v. 38, no. 8, p. 1191–1204.

Erdmer, Philippe, Ghent, E.D., Archibald, D.A., and Stout, M.Z., 1998, Paleozoic and Mesozoic high-pressure metamorphism at the margin of ancestral North America in central Yukon: Geological Society of America Bulletin, v. 110, no. 5, p. 615–629.

Foster, H.L., 1992, Geologic map of the eastern Yukon-Tanana region, Alaska: U.S. Geological Survey Open-File Report 92–313, 26 p., scale 1:500,000.

Foster, H.L., Cushing, G.W., Keith, T.E.C., and Laird, Jo, 1985, Early Mesozoic tectonic history of the Boundary area, east-central Alaska: Geophysical Research Letters, v. 12, no. 9, p 553–556.

Foster, H.L., Keith, T.E.C., and Menzie, W.D., 1994, Geology of the Yukon-Tanana area of east-central Alaska, *in* Plafker, George, and Berg, H.C., eds., The geology of Alaska, v. G–1 *of* The geology of North America: Boulder, Colo., Geological Society of America, p. 205–240.

Foster, H.L., Laird, Jo, Keith, T.E.C., Cushing, G.W., and Menzie, W.D., 1983, Preliminary geologic map of the Circle quadrangle, Alaska: U.S. Geological Survey Open-File Report 83–170–A, 32 p., scale 1:250,000.

Foster, H.L., Menzie, W.D., Cady, J.W., Simpson, S.L., Aleinikoff, J.N., Wilson, F.H., and Tripp, R.B., 1987, The Alaska Mineral Resource Assessment Program—background information to accompany folio of geologic and mineral resource maps of the Circle quadrangle, Alaska: U.S. Geological Survey Circular 986, 22 p.

Hansen, V.L., 1990, Yukon-Tanana terrane; a partial acquittal: Geology, v. 18, no. 4, p. 365–369.

Hansen, V.L., and Dusel-Bacon, Cynthia, 1998, Structural and kinematic evolution of the Yukon-Tanana upland tectonites, east-central Alaska—a record of late Paleozoic to Mesozoic crustal assembly: Geological Society of America Bulletin, v. 110, no. 2, p. 211–230.

Hansen, V.L., Heizler, M.T., and Harrison, T.M., 1991, Mesozoic thermal evolution of the Yukon-Tanana composite terrane—new evidence from $^{40}Ar/^{39}Ar$ data: Tectonics, v. 10, no. 1, p. 51–76.

Heslop, Kate, Dusel-Bacon, Cynthia, and Williams, I.S., 1995, Survival of zircon U-Pb isotopic systems through partial melting and high P-T dynamothermal metamorphism, Yukon-Tanana terrane, Alaska [abs]: Geological Society of America Abstracts with Programs, v. 27, no. 5, p. 26.

Lanphere, M.A., Dalrymple, G.B., Fleck, R.J., and Pringle, M.S., 1990, Intercalibration of mineral standards for K-Ar and $^{40}Ar/^{39}Ar$ age measurements [abs]: Eos (American Geophysical Union Transactions), v. 71, no. 43, p. 1658.

Layer, P.W., Hall, C.M., and York, Derek, 1987, The derivation of $^{40}Ar/^{39}Ar$ age spectra of single grains of hornblende and biotite by laser step heating: Geophysical Research Letters, v. 14, no. 7, p. 757–760.

Ludwig, K.R., 2001, Users manual for Isoplot/Ex rev. 2.49, a geochronological toolkit for Microsoft Excel: Berkeley, Calif., Berkeley Geochronology Center Special Publication 1a, 56 p.

McDougall, Ian, and Harrison, T.M., 1988, Geochronology and thermochronology by the $^{40}Ar/^{39}Ar$ method: New York, Oxford University Press, 212 p.

Mortensen, J.K., 1992, Pre-mid-Mesozoic tectonic evolution of the Yukon-Tanana terrane, Yukon and Alaska: Tectonics, v. 11, no. 4, p. 836–853.

Newberry, R.J., 2000, Mineral deposits and associated Mesozoic and Tertiary igneous rocks within the interior Alaska and adjacent Yukon portions of the "Tintina gold belt"; a

progress report, *in* Tucker, T.L., and Smith, M.T., chairpersons, The Tintina gold belt; concepts, exploration, and discoveries (special volume 2): Vancouver, British Columbia and Yukon Chamber of Mines, p. 59–87.

Pačes, J.B., and Miller, J.D., 1993, U-Pb ages of the Duluth Complex and related mafic intrusions, northeastern Minnesota: geochronologic insights into physical, paleomagnetic and tectonomagmatic processes associated with the 1.1 Ga mid-continent rift system: Journal of Geophysical Research, v. 98, no. B8, p. 13997–14013.

Pavlis, T.L., Sisson, V.B., Foster, H.L., Nokleberg, W.J., and Plafker, George, 1993, Mid-Cretaceous extensional tectonics of the Yukon-Tanana terrane, Trans-Alaskan Crustal Transect (TACT), east-central Alaska: Tectonics, v. 12, no. 1, p. 103–122.

Pearce, J.A., Harris, N.B.W., and Tindle, A.G., 1984, Trace element discrimination diagrams for the tectonic interpretaton of granitic rocks: Journal of Petrology, v. 25, no. 4, p. 956–983.

Poldervaart, Arie, 1956, Zircons in rocks. 2. Igneous rocks: American Journal of Science, v. 254, no. 9, p. 521–554.

Robinson, M.S., Smith, T.E., and Metz, P.A., 1990, Bedrock geology of the Fairbanks Mining District: Alaska Division of Geological and Geophysical Surveys Professional Report 106, 2 sheets, scale 1:63,360.

Samson, S.D., and Alexander, E.C., Jr., 1987, Calibration of the interlaboratory $^{40}Ar/^{39}Ar$ dating standard, MMhb–1: Chemical Geology, v. 66, no. 1–2, p. 27–34.

Silver, L.T., 1969, A geochronological investigation of the anorthosite complex, Adirondack Mountains, New York, *in* Isachsen, Y.W., ed., Origin of anorthosite and related rocks: New York State Museum and Science Service Memoir 18, p. 233–251.

Smith, T.E., Robinson, M.S., Weber, F.R., Waythomas, C.W., and Reifenstuhl, R.R., 1994, Geologic map of the upper Chena River area, eastern Interior Alaska: Alaska Division of Geological and Geophysical Surveys Professional Report 115, 19 p., scale 1:63,360.

Spear, F.S., 1993, Metamorphic phase equilibria and pressure-temperature-time paths: Washington, D.C., Mineralogical Society of America, 799 p.

Steiger, R.H., and Jäger, Emilie, 1977, Subcommission on geochronology; convention on the use of decay constants in geo- and cosmochronology, Earth and Planet Science Letters, v. 36, no. 3, p. 359–362.

van Breemen, Otto, Davidson, Anthony, Loveridge, W.D., and Sullivan, R.W., 1986, U-Pb zircon geochronology of Grenville tectonites, granulites, and igneous precursors, Parry Sound, Ontario, *in* Moore, J.M., ed., The Grenville Province: Geological Association of Canada Special Paper 31, p. 191–207.

van Breemen, Otto, Henderson, J.B., Loveridge, W.D., and Thompson, P.H., 1987, U-Pb zircon and monazite geochronology and zircon morphology of granulites and granite from the Thelon Tectonic Zone, Healy Lake and Artillery Lake mafic areas, N.W.T., *in* Current research, part A: Geological Survey of Canada Paper 87–1A, p. 783–801.

Weber, F.R., Foster, H.F., Keith, T.E.C., and Dusel-Bacon, Cynthia, 1978, Preliminary geologic map of the Big Delta quadrangle, Alaska. U.S. Geological Survey Open-File Report 78–529–A, scale 1:250,000.

Wheeler, J.O., and McFeely, Patricia, 1991, Tectonic assemblage map of the Canadian Cordillera and adjacent parts of the United States of America: Geological Survey of Canada Map 1712A, scale 1:2,000,000.

Williams, I.S., 1998, U-Th-Pb geochronology by ion microprobe; not just ages but histories, *in* McKibben, M.A., Shanks, W.C., and Ridley, W.I., eds., Applications of microanalytical techniques to understanding mineralizing processes: Society of Economic Geologists Reviews in Economic Geology, v. 7, p. 1–35.

Williams, I.S., and Hergt, J.M., 2000, U-Pb dating of Tasmanian dolerites; a cautionary tale of SHRIMP analysis of high-U zircon, *in* Woodhead, J.D., Hergt, J.M., and Noble, W.P., eds., Beyond 2000; New Frontiers in Isotope Geoscience, Lorne, Australia, Abstracts and Proceedings: Victoria, Australia, University of Melbourne, p. 185–188.

Wilson, F.H., Smith, J.G., and Shew, Nora, 1985, Review of radiometric data from the Yukon crystalline terrane, Alaska and Yukon Territory: Canadian Journal of Earth Sciences, v. 22, no. 4, p. 525–537.

York, Derek, Hall, C.M., Yanase, Yotaro, Hanes, J.A., and Kenyon, W.J., 1981, $^{40}Ar/^{39}Ar$ dating of terrestrial minerals with a continuous laser: Geophysical Research Letters, v. 8, no. 11, p. 1136–1138.

Studies by the U.S. Geological Survey in Alaska, 2001
U.S. Geological Survey Professional Paper 1678

Kinematic Analysis from Tectonites in the Northern Part of the Big Delta Quadrangle, East-Central Alaska

By Douglas H. Oliver and Cynthia Dusel-Bacon

Abstract

New structural analysis has helped define a polyphase deformation history in ductilely deformed tectonites between the Chena and Salcha Rivers in the Yukon-Tanana Upland of east-central Alaska. The sedimentary, intrusive, and volcanic protoliths have been metamorphosed and subjected to partitioned noncoaxial shearing. We have integrated kinematic indicators from outcrop motion-plane views and oriented thin sections with nine quartz *c*-axis fabric analyses. Top-to-the-northwest, top-to-the-southeast, and local top-to-the-southwest shear senses that are preserved are the products of discrete deformation events. In other parts of the Yukon-Tanana Upland, the top-to-the-northwest and top-to-the-southeast fabrics previously were suggested to have resulted from Early Jurassic crustal contraction and mid-Cretaceous extension, respectively. The West Point orthogneiss, which occurs in the core of a high-grade igneous-metamorphic complex in the northeastern part of the Big Delta quadrangle, may have been exhumed during the mid-Cretaceous deformational event, but the top-to-the-southwest fabrics contained in the structurally low carbonaceous unit remain problematic. Unusual tectonites containing multiple quartz lattice-preferred-orientation domains provide additional evidence of polyphase deformation. Quartz *c*-axis fabric analysis on a domain-by-domain basis suggests that the analyzed fabric resulted from partial overprinting during strain-partitioned ductile shearing.

Introduction

The metamorphic rocks of the Yukon-Tanana Upland reflect a complex deformational and metamorphic history. These rocks, generally referred to as the Yukon-Tanana terrane, compose the largest tectonostratigraphic terrane in the northern Cordillera. They are fault bounded along most of their length by the right-lateral Tintina and Denali Fault systems on the northeast and southwest, respectively. This polygenetic terrane has been subdivided on the basis of differences in the composition and age of protoliths and the structural and metamorphic histories of its components (for example, Foster and others, 1985, 1994; Nokleberg and others, 1989; Hansen and others, 1991; Dusel-Bacon and Cooper, 1999). Previous kinematic and geochronologic studies have delineated the following three major deformational events across the Yukon-Tanana terrane from the United States-Canadian border to Fairbanks, Alaska (Hansen and others, 1991; Pavlis and others, 1993; Hansen and Dusel-Bacon, 1998; Day and others, 2000; Dusel-Bacon and others, 2002): (1) pre-latest Triassic, northeastward-directed, margin-normal contraction of the structurally high level oceanic Seventymile terrane and structurally high level marginal-basin assemblages of the Yukon-Tanana terrane (the Taylor Mountain assemblage of Hansen and Dusel-Bacon, 1998—recently renamed the Fortymile River assemblage by Dusel-Bacon and others, 2002—and the Nisutlin assemblage of Hansen and Dusel-Bacon, 1998) during west-dipping subduction and closure of the Anvil ocean; (2) Early Jurassic, northwestward-directed, inferred margin-parallel contraction and imbrication that resulted in emplacement of the structurally high, outboard assemblages onto parautochthonous continental-margin rocks of the ancient Pacific margin, including the Lake George assemblage of Dusel-Bacon and Cooper (1999) (previously referred to as the Lake George subterrane of the Yukon-Tanana terrane by Pavlis and others, 1993); and (3) Early Cretaceous southeastward-directed crustal extension that resulted in exposure of the structurally deepest, parautochthonous continental-margin rocks of the Lake George assemblage.

This chapter presents new kinematic data from a study area between the Chena and Salcha Rivers in the northern part of the Big Delta quadrangle (fig. 1). The data were collected during a topical study by Dusel-Bacon and others (1998) of the framework geology and syngenetic base-metal potential of greenschist-facies carbonaceous rocks correlated by Dusel-Bacon and others (1998) with the Nasina assemblage of Wheeler and McFeely (1991), and of a unit of quartz-chlorite-muscovite semischist and associated metasedimentary rocks, marble, and greenstone that was formerly referred to as the Butte subterrane of the Yukon-Tanana terrane by Pavlis and others (1993) hereinafter referred to as the Butte assemblage. We also collected kinematic data in the amphibolite-facies metaigneous and metamorphic rocks of the West Point area to compare the deformational and thermal history of this area with that of the sillimanite-bearing Salcha River gneiss dome (terminology of Dusel-Bacon and others, 2002) to the southeast (fig. 1). U-Pb zircon and $^{40}Ar/^{39}Ar$ mica data relating to those high-grade areas are presented by Dusel-Bacon, Wooden, and Layer (this volume).

Previous Studies in the Chena-Salcha Rivers Area

A detailed reconnaissance map of the study area (fig. 1) was originally made by Weber and others (1978). Subsequent petrologic and field studies defined a sillimanite gneiss dome that structurally underlies the surrounding greenschist-facies rocks in an area that straddles the Salcha River (Dusel-Bacon and Foster, 1983). Later kinematic analysis of the structural contact between the greenschist-facies rocks and the Salcha River gneiss dome revealed the contact to be a folded low-angle extensional detachment that formed during east-southeastward-directed crustal extension (Pavlis and others, 1993). Detailed mapping in the upper Chena River area by Smith and others (1994) formally defined the West Point Complex—a topographically high area of upper amphibolite-facies metamorphic rocks that were intruded by abundant premetamorphic and postmetamorphic felsic to intermediate-composition igneous rocks. Smith and others (1994) interpreted this complex to be gradational into the adjacent unit that forms the lowest unit of a stratigraphic and decreasing metamorphic-grade sequence (from bottom to top) of (1) quartzite-dominant basement rocks (Fairbanks schist unit of Robinson and others, 1990); (2) primarily metavolcanic rocks, marble, augen gneiss, and pelitic schist (Chena River sequence of Smith and others, 1994); (3) calcareous schist and phyllite (Dan Creek unit of Smith and others, 1994); (4) carbonaceous rocks (Nasina assemblage, fig. 1; Blackshell unit of Smith and others, 1994); and (5) phyllite, semischist, and marble (Butte assemblage). Smith and others correlated their Blackshell unit and the overlying Butte assemblage with the Keevy Peak Formation and the Totatlanika Schist, respectively, in the Alaska Range (Wahrhaftig, 1968, 1970).

Throughout the study area (fig. 1), contacts between the various assemblages are not exposed and generally occur in saddles. Results from diamond drilling within the carbonaceous Nasina assemblage in the Teuchet Creek and Munson Creek areas (fig. 1) revealed that the contacts of major lithologic variations within this assemblage are strongly sheared and, in places, are the locus of quartz veining, suggesting some degree of structural modification or even structural emplacement. Drilling within the carbonaceous rocks further revealed that foliation, lithologic contacts, and sulfide bodies all approximately parallel one another at a gentle dip of approximately 20° S. (J.R. Bressler, oral commun., 2002). The contact between the greenschist-facies Butte and Nasina assemblages was interpreted by Foster (1992) and Smith and others (1994) to be a low-angle thrust fault, though not on the basis of any structural data, and so the low-angle fault may, instead, be an extensional detachment. Although an actual fault contact between these units is rarely visible in the field, the best evidence for it is the presence of a sliver of ultramafic rock along the contact, just east of the most highly mineralized sulfide section penetrated during drilling (TC, fig. 1), suggesting structural interleaving of an oceanic rock type between two different continental-margin assemblages.

Deformational History of Tectonites of the Chena-Salcha Rivers Area

The deformed phyllite, schist, and gneiss (tectonites) of the Chena-Salcha Rivers area preserve a complex and poorly understood structural history. As elsewhere in the Yukon-Tanana composite terrane (Pavlis and others, 1993; Hansen and Dusel-Bacon, 1998), rocks in the study area (fig. 1) have undergone multiple episodes of ductile and brittle deformation, metamorphism, and, locally, thermal reheating related to Cretaceous and (or) Tertiary igneous activity. The style of deformation within the various greenschist- and amphibolite-facies units is broadly similar, consisting of flat-lying to gently dipping foliation, locally developed elongation lineation, centimeter- to meter-scale folds, and crenulations and spaced cleavage in the lower-grade rocks. Given the sparse outcrop exposure in the study area and its geologic complexity, an indepth understanding of the deformational history will require more detailed study.

Although the rocks in the study area (fig. 1) show evidence of brittle deformation, this chapter focuses on the ductile-deformational history that largely preceded it. Textures of sedimentary, intrusive, and volcanic protoliths are preserved in some of the greenschist-facies rocks, although primary bedding (S_0) is not commonly observed. Relic protolith textures are less common in the higher-grade amphibolite-facies rocks that make up the West Point Complex and the Salcha River gneiss dome in the northeastern and southwestern parts of the study area, respectively. Most tectonites display a penetrative ductile foliation (S_1) consisting of flattened, commonly elongate, recrystallized and (or) comminuted mineral grains. The intensity of tectonite fabric formation varies significantly both across the study area and within individual outcrops, largely as a result of strain partitioning, as evidenced by the discrete bands of mylonite found in many outcrops across the study area. Microlithons—thin septa of rock whose internal foliation is sharply discordant to the shear bands that enclose it—that are locally well formed further attest to the partial overprinting of earlier formed fabrics, although not all lithologic units may have undergone a common deformational history. Folds, ranging from close to isoclinal in interlimb angle, show no systematic trends with respect to the orientation of their fold axes and likely formed at different times during the deformational history. Though not as common as folds, boudins are also observed, most of which are consistent with northeast-southwestward crustal extension.

Many of the tectonites in the study area (fig. 1) also display a mineral-elongation lineation (L_e) consisting of sheared mica or rodded quartz. The trend of L_e varies considerably across the study area but is mostly northwest-southeastward, although clear northeast-southwestward trends are observed in a few areas, notably in the Nasina assemblage in the Teuchet Creek area and in an isolated area in the Butte assemblage adjacent to the low-angle fault southwest of the ultramafic (peridotite) body near VABM Nail (peridotite of Salcha

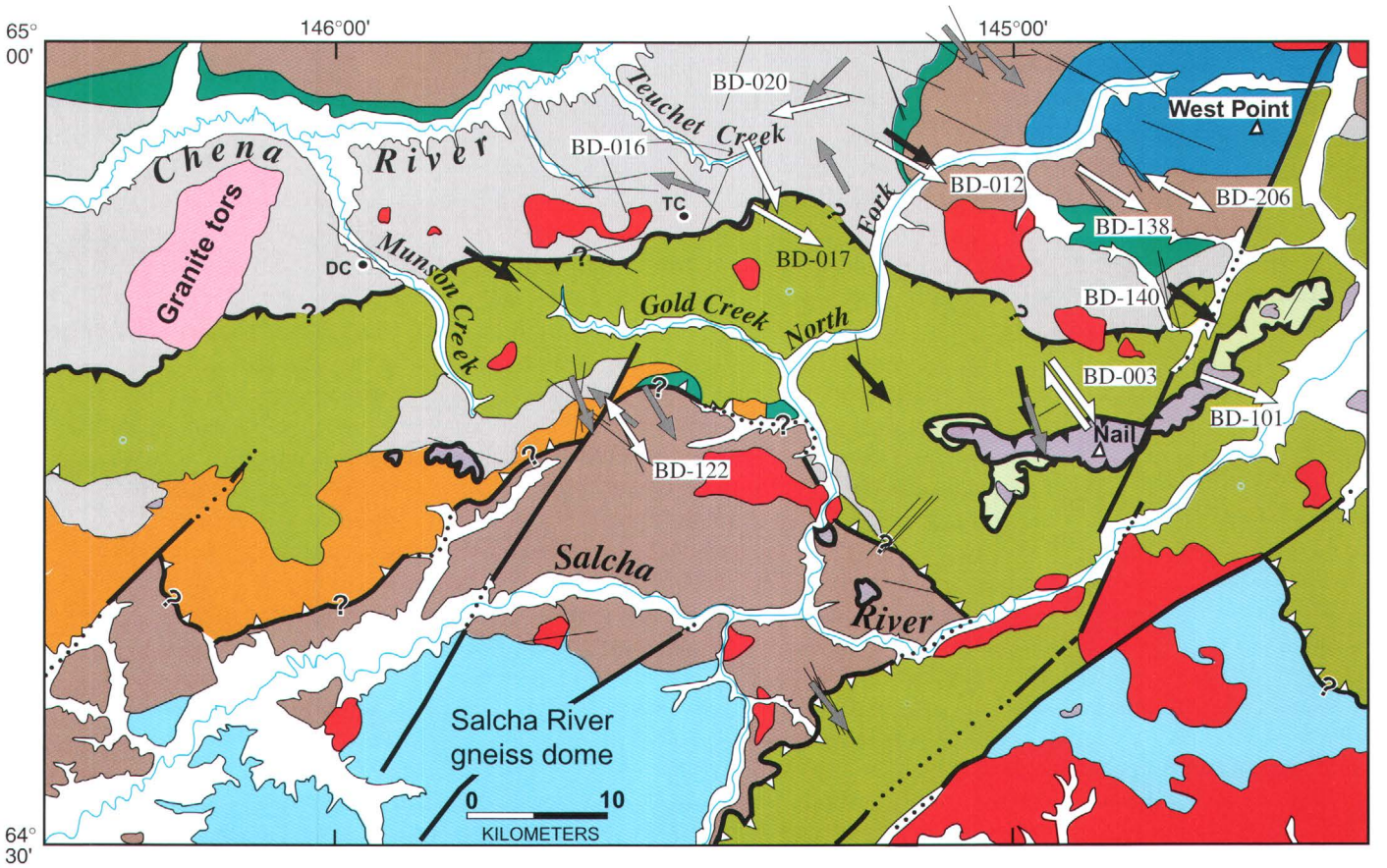

EXPLANATION

Surficial deposits (Quaternary)

Postmetamorphic granitoids (Tertiary and Cretaceous)

STRUCTURALLY HIGHER ROCKS

Peridotite (purple), greenstone, metalimestone, metachert, and metasedimentary rocks (Triassic, Permian, and Mississippian–Seventymile terrane)

Greenschist-facies semischist, phyllite, quartzite, marble, and greenstone (Mississippian and Devonian)–Butte subterrane of the Yukon-Tanana terrane of Pavlis and others (1993)

Greenschist-facies quartzofeldspathic mylonite schist and gneiss (Mississippian and Devonian)

STRUCTURALLY LOWER ROCKS

Greenschist-facies carbonaceous quartzite and phyllite and felsic and mafic metavolcanic rocks (Mississippian and Devonian)–Nasina assemblage of Wheeler and McFeely (1991)

Amphibolite-facies calcareous phyllite and marble

Amphibolite-facies peltic schist, quartzite, marble, and amphibolite

Amphibolite-facies sillimanite gneiss, quartzite, and marble

Amphibolite-facies quartzite, marble, pelitic schist, and orthogneiss–West Point Complex of Smith and others (1994)

Contact

Fault; dotted where concealed

Thrust fault; sawteeth on upper plate, queried where uncertain

Low-angle normal fault; sawteeth on upper plate, dotted where concealed, queried where uncertain

Kinematics based on quartz *c*-axis fabric analysis (top-to-the-northwest and coaxial shear)

Tectonites with multiple quartz lattice-preferred orientation domains showing opposing shear senses based on quartz *c*-axis fabric analysis

Microkinematic indicators (top-to-the-northwest shear)

Mesokinematic and macrokinematic indicators (top-to-the-northwest shear)

Trend of elongation lineation

BD-017 Kinematic samples referred to in text

Mineralized diamond-drill hole at Teuchet Creek (TC) and Drone Creek (DC) properties

Named peak

Figure 1. Geologic map of northern part of the Big Delta quadrangle, east-central Alaska (modified from Weber and others, 1978), showing distribution of linear and planar fabric elements and kinematic interpretations.

River of Foster and others, 1994; "Nail" allochthon of Southworth, 1984; hereinafter referred to as the Nail allochthon). Particularly well formed microlithons are observed both in the Teuchet Creek area (Watkinson, 1992) and in the area of carbonaceous and quartzofeldspathic rocks just west of the northeast-trending fault south of Gold Creek (fig. 1), suggesting local preservation of earlier-formed fabrics that may have been obliterated elsewhere.

As a fabric element, L_e generally forms parallel to the direction of maximum principle extension for the deformational event that formed it (Anderson, 1948). L_e alone, however, cannot uniquely constrain the aggregate sense of shear that the rock has undergone. Relative to the structural reference frame (X parallel to L_e, Z normal to foliation, and Y perpendicular to X and Z), fabric asymmetries in the motion (XZ) plane provide a means of evaluating kinematics (for example, Berthé and others, 1979; Simpson and Schmid, 1983; Hanmer and Passchier, 1991; Passchier and Trouw, 1996).

Motion-plane views observed in the field show relatively few kinematic indicators, mostly consisting of weakly formed S–C fabrics, σ-porphyroclasts (with "tails" of comminuted mineral grains streaming from them), and asymmetric folds. Microshear-sense indicators, however, were present in approximately 20 percent of the motion-plane thin sections. The microkinematic indicators we commonly observed include S–C fabrics, rotated porphyroclasts, σ-porphyroclasts, and quartz grain-shape preferred orientation (GSPO), although the confidence level of these indicators—a function of the number of indicators per thin section, degree of asymmetry, and asymmetric consistency—is generally low. In addition, some opposing shear-sense indicators were observed in closely proximal tectonites (pelitic schist) south of Gold Creek (fig. 1).

Quartz-rich tectonites in the Chena-Salcha Rivers area (fig. 1) commonly display petrofabrics characterized by a well-formed quartz lattice-preferred orientation (LPO) when viewed under crossed polars with the gypsum plate inserted. LPOs result when quartz grains rotate or recrystallize during shearing into crystallographic orientations conducive to ductile deformation. Dislocation glide, the principle mechanism responsible for ductile deformation in quartz, involves propagation of defects through the crystal lattice at moderate to high temperatures. Basal, prism, and rhomb crystallographic planes provide the primary slip surfaces in quartz, with defect migration in the crystallographic <*a*> or <*c*> directions. Measurements of *c*-axis orientations in siliceous tectonites is an accepted kinematic technique for differentiating coaxial from noncoaxial shear, establishing the sense of shear, and also can provide information regarding the physical conditions during deformation (Schmid and Casey, 1986; Law, 1990). Symmetrical (orthorhombic) versus asymmetric (monoclinic or triclinic) stereograms of *c*-axis distributions can be used to differentiate coaxial from noncoaxial shear in quartz-rich tectonites, and shear sense can be determined from the sense of asymmetry (fig. 2).

Quartz *c*-axis fabric analysis was conducted on nine siliceous tectonites that represent mylonitized quartzite or transposed quartz veins. Following the method of Turner and Weiss (1963), we measured quartz *c*-axes in the XZ plane on a petrographic microscope equipped with a universal stage. A minimum of 250 *c*-axes were measured, unless otherwise indicated. Equal-area, lower-hemisphere stereograms with the XZ plane as the perimeter circle are shown in figure 2. Fabric elements of the stereoprojections were evaluated in terms of strength, asymmetry, and active slip systems.

Seven out of the nine thin sections of quartz-rich rocks from the study area (fig. 1) for which we measured quartz *c*-axes exhibit a single well-developed LPO, as evidenced by uniform interference colors when viewed under crossed polars with the gypsum plate inserted, thus indicating a single coherent alignment of the quartz *c*-axes in the sample. However, thin sections of two quartz-rich greenschist-facies tectonites from the study area are unusual in that multiple distinct LPO domains, as indicated by an ordered distribution of interference colors, are preserved. Initial quartz *c*-axis petrofabric analysis of these samples produced stereoplots unlike those typically observed in nature and did not allow for a shear-sense determination. However, by utilizing a detailed analysis of quartz *c*-axes petrofabrics on a domain-by-domain basis across each thin section, consistent patterns of shear sense were revealed. Individual domains in sample BD–003 (fig. 3*A*) show opposing shear senses. For domains with high-order interference colors (blue), the quartz grains indicate top-to-the-northwest shear, whereas domains with low-order interference colors (yellow) show well-defined top-to-the-southeast fabrics. In addition, domains characterized by deep-orange or dark-blue interference colors, indicative of quartz grains whose *c*-axes are normal to the plane of the thin section, show triclinic patterns of quartz *c*-axis distributions. Sample BD–016 (fig. 3*B*) shows a similar pattern of alternating LPO domains that record opposing top-to-the-northwest and top-to-the-southeast shear senses. Microkinematic indicators (GSPO) contained within the LPO domains of this sample also indicate opposing senses of shear, corroborating the results of quartz *c*-axis petrofabric analysis in the various domains. In sample BD–016, the top-to-the-southeast fabrics are more monoclinic, and the top-to-the-northwest fabric asymmetries more triclinic, than for comparable domains in sample BD–003. Sample BD–016 also contains a single domain near extinction (dark blue area, fig. 3*B*) that yielded a strongly triclinic quartz *c*-axis distribution. Tectonites showing multiple LPO domains have previously been reported from geologic units in the Teslin suture zone of the central Yukon Territory, Canada (Oliver, 1998), believed to be correlative with greenschist-facies rocks of the study area (Hansen and others, 1991).

The combination of quartz *c*-axis petrofabrics and macro/microkinematic indicators reveal a complex and somewhat ambiguous deformational history. In the localities where shear sense is evident, both top-to-the-northwest and top-to-the-southeast shear senses are preserved, in some places in close proximity to each other (fig. 1). Only within the vicinity of the West Point Complex are top-to-the-northwest shear fabrics absent. In addition, some quartz *c*-axis petrofabrics do not reveal a clear sense of shear (fig. 2). While some of these fab-

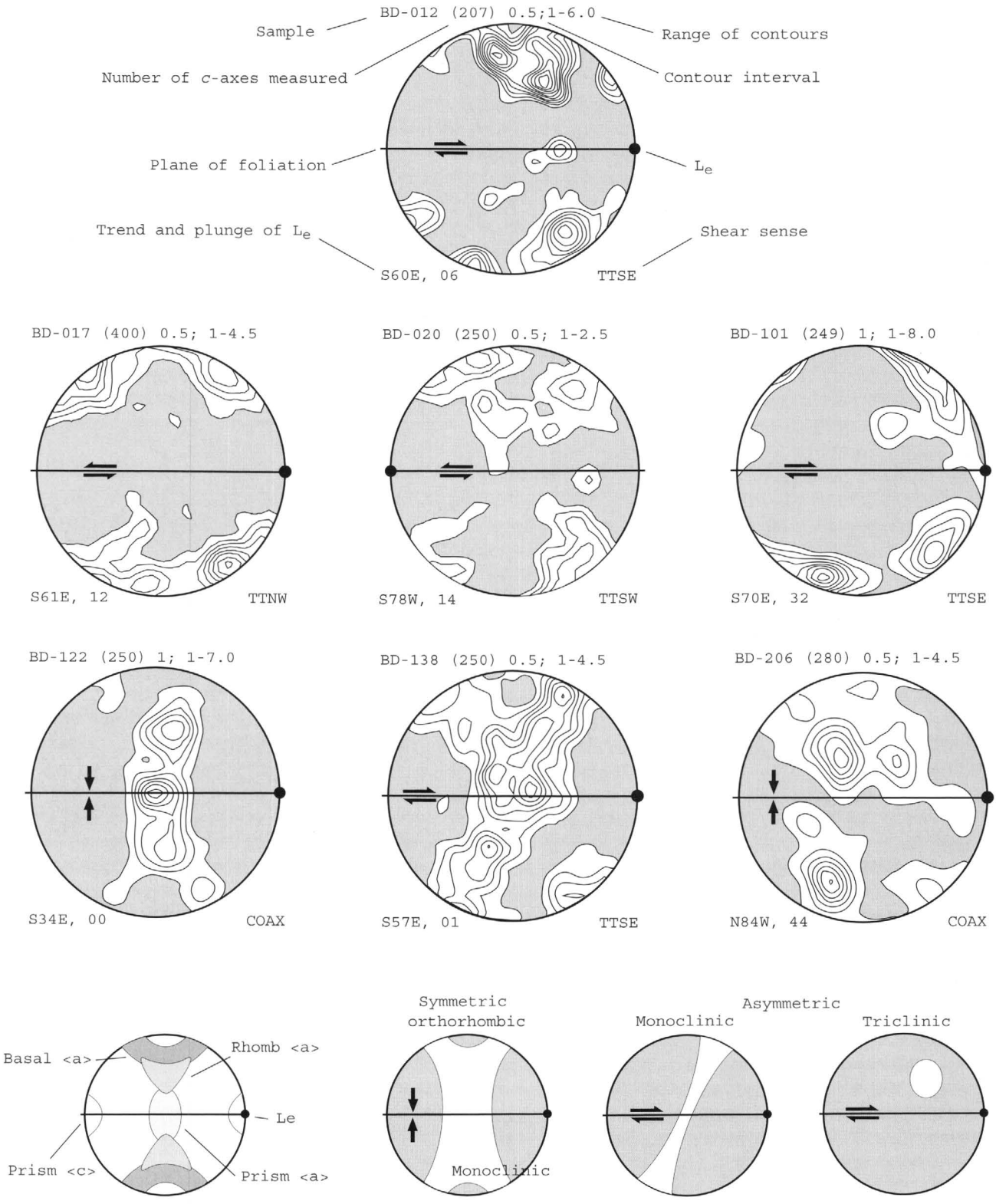

Figure 2. Equal-area, lower-hemisphere stereonet projections of quartz *c*-axis petrofabrics viewed within motion plane (XZ plane—that normal to foliation and parallel to L_e) (see fig. 1 for sample locations and kinematic interpretations). Gray areas represent <1 normal Gaussian distribution with contour intervals representing either 0.5 or 1.0 increments above normal 1 Gaussian distribution. Arrows show shear sense interpreted from fabric asymmetry. Letters at lower right corner denote interpreted shear sense: TTNW, top-to-the-northwest; TTSE, top-to-the-southeast; TTSW, top-to-the-southwest; COAX, coaxial shear or no shear sense determined. Plots were contoured using STEREOPLOTII program (Mancktelow, 1993). Inset at bottom left is a schematic stereogram showing *c*-axis locations indicative of the principal quartz-slip systems. Insets at bottom center and right are schematic stereograms of orthorhombic, monoclinic, and triclinic *c*-axis fabrics.

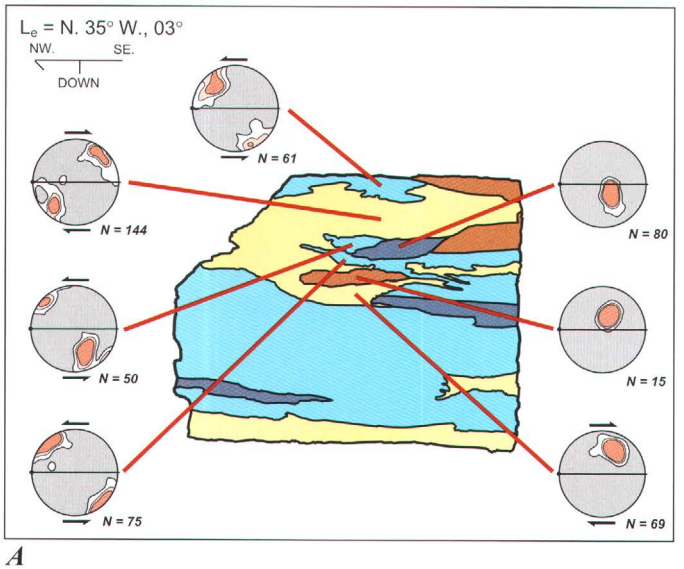

A

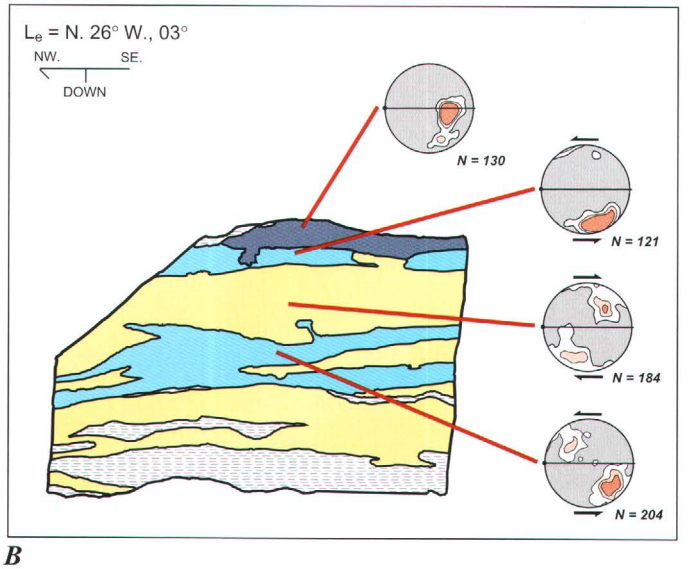

B

Figure 3. Schematic drawing of thin sections of samples BD-003 (*A*) and BD-016 (*B*), showing domains of quartz *c*-axis petrofabrics as determined by interference colors when viewed under crossed polars with gypsum plate inserted. Lower-hemisphere stereonet projections are for *c*-axes contained within specific thin-section domains. Gray areas, <1 normal Gaussian distribution; white, pink, and red areas, 1 to 2, 2 to 3, and >3 normal Gaussian distribution, respectively. Height of thin-section drawings, 2 cm. See text for explanation of colors.

rics are orthorhombic and indicative of coaxial (that is, flattening) deformation (sample BD–122, fig. 2), others lack a coherent pattern but are consistent with coaxial (sample BD–206) or noncoaxial (sample BD–012) shear. Kinematic determinations on structurally low tectonites of the Nasina assemblage record top-to-the-southwest shear senses, in addition to the more widespread top-to-the-northwest fabrics. Top-to-the-southeast fabrics, though not recorded in the Nasina assemblage itself, occur in the subjacent pelitic schist unit west of West Point and at the base of the structurally(?) overlying Butte assemblage north of Gold Creek and south of West Point (fig. 1).

Interpretation of the Kinematic Data

Our kinematic data from the Chena-Salcha Rivers area are consistent with, and support the results of, previous structural investigations of tectonites in assemblages of the Yukon-Tanana Upland farther to the southeast in the southern part of the Eagle quadrangle and in the northeastern part of the Tanacross quadrangle (Hansen and Dusel-Bacon, 1998). In those other areas, both structurally higher and structurally lower rock assemblages commonly display a well-formed top-to-the-northwest fabric that locally has been overprinted by top-to-the-southeast fabrics. The top-to-the-southwest fabrics locally the present in the Nasina assemblage in study area (fig. 1) are anomalous. Previous kinematic studies in east-central Alaska have identified relatively few tectonites with this specific shear sense (Pavlis and others, 1993; Hansen and Dusel-Bacon, 1998). In addition, the top-to-the-northeast shear senses reported in amphibolite-facies rocks of the Taylor Mountain assemblage (recently renamed the Fortymile River assemblage by Dusel-Bacon and others, 2002) to the east were not observed in the Chena-Salcha Rivers area.

Top-to-the-northwest fabrics across the Yukon-Tanana composite terrane are interpreted to have resulted from obduction of outboard oceanic and marginal-basin rocks onto the North American continental margin, with continued imbrication and shortening of both upper- and lower-plate assemblages (for example, Hansen and others, 1991; Pavlis and others, 1993; Dusel-Bacon and others, 1995; Hansen and Dusel-Bacon, 1998). In the eastern Yukon-Tanana Upland, $^{40}Ar/^{39}Ar$ cooling ages constrain this northwestward-directed contraction to the Early Jurassic (Cushing, 1984; Hansen and others, 1991; Dusel-Bacon and others, 2002).

The later, top-to-the-southeast deformation, present in several areas within the Yukon-Tanana Upland, has been attributed to mid-Cretaceous crustal extension that exhumed structurally lower rocks and juxtaposed them against structurally higher assemblages (Pavlis and others, 1993; Dusel-Bacon and others, 1995; Hansen and Dusel-Bacon, 1998). In the study area (fig. 1), these top-to-the-southeast fabrics are best formed around the West Point Complex. Rims of zircon crystals separated from orthogneiss in the core of the West Point Complex yield an ion microprobe U-Pb age of 111±2 Ma (see Dusel-Bacon, Wooden, and Layer, this volume). Dusel-Bacon, Wooden, and Layer (this volume) interpret this age to represent either the time of igneous crystallization of the granitic protolith or, less likely, the time of regional metamorphism of a Devonian or Mississippian intrusion (the U-Pb age of many of the zircon cores), suggesting that the orthogneiss may have been emplaced and (or) metamorphosed during the mid-Cretaceous crustal-extension episode postulated for other areas of the upland. Top-to-the-southeast fabrics are also present around the Salcha River gneiss dome in the vicinity of the

folded low-angle extensional detachment that is inferred to separate it from the overlying lower-grade rocks (Pavlis and others, 1993), and along the southeastern margin of the Nail allochthon (fig. 1), consistent with downdropping of these structurally high klippen during regional crustal extension.

Evidence contained within the polydeformed quartz tectonites is consistent with this interpretation of both contractional and extensional deformation. Preserved fabrics in both samples BD–003 and BD–016 (fig. 3) show opposing top-to-the-northwest and top-to-the-southeast shear fabrics that could have formed as a result of polyphase deformation. In our interpretation, strain partitioning resulted in the preservation of remnants of earlier-formed top-to-the-northwest fabrics within both samples. The ragged boundaries between *c*-axis domains are similar to what has been experimentally created by using octochloropropane during strain partitioning (Win Means, oral commun., 1996). In these experiments, deformation within shear bands superimposed on existing grain orientations was by grain-boundary migration. Because the grains themselves are typically irregular and the shear bands are only a few grains wide, the boundary separating the sheared and unsheared grains is also uneven.

Other possible explanations do not satisfactorily explain these tectonites. The tectonites cannot have resulted from rotation of earlier-formed fabrics during progressive simple-shear deformation. Although feldspars, pyrite, and garnet all are known to rotate as rigid bodies during shearing, quartz deforms ductilely even at moderate temperatures and pressures. In addition, rotations during simple shear occur along an axis parallel to the structural Y-direction. To create the observed fabrics would require a rotation of 180° in the X- or Z-direction. Isoclinal folding is also implausible. Refolding a layer with fabric asymmetries back upon itself will not reverse the sense of shear in the overturned limb. Folding along an axis parallel to the extension direction could create opposing fabrics, but only if the folding occurred after ductile shearing. We know of no evidence suggesting late northeast-southwestward crustal contraction in the Yukon-Tanana Upland. Folding before or during ductile shearing would result in the same shear sense in both limbs. Finally, we consider it unlikely that these fabrics could have resulted from coaxial flattening where differences in the orientations of quartz grains in a primary fabric have been accentuated. Fabric asymmetries are not typically associated with coaxial flattening, and sample BD–016 (fig. 3*B*) contains microkinematic indicators in addition to the quartz *c*-axis fabrics. Furthermore, earlier ductile-deformation events would probably have created a coherent quartz LPO in these tectonites, thus minimizing differences in the initial orientation of quartz grains.

In general, quartz petrofabrics associated with noncoaxial deformation are expected to show monoclinic asymmetries, in that the observed L_e allows the orientation of the motion plane to be established. In contrast, remnant quartz petrofabrics from an earlier deformational event are more likely to be triclinic because the motion planes for both older and more recent deformational events will probably not have the same geometry, and so the now-misaligned monoclinic fabrics from the earlier deformation will appear triclinic. In both our samples with the opposing shear-sense domains, the top-to-the-southeast fabrics are more monoclinic, and the top-to-the-northwest fabrics more triclinic, as would be expected if top-to-the-southeast shearing overprinted existing top-to-the-northwest fabrics. In addition, the strongly triclinic quartz *c*-axis fabrics recorded in LPO domains with deep-orange or dark-blue interference colors may represent a rigid-body rotation of the top-to-the-northwest fabrics along an axis parallel to the extension direction during a later top-to-the-southeast deformation. The multiple triclinic domains observed in sample BD–003 (fig. 3*A*) may represent a progressive rotation of preexisting top-to-the-northwest fabrics through 90° until they are in an orientation conducive to basal <*a*> slip during top-to-the-southeast extension.

The top-to-the-west-southwest direction of tectonic transport measured in the Teuchet Creek area, including sample BD–020 (fig. 2), though unusual for the study area (fig. 1), is close to the due-west direction of tectonic transport determined for amphibolite-facies rocks in the Central Creek area in the southeastern part of the Big Delta quadrangle (Hansen and Dusel-Bacon, 1998; Day and others, 2002; Dusel-Bacon and others, 2002). Day and others (2002) reported new U-Pb ages of 116±4 and 116±2 Ma from spot analyses on the rims of zircons from two different gneiss units in the Central Creek area. They interpreted these ages as the time of prograde mid-Cretaceous metamorphism, which they propose accompanied westward-vergent thrusting in that area.

Absence of asymmetric structural elements in tectonites of the Butte assemblage that contain the anomalous northeast-trending L_e, southwest of the Nail allochthon, makes it impossible to know whether they underwent a southwestward-vergent phase of deformation or whether the tectonites record the northeastward-vergent deformation interpreted to be the oldest (orogen-normal) deformation preserved in the structurally high Fortymile River assemblage (previously named the Taylor Mountain assemblage) in the Fortymile River area near the Alaska-Yukon Territory border (Hansen and Dusel-Bacon, 1998) and at the base of the Nail allochthon (Pavlis and others, 1993). Given the polyphase deformational history and the additional structural complexity resulting from Cenozoic normal faulting, assignment of these anomalous transport directions to a single cause is impossible.

Conclusions

1. Tectonites between the Chena and Salcha Rivers record a complex ductile-deformation history. Kinematic analysis has identified widespread top-to-the-northwest and top-to-the-southeast shear senses and, in the structurally low Nasina assemblage, more local top-to-the-northwest fabrics.
2. Previous structural studies in several areas of the Yukon-Tanana terrane provide a basis for interpreting our kinematic

results. The top-to-the-northwest fabrics are interpreted to have resulted from Early Jurassic thrusting of allochthonous tectonites over the North American continental margin, and the top-to-the-southeast fabrics from mid-Cretaceous crustal extension that exhumed structurally lower rocks. The particularly well formed top-to-the-southeast fabrics around the West Point Complex may have formed during tectonic exhumation of the igneous and metamorphic complex, similar to the exhumation proposed for the Salcha River gneiss dome. The significance of the top-to-the-southwest fabrics is unknown.

3. Unusual siliceous tectonites containing quartz LPO domains record evidence of polyphase deformation. Earlier-formed fabrics exist as remnants after partial overprinting during strain-partitioned ductile shearing. Quartz c-axis fabric analysis on a domain-by-domain basis provides a means of recognizing these earlier events and determining their shear sense.

Acknowledgments

We thank Rainer Newberry (University of Alaska, Fairbanks) and Julie Hunt (Yukon Geology Program) for participating in 5 days of fieldwork during 1997 and 1998, respectively. Kinematic discussions with Vicki Hansen (Southern Methodist University) were extremely helpful. Charlie Bacon (USGS) provided invaluable logistic support in the field, and Melanie Hopkins (USGS) helped with graphic illustrations. We thank Dwight Bradley and Warren Day, both of the USGS, for their helpful reviews of the manuscript.

References Cited

Anderson, E.M., 1948, On lineation and petrofabric structure, and the shearing movement by which they have been produced: Geological Society of London Quarterly Journal, v. 102, no. 104, pt. 1, p. 99–132.

Berthé, Didier, Choukroune, Pierre, and Jégouzo, Pierre, 1979, Orthogneiss, mylonite and non coaxial defornation of granite—the example of the South Armorican shear zone: Journal of Structural Geology, v. 1, no. 1, p. 31–42.

Cushing, G.W., 1984, The tectonic evolution of the eastern Yukon-Tanana upland: Albany, State University of New York, M.S. thesis, 235 p.

Day, W.C., Aleinikoff, J.N., Henning, M.H., Gamble, B.M., and Gough, L.P., 2002, Overview of the bedrock geologic setting of the Big Delta B–2 quadrangle, Alaska [abs.]: Alaska Miners Association Biennial Conference, 18th, Fairbanks, Alaska, 2002, p. 10–11.

Day, W.C., Gamble, B.M., Henning, M.W., and Smith, B.D., 2000, Geologic setting of the Fortymile River area—polyphase deformational history within part of the eastern Yukon-Tanana uplands of Alaska, *in* Kelley, K.D., and Gough, L.P., eds., Geologic studies in Alaska by the U.S. Geological Survey, 1998: U.S. Geological Survey Professional Paper 1615, p. 65–82.

Dusel-Bacon, Cynthia, Bressler, J.R., Takaoka, H., Mortensen, J.K., Oliver, D.H., Leventhal, J.S., Newberry, R.J., and Bundtzen, T.K., 1998, Stratiform zinc-lead mineralization in Nasina assemblage rocks of the Yukon-Tanana Upland in east-central Alaska: U.S. Geological Survey Open-File Report 98–340 [URL http://geopubs.wr.usgs.gov/open-file/of98-340/].

Dusel-Bacon, Cynthia, and Cooper, K.M., 1999, Trace-element geochemistry of metabasaltic rocks from the Yukon-Tanana Upland and implications for the origin of tectonic assemblages in east-central Alaska: Canadian Journal of Earth Sciences, v. 36, no. 10, p. 1671–1695.

Dusel-Bacon, Cynthia, and Foster, H.L., 1983, A sillimanite gneiss dome in the Yukon crystalline terrane, east-central Alaska—petrography and garnet-biotite geothermometry: U.S. Geological Survey Professional Paper 1170–E, 25 p.

Dusel-Bacon, Cynthia, Hansen, V.L., and Scala, J.A., 1995, High-pressure amphibolite-facies dynamic metamorphism and the Mesozoic tectonic evolution of an ancient continental margin, east-central Alaska: Journal of Metamorphic Geology, v. 13, no. 1, p. 9–24.

Dusel-Bacon, Cynthia, Lanphere, M.A., Sharp, W.D., Layer, P.W., and Hansen, V.L., 2002, Mesozoic thermal history and timing of structural events for the Yukon-Tanana Upland, east-central Alaska—$^{40}Ar/^{39}Ar$ data from metamorphic and plutonic rocks: Canadian Journal of Earth Sciences, v. 39, no. 6, p. 1013–1051.

Foster, H.L., 1992, Geologic map of the eastern Yukon-Tanana region, Alaska: U.S. Geological Survey Open-File Report 92–313, 26 p., scale 1:500,000.

Foster, H.L., Cushing, G.W., and Keith, T.E.C., Laird, Jo, 1985, Early Mesozoic tectonic history of the Boundary area, east-central Alaska: Geophysical Research Letters, v. 12, no. 9, p. 553–556.

Foster, H.L., Keith, T.E.C., and Menzie, W.D., 1994, Geology of the Yukon-Tanana area of east-central Alaska, *in* Plafker, George, and Berg, H.C., eds., The geology of Alaska, v. G–1 *of* The geology of North America: Boulder, Colo., Geological Society of America, p. 205–240.

Hanmer, Simon, and Passchier, C.W., 1991, Shear-sense indicators—a review: Geological Survey of Canada Paper 90–17, 72 p.

Hansen, V.L., and Dusel-Bacon, Cynthia, 1998, Structural and kinematic evolution of the Yukon-Tanana upland tectonites, east-central Alaska—a record of late Paleozoic to Mesozoic crustal assembly: Geological Society of America Bulletin, v. 110, no. 2, p. 211–230.

Hansen, V.L., Heizler, M.T., and Harrison, T.M., 1991, Mesozoic thermal evolution of the Yukon-Tanana composite terrane—new evidence from $^{40}Ar/^{39}Ar$ data: Tectonics, v. 10, no. 1, p. 51–76.

Law, R.D., 1990, Crystallographic fabrics; a selective review of their application to research in structural geology, *in*

Knipe, R.J., and Rutter, E.H., eds., Deformation mechanisms, rheology and tectonics: Geological Society of London Special Publication 54, p. 335–352.

Mancktelow, N.S., 1993, Stereoplot II: Zürich, Facelt Resources.

Nokleberg, W.J., Foster, H.L., and Aleinikoff, J.N., 1989, Geology of the northern Copper River Basin, eastern Alaska Range, and southern Yukon-Tanana Basin, southern and east-central Alaska, *in* Nokleberg, W.J., and Fisher, M.A., eds., Alaskan geological and geophysical transect: American Geophysical Union Field Trip Guidebook T104, p. 34–63.

Oliver, D.H., 1998, Lattice preferred orientation (LPO) domains in siliceous tectonites as indicators of polyphase deformation [abs.]: Geological Society of America Abstracts with Programs, v. 30, no. 7, p. A–133.

Passchier, C.W., and Trouw, R.A.J., 1996, Microtectonics: Berlin, Springer-Verlag, 289 p.

Pavlis, T.L., Sisson, V.B., Foster, H.L., Nokleberg, W.J., and Plafker, George, 1993, Mid-Cretaceous extensional tectonics in the Yukon-Tanana terrane, Trans-Alaskan Crustal Transect (TACT), east-central Alaska: Tectonics, v. 12, no. 1, p. 103–122.

Robinson, M.S., Smith, T.E., and Metz, P.A., 1990, Bedrock geology of the Fairbanks Mining District: Alaska Division of Geological and Geophysical Surveys Professional Report 106, 2 sheets, scale 1:63,360.

Schmid, S.M., and Casey, M., 1986, Complete fabric analysis of some commonly observed quartz *c*-axis patterns, *in* Heard, H.C., and Hobbs, B.E., eds., Mineral and rock deformation; laboratory studies (Paterson volume): American Geophysical Union Geophysics Monograph 36, p. 263–286.

Simpson, C., and Schmid, S.M., 1983, An evaluation of the sense of movement in sheared rocks: Geological Society of America Bulletin, v. 94, no. 11, p. 1281–1288.

Smith, T.E., Robinson, M.S., Weber, F.R., Waythomas, C.W., and Reifenstuhl, R.R., 1994, Geologic map of the upper Chena River area, eastern Interior Alaska: Alaska Division of Geological and Geophysical Surveys Professional Report 115, 19 p., scale 1:63,360.

Southworth, D.D., 1984, Geologic and geochemical investigations of the "Nail" allochthon, east-central Alaska: U.S. Bureau of Mines Open-File Report 176–84, 19 p.

Turner, F.J., and Weiss, L.E., 1963, Structural analysis of metamorphic tectonites: New York, McGraw-Hill, 545 p.

Wahrhaftig, Clyde, 1968, Schists of the central Alaska Range: U.S. Geological Survey Bulletin 1254–E, p. E1–E22.

——1970, Geologic map of the Healy D–2 quadrangle, Alaska: U.S. Geological Survey Geologic Quadrangle Map GQ–805, scale 1:63,360.

Watkinson, A.J., 1992, Evaluation of the structural geology of the STN claim areas, WGM Tanana Uplands Project, *in* Bressler, J.R., and Corbett, T.J., Stone Boy Project 1991 Annual Report: Anchorage, WGM, Inc., p. 99–117.

Weber, F.R., Foster, H.F., Keith, T.E.C., and Dusel-Bacon, Cynthia, 1978, Preliminary geologic map of the Big Delta quadrangle, Alaska. U.S. Geological Survey Open-File Report 78–529–A, scale 1:250,000.

Studies by the U.S. Geological Survey in Alaska, 2001
U.S. Geological Survey Professional Paper 1678

Tertiary Volcanic Rocks of the Central Talkeetna Mountains, Alaska

By Katie E. Amos and Ronald B. Cole

Abstract

Volcanic rocks of the central Talkeetna Mountains consist of more than 400 m of shallow-dipping basaltic and andesitic lavas with subordinate dacitic and rhyolitic lavas and tuffs. All of the lavas are intruded by rhyolite and dacite dikes, sills, and small domes and by minor basaltic dikes. The eruption of these rocks began with the outpouring of mafic lavas, followed by alternating mafic, intermediate-composition, and felsic lava flows. The youngest phase of magmatism is recorded by the shallow rhyolite and dacite intrusions that crosscut the lavas. Geochemically, the basalt samples are relatively depleted in light-rare-earth elements (chondrite-normalized La/Yb ratios of 0.9–2.3, with La 9.5–31.3 times chondrite) and have compatible-element contents similar to those of midocean-ridge basalts, indicating a depleted mantle source for the basalts. The felsic lavas and intrusions are the most evolved rocks in the study area (chondrite-normalized La/Yb ratios of 3.7–7.6, with La 32.7–64.0 times chondrite and highest Ba, Rb, Th, and K contents) and evolved from the mafic magmas by a combination of fractional crystallization and crustal assimilation. All of the samples (basalts through rhyolites) show enrichment in Cs, Ba, Th, and Pb, which is consistent with metasomatism of the depleted mantle source.

Introduction

This study is focused on unnamed Tertiary volcanic rocks that are exposed along a northwest- trending belt through the central Talkeetna Mountains (fig. 1). These volcanic rocks occur 50 to 75 km north of the Border Ranges Fault system, which forms the south boundary of the Wrangellia composite terrane. The Wrangellia composite terrane includes varyingly metamorphosed magmatic-arc rocks and oceanic sedimentary rocks of the Wrangellia, Peninsular, and Alexander terranes (Nokleberg and others, 1994). The volcanic rocks of the central Talkeetna Mountains are enigmatic because they were erupted through the Wrangellia composite terrane during an apparent lull in arc magmatism across south-central Alaska, and their tectonic and petrogenetic histories are poorly known. The specific goals of this report are to (1) provide a geologic overview, including new stratigraphic and geochemical results, for Tertiary volcanic rocks at two localities in the northern part of the central Talkeetna Mountains; and (2) to develop a working hypothesis for the origin of the Tertiary volcanic rocks in this area. The two study areas are in the central part of the Talkeetna Mountains 1°×3° quadrangle adjacent to the Tafia vertical-azimuth bench mark (VABM) and the Sedan VABM (fig. 2). The results reported here are based on fieldwork conducted during June 2001 at these two localities with helicopter and logistical support provided by the U.S. Geological Survey Talkeetna Mountains Transect project.

Background

The volcanic rocks of the central Talkeetna Mountains were described by Csejtey and others (1978) as more than 1,500 m of felsic to mafic subaerial volcanic rocks and related shallow-intrusive rocks. Csejtey and others (1978) further described that the lower part of the volcanic sequence consists dominantly of rhyolite and latite small-scale intrusions, lavas, and pyroclastic rocks and that the upper part consists mostly of andesite and basalt flows interlayered with minor amounts of tuff and fluvial conglomerate. More detailed mapping by Adams and others (1985) showed that the volcanic rocks of the central Talkeetna Mountains consist mostly of mafic to intermediate-composition lavas, with subordinate felsic lavas and interbedded tuff, all of which are intruded by dacite and rhyolite dikes and domes and minor mafic dikes. Our field observations are consistent with their mapping.

Existing K-Ar ages yield an Early to Middle Eocene range for the volcanic rocks of the central Talkeetna Mountains. Csejtey and others (1978) reported a K-Ar age of 51.3±2.5 Ma on an andesite whole-rock sample from the middle of the volcanic sequence at the north edge of the volcanic field and an age of 56.3±2.5 Ma on an andesite whole-rock sample from the south edge of the volcanic field (fig. 2A). Csejtey and others (1978) also reported a K-Ar age of 50.4±2.0 Ma on hornblende from an andesite flow in a pod of volcanic rocks exposed about 14 km west of the main part of the central Talkeetna Mountains volcanic field. In addition, hornblende from two rhyodacite dikes that intrude mafic and intermediate-composition lavas in the central

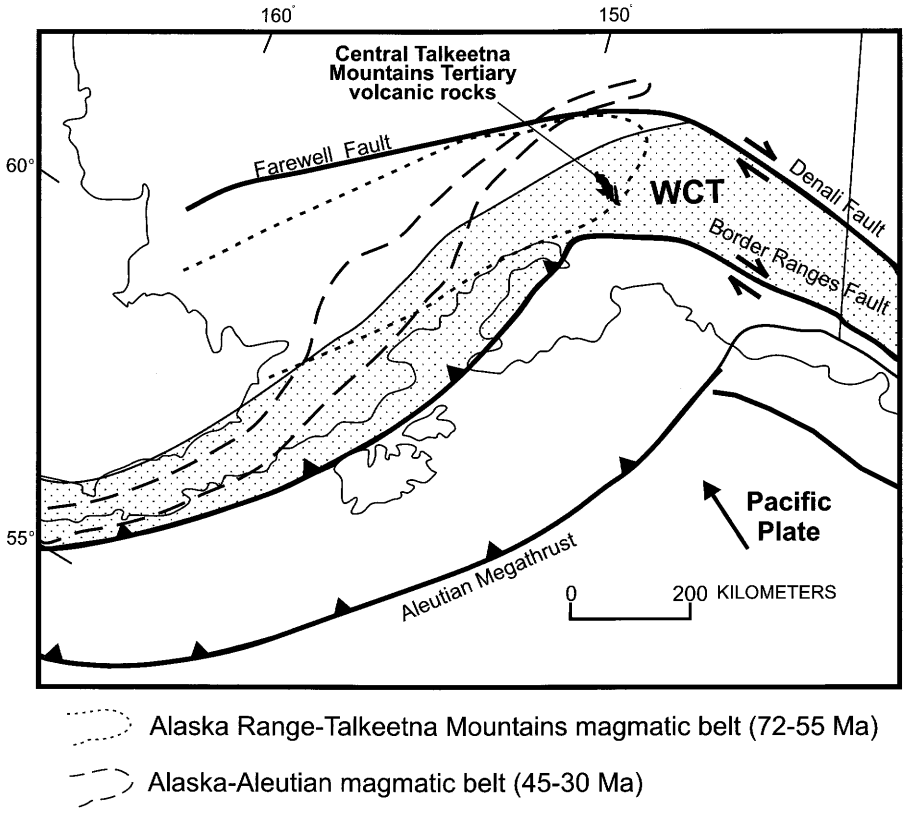

Figure 1. South-central Alaska, showing volcanic rocks of the central Talkeetna Mountains, major fault systems, the Wrangellia composite terrane (WCT), and regional magmatic belts. Boundaries of WCT from Nokleberg and others (1994) and of magmatic belts from Moll-Stalcup and others (1994).

Talkeetna Mountains yielded K-Ar ages of 39.8±2.5 and 43.6±2.6 Ma (fig. 2*A*; Adams and others, 1985; Little, 1988).

The volcanic rocks of the central Talkeetna Mountains overlie Late Paleozoic and Jurassic rocks (fig. 2). The Late Paleozoic rocks include Pennsylvanian(?) and Early Permian basaltic to andesitic metavolcanic rocks, with subordinate mudstone, bioclastic marble, and dark-gray to black phyllite (Csejtey and others, 1978). These rocks are tightly folded and complexly faulted and are regionally metamorphosed to greenschist and, locally, amphibolite facies (Csejtey and others, 1978). The Jurassic rocks include Lower to Upper Jurassic trondhjemite, granodiorite, quartz diorite, amphibolite, and migmatite, with lesser greenstone and pelitic mica schist (Csejtey and others, 1978).

Volcanic and Shallow-Intrusive Rocks

Approximately 400 m of horizontal to shallow-dipping lavas, minor pyroclastic units, and small intrusions is exposed in the Tafia and Sedan study areas (figs. 3, 4). On the basis of their silica and alkali composition, the rocks include basalt, basaltic andesite, andesite, dacite, and rhyolite (fig. 5). The lavas are predominantly basaltic through andesitic, with subordinate dacite and rhyolite flows (figs. 2*B*, 2*C*). The intrusive rocks are predominantly dacite and rhyolite dikes and small stocks, with subordinate basaltic dikes. The general stratigraphic sequence in the study areas includes a lower interval of mafic lavas, overlain by interlayered mafic, intermediate-composition, and felsic lavas. In the Sedan study area, a felsic pyroclastic lens that is present at the base of the volcanic sequence unconformably overlies folded and sheared Paleozoic metamorphic rocks. Pyroclastic deposits are also present as minor lenses throughout the sequence. The dacite and rhyolite intrusions are the youngest units observed in the study areas.

Mafic Lavas

Mafic lavas, including basalt and basaltic andesite, are the most abundant lavas observed. Individual lava flows range from about 2 to 8 m in thickness and typically form elongate lenses that extend for a few to tens of meters across. Several beds display internal flow folding, and overall the mafic lava beds are generally less vesicular at the base and highly vesicular to scoriaceous at the top. Weathering colors range from light medium gray to red-brown, and fresh colors are typically dark gray to black. Nearly all of the mafic lavas are aphanitic to finely porphyritic, with phenocrysts of plagioclase, pyroxene, minor olivine, and Fe-Ti oxides in a glassy

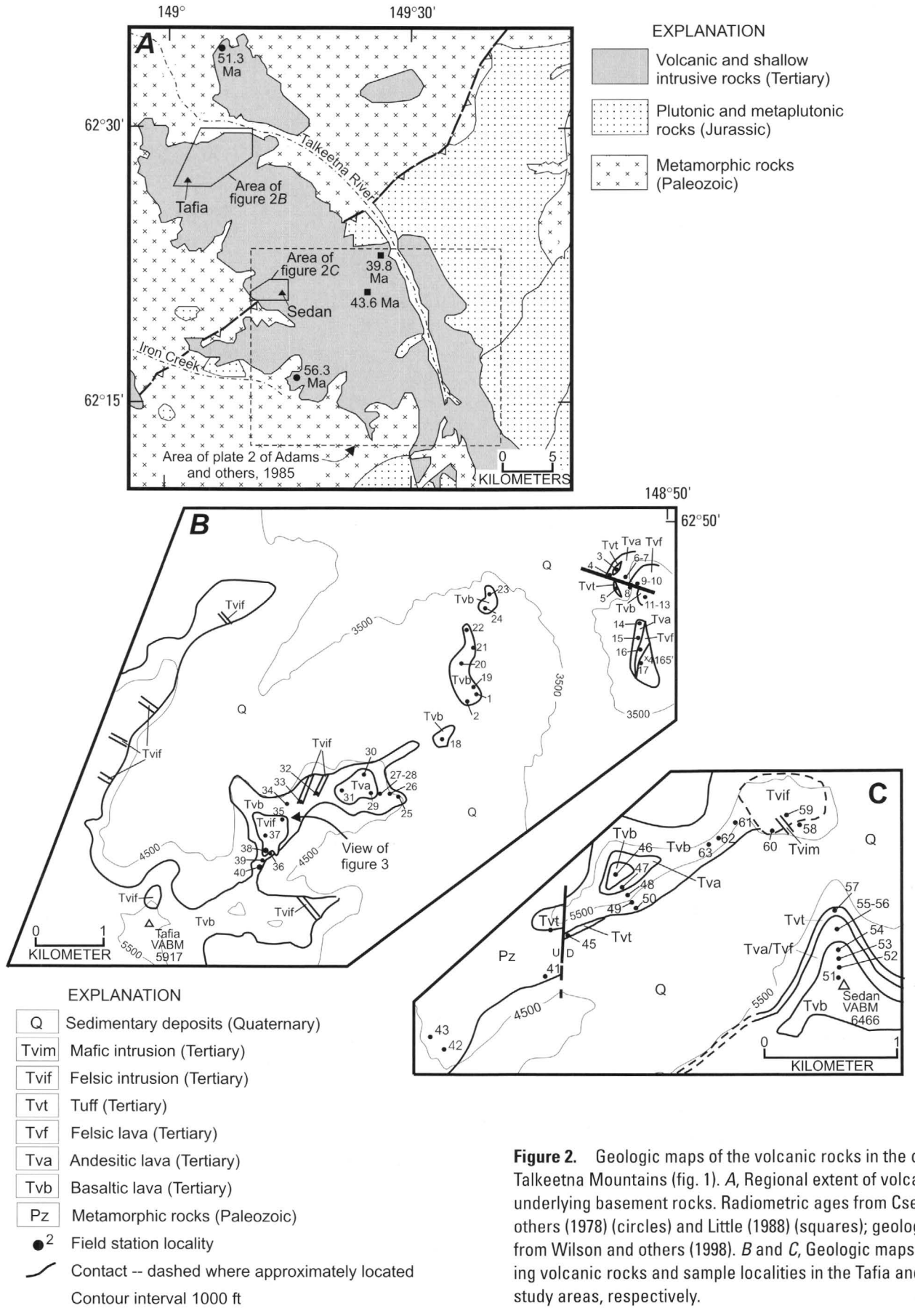

Figure 2. Geologic maps of the volcanic rocks in the central Talkeetna Mountains (fig. 1). *A*, Regional extent of volcanic and underlying basement rocks. Radiometric ages from Csejtey and others (1978) (circles) and Little (1988) (squares); geologic base from Wilson and others (1998). *B* and *C*, Geologic maps showing volcanic rocks and sample localities in the Tafia and Sedan study areas, respectively.

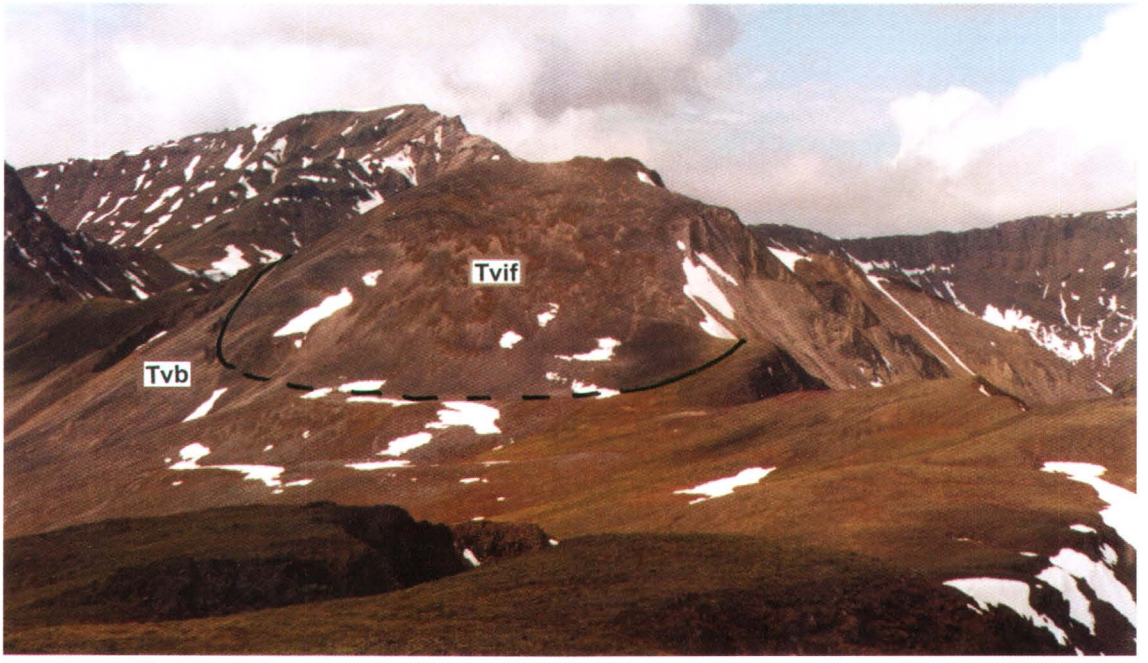

Figure 3. Rhyolite-dacite dome (unit Tvif, fig. 2) intruded through shallow-dipping basalt lava flows (Tvb) in the Tafia study area (fig. 2*B*). Dome is approximately 200 m across.

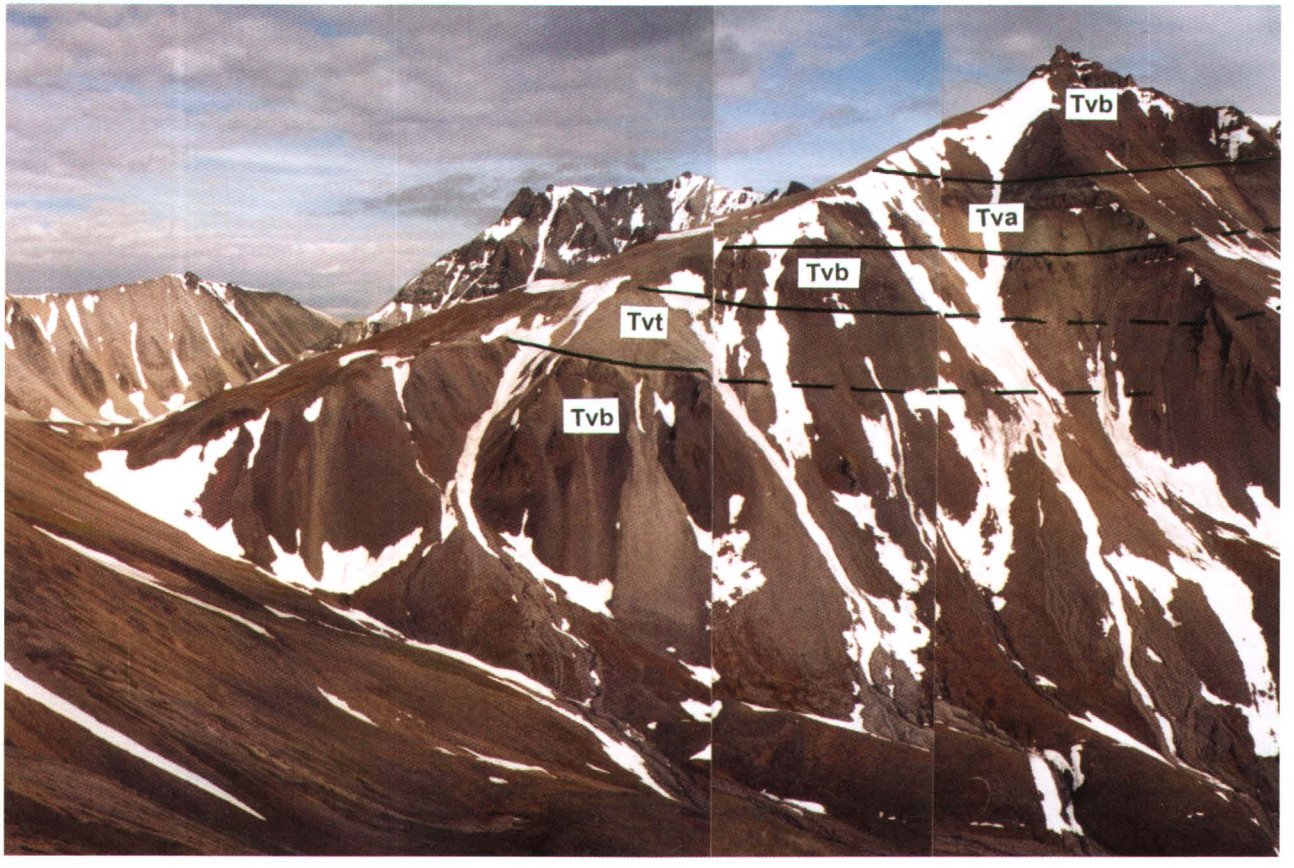

Figure 4. Basalt (unit Tvb, fig. 2) and andesite (unit Tva) lavas with interbedded tuff (unit Tvt) in the Sedan study area (fig. 2*C*); vertical-azimuth bench mark (VABM) Sedan (elev 1,971 m) is located at peak.

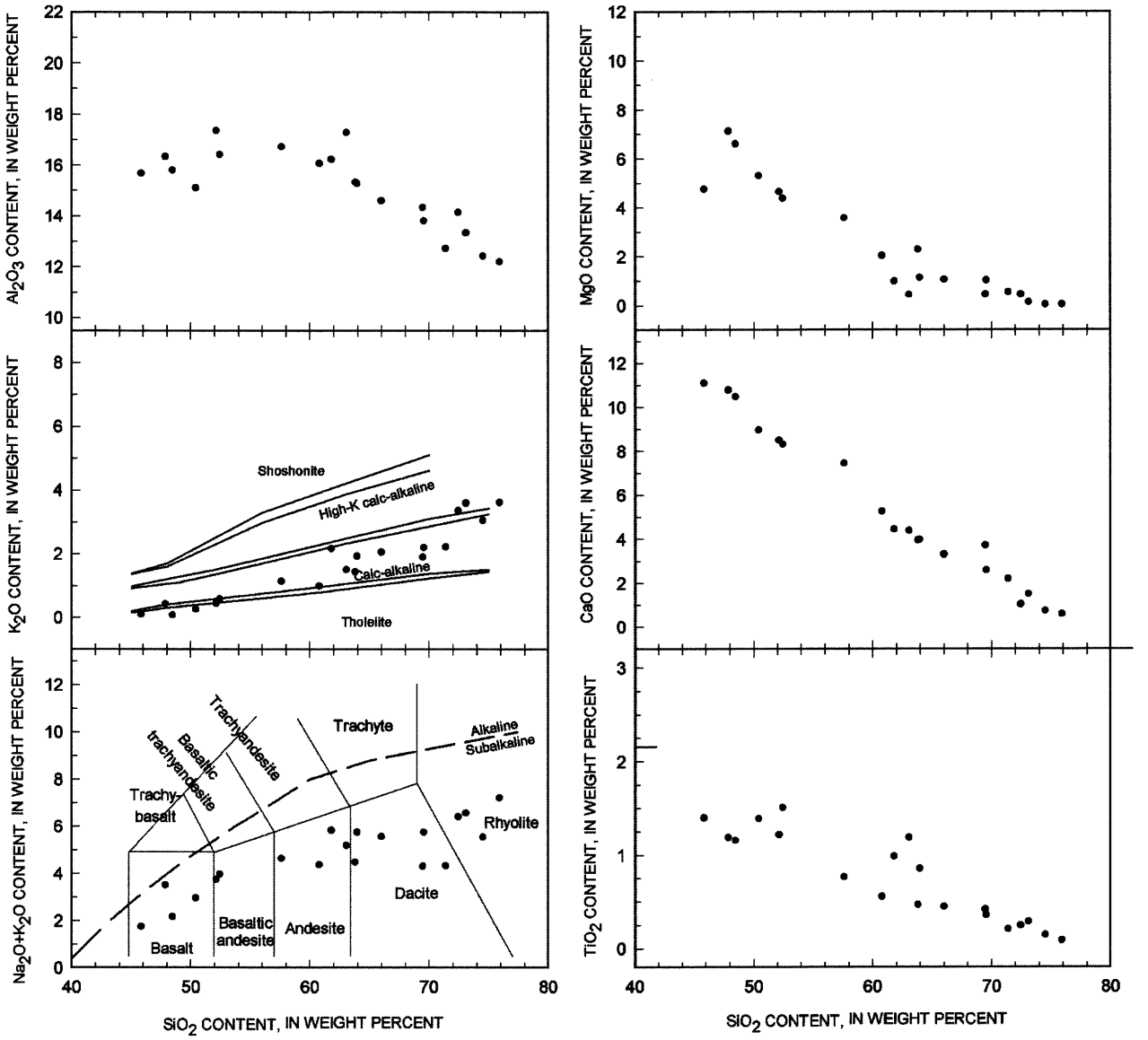

Figure 5. Major-element variation diagrams for volcanic rocks of the central Talkeetna Mountains (fig. 1). Rock classification scheme from Le Bas and others (1986); rock series from Rickwood (1989).

and (or) plagioclase-rich matrix. The pyroxene and plagioclase phenocrysts are commonly intergrown, and ophitic texture is common. Secondary replacement of plagioclase with calcite is also common.

Intermediate-Composition Lavas

The andesitic lavas are interbedded with the mafic lavas. Individual andesite flows are approximately 5 to 10 m thick and form broad lenses. Individual lava flows are commonly vesicular and amygdaloidal. Weathering colors include light gray, light green, and red-brown, and fresh colors are typically medium to dark gray. The rocks are aphanitic to porphyritic, with plagioclase and minor pyroxene phenocrysts in a glassy, devitrified-glass, and plagioclase-rich matrix. Plagioclase phenocrysts are commonly zoned and exhibit resorption textures.

Felsic Lavas

The felsic lavas include dacite and rhyolite and are less abundant than the mafic and intermediate-composition lavas. Beds are massive and generally more than 5 m thick, although bedding contacts are difficult to discern. Thin wispy laminations and banding are typical in the felsic lavas. Weathering colors range from tan through light gray to light purple, and fresh colors are light pink to light gray. The felsic rocks range in texture from aphanitic to coarsely porphyritic. The felsic lavas are typically hypocrystalline,

with a glassy matrix containing phenocrysts of quartz and zoned plagioclase. The dacites also include some amphibole and rare pyroxene phenocrysts. Embayments are typical in all phenocrysts.

Pyroclastic Deposits

Lithic vitric tuff and lapilli tuff deposits occur at several localities within the study areas. These pyroclastic deposits are typically lens shaped and range in thickness from tens of centimeters to about 10 m. The predominant grains within the deposits include cuspate glass shards, pumice grains (approx 0.5–3-cm diam), felsic porphyritic lithic grains (approx 1–12-cm diam), and dark-gray to black argillite grains (approx 1–6-cm diam).

Felsic Intrusive Rocks

Felsic intrusive rocks crosscut all of the lavas in the Tafia and Sedan study areas (figs. 3, 4). These intrusive rocks range in composition from dacite to rhyolite and in size from small dikes (0.5–1 m across) to small domes (a few hundred meters across) (fig. 3). In the Tafia study area, a radial pattern of felsic dikes is apparent around a rhyodacite dome (fig. 2*B*) that exhibits well-developed columnar jointing. Weathering colors in the felsic intrusive rocks are light gray, tan, and pink, and fresh color is typically light gray. The felsic intrusive rocks are typically porphyritic, with phenocrysts of zoned plagioclase and quartz and minor biotite and amphibole in a glassy or plagioclase-rich matrix. Embayments are common in all mineral phases.

Geochemical Results

New major- and trace-element data were collected for 20 samples of volcanic and intrusive rocks in the central Talkeetna Mountains (tables 1, 2). The samples were prepared and powdered by using an alumina ceramic mixing mill at Allegheny College and analyzed for major oxides by X-ray fluorescence and for trace elements by inductively coupled mass spectrometry at ALS Chemex Labs, Inc.

The volcanic and shallow-intrusive rocks of the central Talkeetna Mountains are subalkalic and lie in the medium-K calc-alkaline field of Rickwood (1989) (fig. 5). The entire suite of rocks shows coherent trends among major oxides, with decreases in MgO, CaO, and Al_2O_3 contents and an increase in K_2O content with increasing SiO_2 content.

All but one of the samples exhibit some degree of light-rare-earth-element (LREE) enrichment (fig. 6), with La(n)/Yb(n) ratios of 0.9 to 2.3 for basalts, 3.4 to 4.5 for andesites, and 3.7 to 7.6 for rhyolites and dacites. Basalt sample CTM01–AC49, which shows a slight LREE depletion, represents the most primitive sample in the set. Overall, the basalt samples exhibit relatively flat to slightly enriched LREE patterns. Progressive LREE enrichment and Eu depletion occurs from the basalt through the andesite, dacite, and rhyolite samples.

Normalized to chondrite, the basalt samples exhibit moderate Ba enrichment, a high degree of Th enrichment, and low Rb and K contents relative to Ba and Th (fig. 7). The basalt samples show less overall variation in the more compatible trace elements (Zr, Hf, Ti, Y, and rare-earth elements) and have relatively high Ta contents relative to Nb (fig. 7). This trend is also apparent by comparing the basalt samples with midocean-ridge basalt (MORB) (fig. 8); for the more compatible trace elements, the basalts display flat MORB-normalized patterns that are close to unity, especially for sample CTM01–AC49. All of the basalt samples exhibit varying enrichment of Sr, P, and Zr. Relative to the basalt samples, the andesite, dacite, and rhyolite samples show a progressive enrichment of incompatible elements, especially Rb and K (fig. 7). The andesite, dacite, and rhyolite samples also show progressive depletion in Sr, Eu, P, and Ti. All of the samples of volcanic rocks of the central Talkeetna Mountains have a relatively high Ta/Nb ratio.

Discussion

The stratigraphy of the volcanic rocks of the central Talkeetna Mountains reveals that a volcanic episode began with the outpouring of mafic lavas punctuated by minor felsic pyroclastic eruptions. Felsic lavas were erupted intermittently with intermediate-composition and mafic lavas after the initial mafic outpouring. This eruptive sequence suggests to us that mafic magmas were formed and erupted first and that the intermediate-composition and felsic magmas evolved later, probably from the mafic magmas.

All the basalt samples show some degree of fractionation or enrichment in incompatible elements and have relatively low Mg numbers of 0.35 to 0.42 (determined as MgO/(MgO+total FeO), where total FeO is calculated from Fe_2O_3). Although the basalts are not likely primary, sample CTM01–AC49 (figs. 6–8; tables 1, 2) shows the least incompatible-element enrichment and is the most reasonable sample for estimating primary magma composition. Its depletion in LREEs relative to chondrite (fig. 6) and its uniform contents of compatible trace elements similar to that of MORB (fig. 8) indicates a depleted mantle source for the primary magmas. The remaining basalt samples show some degree of LREE enrichment, but they all exhibit chondrite-normalized rare-earth-element contents and La(n)/Yb(n) ratios in the range of normal to enriched MORB (fig. 6). Some of the trace-element trends for basalt sample CTM01–AC47A (figs. 6–8; tables 1, 2) are similar to that of average oceanic-island basalts of Hawaii (fig. 7); however, this sample has a lower La(n)/Yb(n) ratio and less enrichment of more compatible elements (Zr, Hf, Ti, HREE) than do average Hawaii basalts

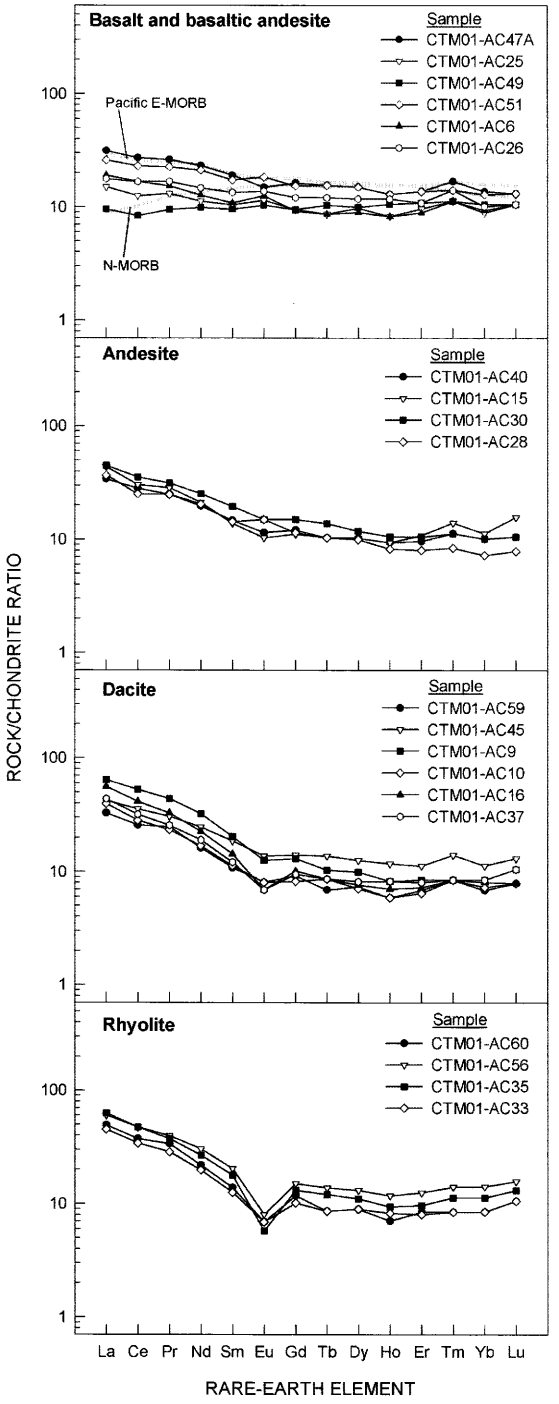

Figure 6. Chondrite-normalized rare-earth-element diagrams for volcanic rocks of the central Talkeetna Mountains (fig. 1). Normalizing values from Taylor and McLennan (1985); data for normal midocean-ridge basalt (N–MORB) and Pacific enriched midocean-ridge basalt (E–MORB) from Klein and Langmuir (2000).

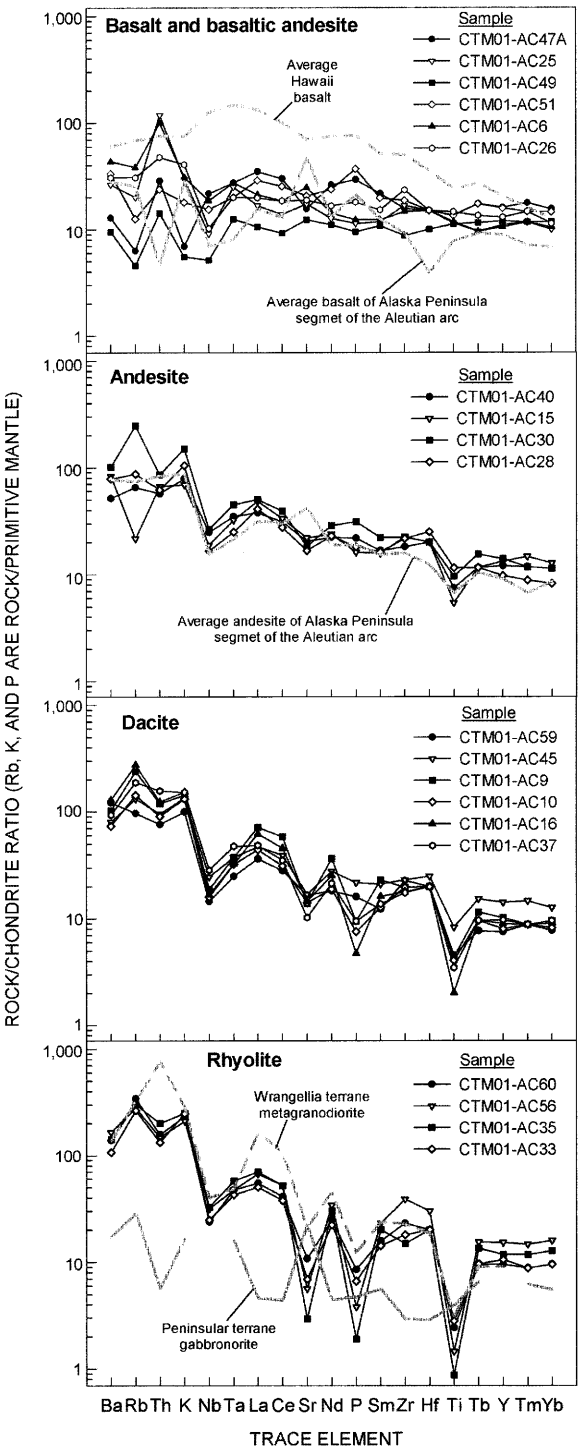

Figure 7. Normalized trace-element plots for volcanic rocks of the central Talkeetna Mountains (fig. 1). Normalizing values from Thompson and others (1984) and Sun (1980). Data for average Hawaii basalt compiled from Feigenson and Spera (1983), Hofman and others (1984, 1987), Spengler and Garcia (1988), Wright and Helz (1996), and Sims and others (1999); average Aleutian Alaska Peninsula basalt and andesite compiled from Hildreth (1983), Nye and Turner (1990), Nye and others (1994), Till and others (1994), Johnson and others (1996), Coombs and others (2000); and Wrangellia and Peninsular terrane rocks from Plafker and others (1989).

Table 1. Major-element composition of samples of volcanic rocks of the central Talkeetna Mountains.

[All values in weight percent. See figure 1 for locations. Do., ditto]

Sample	Description	SiO_2	Al_2O_3	Fe_2O_3	MgO	CaO	Na_2O	K_2O	TiO_2	P_2O_5	MnO	LOI	Total
						Tafia study area							
CTM01-AC25	Basalt	47.86	16.34	10.77	7.14	10.79	3.09	0.43	1.19	0.12	0.16	1.38	99.27
CTM01-AC6	Basaltic andesite	52.11	17.36	9.84	4.67	8.51	3.3	.45	1.22	.13	.16	1.46	99.51
CTM01-AC26	do	52.41	16.42	10.85	4.39	8.33	3.39	.59	1.51	.19	.17	1.04	99.29
CTM01-AC40	Andesite	57.59	16.73	7.18	3.58	7.45	3.51	1.14	.77	.23	.15	.65	98.98
CTM01-AC15	do	60.77	16.08	4.83	2.05	5.27	3.38	1.00	.56	.17	.09	4.29	98.49
CTM01-AC30	do	61.79	16.23	5.33	1.00	4.46	3.67	2.17	.99	.33	.1	3.09	99.16
CTM01-AC28	Dacite	63.04	17.29	5.53	.45	4.39	3.69	1.51	1.19	.19	.05	2.5	99.83
CTM01-AC9	do	65.98	14.61	3.66	1.07	3.32	3.52	2.06	.45	.1	.07	4.44	99.28
CTM01-AC10	do	69.46	14.34	2.27	.46	3.73	2.42	1.9	.42	.08	.02	4.62	99.72
CTM01-AC16	do	71.39	12.73	1.95	.55	2.2	2.12	2.22	.21	.05	.03	6.06	99.51
CTM01-AC33	Rhyolite dike	73.09	13.34	2.55	.15	1.51	2.97	3.6	.29	.07	.05	1.71	99.33
CTM01-AC37	Rhyolite-dacite plug	69.54	13.82	3.35	1.04	2.59	3.56	2.2	.36	.1	.04	2.42	99.02
CTM01-AC35	do	75.89	12.21	1.39	.05	.6	3.6	3.62	.09	.02	.03	1.29	98.79
						Sedan study area							
CTM01-47A	Basalt	45.81	15.69	9.99	4.77	11.1	1.65	0.1	1.4	0.31	0.18	8.45	99.45
CTM01-AC49	do	48.46	15.81	10.33	6.62	10.49	2.09	.08	1.16	.1	.15	4.45	99.74
CTM01-AC51	do	50.4	15.11	11.42	5.32	8.97	2.7	.26	1.39	.39	.18	2.61	98.75
CTM01-AC59	Rhyolite-dacite plug	63.79	15.34	4.8	2.30	3.96	3.05	1.44	.47	.17	.06	4.25	99.63
CTM01-AC45	Dacite	63.94	15.28	5.12	1.15	3.99	3.83	1.93	.86	.23	.11	1.55	97.99
CTM01-AC60	Rhyolite-dacite plug	72.43	14.15	2.59	.46	1.04	3.06	3.36	.25	.09	.04	2.23	99.7
CTM01-AC56	Rhyolite	74.5	12.43	2.07	.05	.74	2.5	3.05	.15	.04	.04	2.34	97.91
Limit of detection		.01	.01	.01	.01	.01	.01	.01	.01	.01	.01	.01	.01

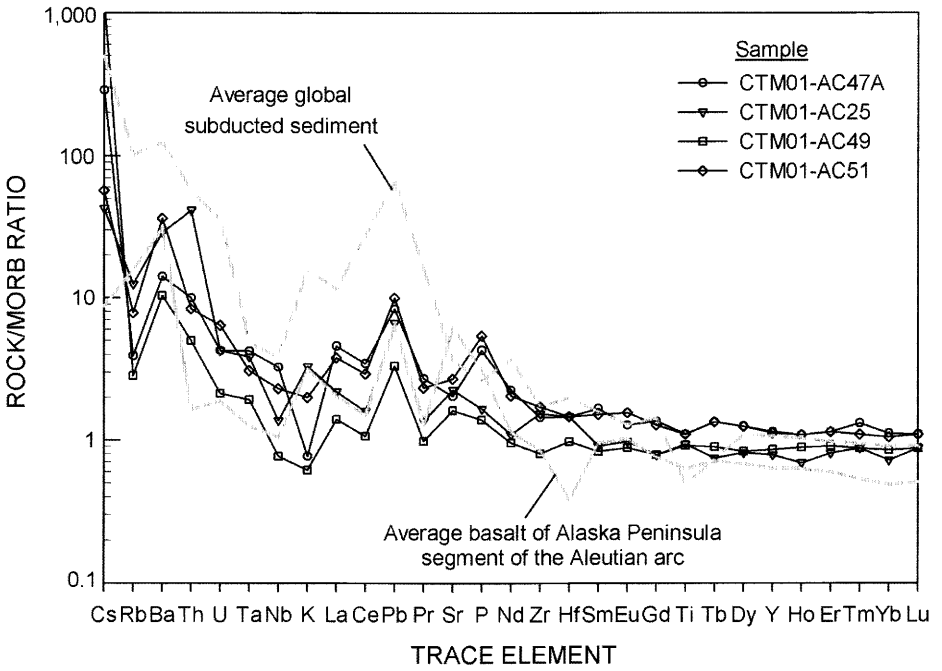

Figure 8. Midocean-ridge basalt (MORB)-normalized trace-element plot for volcanic rocks of the central Talkeetna Mountains (fig. 1). Normalizing values and arrangement of elements from Pearce and Parkinson (1993); data for average Aleutian basalt from same references as cited in figure 7; data for average subducted sedimentary rocks from Plank and Langmuir (1998).

Table 2. Trace-element composition of samples of volcanic rocks of the central Talkeetna Mountains.

[All values in parts per million. Descriptions: A, andesite; B, basalt; BA, basaltic andesite; D, dacite; R, rhyolite. See figure 1 for locations]

Sample	Description	Ag	Ba	Be	Cd	Ce	Co	Cr	Cs	Cu	Dy	Er	Eu	Ga	Gd	Ge	Hf	Ho	La	Lu	Mo
CTM01-AC47A	B	0.3	89	0.5	0.08	26	43.8	69	2	56.9	5.7	3.4	1.3	17.4	5	0.25	3	1.1	11.5	0.5	0.6
CTM01-AC25	B	.4	182.5	.6	.1	12	35.7	72	.3	47	3.7	2.4	1	17.55	2.9	.15	3	.7	5.5	.4	.55
CTM01-AC49	B	.06	65.5	.3	.06	8	46.1	141	8.1	84.4	3.8	2.7	.9	16.35	2.9	.15	2	.9	3.5	.4	.5
CTM01-AC51	B	.24	230	.65	.1	22	33.2	80	.4	59.7	5.7	3.4	1.6	16.85	4.7	.25	3	1.1	9.5	.5	.65
CTM01-AC6	BA	.28	301	.55	.08	16	28.6	39	.4	42.4	3.4	2.2	1.1	19.7	2.8	.15	3	.7	7	.4	.9
CTM01-AC26	BA	.4	213	.65	.08	16	32.4	20	.3	44.2	4.5	2.7	1.2	19.2	3.7	.25	3	1	6.5	.4	1.35
CTM01-AC40	A	.44	356	.95	.1	27	21.8	19	.6	44.2	3.9	2.4	1	16.9	3.7	.15	4	.8	12.5	.4	.95
CTM01-AC15	A	.1	577	1	.16	29	11.5	34	.4	37.2	3.9	2.7	.9	17.25	3.4	.2	4	.8	16	.6	.8
CTM01-AC30	A	.66	700	1.85	.08	34	7.7	9	4.4	19.6	4.5	2.6	1.3	21.3	4.6	.2	4	.9	16.5	.4	1.15
CTM01-AC28	D	.48	542	.95	.06	24	8.7	6	.9	21.8	3.8	2	1.3	20.15	3.5	.2	5	.7	13.5	.3	.85
CTM01-AC59	R-D plug	.28	843	.65	.04	24.5	11.2	47	1.5	29.4	2.8	1.7	.7	15.05	2.8	.15	4	.5	12	.3	.7
CTM01-AC45	D	.5	555	.95	.08	34	8.2	16	.7	22.6	4.8	2.8	1.2	17.1	4.3	.25	5	1	15.5	.5	1.4
CTM01-AC9	D	.24	706	1.45	.08	50.5	6.5	27	5.7	29.2	3.8	2.1	1.1	15.85	4	.15	4	.7	23.5	.4	1.3
CTM01-AC10	D	.04	508	1.75	.04	27	3.8	22	7.1	21.6	2.7	1.6	.7	14.6	2.5	.05	4	.5	14.5	.3	.55
CTM01-AC37	R-D plug	.48	646	1.15	.02	30.5	6.2	30	1.5	20.2	3.1	2	.6	15.5	2.9	.2	4	.7	16	.4	1.2
CTM01-AC16	D	< .1	892	1.2	.06	39.5	2.4	22	6.6	11.8	2.9	1.8	.6	14.15	3.1	.15	4	.6	20.5	.3	.95
CTM01-AC60	R-D plug	.4	957	1.95	.06	35.5	2.6	14	5.4	14	3.4	2.1	.6	16.65	3.6	.15	4	.6	18	.4	.7
CTM01-AC33	R dike	.56	740	1.2	.1	32.5	3.3	16	1.3	15.2	3.4	2	.6	14.15	3.1	.15	4	.7	16.5	.4	1
CTM01-AC56	R	.5	1,145	1.5	.06	45	1	11	4.5	12	5	3.1	.7	14.35	4.6	.15	6	1	22	.6	.85
CTM01-AC35	R-D plug	.52	978	1.45	.02	45	.6	28	2.5	9.2	4.2	2.4	.5	13.95	4	.15	4	.8	23	.5	1.8
Limit of detection		.1	.5	.1	.02	.5	.5	5	.1	5	.1	.1	.1	1	.1	.05	1	.1	.5	.1	.5

Sample	Description	Nb	Nd	Ni	Pb	Pr	Rb	Sm	Sn	Sr	Ta	Tb	Th	Tm	U	V	W	Y	Yb	Zn	Zr
CTM01-AC47A	B	7.6	16.5	70.9	2.5	3.6	2.2	4.4	0.4	184	0.55	0.9	1.2	0.6	0.2	204	1.1	32	3.4	80	107
CTM01-AC25	B	3.2	8	49.6	2	1.8	7	2.4	.4	204	.5	.5	5	.4	.2	219	.3	22	2.2	74	114
CTM01-AC49	B	1.8	7	137.5	1	1.3	1.6	2.2	.4	146	.25	.6	.6	.4	.1	251	.1	24	2.6	66	59.5
CTM01-AC51	B	5.4	15	69.9	3	3.1	4.4	4	.6	244	.4	.9	1	.5	.3	174	.5	31.5	3.2	76	127.5
CTM01-AC6	BA	6.5	9	11.8	4.5	2.1	13.4	2.5	.6	293	.55	.5	4.2	.4	.5	191	.4	21	2.3	86	100.5
CTM01-AC26	BA	3.6	10.5	23.4	2.5	2.3	10.8	3.1	.6	222	.4	.7	2	.5	.3	238	.3	26	2.5	84	160.5
CTM01-AC40	A	8.7	14	17	4.5	3.4	22.8	3.4	.6	242	.7	.6	2.4	.4	.7	137	.5	24	2.5	68	124
CTM01-AC15	A	6.6	15	18.2	7	3.9	7.6	3.2	.8	260	.65	.6	2.8	.5	.9	84	.4	26.5	2.8	72	153.5
CTM01-AC30	A	9.3	18	2.2	12.5	4.3	86.4	4.5	1.8	217	.9	.8	3.6	.4	1.8	93	1.2	28	2.5	94	152
CTM01-AC28	D	5.8	14.5	2	7	3.4	30.4	3.3	1	196.5	.5	.6	2.6	.3	.8	108	.4	19.5	1.8	96	148.5
CTM01-AC59	R-D plug	5.1	11.5	21.2	5	3.4	33.8	2.5	.6	197	.5	.4	3.2	.3	.9	84	.5	15	1.7	54	155.5
CTM01-AC45	D	8.6	17.5	2.4	7	4.2	46.2	4.3	1	199.5	.75	.8	4	.5	1.3	64	.6	28.5	2.8	62	158
CTM01-AC9	D	6.6	23	6.4	11	6	83.6	4.7	1.4	165	.75	.6	5	.3	2.6	47	1.1	20.5	2.1	50	134.5
CTM01-AC10	D	5.6	12	5.4	7.5	3.2	49.8	2.6	1.2	167	.65	.5	3.8	.3	1.1	41	3.1	16	1.8	28	134.5
CTM01-AC37	R-D plug	10.0	13.5	9.4	7.5	3.5	66	2.8	.8	121	.95	.5	6.6	.3	2	44	.8	19.5	2.1	46	120
CTM01-AC16	D	5.9	16	3	11	4.5	96.2	3.3	1.4	172.5	.65	.5	5.2	.3	2.4	16	.7	18	2	40	123
CTM01-AC60	R-D plug	8.3	15.5	2.6	13.5	4.6	120	3.2	2.2	127.5	.95	.5	6.6	.3	4	17	1.1	19	2.1	46	158
CTM01-AC33	R dike	8.7	14	3.4	9	3.9	93.2	2.9	.8	81.9	.85	.5	5.6	.3	2.1	25	1	21	2.1	50	123
CTM01-AC56	R	11.1	21.5	2.6	10.5	5.4	97.6	4.7	1.4	66.8	.95	.8	6.2	.5	3	3	3.1	30.5	3.5	46	265
CTM01-AC35	R-D plug	11.4	19	1.6	14.5	5.1	106	4.1	1	34.7	1.15	.7	8.4	.4	2.4	<1	.8	23.5	2.8	34	102
Limit of detection		.5	.5	2	1	.1	.2	.1	.2	.1	.5	.1	.2	.1	.1	1	.1	.5	.1	2	.5

(fig. 7). Our working hypothesis is that the central Talkeetna Mountain basalts were derived from a depleted source, similar to that of normal to enriched MORB.

The enrichment of Cs, Ba, Th, and Pb, coupled with the low Rb and K contents of the basalt samples, especially samples CTM01–AC49 and CTM01–AC47A (figs. 6–8; tables 1, 2), probably reflects characteristics of the mantle source, as opposed to crustal contamination of the basaltic magmas. If the basaltic magmas had undergone extensive crustal contamination, we would expect to find higher Rb and K contents, along with an increase in the contents of other incompatible elements, as is supported by the geochemical data of Plafker and others (1989) for rocks of the Wrangellia composite terrane, which forms the crust beneath much of south-central Alaska. The rocks of the Wrangellia composite terrane generally are more enriched in Rb and K and more depleted in Th relative to basalts of the central Talkeetna Mountains (fig. 7). One exception is a sample of Pennsylvanian metagranodiorite from the Wrangellia composite terrane (sample 84ANK186A of Plafker and others, 1989) that has a very high Th content (fig. 7). If this type of rock unit is present in the Talkeetna Mountains area, then the high Th content of the basalts in the central Talkeetna Mountains could reflect some degree of crustal contamination. This comparison is not ideal, however, because the data for the Wrangellia composite terrane are from samples collected in the Copper River Basin area, about 150 km southeast of the central Talkeetna Mountains. Geochemical studies of rocks of the Wrangellia composite terrane in the Talkeetna Mountains area are needed to better constrain the composition of the crust and the potential degree of crustal contamination during Tertiary magmatism in this region. Assuming, however, that crustal rocks generally have high incompatible-element contents (Taylor and McLennan, 1985), the progressive enrichment of LREEs and Ba, Rb, Th, and K from the basalts through the andesites, dacites, and rhyolites of the central Talkeetna Mountains (fig. 7) indicates that crustal assimilation was important in the formation of the felsic magmas (Thompson and others, 1984). The progressive depletion of Sr, Eu, P, and Ti from the basalts through the andesites, dacites, and rhyolites indicates that fractional crystallization of plagioclase, apatite, and Fe-Ti oxides also played a role in the evolution of the felsic magmas (Thompson and others, 1984).

The evolution of the volcanic rocks of the central Talkeetna Mountains from a depleted magma source, as well as the apparent age range of these volcanic rocks (approx 40–56 Ma, based on K-Ar ages of Csejtey and others, 1978, and Little, 1988), is enigmatic for Tertiary magmatism in south-central Alaska. Within this time frame, a lull in regional magmatic activity occurred across Alaska. The Alaska Range-Talkeetna Mountains magmatic belt, attributed to Kula Plate subduction, ranges in age from about 56 to 72 Ma (Wallace and Engebretson, 1984; Moll-Stalcup, 1994) (fig. 1). The Alaska-Aleutian Arc, a precursor to the modern Aleutian Arc, ranges in age from about 30 to 45 Ma (fig. 1; Moll-Stalcup, 1994). The volcanic rocks of the central Talkeetna Mountains were erupted during the time between these two regional magmatic episodes. Spatially, the volcanic rocks of the central Talkeetna Mountains are more closely related to the older Alaska Range-Talkeetna Mountains belt than to the younger Alaska-Aleutian Arc. The volcanic rocks of the central Talkeetna Mountains may represent the youngest and easternmost phase of Alaska Range-Talkeetna Mountains belt magmatism, a relation consistent with a general age trend illustrated by Moll-Stalcup and others (1994) in which the northeastern part of this belt is younger (mostly 55–65 Ma) than the rest of the belt (mostly 60–72 Ma). Although the volcanic rocks of the central Talkeetna Mountains do lie within the boundaries of the Alaska Range-Talkeetna Mountains magmatic belt and do display geochemical characteristics that are attributable to subduction-related processes, they also have characteristics that differ from those of typical subduction-related volcanic rocks.

The high Cs, Ba, Th, and Pb contents in the basalts of the central Talkeetna Mountains are characteristic of arc basalts, including basalts erupted along the Alaska Peninsula segment of the modern Aleutian Arc (figs. 7, 8). Of these elements, Cs, Ba, and Pb are highly mobile in fluids and are typically released into the mantle wedge beneath arcs during dehydration of the subducted slab (Kay, 1984; Class and others, 2000; Hochstaedter and others, 2001). Th is relatively immobile in fluids but is enriched in subducted sediment (fig. 8; Plank and Langmuir, 1998) and can be released into the mantle wedge beneath arcs during partial melting of subducted sediments (Class and others, 2000). Accordingly, the high Cs, Ba, Th, and Pb contents in the basalt samples could represent enrichment of the mantle beneath the Wrangellia composite terrane by fluids and partial melts derived from a subducted slab during the final phase of the Alaska Range-Talkeetna Mountains magmatic episode. The high Th content might also reflect some degree of crustal contamination, as discussed earlier. Except for a varying Rb content, the andesite samples from the central Talkeetna Mountains display chondrite-normalized trace-element concentrations that are nearly identical to those of modern andesites erupted along the Alaska Peninsula segment of the Aleutian Arc (fig. 7).

The characteristics of the basalts of the central Talkeetna Mountains that differ from those of typical subduction-related volcanic rocks include the absence of a paired Nb-Ta-depletion trend, high Ta contents (average Nb/Ta ratio of 10.3 among the basalts versus an average of 15 for Aleutian Arc basalts), low La/Nb ratios among the basalts (average of 1.64 versus an average of ~3 for Aleutian Arc basalts), and low Ba/Ta ratios (average of 407 and 815 for the basalts and andesites versus averages of 1,294 and 2,471 for Aleutian Arc basalts and andesites, respectively; see references in fig. 7). The primary source for the volcanic rocks of the central Talkeetna Mountains was therefore depleted mantle that was probably enriched in Ta relative to the mantle sources of average subduction-related volcanic rocks.

Conclusions

The results of this study provide new insight into the tectonomagmatic history of south-central Alaska. First, the timing and extent of subduction-related magmatism is poorly defined for early Tertiary time in south-central Alaska. The geochemistry of the volcanic rocks of the central Talkeetna Mountains indicates that subduction-related magmatic processes were important in the evolution of these rocks but that these rocks also lack some "typical" arc-volcanic geochemical affinities. This trend is consistent with the interpretation by Moll-Stalcup (1994) that in western Alaska, between about 56 and 50 Ma, there was "a transition from subduction-related magmatism to post subduction, possibly intraplate, magmatism during which rocks typical of both environments erupted." The mixed geochemical affinity of the volcanic rocks of the central Talkeetna Mountains indicates that a similar transition occurred in south-central Alaska during Eocene time. Second, the composition of the mantle beneath the Wrangellia composite terrane in south-central Alaska is poorly known. Our results indicate that a depleted mantle reservoir existed beneath south-central Alaska during early Tertiary time. This depleted mantle reservoir could represent the original composition of the upper mantle beneath the Wrangellia composite terrane, or it could have formed as a slab window beneath south-central Alaska after the passage of a trench-spreading ridge-trench triple junction (Bradley and others, 1993). Our ongoing work to compile the ages and regional geochemical trends of Tertiary volcanic rocks in south-central Alaska will help to further constrain these tectonomagmatic models.

Acknowledgments

This research was funded by National Science Foundation grant EAR9814377. The U.S. Geological Survey Talkeetna Mountains project provided helicopter and base-camp support for this project. We thank Jeanine Schmidt, Steve Nelson, and Peter Oswald for discussions about the Tertiary volcanic rocks in the central Talkeetna Mountains. Charles Cunningham and John Pallister reviewed the manuscript.

References Cited

Adams, D.D., Burns, L.E., Pessel, G.H., Little, T.A., Newberry, R.J., and Flynn, L.R., 1985, Preliminary geologic map of the central Talkeetna Mountains, Alaska: Alaska Division of Geological and Geophysical Surveys Public Data File 85–20, 2 sheets, scale 1:25,000.

Bradley, D.C., Haeussler, P.J., and Kusky, T.M., 1993, Timing of Early Tertiary ridge subduction in southern Alaska, *in* Dusel-Bacon, Cynthia, and Till, A.B., eds., Geologic studies in Alaska by the U.S. Geological Survey, 1992: U.S. Geological Survey Bulletin 2068, p. 163–177.

Class, Cornelia, Miller, D.M., Goldstein, S.L., and Langmuir, C.H., 2000, Distinguishing melt and fluid subduction components in Umnak volcanics, Aleutian Arc: Geochemistry, Geophysics, Geosystems, v. 1, paper 1999GC000010, 34 p.

Coombs, M.L., Eichelberger, J.C., and Rutherford, M.J., 2000, Magma storage and mixing conditions for the 1953–1974 eruptions of southwest Trident Volcano, Katmai National Park, Alaska: Contributions to Mineralogy and Petrology, v. 140, p. 99–118.

Csejtey, Béla, Jr., Nelson, W.H., Jones, D.L., Silberling, N.J., Dean, R.M., Morris, M.S., Lanphere, M.A., Smith, J.G., and Silberman, M.L., 1978, Reconnaissance geologic map and geochronology, Talkeetna Mountains quadrangle, northern part of Anchorage quadrangle, and southwest corner of Healy quadrangle, Alaska: U.S. Geological Survey Open-File Report 78–558–A, 1:250,000.

Feigenson, M.D., and Spera, F.J., 1983, Case studies on the origin of basalt II—the transition from tholeiitic to alkalic volcanism on Kohala Volcano, Hawaii: Contributions to Mineralogy and Petrology, v. 84, no. 4, p. 390–405.

Hildreth, Wes, 1983, The compositionally zoned eruption of 1912 in the Valley of Ten Thousand Smokes, Katmai National Park, Alaska: Journal of Volcanology and Geothermal Research, v. 18, no. 1–4, p. 1–56.

Hochstaedter, Alfred, Gill, James, Peters, Robert, Broughton, Phil, Holden, Peter, and Taylor, Brian, 2001, Across-arc geochemical trends in the Izu-Bonin arc—contributions from the subducting slab: Geochemistry, Geophysics, Geosystems, v. 2, paper 2000GC000105, 44 p.

Hofmann, A.W., Feigenson, M.D., and Raczek, Ingrid, 1984, Case studies on the origin of basalt III—petrogenesis of the Mauna Ulu eruption, Kilauea, 1969–1971: Contributions to Mineralogy and Petrology, v. 88, no. 1–2, p. 24–35.

———1987, Kohala revisited: Contributions to Mineralogy and Petrology, v. 95, no. 1, p. 114–122.

Johnson, K.E., Harmon, R.S., Richardson, J.M., Moorbath, Stephen, and Strong, D.F., 1996, Isotope and trace element geochemistry of Augustine Volcano, Alaska—implications for magmatic evolution: Journal of Petrology, v. 37, no. 1, p. 95–115.

Kay, R.W., 1984, Elemental abundances relevant to the identification of magma sources: Royal Society of London Philosophical Transactions, ser. A, v. 310, no. 1514, p. 535–547.

Le Bas, M.J., LeMaitre, R.W., Streckeisen, Arthur, and Zanettin, B.A., 1986, A chemical classification of volcanic rocks based on the total alkali-silica diagram: Journal of Petrology, v. 27, no. 3, p. 745–750.

Little, T.A., 1988, Tertiary tectonics of the Border Ranges fault system, north-central Chugach Mountains, Alaska—sedimentation, deformation and uplift along the inboard edge of a subduction complex: Stanford, Calif., Stanford University, Ph.D. thesis, 343 p.

Moll-Stalcup, E.J., 1994, Latest Cretaceous and Cenozoic magmatism in mainland Alaska, *in* Plafker, George, and Berg, H.C., eds., The geology of Alaska, v. G–1 *of* The geology of North America: Boulder, Colo., Geological Society of America, p. 589–619.

Moll-Stalcup, E.J., Brew, D.A., and Vallier, T.L., 1994, Latest

Cretaceous and Cenozoic magmatic rocks of Alaska, pl. 5 *of* Plafker, George, and Berg, H.C., eds., The geology of Alaska, v. G–1 *of* The geology of North America: Boulder, Colo., Geological Society of America, scale 1:2,500,000.

Nokleberg, W.J., Plafker, George, and Wilson, F.H., 1994, Geology of south-central Alaska, *in* Plafker, George, and Berg. H.C., eds., The geology of Alaska, v. G–1 *of* The geology of North America: Boulder, Colo., Geological Society of America, p. 311–366.

Nye, C.J., Swanson, S.E., Avery, V.F., and Miller, T.P., 1994, Geochemistry of the 1989–1990 Eruption of Redoubt Volcano; part I, Whole-rock major- and trace-element chemistry: Journal of Volcanology and Geothermal Research, v. 62. no. 1–4, p. 429–452.

Nye, C.J., and Turner, D.L., 1990, Petrology, geochemistry, and age of the Spurr volcano complex, eastern Aleutian arc: Bulletin of Volcanology, v. 52, no. 3, p. 205–226.

Pearce, J.A., and Parkinson, I.J., 1993, Trace element models for mantle melting—application to volcanic arc petrogenesis, *in* Prichard, H.M., Alabaster, Tony, Harris, N.B.W., and Neary, C.R., eds., Magmatic processes and plate tectonics (Gass volume): Geological Society of London Special Publication 76, p. 373–403.

Plafker, George, Nokleberg, W.J., and Lull, J.S., 1989, Bedrock geology and tectonic evolution of the Wrangellia, Peninsular, and Chugach Terranes along the Trans-Alaska Crustal Transect in the Chugach Mountains and southern Copper River Basin, Alaska: Journal of Geophysical Research, v. 94, no. B4, p. 4255–4295.

Plank, Terry, and Langmuir, C.H., 1998, The chemical composition of subducting sediment and its consequences for the crust and mantle: Chemical Geology, v. 145, no. 3–4, p. 325–394.

Rickwood, P.C., 1989, Boundary lines within petrologic diagrams which use oxides of major and minor elements: Lithos, v. 22, no. 4, p. 247–263.

Sims, K.W.W., DePaolo, D.J., Murrell, M.T., Baldridge, W.S., Goldstein, S.J., Clague, D.A., and Jull, M.G., 1999, Porosity of the melting zone and variations in the solid mantle upwelling rate beneath Hawaii—inferences from ^{238}U-^{230}Th-^{226}Ra and ^{235}U-^{231}Ra disequilibria: Geochimica et Cosmochimica Acta, v. 63, no. 23–24, p. 4119–4138.

Spengler, S.R., and Garcia, M.O., 1988, Geochemistry of the Hawi lavas, Kohala volcano, Hawaii: Contributions to Mineralogy and Petrology, v. 99, no. 1, p. 90–104.

Sun, S.-S., 1980, Lead isotopic study of young volcanic rocks from mid-ocean ridges, ocean islands and island arcs: Royal Society of London Philosophical Transactions, ser. A, v. 297, no. 1431, p. 409–445.

Taylor, S.R., and McLennan, S.M., 1985, The continental crust—its composition and evolution: Oxford, U.K., Blackwell Scientific, 312 p.

Thompson, R.N., Morrison, M.A., Hendry, G.L., and Parry, S.J., 1984, An assessment of the relative roles of crust and mantle in magma genesis—an elemental approach: Royal Society of London Philosophical Transactions, ser. A, v. 310, no. 1514, p. 549–590.

Till, A.B., Yount, M.E., and Bevier, M.L., 1994, The geologic history of Redoubt volcano, Alaska: Journal of Volcanology and Geothermal Research, v. 62, no. 1–4, p. 11–30.

Wallace, W.K., and Engebretson, D.C., 1984, Relationship between plate motions and Late Cretaceous to Paleogene magmatim in southwestern Alaska: Tectonics, v. 3, no. 2, p. 293–315.

Wilson, F.H., Dover, J.H., Bradley, D.C., Weber, F.R., Bundtzen, T.K., and Haeussler, P.J., 1998, Geologic map of central (interior) Alaska: U.S. Geological Survey Open File Report 98–133, scale 1:500,000.

Wright, T.L., and Helz, R.T., 1996, Differentiation and magma mixing on Kilauea's East Rift Zone; a further look at the eruptions of 1955 and 1960. 2, The 1960 lavas: Bulletin of Volcanology, v. 57, no. 8, p. 602–630.

Studies by the U.S. Geological Survey in Alaska, 2001
U.S. Geological Survey Professional Paper 1678

Mesozoic Sedimentation and Deformation Along the Talkeetna Thrust Fault, South-Central Alaska—New Insights and Their Regional Tectonic Significance

By J. Michael O'Neill, Kenneth D. Ridgway, and Kevin R. Eastham

Abstract

Recent work in the Talkeetna Mountains of south-central Alaska involving sedimentologic and structural investigations along the trace of the Talkeetna thrust fault reveals the following relations: (1) the Kahiltna assemblage in the footwall of the Talkeetna thrust fault represents proximal submarine-fan deposits that were derived from strata exposed in the adjacent hanging wall of the fault; and (2) the structure along the exposed trace of the fault is that of minor thrust slices in the juxtaposed upper and lower plates, is nonpenetrative, and is restricted to within 20 to 50 m of the thrust fault. Lower-plate rocks containing rounded pebble to boulder clasts and delicate bivalve macrofossils adjacent to the fault are undeformed. The proximal sedimentary relation between the footwall and hanging-wall rocks, coupled with the absence of well-developed penetrative-deformation fabrics, suggests that the Talkeetna thrust fault is not a major nappelike structure with tens of kilometers of tectonic transport, as originally interpreted, and so this individual fault zone does not mark a major tectonic terrane boundary in the accretionary tectonic landscape of south-central Alaska.

Introduction

The tectonic evolution of south-central Alaska is largely known from reconnaissance geologic mapping in the Talkeetna Mountains quadrangle (Csejtey and others, 1978) and adjacent Healy quadrangle (Csejtey and others, 1992). These studies showed that the regional geologic framework of the region between the Alaska Range on the north and the Border Ranges of the Chugach terrane on the south represents a composite of two allochthonous terranes and associated basins that were sutured to the North American craton during mid-Cretaceous and Late Cretaceous time. The four major tectonostratigraphic units involved in this collisional event are, from north to south, the North American, Kahiltna, Wrangellia, and Peninsular terranes (fig. 1). The narrow, elongate Peninsular and Wrangellia terranes evolved separately during the Paleozoic at latitudes far south of their present position and were not in their present positions during Early Cretaceous time (Packer and Stone, 1974; Jones and others, 1977). The two terranes were apparently sutured together as early as late Paleozoic, because they share a common geologic history throughout the Mesozoic (Csejtey and others, 1982; Gardner and others, 1988); they have since acted as a structurally cohesive unit and, as such, were termed the "Talkeetna superterrane" by Csejtey and others (1982) and the Wrangellia composite terrane by Plafker and Berg (1994). The Kahiltna assemblage consists of strata deposited in sedimentary basins between the Wrangellia composite terrane and the North American craton (fig. 1). Exposed within the Kahiltna assemblage are what have been called miniterranes, composed of geologically dissimilar fault-bounded blocks, interpreted to have been tectonically intermixed with the Kahiltna assemblage during the collisional event that joined the Wrangellia composite terrane to the continental margin (Csejtey and others, 1982, p. 3747). The miniterranes, the best known of which is the Chulitna terrane (fig. 1), have been interpreted to represent klippen directly tied to a major nappelike structure emplaced along the Talkeetna thrust fault (Csejtey and others, 1978, 1982, 1992). Thus, the Talkeetna thrust fault was interpreted to represent a major terrane boundary that marks the northwest edge of the Wrangellia composite terrane.

Recent geologic mapping along a northwest-trending transect across the Talkeetna Mountains allowed us to examine the Talkeetna thrust fault where it is well exposed. This chapter describes the structural characteristics of the Talkeetna thrust fault and the stratigraphy and sedimentology of footwall strata of the overthrust Late Jurassic and Early Cretaceous Kahiltna assemblage, and discusses the tectonic implications of these observations.

Talkeetna Thrust Fault

The Talkeetna thrust fault, as previously described by Csejtey and others (1982), dips moderately to steeply southeast and everywhere marks the boundary between Triassic and Permian metavolcanic and metasedimentary strata of the

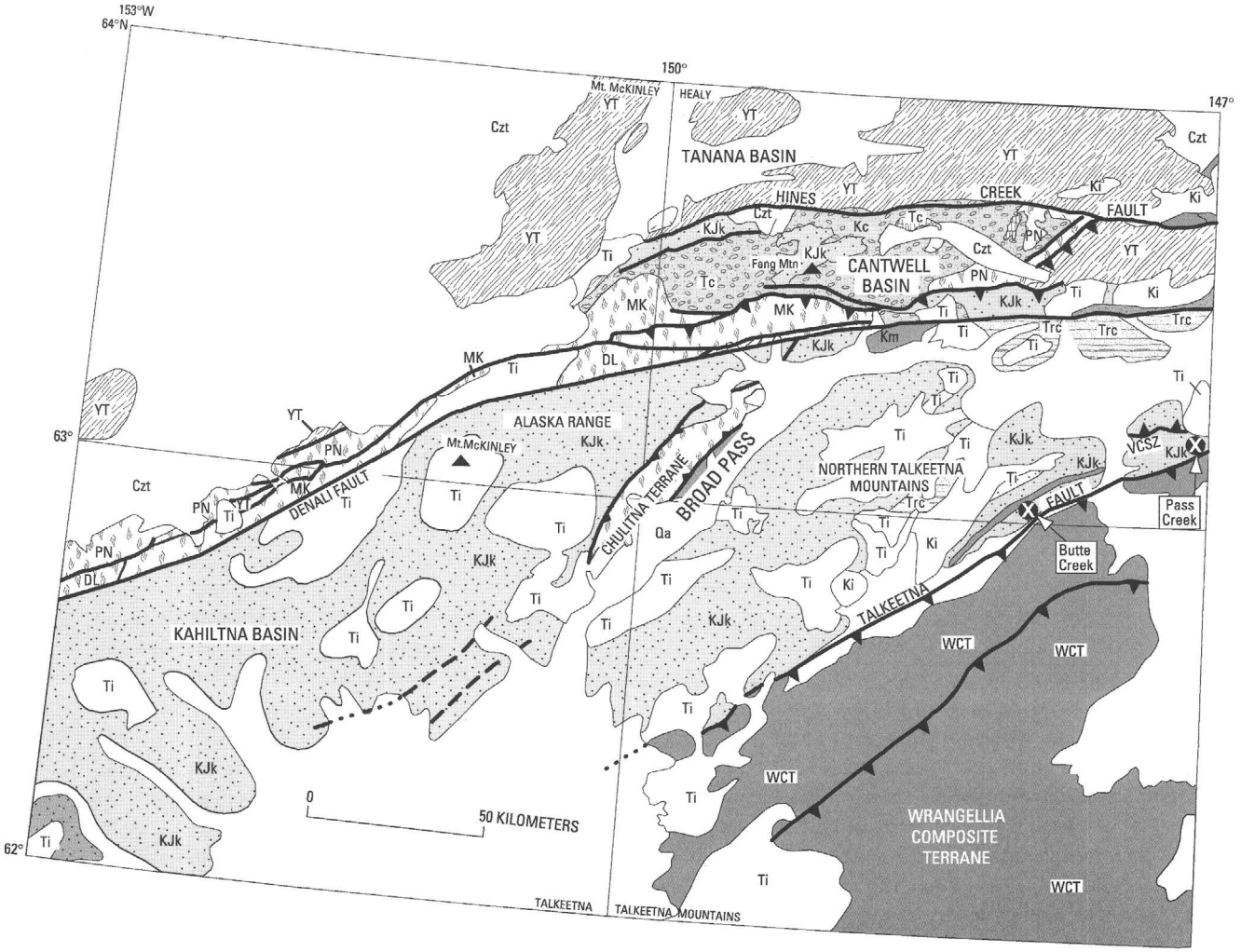

EXPLANATION

Contact, dotted where concealed

Fault, dashed where inferred, dotted where concealed

Thrust fault, dashed where inferred, dotted where concealed, teeth on upper plate

CF	Castle Mountain Fault
CG	Chugach terrane
Czt	Tanana Basin deposits (Cenozoic)
DF	Denali Fault
DL	Dillinger terrane
Kc	Cantwell Basin sedimentary strata (Cretaceous)
KH	Kahiltna assemblage
Ki	Igneous rocks (Cretaceous)
KJk	Kahiltna assemblage (Late Jurassic to Late Cretaceous)
Km	Melange (Cretaceous)
MK	McKinley terrane
NA	North American craton
PN	Pingston terrane
Qa	Alluvium (Quaternary)
Tc	Cantwell Basin volcanic strata (Tertiary)
TF	Tintina Fault
Ti	Igneous rocks (Tertiary)
TKF	Talkeetna thrust fault
Trc	Calcareous sedimentary rocks (Late Triassic)
VCSZ	Valdez Creek shear zone
WCT	Wrangellia composite terrane
YK	Yakutat terrane
YT	Yukon-Tanana terrane

INDEX MAP

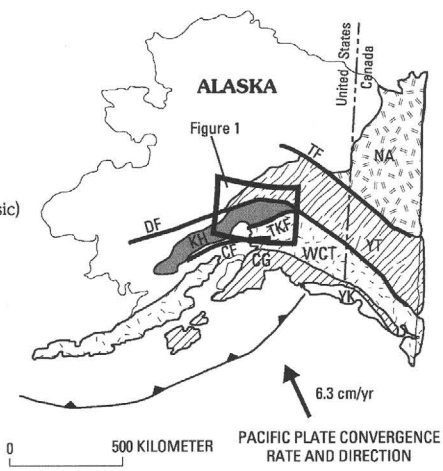

Figure 1. Generalized lithotectonic map of south-central Alaska, showing locations of Butte Creek and Pass Creek study areas.

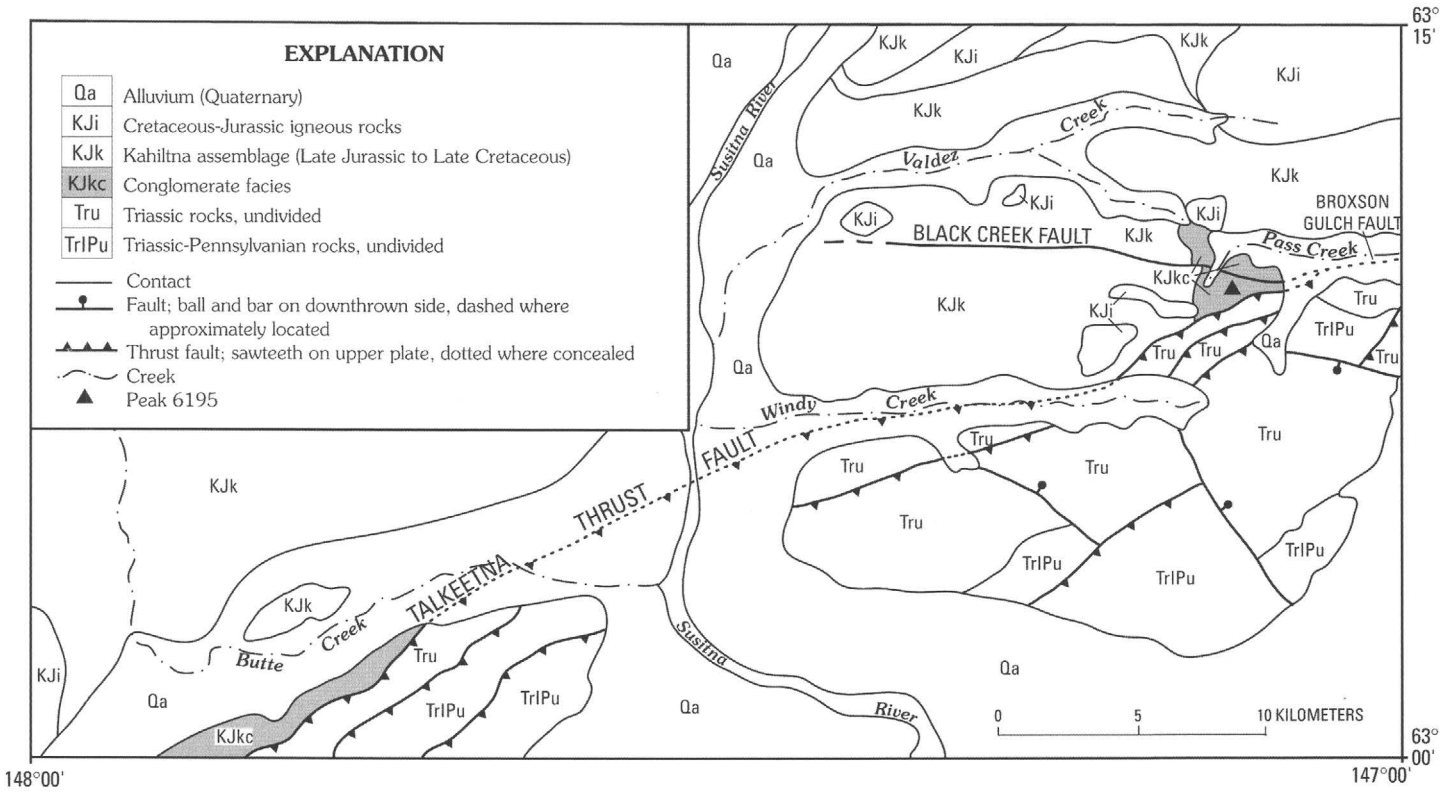

Figure 2. Geologic map of the Butte Creek and Pass Creek study areas, south-central Alaska (modified from Csejtey and others, 1992).

Talkeetna superterrane (Wrangellia composite terrane) on the south and sedimentary strata of the Kahiltna assemblage on the north (fig. 1). The thrust was most recently interpreted to terminate against the younger, north-dipping Broxson thrust fault on the east (fig. 2; Nokleberg and others, 1994). On the west, much of the thrust zone is either intruded by younger plutons and (or) covered by their volcanic counterparts (Csejtey and others, 1978). Complex structural relations are interpreted to exist along this terrane-bounding thrust fault. Csejtey and others (1982) described the thrust zone as a series of southeast-dipping thrust slices that consistently bring older rocks of the Wrangellia terrane over the Kahiltna assemblage. Folds associated with the thrust fault are tight to isoclinal and verge northwest. About 40 to 80 km northwest of the mapped trace of the Talkeetna thrust fault are exposures of Triassic and older rocks interpreted to be crustal blocks (miniterranes) derived from the Wrangellia terrane by displacements along the Talkeetna thrust system. The allochthonous miniterrane interpretation requires that a 6-km-thick nappelike structure consisting of an imbricate stack of thrust slices with northwestward-directed tectonic transport of as much as 80 km be emplaced above strata of the Kahiltna Basin (Csejtey and others, 1982, figs. 5–7). Displacement along the Talkeetna thrust fault and deformation of the Wrangellia terrane and the adjacent Kahiltna assemblage was interpreted as a mid-Cretaceous and Late Cretaceous event that accreted the Wrangellia composite terrane to Alaska.

Geologic Observations of the Talkeetna Thrust Fault and the Kahiltna Assemblage

The Talkeetna thrust fault and associated footwall rocks are largely covered by Tertiary and Quaternary valley-fill sedimentary deposits along most of its length. The thrust fault is best exposed directly south of Butte Creek in the Healy and Talkeetna Mountains quadrangles, and in the Clearwater Mountains to the east at the headwaters of Pass Creek (fig. 1).

Butte Creek Area

Structural Geology

The Talkeetna thrust fault is exposed in the rugged mountains directly south of Butte Creek in the southeastern part of the Healy and adjacent Talkeetna Mountains quadrangles (Smith and others, 1988), where it can be traced for about 8 km (fig. 2). Hanging-wall rocks consist of Triassic mafic metavolcanic flows, gabbroic sills, and interlayered Triassic fine-grained clastic and carbonate rocks. The footwall rocks consist of Jurassic and Cretaceous sedimentary strata consisting of about 75 m of interbedded shale, siltstone, sandstone, and marl that overlie more than 500

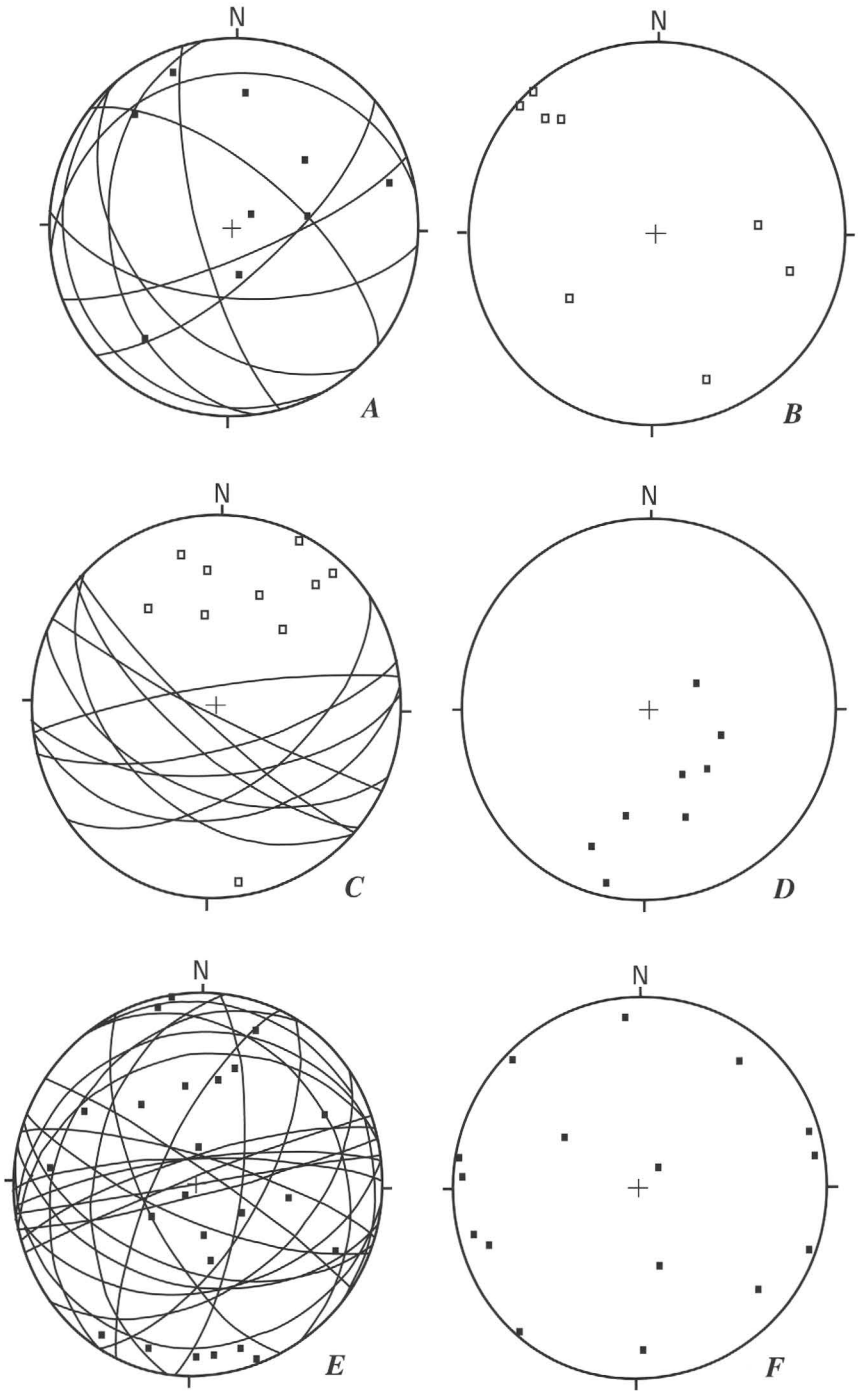

Figure 3. Lower-hemisphere, equal-area stereographic projections showing orientation of fabric elements in Butte Creek and Pass Creek study areas (figs. 1, 2). *A*, Orientation of secondary fractures (planes and poles to those planes; *n*=9) in footwall rocks adjacent to the Talkeetna thrust fault at Butte Creek. *B*, Orientation of slickenlines on fractures (*n*=8) in footwall rocks at Butte Creek. *C*, Orientation of secondary fractures (planes and poles to those planes; *n*=10) in footwall rocks associated with the Talkeetna thrust fault at Pass Creek. *D*, Orientation of slickenlines associated with fractures (*n*=8) at the Talkeetna thrust fault at Pass Creek. *E*, Orientation of fractures (planes and poles to those planes; *n*=24) associated with the Black Creek Fault/Broxson Gulch thrust fault zone. *F*, Orientation of slickenlines on fractures (*n*=17) in the Black Creek Fault/Broxson Gulch thrust fault zone.

m of pebble to boulder conglomerate. The thrust fault dips gently to moderately south-southwest in this area. Secondary fractures in footwall rocks containing slickenlines on their surfaces are variously oriented; most fractures dip moderately southwest (fig. 3*A*). The fractures are associated with a poorly developed cleavage that consistently strikes east-northeast and dips steeply southeast. Slickenlines are predominantly subhorizontal, and their azimuth and associated Reidel shears indicate tectonic transport to the northwest (fig. 3*B*). Bedding in the fine-grained clastic strata directly beneath the hanging wall is weakly to moderately folded about axes that plunge gently southwest. A 1- to 3-m-thick bed of marl about 20 m below the main fault contains abundant undeformed pelecypods of Cretaceous age (fig. 4). Folding, fracturing with slickenlines, and cleavage are confined to beds within 50 m of the thrust fault; the underlying conglomerate is essentially undeformed (fig. 5). At this locality the overall structural characteristics of the rocks 0 to 20 m directly below the thrust fault show an absence of intense, penetrative deformation.

Kahiltna Assemblage

The Kahiltna assemblage in the Butte Creek area directly below the Talkeetna thrust fault consists of three dominant lithofacies: (1) pebble to boulder conglomerate, (2) horizontally stratified sandstone, and (3) laminated siltstone (fig. 6).

The conglomerate lithofacies forms discontinuous lens-shaped packages of conglomerate and finer grained rocks that are 20 to 50 m long and as much as 25 m thick. Internally, this lithofacies consists of normally graded, moderately sorted conglomerate in 0.5- to 1.5-m-thick beds that fine upward into siltstone (for example, 200–216 m, fig. 6). The conglomerate is clast supported and contains subrounded pebbles and cobbles. The conglomerate lithofacies is commonly interbedded with laminated

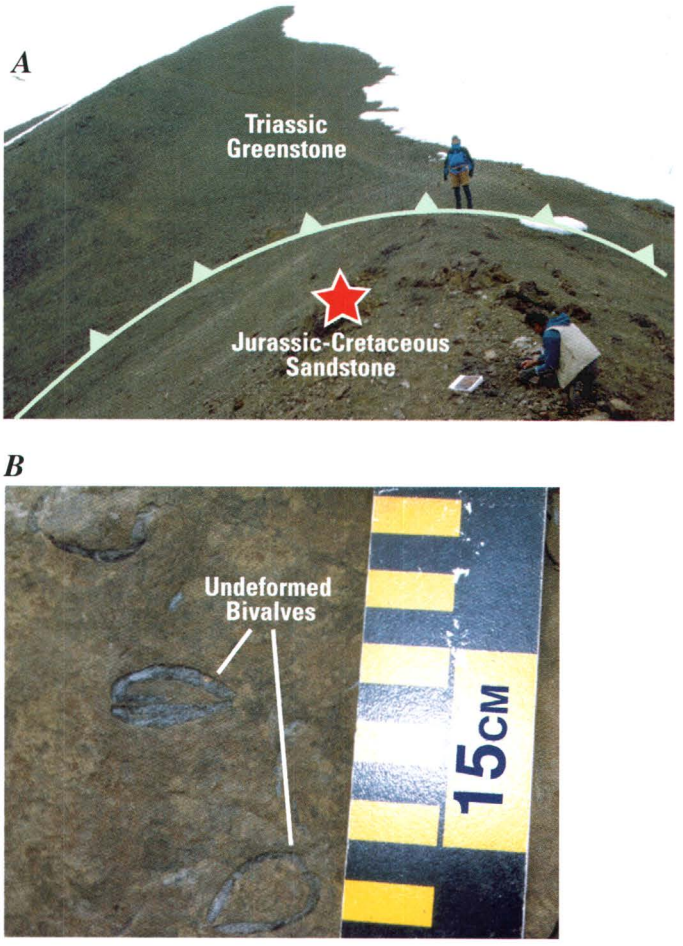

Figure 4. Talkeetna thrust fault in Butte Creek study area, south-central Alaska (figs. 1, 2). *A*, Trace of fault, showing Triassic greenstone structurally overlying Jurassic-Cretaceous sandstone. *B*, Marl of the Kahiltna assemblage and enclosed, undeformed pelecypod bivalves.

Figure 5. Conglomerate of the Kahiltna assemblage (undeformed volcanic-rock and limestone clasts) at Butte Creek (figs. 1, 2). Pen is 14 cm long.

siltstone and shale sequences that are tens of meters thick (230–297 m, fig. 5). The normal grading, overall grain size, and moderate sorting of rocks in the conglomerate lithofacies all suggest deposition from gravelly to sandy turbidity currents. Clast grading probably resulted from decreasing current velocity, which allowed progressively smaller clasts to settle (for example, Hein, 1982). Imbrication of clasts is rare in these conglomerate beds. Also present in the Butte Creek section are nongraded, laterally discontinuous lenses of boulder conglomerate (308–334 m, fig. 6) that contain poorly sorted, subangular clasts ranging in size from 0.1 to more than 7 m across. Because of the wide range of clast sizes (especially the very large clasts), the angularity of the clasts, and the absence of grading, we interpret these deposits as submarine rockfalls and (or) avalanche and debris flows that formed in the proximal part of a submarine-fan system, adjacent to submarine canyons (for example, Lowe, 1982; Stow and others, 1996).

The sandstone lithofacies is fine to coarse grained and is commonly part of upward-fining packages. Beds range in thickness from 10 to 50 cm and typically display sharp bases. Horizontal stratification is the most common sedimentary structure observed in the sandstone beds (360–429 m, fig. 6). According to Bouma's (1962) classification for turbidite deposits, the sandstone beds are described as Ta (massive, graded sandstone), Tab (Ta unit overlain by horizontally laminated sandstone), and Tabd (Tab unit overlain by laminated siltstone and mudstone). Well-preserved pelecypods (*Buchia*) and ammonites were collected 525 m above the base of the section in the sandstone lithofacies.

The siltstone lithofacies is laminated (0–54, 230–297, 476–522 m, fig. 5). We interpret this lithofacies to indicate pelagic sedimentation and (or) very fine grained, low-density turbidity-current deposition (Bouma, 1962).

Clast composition changes upsection in conglomerate beds of the Butte Creek section. In the lower part of the section, clasts consist mainly of black argillite (53 volume percent), gray limestone (22 volume percent), and siltstone (11 volume percent) (fig. 7*A*); in the middle of the section, clasts consist mainly of gray limestone (86 volume percent) and black argillite (9 volume percent) (fig. 7*B*); and in the uppermost part of the section, clasts consist mainly of greenstone (60 volume percent) and chert (17 volume percent) chert clasts (fig. 7*C*). We interpret the upsection clast-compositional trend from argillite through limestone to volcanic rock (greenstone) dominated as representing the progressive unroofing of the nearby Wrangellia terrane (northern part of the Wrangellia composite terrane). The Wrangellia terrane consists of more than 3,000 m of middle and (or) Late Triassic volcanic rocks (Nikolai Greenstone), overlain by 1,100 m of Upper Triassic carbonate strata (Chitistone and Nizina Limestones) and capped by 600 m of Upper and Lower Triassic to Jurassic argillite (McCarthy Formation). These rocks are exposed in the hanging wall of the Talkeetna thrust fault (Csejtey and others, 1978, fig. 1).

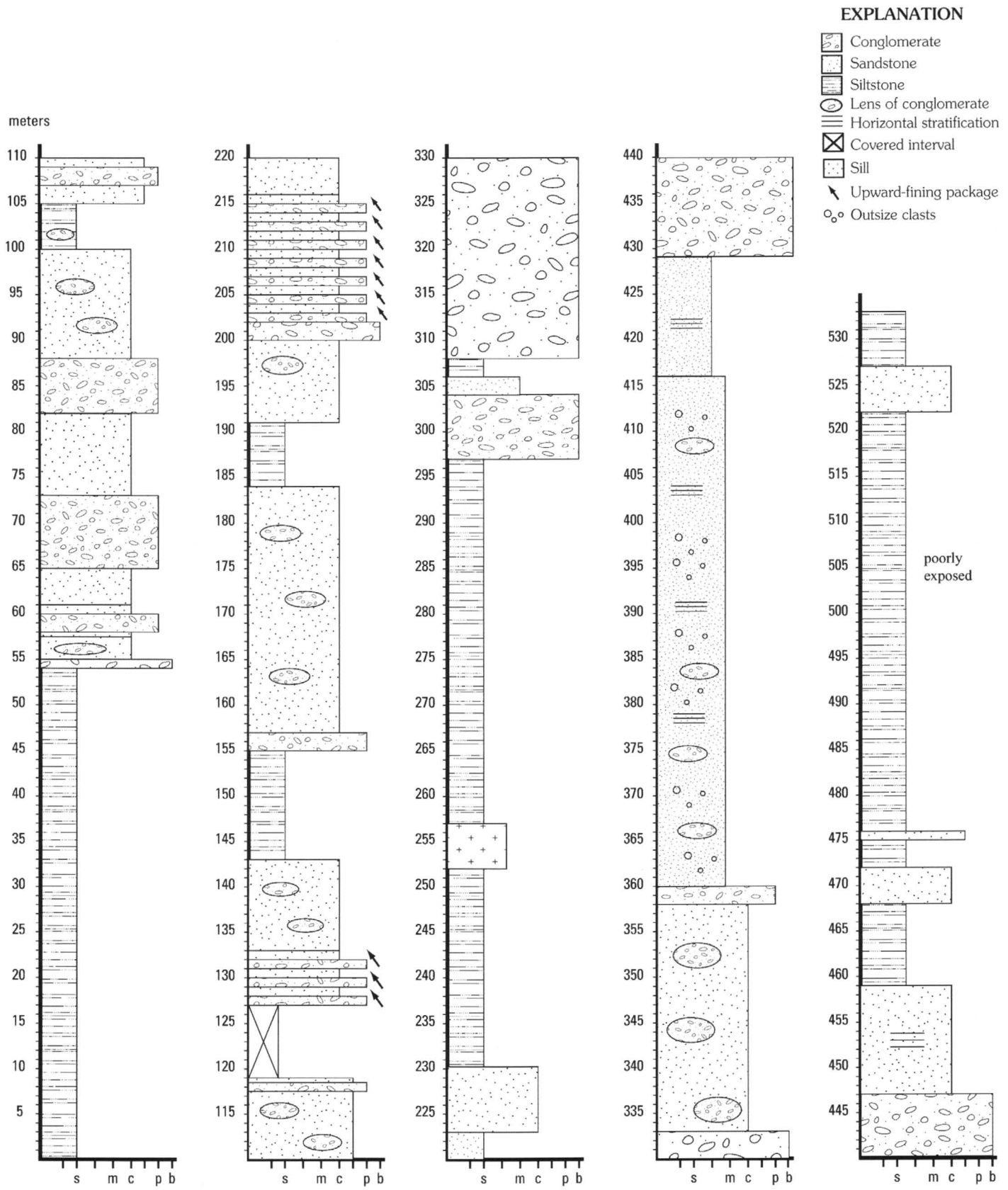

Figure 6. Measured stratigraphic section at Butte Creek (figs. 1, 2) Rock types: b, boulders; c, coarse-grained sandstone; m, medium-grained sandstone; p, pebbles; s, siltstone.

Pass Creek Area

Structural Geology

The Talkeetna thrust fault is not exposed between the Butte Creek area and the Pass Creek area in the Clearwater Mountains to the east, a distance of nearly 45 km (fig. 1). In the Pass Creek area, the trace of the thrust is exposed over a distance of about 8 km between Windy Creek and Pass Creek (fig. 2). The thrust trends east-northeast in this area and, on the northeast, joins the buried trace of the Broxson Gulch thrust fault of Nokleberg and others (1994); the nature of this join is unknown because it is concealed beneath surficial deposits of Pass Creek. Nokleberg and others (1994) interpreted the Broxson Gulch thrust fault to truncate the Talkeetna thrust fault at Pass Creek but did not locate the trace of the Broxson Gulch thrust fault beyond the point of truncation. Silberling and others (1981) mapped the Talkeetna and Broxson Gulch thrust faults as continuous structures within the same thrust zone. A high-angle fault mapped across the southern Clearwater Mountains by Smith (1981) and Adams and others (1991) merges with the Talkeetna thrust fault at Pass Creek. Named the Black Creek Fault by Adams and others (1991), their high-angle fault was later interpreted by Csejtey and others (1992) as a southward-directed reverse fault that truncates the Talkeetna thrust fault.

The Broxson Gulch thrust fault is interpreted to have a long and complex history of movement. To paraphrase Nokleberg and others (1994), the first movement involved thrusting along a south-dipping fault that placed the Wrangellia terrane onto the Kahiltna assemblage in the Maclaran Glacier area (Maclaran terrane of Nokleberg and others). A second period of movement involved strike-slip displacement, followed by a third period of displacement wherein the original south-dipping thrust fault was overturned to a north-dipping structure that then placed rocks of the Wrangellia terrane over Tertiary and Quaternary deposits.

At peak 6195 (fig. 2), directly south of Pass Creek, are two faults with completely different displacement histories. The Talkeetna thrust fault is clearly an east-northeast-trending fault that places older Triassic metasedimentary and metavolcanic rocks on coarse conglomerate of the Kahiltna assemblage (Silberling and others, 1981; Smith, 1981; Adams and others, 1991). The fault dips moderately south; associated fractures in the upper and lower plates dip moderately to steeply southward (fig. 3*C*). Slickenlines consistently plunge downdip (fig. 3*D*), and associated kinematic indicators show tectonic transport nearly due northward. Deformation of upper- and lower-plate rocks is restricted to brecciation at the fault contact, decreasing outward into minor folding and fracturing within 20 m of the fault trace. Minor northward-directed bedding-plane slippage is present locally at greater distances beneath the thrust fault. Evidence of stretching or flattening of conglomerate clasts is absent in the underlying Kahiltna assemblage.

At peak 6195 (fig. 2), the Broxson Gulch fault (Black Creek Fault of Adams and others (1991) and the unnamed fault of Smith (1981) form a zone of shearing and brecciation, as much as 200 m wide. The Kahiltna assemblage is present on both sides of the fault zone. Fractures with slickensided surfaces within this zone range in attitude from subhorizontal to steeply inclined in this east-trending fault zone (fig. 3*E*). The fault zone is marked by major topographic breaks and strongly brecciated and broken, limonite-stained rock where it crosses glacial arêtes at peak 6195. Similar topographic breaks persist for 15 km westward, where the fault zone cuts through strongly glaciated terrane before it apparently dies out in the western Clearwater Mountains.

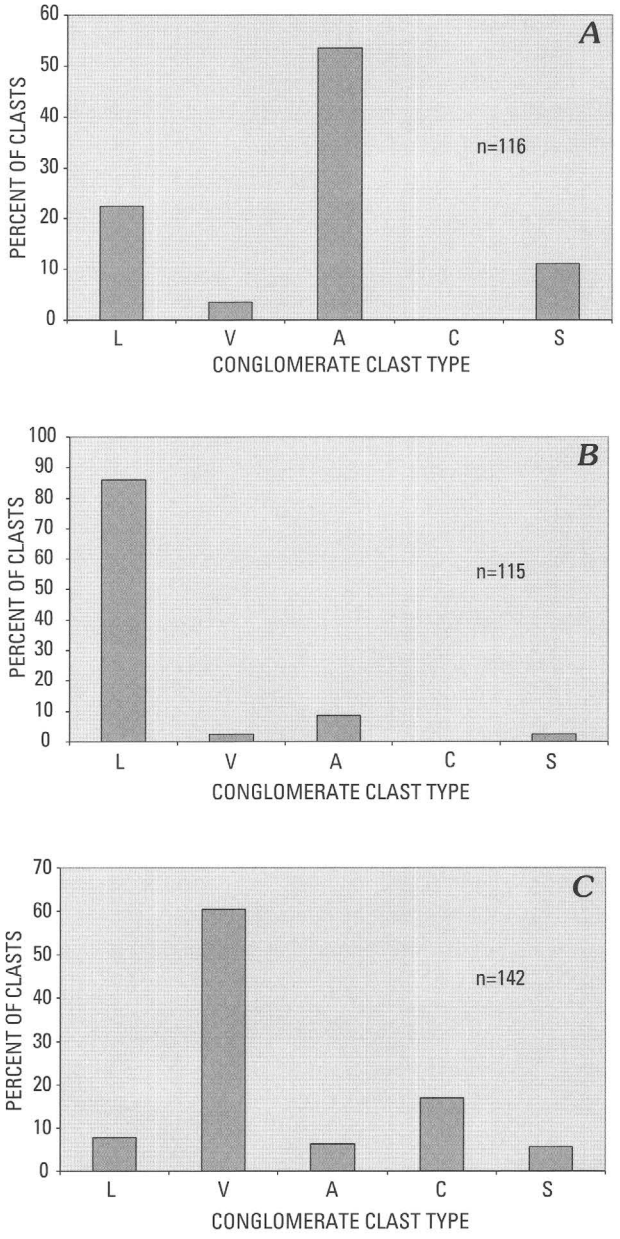

Figure 7. Clast-count data from stratigraphic section at Butte Creek (figs. 1, 2, 6). *A*, 59 m. *B*, 320 m. *C*, 470 m. Clast types: A, argillite; C, chert;, L, limestone; S, siltstone; V, volcanic rocks.

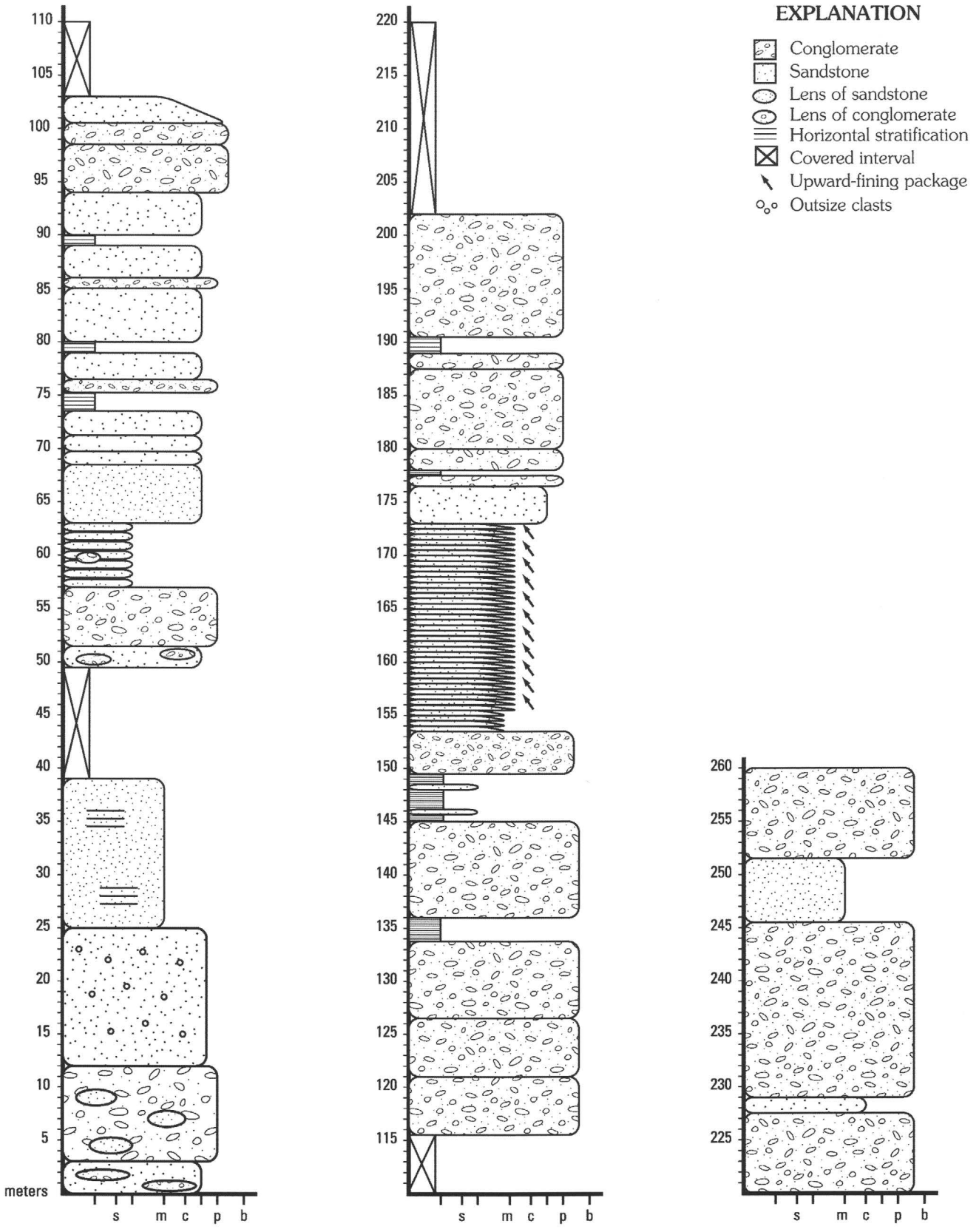

Figure 8. Measured stratigraphic section at Pass Creek (figs. 1, 2). Rock types: b, boulders; c, coarse-grained sandstone; m, medium-grained sandstone; p, pebbles; s, siltstone.

No large displacement was determined for the Broxson Gulch fault. At peak 6195 (fig. 2), conglomerate of the Kahiltna assemblage on the south is juxtaposed variously on the north with conglomerate and finer grained Kahiltna strata. Kinematic indicators—tension gashes, cleavage, and Reidel shears associated with slickensides—are best developed on subvertical surfaces that show strike-slip displacement (fig. 3*F*). Strike-slip displacement is dextral. Moderately north- and south-dipping high-angle faults within the fault zone show normal displacement (fig. 3*F*).

Kahiltna Assemblage

The Kahiltna assemblage in the Pass Creek area of the Clearwater Mountains (fig. 1) is exposed in the footwall of the Talkeetna thrust fault. In the Pass Creek area, the Kahiltna assemblage is similar to that described in the Butte Creek area and consists of the same three dominant lithofacies—pebble to boulder conglomerate, horizontally stratified sandstone, and laminated siltstone. The main difference between the two areas is the greater abundance of the pebble to boulder conglomerate lithofacies in the Pass Creek area (fig. 8). Conglomerate beds in the Pass Creek area do not exhibit the upsection clast-compositional trend characteristic of the Butte Creek area (fig. 7); instead, the conglomerate beds throughout the studied section are dominated by greenstone clasts. As at Butte Creek, the Pass Creek section is interpreted as proximal submarine-fan deposits that were derived from the Wrangellia terrane exposed in the hanging wall of the Talkeetna thrust fault.

Discussion and Conclusion

First, structural and stratigraphic relations at Butte Creek and Pass Creek lead us to conclude that major contractional displacements have not occurred along the Talkeetna thrust fault. The absence of major penetrative deformation associated with the thrust fault in these two areas indicates that displacement along the fault is relatively minor and did not involve shortening measured in tens of kilometers, as suggested by previous workers. The overthrust Kahiltna assemblage represents proximal, synorogenic submarine-fan facies derived from the Wrangellia terrane that is exposed in the hanging wall of the Talkeetna thrust fault. The proximal, coarse conglomeratic Jurassic and Cretaceous Kahiltna assemblage was deposited directly adjacent to the Wrangellia terrane and is still adjacent to that source terrane, even though their present contact is a thrust fault. The composition of conglomerate clasts in the Kahiltna assemblage near Butte and Pass Creeks can be readily matched with lithologies of the Wrangellia terrane in the hanging wall of the Talkeetna thrust fault. In addition, excellent exposures of the Kahiltna assemblage in the footwall of the Talkeetna thrust fault in the Butte and Pass Creek areas show little deformation. We conclude that the Talkeetna thrust fault has undergone relatively minor displacement and does not represent a major tectonic terrane boundary.

Second, displacements on this relatively small thrust fault could not accommodate the tens of kilometers of tectonic transport required to emplace exotic miniterranes 40 to 80 km northwest of the fault trace. The actual join of the Wrangellia composite terrane with the North American craton must be zone located northwest of the Talkeetna thrust fault. Additional fieldwork in summer 2002 has shown that the exotic miniterranes in the northern Talkeetna Mountains south of Broad Pass (fig. 1) are, in fact, parautochthonous basement rocks of Wrangellia affinity that unconformably underlie the Kahiltna assemblage. On the basis of these more recent observations, the miniterranes exposed in the northern Talkeetna Mountains represent uplifted basement rocks of Wrangellia; the actual suture zone between Wrangellia and the North American craton is northwest of the Talkeetna Mountains and, we would suggest, likely underlies Broad Pass.

Third, the Broxson thrust fault of Nokleberg and others (1994) is a younger feature partly superimposed on the Talkeetna thrust fault. Tertiary and Quaternary dextral strike-slip displacements and southward-directed contractional movement along the Black Creek Fault/Broxson Gulch thrust fault suggest that the fault has a strong kinematic tie to the larger and longer right-lateral strike-slip Denali Fault, with which it merges. The Talkeetna thrust fault of Csejtey and others (1992) and the Broxson Gulch thrust fault of Nokleberg and others (1994) are collinear and superimposed on the east; the Black Creek Fault/Broxson Gulch thrust fault truncates the Talkeetna thrust fault at Pass Creek, where it diverges from the trace of the older feature. Thus, the two faults in the Pass Creek area are not kinematically related.

References Cited

Adams, D.D., Freeman, C.J., and Brown, D.R., 1991, Timberline Creek gold lode project, Valdez Creek mining district, Alaska: Anchorage, final report prepared for the Mineres Co., 59 p.

Bouma, A.H., 1962, Sedimentology of some flysch deposits—a graphic approach to facies interpretation: New York, Elsevier, 168 p.

Csejtey, Béla, Jr., Cox, D.P., Evarts, R.C., Stricker, G.D., and Foster, H.L., 1982, The Cenozoic Denali fault system and the Cretaceous accretionary development of southern Alaska: Journal of Geophysical Research, v. 87, no. B5, p. 3741–3754.

Csejtey, Béla, Jr., Mullen, M.W., Cox, D.P., and Stricker, G.D., 1992, Geology and geochronology of the Healy quadrangle, south-central Alaska: U.S. Geological Survey Miscellaneous Investigations Series Map I–1961, 63 p., 2 plates, scales 1: 250,000, 1:360,000.

Csejtey, Béla, Jr., Nelson, W.H., Jones, D.L., Silberling, N.J., Dean, R.M., Morris, M.S., Lanphere, M.A., Smith, J.G., and

Silberman, M.L., 1978, Reconnaissance geologic map and geochronology, Talkeetna Mountains Quadrangle, northern part of Anchorage Quadrangle, and southwestern corner of Healy Quadrangle, Alaska: U.S. Geological Survey Open-File Report 78–558–A, 62 p., scale 1:250,000.

Gardner, M.C., Bergman, S.C., Cushing, G.W., MacKevett, E.M., Plafker, G., Campbell, R.B., Dodds, C.J., McClelland, W.C., and Mueller, P.A., 1988, Pennsylvanian pluton stitching of Wrangellia and the Alexander terrane, Wrangell Mountains, Alaska: Geology, v. 16, no. 11, p. 967–971.

Hein, F.J., 1982, Depositional mechanisms of deep-sea coarse clastic sediments, Cap Enrage Formation, Quebec: Canadian Journal of Earth Sciences, v. 19, no. 2, p. 267–287.

Jones, D.L., Silberling, N.J., and Hillhouse, J.W., 1977, Wrangellia—a displaced terrane in northwestern North America: Canadian Journal of Earth Science, v. 14, no. 11, p. 2565–2577.

Lowe, D.R., 1982, Sediment gravity flows; depositional models with special reference to the deposits of high-density turbidity currents: Journal of Sedimentary Petrology, v. 52, no. 1, p. 279–297.

Nokleberg, W.J., Plafker, George, and Wilson, F.H., 1994, Geology of south-central Alaska, *in* Plafker, George, and Berg, H.C., eds., The geology of Alaska, v. G–1 *of* The geology of North America: Boulder, Colo., Geological Society of America, p. 311–366.

Packer, D.R., and Stone, D.B., 1974, Paleomagnetism of Jurassic rocks from southwestern Alaska and their tectonic implication: Canadian Journal of Earth Science, v. 11, no. 7, p. 976–997.

Plafker, George, and Berg, H.C., 1994, Overview of the geology and tectonic evolution of Alaska, *in* Plafker, George, and Berg, H.C., eds., The geology of Alaska, v. G–1 *of* The geology of North America: Boulder, Colo., Geological Society of America, p. 989–1021.

Silberling, N.J., Richter, D.H., Jones, D.L., and Coney, P.J., 1981, Geologic map of the bedrock part of the Healy A–1 quadrangle south of the Talkeetna-Broxson Gulch fault system, Clearwater Mountains, Alaska: U.S. Geological Survey Open-File Report 81–1288, scale 1:63,360.

Smith, T.E., 1981, Geology of the Clearwater Mountains, south-central Alaska: Alaska Division of Geological and Geophysical Surveys Geologic Report 60, 69 p., scale 1: 36,360.

Smith, T.E., Albanese, M.D., and Kline, G.L., 1988, Geologic map of the Healy A–2 quadrangle, Alaska: Alaska Division of Geological and Geophysical Surveys Professional Report 95, scale 1:63,360.

Stow, D.A., Reading, H.G., and Collinson, J.D., 1996, Deep seas, *in* Reading, H.G., ed., Sedimentary environments; processes, facies and stratigraphy: Oxford, U.K., Blackwell Science, p. 395–453.

Studies by the U.S. Geological Survey in Alaska, 2001
U.S. Geological Survey Professional Paper 1678

The Clark Bar Prospect: Granite-Hosted Sn-Mo-Ag Mineralization in the Northern Talkeetna Mountains, Southern Alaska

By Jeanine M. Schmidt and Bruce M. Gamble

Abstract

Clark Bar is a strongly altered and oxidized zone of Paleocene granitic rocks intruded by aplitic to aphanitic felsic dikes along Clark Creek in the northern Talkeetna Mountains, southern Alaska. Major-, minor-, and trace-element geochemistry of fresh plutonic host rocks, altered rocks, and stream sediment suggest that the prospect has a potential to host granitoid Sn-Mo-Ag mineralization. Regional mapping and lithogeochemistry suggest that many of the Tertiary plutonic rocks exposed in the northern Talkeetna Mountains belong to the "specialized" granite or granophile suite. Much of the area of the northern Talkeetna Mountains where these granites are exposed is prospective for various Sn-, Mo-, and Ag-enriched granophile deposits.

Location

The Clark Bar prospect is located in the northern Talkeetna Mountains (D–4 quadrangle), 15 km north of a conspicuous bend in the westward-flowing Susitna River (fig. 1).

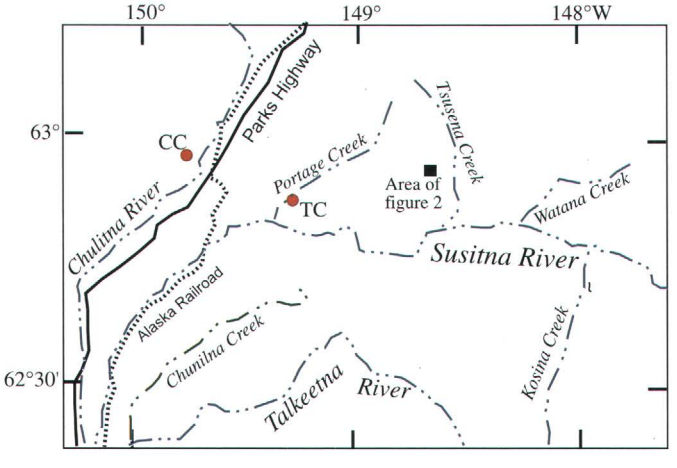

Figure 1. Northern Talkeetna Mountains, southern Alaska, showing locations of Clark Bar prospect (fig. 2) and other prospects mentioned in text. CC, Coal Creek; TC, Treasure Creek.

Topography in the area is steep and glaciated, with elevations ranging from 1,500 ft along the Susitna River to 5,700 ft in the mountains. Bare rock ridges at high elevations give way to discontinuous tundra and shrub vegetation on the side slopes; trees are limited to creek and valley bottoms.

Clark Bar is a conspicuous orange-weathering grus zone, several hundred square meters in area, along a ridge in sec. 14, T. 33 N., R. 3 E., immediately east of Clark Creek, a southeastward-flowing tributary of Tsusena Creek (figs. 1, 2). Access to the prospect is by helicopter only. Tsusena Butte, which has float- and fixed-wing plane access on private lands, is 5 km to the southeast.

Work Done

The Clark Bar prospect was examined briefly and sampled in July 1999 and again in June 2000, when extensive snow cover severely limited the exposures. In July 2001, stream-sediment and panned-concentrate samples were collected from a small tributary draining the prospect for comparison with regional sediment data collected in 1977 (Miller and others, 1978) under the auspices of the Alaska Mineral Resource Appraisal Program (AMRAP).

Two samples of unaltered plutonic rocks from the ridgeline and north-facing slope at Clark Bar were analyzed for major, minor, and trace elements (table 1; see Jackson and others, 1987, for description of methods). Five samples of typical unaltered granite and granodiorite in the nearby area (max 25 km away) were collected for comparison and analyzed by the same methods (fig. 2; table 1).

Seven mineralized and altered rock samples and one sample of poorly developed soil were collected at the Clark Bar prospect and analyzed for various metallic and trace elements (table 2). Stream-sediment and panned-concentrate samples were taken from the stream draining Clark Bar and analyzed for minor and trace elements (table 3). Remainders from the stream-sediment and panned-concentrate samples collected from the same site during a 1977 regional drainage survey (Miller and others, 1978) were reanalyzed by

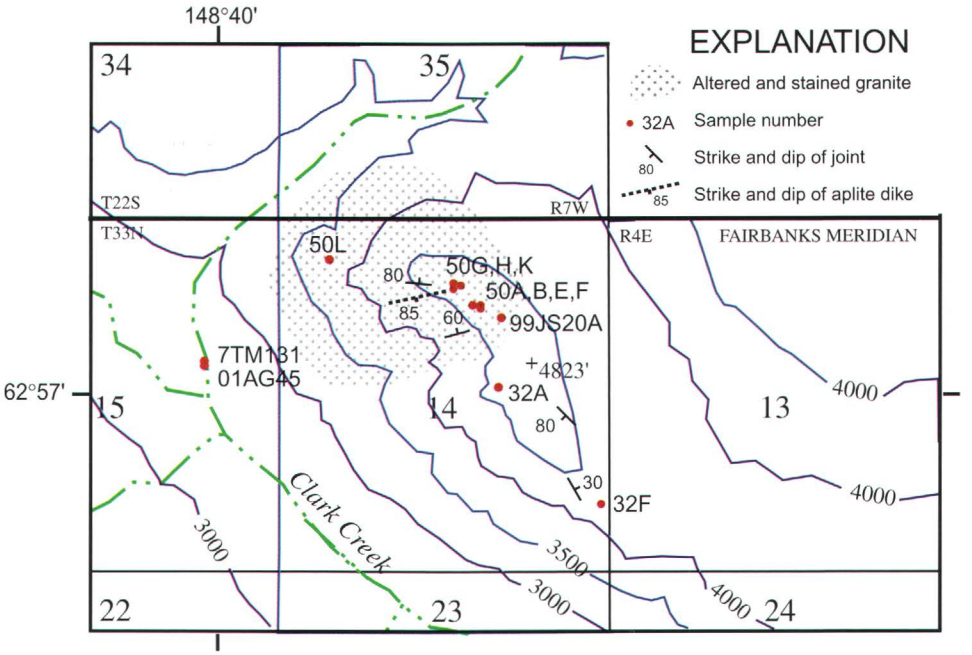

Figure 2. Clark Bar prospect area, northern Talkeetna Mountains, southern Alaska (fig. 1), showing locations of fresh granite (table 1), altered rock and soil (table 2), and stream-sediment and panned-concentrate samples. Field numbers "32" or "50" are preceded by "00JS". Elevations are feet above sea level; section lines are 1 mi apart.

the same methods (see Grimes and Marranzino, 1968, for description) for comparison with the original semiquantitative analytical results (table 3).

Regional Geology

The Clark Bar prospect lies within an overlap assemblage composed of Jurassic and Early Cretaceous flysch, between the Wrangellia and North American tectonostratigraphic terranes (Csejtey and others, 1978; Nokleberg and others, 1994). The flysch is a marine turbidite sequence, dominated by shale, that was previously assigned to the Kahiltna assemblage (Nokleberg and others, 1994). New stratigraphic and provenance data (Eastham and others, 2000; Eastham and Ridgway, 2001), however, suggest that the source of the flysch of the northern Talkeetna Mountains was the Wrangellia terrane to the southeast, with transport directions to the west and northwest. This flysch contrasts with flysch of the type section of the Kahiltna assemblage in the western Alaska Range, which was derived from sources to the northwest and transported eastward and southeastward. These two flysch sequences were deposited in separate basins and may have significantly different overall chemical compositions, a difference that would affect the composition of granitic melts derived from them.

Flysch of the northern Talkeetna Mountains is intruded by abundant granitic stocks of Tertiary age (Csejtey and others, 1978; J.M. Schmidt and others, unpub. data, 2000–2), producing contact aureoles of biotite-, andalusite-, or sillimanite-bearing hornfels. Uncommon mafic to felsic dikes that cut both flysch and plutons in the vicinity of Clark Bar are subvolcanic feeders to Eocene volcanic rocks that once overlay much of the northern Talkeetna Mountains (Csejtey and others, 1978; J.M. Schmidt and others, unpub. data, 2000–2).

Granitic Plutons

Granitic plutons exposed in the northern Talkeetna Mountains are subalkaline, quartz-normative peraluminous to metaluminous, biotite-bearing granite and granodiorite, with varying amounts of hornblende or white mica. The dominant lithology regionally is a fine-grained equigranular, salt-and-pepper granite to granodiorite containing 15 to 30 volume percent quartz, plagioclase greater than K-feldspar, a color index of 4 to 10, and biotite greater than hornblende. Foliated, biotite-rich (color index, ≤35) granodiorite occurs as inclusions in the equigranular rock and is compositionally similar to biotite-quartz-plagioclase gneissic wallrocks derived from the flysch. Granites near the Clark Bar prospect are multiphase, contain both biotite and hornblende, and vary in texture and mineralogy within a few tens of meters.

We sampled fresh intrusive rocks from the Clark Bar prospect and from several nearby plutons (fig. 2; table 1) to determine unmineralized background values and the variation within granites of the northern Talkeetna Mountains. A relatively fresh hornblende-biotite granite (field No. 00JS50G, table 1) and a crosscutting aplite dike (field No. 00JS50E)

Table 1. Major-element-oxide and minor- and selected trace-element analyses of fresh granitic rocks near Clark Creek, Talkeetna Mountains D–4 quadrangle, southern Alaska.

[Major-element-oxide analyses by wavelength-dispersive X-ray fluorescence in weight percent; data for average granite from Carmichael (1982). Minor- and selected trace-element analyses by cold-vapor atomic absorption spectroscopy (Hg), energy-dispersive X-ray fluorescence (Cr, Cs, Rb, Sn, Th, U, Y), fire assay (Au), instrumental neutron-activation analysis (W), or inductively coupled plasma atomic-absorption spectroscopy (all other elements) in parts per million; data for average granite from Krauskopf (1967). Lower limits of detection (in parts per million) of selected trace elements: cold-vapor atomic absorption, Hg (0.02); energy-dispersive X-ray fluorescence, Cr (3), Mo (1), Rb (2), Th (2), U (2), Y (2), and Zr (5); fire assay, Au (0.005); 10-element inductively coupled plasma atomic-emission spectroscopy, Ag (0.08), As (1), Bi (1), Cd (0,05), Cu (0.05), Mo (0.2), Pb (1), and Sb (1); 40-element inductively coupled plasma atomic-emission spectroscopy, Ce (5), La (2), Li (2), Mn (4), Nd (9), Sn (50), Th (6), Y (2) and Zn (2); neutron activation, W (0.5). Do., ditto]

Field No.	Location	Latitude N.	Longitude W.	Description	Low values consistent with granophile suite	High values consistent with granophile suite	Al_2O_3	CaO	Total Fe_2O_3	K_2O	MgO	MnO
00JS50G	Clark Bar---------	62° 57′ 19″	148° 38′ 34″	Hornblende-biotite granite.	MgO, TiO_2, Sr, V	Cs, Zn	13.5	1.05	2.15	4.21	0.11	0.06
00JS50E	Do----------	62° 57′ 19″	148° 38′ 34″	Aplite----------	CaO, Ce, FeO, MgO, TiO_2, Ba, Cr, La, Sr, V	SiO_2, Nb, Rb, Th, U, Zn	12.8	.14	.44	4.02	.06	<.01
00JS32A	Ridgeline 0.2 km S.of Clark Bar.	62° 56′ 56″	148° 38′ 11″	Biotite granite; fine-grained, light-colored, most common.	MgO, Ce, Cu, La, V	Cs	14.9	2.23	1.22	3.31	.44	.02
00JS32F	Do----------	62° 56′ 43″	148° 37′ 39″	Foliated biotite granodiorite.	Cu	Cs, Zn	16.1	4.08	3.46	2.32	1.24	.05
00JS48A	2.5 km SW. of Clark Bar; W. of Clark Creek.	62° 56′ 45″	148° 41′ 55″	Leucocratic granite----------	CaO, FeO, MgO, TiO_2, Cu, Sr, V		13.6	.72	1.96	4.17	.10	.06
00JS39A	3 mi WSW. of Clark Bar	62° 56′ 13″	148° 43′ 36″	Fine-grained biotite granite.	Cu	Cs, Li, Zn	17.1	3.76	2.95	2.68	.97	.03
00JS08W	Devil Creek, 23 km W. of Clark Bar.	62° 54′ 31″	149° 02′ 18″	Equigranular, garnet-bearing muscovite-biotite granite.	CaO, FeO, MgO, TiO_2, Ba, Ce, Cr, Cu, La, Sr, V	SiO_2, Be, Li, Sn, U	14.6	.53	.66	3.42	.04	.10
				Average granite----------			13.9	1.33		5.46	.52	.06
				Specialized granite suites----------			--	Depleted	--	>4.0	Depleted	--

Na_2O	P_2O_5	SiO_2	TiO_2	LOI	Total	Ba	Be	Ce	Cr	Cs	Cu	Ga	La	Li	Mn	Mo	Nb	Pb	Rb	Sn	Sr	Th	U	V	Y	Zn	Zr
4.22	<0.01	73.3	0.160	0.3	98.76	1,610	3	84	8	23	12	22	43	21	428	2	14	26	138	5	122	9	5	4	42	145	245
3.25	<.01	78.3	.063	1.0	99.07	225	4	11	3	4	11	26	22	10	<4	2	32	12	251	4	13	41	11	<2	41	105	203
3.94	.13	72.0	.215	1.1	98.41	2,170	<1	21	9	24	<2	22	14	17	121	1	<4	16	69	4	576	2	2	6	10	66	144
3.30	.18	68.8	.586	.5	100.12	2,390	2	53	25	15	4	25	25	41	347	2	14	12	60	3	568	4	3	42	8	140	182
4.24	<.01	73.7	.165	.4	98.72	1,680	2	67	9	8	3	21	33	16	351	1	10	14	119	4	123	8	4	3	43	87	251
4.31	. 13	65.3	.551	.7	97.78	3,130	2	109	12	22	2	16	53	61	153	2	22	10	51	3	1,150	2	3	16	3	120	280
4.54	.09	74.0	.031	1.1	98.01	42	8	7	<3	8	<2	25	3	43	646	<1	5	16	193	12	13	<2	7	<2	11	44	35
3.08	.18	72.1	.370	--	--	600	5	87	4	5	10	18	40	30	400	2	20	20	150	3	285	17	4.8	20	40	40	180
--	--	>73.0	Depleted	--	--	Low	High	--	Low	High	Low	--	Low	High	--	High	High	High	High	High	Low	High	High	Low	High	--	Low

Table 2. Selected trace- and metallic-element analyses of altered rock and soil from the Clark Bar prospect, Talkeetna Mountains D–4 quadrangle, southern Alaska.

[All analyses in parts per million except for Fe (in weight percent); crustal abundances and data for average granite from Krauskopf (1967). Columns for elements anomalous at the 90th- and 98th-percentile levels are in comparison with all altered rocks collected in the northern Talkeetna Mountains (J.M. Schmidt and others, unpub. data, 1999–2001)]

Field No.	Sample description	Elements anomalous at 90th percentile	Elements anomalous at 98th percentile	Ag	As	Au		Ba
						FA	ICP	
99JS20A	Quartz-pyrite cobble from top of orange-stained area.	Au, Be, Pb, W	---	0.2	2	0.020	0.2	1,430
00JS50A	Chalky altered leucogranodiorite----------	Bi	---	.3	18	<.005	<.1	1,120
00JS50B	Fracture-controlled iron oxides in biotite granite.	Be,Yb, Zn	Ce, La, Nd, Y	<.08	21	<.005	<.1	1,600
00JS50F	Minor silicified aplite----------	---	---	<.08	7	<.005	<.1	853
00JS50H	Pyritic fractures In aplite----------	Bi, La, Nd, Th	Ag, Cd, Li, Mn, Pb, Zn	4.9	4	<.005	.2	1,180
00JS50K	Pyrite-quartz veinlet in aplite----------	As, Be, Hg	Ag, Bi, Cd, Li, Pb, Sb, Sn, Zn	25.1	47	<.005	.2	396
00JS50L	Dark brown to black Fe oxide-stained aplite---------	Ba, Ga, Mo, Nd	Ag, Bi, Cd, Ce, Cu, La, Mn, Pb, Sn, Th, Zn	26.6	11	<.005	.1	2,220
00JS50C	Orange soil ----------	Ce, Ho, La, Nd, Th, Yb	Y	<.08	19	<.005	.1	1,440
	~90th percentile for Talkeetna Mountains samples ----------			≥1.0	≥30	≥.012	≥.3	≥2,000
	~98th percentile for Talkeetna Mountains samples ----------			≥10.0	≥70	≥.050	≥1.0	≥5,000
	Crustal abundance ----------			.07	1.8	<.050	<.05	425
	Average granite ----------			.04	1.5	--	--	600

Be	Bi	Cd	Ce	Cu	Eu	Fe	Ga	Hg	Ho	La	Li	Mn	Mo	Nd	Pb	Sb	Sn	Th	W	Y	Yb	Zn
3	<1	0.35	43	3.2	<2	1.06	19	<0.02	<4	34	17	73	3.9	26	8	<1	<50	9	4.1	24	2	88
2	2	<.05	45	1.0	<2	.25	25	<.02	<4	26	27	<4	6.5	28	9	<1	<50	10	.6	29	3	12
3	<1	.39	132	4.6	3	1.21	23	<.02	<4	150	9	96	5.9	140	13	<1	<50	9	1.3	70	5	184
2	<1	<.05	23	1.3	<2	.3	16	<.02	<4	21	40	7	1.8	26	8	<1	<50	6	.5	21	2	13
2	2	3.03	74	35.6	<2	2.17	32	<.02	<4	41	186	4,380	1.4	43	367	<1	<50	13	1.3	26	2	597
3	6	8.85	42	91.5	<2	3.67	19	.18	<4	27	180	385	8.8	26	1,120	10	76	<6	1.5	25	2	2,130
2	15	126	108	1,480	<2	8.61	38	.02	<4	58	23	4,150	16.4	56	1,660	<1	81	16	.7	24	2	18,900
2	1	.33	75	3.2	<2	1.8	28	.02	5	42	18	255	5.4	49	13	<1	<50	14	1.3	46	5	112
≥3	≥2	≥1	≥75	≥160	≥3	≥9.0	≥36	≥.1	≥5	≥35	≥50	≥1,400	≥9	≥39	≥14	≥3		≥12	≥3	≥30	≥4	≥140
>4	≥5	≥2	≥100	≥500	--	≥14.0	≥45	≥.4	≥6	≥50	≥100	≥2,000	>22	≥70	≥100	≥10	≥50	≥14	≥5	≥40	≥5	≥500
2.8	.17	.2	67	55	1.2	5.6	15	.08	1.5	25	20	950	1.5	28	12.5	.2	2	9.6	1.5	33	3	70
5	.18	.2	87	10	1.5	2.7	18	.08	1.9	40	30	400	2	35	20	.2	3	17	2	40	3.8	40

Table 3. Selected trace- and metallic element analyses of stream-sediment and panned-concentrate samples from streams draining the Clark Bar prospect, Talkeetna Mountains D–4 quadrangle, southern Alaska.

[All values in parts per million except for Fe (in weight percent). Analytical methods: cold-vapor atomic-absorption spectroscopy (Hg), instrumental neutron-activation analysis (W), 10-element inductively coupled plasma atomic-emission spectroscopy (Ag, As, Au, Bi, Cd, Cu, Mo, Pb, Y, Zn), 40-element inductively coupled plasma atomic-emission spectroscopy (Ba, Ce, Co, Cr, Fe, Ga, La, Li, Mn, Nb, Nd, Ni, Sc, Sn, Th, V, Y). Original analyses of samples with field Nos. 7TM131C and 7TM131S were by semiquantitative emission spectroscopy. N, not detected at parts-per-million level indicated]

Field No.	Sample type	Type of analysis and year	Ag	As	Au	Ba	Bi	Cd	Ce	Co	Cr	Cu
7TM131S	Stream sediment----	Emission spectroscopy, 1977	N0.5	N200	N10	1,500	N10	N20	--	10	20	20
7TM131S	do----------	ICP–AES, INAA, CV–AAS, 2001	.1	6	.1	1,230	<1	.47	251	4	8	11
01AG45DS	do----------	ICP–AES, INAA, CV–AAS, 2001	.1	7	.3	1,110	1	.7	170	8	10	13.1
7TM131C3	Panned concentrate--	Emission spectroscopy, 1977	N1	N500	N20	300	N20	N50	--	<10	20	50
01AG45C	do----------	ICP–AES, INAA, CV–AAS, 2001	<.08	4	<.1	1,200	<1	.3	218	6	7	12.2
	Crustal abundance----------		.07	1.8	<.05	425	.17	.2	67	25	100	55
	Average granite----------		.04	1.5	------	600	.18	.2	87	1	4	10

Fe	Ga	Hg	La	Li	Mn	Mo	Nb	Nd	Ni	Pb	Sc	Sn	Th	V	W	Y	Zn
7	--	--	300	--	1,000	N5	<20	--	10	70	30	N10	--	50	N10	100	N200
2.86	4	.04	130	37	658	.8	16	100	4	19	14	<50	18	43	.7	31	131
2.91	20	<.02	89	35	689	.9	17	76	5	19	13	<50	11	62	<.5	38	125
3	--	--	200	--	700	N10	200	--	<10	50	70	1,000	N200	100	N100	200	N500
3.15	<4	<.02	117	32	709	.7	15	86	4	13	13	<50	15	67	.7	29	113
5.6	15	.08	25	20	950	1.5	20	28	75	12.5	22	2	9.6	135	1.5	33	70
2.7	18	.08	40	30	400	2	20	35	.5	20	5	3	17	20	2	40	40

were sampled from the immediate prospect area (fig. 2). Along the unaltered ridgeline to the south (fig. 2), the predominant biotite granite (field No. 00JS32A) and a common, though less abundant, foliated biotite granodiorite (field No. 00JS32F) were sampled. The samples with field Nos. 00JS48A and 00JS39A, collected 3 and 5 km, respectively, west of Clark Bar, represent the main phases of leucogranite and biotite granodiorite plutons in the Clark-Tsusena River area.

About 23 km west of Clark Bar, a muscovite-biotite-garnet-bearing granite at Devil Creek has been dated at 59±0.2 Ma ($^{40}Ar/^{39}Ar$ age on muscovite; L.W. Snee, written commun., 2001). It is similar in mineralogy and age to the McKinley sequence granites of the Alaska Range (West, 1994), which are peraluminous S-type plutons (Lanphere and Reed, 1985) derived by assimilation of the Jurassic and Cretaceous flysch (Lanphere and Reed, 1985, 1990). Table 1 includes one analysis (field No. 00JS08W) from the Devil Creek stock for comparison with the common biotite-only or biotite-hornblende granites and granodiorites.

Hornblende-biotite granite from the Clark Bar prospect (field No. 00JS50G, table 1) has yielded a preliminary $^{40}Ar/^{39}Ar$ age of 58.5 Ma on biotite (L.W. Snee, written commun., 2001). The similarity of chemistry and tentative age correlation between the Devil Creek stock and the regionally extensive hornblende-biotite granite to granodiorite suggest that they are part of a single intrusive suite emplaced during the late Paleocene. This late Paleocene magmatic suite in the northern Talkeetna Mountains is similar in age and chemistry to the McKinley sequence in the Alaska Range (Lanphere and Reed, 1985, 1990). Any paleogeographic or genetic connection, however, remains to be determined by additional mapping and petrologic and tectonic studies.

"Specialized" Granite Chemistry

Reed (1986b, c), in discussing the origin of Sn deposits, invoked a "specialized" granite, with high SiO_2 content (>73 weight percent), enriched in K, Sn, F, Rb, Li, Be, Nb, Cs, U, Th, B, Mo, and rare-earth elements (REEs) relative to typical calc-alkaline, arc-related granites. Strong (1988), in categorizing granitic-rock-hosted mineral deposits, identified a group of quartz-rich, leucocratic granites enriched in what he termed "granophile" elements. The granophile elements include three subgroups—(1) large, highly charged cations: Sn^{4+}, W^{6+}, U^{6+}, Mo^{6+}; (2) small, varyingly charged cations: Be^{2+}, B^{2+}, Li^{+}, and P and anions; and (3) CO_3^{2-}, Cl^{-}, F^{-}; Strong, 1988)—each associated with distinctive mineral deposits. Both subgroups 2 and 3 of granophile elements help control magma-solidification processes (Strong, 1988), which, in turn, control the contents of subgroup 1. Strong interpreted these granophile plutons to be anatectic or partial melts, containing abundant magmatic water, formed at 15- to 25-km depth and intruded to 8- to 15-km depth.

McKinley-sequence granites from the Alaska Range show a twofold enrichment in B, Cs, U, Pb, and Li (Lanphere and Reed, 1985) relative to average granites, suggesting that they have some characteristics of the "specialized" or granophile type. They are corundum normative, contain accessory tourmaline, and have compositions similar to "minimum melts" crystallized at shallow (1.5–3 km) depth (West, 1994).

The granitic plutons of the northern Talkeetna Mountains as a group (table 1) are depleted in Ce, Cu, FeO, La, MgO, TiO_2, and V and enriched in Cs and Sn, consistent with the "specialized" or granophile suite. In particular, the aplite sample from Clark Bar (field No. 00JS50E, table 1) and the two-mica Devil Creek stock sample (field No. 00JS08W) have major- and trace-element compositions characteristic of the granophile suite.

Alteration and Mineralization

At the Clark Bar prospect, biotite granite and granodiorite along the southern ridgeline are in sharp contact to the north with a bright-orange-weathering grus zone (figs. 2, 3*A*, 3*B*) derived from a medium-grained granitoid.

The predominant rock type at the prospect is a biotite-bearing, equigranular, medium-grained (2–4 mm) granite with a low color index (5–12), containing approximately 30 volume percent quartz and traces of weathered sulfide. The granite is crosscut by numerous steep joints and iron-stained fractures that weather to form resistant (quartz rich?) 2- to 10-cm-wide veins forming a boxwork texture surrounding meter-wide patches of grus (fig. 3*C*). Fracture surfaces locally have slickensides along them but show no significant or consistent offset. Some chalky clay-altered light-colored granite is cut by crackle veinlets, a few centimeters long, with associated iron oxides, which form a type of granitic "breccia" texture.

Thin (8–10 cm wide), but uncommon, steeply dipping aplite dikes crosscut the main biotite granite. The aplites have a fine-grained (≤0.5 mm) micrographic texture, contain less than 2 volume percent biotite, are locally altered to chlorite, and contain minor pyrite along fractures and in dark-gray quartz veinlets. No other sulfide minerals were identified at the surface at Clark Bar, owing to the extreme weathering of the rocks.

Geochemistry of Altered Rock Samples and Soil

Seven samples of fractured and veined aplite and granite and of altered, stained, and pyrite-bearing rocks at the Clark Bar prospect were analyzed for metallic and trace elements (figs. 2, 3*D*; table 2). One sample of orange soil derived from barely decomposed granitic material was also analyzed. Results of these analyses were compared with the set of 155 altered and mineralized samples collected in the northern Talkeetna Mountains during 1999–2001 (U.S. Geological Survey, unpub. Data, 2000–2) and with worldwide averages for granites (Krauskopf, 1967). Elemental concentrations anomalous at the 90th- and 98th-percentile levels for the Talkeetna Mountains sample population are identified in table 2.

Figure 3. Clark Bar prospect, northern Talkeetna Mountains, southern Alaska (fig. 1). *A*, View southward from approximate location of sample with field No. 00JS50A (fig. 2) toward contact of orange-weathering altered grus zone and fresh granodiorite (dark cliffs in shadows at midground). *B*, View northeastward from approximate location of sample with field No. 99JS20A (fig. 2) toward altered and fractured granite near locations of samples with field Nos. 00JS50G through 00JS50K. *C*, Resistant-weathering quartz-rich joint surfaces and veins in granite, with patches of low-relief grus between. Quartz veins contain disseminated Fe oxides and rare pyrite. *D*, Fe oxide-stained, veined and fractured granite with field No. 00JS50A. Pyrite is only sulfide identified to date at Clark Bar.

Altered rock samples from Clark Bar contain as much as 26.6 ppm Ag, 47 ppm As, 20 ppb Au, 15 ppm Bi, 1,480 ppm Cu, 180 ppb Hg, 16.4 ppm Mo, 1,660 ppm Pb, 10 ppm Sb, 81 ppm Sn, 4.1 ppm W, and 1.89 weight percent Zn.

Ag, As, Bi, Cd, Cu, Li, Mn, Mo, Pb, Sb, Sn, and Zn contents are anomalous at the 90th-percentile level or higher, with values 4.5 to 740 times those of average granites (Krauskopf, 1967) in one to four samples each. One to four samples at Clark Bar are anomalous in each of the elements Ba, Be, Ce, Eu, Ga, Hg, Ho, La, Nd, Th, W, Y, and Yb at the 90th-percentile level for the Talkeetna Mountains, but fall nearer (≤4×) the values for worldwide granitic rocks (Krauskopf, 1967). Only one sample, a silicified aplite (field No. 00JS50F, table 2), has no elements anomalous at the 90th-percentile level or above, or significantly above average granite values, probably because the addition of SiO_2 reduced the relative contents of all other elements.

Ag, As, Ba, Bi, Cd, Cu, Ga, and Zn contents at Clark Bar are consistently higher than worldwide averages for granite (Krauskopf, 1967), although they are not necessarily anomalous relative to the northern Talkeetna Mountains data set (table 2; J.M. Schmidt, unpub. data, 2002). Conversely, Be, Ce La, Hg, Mn, Pb, Th, W, Y, and Yb contents at Clark Bar are low relative to average granites, although they are higher than in many areas of the Talkeetna Mountains (J.M. Schmidt, unpub. data, 2002). All the altered rock and soil samples from Clark Bar contain relatively low Cr (≤4 ppm), Nb (≤19 ppm), Sc (≤9 ppm), Sr(≤100 ppm), and V (≤6 ppm), and no detectable Co (at 2-ppm lower detection limit) or Ni (<3 ppm) (J.M. Schmidt, unpub. data, 2002).

Enrichment in lithophile or granophile elements is characteristic of mineralized systems developed from late magmatic fluids associated with S-type or "specialized" granites discussed above. Of the indicator elements for granophile or "specialized" granite suites (Reed, 1986b, c; Strong, 1988), we have analyses at Clark Bar for Be, Li, Mo, Nb, Pb, Sn, Th, W, and Y, which should be enriched, and Ba, Cr, Cu, La, Sr, and V, which should be depleted. The Clark Bar data are similar to the overall granophile signature but have higher Ba and Cu contents than expected and relatively low Be, Pb, Th, and W contents. This pattern and the occurrence of a few high Au, Bi, and Sb values suggest that the Clark Bar area and similar Paleocene plutons of the northern Talkeetna Mountains could host mineralized systems with Sn-Mo-Ag potential and possible Au or base-metal enrichment.

Stream-Sediment and Panned-Concentrate Data

The elemental concentrations in stream-sediment and panned-concentrate samples collected from a small tributary that drains the northern Clark Bar prospect and flows westward into Clark Creek (fig. 2) are listed in table 3. Two of the samples (field Nos. 7TM131S, 7TM131C) were collected in 1977 as part of the U.S. Geological Survey AMRAP regional drainage-sampling program (Miller and others, 1978). This method reported data in steps (in the series 1, 1.5, 2, 3, 5, 7, 10, 15, and so on), and had high lower detection limits for many elements (Grimes and Marranzino, 1968). During July 2001, we collected new stream-sediment and panned-concentrate samples from the same stream at approximately the same location. The two new samples and the rest of the 1977 stream-sediment sample were analyzed in 2001 by XRAL Laboratories under contract to the USGS; not enough of the 1977 panned-concentrate sample remained to allow its reanalysis.

The stream-sediment and panned-concentrate samples from Clark Bar contain as much as 0.1 ppm Ag, 7 ppm As, 1 ppm Bi, 251 ppm Ce, 8 ppm Co, 20 ppm Ga, 40 ppb Hg, 130 ppm La, 37 ppm Li, 0.9 ppm Mo, 100 ppm Nd, 5 ppm Ni, 14 ppm Sc, and 67 ppm V (table 3). Both the stream-sediment and panned-concentrate samples contain relatively low Cu (≤13.1 ppm), Mn (≤709 ppm) Pb (≤19 ppm) and Zn (≤131 ppm) contents. An analysis of 1,000 ppm Sn in the 1977 panned-concentrate sample was not duplicated in the 2001 sample, possibly owing to a nugget effect from individual grains of cassiterite in the 1977 sample, but no petrographic examination of the sample was completed before its analysis. The stream-sediment samples contain significantly more Ce and V than any of the altered or fresh rocks from the prospect but have Ba, Cr, Ga, Li, Nb, Th and Y contents nearly identical to those of fresh granitic rocks from the area (table 1).

Most metallic and trace elements are not significantly enriched in the panned-concentrate relative to the stream-sediment samples (table 3). Because this heavily glaciated area is dominated by mechanical rather than chemical weathering, the stream sediment itself is a fine-sand-size accumulation of broken rock containing few fines or silt- or clay-size material. Panning to a concentrate, therefore, removes the smaller rock fragments rather than a material of significantly different mineralogy or composition.

Applicable Deposit Models

Alteration minerals and high metallic-element contents at Clark Bar are confined to felsic intrusive rocks, are mainly fracture controlled, and are spatially associated with aplite dikes that crosscut the biotite granite. Mineral-deposit models that are consistent with the geologic setting and lithogeochemistry of the Clark Bar prospect include late-stage magmatic, pneumatolytic, pegmatitic, and early-stage hydrothermal deposit types related to granitic intrusion (table 4). These models include large-tonnage disseminated and high-grade vein deposits related to the latest or most fractionated stages of felsic magmatic intrusion and cooling, as well as the formation of vapor- and water-rich phases.

Strong (1988) developed a classification scheme for granite-related mineral deposits that differentiated porphyry-type hydrothermal systems from granophile late-stage magmatic deposits, which include Sn, W, U, and Mo deposits associated

Table 4. Granophile and granite-related mineral-deposit models applicable to the Clark Bar prospect, Talkeetna Mountains D–4 quadrangle, southern Alaska, and nearby late Paleocene plutons.

[REEs, rare-earth elements. Do., ditto]

Mineral-deposit model	Type of mineralization	Ore characteristics	Igneous rock	Comments	References
Climax Mo (granite molybdenite).	Stockwork veins and veinlets-----	50th-percentile tonnage and grade: 200 million t containing 0.19 weight percent Sn.	High-silica (>75 weight percent SiO_2); granite-rhyolite stocks and radial dikes.	Host rocks at Clark Bar are dominantly intrusive; subvolcanic feeders to nearby Tertiary volcanic rocks may occur.	Ludington (1986), Singer and others (1986).
Granite-related Mo deposits.	Disseminated and stockwork veinlets in pluton and host rocks.	50th-percentile tonnage and grade: 81 million t containing 0.1 weight percent Mo.	Metaluminous to alkaline, high-silica granite and rhyolite.	Host rocks at Clark Bar are metaluminous to peraluminous.	Carten and others (1993), Kirkham and Sinclair (1995).
Granitic pegmatites: rare-element, Li-Cs-Ta family.	Pods of complex mineralogy in schist, gneiss, and felsic intrusions.	Contain Li, Rb, Cs, Be, Sn, Ga, Ta>Nb, B, P, and F.	Peraluminous, S-type granites----------	Similar host rocks occur at Clark Bar--	Černý (1993), Sinclair (1995a).
Granitic pegmatites: rare-element, Nb-Y-F family.	do----------	Contain Nb>Ta, Ti, Y, Sc, REEs, Zr, U, Th, and F.	Subaluminous to metaluminous granites.	Host rocks at Clark Bar are metaluminous to peraluminous.	Do.
Granophile deposits---------	Pegmatite, greisen, and veins at and near margins of intrusive bodies.	Zoned from Sn, W, As, and U outward to Ni-Co.	Quartz-rich leucocratic granitoids enriched in granophile elements.	Similar host rocks occur at Clark Bar--	Strong (1988).
Low-F porphyry Mo---------	Disseminated and stockwork veinlets in pluton and host rock.	50th-percentile tonnage and grade: 94 million t containing 0.085 weight percent Mo.	Calc-alkaline tonalite, granodiorite, and monzogranite.	Host rocks at Clark Bar are generally more siliceous.	Menzie and Theodore (1986), Theodore (1986), Kirkham and Sinclair (1995).
Polymetallic veins (felsic intrusion associated Ag-Pb-Zn).	Multiphase veins----------	50th-percentile tonnage and grade: 0.0076 million t containing 820 g Ag/t.	Calc-alkaline to alkaline small diorite to monzogranite intrusions and plugs.	do----------	Cox (1986a), Bliss and Cox (1986).
Polytype W deposits---------	Pegmatite, granite, greisen, replacement, and quartz vein types.	Sn-Mo-Bi; W-Sn; Mo-W; varying proportions.	Granite, commonly siliceous and muscovite bearing.	Similar host rocks occur at Clark Bar--	Sinclair (1995b); Deposit types 1, 2, 3, 5, and 6 of Yidou (1993).
Porphyry Cu-Mo----------	Disseminated and stockwork veinlets in pluton and host rock.	50th-percentile tonnage and grade: 500 million t containing 0.016 weight percent Mo, 1.2 g Ag/t.	Tonalite to monzogranite, commonly porphyritic.	Host rocks at Clark Bar are more siliceous.	Cox (1986b), Singer and others (1986), Kirkham and Sinclair (1995).
Porphyry Sn (subvolcanic Sn).	Disseminated, veinlet and breccia.	Zoned from Sn-B to Sn-Ag-As-Sb-base metals outward.	Intermediate to felsic quartz porphyry stocks and calc-alkaline lavas.	Host rocks at Clark Bar are dominantly intrusive; subvolcanic feeders to nearby Tertiary volcanic rocks may occur.	Reed (1986a), Kirkham and Sinclair (1995).
Sn greisens----------	Disseminated mineralization in greisen, and veinlets in host rocks.	50th-percentile tonnage and grade: 7.2 million t containing 0.28 weight percent Sn.	Specialized two-mica, S-type leucogranite.	Similar host rocks occur near Clark Bar.	Menzie and Reed (1986a), Reed (1986b).
Sn polymetallic veins, subvolcanic.	Multistage veins and breccia pipes.	Cu-Zn-Sn-Ag; zoned from Sn-W to Cu-Sn to Pb-Ag outward from center.	Felsic subvolcanic and ignimbritic rocks.	Host rocks at Clark Bar are dominantly intrusive; subvolcanic feeders to nearby Tertiary volcanic rocks may occur.	Togashi (1986).
Sn veins (Cornish lodes)----	Veins, brecciated and banded veins, and replacement lodes.	50th-percentile tonnage and grade: 0.24 million t containing 1.3 weight percent Sn.	Felsic plutonic rocks; specialized two-mica granite common.	Similar host rocks occur at Clark Bar--	Menzie and Reed (1986b), Reed (1986c), Sinclair (1995b).

with quartz-rich leucocratic granitoids. Granophile deposits, according to Strong (1988), form from magmatic water early in the crystallization history of the magmas at higher temperatures and deeper emplacement levels than do typical porphyry deposits, are dominated by oxide minerals rather than sulfides, and commonly contain pegmatitic or other late-stage magmatic textures. Greisenization (white mica, quartz, topaz, tourmaline, fluorite) and the addition of Li, Be, B, F, and Si to wallrocks are typical signs of alteration. In aluminosilicate host rocks, such as those in the vicinity of Clark Bar, Strong's (1988) granophile deposits can include topaz-quartz greisens within a pluton, tourmaline- and mica-rich pegmatites at the contact with wallrocks, and quartz-dominated vein systems in greisenized and hornfels wallrocks (Strong, 1988).

Sn-Ag±Mo-W porphyry, vein, and greisen deposits (Reed, 1986a–c; Yidou, 1993; Kirkham and Sinclair, 1995; Sinclair, 1995a, b) are most consistent with the geologic setting and lithogeochemistry of the Clark Bar area as currently understood. Greisen deposits would occur mainly within the felsic intrusions. Vein systems and related disseminated mineralization could be hosted either by the granites or by the hornfelsed Jurassic and Cretaceous flysch that the granites intruded. Evolved two-mica leucogranites are also associated with the occurrence of rare-element (Cs, Ga, Nb, Rb, REEs, Sc, Ta, Th, U, Y) and Li, U, or Sn pegmatite deposits (Černý, 1993; Sinclair, 1995a) of several types (table 4). The absence of any known calcareous wallrocks in the vicinity of Clark Bar suggests that the potential for related Sn-bearing skarn or replacement deposits (models 14b, 14c; Cox and Singer, 1986) is low. Placers concentrated from a lower-grade disseminated Sn-Mo-Ag lode source are unlikely because they would have had little time to form in this rugged, heavily glaciated area.

Analogs

The Clark Bar prospect is similar to other Sn-, Mo-, or W-mineralized areas of southern Alaska, some of which have been genetically linked to the McKinley sequence or other Paleocene granites (Nokleberg and others, 1987; Hudson and Reed, 1997). The Treasure Creek Mo prospect (Kurtak and others, 1992) lies approximately 40 km southwest of Clark Bar (fig. 1) and 15 km from the Devil Creek two-mica, garnet-bearing stock (table 1). Treasure Creek comprises disseminated sulfide mineralization containing as much as 1.0 weight percent Mo, 2.65 weight percent Zn, and 58 ppm Ag in a silicified and fluorite-altered stock of unknown, probable Tertiary age that crosscuts the Jurassic and Cretaceous flysch of the northern Talkeetna Mountains.

At Coal Creek (fig. 1), an estimated resource of 5 million t of rock containing 0.28 weight percent Sn and 0.5 weight percent Cu is present in sheeted and stockwork veins and disseminated mineralization (Nokleberg and others, 1987; Thurow and Warner, 1994). Grab samples of cassiterite and sulfide mineralization contain as much as 1.5 weight percent Sn, 148 g Ag/t, 0.5 ppm Au, and 720 ppm W (Balen, 1990). Greisenization (topaz, tourmaline, quartz, sericite fluorite) occurs in vein envelopes and as a pervasive alteration of the McKinley-sequence granite, which intrudes Paleozoic argillite and graywacke (Thurow and Warner, 1994).

Two granite-hosted prospects occur in the Alaska Range, where Paleocene McKinley sequence stocks intrude flysch of the Kahiltna assemblage. At Ohio Creek, Nb oxides and mineralized rocks containing as much as 1.25 weight percent W, 5,042 g Ag/t, and 0.1 weight percent Sn are hosted in muscovite-tourmaline greisen and pegmatitic quartz-arsenopyrite veins (Balen, 1990). At Hidden Creek, cassiterite occurs in quartz-tourmaline-muscovite veins that cut the granite. Sn-Ag vein and skarn mineralization at Ready Cash and Boulder Creek/Purkeypile (Balen, 1990; Millholland, 1999) are also genetically related to the McKinley sequence granites.

A similar metallogenetic setting occurs west of the Alaska Range, where felsic plugs of Late Cretaceous or early Tertiary age intrude Late Cretaceous Kuskokwim Group marine sandstone and shale. The Won, Win, and Bismark Creek prospects in the Kuskokwim Mountains are Sn-Ag-rich sheeted or stockwork veins with complex, sulfosalt-rich mineralogy in addition to cassiterite (Hudson and Reed, 1997). Tourmaline is common, and B rather than F is enriched in these shallow-level subvolcanic systems. At Sleitat in the southern Taylor Mountains, a 57-Ma two-mica granite has produced Sn-W mineralization in topaz- and tourmaline-bearing greisen (Burleigh, 1991; Hudson, 2001).

Though varying widely in host rock and geographic location, all these prospects share a close association with late-stage, quartz-rich granites, similar to the granophile and specialized suites discussed above. If all the granitic stocks of the northern Talkeetna Mountains can be shown to be of similar composition and origin, then the northern Talkeetna Mountains could have a potential for deposits of Nb, rare elements, or W, as well as the Sn-Ag-Mo association noted at Clark Bar.

Summary

Although our observations and sampling of the Clark Bar prospect were limited, some conclusions can be drawn concerning the mineral potential of the area. Strongly altered rocks at Clark Bar are enriched in Ag, Be, Ce, La, Li, Mo, Sn, and Zn and somewhat enriched in Bi, Hg, and Sb. Associated Paleocene granitic rocks are silica rich and have a trace-element chemistry consistent with granophile or "specialized," S-type granites. The two-mica, garnet-bearing stock at Devil Creek may be an example of a late-stage, volatile-rich phase of the larger regional composite plutons that are dominantly granodioritic in composition. Both the Clark Bar prospect and the regionally extensive Paleocene plutons have a moderate potential to host Sn-Ag-Mo and or W and rare-element deposits related to the most differentiated, water-rich stages of felsic intrusion.

Grid sampling of rocks and soils and more detailed stream-sediment sampling of all creeks draining the altered area at Clark Bar could determine the extent and metal content of possible mineralization at the prospect. Additional geologic mapping might indicate key indicator minerals in rock samples (muscovite, fluorite, tourmaline, topaz) or panned-stream concentrates (cassiterite, molybdenite, fluorite). Analysis of new and existing samples for such additional elements as F and B, and analytical methods with lower detection limits for such elements as U and W, would narrow down the range of possible deposit models to pursue in this region.

Acknowledgments

We thank our helicopter pilots, Gary Brogdon and Bill Merkley, for their tireless efforts to take us to sites that only a geologist could love. Thanks also to Skip Cunningham for his optimism about the mineral potential of the northern Talkeetna Mountains.

References Cited

Balen, M.D., 1990, Geochemical sampling results from Bureau of Mines investigations in the Valdez Creek mining district, Alaska; U.S. Bureau of Mines Open-File Report 34–90, 250 p.

Bliss, J.D., and Cox, D.P., 1986, Grade and tonnage model of polymetallic veins, model 22c *of* Cox, D.P., and Singer, D.A., eds., Mineral deposit models: U.S. Geological Survey Bulletin 1693, p. 125–129.

Burleigh, R.E., 1991, Geology and geochemistry of the Sleitat Mountain tin deposit, southwestern Alaska, *in* Reger, R.D., ed., Short notes on Alaskan geology, 1991: Alaska Division of Geological and Geophysical Surveys Professional Report 111, p. 29–40.

Carmichael, R.S., ed., 1982, Handbook of physical properties of rocks: Boca Raton, Fla., CRC Press, 3 v.

Carten, R.B., White, W.H., and Stein, H.J., 1993, High-grade granite-related molybdenum systems; classification and origin, *in* Kirkham, R.V., Sinclair, W.D., Thorpe, R.I., and Duke, J.M., eds., Mineral deposit modeling: Geological Association of Canada Special Paper 40, p. 521–554.

Černý, Petr, 1993, Rare-element granitic pegmatites, part I. Anatomy and internal evolution of pegmatite deposits, *in* Sheahan, P.A., and Cherry, M.E., eds., Ore deposit models (Geoscience Canada Reprint Series, v. 6): St. John's, Newfoundland, Geological Association of Canada, v. 2, p. 29–48.

Cox, D.P., 1986a, Descriptive model of polymetallic veins, model 22c *of* Cox, D.P., and Singer, D.A., eds., Mineral deposit models: U.S. Geological Survey Bulletin 1693, p. 125.

———1986b, Descriptive model of porphyry Cu-Mo, model 21a *of* Cox, D.P., and Singer, D.A., eds., Mineral deposit models: U.S. Geological Survey Bulletin 1693, p. 115.

Cox, D.P., and Singer, D.A., 1986, Mineral deposit models: U.S. Geological Survey Bulletin 1693, 379 p.

Csejtey, Béla, Jr., Nelson, W.H., Jones, D.L., Silberling, N.J., Dean, R.M., Morris, M.S., Lanphere, M.A., Smith, J.G., and Silberman, J.L., 1978, Reconnaissance geologic map and geochronology, Talkeetna Mountains quadrangle, northern part of Anchorage quadrangle, and southwest corner of Healy quadrangle, Alaska: U.S. Geological Survey Open-File Report 78–558–A, 62 p., scale 1:250,000.

Eastham, K.R., and Ridgway, K.D., 2001, Jurassic-Cretaceous basin development and structural configuration, Alaska Range suture zone [abs.]: Geological Society of America Abstracts with Programs, v. 33, no. 6, p. 390–391.

Eastham, K.R., Ridgway, K.D., and Lesh, M.E., 2000, Structural configuration and stratigraphy of the Kahiltna basin(s)—a detailed look at the "black crap" of central Alaska [abs.]: Geological Society of America Abstracts with Programs, v. 32, no. 7, p. A171.

Grimes, D.J., and Marranzino, A.P., 1968, Direct current arc and alternating-current spark emission spectrographic field methods for the semiquantitative analysis of geologic materials: U.S. Geological Survey Circular 591, 6 p.

Hudson, T.L., 2001, Alaska Resource Data File (ARDF) for the Taylor Mountains quadrangle: U.S. Geological Survey Open-File Report 01–200, 51 p.

Hudson, T.L., and Reed, B.L., 1997, Tin deposits in Alaska, *in* Goldfarb, R.J., and Miller, L.D., eds., Mineral deposits of Alaska (Economic Geology Monograph 9): Stanford, Calif., Economic Geology Publishing Co., p. 450–465.

Jackson, L.L., Brown, F.W., and Neil, S.T., 1987, Major and minor elements requiring individual determination, classical whole rock analysis, and rapid rock analysis, *in* Baedecker, P.A., ed., Methods for geochemical analysis: U.S. Geological Survey Bulletin 1770, p. G1–G23.

Kirkham, R.V., and Sinclair, W.D., 1995, Porphyry copper, gold, molybdenum, tungsten, tin, silver, chap. 19 *of* Eckstrand, O.R., Sinclair, W.D. and Thorpe, R.I., eds., Geology of Canadian mineral deposit types, v. P–1 *of* The geology of North America: Ottawa, Ontario, Geological Survey of Canada, p. 421–446.

Krauskopf, K.B., 1967, Introduction to geochemistry: San Francisco, McGraw-Hill, 721 p.

Kurtak, J.M., Southworth, D.D., Balen, M.D., and Clautice, K.H., 1992, Mineral investigations in the Valdez Creek mining district, south-central Alaska, U.S. Bureau of Mines Open-File Report 1–92, 658 p.

Lanphere, M.A., and Reed, B.L., 1985, The McKinley sequence of granitic rocks; a key element in the accretionary history of southern Alaska: Journal of Geophysical Research, v. 90, no. B13, p. 11413–11430.

———1990, Origin of the McKinley sequence of granitic rocks; constraints from Nd, Sr, and O isotopic data [abs.]: Geological Society of America Abstracts with Programs, v. 22, no. 3, p. 36.

Ludington, S.D., 1986, Descriptive model of Climax Mo deposits, model 16 *of* Cox, D.P., and Singer, D.A., eds.,

Mineral deposit models: U.S. Geological Survey Bulletin 1693, p. 73.

Menzie, W.D., and Reed, B.L., 1986a, Grade and tonnage model of Sn greisen deposits, model 15c *of* Cox, D.P., and Singer, D.A., eds., Mineral deposit models: U.S. Geological Survey Bulletin 1693, p. 71–72.

———1986b, Grade and tonnage model of Sn veins, model 15b *of* Cox, D.P., and Singer, D.A., eds., Mineral deposit models: U.S. Geological Survey Bulletin 1693, p. 67–69.

Menzie, W.D., and Theodore, T.G., 1986, Grade and tonnage model of porphyry Mo, low-F, model 21b *of* Cox, D.P., and Singer, D.A., eds., Mineral deposit models: U.S. Geological Survey Bulletin 1693, p. 120–122.

Miller, R.J., Cooley, E.F., O'Leary, R.M., Garmezy, Lawrence, Csejtey, Béla, Jr., Smith, T.E., and Cleveland, M.N., 1978, Analyses of geochemical samples from the Talkeetna Mountains Quadrangle: U.S. Geological Survey Open-File Report 78–1052, 279 p.

Millholland, Madelyn, 1999, Alaska Resource Data File (ARDF) for the Taylor Mountains quadrangle: U.S. Geological Survey Open-File Report 99–139, 183p.

Nokleberg, W.J., Bundtzen, T.K., Berg, H.C., Brew, D.A., Grybeck, Donald, Robinson, M.S., Smith, T.E., and Yeend, W.E., 1987, Significant metalliferous lode deposits and placer districts of Alaska: U.S. Geological Survey Bulletin 1786, 104 p., 2 plates, scale 1:5,000,000.

Nokleberg, W.J., Plafker, George, and Wilson, F.H., 1994, Geology of south-central Alaska, chap. 10 *of* Plafker, George, and Berg, H.C., eds., The geology of Alaska, v. G–1 *of* The geology of North America: Boulder, Colo., Geological Society of America,, p. 311–366.

Reed, B.L., 1986a, Descriptive model of porphyry Sn, model 20a *of* Cox, D.P., and Singer, D.A., eds., Mineral deposit models: U.S. Geological Survey Bulletin 1693, p. 108.

———1986b, Descriptive model of Sn greisen deposits, model 15c *of* Cox, D.P., and Singer, D.A., eds., Mineral deposit models: U.S. Geological Survey Bulletin 1693, p. 70.

———1986c, Descriptive model of Sn veins, model 15b *of* Cox, D.P., and Singer, D.A., eds., Mineral deposit models: U.S. Geological Survey Bulletin 1693, p. 67.

Sinclair, W.D., 1995a, Granitic pegmatites, chap. 21 *of* Eckstrand, O.R., Sinclair, W.D., and Thorpe, R.I., eds., Geology of Canadian mineral deposit types, v. P–1 *of* The geology of North America: Ottawa, Ontario, Geological Survey of Canada, p. 503–512.

———1995b, Vein-stockwork tin, tungsten, chap. 18 *of* Eckstrand, O.R., Sinclair, W.D., and Thorpe, R.I., eds., Geology of Canadian mineral deposit types, v. P–1 *of* The geology of North America: Ottawa, Ontario, Geological Survey of Canada, p. 409–420.

Singer, D.A., Cox, D.P., and Mosier, D.L., 1986, Grade and tonnage model of porphyry Cu-Mo, model 21a *of* Cox, D.P., and Singer, D.A., eds., Mineral deposit models: U.S. Geological Survey Bulletin 1693, p. 116–119.

Singer, D.A., Theodore, T.G., and Mosier, D.L., 1986, Grade and tonnage model of Climax Mo deposits, model 16 *of* Cox, D.P., and Singer, D.A., eds., Mineral deposit models: U.S. Geological Survey Bulletin 1693, p.73–75.

Strong, D.F., 1988, A model for granophile mineral deposits, *in* Roberts, R.G., and Sheahan, P.A., eds., Ore deposit models (Geoscience Canada Reprint Series, v. 3): St. John's, Newfoundland, Geological Association of Canada, v. 1, p. 59–66.

Theodore, T.G., 1986, Descriptive model of porphyry Mo, low-F, model 21b *of* Cox, D.P., and Singer, D.A., eds., Mineral deposit models: U.S. Geological Survey Bulletin 1693, p. 120.

Thurow, Greg, and Warner, J.D., 1994, Coal Creek Sn deposit, *in* Nokleberg, W.J., Brew, D.A., and others, Metallogeny and major mineral deposits of Alaska, chap. 29 *of* Plafker, George, and Berg, H.C., eds., The geology of Alaska, v. G–1 *of* The geology of North America: Boulder, Colo., Geological Society of America, p. 878.

Togashi, Yukio, 1986, Descriptive model of Sn-polymetallic veins, model 20b *of* Cox, D.P., and Singer, D.A., eds., Mineral deposit models: U.S. Geological Survey Bulletin 1693, p.109.

West, A.W., 1994, A petrologic and geochronologic study of the McKinley pluton, Alaska: Fairbanks, University of Alaska, M.S. thesis, 181 p.

Yidou, Li, 1993, Poly-type model for tungsten deposits and vertical structural zoning model for vein-type tungsten deposits in south China, *in* Kirkham, R.V., Sinclair, W.D., Thorpe, R.I., and Duke, J.M., eds., Mineral deposit modeling: Geological Association of Canada Special Paper 40, p. 555–568.

Studies by the U.S. Geological Survey in Alaska, 2001
U.S. Geological Survey Professional Paper 1678

Early Middle Devonian (Eifelian) Gastropods from the Wadleigh Limestone in the Alexander Terrane of Southeastern Alaska Demonstrate Biogeographic Affinities with Central Alaskan Terranes (Farewell and Livengood) and Eurasia

By Robert B. Blodgett, David M. Rohr, Susan M. Karl, and James F. Baichtal

Abstract

Silicified Eifelian (early Middle Devonian) gastropods form the dominant component of a mollusk-rich fauna from U.S. Geological Survey fossil locality M1299–SD, on a small islet in the NW¼NE¼ sec. 34, T. 70 S., R. 79 E., of the Craig D–4 quadrangle, southeastern Alaska (Alexander terrane). Six species are recognized from this locality of the Wadleigh Limestone, most of which are conspecific or closely allied with coeval gastropod faunas known from the Nixon Fork subterrane of the Farewell terrane of west-central Alaska and the Livengood terrane of east-central Alaska. None of these species is known from contemporaneous, miogeoclinal strata of western Canada. None of the species discussed herein has been recognized within coeval rocks of nonaccreted western North America, and these close affinities suggest that the Alexander terrane, like the related Farewell and Livengood terranes, is of Eurasian origin, most likely representing rifted marginal parts of the Siberian paleocontinent or, less likely, part of northeastern Baltica. Similarly strong biogeographic linkages are also noted in older (Late Silurian and Early Devonian) faunas of the Alexander terrane.

Introduction

The Wadleigh Limestone, named by Eberlein and Churkin (1970), is a medium- to thick-bedded "relatively pure, fossil-fragmental limestone," with interbedded argillaceous limestone and calcareous shale in the lower part of the unit. The limestone is rich in corals, crinoid columnals, and the stromatoporoid Amphipora and contains less abundant brachiopods, gastropods, bivalves, nautiloids, ammonoids, and ostracodes. The unit is inferred to represent patch reefs, reef breccia, and reef-peripheral deposits (Eberlein and Churkin, 1970). The unit is assigned an Eifelian to Famennian (Middle and Late Devonian) age (Eberlein and others, 1983). The unit concordantly and gradationally overlies red beds of the Lower Devonian Karheen Formation.

Although the Wadleigh Limestone is richly fossiliferous, very few megafossils have been described or illustrated from it. Previous publications addressing various elements of the Wadleigh megafauna include Oliver and others (1975) on Middle Devonian and Frasnian corals, Savage and Baxter (1995) on Frasnian brachiopods, and Blodgett and Cook (2002) with a description of a single gastropod species, *Cheeneetnukia frydai*, noted from the U.S. Geological Survey (USGS) fossil locality (M1299–SD) discussed here. Nautiloids from the same general horizon as USGS fossil locality M1299–SD were also discussed by Zavala and others (1995) and Soja and others (1996).

In this chapter, we discuss a small, but biogeographically important, silicified gastropod fauna from Eifelian strata of the Wadleigh Limestone in the Craig D–4 quadrangle, southeastern Alaska (Alexander terrane). The fauna is represented by a single collection made by J.W. Evans of the USGS in 1968 (his field No. 68AEs596) at a locality that was subsequently designated USGS fossil locality M1299–SD. The fossil locality is on the shoreline of a small islet in the NW¼NE¼ sec. 34, T. 70 S., R. 79 E., of the Craig D–4 quadrangle (fig. 1). This locality is approximately equivalent to fossil locality F–44 of Eberlein and others (1983). The specimens are coarsely silicified, but enough characteristics of the teleoconchs are preserved to allow significant taxonomic and biogeographic conclusions to be drawn. In our experience, Paleozoic gastropod faunas are more provincial than nearly every other faunal group, and so they have important biogeographic implications for terrane accretion in southern Alaska.

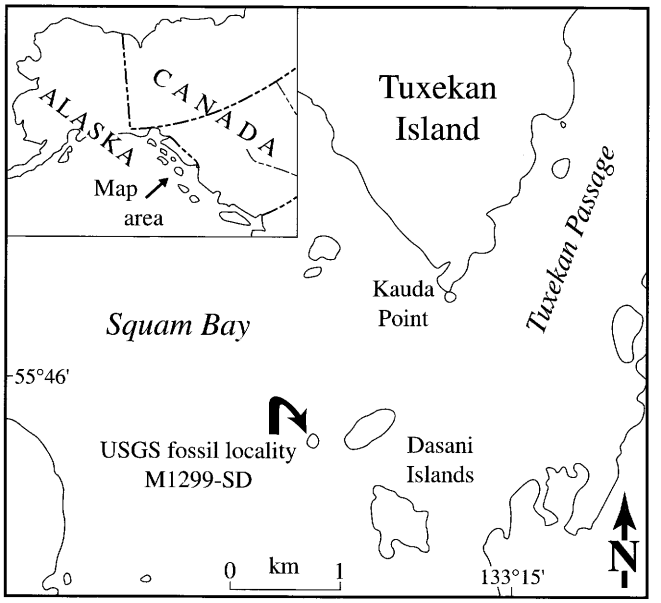

Figure 1. Islet in Tuxekan Narrows-Karheen Strait area, Craig D–4 quadrangle, southeastern Alaska, showing location of U.S. Geological Survey fossil locality M1299–SD (modified from Soja and others, 1996).

Gastropod Fauna

The following species are recognized from U.S. Geological Survey locality M1299–SD:

Cheeneetnukia frydai Blodgett and Cook, 2002—11 specimens

Astralites sp.—14 specimens

Kitakamispira ormistoni (Blodgett, 1992)—3 specimens

Paffrathopsis n.sp.—28 specimens

Euryzone sp.—15 specimens

Subulites (Fusispira) sp.—3 specimens

The most distinctive gastropod in the collection is *Cheeneetnukia frydai* Blodgett and Cook, 2002 (pl. 1, fig. 5), a species whose type area is from the upper part (of middle Eifelian age) of the Cheeneetnuk Limestone (Blodgett and Gilbert, 1983) of the McGrath A–4 and A–5 quadrangles, west-central Alaska. The Cheeneetnuk Limestone represents the uppermost Devonian platform carbonate unit recognized in the Nixon Fork subterrane stratigraphy of the McGrath quadrangle and is equivalent to the uppermost Devonian platform carbonate rocks of the type area of the Nixon Fork subterrane in the Medfra quadrangle, where it represents the upper part of the Whirlwind Creek Formation (Dutro and Patton, 1982). The Whirlwind Creek Formation was described by Dutro and Patton (1982, p. H19) as "an Upper Silurian to Upper Devonian sequence of predominantly shallow-water carbonate rocks, 1,000–1,500 m thick." Blodgett and others (2000) subsequently raised this formation to group status.

Three specimens of *Kitakamispira ormistoni* (Blodgett, 1992) are present in the Wadleigh Limestone collection (pl. 1, fig. 6). This species was originally described from the "Cascaden Ridge unit" of the Livengood quadrangle and was assigned to the closely related genus *Gyronema*; however, reconsideration of its distinctly nodose ornament now favors its placement in the genus *Kitakamispira* Kase and Nishida, 1988. This option was earlier considered by Blodgett (1992) but was rejected at the time it was established. Poorly preserved, silicified specimens of a nearly identical species were also noted in Blodgett (1992, p. 151) to be present in the uppermost part of the Whirlwind Creek Group of the Medfra B–3 quadrangle, west-central Alaska, and these specimens were suggested to probably be conspecific with the Livengood species.

The genus *Paffrathopsis* was recently proposed by Frýda (2000), the type species being *Nerita subcostata* Dechen (1832), which was reillustrated by D'Archiac and DeVerneuil (1842, pl. 34, figs. 5, 5a, 6) under the name *Natica subcostata*. The particular species of *Paffrathopsis* present in the Wadleigh Limestone collection (pl. 1, figs. 7–8) is also the most abundant, represented by 28 specimens. The silicification is quite coarse, but nonetheless, this species appears to represent a new species that differs from the type species, *P. subcostata* (D'Archiac and DeVerneuil, 1842).

The pseudophorid gastropod genus *Astralites* Whiteaves, 1892, was described originally from Givetian beds of the Winnipegosis Formation of Manitoba. The type species is *A. fimbriatus* Whiteaves. A total of 14 specimens are present in USGS collection M1299–SD, which can be ascribed to this genus (pl. 2, figs. 1–3). Heidelberger (2001) ascribed two German species from the Givetian to the genus: *A. sublimbatus* (D'Orbigny, 1850) and *A. muelleri* Heidelberger, 2001. The genus is also present in the upper part (Eifelian) of the Cheeneetnuk Limestone,

The genus *Euryzone* is represented by 15 specimens in USGS collection M1299–SD, most of which are coarsely silicified (pl. 1, figs. 1–4), although 1 specimen (pl. 1, fig. 4) is preserved well enough to show the typical placement of the selenizone on the upper whorl face that is associated with the genus. The type species of the genus is *E. delphinuloides* (Schlotheim) from the Givetian of Germany. The genus is widespread in many Givetian localities worldwide. The Wadleigh species illustrated here closely approaches the type species, but the preservation of the Alaskan material is too coarse to confirm species level identity with the type species. Another *Euryzone* species, *Euryzone* n.sp. Blodgett, 1992, has been previously described from the Eifelian strata of the "Cascaden Ridge unit," Livengood B–3 quadrangle, east-central Alaska (Livengood terrane). However, the Livengood terrane species differs in having a more angular whorl profile, in contrast to the smooth, evenly rounded whorls found in the Wadleigh Limestone specimens.

Subulites (*Fusispira*) sp. (pl. 1, fig. 9; pl. 2, fig. 4) is represented in USGS collection M1299–SD by three specimens that appear to be conspecific, or closely allied with *Subulites* (*Fusispira*) sp. Blodgett, 1992, described from Eifelian beds of the "Cascaden Ridge unit" in exposures of the Livengood terrane of the Livengood B–3 quadrangle, east-central Alaska. As noted by Blodgett (1992, p. 160), the Livengood terrane species is also present in Eifelian beds of the uppermost part of the Cheeneetnuk Limestone, McGrath A–5 quadrangle, west-central Alaska (part of the Nixon Fork subterrane of the Farewell terrane).

Biogeographic Implications

The Eifelian gastropod fauna known from the Wadleigh Limestone (USGS fossil loc. M1299–SD) is essentially identical at the species level with coeval faunas known from the Nixon Fork subterrane of the Farewell terrane of west-central Alaska and the Livengood terrane east-central Alaska (see fig. 2). None of these gastropod species is recognized in nonaccreted rocks of western North America. Their extremely close similarities suggest a similar Eurasian origin, mostly

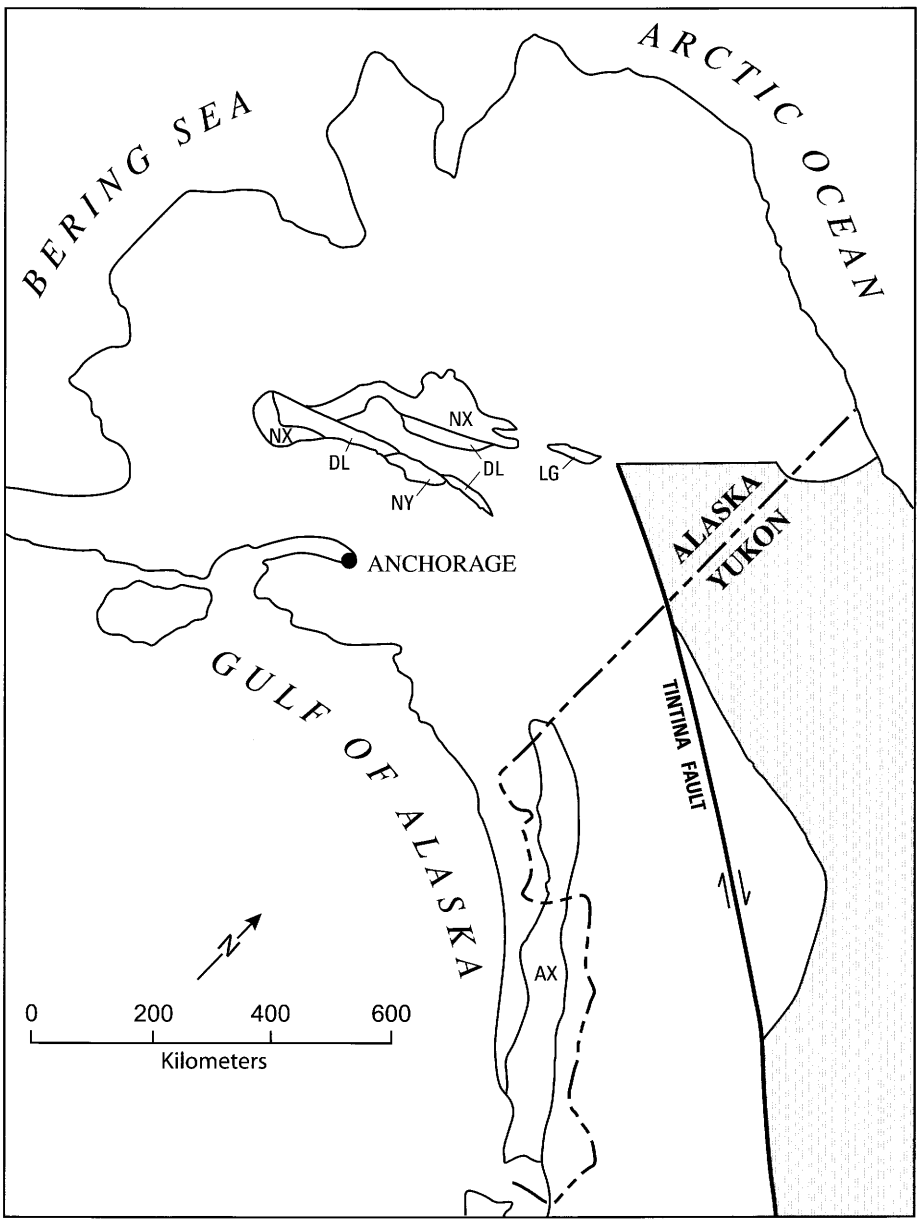

Figure 2. Tectonostratigraphic terranes and component subterranes in Alaska (modified from Blodgett and others, 2002). AX, Alexander terrane; LG, Livengood terrane. Subterranes of the Farewell terrane: DL, Dillinger; MY, Mystic; NX, Nixon Fork. Shaded area, North American autochthonous basement.

likely from a marginal part of the Siberian paleocontinent, as indicated by biogeographic affinities (primarily based on brachiopods) of the Farewell terrane (Blodgett and Brease, 1997; Blodgett, 1998; Blodgett and Boucot, 1999; Garcia-Alcalde and Blodgett, 2001; Blodgett and others, 2002).

Close alliance of the Alexander terrane Eifelian gastropod fauna with that of the Farewell and Livengood terranes is also supported by another Eifelian age collection recovered in 1958 by Donald J. Miller of the USGS from the Chilkat Mountains of the Juneau D–6 quadrangle, part of the Alexander terrane in southeastern Alaska. This small collection contained several brachiopod species, as well as several gastropod species and the dasyclad alga genus *Coelotrochium*. Many of these species were conspecific with species in the Cheeneetnuk Limestone of the Farewell terrane (Blodgett and others, 2002). As noted elsewhere, the alga genus *Coelotrochium* is almost a hallmark for the shallow-water, inner-carbonate-platform facies of Eifelian rocks of the Farewell terrane and is also known from northern Europe (Baltica), but it has never been reported from cratonic or miogeoclinal rocks of North America.

Rugose corals from Middle Devonian strata of the Alexander terrane also have non-North American affinity. Oliver and others (1975, p. 19) noted that the Middle Devonian coral fauna from the Wadleigh Limestone of southeastern Alaska was distinct from that of western North America, stating that "none of these corals from southeastern Alaska seems conspecific or very closely related to Hume [Shale of Northwest Territories] or Great Basin species."

An unusually rich, biogeographically distinctive fossil fauna of Emsian (late Early Devonian) age is known from Kasaan Island on the east side of Prince of Wales Island, southeastern Alaska. The earliest mention of this fauna is by Kindle (1907), who provided a faunal list from these beds and noted that the entire fauna was more strongly allied with Asiatic and European faunas than with contemporaneous North American faunas outside of Alaska. The foreign affinities were particularly emphasized by the presence of the bivalve *Hercynella* in a single horizon in the lower part of the Devonian section on Kasaan Island. Forney and others (1981, p. 131) noted the presence of typical "Bohemian" molluscan elements in the Emsian strata of Kasaan Island, including the distinctive bivalve *Hercynella* cf. *H. bohemica* Barrande, the oriostomatid gastropod *Oriostoma* sp. aff. *O. princeps* Oehlert, and the tremanotid gastropod *Boiotremus* cf. *B. fortis* Frech. We note that Lower Devonian Bohemian (or Barrandian) faunas have close biogeographic affinities with Uralian faunas of Russia. Blodgett and others (1988) illustrated two gastropod species from the Kasaan beds: Oriostoma sp. (their figs. 6.7, 6.8) and *Tubina* sp. (their figs. 6.5, 6.6). The oriostomatid genus Tubina is foreign to North America, and no previous reports of the taxon are known from the Western Hemisphere. In a broad survey of all known Emsian gastropod collections from western or Arctic North America, not one species of the richly diverse Kasaan Island fauna is shared with faunas of undoubted North American origin. The closest related fauna from western North America is that from the Nixon Fork subterrane of the Farewell terrane exposed on the south flank of Limestone Mountain, Medfra B–4 quadrangle, west-central Alaska (Blodgett and others, 1988, 2002; Blodgett and Rohr, 1989; Frýda and Blodgett, 1998 and in press). Emsian brachiopods from Kasaan Island also are characterized by close affinities with contemporaneous Uralian and (or) Siberian faunas (Soja, 1988; Blodgett and others, 2002). Early Devonian corals from Noyes Island, off the west side of Prince of Wales Island, were also noted by Churkin and others (1969, 1970) as showing their closest affinities with those of the former USSR, notably the Asiatic part (Siberia and Kolyma).

The Upper Lower to Upper Silurian Heceta Limestone of southeastern Alaska contains a diverse brachiopod fauna of Uralian-Cordilleran affinities (Blodgett and others, 2002). At the species level, however, as noted by Kirk and Amsden (1952, p. 54), the Heceta brachiopod faunas most closely resemble Late Silurian faunas described by Khodalevich (1939) from the east slope of the Urals.

Late Silurian gastropods from the Glacier Bay region of southeastern Alaska (part of the Alexander terrane) likewise are biogeographically most closely allied to Late Silurian faunas known from the Ural Mountains of Russia and the Farewell terrane of southwestern and west-central Alaska (Rohr and others, in press; Rohr and Blodgett, this volume). Like contemporaneous rocks of the Farewell terrane of southwestern and west-central Alaska, the Heceta Limestone of the Alexander terrane contains extensive Late Silurian algal-reef-mound complexes with an algal flora and associated aphrosalpingid sphinctozoan sponges that are also known in the Urals (Riding and Soja, 1993; Rigby and others, 1994; Soja, 1994; Soja and Antoshkina, 1997; Blodgett and others, 2002). Similar complexes are unknown from rocks of equivalent age in the North America craton.

In summary, Silurian and Devonian megafossils from the Alexander terrane lack affinities with North America faunas from the western Cordillera of the United States or western or Arctic Canada but are closely allied with faunas described from the Urals, Central Asia, and the Kuznetsk Basin of Siberia. Their closest consistent biotic ties, however, are with the Farewell terrane of southwestern Alaska, suggesting that although they are dominated by differing sedimentologic regimes, these terranes were close enough to one another during Silurian and Devonian time to produce commonality among a large proportion of their fossil biota.

Acknowledgments

The first author thanks the Alexander von Humboldt Stiftung (Bonn, Germany) for providing financial support that allowed him a 6-month stay in Germany to study European Devonian gastropods. We also acknowledge Arthur J. Boucot and Ning Zhang (both of Oregon State University, Corvallis) for their reviews of the manuscript.

References Cited

Blodgett, R.B., 1992, Taxonomy and paleobiogeographic affinities of an early Middle Devonian (Eifelian) gastropod faunule from the Livengood quadrangle, east-central Alaska: Palaeontographica, Abteilung A, v. 221, p. 125–168.

———1998, Emsian (Late Early Devonian) fossils indicate a Siberian origin for the Farewell terrane, *in* Clough, J.G., and Larson, Frank, eds., Short notes on Alaskan geology, 1997: Alaska Division of Geological & Geophysical Surveys Professional Report 118, p. 27–34.

Blodgett, R.B., and Boucot, A.J., 1999, Late Early Devonian (late Emsian) eospiriferinid brachiopods from Shellabarger Pass, Talkeetna C–6 quadrangle, south-central Alaska and their biogeographic importance; further evidence for a Siberian origin of the Farewell and allied Alaskan accreted terranes: Senckenbergiana Lethaea, v. 72, no. 1, p. 209–221.

Blodgett, R.B., and Brease, P.F., 1997, Emsian (late Early Devonian) brachiopods from Shellabarger Pass, Talkeetna C–6 quadrangle, Denali National Park, Alaska indicate Siberian origin for Farewell terrane [abs.]: Geological Society of America Abstracts with Programs, v. 29, no. 5, p. 5.

Blodgett, R.B., and Cook, A.G., 2002, Cheeneetnukiidae, a new Middle Devonian murchisonioid gastropod family, including the new genera *Cheeneetnukia* and *Ulungaratoconcha* based on representatives from Alaska and Australia: Memoirs of the Queensland Museum, v. 48, no. 1, p. 17–28.

Blodgett, R.B., and Gilbert, W.G., 1983, The Cheeneetnuk Limestone, a new Early(?)–Middle Devonian formation in the McGrath A–4 and A–5 quadrangles, west-central Alaska: Alaska Division Geological & Geophysical Surveys Professional Report 85, 6 p.

Blodgett, R.B., and Rohr, D.M., 1989, Two new Devonian spine-bearing pleurotomariacean gastropod genera from Alaska: Journal of Paleontology, v. 63, no. 1, p. 47–53.

Blodgett, R.B., Rohr, D.M., and Boucot, A.J., 1988, Lower Devonian gastropod biogeography of the Western Hemisphere, *in* McMillan, N.J., Embry, A.F., and Glass, D.J., eds., Devonian of the World: Canadian Society of Petroleum Geologists Memoir 14, v. 3, p. 285–305.

———1990, Early and Middle Devonian gastropod biogeography, *in* McKerrow, W.S., and Scotese, C.R., eds., Palaeozoic paleogeography and biogeography: Geological Society (London) Memoir 12, p. 277–284.

———2002, Paleozoic links among some Alaskan accreted terranes and Siberia based on megafossils, *in* Miller, E.L., Grantz, Art, and Klemperer, S.L., eds., Tectonic evolution of the Bering Shelf-Chukchi Sea-Arctic margin and adjacent landmasses: Geological Society of America Special Paper 360, p. 273–291.

Blodgett, R.B., Rohr, D.M., Measures, E.A., Savage, N.M., Pedder, A.E.H., and Chalmers, R.W., 2000, The Soda Creek Limestone, a new upper Lower Devonian formation in the Medfra quadrangle, west-central Alaska, *in* Pinney, D.S., and Kauth, P.K., eds., Short notes on Alaska geology, 1999: Alaska Division of Geological & Geophysical Surveys Professional Report 119, p. 1–9.

Churkin, Michael, Jr., Eberlein, G.D., Hueber, F.M., and Mamay, S.H., 1969, Lower Devonian land plants from graptolitic shale in southeastern Alaska: Palaeontology, v. 12, no. 4, p. 559–573.

Churkin, Michael, Jr., Jaeger, Hermann, and Eberlein, G.D., 1970, Lower Devonian graptolites from southeastern Alaska: Lethaia, v. 3, no. 2, p. 183–202.

D'Archiac, E.J.A., and DeVerneuil, E.P., 1842, On the fossils of the older deposits in the Rhenish provinces, preceded by a general survey of the fauna of Palaeozoic rocks, and followed by a tabular list of the organic remains of the Devonian System in Europe: Geological Society of London Transactions, v. 6, p. 303–410.

von Dechen, E.H.C., *in* De la Beche, H.T., Handbuch der Geognosie: Berlin, p. 533–534

D'Orbigny, Alcide, 1850, Prodrome de paléontologie stratigraphique universelle des animaux mollusques et rayonnés faisant suite au cours élémentaire de paléontologie et de géologie stratigraphiques: Paris, 392 p.

Dutro, J.T., Jr., and Patton, W.W., Jr., 1982, New Paleozoic platform formations in the northern Kuskokwim Mountains, west-central Alaska, *in* Stratigraphic notes, 1980–1982: U.S. Geological Survey Bulletin 1529–H, p. H13–H22.

Eberlein, G.D., and Churkin, Michael, Jr., 1970, Paleozoic stratigraphy in the northwest coastal area of Prince of Wales Island, southeastern Alaska: U.S. Geological Survey Bulletin 1284, 67 p.

Eberlein, G.D., Churkin, Michael, Jr., Carter, Claire, Berg, H.C., and Ovenshine, A.T., 1983, Geology of the Craig quadrangle, Alaska: U.S. Geological Survey Open-File Report 83–91, 53 p., 4 sheets, scale 1:250,000.

Forney, G.G., Boucot, A.J., and Rohr, D.M., 1981, Silurian and Lower Devonian zoogeography of selected molluscan genera, *in* Gray, Jane, Boucot, A.J., and Berry, W.B.N., eds., Communities of the past: Stroudsberg, Penn., Hutchinson Ross, p. 119–164.

Frýda, Jiří, 2000, Some new Givetian (late Middle Devonian) gastropods from the Paffrath area (Bergisches Land, Germany): Queensland Museum Memoirs, v. 45, no. 2, p. 359–374.

Frýda, Jiří, and Blodgett, R.B., 1998, Two new cirroidean genera (Vetigastropoda, Archaeogastropoda) from the Emsian (Late Early Devonian) of Alaska with notes on the early phylogeny of Cirroidea: Journal of Paleontology, v. 72, no. 2, p. 265–273.

——— in press, New Emsian (Late Early Devonian) gastropods from Limestone Mountain, Medfra B–4 quadrangle, west-central Alaska (Farewell terrane), and their paleobiogeographic affinities and evolutionary significance: Journal of Paleontology, v. 78, no. 1, p. 111–132.

Garcia-Alcalde, J.L., and Blodgett, R.B., 2001, New Lower Devonian (Upper Emsian) *Myriospirifer* (Brachiopoda, Eospiriferinae) species from Alaska and northern Spain and the paleogeographic distribution of the genus *Myriospirifer*: Czech Geological Society Journal, v. 46, no. 3–4, p. 59–68.

Heidelberger, Doris, 2001, Mitteldevonische (Givetische) Gastropoden (Mollusca) aus der Lahnmulde (südliches Rheinisches Schiefergebirge): Geologische Abhandlungen Hessen, v. 106, 291 p.

Kase, Tomoki, and Nishida, Tamio, 1988, Two new Middle Devonian gastropods from the Nakazato Formation of Kitakami, Northeast Japan, in Professor Tamio Kotaka commemorative volume on molluscan paleontology (Studies on Japanese Trilobites and Associated Fossils, no. 41): Saito Ho-on Kai Museum Special Publication 2, p. 257–261.

Khodalevich, A.N., 1939, Verkhnesiluriiskie brakhiopody vostochnogo sklona urala: Trudy Uralskogo Geologicheskogo Upraveleniya, Izdanie Uralgeoupravleniya, Sverdlovsk, 135 p.

Kindle, E.M., 1907, Notes on the Paleozoic faunas and stratigraphy of southeastern Alaska: Journal of Geology, v. 15, no. 4, p. 314–337.

Kirk, Edwin, and Amsden, T.W., 1952, Upper Silurian brachiopods from southeastern Alaska: U.S. Geological Survey Professional Paper 233–C, p. 53–66.

Oliver, W.A., Jr., Merriam, C.W., and Churkin, Michael, Jr., 1975, Ordovician, Silurian, and Devonian corals of Alaska: U.S. Geological Survey Professional Paper 823–B, p. B13–B43.

Riding, Robert, and Soja, C.M., 1993, Silurian calcareous algae, cyanobacteria, and microproblematica from the Alexander terrane: Journal of Paleontology, v. 67, no. 5, p. 710–728.

Rigby, J.K., Nitecki, M.H., Soja, C.M., and Blodgett, R.B., 1994, Silurian aphrosalpingid sphinctozoans from Alaska and Russia: Acta Palaeontologica Polonica, v. 39, no. 4, p. 341–391.

Rohr, D.M., Blodgett, R.B., and Frýda, Jiří, 2003, New Silurian murchisoniid gastropods from Alaska and a review of the genus *Coelocaulus*, *in* Clautice, K.H., and Davis, P.K., eds., Short notes on Alaska geology, 2003: Alaska Division of Geological & Geophysical Surveys Professional Report 120, p. 87–93.

Savage, N.M., and Baxter, M.E., 1995, Late Devonian (Frasnian) brachiopods from the Wadleigh Limestone, southeastern Alaska: Journal of Paleontology, v. 69, no. 6, p. 1029–1046.

Soja, C.M., 1988, Lower Devonian (Emsian) brachiopods from southeastern Alaska: Palaeontographica, Abteilung A, v. 201, p. 129–193.

———1994, Significance of Silurian stromatolite-sphinctozoan reefs: Geology, v. 22, no. 4, p. 355–358.

Soja, C.M., and Antoshkina, A.I., 1997, Coeval development of Silurian stromatolite reefs in Alaska and the Urals Mountains; implications for paleogeography of the Alexander terrane: Geology, v. 25, no. 6, p. 539–542.

Soja, C.M., Gobetz, K.E., Thibeau, Jennifer, Zavala, Erika, and White, Brian, 1996, Taphonomy and paleobiological implications of Middle Devonian (Eifelian) nautiloid concentrates, Alaska: Palaios, v. 11, no. 5, p. 422–436.

Whiteaves, J.F., 1892, The fossils of the Devonian rocks of the islands, shores or immediate vicinity of Lakes Manitoba and Winnipegosis: Geological Survey of Canada Contributions to Canadian Palaeontology, v. 1, no. 4, p. 255–359.

Zavala, Erika, Thibeau, Jennifer, Gobetz, K.E., and Soja, C.M., 1995, Origin of Middle Devonian nautiloid deposits, southeastern Alaska [abs.]: Geological Society of America Abstracts with Programs, v. 27, no. 1, p. 94.

PLATES 1, 2

Plate 1. Eifelian (early Middle Devonian) gastropods from USGS fossil locality M1299–SD.

Figures 1–4. *Euryzone* sp.

1, 2, 3. Apertural, apical, and basal views of coarsely silicified specimen. Magnification, ×1.5.

4. Oblique apical view of partial shell fragment, showing preserved trace of selenizone on final whorl. Magnification, ×2.

5. *Cheeneetnukia frydai* Blodgett and Cook, 2002. Side view. Magnification, ×1.5.

6. *Kitakamispira ormistoni* (Blodgett, 1992). Side view. Magnification, ×1.

7, 8. *Paffrathopsis* sp., abapertural and apical views. Magnification, ×2.0.

9. *Subulites* (*Fusispira*) sp. Blodgett, 1992. Side view of medium-size shell. Magnification, ×2.0.

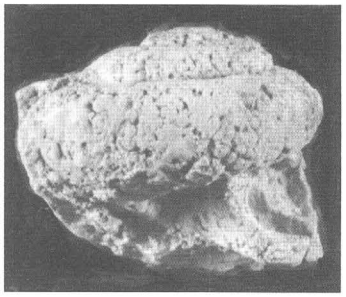

1

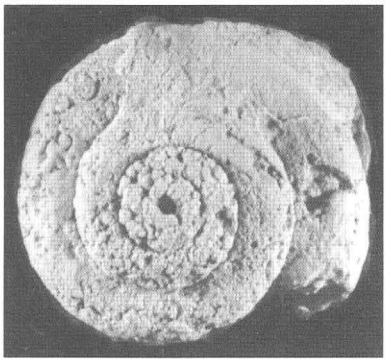

2

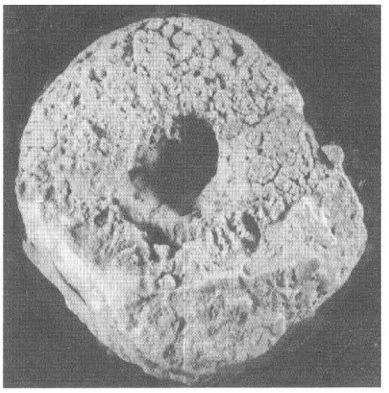

3

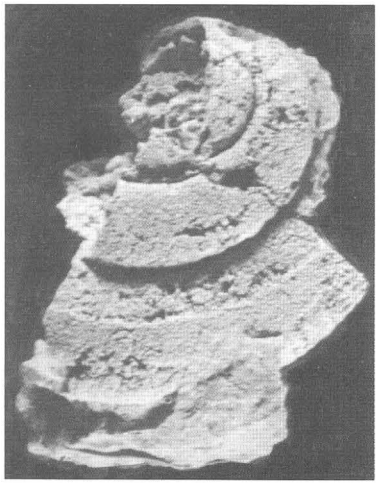

4

5

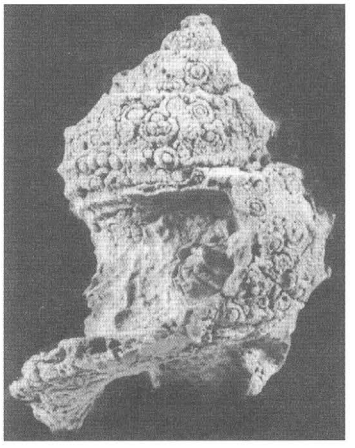

6

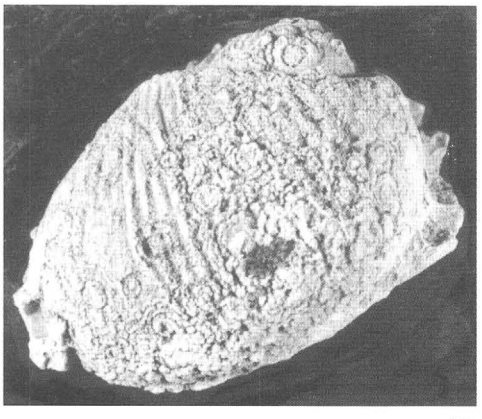

7

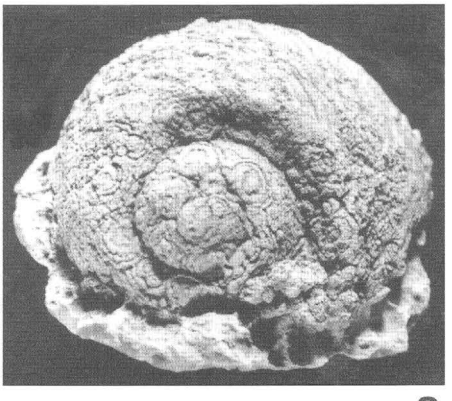

8

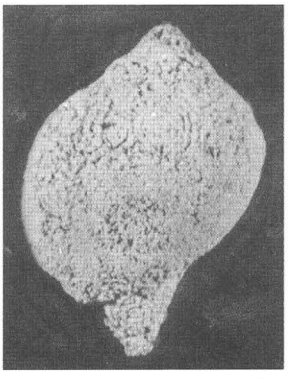

9

Plate 2. Eifelian (early Middle Devonian) gastropods from USGS fossil locality M1299–SD.

Figures 1–3. *Astralites* sp.

1, 2, 3. Side, oblique side, and apical views of relatively large shell. Magnification, ×1.5.

4. *Subulites* (*Fusispira*) sp. Blodgett, 1992. Apertural view of large shell. Magnification, ×1.5.

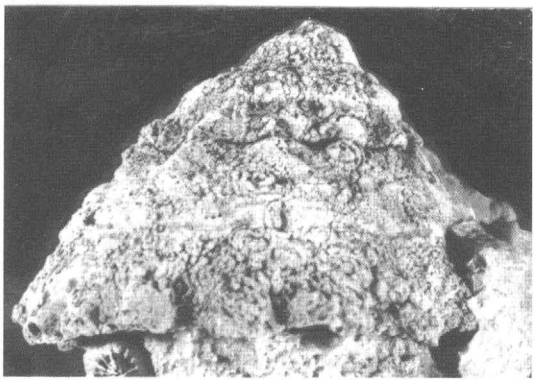

1

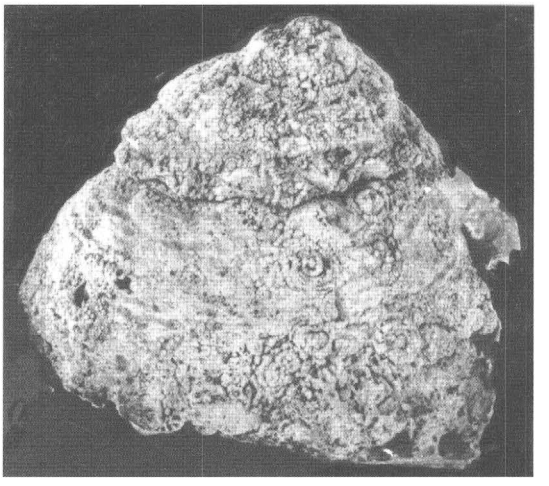

2

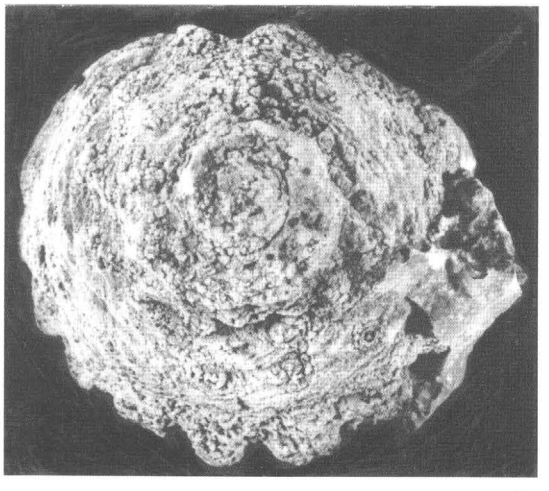

3

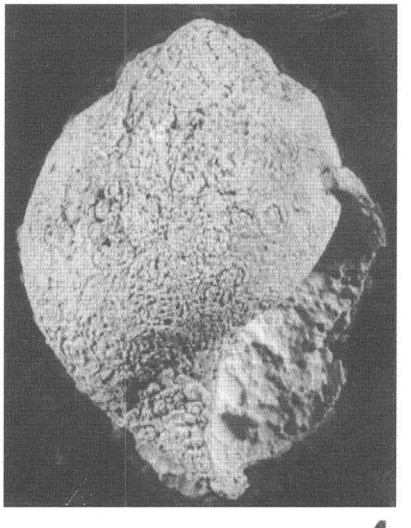

4

Studies by the U.S. Geological Survey in Alaska, 2001
U.S. Geological Survey Professional Paper 1678

Kirkospira, a New Silurian Gastropod from Glacier Bay, Southeastern Alaska

By David M. Rohr and Robert B. Blodgett

Abstract

Kirkospira glacialis n.gen., n.sp., is described from the Upper Silurian part of the Willoughby Limestone of Glacier Bay, southeastern Alaska. The examined material, which was collected by two U.S. Geological Survey geologists, F.E. Wright in 1906 and Edwin Kirk in 1917, from one of two small islands situated immediately northeast of Willoughby Island, is part of a large-shelled molluscan facies that is observed on both Willoughby and Drake Islands. This fauna of the Alexander terrane is biogeographically most closely allied to other Late Silurian faunas known from the Ural Mountains of Russia and the Farewell terrane of southwestern Alaska.

Introduction

The Willoughby Limestone was named by Rossman (1963) for exposures on Willoughby Island, where the best and most typical section is situated. Kirk (1927b) considered the strata exposed there to be Late Silurian. Although Gryc and others (1967) modified the age to Middle Devonian, subsequent workers, such as Churkin (1973) and Soja and others (2000), retain Silurian and Late Silurian ages, respectively.

F.E. Wright and Edwin Kirk of the U.S. Geological Survey (USGS) collected a Silurian fauna, including gastropods, from Drake and Willoughby Islands in southeastern Alaska during 1906 and 1917, respectively. Descriptions of the bivalve genus *Pycnodesma* Kirk, 1927b, (subsequently renamed *Pycinodesma*, Kirk, 1927a) and the gastropod genus *Bathmopterus* Kirk, 1928 (=*Euomphalopterus* Fischer, 1887) were published in subsequent years.

The specimens described here were collected by F.E. Wright in 1906 and by Edwin Kirk in 1917. They bear the respective labels "873, Glacier Bay, small island 500′ east of Willoughby Island, Alaska" and "993, Small island lying off northeast end of Willoughby Island, Glacier Bay, Alaska" (two islands lying off the northeast end of Willoughby Island, fig. 1). The numbers "873" and "993" refer to their catalog number in the USGS Silurian-Devonian locality register. Examination of Kirk's collection indicates that the species was part of a large-shelled molluscan assemblage which included *Euomphalopterus liratus* (Kirk, 1928), *Coelocaulus karlae* Rohr and others (in press), *Holopea* sp., and a large pleurotomaroid shell described here for the first time. Specimen numbers with a prefix of "USNM" are from the National Museum of Natural History, Washington, D.C., where the specimens are deposited. Enclosed in one gastropod shell is a large leperditiid ostracode. Soja and others (2000) reported this same molluscan fauna from Drake Island, where they are part of a carbonate lagoonal facies associated with a stromatolite reef. As noted by Blodgett and Rohr (1990, 1991), Silurian gastropods are poorly known from Alaska, and this chapter and the report by Rohr and others (in press) should provide a more detailed view of the gastropod fauna of that age from southern Alaska's accreted terranes.

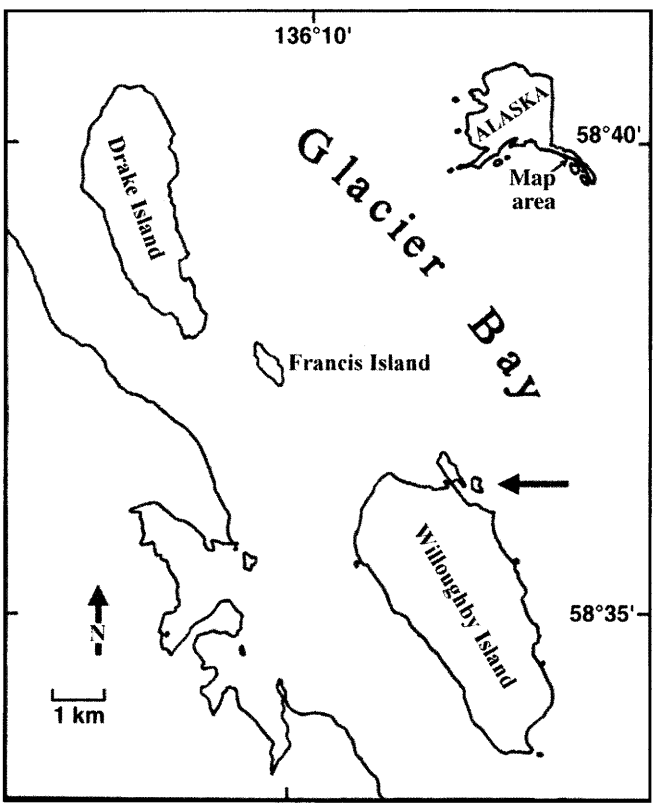

Figure 1. Glacier Bay, Alaska, showing location of Edwin Kirk's U.S. Geological Survey fossil locality 993–SD on a small island (arrow) northeast of Willoughby Island.

Paleobiogeographic Affinities of Silurian Faunas of the Alexander Terrane

In recent years, the concept that nearly all of Alaska, as well as much of the western Cordillera of North America, is composed of numerous discrete, accreted tectonostratigraphic terranes (Coney and others, 1980; Jones and others, 1981, 1982, 1986, 1987; Nokleberg and others, 1994) has gained general acceptance. Much of southeastern Alaska is considered part of the Alexander terrane. Despite having been better studied paleontologically than the rest of Alaska, the Alexander terrane of southeastern Alaska still remains relatively poorly known in comparison with cratonic North America. Nevertheless, the Silurian and Devonian shelly faunas of the Alexander terrane clearly demonstrate non-North American affinities and closer affinity with the Farewell terrane of southwestern Alaska, as well as with the Ural Mountains of Russia (Blodgett and others, in press). Although few faunal studies exist on Late Silurian gastropods from either Alaska or Russia, our limited data base indicates strong faunal ties between the gastropod faunas of the Alexander terrane with that of the Farewell terrane of southwestern Alaska (Rohr and others, in press) and the Ural Mountains (Chernyshev, 1893). Chernyshev focused on Early Devonian faunas of the Urals; however, the gastropod fauna particularly similar to the Late Silurian faunas of the Alexander and Farewell terranes is that reported from the Taltiya River (at the mouth of the Bobrovka), now considered to be of Ludlovian (middle Late Silurian) age (Melnikov and Khodalevich, 1965, p. 177).

The Late Silurian brachiopod fauna of the Alexander terrane shows its strongest affinity with that of the Ural Mountains of Russia, as is well demonstrated by the large distinctive pentamerid genera *Brooksina* Kirk, 1922, *Harpidium* Kirk, 1925, and *Cymbidium* Kirk, 1926, all based on specimens found in the Heceta Limestone in the area of Prince of Wales Island. These three genera occur together in one single collection, from USGS fossil locality 1005–SD in the Vermont Marble prospect on the south shore of Kosciusko Island (Kirk and Amsden, 1952, p. 53). In terms of overall brachiopod taxic composition, the faunal association from that locality closely matches the *Brooksina* Community of Sapelnikov and others (1999) on the basis of collections from the Lozva River, Ivdel region, east slope of the Northern Urals. As noted by Kirk and Amsden (1952, p. 54), the Heceta faunas most closely resemble Late Silurian faunas described by Khodalevich (1939) from the east slope of the Urals. The genus *Brooksina*, according to Sapelnikov (1985), is known from strata of late Wenlockian to Ludlovian age and occurs in both the east and west slopes of the Urals, Gornyi Altai, southern Tien Shan, Kazakhstan, and northeastern Siberia, as well as in Ludlovian strata of southeastern Alaska and Nevada (Johnson and others, 1976). The genus *Cymbidium*, according to Sapelnikov (1985), occurs in Ludlovian strata of southeastern Alaska and central Nevada and questionably in northeastern Siberia (the Omulevsk Mountains). The genus has also been recognized recently from Wenlockian strata on Baillie Hamilton Island, Canadian Arctic Islands (Zhang, 1989). The genus *Harpidium*, according to Sapelnikov (1985), ranges in age from late Llandoverian to Ludlovian and is much more widespread in distribution than the first two genera, occurring in the Urals, the Central Asia part of the former USSR, Kazakhstan, the Goryni Altai, northeastern USSR, southeastern Alaska, the midcontinental region of the United States (Iowa, Wisconsin, Ohio, and Illinois), and Greenland. The overall affinities of these three distinctive genera of the Alexander terrane remain closest to the Urals; although the genus *Cymbidium* has not been reported from there, it is reported questionably from the Kolyma region of Siberia.

As in the Farewell terrane, the Heceta Limestone of the Alexander terrane contains extensive buildups of Late Silurian algal-reef-mound complexes, containing an algal flora and associated sphinctozoan sponge complex known also in the Urals and the Farewell terrane (Riding and Soja, 1993; Soja and Riding, 1993; Rigby and others, 1994; Soja, 1994; Soja and Antoshkina, 1997; Soja and others, 2000). Similar buildups are unknown from nonaccreted rocks of equivalent age in North America.

Systematic Paleontology

Family PLETHOSPIRIDAE Wenz, 1938

Discussion.—In the classification of Wenz (1938), the subfamily Plethospiridae Wenz, 1938, was regarded as belonging to the Pleurotomarioidea. Knight and others (1960) transferred this subfamily and raised it in rank to a family within the superfamily Murchisonioidea Koken, 1896, without written explanation of evidence supporting this transferral.

KIRKOSPIRA n.gen.

Diagnosis.—Large, turbiniform gastropod with apical angle about 95°, extended narrowly phaneromphalous base, with thick, reflexed columellar lip. Selenizone above midwhorl, fine spiral ornamentation.

Type species.—*Kirkospira glacialis* n.sp.

Comparison.—The shell is similar in shape to *Phanerotrema* Fischer, 1885, but the selenizone is not as high on the whorl, and it lacks the ornamentation. The genus has a similar shape but has a less acute apical angle than *Plethospira* Ulrich in Ulrich and Scofield, 1897, and *Seelya* Ulrich in Ulrich and Scofield, 1897. The latter genera have been illustrated with inwardly reflexed columellar lips (Knight and others, 1960), but this feature is not shown well on the actual specimens (see Knight, 1941).

Etymology.—Genus named after Edwin Kirk, whose early studies of Alaskan fossils are the basis of this report.

Included species.—Only the type species.

Known stratigraphic range.—Late Silurian.

Known geographic range.—Southeastern Alaska (Alexander terrane)

***Kirkospira glacialis* n.sp.**
(Pl. 1, Figs. 2, 3)

Diagnosis.—By monotypy, same as the genus.

Holotype.—USNM specimen 520613. Paratypes USNM 520614–520617, both from USGS fossil locality 993–SD.

Etymology.—glacialis, Latin for ice, in reference to Glacier Bay, Alaska.

Description.—Relatively large (10 cm high), rounded gastropods with an apical angle of about 95° and a narrow, raised selenizone located above midwhorl. Whorl cross section rounded, rhombic, about twice as high as wide. Depth of sinus or slit unknown. Whorl surface curves convexly downward and outward from impressed suture to selenizone and then curves convexly downward and inward to meet columellar lip. Thick, outwardly reflexed columellar lip. Growth lines prosocline above selenizone and nearly orthocline below. Fine spiral ornamentation on some specimens. Cross sections show a deep, narrow umbilicus, possibly formed by the reflexed columella.

Discussion.—The description is based on 15 large, nonsilicified specimens that were separated from the limestone matrix by Edwin Kirk.

Occurrence.—USGS fossil localities 873–SD and 993–SD, "small island lying off northeast end of Willoughby Island, Glacier Bay, Alaska."

Acknowledgment

We thank A.J. Boucot and Ning Zhang, Department of Zoology, Oregon State University, for their helpful reviews of the manuscript.

References Cited

Blodgett, R.B., and Rohr, D.M., 1990, Silurian-Devonian gastropod biogeography of Alaska [abs.]: Geological Society of America Abstracts with Programs, v. 22, no. 7, p. A221.

———1991, Silurian and Devonian gastropods of Alaska, *in* Abstracts and proceedings of the annual meeting of the Western Society of Malacologists on current directions in Alaskan malacology: Western Society of Malacologists Annual Report, v. 23, p. 15–16.

Blodgett, R.B., Rohr, D.M., and Boucot, A.J., 2002, Paleozoic links among some Alaskan accreted terranes and Siberia based on megafossils, *in* Miller, Elizabeth, Grantz, Art, and Klemperer, Simon, eds., Tectonic evolution of the Bering Shelf-Chukchi Sea-Arctic margin and adjacent landmasses: Geological Society of America Special Paper 360, p. 273–291.

Chernyshev, F.N., 1893, Fauna nizhnyago devona vostochnago sklona urala: Trudy Geologiceskago Komiteta, v. 4, no. 3, 221 p.

Churkin, Michael, Jr., 1973, Paleozoic and Precambrian rocks of Alaska and their roles in its structural evolution: U.S. Geological Survey Professional Paper 740, 64 p.

Coney, P.J., Jones, D.L., and Monger, J.W.H. 1980, Cordilleran suspect terranes: Nature, v. 288, no. 5789, p. 329–333.

Fischer, P.H., 1887, Manuel de conchyliologie et de paléontologie conchyliologique, ou histoire naturelle des mollusques vivants et fossiles: Paris, F. Savy, 1,369 p.

Gryc, George, Dutro, J.T., Jr., Brosge, W.P., Tailleur, I.L., and Churkin, Michael, Jr., 1967, Devonian of Alaska, *in* Oswald, D.H., ed., International symposium on the Devonian System: Calgary, Alberta Society of Petroleum Geologists International Symposium on the Devonian System, v. 1, p. 703–716.

Johnson, J.G., Boucot, A.J., and Murphy, M.A., 1976, Wenlockian and Ludlovian age brachiopods from the Roberts Mountains of central Nevada: University of California Publications in Geological Sciences, v. 115, 102 p.

Jones, D.L., Silberling, N.J., Berg, H.C., and Plafker, George, 1981, Map showing tectonostratigraphic terranes of Alaska, columnar sections, and summary description of terranes: U.S. Geological Survey Open-File 81–792, 20 p., 2 sheets, scale 1:2,500,000.

Jones, D.L., Silberling, N.J., and Coney, P.J., 1986, Collision tectonics in the Cordillera of western North America; examples from Alaska, *in* Coward, M.P., and Ries, A.C., eds., Collision tectonics: Geological Society of London Special Publication 19, p. 367–387.

Jones, D.L., Silberling, N.J., Coney, P.J., and Plafker, George, 1987, Lithotectonic terrane map of Alaska (west of the 141st Meridian): U.S. Geological Survey Map MF–1874–A, scale 1:2,500,000.

Jones, D.L., Silberling, N.J., Gilbert, W.G., and Coney, P.J., 1982, Character, distribution, and tectonic significance of accretionary terranes in the central Alaska Range: Journal of Geophysical Research, v. 87, no. B5, p. 3709–3717.

Khodalevich, A.N., 1939, Verkhnesiluriiskie brakhiopody vostochnogo sklona urala: Trudy Uralskogo Geologicheskogo Upraveleniya, Izdanie Uralgeoupravleniya, Sverdlovsk, 135 p.

Kirk, Edwin, 1922, *Brooksina*, a new pentameroid genus from the Upper Silurian of southeastern Alaska: U.S. National Museum Proceedings, v. 60, art. 19, p. 1–8.

———1925, *Harpidium*, a new pentameroid brachiopod genus from southeastern Alaska: U.S. National Museum Proceedings, v. 66, art. 32, p. 1–7.

———1926, *Cymbidium*, a new genus of Silurian pentameroid brachiopods from Alaska: U.S. National Museum Proceedings, v. 69, art. 23, p. 1–5.

———1927a, *Pycinodesma*, a new name for Pycnodesma Kirk not Schrammen: Washington Academy of Sciences Journal, v. 17, p. 543.

———1927b, *Pycnodesma*, a new molluscan genus from the

Silurian of Alaska: U.S. National Museum Proceedings, v. 71, art. 20, 9 p.

———1928, *Bathmopterus*, a new fossil gasteropod genus from the Silurian of Alaska: U.S. National Museum Proceedings, v. 74, art. 18, p. 1–4.

Kirk, Edwin, and Amsden, T.W., 1952, Upper Silurian brachiopods from southeastern Alaska: U.S. Geological Survey Professional Paper 233–C, p. 53–66.

Knight, J.B. 1941, Paleozoic gastropod genotypes: Geological Society of America Memoir 32, 510 p.

Knight, J.B., Batten, R.L., Cox, L.R., Keen, A.M., Robertson, Robert, and Yochelson, E.L., 1960, Systematic descriptions [Archaeogastropoda], *in* Moore, R.C.., ed., Mollusca, pt. 1 *of* Treatise on invertebrate paleontology: Lawrence, Kans., Geological Society of America and University of Kansas Press, p. I169–I310.

Koken, Ernst, 1896, Die Leitfossilien; ein Handbuch für den Unterricht und für das Bestimmen von Versteinerungen: Leipzig, C.H. Tauchnitz, 848 p.

Melnikov, A.S., and Khodalevich, A.N., 1965, Vostochnogo sklon urala—severnyi i srednii ural, *in* Nikiforova, O.I., and Obut, A.M., eds., Stratigrafiya SSSR v chetyrnatsati tomakh, Siluriiskaya Sistema: Moscow, Izdatelstvo "Nedra," p. 171–182.

Nokleberg, W.J., Moll-Stalcup, E.J., Miller, T.P., Brew, D.A., Grantz, Art, Reed, J.C., Jr., Plafker, George, Moore, T.E., Silva, S.R., and Patton, W.W., Jr., *with contributions on specific regions by* Blodgett, R.B., Box, S.E., Bradley, D.C., Bundtzen, T.K., Dusel-Bacon, Cynthia, Gamble, B.M., Howell, D.G., Foster, H.L., Karl, S.M., Miller, M.L., and Nelson, S.W., 1994, Tectonostratigaphic terrane and overlap assemblage map of Alaska: U.S. Geological Survey Open-File Report 94–194, 53 p., scale 1:2,500,000.

Riding, Robert, and Soja, C.M., 1993, Silurian calcareous algae, cyanobacteria, and microproblematica from the Alexander Terrane, Alaska: Journal of Paleontology, v. 67, no. 5, p. 710–728.

Rigby, J.K., Nitecki, M.H., Soja, C.M., and Blodgett, R.B., 1994, Silurian aphrosalpingid sphinctozoans from Alaska and Russia: Acta Palaeontologica Polonica, v. 39, no. 4, p. 341–391.

Rohr, D.M., Blodgett, R.B., and Frýda, Jiří, in press, New Silurian murchisoniid gastropods from Alaska and a review of the genus Coelocaulus, in Clautice, K.H., eds., Short notes on Alaska geology, 2001: Alaska Division of Geological & Geophysical Surveys Professional Report.

Rossman, D.L., 1963, Geology of the eastern part of the Mount Fairweather quadrangle, Glacier Bay, Alaska, *in* Contributions to general geology, 1960: U.S. Geological Survey Bulletin 1121–K, p. K1–K57.

Sapelnikov, V.P., 1985, Sistema i stratigraficheskoe znachenie brakhiopod podotryada pentameridin: Moskva, "Nauka," 208 p.

Sapelnikov, V.P., Bogoyavlenskaya, O.V., Mizens, L.I., and Shuysky, V.P., 1999, Silurian and Early Devonian benthic communities of the Ural-Tien Shan region, *in* Boucot, A.J., and Lawson, J.D., eds., Paleocommunities—a case study from the Silurian and Lower Devonian. New York, Cambridge University Press p. 510–544.

Soja, C.M., and Antoshkina, A.I., 1997, Coeval development of Silurian stromatolite reefs in Alaska and the Urals Mountains; implications for paleogeography of the Alexander terrane: Geology, v. 25, no. 6, p. 539–542.

Soja, C.M., and Riding, Robert, 1993, Silurian microbial associations from the Alexander terrane: Journal of Paleontology, v. 67, no. 5, p. 728–738.

Soja, C.M., White, Brian, Antoshkina, Anna, Joyce, Stacey, Mayhew, Lisa, Flynn, Brian, and Gleason, Alison, 2000, Development and decline of a Silurian stromatolite reef complex, Glacier Bay National Park, Alaska: Palaios, v. 15, no. 4, p. 273–292.

Ulrich, E.O., and Scofield, W.H., 1897, The Lower Silurian Gastropoda of Minnesota, pt. 2 *of* Paleontology, v. 3 *of* The geology of Minnesota: Minneapolis, Minnesota Geological Survey, p. 813–1081.

Wenz, Wilhelm, 1938, Allgemeiner Teil und Prosobranchia, pt. 1 *of* Schindewolf, O.H., ed., Gastropoda, v. 6 *of* Handbuch der Paläozoologie: Berlin, Gebrüder Borntraeger, p. 1–240.

Zhang, Ning, 1989, Wenlockian (Silurian) brachiopods of the Cape Phillips Formation, Baillie Hamilton Island, Arctic Canada, part II: Palaeontolographica, pt. A, v. 206, p. 99–135.

PLATES 1, 2

Plate 1.

Figures 1–4. *Kirkospira glacialis* n.sp. from Upper Silurian part of the Willoughby Limestone.

1. Side view showing peripheral band above midwhorl. U.S. National Museum (USNM) paratype 520614. Magnification, ×1.
2. Detail of growth lines and fine, spiral threads. USNM paratype 520615. Magnification, ×2.
3. Side of view, ×1, showing shape of whorl and columellar lip. USNM holotype 520613. Magnification, ×1.
4. Side view of fragmentary specimen. USNM paratype 520616. Magnification, ×1.

1

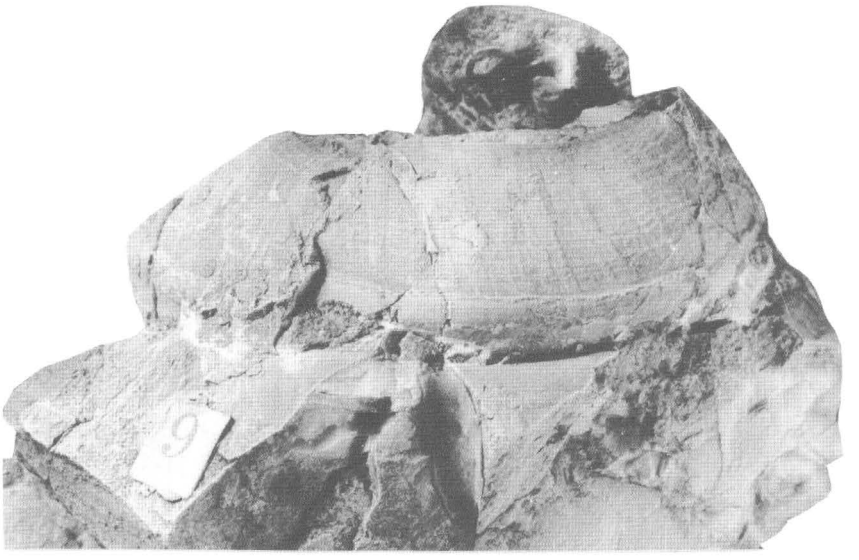

2

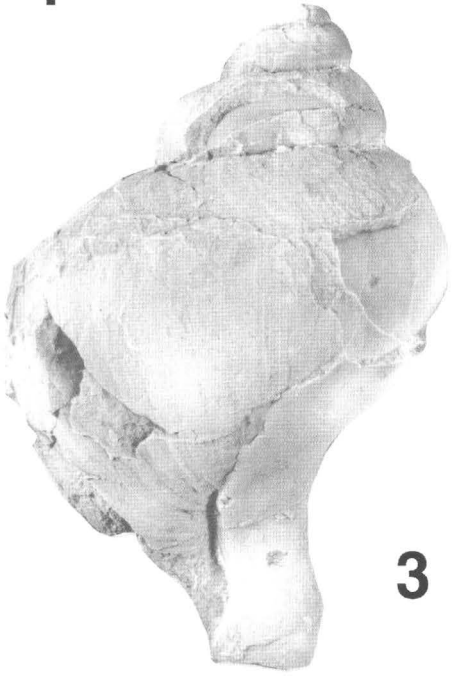

3

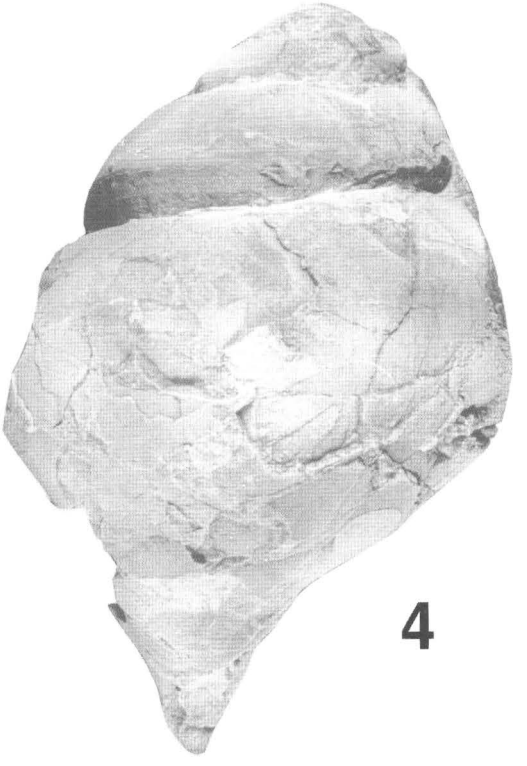

4

Plate 2.

Kirkospira glacialis n.sp. at U.S. Geological Survey locality 993–SD. Upper Silurian part of the Willoughby Limestone. Cross-sectional views showing narrow umbilicus. USNM paratypes 520617a and 520617b. Magnification, ×1

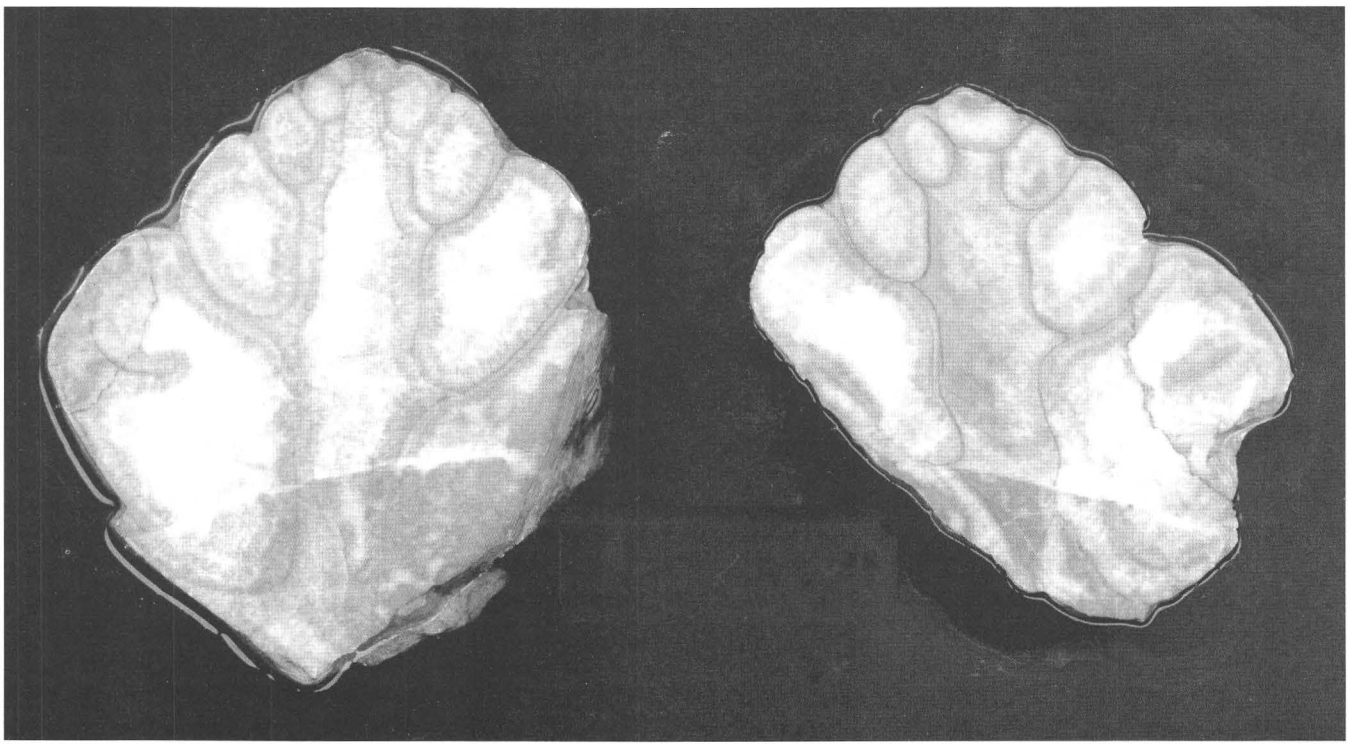

Studies by the U.S. Geological Survey in Alaska, 2001
U.S. Geological Survey Professional Paper 1678

Soil Temperature, Moisture, and Carbon and Nitrogen Mineralization at a Taiga-Tundra Ecotone, Noatak National Preserve, Northwestern Alaska

By Robert Stottlemyer, Charles Rhoades, and Heidi Steltzer

Abstract

Northwestern Alaska has been warming (0.3°C/yr) since the early 1990s. Ecotonal (treeline) Arctic ecosystems are expected to exhibit the effects of climate change earliest. High-latitude terrestrial ecosystems contain from 30 to 45 percent of the global organic-C pool. Soil warming may enhance release of CO_2 and CH_4, soil N mineralization, and the production and export of dissolved organic C and N to the aquatic ecosystem. In 1990, we began our research on climate-change effects in the small (800-ha area) Asik watershed, Noatak National Preserve, northwestern Alaska. We report results here from an intensive study conducted during 1997–98 on the relation between soil temperature, moisture, and C and N mineralization rates across a treeline taiga-tundra ecotone within the watershed. Soil C and N contents and C/N ratio were greater ($p<0.05$) beneath tundra. The depth of the soil active layer (annual thaw depth) increased ($p<0.001$) more than 40 cm during the growing season. Thaw depths reached most of the deeper layers of surface organic matter. Despite this warming, most plots did not show a clear relation between soil temperature and soil respiration (CO_2 efflux). Peak soil temperatures were below the threshold needed for a respiration response to temperature, and the thawing resulted in saturated deeper soils keeping temperatures low. Soil C respiration rates did increase through the summer. Soil inorganic-N pools were larger early in summer ($p<0.001$) and beneath tundra ($p<0.05$). Net N mineralization rates were higher ($p<0.01$) in spruce but were positive only during early summer. Rates were negative for tundra and the taiga-tundra transition zone. In midsummer, soil microbial N consumption exceeded gross N mineralization rates except beneath tundra. Rates of gross ammonification ($p<0.01$) and microbial N consumption ($p=0.05$) increased with moisture content in the surface organic matter (Oa soil horizon). Soil-water organic and inorganic chemistry did not reflect the patterns in stream water, suggesting that the processes observed within these plots may not dominate at the watershed level. Stream-water NO_3^- concentrations at the mouth of the watershed increased with discharge ($p<0.01$, $r^2=0.52$), and autumn inorganic-N flux from the watershed increased tenfold from summer lows.

Introduction

Ecotonal Arctic and high-latitude boreal ecosystems are expected to exhibit the effects of climate change earliest and to a greater degree than other regions (Shaver and others, 1992). High-latitude taiga and tundra ecosystems have large, mostly unavailable organic reservoirs of carbon, nitrogen, and phosphorus. Typically, more than 95 percent of total ecosystem carbon, nitrogen, and phosphorus is contained in soil organic matter (SOM). The nutrient and C storage in SOM pools is a function of high soil moisture and low temperature, which slow decomposition. The percentage of an ecosystem's organic-matter pools stored in the soil increases with latitude, further limiting nutrient availability.

In the Alaska taiga-tundra ecotone at the northward extent of the boreal biome, much of this organic matter is deeper than the annual soil thaw zone (soil active layer) and unavailable to the C or nutrient cycles. In this extensive taiga-tundra region, any factor that increases the depth or temperature of the soil active layer could reduce soil moisture content but increase SOM decomposition, nutrient availability and cycling rates, and soil respiration rate (Chapin and others, 1995; Jonasson and others, 1999). Our studies in the southern boreal Wallace Lake watershed, Isle Royale National Park, Mich., show that slight gains in SOM decomposition will increase available nutrients as inorganic N in amounts greater than the sum of other nitrogen sources (precipitation, fixation) (Stottlemyer and Toczydlowski, 1999a, b). An increase in N availability will alter above- or below-ground C/N ratios, which, in turn, could accelerate above-ground production or below-ground heterotrophic respiration (Shaver and others, 1992). Which process occurs most rapidly could determine whether the ecosystem becomes a C source or sink. Change in such processes, especially in the taiga-tundra ecotone, may lead to altered patterns of treeline advance (Lloyd and Graumlich, 1997; Suarez and others, 1999).

The strong interaction of the C cycle with nutrients complicates prediction of the taiga-tundra and boreal ecosystem response to climate change (Shaver and others, 1992; Stottlemyer and others, 1995; McKane and others, 1997). The effect of climate change on the N cycle, in particular, will determine or constrain the effect of such change on the C cycle. Soil C provides energy for microbial transformations that, in turn, regulate ecosystem N availability, and N availability largely determines biomass-production rates in the taiga-tundra ecotone.

An additional dimension in assessing the effects of climate change on high-latitude ecosystems is the likely variation in export of dissolved organic carbon (DOC) and dissolved organic nitrogen (DON). Changes in N availability due to climate change could increase forest-floor and soil DOC and DON production. However, there has been little study of how a change in N availability might alter DOC and DON production and export to the aquatic ecosystem, where these more labile organic C and N forms are important energy and nutrient sources. The export of DOC and DON to the aquatic ecosystem is primarily a function of seasonal flowpath (Rice and Bricker, 1995; McNamara and others, 1997; Kallbitz and others, 2000) and, probably, soil temperature, moisture, total C and N pool size and quality, and (inorganic) N availability (Sommaruga and others, 1999; Kallbitz and others, 2000; Lipson and others, 2000).

Research was initiated in 1990 in the treeline Asik watershed (800-ha area), a U.S. Geological Survey Reference Ecosystem in Noatak National Preserve, northwestern Alaska (Binkley and others, 1994, 1995; Suarez and others, 1999; Rhoades and others, 2001; Stottlemyer, 2001). Much of this study has focused on quantifying the sensitivity of the terrestrial ecosystem to climate change, especially temperature and available nitrogen. This chapter updates results from studies on treeline sensitivity to climate change and presents (1) preliminary results from a recent intensive study of below-ground processes in taiga, tundra, and the taiga-tundra transition zone; and (2) a summary of current and planned site research.

Methods

Site Description

The 800-ha-area treeline Asik watershed (lat 67°58′ N., long 162°15′ W.) is in Noatak National Preserve, 95 km north-

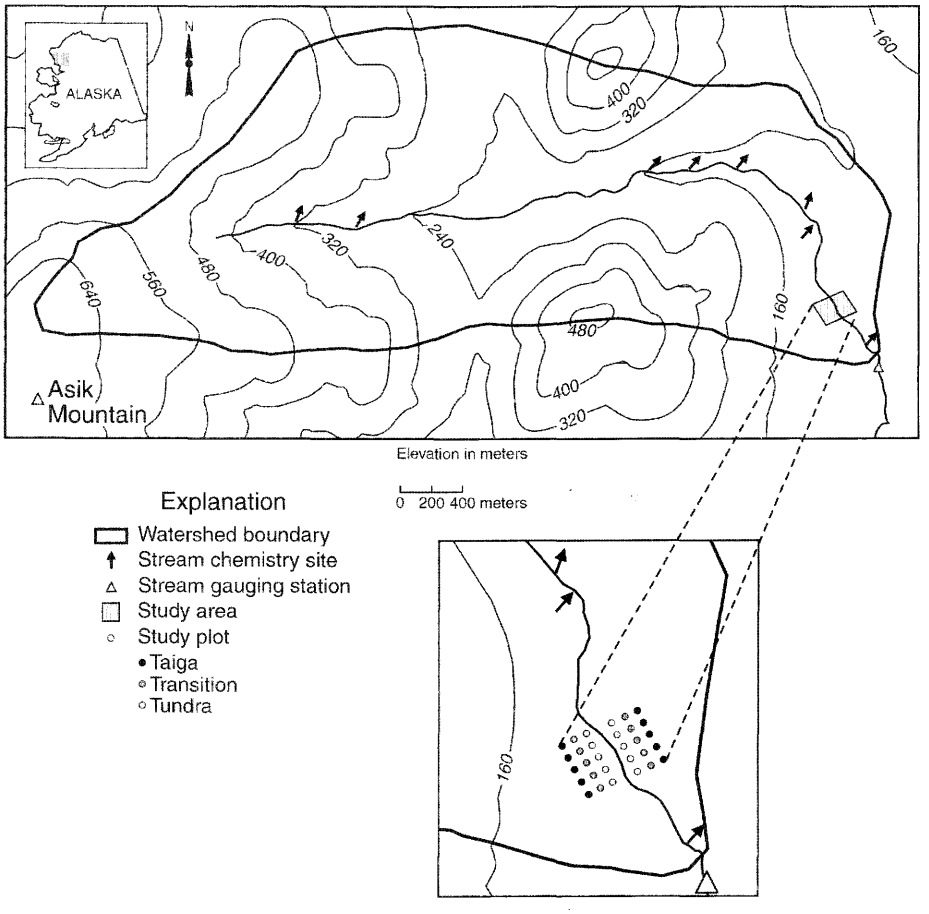

Figure 1. Asik watershed (lat 67°58′ N., long 162°15′ W.), Agashashok River drainage, Noatak National Preserve, northwestern Alaska, showing location of study area.

east of Kotzebue, Alaska (fig. 1). Watershed elevation ranges from 100 to 725 m, and its first-order stream drains from the north and northwest into the Agashashok River. Temperatures in the Arctic region and locally have been warming (Illeris and Jonasson, 1999; Herrmann and others, 2000). National Oceanographic Atmospheric Administration (NOAA) temperature data from northwestern Alaska show a warming trend (0.3°C/yr) since the late 1980s, approaching the maximum recorded. However, no annual trend in precipitation has been observed. During the 1997–98 growing season in the Asik watershed, the mean daily air temperature was 11.6°C, about 1°C warmer than in previous and subsequent summers.

The soils of the Asik watershed are dominated by volcanic ash and loess. At the subgroup level, the soils are generally considered as Histic Pergelic Cryaquepts. Discontinuous permafrost exists in the watershed, especially where no forest is present. The bedrock is sedimentary and metamorphic rock, and 5 to 7 percent of the watershed area is covered by talus.

About 60 percent of the watershed area is forested. Better-drained parts of the lower third and most of the middle half of the watershed are dominated by white spruce (*Picea glauca* [Moench] Voss). Spruce basal area ranges from 23 m^2/ha in bottom land to 4 m^2/ha on southern aspects (Suarez and others, 1999). Forest understory consists primarily of *Hylocomium splendens* (Hedw.) B.S.G, *Equisetum arvense* L., and *Boykinia richardsonii* (Hook.) Gray, with shrubs of *Salix* and *Vaccinium uliginosum* L. The understory of the taiga-tundra transition zone and tundra is dominated by tussocks of *Eriophorum vaginatum* L., *Vaccinium uliginosum*, *Potentilla fruticosa* L., and *Betula nana* L. A more detailed site description of the watershed was presented by Stottlemyer (2001).

This study was conducted in the lower third of the watershed above the stream-gauging station at the mouth (fig. 1). A total of 30 25-m^2-area plots, at least 15 m apart, were established in a rough grid pattern; 15 plots were located on an eastern aspect (slope 10 percent), with transects of 5 plots each in wet sedge tundra at the toe of the slope, the transition between tundra and taiga, and in spruce. This layout was repeated across the stream, opposite the first array, in an area with a slope of 10 to 12 percent and a western aspect. In the study plots, surface mineral soils were typically covered by 20 to 30 cm of organic matter consisting of recent litterfall (Oi horizon) and partially decomposed debris (Oa horizon).

The center of each plot was flagged. Each plot was equipped with a tension lysimeter (at 30-cm depth in the Oi horizon) to sample the soil solution. A subset of six plots was equipped with Licor dataloggers that continuously monitored air temperature, as well as temperature at 5-, 10-, and 20-cm depth in the Oi horizon. All the data presented here were collected from these six plots.

The depth of the soil active layer (thaw depth) was measured by driving in a pointed stainless-steel rod at 10 additional plots located along a transect tangential to the stream and conterminous with the south boundary of the soil-process plot layout. At each plot and sampling date, four measurements were taken and averaged.

Nitrogen and Carbon Mineralization and Pools

Measurements were made of net NO_3^-, NH_4^+, and total inorganic-N mineralization in each plot at intervals of 3 or 4 weeks, using the buried-polyethylene-bag method (Eno, 1960). With this method, net mineralization is the sum of mineralized NH_4^+ plus NO_3^- from organic N, minus microbial immobilization of NH_4^+ and NO_3^-. Net nitrification is the sum of NO_3^- from both organic N and NH_4^+, minus microbial immobilization of NO_3^-.

After the surface organic matter (Oi soil horizon) was removed intact, the uppermost 10 cm of the Oa/Oe horizon was sampled with a 5-cm-diameter soil corer. Paired cores were retained from each plot. One core from each pair, representing a nonincubated sample, was placed in a Whirl Pac and brought to the field laboratory; the other core was placed in a 0.025-mm-thick polyethylene bag and returned to the same hole for incubation. The surface organic matter was then replaced. After about 20 to 25 days, the field-incubated sample was removed and returned to the field laboratory for processing.

Soil moisture was determined by oven drying (105°C for 24–30 hours) a subsample, with the moisture content (in percent) equal to the weight of water lost per soil dry weight times 100. Bulk density was calculated from the ratio of total oven-dry weight to total soil volume. A large subsample was then sieved in a 2-mm sieve. The <2-mm fraction was weighed and divided into two samples; one subsample was extracted for NO_3^- and NH_4^+ by using 2M KCl, and the other frozen for total C and N analyses on a Leco CHN analyzer at our laboratory in Fort Collins, Colo.

The ^{15}N isotope-dilution method was used to estimate inplace gross N ammonification and nitrification rates. Field incubations were conducted in early July 1997. Gross mineralization is defined as the sum of NH_4^+ from organic N, and gross nitrification as the sum of NO_3^- from NH_4^+ and organic-N substrates. On the date of the analysis, net mineralization and nitrification were estimated by the methods described above. Initial inorganic-N pools in the soils were determined, and a net mineralization and nitrification incubation (20–25 days) started as described above. In addition, a separate set of intact soil cores was collected immediately adjacent to the net incubation samples and processed as follows. Using a spinal needle (18 gauge, 10 cm long) and syringe, one intact core received a 6-mL aliquot of $Na^{15}NO_3$ solution, providing about 2 µg N/g of soil (dry-weight equivalent). A separate intact core received 6 mL of $(^{15}NH_4)_2SO_4$ solution, again providing about 2 µg N/g of soil.

After a 24-hour inplace incubation period, the cores were retrieved, taken to the field laboratory, and mixed, and a subsample was extracted by using 2M KCl. After at least 1 hour of mixing, all KCl extractions were filtered through Whatman No. 1 filters prerinsed with 2M KCl. The samples were forwarded to our laboratory in Fort Collins, Colo., where NH_4^+ and NO_3^- analyses were made on a Lachat flow-injection autoanalyzer. Nitrogen diffusion (Brooks and others, 1989)

was used to prepare the samples for ^{15}N analyses by using glass-fiber filter traps. Gross NH_4^+ immobilization and mineralization rates were calculated for the cores labeled with $^{15}NH_4^+$ by the isotope-dilution method of Kirkham and Bartholomew (1954), and gross NO_3^- immobilization and mineralization rates were calculated for cores labeled with $^{15}NO_3^-$ by using the same method but replacing NO_3^- for NH_4^+. The ^{15}N-enriched samples were analyzed by mass spectroscopy at the University of California, Davis.

Soil respiration rates, as indicated by surface CO_2 efflux, were determined by using the dynamic method on a PP Systems portable infrared gas analyzer.

Stream and Lysimeter Samples

Stream samples were collected weekly just above the gauging station, using 500-mL amber polyethylene bottles. Soil solution was collected from tension porous-cup lysimeters. Tension was placed on the lysimeters 24 hours before sample collection. Stream- and soil-water samples were taken to the field laboratory, where pH, alkalinity, and specific conductance were measured and a subsample filtered (0.45 µm) for ion or dissolved-organic-matter analyses. Field analyses were generally completed within 8 to 12 hours after sample collection.

The filtered subsamples were then shipped to our laboratory in Fort Collins and analyzed for macroions (Ca^{2+}, Mg^{2+}, Na^+, K^+, NH_4^+, PO_4^{3-}, Cl^-, NO_3^-, SO_4^{2-}) on a Waters ion chromatograph. DOC content was determined on filtered samples kept frozen until analyzed on a Shimadzu TOC–5000 Series analyzer.

Data Analyses

We used ANOVA to test for differences by vegetation type, soil depth, and date. The homogeneity of variance was checked (Bartlett's test) for each variable analyzed. The plot layout was on gradually sloping areas with clearly defined taiga-tundra gradients on eastern and western aspects. Although slopes were slight, we checked for any differences by aspect; none were present. Statistical analyses were done by using Systat modules (Wilkinson, 1990).

Results

Soil Thaw Depth, Temperature, and Moisture Content

The depth of the soil active layer (thaw depth) was similar beneath the three vegetation types but increased ($p<0.001$) to more than 40 cm during the growing season (fig. 2; table 1). Soil temperatures at 10-cm depth in the Oa horizon increased ($p<0.001$, $r^2=0.5$) during the growing season and were correlated ($p<0.001$, $r^2=0.58$) with thaw depth. The maximum seasonal mean temperature in the Oa horizon occurred beneath tundra in early August. At the continuously monitored subset of plots, daily soil temperatures at 5-, 10-, and 20-cm depth in the Oa horizon also increased ($p<0.001$, $r^2>0.2$; not plotted) during the growing season. Daily mean temperatures at 5-cm depth in the Oa horizon ranged from 2.6 to 10.5°C, at 10-cm depth from 1.4 to 8.7°C, and at 20-cm depth from 0.3 to 5.6°C.

Soil moisture content, expressed as a percentage of soil dry weight, was more than 200 percent throughout the growing season; it showed no seasonal trend (fig. 2).

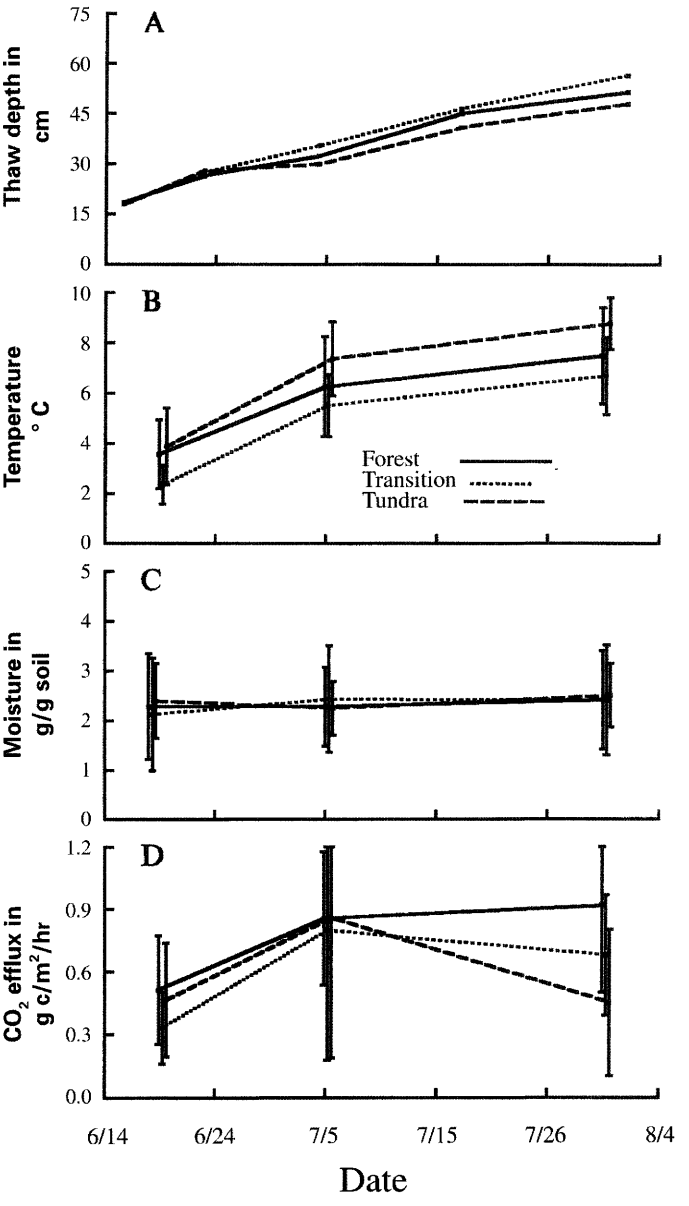

Figure 2. Seasonal changes in the Asik watershed, Noatak National Preserve, northwestern Alaska, during June–August 1997, *A*, Depth of thaw (soil active layer) from surface of Oi. *B*, Soil temperature at 10-cm depth in Oa. *C*, Soil moisture at 1 to 10 cm depth in Oa. *D*, Soil CO_2 efflux from Oa surface.

Table 1. Change in soil physical properties, N pools, and processes during the growing season from early to late summer 1997 in the Asik watershed, Noatak National Preserve, northwestern Alaska.

[All measurements except thaw depth and CO_2 efflux were taken in the top 10 cm of the Oa soil horizon. ns, not significant]

	Probability (p)	Increase (+) or decrease (−)
Soil thaw depth	<0.001	+
Soil temperature	<.001	+
Soil moisture content	>.05	ns
Soil inorganic-N pool	<.001	−
Soil NO_3^- pool	<.001	−
Soil CO_2 efflux	<.001	+
Net N mineralization	>.05	ns
Net nitrification	>.05	ns

Soil Carbon and Nitrogen Pools

In the surface organic matter (Oa and Oe soil horizons), C and N percentages were greater (p<0.05) beneath tundra than in either spruce or the transition zone, and the C/N ratio was greater beneath tundra than in spruce (fig. 3). The C content (p<0.01) and N content (p<0.05) were greater beneath tundra than in either spruce or the transition zone. The C and N contents in the Oa soil horizon were lower (p<0.001) than in the Oe soil horizon.

The inorganic-N pool size differed by vegetation type (p<0.05) and season (p<0.001) (fig. 4; table 1). Pools were greater beneath tundra (mean, 239 mg N/m^2). The average N pool size was 169 mg N/m^2 in the transition zone and 189 mg N/m^2 in the forest. Seasonally among all vegetation types, the inorganic-N pool size decreased from 234 mg N/m^2 in early July to 52 mg N/m^2 in August. The variation in seasonal inorganic-N pool size was greatest beneath tundra (180–929 mg N/m^2). The NO_3^--N pool did not differ by vegetation type but declined (p<0.001) during the growing season. The NO_3^--N pool made up 13 percent of the total inorganic N.

Soil Respiration and Nitrogen Mineralization

Soil respiration rates, as estimated by CO_2 efflux (fig. 2) in the Oi horizon, did not differ by vegetation type. Pooling the results from all plots, CO_2-efflux rates were lower (p<0.001) in June than in July or August. For all sample dates combined, CO_2 efflux was unrelated to the soil temperature measured at 10-cm depth in the Oi horizon. In June, however, there was a weak (p<0.05, r^2=0.16) positive correlation of CO_2 efflux with temperature for all vegetation types. For the growing season, only spruce showed a positive, but weak,

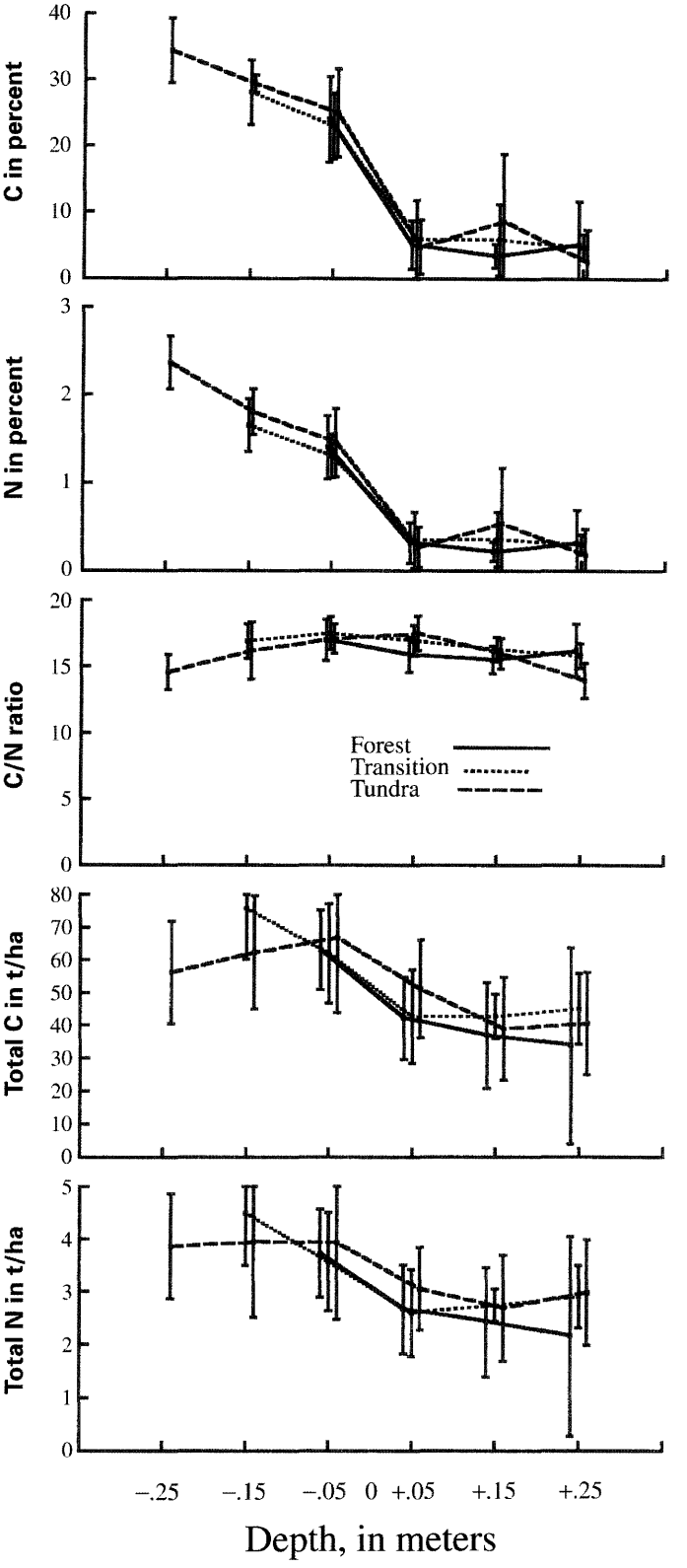

Figure 3. Total C and N contents in surface organic matter and mineral soils, C/N ratios, and organic-C and organic-N pool sizes, by vegetation type, at plots in the Asik watershed, Noatak National Preserve, northwestern Alaska,. 0-m reference depth is interface between Oa and Oe soil horizons. Samples were collected July 31-August 1, 1997.

correlation ($p<0.05$, $r^2=0.18$) between CO_2 efflux and surface temperature. The averaged mean daily temperatures monitored by data loggers at three depths (5, 10, and 20 cm) in the Oi horizon in spruce showed an inverse relation ($p<0.01$, $r^2=0.26$) between CO_2 efflux and soil temperature in early August.

Net N mineralization rates from mid-June to early August were negative except in spruce (table 2). By vegetation type, net ammonification and nitrification rates were higher ($p<0.05$) in spruce, as were net N mineralization rates ($p<0.01$). Sampling frequency was insufficient to analyze for seasonal trends. The net ammonification, nitrification, and total N mineralization rates were negatively correlated ($p<0.001$) with inorganic-N pool size.

Gross N mineralization and microbial consumption rates, as determined by the enriched ^{15}N dilution procedure, showed that total mean microbial N consumption exceeded ammonification and nitrification rates everywhere except beneath the sedge tundra (table 2). In spruce, the NH_4^+-N consumption rate exceeded ($p<0.05$) the gross ammonification rate. Pooling the results from all three vegetation types, NO_3^--N consumption exceeded ($p<0.001$) gross nitrification rates. Differences were most evident in spruce ($p<0.001$) and beneath sedge tundra ($p<0.01$).

Although gross N ammonification rates increased with temperature at 10-cm depth in the Oa horizon, the relation was not significant ($p=0.2$). Gross N ammonification rates increased ($p<0.01$) with soil moisture content, as did microbial consumption ($p=0.05$) at 0- to 10-cm depth in the Oa horizon. Gross nitrification rates were correlated with the initial NH_4^+ pool ($p<0.01$), NO_3^- pool, and total inorganic-N pool size ($p<0.001$). Gross NO_3^- consumption was also related ($p<0.05$) to the initial inorganic-N pool size.

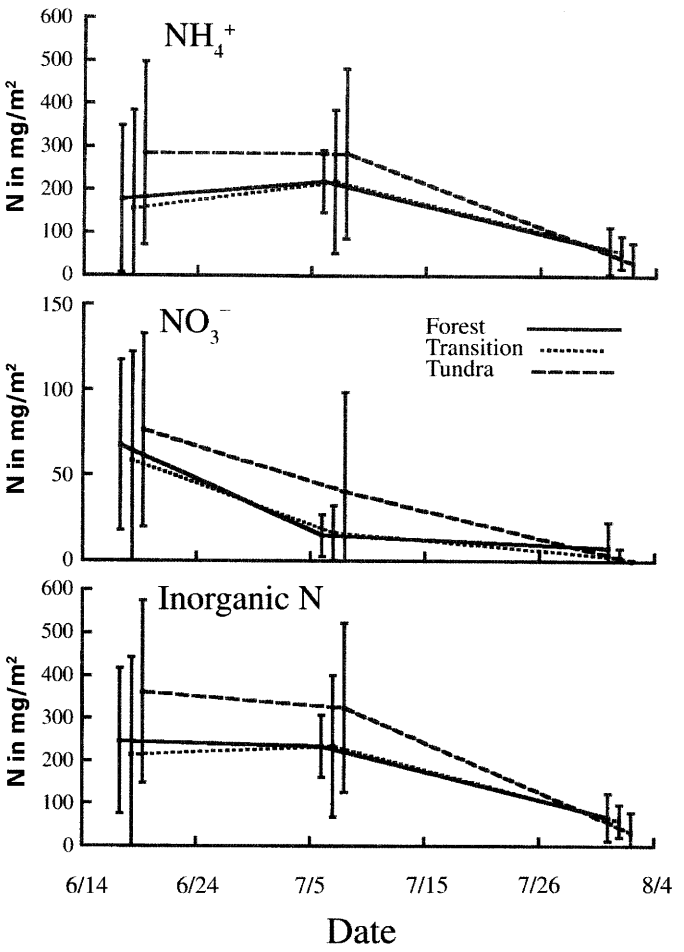

Figure 4. Seasonal changes during June–August 1997 in soil inorganic-N pool size, by vegetation type, at plots in the Asik watershed, Noatak National Preserve, northwestern Alaska.

Soil and Stream Water

Soil water may not have been sampled frequently enough to provide a temporal comparison with stream water. Many of the lysimeters were frozen well into July. Ca^{2+} concentrations (1,753±450 μequiv/L, table 3) in soil water averaged 70 percent of those in stream water at the mouth of the watershed. NO_3^- concentrations in soil water were 16 percent, and SO_4^{2-} concentrations 25 percent, of those in stream water. In contrast, the DOC content of soil water was more than 6 times that of stream water.

During the year, stream-water NO_3^- concentrations at the mouth of the watershed increased with discharge ($p<0.01$, $r^2=0.52$, fig. 5), whereas stream-water base-cation (CB) concentrations, as indicated by Ca^{2+} concentration, did not show the usual inverse relation with discharge.

Discussion

Soil Thaw Depth, Temperature, and Moisture

The increase in thaw depth during the growing season reached all layers of surface organic matter and the shallow mineral soils (figs. 2, 3). Thaw depths could already reflect the recent warming-trend ecologic responses to change in thaw depth that can occur within a few years, and have been documented in central Alaska for the early 1990s (Jorgenson and others, 2001). With the increase in regional temperatures since the 1960s, particularly in late spring (Herrmann and others, 2000), the rate and depth of annual thaw will likely increase. Increases could be accentuated on steeper, better-drained slopes, especially on southern aspects at this latitude. At present, thaw depths include soils with the highest C and N contents (figs. 2, 3). Any change in temperature or moisture content at these depths could alter C and N mineralization rates, increase CO_2 loss from organic-C decomposition, and increase NH_4^+ and NO_3^- availability for microbial or above-ground plant uptake (Stottlemyer, 2001).

Several factors, however, complicate estimating the degree to which this ecosystem might become a C source. The interaction between surface-organic-matter thickness and

Table 2. Net N mineralization and nitrification rates during two incubation periods from June 15 to August 5, 1997, and gross N mineralization, nitrification, and consumption rates during July 4–5, 1997, in the Asik watershed, Noatak National Preserve, northwestern Alaska.

[All values in milligrams per square meter per day]

	N Mineralization		Total inorganic N	N Consumption	
	NH_4^+-N	NO_3^--N		NH_4^+-N	NO_3^--N
Net rates (June 15–Aug. 5)					
Spruce	1.0	–0.3	0.6	--	--
Transition	–1.2	–1.1	–2.3	--	--
Tundra	–4.8	–1.9	–6.8	--	--
Gross rates (July 4–5)					
Spruce	483	21	--	541	135
Transition	417	75	--	464	186
Tundra	354	124	--	339	242

soil temperature and moisture content determines much of the productivity from these taiga-tundra sites. The thick layers of surface organic matter in our plots have a low bulk density (<0.3), which helps insulate deeper soils against temperature change and partly explains why the soil-temperature increase at 20-cm depth was only half that at 5-cm depth during the growing season. Another factor is the high soil moisture content that occurs as a result of thaw. Saturated deeper soils could offset some of the effect of shallower soil warming on respiration and N mineralization rates. Seasonal change in the depth of subsurface flowpath would have a similar effect. In the present study, the July increase in discharge (fig. 5) was the result of rainfall on relatively wet soils. The Asik watershed generally has two annual peaks in stream discharge (Stottlemyer, 2001). The high discharge in spring and early summer results from snowmelt and icemelt, whereas the high discharge in autumn partly results from continued soil thawing, because soil temperatures peak in August, a month later than air temperatures. The increase in stream-water NO_3^- concentration with discharge, especially in autumn, indicates increasing shallow subsurface lateral flow through the biologically active soils relative to the dormant season.

Soil Carbon and Nitrogen Pools

The soil C pool size was midway in the range of values measured across a long gradient on the North Slope that included sites ranging from a northern foothills ridgetop to the coastal-plain tundra near Barrow (Michaelson and others, 1996). The C and N pool sizes in the Oe soil horizon were more than 40 percent higher than in the surface organic matter (fig. 3). However, C/N ratios remained somewhat constant throughout the surface organic matter and matched those generally measured in Arctic soils (Shaver and others, 1992). Above-ground live-biomass C/N ratios range from 35 to 66, or 2 to 4 times the ratio below ground (Robert Stottlemyer, unpub. data, 1999–2001). Such a C/N-ratio gradient indicates that nitrogen is relatively more abundant for mineralization by the soil microbial community. Any factor that increases below-ground N mineralization rates increases N availability as NH_4^+ or NO_3^-, which can then be taken up by roots, in turn affecting above-ground plant production. The degree to which soil organic-C and organic-N mineralization rates differ in response to such factors as soil temperature or moisture content will determine the rate at which inorganic N may be transferred above ground.

The seasonal change in soil inorganic-N pool size in the present study (fig. 4) was similar to that in a later study of 50 plots in the watershed (Stottlemyer, 2001). However, in the present study, the amounts were less than half the watershed levels found in the later study. We attribute this difference primarily to the consistently high soil moisture content and low temperature in the present study.

Soil Respiration and Nitrogen Mineralization

The relation between soil CO_2 efflux and temperature varied by vegetation type and soil depth. Soil respiration rates were unrelated to thaw depth during the growing season, probably as a result of increasing soil moisture with depth. Only spruce showed a positive correlation between soil CO_2 efflux and temperature at 10-cm depth. In the later study in five vegetation types throughout the watershed, soil CO_2 efflux generally increased with temperature (Stottlemyer, 2001). In the present study, the inverse relation between mean temperature, recorded continuously at three depths, and soil CO_2 efflux in spruce in August is attributable to the high soil moisture at depth offsetting the effect on respiration of a slight temperature increase. Nadelhoffer and others (1991) found Arctic soil C mineralization rates in laboratory incubations insensitive to temperatures below 9°C. In the present study, mean daily shallow-soil temperatures peaked at 8°C (fig. 2). Our field results appear to confirm the laboratory results of Nadelhoffer and others (1991).

Because of the warming trend throughout northern Alaska, the region appears to be shifting from a C sink to a C source (Oechel and others, 1993). On a site-by-site basis, this relation varies as a result of changes in soil temperature and moisture (Oechel and others, 1995). In tundra along the North Slope, cooler and moister habitats continue to be C sinks,

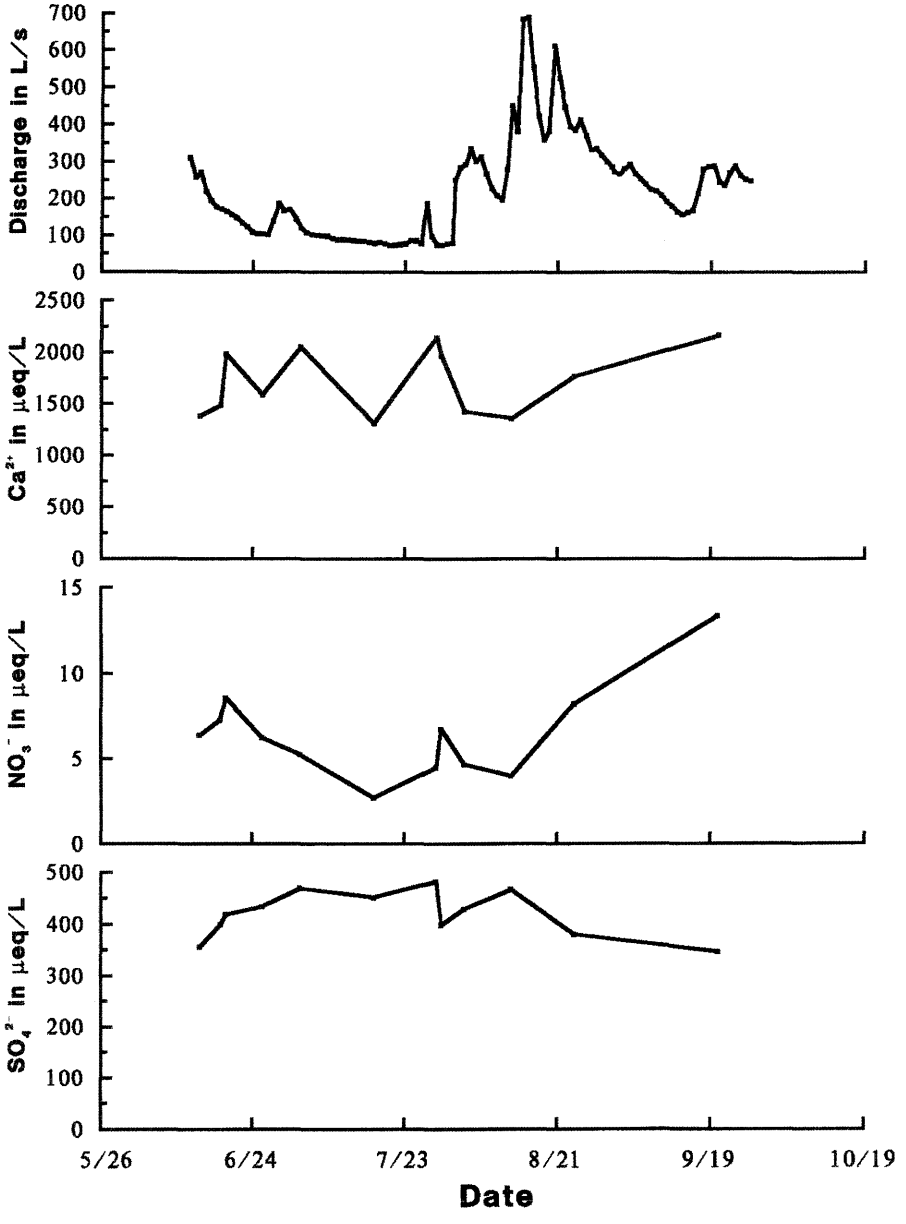

Figure 5. Seasonal changes during June–September 1997 in stream-water discharge and ion concentrations at mouth of the Asik watershed, Noatak National Preserve, northwestern Alaska.

whereas warmer and drier sites are C sources. However, long-term comparative data from Arctic tundra ecosystems also suggests that continued warming and drying could diminish, if not reverse, the trend toward a C source (Oechel and others, 2000).

The inverse correlation between inorganic-N pool size and net ammonification, nitrification, and total N mineralization rates suggests that the response of soil processes mineralizing N and N uptake by the soil microbial community differ (Hart and others, 1994). The results of the present study are consistent with later work (Stottlemyer, 2001) and suggest that during the growing season, mineralized N is sequestered in the surface organic matter, a result consistent with observations on stream-water inorganic-N export. The C and N cycles are closely linked, and the seasonal N retention suggests also that this ecosystem is currently a C sink.

The results from the inplace study of gross N mineralization and immobilization rates lend support to the observations of net N mineralization. The gross rates, which estimate total N cycling, indicate that the cycling of inorganic N is orders of magnitude greater than suggested by net N mineralization rates. Gross ammonification rates in the Asik watershed were equal to, and nitrification rates greater than, those recorded at the southward extent of the boreal biome (Stottlemyer and Toczydlowski, 1999b). However, in most research plots at Asik, microbial N consumption exceeded mineralization rates, at least during the growing season, a result consistent with the negative net N mineralization rates and again suggesting that, except for early summer, this part of the watershed is losing little inorganic N during the growing season.

In comparing net and gross N mineralization rates, the results depend on the method used. Regardless of method, such potentially confounding factors as change in soil N leaching, moisture content, and root uptake are absent in these studies. The study of net N mineralization was conducted during much of the growing season, when microbial processes must integrate the effects of trends in soil temperature, availability of labile C, and other changing conditions. The factors regulating N mineralization and consumption rates generally do not affect both processes equally. Soil microbial functional composition also changes rather rapidly over time and would be reflected more in the net mineralization results than in the study of short-term gross N mineralization and consumption. Because of the short growing season, no attempt was made to examine the likely seasonal change in gross N mineralization rates, as reported in other studies (Stottlemyer and Toczydlowski, 1999b).

Soil and Stream Water

The differences in soil solution and stream-water DOC concentrations suggest poor linkage between the research plots and the stream during the growing season, as was true for such ions as Ca^{2+} and SO_4^{2-}, and for biologically derived NO_3^-. More intensive sampling of the soil-water lysimeters might have shown a better correlation between plot soil-water chemistry and stream-water chemistry. However, the wide variation in rate of soil processes (fig. 4) and the lagtime in soil water reaching the stream could also account for the absence of correlation. The plots in the present study were located to examine soil processes across a taiga-tundra ecotone. Although this zone occurs throughout the watershed, it is not the dominant vegetation condition; most of the watershed is forest or tundra. Other studies in the Asik watershed show the large influence on stream-water solute concentrations and flux exerted by the alpine system (Stottlemyer, 2001). The study plots reported here are but a small part of the total vegetated area in the watershed (fig. 1).

Table 3. Mean concentrations of selected ions and DOC in soil solution during the 1997 growing season in the Asik watershed, Noatak National Preserve, northwestern Alaska.

[DOC, dissolved organic carbon. Standard deviations in parentheses]

	Ca^{2+} (μequiv /L)	NO_3^- (μequiv /L)	SO_4^{2-} (μequiv /L)	DOC (mg/L)
Spruce ----------	2,452 (713)	1.0 (2)	84 (63)	9.5 (6)
Transition ------	2,533 (1,027)	.5 (1.0)	149 (281)	12 (5)
Tundra ----------	2,533 (1,072)	.02 (0.1)	59 (195)	12 (4)

Although the stream is gauged year round, only seasonal flow can be measured in the Asik watershed. From late September to May, the stream is frozen from the bottom up, and little, if any, flow occurs. On the basis of seasonal flow measurements, discharge in 1997–98 did not greatly differ from that in other years (Robert Stottlemyer, unpub. data, 1995–2001). The inverse relation between stream discharge and Ca^{2+}, Mg^{2+}, and SO_4^{2-} concentrations previously observed in the Asik watershed was not apparent in 1997–98 (Stottlemyer, 2001). At the watershed level, this absence of correlation suggests that waters were well mixed from various depths before reaching the stream. The correlation between stream discharge and NO_3^- concentration was also unusual. The stream-water NO_3^- flux was 10 times greater in September than in midsummer, indicating that much of the autumn increase in runoff—the product of reduced evapotranspiration, maximum soil thawing, and some increase in precipitation—was moving laterally through shallow soils and removing the mobile NO_3^-.

In the Asik watershed, inorganic-N outputs, almost all as NO_3^-, exceed inputs by an average of 70 percent. Results from the present study suggest that most of this excess inorganic N is lost, partly during the spring runoff but especially in autumn. Obviously, if this ecosystem is N limited, outputs can-

not exceed inputs over a long period. At the watershed level, another study shows soil inorganic-N pools and early summer net N mineralization rates to be positively related to temperature (Stottlemyer, 2001). Warming regional temperatures could be accounting for the present net N loss from the watershed. However, year-to-year hydrologic variation can be a major source of change in watershed N output, and the short-term present study will not detect such change. Finally, N fixation occurs in this watershed at various places, especially in alder (Rhoades and others, 2001), and some of the N output could be the result of this process.

Conclusion

In this high-latitude ecosystem, changes in the C and N budgets appear to be closely linked. The potential effects of seasonal changes in above-ground temperature and moisture content may be partly offset by significant increases in below-ground moisture content from thawing. The absence of correlation between soil respiration rates, thaw depth, and temperature suggests that high soil moisture content limited the response of soil processes to temperature increases. Such offsetting conditions make it difficult to link year-to-year climatic variation to any change in soil processes in the short term. The plots selected for this study were deliberately placed in or conterminous with a taiga-tundra transition zone. Considerable local variation occurs in soil temperature and moisture content and in the depth of surface organic matter across such a gradient. Soils were commonly saturated below 10-cm depth, and surface overland flow occurred in the sedge tundra. As observed in the more extensive 50-plot study of a subset of the processes examined in the present study, the taiga-tundra transition zone commonly showed relations between processes and soil characteristics not observed within the conterminous tundra or taiga (Stottlemyer, 2001). Much of this variation appeared to result from changes in soil moisture content and subsurface flowpath. Except for the high early-summer NO_3^- flux in stream water concurrent with a high soil NO_3^- pool, no evidence was observed of a direct linkage between soil processes at the plot level and stream-water chemistry during the growing season.

Ongoing Related Research in Fiscal Year 2002

Routine monitoring of weather, soil temperature, hydrology, and stream-water and precipitation chemistry in the Asik watershed is ongoing. During fiscal year 2002, intensive comparative study of N-fertilized and nonfertilized plots in all major vegetation types of the watershed will continue. An intensive study will be conducted of the watershed source areas for alpine and subalpine stream-water DOC and DON contents, using $^{15}N/^{14}N$ and $^{13}C/^{12}C$ natural-isotope-abundance analyses. This study will also look at trends in isotopic ratios with depth of organic matter in soils to assess seasonal contributions from varying soil horizons. Finally, the study of "tree islands" in tundra will be continued to better define what soil conditions or processes account for island expansion or contraction.

References Cited

Binkley, Dan, Stottlemyer, Robert, Suarez, Frank, and Cortina, J., 1994, Soil nitrogen availability in some Arctic ecosystems in Northwest Alaska; responses to temperature and moisture: Ecoscience, v. 1, no. 1, p. 64–70.

Binkley, Dan, Suarez, Frank, Rhoades, Charles, Stottlemyer, Robert, and Valentine, David, 1995, Parent material depth controls ecosystem composition and function on a riverside terrace in northwestern Alaska: Ecoscience, v. 2, no. 4, p. 377–381.

Brooks, P.D., Stark, J.M., McInteer, B.B., and Preston, T., 1989, Diffusion method to prepare soil extracts for automated nitrogen-15 analysis: Soil Science Society of America Journal, v. 53, p. 1707–1711.

Chapin, F.S., III, Shaver, G.R., Giblin, A.E., Nadelhoffer, K.J., and Laundre, J.A., 1995, Responses of Arctic tundra to experimental and observed changes in climate: Ecology, v. 76, p. 694–711.

Eno, F., 1960, Nitrate production in the field by incubating the soil in polyethylene bags: Soil Science Society of America Proceedings, v. 24, p. 277–279.

Hart, S.C., Nason, G.E., Myrold, D.D., and Perry, D.A., 1994, Dynamics of gross nitrogen transformations in an old-growth forest; the carbon connection: Ecology, v. 75, no. 4, p. 880–891.

Herrmann, Raymond, Stottlemyer, Robert, Zak, J.C., Edmonds, R.L., and Van Miegroet, Helga, 2000, Biogeochemical effects of global change on U.S. National Parks: American Water Resources Association Journal, v. 36, no. 2, p. 337–346.

Illeris, L., and Jonasson, Sven, 1999, Soil and plant CO_2 emission in response to variations in soil moisture and temperature and to amendment with nitrogen, phosphorus, and carbon in Northern Scandinavia: Arctic, Antarctic, and Alpine Research, v. 31, no. 3, p. 264–271.

Jonasson, Sven, Michelsen, A., Schmidt, I.K., and Nielsen, E.V., 1999, Responses in microbes and plants to changed temperature, nutrient, and light regimes in the Arctic: Ecology, v. 80, no. 6, p. 1828–1843.

Jorgenson, M.T., Racine, C.H., Walters, J.C., and Osterkamp, T.E., 2001, Permafrost degradation and ecological changes associated with a warming climate in central Alaska: Climate Change, v. 48, no. 4, p. 551–579.

Kallbitz, Karsten, Solinger, Stephen, Park, J.H., Michalzik, B., and Matzner, Egbert, 2000, Controls on the dynamics of

dissolved organic matter in soils; a review: Soil Science, v. 165, no. 4, p. 277–304.

Kirkham, Don, and Bartholomew, W.V., 1954, Equations for following nutrient transformation in soil, utilizing tracer data: Soil Science Society of America Proceedings, v. 18, p. 33–34.

Lipson, D.A., Schmidt, S.K., and Monson, R.K., 2000, Carbon availability and temperature control the post-snowmelt decline in alpine soil microbial biomass: Soil Biology and Biogeochemistry, v. 32, p. 441–448.

Lloyd, A.H., and Graumlich, L.J., 1997, Holocene dynamics of tree line forests in the Sierra Nevada: Ecology, v. 78, no. 4, p. 1199–1210.

McKane, R.B., Rastetter, E.B., Shaver, G.R., Nadelhoffer, K.J., Giblin, A.E., Laundre, J.A., and Chapin, F.S., III, 1997, Climatic effects on tundra carbon storage inferred from experimental data and a model: Ecology, v. 78, no. 4, p. 1170–1187.

McNamara, J.P., Kane, D.L., and Hinzman, L.D., 1997, Hydrograph separations in an Arctic watershed using mixing model and graphical techniques: Water Resources Research, v. 33, no. 7, p. 1707–1719.

Michaelson, G.J., Ping, C.L., and Kimble, J.M., 1996, Carbon storage and distribution in tundra soils of Arctic Alaska, U.S.A.: Arctic and Alpine Research, v. 28, no. 4, p. 414–424.

Nadelhoffer, K.J., Giblin, A.E., Shaver, G.R., and Laundre, J.A., 1991, Effects of temperature and substrate quality on element mineralization in six Arctic soils: Ecology, v. 72, no. 1, p. 242–253.

Oechel, W.C., Hastings, S.J., Vourlitis, G.H., Jenkins, Mitchell, Riechers, George, and Grulke, Nancy, 1993, Recent change of Arctic tundra ecosystems from a net carbon dioxide sink to a source: Nature, v. 361, no. 6412, p. 520–523.

Oechel, W.C., Vourlitis, G.H., Hastings, S.J., and Bochkarev, S.A., 1995, Change in Arctic CO_2 flux over two decades; effects of climate change at Barrow, Alaska: Ecological Applications, v. 5, p. 846–855.

Oechel, W.C., Vourlitis, G.H., Hastings, S.J., Zulueta, R.C., Hinzman, Larry, and Kane, Douglas, 2000, Acclimation of ecosystem CO_2 exchange in the Alaskan Arctic in response to decadal climate warming: Nature, v. 406, no. 6799, p. 978–981.

Rhoades, Charles, Oskarsson, Hlynur, Binkley, Dan, and Stottlemyer, Robert, 2001, Alder (*Alnus crispa*) effects on soils in ecosystems of the Agashashok River valley, northwest Alaska: Ecoscience, v. 8, no. 1, p. 89–95.

Rice, K.C., and Bricker, O.P., 1995, Seasonal cycles of dissolved constituents in streamwater in two forested catchments in the mid-Atlantic region of the eastern USA: Journal of Hydrology, v. 170, p. 137–158.

Shaver, G.R., Billings, W.D., Chapin, F.S., III, Giblin, A.E., Nadelhoffer, K.J., Oechel, W.C., and Rastetter, E.B., 1992, Global change and the carbon balance of Arctic ecosystems: BioScience, v. 42, no. 6, p. 433–441.

Sommaruga, Ruben, Psenner, Roland, Schafferer, Ellen, Koinig, K.A., and Sommaruga-Wograth, Sabine, 1999, Dissolved organic-carbon concentration and phytoplankton biomass in high-mountain lakes of the Austrian Alps; potential effect of climatic warming on UV underwater attenuation: Arctic, Antarctic, and Alpine Research, v. 31, no. 3, p. 247–253.

Stottlemyer, Robert, 2001, Biogeochemistry of a treeline watershed, Northwestern Alaska: Journal of Environmental Quality, v. 30, p. 1990–1998.

Stottlemyer, Robert, 1999a, Soil nitrogen cycling in a mature boreal forest, Isle Royale, Michigan: Journal of Environmental Quality, v. 28, no. 2, p. 709–720.

Stottlemyer, Robert, and Toczydlowski, David, 1999b, Seasonal relationships between precipitation, soil, and streamwater nitrogen, Isle Royale, Michigan: Soil Science Society of America Journal, v. 63, no. 2, p. 389–398.

Stottlemyer, Robert, Travis, Benjamin, and Toczydlowski, David, 1995, Nitrogen mineralization in boreal forest stands of Isle Royale, Northern Michigan: Water, Air & Soil Pollution, v. 82, p. 191–202.

Suarez, Frank, Binkley, Dan, Kaye, M., and Stottlemyer, Robert, 1999, Expansion of forest stands into tundra in the Noatak National Preserve, Northwest Alaska: Ecoscience, v. 6, no. 3, p. 465–470.

Wilkinson, Leland, 1990, Systat; the system for statistics: Evanston, Ill., Systat, Inc., 676 p.

Studies by the U.S. Geological Survey in Alaska, 2001
U.S. Geological Survey Professional Paper 1678

Soil Drainage and Its Potential for Influencing Wildfires in Alaska

By Jennifer W. Harden, Rose Meier, Cherie Silapaswan, David K. Swanson, and Anthony D. McGuire

Abstract

Soil drainage, as defined by water-holding capacity, hydraulic conductivity, and position of seasonal water table, is closely associated with soil C storage because of controls on plant production, decomposition, fire severity, and fire frequency. As an initial regional assessment, we have used the U.S. Department of Agriculture's Natural Resource Conservation Service (NRCS) map (scale 1:1,000,000) to categorize areas in Alaska according to seven soil-drainage classes, using a simple numeric scale and an area weighting of mapped polygons. The seven NRCS soil-drainage classes were ranked numerically, from 1 (excessively drained: very high hydraulic conductivity and low water-holding capacity, water table >2 m deep) to 7 (very poorly drained: low hydraulic conductivity, water table <30 cm deep throughout the year). Area-weighted scores for each polygon were computed and plotted. About 50 percent of Alaskan landscapes have low hydraulic conductivity and high (<1-m depth) water table, which in many areas are related to shallow permafrost. Less than a third of the landscape (~26 percent) is moderately to excessively drained, and ~4 percent qualifies as very poorly drained wetlands. A statistical correlation exists between more poorly drained wet areas (drainage class, >5) and historical burning (since 1950), which we hypothesize to be related to high soil C storage and continuous cover of fuels typical of black spruce/feathermoss systems underlain by shallow permafrost.

Introduction

The spatial occurrence of boreal forests currently coincides largely with the zone of discontinuous permafrost (Brown and others, 1997), very large wildfires (Stocks, 1991, 1993; Kasischke and others, 1995) and very large carbon stocks (Eswaran and others, 1993; Tarnocai, 1998). Much of the terrestrial C of these regions is stored in soils, particularly in areas underlain by wetlands or permafrost (Gorham, 1991).

A closer examination of boreal forest systems reveals a hundredfold variation in soil C storage, ranging from about 3 to 5 kg C/m^2 in sandy, permeable soils to as much as 120 kg C/m^2 in well-established wetland peats (fig. 1). A recent evaluation of the long-term C accumulation on land (Harden and others, 2000) suggests that although net primary production varies threefold among these systems (Trumbore and Harden, 1997), C losses vary tenfold to a hundredfold, resulting in large variations in net C accumulation and storage. Variations in decomposition rates have been evaluated for temperature (Trumbore and others, 1996) and nutrient gradients (Bubier, 1995) within boreal systems. However, a recent evaluation of fire and decomposition along a soil-drainage gradient emphasized the role that wetness plays in protecting C stocks from fire (Harden and others, 2000). In general, northern soils are accumulating carbon (net ecosystem production is positive) and fall below the "steady state" line (fig. 2). Soils that are well drained, with rapid decomposition rates (turnover, <10 years; Trumbore and Harden, 1997), have relatively low ground fuels and burn emissions (fig. 2). In wetland soils that are very poorly drained, not only are decomposition losses low, but also average burn emissions are low because of sustained, high water tables. Between these two extremes, soils that are intermediate in drainage have the potential for large amounts of ground fuels and high fire emissions. During normal fire years, these systems may lose significant amounts of C to fire relative to their drier or wetter counterparts.

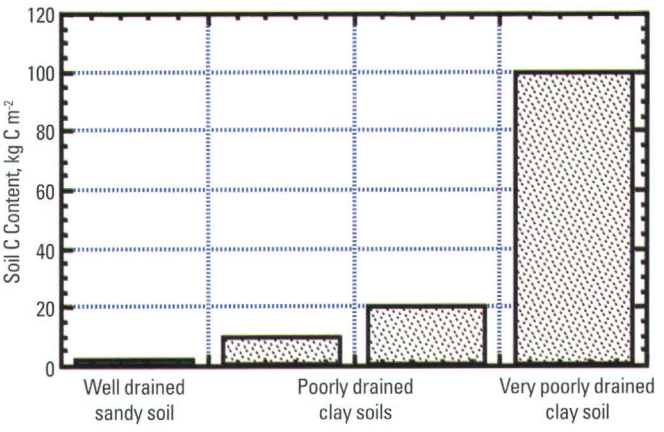

Figure 1. Soil C storage in soils of different drainage classes (Harden and others, 1997), based on data from soils of northern Manitoba, Canada. Well-drained soils are covered by jack pine and lichen, poorly drained soils covered by black spruce/feathermosses and black spruce/sphagnum mosses, and very poorly drained soils are covered by brown mosses and sedges.

Because significant amounts of C are stored in deep organic layers, unusually dry periods have the potential to expose very large C stocks to severe fires. In contrast, periods of wet summers could result in higher C storage and low emissions.

We hypothesize that large-scale patterns of fire are partly controlled by soil drainage and that permafrost-laden systems are particularly "elastic" in their ability to store, release, and sequester carbon onto land (fig. 2). This elasticity is derived from the unique thermal-moisture relations that govern peatland and wetland occurrence (Halsey and others, 1997). This hypothesis motivated us to extract spatial information on soil drainage in Alaska. For evaluation purposes, we compared a spatial overlay of fire history as a first test of our hypotheses.

Methods

Analysis of soil drainage is based directly on the U.S. Department of Agriculture's Natural Resource Conservation Service (NRCS) 1:1,000,000-scale soil map of Alaska (Rieger and others, 1979), available through the State Soil Geographic (STATSGO) Alaska data base (Natural Resource Conservation Service, 1991). Soil-drainage classes were assigned by NRCS soil scientists to subunits within each soil-mapping unit on the basis of field observations during the soil survey. Field observations included both soil-wetness state or depth to water table in soil pits and soil-morphologic properties that are associated with dry or wet soils. Wetness must be inferred from soil morphology because soil wetness can vary greatly over time, such that one-time observation of wetness may not be representative. The main soil morphologic properties used to infer wetness conditions include the presence or absence of features that are produced by biochemical reduction of Fe and other elements; accumulation of organic matter at the surface due to restricted decomposition under water-saturated conditions; and the permeability of soil layers, which indirectly indicates water retention. Although landscape properties, such as vegetation and topography, aid the soil scientist in delineating the extent of a given soil, the decisive criteria in assigning drainage classes are soil morphology and observations of the soil-wetness state. In the STATSGO Alaska data base, the properties of soil-drainage classes can be summarized as follows; the sources used include unpublished NRCS guidelines and the STATSGO data base itself.

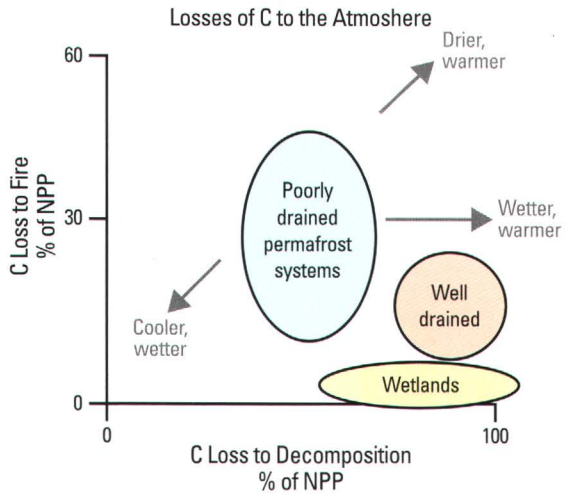

Figure 2. C losses to fire and decomposition for soils of different drainage classes, and conceptualizations of sensitivity to climate change, based on data and models of Harden and others (2000). Climate-change sensitivity is based on the logic that wet periods would favor suppression of fire and cold periods would favor suppression of decomposition. Poorly drained soils, particularly those with shallow permafrost, are conceived as most "elastic" or sensitive to climate change because of changes in active-layer thickness, perched water table, and sensitivity of fire severity to permafrost depth.

Excessively drained.—Excessively drained soils are almost exclusively coarse-grained Entisols, with very high permeability, little horizon development, and no redoximorphic features (reduced colors).

Somewhat excessively drained.—Somewhat excessively drained soils are mostly not represented in the STATSGO data base (2 out of 1,664 records).

Well drained.—Well-drained soils include a wide variety of morphologies (Inceptisols, Andisols, Spodosols, Entisols), but their common property is no to very weak redoximorphic features within 75 cm of the surface and a thin (<20 cm thick) surface organic layer. Saturation of the soil above 75-cm depth can occur, but it must be brief (<2 weeks per year). Some of these soils have permafrost, but it does not result in a wet soil for various reasons: the soils thaw deeply (generally >1 m deep), are generally coarse grained or shallow over bedrock, and are mostly on steep slopes.

Moderately well drained.—Moderately well drained soils are mostly not represented in the STATSGO data base (2 out of 1,664 records; some mixed moderately well drained and other soils are listed, but only a few).

Somewhat poorly drained.—Somewhat poorly drained soils generally show some morphologic effects of wetness in the form of reduced colors above 75-cm depth, and saturation at 50- to 75-cm depth can be prolonged. However, the surface organic layer is still thin (<20 cm thick), and any saturation above 50-cm depth should be brief (<2 weeks), including soils with and without permafrost. In soils with permafrost, some factor, such as coarse texture or slope, prevents continuous perching of water high in the profile; in the soils without permafrost, fine texture and (or) landscape position causes the soil to be wet part of the year.

Poorly drained.—Poorly drained soils generally show strong morphologic signs of wetness—dominantly, reduced colors above 50-cm depth, and in some soils a thick (max 40 cm) surface organic layer. Saturation is prolonged at 25- to 50-cm depth but brief (<2 weeks) above this depth. In northern and central Alaska, these soils generally have permafrost that thaws to about 50-cm depth in the summer; in areas that lack permafrost, other factors, such as fine texture, flat slope, and high regional ground-water table, keep the soils wet.

Table 1. Numerical-value assignments to Natural Resource Conservation Service soil-drainage classes.

[From Rieger and others (1979)]

Value	Soil-drainage class	Description
1	Excessively drained----------	Very high hydraulic conductivity and low water-holding capacity, water table >2.0 m deep.
2	Somewhat excessively drained---	High hydraulic conductivity and low water-holding capacity, water table >2.0 m deep.
3	Well drained----------	Intermediate water-holding capacity, water table >2.0 m deep.
4	Moderately well drained----------	Low hydraulic conductivity, wet state high in profile, water table 1.0–2.0 m deep.
5	Somewhat poorly drained---------	Low hydraulic conductivity, wet state high in profile, water table 0.3–1.0 m deep.
6	Poorly drained----------	Saturated zone or layer of low hydraulic conductivity, water table <25 cm deep.
7	Very poorly drained----------	Saturated, water table <30 cm deep throughout the year.

Very poorly drained.—Very poorly drained soils are saturated with water below 25-cm depth for at least 2 weeks per year and commonly longer—most of the growing season for many such soils. In Alaska, these surface soils have a surface organic layer that is at least 20 cm (commonly >40 cm) thick. Mineral soil, if present, is generally reduced. In northern and central Alaska, these soils commonly have permafrost and thaw 0.5 m or less each summer. In southern Alaska, the soils lack permafrost but are still organic and continuously saturated near the surface.

Data are organized by map unit in the STATSGO data base. A map unit is represented by one or more polygons on the map (Rieger and others, 1979) and has a single data set with many attributes. We selected the attributes rock, open water, and soil-drainage class to portray soil-drainage conditions, and converted the qualitative soil-drainage classes to numerical soil-drainage classes from 1 (excessively drained) to 7 (very poorly drained) (table 1).

A map unit may have as many as seven components or subunits, corresponding to spatially distinct areas with different soils. Although the locations of these subunits are not shown on the map (Rieger and others, 1979), the areal percentage of the component is represented along with its associated soil-drainage class. To quantify the composite drainage class of each map unit, we first subtracted the percentage of area represented by rock, ice, or open water, and then recalculated the proportional areas representing soil-drainage classes 1 through 7. To assign a single drainage value to each map unit, we multiplied each drainage rank by its proportional area and summed the products to represent the drainage in each polygon, according to the strategy of Rapalee and others (1999). The resulting soil-drainage map (fig. 3) displays only six broad soil-drainage classes, calculated from the relation

$$A = \frac{\sum (R * P)_{1...n}}{n}, \qquad (1)$$

where A is the area-weighted soil-drainage class for each map unit, R is the soil-drainage class for each subunit within the polygon, P is the areal percentage of each subunit, and n is the total number of subunits.

Fire-History Maps

A data base for historical fire occurrence was developed from data of the Alaska Fire Service (Kasischke and Stocks, 2000; Murphy and others, 2000). The polygons of fire scars were digitized and registered, and the resulting file was converted to a grid format, using ArcInfo software, with 1-km grid-cell spatial resolution. The associated files (fire, drainage) were projected together, coregistered, and then reclassified according to burning (burned, unburned) and drainage (wet, dry).

Statistical Analysis

The size of soil-drainage polygons and the size of historical burns are generally quite large; for example, three or four burns account for most of the area burned in any given year. The average polygon size of fires, about 10,000 ha, is about one-sixth the size of the average polygon (~65,000 ha) of the soil map unit. As a result, the utility of comparing fire history and soil drainage on a detailed spatial or historical scale is limited to more general parametric approaches. To test whether fire and soil drainage are associated or collocated, we distinguished 1-km^2-area cells with soil-drainage values >5 ("wet") from those with soil-drainage values <5 ("dry"), and distinguished cells that had burned since about 1950 from those that had not. Using a chi-square statistic, we tested for the null hypothesis of no correlation between burning and drainage class as follows. For the entire population of 1-km^2-area cells, we generated the observed frequency

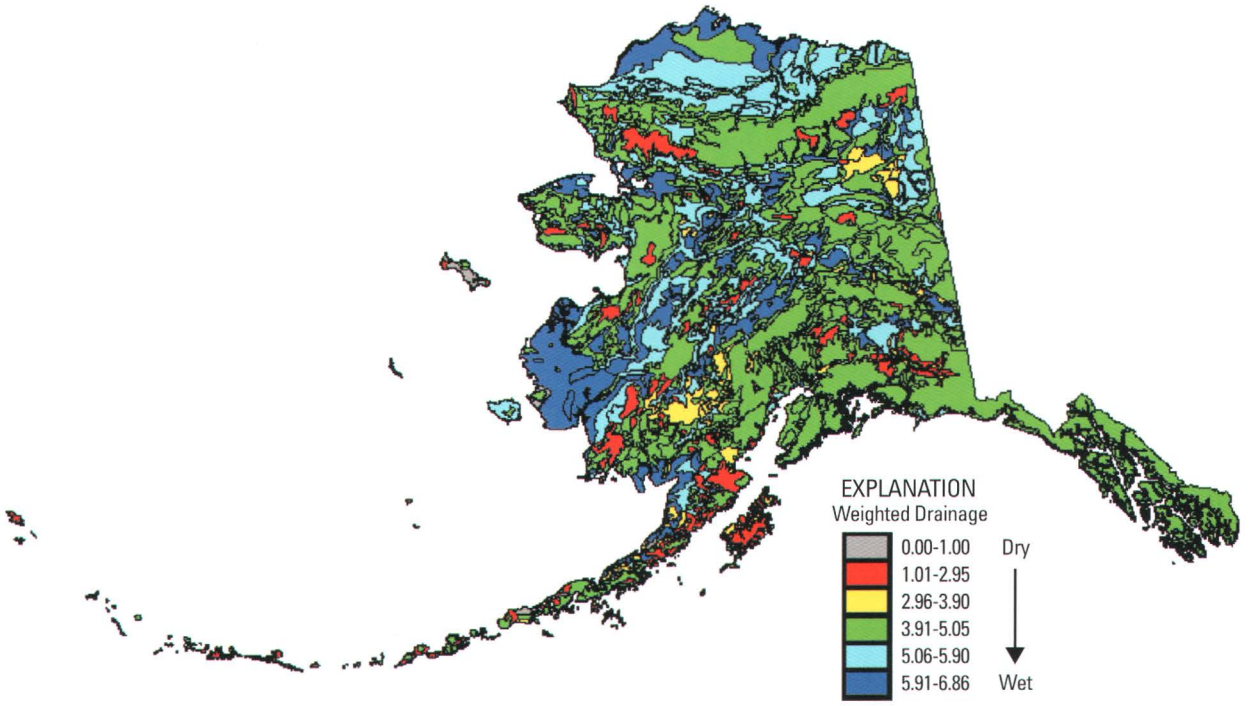

Figure 3. Soil-drainage map of Alaska (from Rieger and others, 1979).

of each unburned, burned, wet, and dry populations of cells. Then, for cells that burned, we generated a similar (expected) frequency of wet and dry populations as was found for the entire population. If a significant difference exists between the expected and actual populations, then the null hypothesis is rejected.

Results

About 40 percent of Alaska is composed of soils that are "wet" (soil-drainage class >5, figs. 3, 4). Many of these soils are likely to be underlain by shallow permafrost, as indicated by a wet state high in the soil profile (table 1). Wetlands (very poorly drained soils) represent about 10 percent of the nonrock, non-open-water cells (soil-drainage class 7, fig. 3). About 15 percent of Alaska is well drained, typically south-facing slopes or steep uplands or coarse-grained deposits with deep water tables. Much (~40 percent) of Alaska is "moderately well drained" (soil-drainage class 4–5). As noted above, few soils are actually rated as 4 (moderately well drained), and so a soil-drainage class of 4 for a polygon is obtained from a mixture of wetter and drier soil-drainage classes—mostly hilly or mountainous regions where soil drainage varies greatly with slope position (see fig. 1, where soil-drainage-class 4 areas occur in and near mountain ranges).

The statistical approach rejected the null hypotheses for the combination of drainage and burning (table 2), indicating a significant positive association between burned areas and wetter soil-drainage classes (fig. 5).

Discussion

Despite the huge, stand-killing fires that typify North American boreal forests (Stocks, 1993), a positive correlation exists between poorly drained soils and the extent of burning (table 2). Another conundrum of the association between wetness and burning is that on the basis of tree coring and stand-age histories in the Canadian Shield region, dry areas would be expected to burn more frequently, with fire-return intervals of 80 to 100 years in well-drained areas (Stocks, 1989) and of 150 to 200 years in more poorly drained stands (Stocks, 1980). Thus, we would expect drier areas to be positively correlated with fire occurrence, rather than wetter areas, as we found (table 2).

Our result probably stems from the fact that in interior Alaska, fire-return interval and fire occurrence may depend

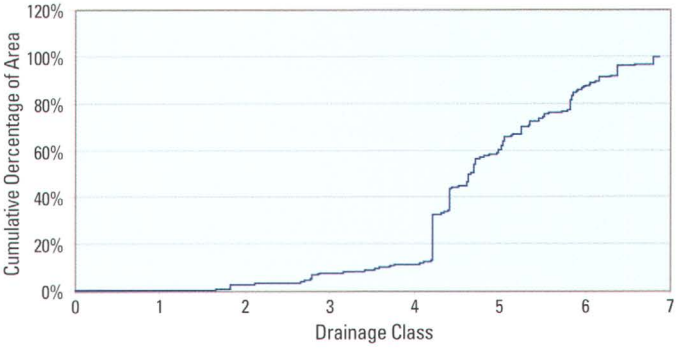

Figure 4. Percentage of map areas represented by soil-drainage classes, based on attribute tables of map subunits from Rieger and others (1979).

more on fuels and fire weather—the quality and quantity of organic matter—than on soil wetness. For example, highly flammable fuels can accumulate on wet soils, and under the right conditions, these wetter areas burn, as in the Alaskan taiga, where highly flammable black spruce and feathermosses commonly grow on wet soils. In addition, an important effect of large fires and severe fire weather may not be well reflected by the fire-return intervals calculated from stand ages. For example, historical data (Murphy and others, 2000) show that most of the burning within a given decade occurs during a single high-fire year, as is supported by climate analyses of fire weather (Hess and others, 2001). Regrowing vegetation and its influence on recurrent burns are also important. Manies and others (this volume) report that although "fire mosses" regenerate quickly after fire, feathermosses and ground fuels take at least 20 years to produce a "dead moss" layer. Also, many stands pass through a longer stage of less flammable deciduous cover before returning to more flammable evergreen vegetation (Viereck, 1975; Foot, 1983).

Conclusion

From the perspective of the long-term C budget of soil C studies, the greater long-term C storage in wetter soils suggests that because fire occurrence (return interval) is higher for "wetter" than drier soil types, fire severity (total combustion losses) must be lower for wet than for dry systems. This

Table 2. Chi square tests on colocation of burning and wetness.

[Low *P* value indicates a positive correlation between "wet" soils and historical burning, where "burning" is defined as having burned since 1950 and "wetness" is defined as a soil-drainage class >5 ("wet") or <5 ("dry"). df, degrees of freedom]

		Burned		
		Yes	No	row marginals
Drainage	>5	75746	527793	603539
	<5	54548	843175	897723
	col marginals	130294	1370968	1501262
	Expected =	52380.9	551158.1	
		77913.1	819809.9	
	Fo - Fe =	23365.1	-23365.1	
		-23365.1	23365.1	
	(Fo-Fe)^2/Fe =	10422.2	990.5	
		7006.9	665.9	
	Chi sq =	19085.5		
	df =	1.0		

Chi Squared critical at .05 with 1df is 3.84

For df=1, the calculated value of chi-sq is corrected for continuity

Corrected Chi sq =	19084.7
p = < 0.0001	

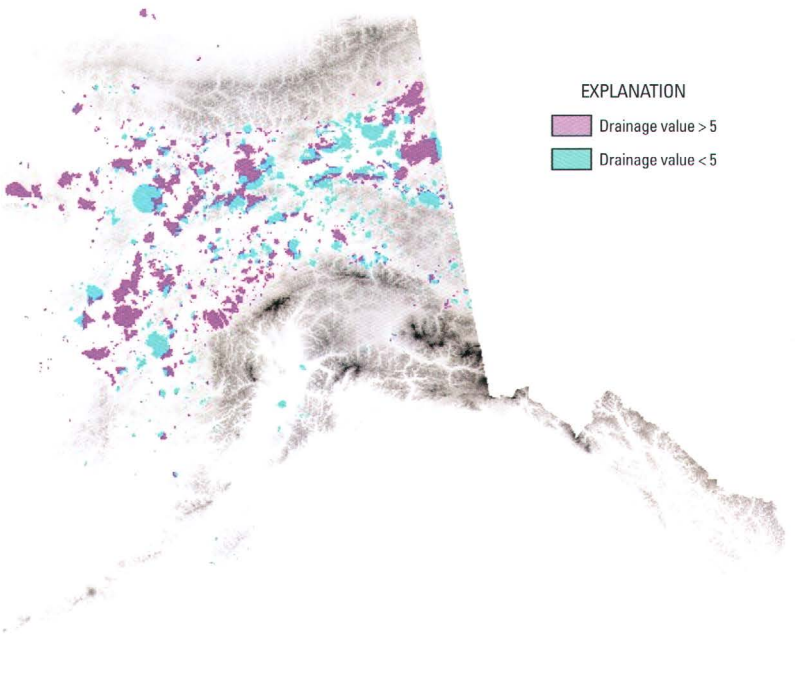

Figure 5. Alaska, showing locations of fire-scar areas (1950–97) that are underlain by two classes of soils: well to moderately well drained (drainage classes <5) and poorly draiend (classes >5) soils, which include soils underlain by shallow permafrost.

argument stems from the observation that net primary production and decomposition losses are more similar in magnitude than deep C contents of wet and dry soils (Harden and others, 2000). Permafrost in these wet soils may play a central role in limiting fire severity to shallow layers (see Swanson, 1986), while also allowing large fuel buildup and large fires to occur. To date, the data on fire severity, combustion losses, climate change and spatial variability, and soil-drainage class are insufficient to separate these factors.

Climatic shifts will influence the control of fire by soil drainage, first and most rapidly by influencing fire weather and secondarily and more gradually by affecting long-term water tables and active layers (fig. 2). Whereas some attributes of soil drainage, such as permeability and elevation, are stable in the climatic environment, other attributes, such as depths to the active layer and water table, are responsive to climate change. If climate change were to lead to greater extremes in extreme drought, the likelihood of wetlands burning greatly increases. In the future, new perspectives are needed to explore the interactions between fire-weather patterns and landscape drainage patterns, vegetation- and fuel-buildup associations, and fire extent and severity.

References Cited

Brown, Jerry, Ferrians, O.J., Jr., Heginbottom, J.A., and Melnikov, E.S., 1997, Circum-Arctic map of permafrost and ground-ice conditions: U.S. Geological Survey Circum-Pacific Map Series Map CP–45, scale 1:10,000,000.

Bubier, J.L., 1995, The relationship of vegetation to methane emission and hydrochemical gradients in northern peatlands: Journal of Ecology, v. 83, p. 403–420.

Eswaran, Hari, Van den Berg, Everet, and Reich, Paul, 1993, Organic carbon in soils of the world: Soil Science Society of America Journal, v. 57, p. 192–194.

Foot, M.J., 1983, Classification, description, and dynamics of plant communities after fire in the taiga of interior Alaska: U.S. Forest Service Research Paper PNW–307, 108 p.

Gorham, Eville, 1991, Northern Peatlands; role in the carbon cycle and probable responses to climatic warming: Ecological Applications, v. 1, p. 182–195.

Halsey, L.A., Vitt, D.H., and Zoltai, Stephen, 1997, Climatic and physiographic controls on wetland type and distribution in Manitoba, Canada: Wetlands, v. 17, no. 2, p. 243–262.

Harden, J.W., O'Neill, K.P., Trumbore, S.E., Veldhuis, Hugo, and Stocks, B.J., 1997, Moss and soil contributions to the annual net carbon flux of a maturing boreal forest: Journal of Geophysical Research, v. 102, no. D24, p. 28805–28816.

Harden, J.W., Trumbore, S.E., Stocks, B.J., Hirsch, A., Gower, S.T., O'Neill, K.P., and Kasischke, E.S., 2000, The role of fire in the boreal carbon budget: Global Change Biology, v. 6, supp. 1, p. 174–184.

Kasischke, E.S. and Stocks, B.J. 2000. Fire, climate change, and carbon cycling in the boreal forest: New York, Springer-Verlag, 461 p.

Kasischke, E.S., Christensen, N.L., and Stocks, B.J. 1995, Fire, global warming and the carbon balance of boreal forests: Ecological Applications, v. 5, p. 437–451.

Murphy, P.J., Mudd, J.P., Stocks, B.J., Kasischke, E.S., Barry, D., Alexander, M.E. and French, N.F., 2000, Historical fire records in the North American Boreal Forest, *in* Kasischke, E.S., and Stocks, B.J., eds., Fire, climate change, and carbon cycling in the boreal forest: New York, Springer-Verlag, 461 p.

Natural Resources Conservation Service, 1991, State soil geographic (STATSGO) data base: National Soil Survey Center Miscellaneous Publication 1492, 113 p.

Rapalee, Gloria, Trumbore, S.E., Davidson, E.A., Harden, J.W. and Veldhuis, Hugo, 1998, Soil carbon stocks their rates of accumulation and loss in a boreal forest landscape: Global Biogeochemical Cycles, v. 12, no. 4, p. 687–701.

Rieger, Samuel, Schoephorster, D.B., and Furbush, C.E., 1979, Exploratory soil survey of Alaska: Washington, D.C., Soil Conservation Service, 213 p.

Stocks, B.J., 1980, Black spruce crown fuel weights in Ontario, Canada: Canadian Journal of Forest Research, v. 10, p. 498–501.

Stocks, B.J., 1989, Fire behavior in mature jack pine: Journal of Forest Ecology, v. 19, p. 783–799.

Stocks, B.J., 1991, The extent and impact of forest fires in northern circumpolar countries In: Levine, J.S., ed., Global biomass burning; atmospheric, climatic, and biospheric implications: Cambridge, Mass., MIT Press, p. 197–202.

Stocks, B.J., 1993, Global warming and forest fires in Canada: Forestry Chronicles, v. 69, p. 290–293.

Swanson, D.K.,1986, Susceptibility of permafrost soils to deep thaw after forest fires in interior Alaska, U.S.A., and some ecologic implications: Arctic and Alpine Research, v. 28, p. 217–227.

Tarnocai, Charles, 1998, The amount of organic carbon in various soil orders and ecological provinces in Canada, *in* Lal, Rattan, Kimble, J.M., Follett, R.F., and Stewart, B.A., eds., Soil processes and the carbon cycle: Boca Raton, Fla., CRC Press, p. 81–92.

Trumbore, S.E., Chadwick, O.A., and Amundson, Ronald, 1996, Rapid exchange between soil carbon and atmospheric carbon dioxide driven by temperature change: Science, v. 272, no. 5360, p. 393–396.

Trumbore, S.E., and Harden, J.W., 1997, Input, accumulation and turnover of carbon in soils of the BOREAS northern study area: Journal of Geophysical Research, v. 102, no. D24, p. 28816–28923.

Van Cleve, Keith, Chapin F.S., III, Flanagan, P.W., Viereck, L.A., and Dyrness, C.T., eds., 1986, Forest ecosystems in the Alaskan taiga; a synthesis of structure and function: New York, Springer-Verlag, 230 p.

Viereck, L.A., 1975, Forest ecology of the Alaska taiga: Circumpolar Conference on Northern Ecology, Ottawa, Ontario, Canada, 1975, Proceedings, p. I–1 to I–22.

Studies by the U.S. Geological Survey in Alaska, 2001
U.S. Geological Survey Professional Paper 1678

The Effect of Soil Drainage on Fire and Carbon Cycling in Central Alaska

By Kristen L. Manies, Jennifer W. Harden, Kenji Yoshikawa, and Jim Randerson

Abstract

Relatively high rates of plant production coupled with low rates of decomposition allow boreal forests to store large amounts of carbon. Fire, the main disturbance of this ecosystem, also plays a key role in regulating this biome's C storage. All three of these factors are sensitive to climate change. For this reason, it is important to understand the interactions between fire, productivity, and decomposition, as well as how these interactions vary with soil drainage.

We are currently investigating the effects of fire on soil temperature and vegetative regrowth for different soil-drainage classes. Various soil, thermal, and vegetative properties are being measured within different-age black spruce (*Picea mariana* (Mill.) BSP) stands in well-drained, moderately well drained, and poorly drained areas. While the absolute amount of organic matter lost to fire is greater at moderately well drained sites, the relative amount of organic-matter loss is greatest at well-drained sites. Loss of any organic matter profoundly affects soil temperature—differences between burned and unburned plots ranged as high as 13°C. Soil drainage also affected which species were dominant postburn. Quantifying the effect of soil drainage on such factors as depth of organic matter, soil temperature, and vegetative regrowth will aid in understanding the impact of fire on boreal-forest C storage.

Introduction

Boreal forests are conifer-dominated ecosystems with thick deposits of organic matter that generally occur between lat 45° and 70° N. One of the largest biomes in the world, these forests play an important role in the global C cycle. They contain more than 300 Gt C, of which approximately 60 percent occurs within organic soil layers and mineral-soil horizons (McGuire and others, 1997). Large amounts of carbon are stored in boreal forests as a result of the unique combination of solar illumination, temperature, and precipitation within these ecosystems (Kasischke, 2000). Long summer days allow relatively high rates of net primary production, whereas cold annual temperatures protect this carbon from decomposition. Discontinuous permafrost also underlies many of these forests. Permafrost not only influences soil temperature but also strongly affects soil drainage.

The importance of such factors as soil temperature to these ecosystems makes the boreal region sensitive to climate change (Cubasch and others, 2001). Further increases in temperature will likely degrade much of the permafrost, in turn raising soil temperatures and lowering water tables. This climate change could also affect the frequency and severity of wildfire in the boreal region. Because fire is the dominant disturbance in this region, changes in the fire-return interval and (or) fire severity can greatly affect the exchange of atmospheric and terrestrial C. Fire affects C storage of the boreal forest both directly (for example, fire emissions) and indirectly. Because most of the postburn soil surface consists of relatively unshaded, black, charred material that has a lower albedo than that of a living forest, fire tends to increase soil temperature (Viereck, 1981). Postfire soil is also subject to greater degrees of heating and cooling because the organic layers, which play an important role in soil insulation, have been removed (Viereck, 1981). Changes in soil temperature directly affect decomposition rates, vegetative regrowth, soil-moisture regimes, and rates of evaporation and transpiration.

The affect of climate change on fire may depend on soil drainage. Soil-drainage class affects such factors as fire frequency and severity (Harden and others, 2000), vegetation recovery (Viereck and others, 1983), and rates of decomposition (Flanagan and Van Cleve, 1983). Because 40 to 60 percent of Alaska consists of poorly drained soils (Meier and others, 2000), it is important to understand not only how fire affects the C storage of boreal forests, but also how this response varies with drainage type. Therefore, the U.S. Geological Survey (USGS) has undertaken a study to examine the C cycling of various drainage types within interior Alaska. The USGS is currently measuring various soil, vegetation, and thermal properties in collaboration with many other investigators and institutions. Here, we outline the format of our site establishment, report on the status of measurements (underway and planned), and provide a general synthesis of organic-layer thickness, canopy density, and temperature levels within our site matrix.

Methods

Field Sites

All field sites are in central Alaska. The first study area is in Donnelly Flats (lat 63° N., long 145° W.), about 80 mi southeast of Fairbanks near Delta Junction (fig. 1). During summer 1999, a wildfire burned more than 18,000 acres of moderately well drained and well-drained land. Plots have been established within burned areas of both of these drainage types. Several other sites near Donnelly Flats, representing different stand ages (time since last fire) and soil-drainage conditions, are also being investigated (table 1). The results presented here are from sites within the Donnelly Flats study area.

The second study area is in Tanana Flats, about 12 mi southwest of Fairbanks (lat 64° N., long 148° W., fig 1). During summer 2001, a wildfire called the Survey Line fire occurred within several poorly drained parts of the area. Plots are currently being set up within this new burn, along with two nearby stands representing different stages of ecosystem recovery (table 1).

Plot Setup

Plots at sites within the Donnelly Flats study area were set up along two transects that were arranged in an "L" formation. The purpose of this setup was to capture each site's spatial variation, as well as negate directional effects on any measurements (for example, the affect of the dominant wind direction on woody-debris orientation). Measurements are taken within plots located along or just inside these transects.

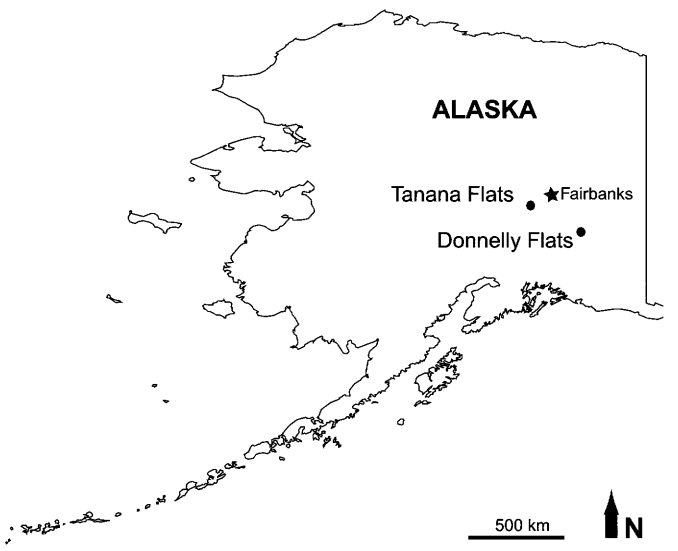

Figure 1. Sketch map of Alaska, showing locations of Donnelly Flats and Tanana Flats study areas.

These measurements include ground cover (percentage of coverage for different moss species and lichen), tree density, organic-layer/soil-horizon thickness, and temperature and moisture content at various organic-layer/mineral-soil horizons (table 2). Other measurements recorded at these sites include the C and N contents of each organic layer/soil horizon and woody-debris inventories (table 2; data not presented here). Plots, using the same format, are currently being implemented at sites in the Tanana Flats study area.

We note that all of the research discussed here is highly collaborative, with various funding institutions and scientific investigators. These partnerships are providing a more complete picture of the effects of both fire and soil drainage on the C cycle. Additional data being collected include eddy flux (Jim Randerson, California Institute of Technology); net primary production and N cycling (Michelle Mack, University of Florida); forest productivity, using remote sensing (Erik Kasischke, University of Maryland); dissolved organic C in leachate (Jason Neff, USGS); and chamber flux measurements (Ted Schuur, University of Florida).

Ground Cover and Tree Density

Ground cover (for example, moss, lichen) was digitally measured, using either 60- or 100-cm^2 area plots permanently located along our transects. First, polygons dominated by different moss species within each plot were delineated by using dyed Q-tips. These marked plots were photographed with a digital camera. At the same time, a rough sketch of each plot was made to record the relative percentage of cover for each moss species within each polygon. The digital photographs were imported into ESRI ArcGIS software, and coordinates that corresponded to each plot's borders on a 60- by 60-cm or 100- by 100-cm grid were assigned. Using a combination of ESRI ArcMap and ArcCatalog software, polygon boundaries were digitized (traced), allowing the area of each polygon to be calculated. Percentage of cover of each moss type was then averaged for the site (n=7–9 for 60-cm^2-area plots, n=13 for 100-cm^2-area plots).

Stand density was determined by using regularly spaced points placed every 30 or 40 m, depending on site, along the transect. Density of trees >3 m tall was measured by using the point-center-quarter method (Cottam and Curtis, 1956). Species, diameter at breast height, and distance from the point were recorded for the closest tree (live or dead) in each of the four quadrants (northeast, southeast, southwest, northwest) surrounding the point. Density is calculated from the formula

$$A = \left[\frac{\frac{1}{n}(\Sigma d)}{c} \right]^2, \qquad (1)$$

Table 1. Matrix of study areas (fig. 1) by soil-drainage class and relative time since last fire.

[Each four-character site name is followed by the name of the study area in which its located. Site in parentheses is planned]

Drainage	Relative time since burn				
	Recent		Recovering		Mature
Well drained-------	DFTB: Donnelly Flats		DF87: Donnelly Flats		DFTC: Donnelly Flats
Moderately well drained.	DFCB: Donnelly Flats	DF94: Donnelly Flats		DF56: Donnelly Flats	DFCC: Donnelly Flats
Poorly drained-----	TFSB: Tanana Flats		(TFSR: Tanana Flats)		TFSC: Tanana Flats

Table 2. Year in which measurements are occurring at each U.S. Geological Survey study site.

[Tree cover: aspen, *Populus tremuloides* (Michx.); black spruce, *Picea mariana* (Mill.) BSP. Soil measurements include horizon thickness, bulk density, C and N content, ^{13}C content, and for some sites, ^{14}C content. Letters in parentheses, chief data collector, by collaborator: K, Erik Kasischke (University of Maryland); M, Michelle Mack (University of Florida); R, Jim Randerson (California Institute of Technology). Do., ditto]

Site	Year of last burn	Tree cover	Moss cover	Soil	Suction lysimeters	Tree density/ moss cover	Net primary production	Soil moisture (continuous)	Soil temperature (continuous)
Donnelly Flats									
DFTB	1999	----	Feathermoss-------	2000	2000	2000	2001 (M)	1999 (R)	1999 (R)
DFCB	1999	----	do----------	2000	2001	2001	2001 (M)	2000	2001
DF94	1994	Aspen----------	*Ceratodon* sp-----	2001	--	2001	2001 (M)	--	2000 (K)
DF87	1987	do----------	Feathermoss-------	2001	--	2001	2001 (M)	--	--
DF56	1956	Black spruce----	do----------	2001	--	2001	2001 (M)	--	--
DFTC	<1900	do----------	do----------	2000	2000	2000	2001 (M)	1999 (R)	1999 (R)
DFCC	<1900	do----------	do----------	2000	2001	2001	2001 (M)	2001	2001
Tanana Flats									
TFSB	2001	Black spruce----	*Sphagnum* sp------	2002	--	2003/4	2003/4	2003/4	2003/4
TFSR	1985	do----------	Feathermoss and *Sphagnum* sp.	2003/4	--	2003/4	2003/4	2003/4	2003/4
TFSC	<1900	do----------	*Sphagnum* sp------	2003/4	--	2003/4	2003/4	2003/4	2003/4

where A is the mean area (in square meters) per tree, d is the distance (in meters) of each tree to the point, n is the number of trees, and c is a correction factor based on the number of trees per point (1 tree, 0.50; 2 trees, 0.66; 3 trees, 0.81; 4 trees, 1.00; Cottam and Curtis, 1956). Stand density at each point (in trees per hectare), D, was calculated from the formula

$$D = \frac{1}{A} \times 10^5. \quad (2)$$

Because A can be corrected for the number of trees per point and both live and dead trees were recorded, overall, live-tree, and dead-tree density can all be calculated. Density of trees <3 m tall were measured by using 2-m-radius plots located at each point. Generally, all live and dead trees >0.5 m tall were recorded; trees <0.5 m were measured in understory-biomass plots (data not presented here).

Organic-Layer and Mineral-Soil Characterization

Multiple plots at each site were described by dividing soil profiles into horizons containing mineral soil or one of the following five types of organic matter: live moss/litter (L), dead moss (D), fibric matter (F, similar to an Oi soil horizon; Birkeland, 1999), mesic matter (M, similar to an Oe soil horizon), or humic matter (H, similar to an Oa soil horizon). Dead-moss layers are composed of more dead-moss material than roots. The F, M, and H soil horizons contain roots and decomposing organic matter, the level of which varies by category. A small "b" was added to the horizon description for charred layers (for example, "bD" is burned dead moss). At most sites, a subset of these plots were sampled for analytical purposes. Bulk density and moisture content, which were also measured, were used in combination with nutrient-content measurements to calculate C and N storage at each site (data not presented here).

Temperature

Soil temperatures at sites in the Donnelly Flats study area were measured by using several different types of instruments. Two sites (DFCC, DFCB, fig. 4) used negative-temperature-coefficient thermistors (Alpha Sensors, Inc., No. 14A5001C2) attached to a CR10X data logger (Campbell Scientific). Because we calibrated each thermistor before it was installed, the accuracy of these instruments should be within 0.01°C. Another two sites (DFTC, DFTB, fig. 5) used 105T thermocouples (Campbell Scientific), also attached to CR10X dataloggers. Data from these instruments have, in the worst case, error rates of ±2.5°C, although error rates in the field are commonly much less. The last site (DF94; data not shown here) used HoboPro thermistors (Onset Computer Corp.), which have a slightly lower accuracy (±0.41°C).

Results and Discussion

Effects of Fire on Organic Layers

Because the forest floor comprises much of the fuel consumed during boreal fires (Stocks and Kauffman, 1997), surface organic layers are considerably changed postburn. These organic layers can be affected by a fire in one of two ways: they can be completely volatilized, or they can become charred. On average, in the Donnelly Flats study area, the well-drained site (DFTB, fig. 5; table 3) lost 7.0 cm of organic matter to the fire, whereas the moderately well drained site (DFCB, fig. 4; table 3) lost 9.2 cm. However, the preburn organic layer was significantly thicker at the wetter site. Therefore, the well-drained site lost 67 percent of its preburn organic matter whereas the moderately well drained site lost only 46 percent. As a result, the moderately well drained site both had more C combusted from the surface organic layer and retained thicker organic layers (fig. 2), which, in turn, provide better soil insulation than at the well-drained site. Those organic layers not burned during a fire play an important role in the long-term C buildup (Harden and others, 2000) because these layers eventually become reburied by moss, providing protection of their carbon from decomposition.

The thickness of organic layers varies not only with fire severity (fig. 2), but also with stand age (table 3). Although these data vary somewhat (see inset, fig. 2), a few interesting trends are noticeable. First, even 45 years after a fire (for example, site DF56; table 3), some evidence of a burn remains in the form of a recognizable char layer. In addition, not until late in the recovery process (>45 years) are dead-moss layers thick enough to be recognized. The late recovery of this layer is likely related to colonization by certain species of feathermoss (see below), which must have either higher rates of production and (or) slower rates of decomposition than early colonization species. Finally, we note that for the moderately well drained sites, the thickness of organic matter decreases

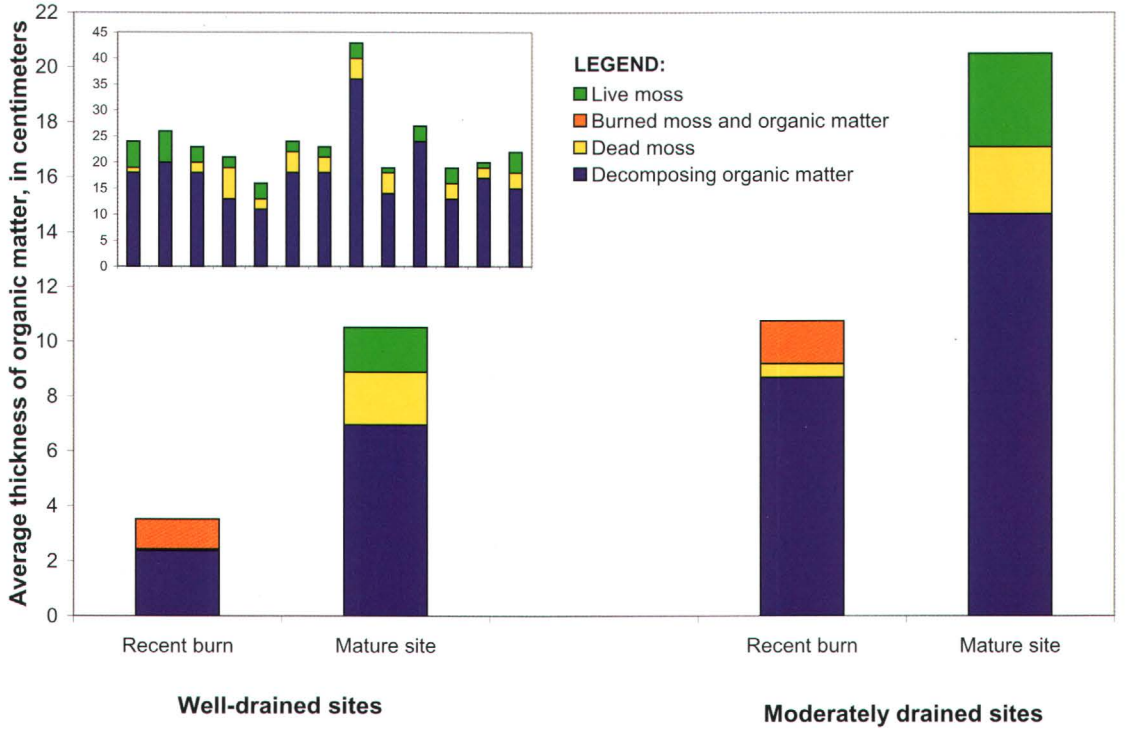

Figure 2. Bar chart comparing preburn and postburn average organic-layer thickness for sites in the Donnelly Flats study area, Alaska (fig. 1). Moderately drained sites have more organic matter, both preburn and postburn, than do well-drained sites. Inset shows variation in individual measurements of horizon thickness within mature, moderately well drained site.

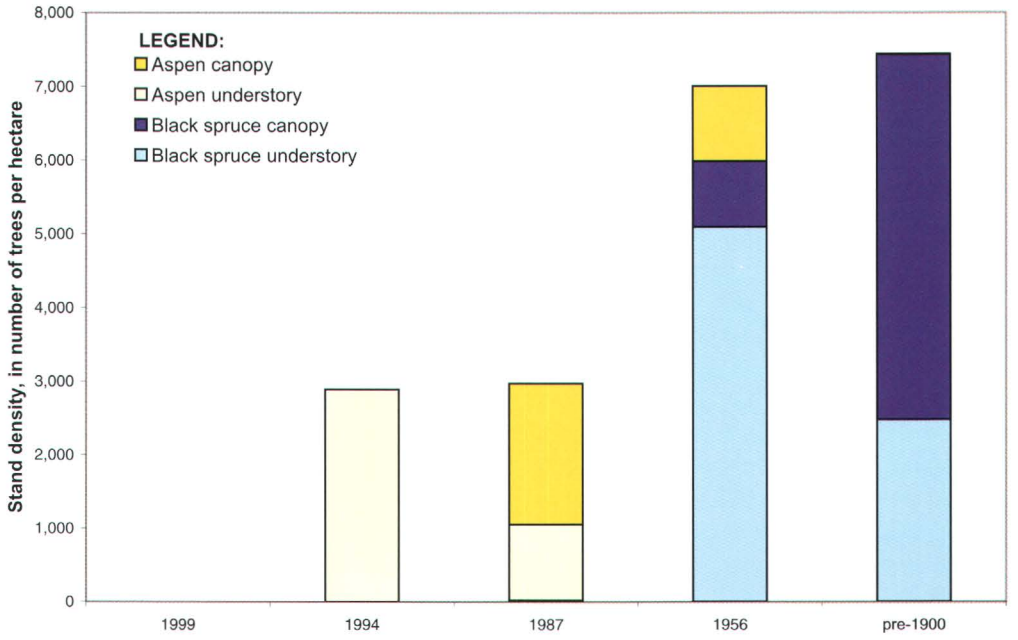

Figure 3. Stand density at sites in the Donnelly Flats study area, Alaska (fig. 1), showing how species composition of both understory (<3 m tall) and canopy (≥3 m tall) changes over time.

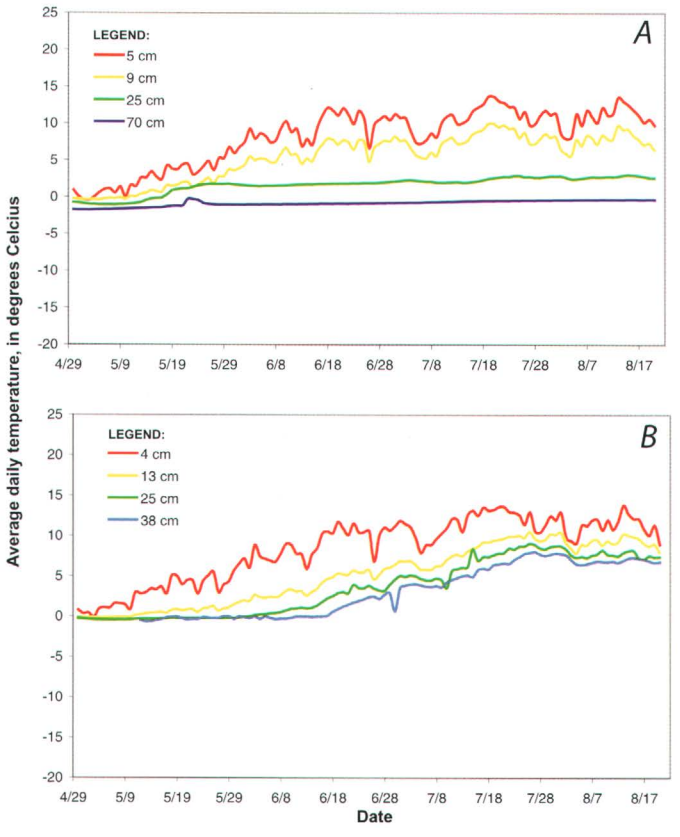

Figure 4. Average daily temperature in 2001 at various depths at moderately well drained sites (DFCB, DFCC) in the Donnelly Flats study area, Alaska (fig. 1). Lower and more even average daily temperatures are measured at mature site (*A*) than at recently burned site (*B*). Temperature probes at 25-cm depth, both in mineral soil, are most comparable.

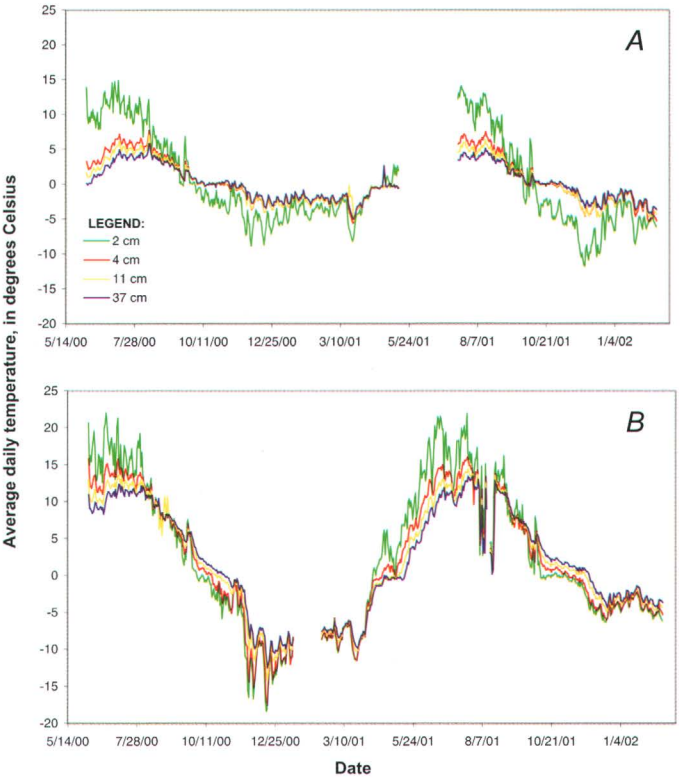

Figure 5. Average daily temperature in 2000–2 at various depths at well-drained sites (DFTB, DFTC) in the Donnelly Flats study area, Alaska (fig. 1). Seasonal amplitude is lower at mature site (*A*) than at recently burned site (*B*).

Table 3. Average thickness of organic layers at site in the Donnelly Flats study area (fig. 1), by drainage type.

[All values in centimeters. Classifications: bL, bD, bF, bM, and bH, burned moss and organic matter; D, dead moss; F, M, and H, decomposing organic matter; L, live moss. See text for definitions]

	Well-drained sites			Moderately well drained sites			
Year of burn	1999	1987	pre-1900	1999	1994	1956	pre-1900
Site	DFTB	DF87	DFTC	DFCB	DF94	DF56	DFCC
Live moss	0.0	0.6	1.6	0.0	1.0	3.4	2.9
Burned moss and organic matter.	1.1	3.7	.0	1.6	3.6	1.0	.0
Dead moss	.0	.0	1.9	.5	.0	.0	2.4
Decomposing organic matter.	2.4	1.2	7.0	8.7	.6	1.9	14.7
Total organic matter	3.5	5.4	10.5	10.8	5.2	6.3	20.0
Number of samples	20	12	26	12	11	10	14

Table 4. Differences in 2001 vegetation by drainage type and years since last fire.

[All values in percent. Study areas: DF, Donnelly Flats; TF, Tanana Flats. Average cover data are for moss, lichen, and other materials; average composition of moss cover lists the most prevalent (>5 percent) species within the moss cover. Because Tanana Flats sites were not measured until 2002, data for those sites (Xs) are based on field observations only]

	Well-drained sites			Moderately well drained sites				Poorly drained sites		
Site	DFTB	DF87	DFTC	DFCB	DF94	DF56	DFCC	TFSB	TFSR	TFSC
Average cover										
Moss (all species)	5	58	64	5	78	56	87	--	--	--
Lichen (all species)	0	4	28	6	5	2	10	--	--	--
Other (for example, soil, wood).	95	38	8	89	17	42	3	--	--	--
Average composition of moss cover										
Aulacomnium sp	--	--	--	--	--	78	22	--	--	--
Ceratodon sp	49	30	--	9	90	--	--	--	--	--
Dicranum sp	49	--	--	9	--	--	--	--	--	--
Hylocomium sp	--	--	91	--	--	16	54	--	--	--
Pluerozium sp	--	--	--	--	--	--	10	--	--	--
Polytrichum sp	--	70	--	82	10	--	9	--	--	--
Rhytidium sp	--	--	7	--	--	--	--	--	--	--
Sphagnum sp	--	--	--	--	--	--	--	--	X	X
None	--	--	--	--	--	--	--	X	--	--

drastically after a burn and recovers only very slowly (table 3). This change is likely due to the minimization of soil C inputs (net primary production) with the continuation, or increase, in C losses (decomposition).

Recovery of Vegetation

Fires within the boreal forest are generally stand replacing, meaning that little, if any, live vegetation exists immediately postburn. Therefore, both canopy and understory species go through a series of changes, known as succession. The first vegetation to colonize burned sites includes moss species, such as *Ceratodon* sp., *Dicranum* sp., and *Polytrichum* sp. (table 4). These species colonize sites quickly because they have lightweight spores or other physiologic adaptations that allow them to rapidly spread after a burn (Johnson, 1981). Which of these three species dominates the site appears to depend on drainage—the well-drained site (DFTB, table 4) is dominated by *Ceratodon* sp. and *Dicranum* sp., whereas most of the moss at the moderately well drained site (DFCB, table 4) is Polytrichum sp.

Vegetative recovery is also affected by changes in soil insulation and shading. Because no living trees remain immediately after a fire, the open stands provide an optimum environment for shade-intolerant species. One such species, aspen (*Populus tremuloides* Michx.), begins to dominate these stands within years after a fire (fig. 3). Because, on a stand level, aspen can intercept more sunlight than can black spruce (*Picea marina* (Mill.) BSP), changes in canopy cover to this tree species may affect the composition of understory and moss species. Mosses also generally do not survive the heavy litterfall below mature aspen stands (Viereck and others, 1983). Additionally, snow interception by aspen, a deciduous species, may be much less than by black spruce, resulting in warmer winter temperatures.

Over time, early-successional tree species give way to black spruce (fig. 3), which differs from aspen in that it does not provide as much canopy cover (at the stand level) as it does year-round shading. At this time, sites become dominated by late successional moss species, such *Hylocomium* sp. and *Aulacomnium* sp. (table 4; Viereck and others, 1983). Again, drainage plays a role in species prevalence; whereas most of the moss at the mature sites is *Hylocomium* sp., the moderately well drained control site (DFCC, table 4) also has significant populations of *Aulacomnium* sp. Additionally, the well-drained mature site (DFTC) has less total moss cover than the moderately well drained site (DFCC) and has significant cover by lichens (table 4). Therefore, soil drainage undoubtedly plays an important role in determining the amount and types of moss cover in both younger and older stands.

Temperature

Drainage also plays a role in soil temperature regimes. Mean late-summer mineral-soil temperatures were ~1.4°C cooler at the unburned, moderately well drained permafrost site (25-cm depth at site DFCC, fig. 4) than at the unburned, well-drained site (37-cm depth at site DFTC, fig. 5). Cooler, more stable soil temperatures at the moderately well drained site likely reflect several interrelated factors, one of which is difference in insulation by organic layers, which are thicker at the moderately well drained site. Differences also exist between the sites in water retention by both permafrost and deep mineral-soil horizons.

Fire affects soil-temperature regimes by increasing both seasonal and daily amplitudes (figs. 4, 5). Differences between burned and unburned plots ranged as high as 13°C. Two years postfire, differences in soil temperatures between burned and unburned moderately well drained sites are less pronounced than differences between burned and unburned well-drained locations (fig. 6). Thus, the thickness of insulating organic layers appears to be an important control on soil-temperature regimes in both burned and unburned stands.

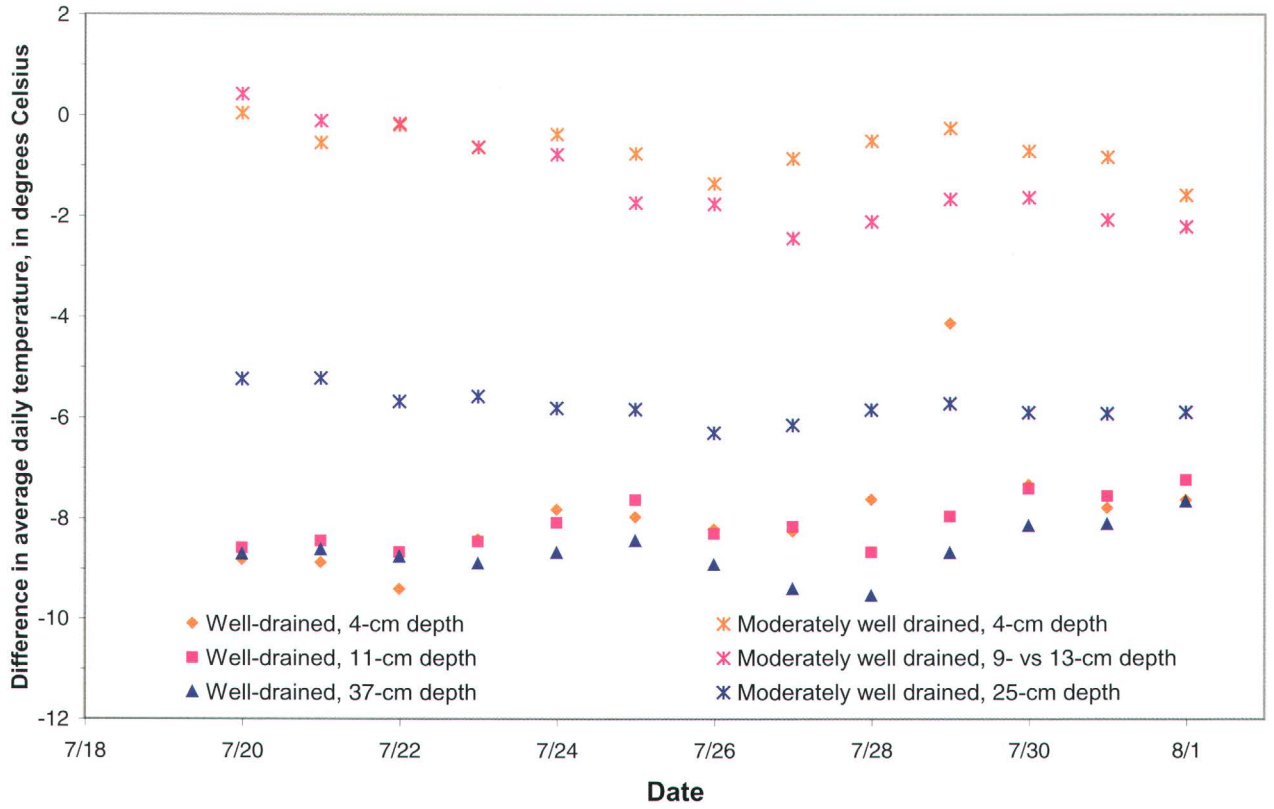

Figure 6. Difference in average daily temperature in 2001 for different soil-drainage classes at mature and burned sites in the Donnelly Flats study area, Alaska (fig. 1). Negative values indicate that temperatures are higher at burned site than at mature site. Differences are greater at well-drained than at moderately well drained site.

Conclusions

Soil drainage, and its dynamic state in the presence of permafrost, exert a major control on both ecosystem structure (for example, species occurrence) and function (for example, how species respond). Whereas fire forces major changes in the physical and chemical states of an ecosystem, soil drainage, with its control on vegetation, moderates the way ecosystems recover. The effects of soil drainage on postfire recovery are clearest during the first few years after a fire, when the vegetation responds immediately to fire severity and melting permafrost in its revegetation responses. However, soil drainage also affects long-term recovery because wetter sites regenerate moss cover of different species at different rates (table 4). The most significant effect of fire is an increase in the amplitude between summer and winter soil temperatures. Differences in temperature between burned and unburned plots at sites in the Donnelly Flats study area ranged as high as 13°C in the shallow organic layers and above 10°C for the deeper mineral-soil horizons (figs. 4, 5). O'Neill and others (2003) also observed warmer summer temperatures in burned areas.

Understanding the feedbacks between soil drainage, fire severity, and postfire revegetation will be important for predicting how fire affects boreal-forest C storage. One of our main goals is to quantify preburn and postburn organic layers, because they have been shown to strongly affect soil temperature (Viereck, 1982; O'Neill and others, 2003) and revegetation (Van Cleve and Viereck, 1984), which, in turn, affect C cycling (Zimov and others, 1999). Along with our collaborators, we are also collecting data that will allow us to quantify net primary production, nutrient inputs and losses, fire-related inputs to the soil (for example, woody debris), and C loss through decomposition (R_h). Each of these components is being examined along various drainage types so that we may better understand how fire affects the C storage in boreal forests and how this effect depends on soil drainage.

References Cited

Birkeland, P.W., 1999, Soils and geomorphology (3d ed.): New York, Oxford University Press, 430 p.

Cottam, Grant, and Curtis, J.T., 1956, The use of distance measures in phytosociological sampling: Ecology, v. 37, p. 451–460.

Cubasch, Ulrich, Dai, X., Ding, Y., Griggs, D.J., Hewitson, Bruce, Houghton, J.T., Isaksen, I.S.A., Karl, T., McFarland, M., Meleshko, V.P., Mitchell, J.F.B., Noguer, M., Nyenzi, B.S., Oppenheimer, M., Penner, J.E., Pollonais, S., Stocker, T., and Trenberth, K.E., 2001, Technical summary of IPCC report climate change 2001—the scientific basis: Intergovernmental Panel on Climate Change Working Group I.

Flanagan, P.W., and Van Cleve, Keith, 1983, Nutrient cycling in relation to decomposition and organic-matter quality in taiga ecosystems: Canadian Journal of Forest Research, v. 13, p. 795–817.

Harden, J.W., Trumbore, S.E., Stocks, B.J., Hirsch, A., Gower, S.T., O'Neill, K.P., and Kasischke, E.S., 2000, The role of fire in the boreal carbon budget: Global Change Biology, v. 6, p. S174–S184.

Johnson, E.A., 1981, Vegetation organization and dynamics of lichen woodland communities in the Northwest Territories, Canada: Ecology, v. 62, p. 200–215.

Kasischke, E.S., 2000, Boreal ecosystems in the global carbon cycle, *in* Kasischke, E.S., and Stocks, B.J., eds., Fire, climate change, and carbon cycling in the boreal forest: New York, Springer-Verlag, p. 19–30.

McGuire, A.D., Melillo, J.M., Kicklighter, D.W., Pan, Y., Xiao, X., Helfrich, J.V.K., III, Moore, B., III, Vorosmarty, C.J., and Schloss, A.L., 1997, Equilibrium responses of global net primary production and carbon storage to doubled atmospheric carbon dioxide; sensitivity to changes in vegetation nitrogen concentration: Global Biogeochemical Cycles, v. 11, p. 173–189.

Meier, R., Harden, J.W., Silapaswan, C., Swanson, D.K., Zhuang, Qianlai, and McGuire, A.D., 2000, Characterization of soil drainage classes for the study of soil carbon storage in Alaska [abs]: Eos (American Geophysical Union Transactions), v. 81, p. 1353.

O'Neill, K.P., Kasischke, E.S., and Richter, D.D., 2003, Seasonal and decadal patterns of soil carbon uptake and emission along an age-sequence of burned black spruce stands in interior Alaska: Journal of Geophysical Research, v. 108, no. D1, doi: 1029/2001 JD000443.

Stocks, B.J., and Kauffman, J.B., 1997, Biomass consumption and behavior of wildland fires in boreal, temperate, and tropical ecosystems: parameters necessary to interpret historic fire regimes and future fire scenarios, *in* Clark, J.S., Cachier, H., Goldammer, J.G., and Stocks, B.J., eds., Sediment records of biomass burning and global change: Berlin, Springer-Verlag, p. 169–188.

Van Cleve, Keith, and Viereck, L.A., 1984, A comparison of successional sequences following fire on permafrost-dominated and permafrost-free sites in interior Alaska, in International Conference on Permafrost, 4th, Fairbanks, Alaska, 1983, Proceedings: Washington, D.C., National Academy Press, p. 1286–1291.

Viereck, L.A., 1982, Effects of fire and firelines on active layer thickness and soil temperatures in interior Alaska, *in* French, H.M., ed., Canadian Permafrost Conference, 4th, Calgary, Alberta, 1981, Proceedings, National Research Council of Canada, p. 123–135.

Viereck, L.A., Dyrness, C.T., Van Cleve, Keith, and Foote, M.J., 1983, Vegetation, soils, and forest productivity in selected forest types in interior Alaska: Canadian Journal of Forest Research, v. 13, p. 703–720.

Zimov, S.A., Davidov, S.P., Zimova, G.M., Davidova, A.I., Chapin, F.S., III, Chapin, M.C., and Reynolds, J.F., 1999, Contribution of disturbance to increasing seasonal amplitude of atmospheric CO_2: Science, v. 284, no. 5422, p. 1973–1976.

Studies by the U.S. Geological Survey in Alaska, 2001
U.S. Geological Survey Professional Paper 1678

Trident Volcano: Four Contiguous Stratocones Adjacent to Katmai Pass, Alaska Peninsula

By Wes Hildreth, Judy Fierstein, Marvin A. Lanphere, and David F. Siems

"It was thither the travellers were bound, headed toward Katmai Pass, which is no more than a gap between peaks, through which the hibernal gales suck and swirl. This pass is even balder than the surrounding barrens, for it forms a funnel at each end, confining the winds and affording them freer course... [Later] the storm was upon them, sweeping through the chute wherein they stood with rapidly increasing violence... It was Dante's third circle of hell let loose—Cerberus baying through his wide, threefold throat, and the voices of tormented souls shrilling through the infernal shades. It came from behind them, lifting the fur on the backs of the wolf-dogs and filling it with powder, pelting their hides with sharp particles until they refused to stand before it..."

Rex Beach, *The Silver Horde* (1909)

Abstract

Trident Volcano lies between Katmai Pass and Mount Katmai along the volcanic front of the Alaska Peninsula reach of the Aleutian Arc. Trident consists of four contiguous stratovolcanoes and several peripheral lava domes, all andesitic-dacitic in composition. Construction of the four principal edifices proceeded stepwise from northeast to southwest. The oldest edifice, East Trident, grew into a 7-km^3-volume stratocone, about 1,000 m high, during a brief eruptive lifetime around 143±8 ka. The central and highest peak, Trident I, buttressed by East Trident, grew into an adjacent 8-km^3-volume stratocone and ended its activity by about 58±15 ka. The third center, West Trident, is a 900-m-high edifice that overlaps the west flank of Trident I; accumulation of its 3- to 4-km^3 eruptive volume was largely completed by 44±12 ka. After glacial dissection of the three Pleistocene cones, a fourth edifice, Southwest Trident, was constructed between 1953 and 1974, overlapping the southwest flanks of two of the older cones. The young volcano produced about 0.7 km^3 of lava and ejecta, including four blocky lava flows and a 3-km^2-area composite cone that remains fumarolically active. Several glaciated dacitic lava domes at the periphery of the Trident group have compositional affinity with the main cones, and all of the lava domes appear to predate some of the lava flows that issued from West Trident and Trident I. The only domes dated are Falling Mountain (70±8 ka) and Mount Cerberus (114±46 ka), which together frame the entrance to Katmai Pass. Two clusters of warm springs and two fields of sulfurous fumaroles have been studied by other workers. Geophysical anomalies that are centered near Katmai Pass and overlap the western part of the Trident group include traveltime delays and attenuation of seismic waves, a Bouguer gravity low, hundreds of small shallow earthquakes each year, and several centimeters of recent uplift detected by synthetic-aperture-radar interferometry. Reconstruction of the eroded edifices yields an estimated eruptive volume for the whole Trident group of 21±4 km^3. Averaged over 143±8 k.y., this output gives a long-term eruption rate of 0.11 to 0.18 km^3/k.y., far smaller than the rates calculated for neighboring Mageik and Katmai Volcanoes.

Introduction

Trident Volcano is actually a group of four stratovolcanoes and several lava domes, part of the Katmai volcanic cluster on the upper Alaska Peninsula (fig. 1). As the main summits of Trident form part of the peninsular drainage divide, their eruptive products have flowed down both sides of the volcanic axis. Eruptive activity at Trident began by 143 ka, before initiation of the neighboring Mageik and Katmai Volcanoes. Accordingly, most components of the Trident group have been sharply dissected during several periods of glacial expansion. From Trident, nonetheless, there also issued the Katmai cluster's most recent eruptive episode, which built a new stratocone and a derivative lava-flow apron between 1953 and 1974. Of the several volcanoes in the Katmai cluster (fig. 1), Trident is the closest to Novarupta (fig. 2), where a new vent opened through Jurassic basement rocks in 1912 to release the world's most voluminous 20th-century eruption (Fierstein and Hildreth,

1992). In the course of studying the products of that eruption, we undertook a detailed reconnaissance of the Trident group (fig. 3), much of which is blanketed by 1912 pumice-fall deposits (figs. 3, 4). We report the results of that reconnaissance investigation here.

Previous Work

Trident was named during the National Geographic Society expedition of 1916, which began as an investigation into the ecologic effects of the 1912 eruption (Griggs, 1922). The fine 1916 photograph of Trident (Griggs, 1922, p. 98), a view northwestward from the mouth of Mageik Creek canyon (a site just east of that of our fig. 4), actually shows the fourth peak of the group (West Trident, figs. 2–4), in addition to the three higher summits prominent from that viewpoint. Evidently, however, the name "Quadrident" lacked sufficient euphony to appeal to Griggs' late Edwardian taste. Just as well, as a fifth summit was constructed after 1953.

Trident received little attention before the onset of its eruption in 1953. After crossing Katmai Pass in 1898, Spurr (1900) noted that two volcanoes (then unnamed) flank the pass, and he mentioned thermal springs south of the pass. Reporting on his 1915–19 expeditions, Griggs repeatedly

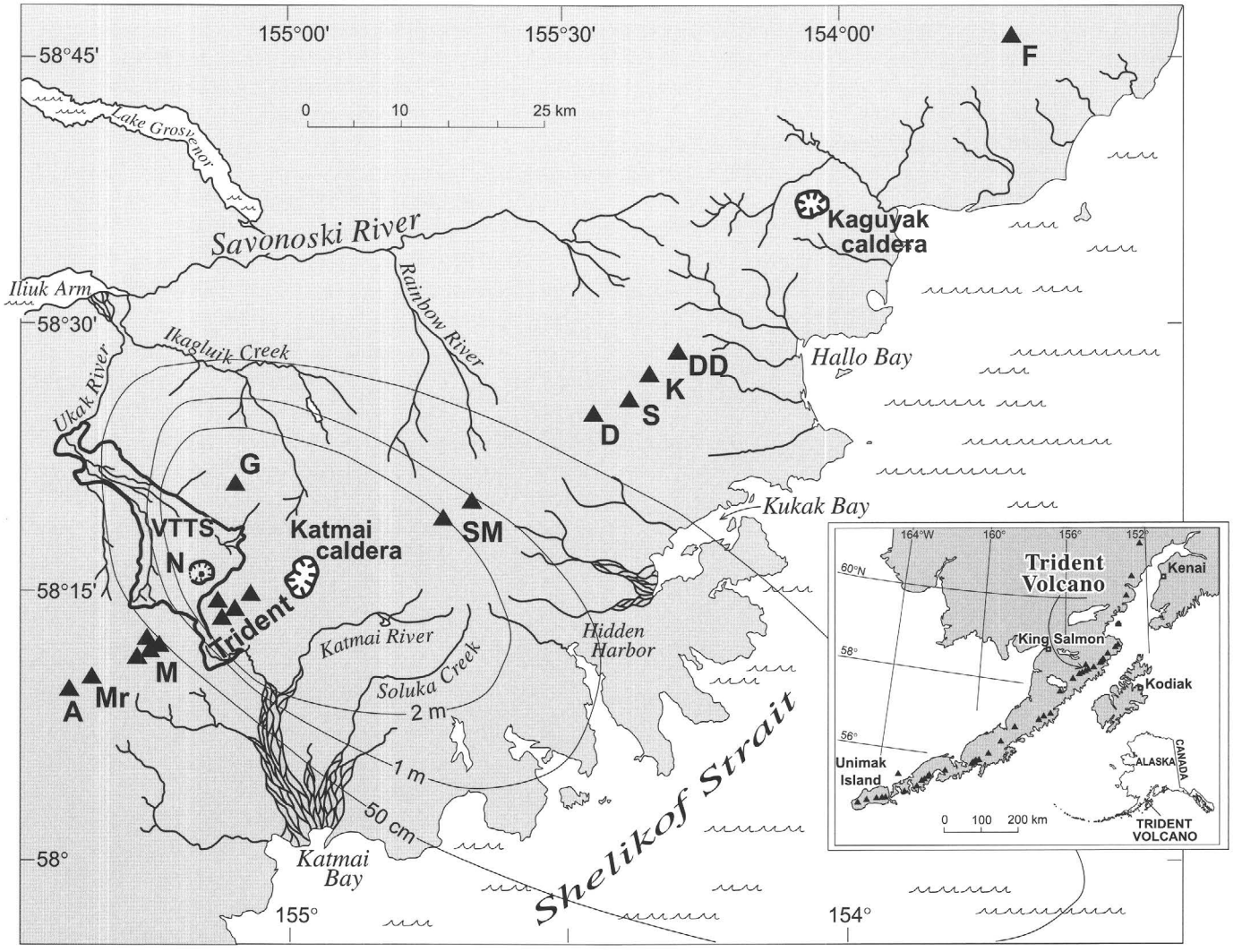

Figure 1. Southern Alaska, showing location of Trident Volcano, a cluster of four cones, along late Quaternary volcanic axis, which straddles drainage divide on this stretch of the Alaska Peninsula. Triangles, andesite-dacite stratovolcanoes: A, Alagogshak; D, Denison; DD, Devils Desk; F, Fourpeaked, G, Griggs; K, Kukak; M, Mageik (cluster of four); Mr, Martin; S, Steller; SM, Snowy Mountain (two cones). VTTS, Valley of Ten Thousand Smokes ash-flow sheet (outlined area), which erupted at Novarupta (N) in June 1912 and also poured southward through Katmai Pass between Trident and Mageik Volcanoes. Isopachs show thickness of cumulative plinian fallout from Novarupta, originally 2 to 10 m thick over Trident Volcano. Inset shows town of King Salmon just west of elongate Naknek Lake, of which the Iliuk Arm is southeastern branch.

referred to Trident as an "old volcano"; he, too, mentioned the thermal springs at its southwest toe, and he illustrated a fumarolic plume on its southeast flank (Griggs, 1922, p. 98). Sporadic observations of the 1953–74 eruptive activity were summarized by Muller and others (1954), Snyder (1954), Decker (1963), Ward and Matumoto (1967), and Simkin and Siebert (1994). The 1953–63 eruptive products were studied petrologically by Ray (1967) and in detail, analytically and experimentally, by Coombs and others (2000). Several unlocated grab samples from the prehistoric edifices of Trident were studied petrologically by Kosco (1981). Progress reports touching on our own intermittent work at Trident were summarized in Hildreth (1987, 1990), Fierstein and Hildreth (2000), and Hildreth and Fierstein (2000).

Basement Rocks

Quaternary volcanoes of the Katmai cluster are built atop a rugged set of glaciated ridges carved from subhorizontal to gently warped marine siltstone and sandstone (fig. 4) of the Jurassic Naknek Formation (Riehle and others, 1993; Detterman and others, 1996). These well-stratified rocks are intruded locally by porphyritic granitoid stocks of Tertiary age. Although both types of basement rock crop out as high as 4,500 ft (1,370 m) near the col between Trident and Mount Katmai (fig. 3), the Trident lavas drape and conceal most of the basement down to elevations no higher than 2,600 ft (790 m) to the southeast and 1,500 ft (460 m) to the south. At the western and northern margins of the Trident group, where

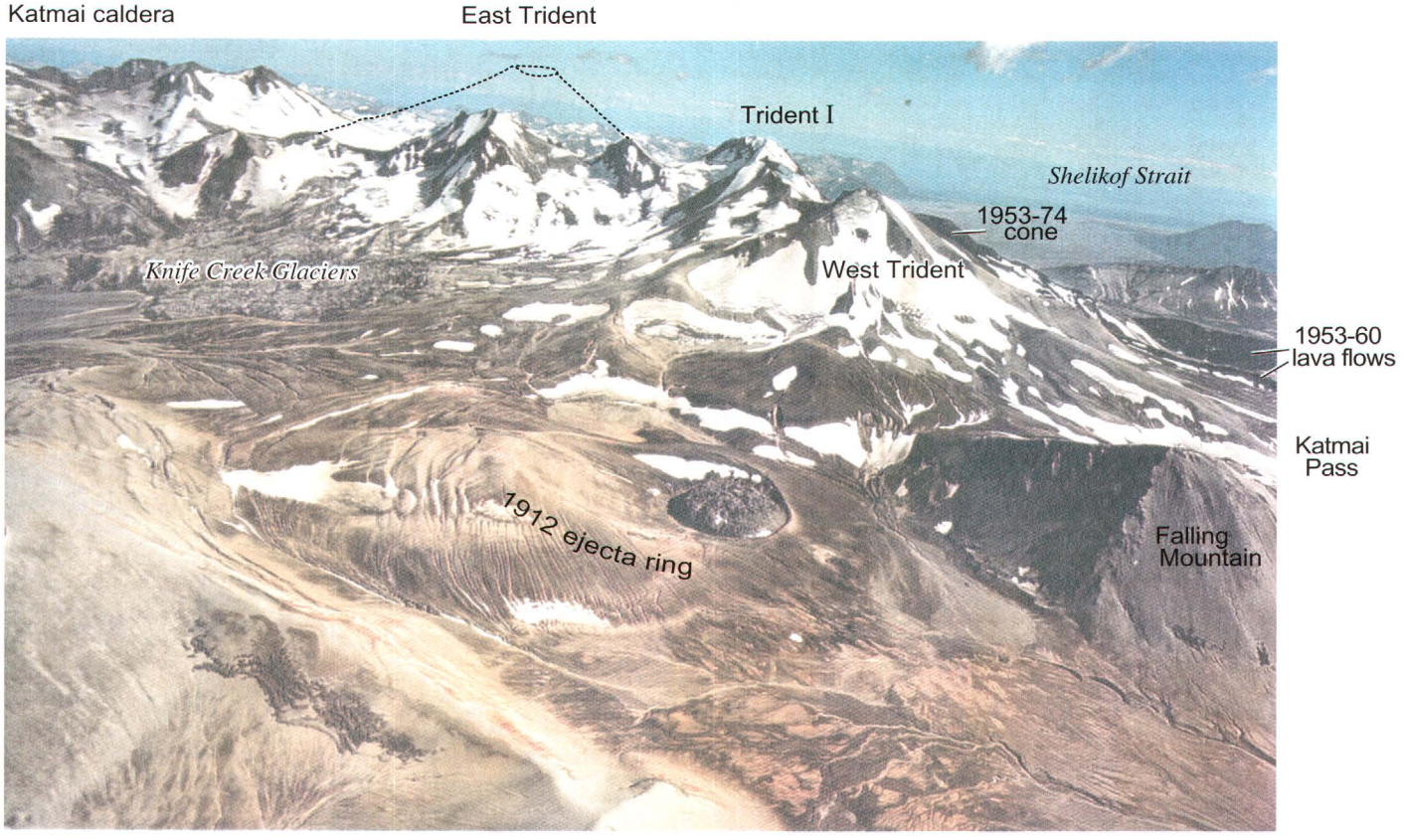

Figure 2. Aerial panorama of Trident Volcano southeastward over 1912 vent depression and small circular lava dome, Novarupta, in central foreground (see fig. 1 for locations). At upper left, Katmai caldera (centered 10 km east of Novarupta) is separated by a low saddle from four prominent peaks of the Trident group. Eastern two peaks are glaciated remnants of East Trident Volcano (as schematically reconstructed); highest is Trident I Volcano, and 3 km behind Novarupta is snowclad West Trident Volcano. Partly hidden behind West Trident is black cone of Southwest Trident (1953–74) and its lava-flow apron (at far right) in Katmai Pass and Mageik Creek. Flat in distance is alluvial plain of Katmai River, which joins Shelikof Strait at Katmai Bay. On blue horizon beyond strait is Kodiak Island. Foreground is dominated by 1912 vent depression, which extends 2.5 km northeastward (to left) from base of 400-m-high scarp of Falling Mountain dacite dome (lower right), a member of the Trident group. 1912 vent funnel was backfilled by welded ignimbrite and fallback ejecta, deformed by compaction-induced faulting, and plugged by 380-m-wide Novarupta rhyolite dome, which is surrounded by a strongly asymmetric ejecta ring. Low gray lobes in left middle distance at foot of East Trident and Mount Katmai are Knife Creek Glaciers, still covered by 1912 ejecta.

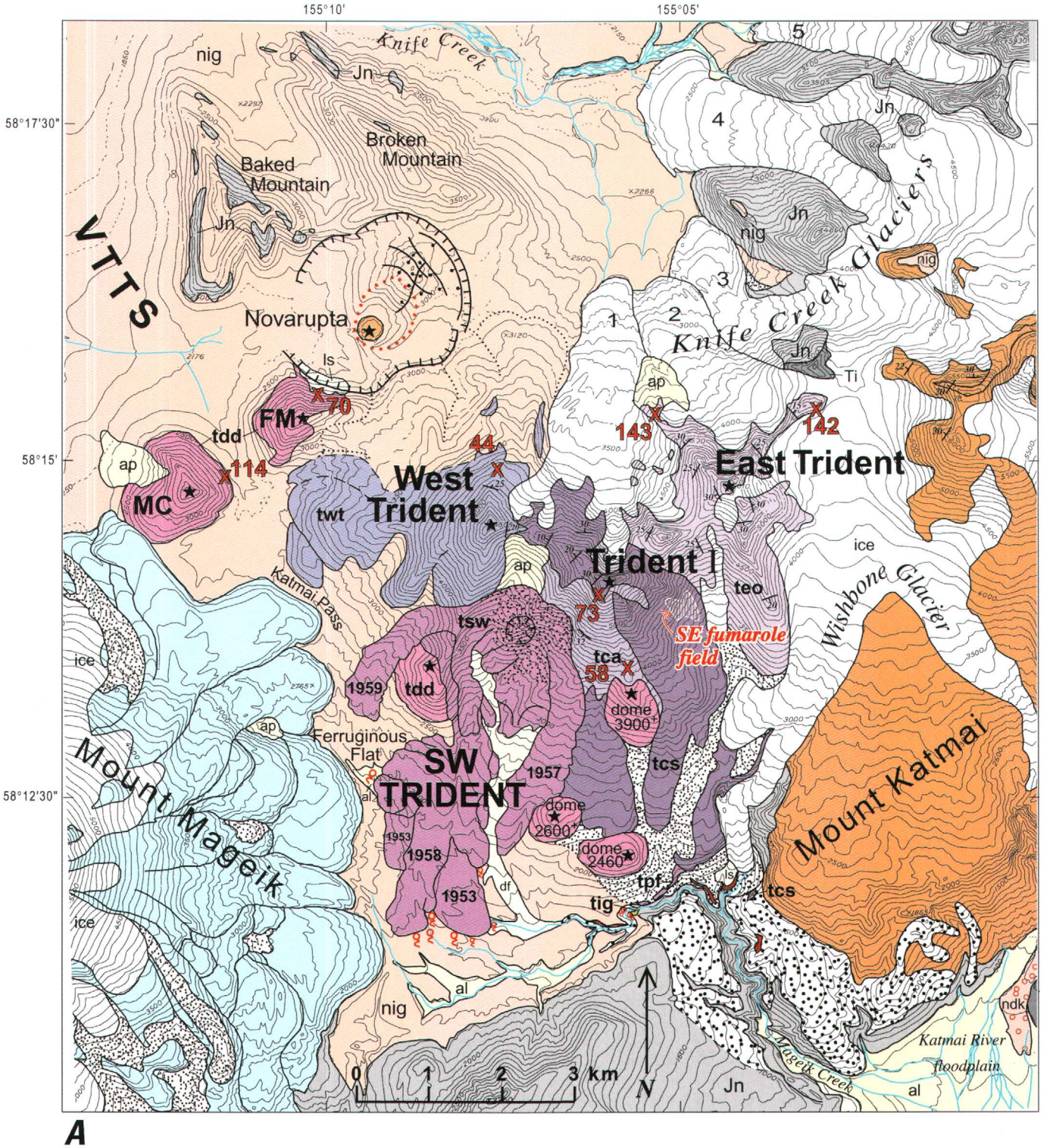

Figure 3. Geologic and topographic maps of the Trident group, flanked by Katmai and Mageik Volcanoes, southern Alaska (see fig. 1 for locations). *A*, Simplified geologic map. To north is the Valley of Ten Thousand Smokes (VTTS), floored by 1912 ignimbrite (unit nig), which also flowed through Katmai Pass from vent at Novarupta (hachured depression) into upper basin of Mageik Creek. Main Trident cones are labeled, and their three-letter unit labels (tca, tcs, teo, tsw, twt) are explained in text. Year of emplacement is labeled for principal lava flows of Southwest Trident, outline of which is drawn from aerial photographs atop preeruptive 1951 topography. Site of initial 1953 outbreak was beneath present crater (hachures) but was subsequently buried by incremental growth of fragmental cone (stippling). Six Trident lava domes (unit tdd) are distinguished, two largest of which are Mount Cerberus (MC) and Falling Mountain (FM). Along Mageik Creek canyon, unit tig (tiny, in green, due south of dome 2460) is dacitic ignimbrite remnant, and unit tpf is lithic pyroclas-

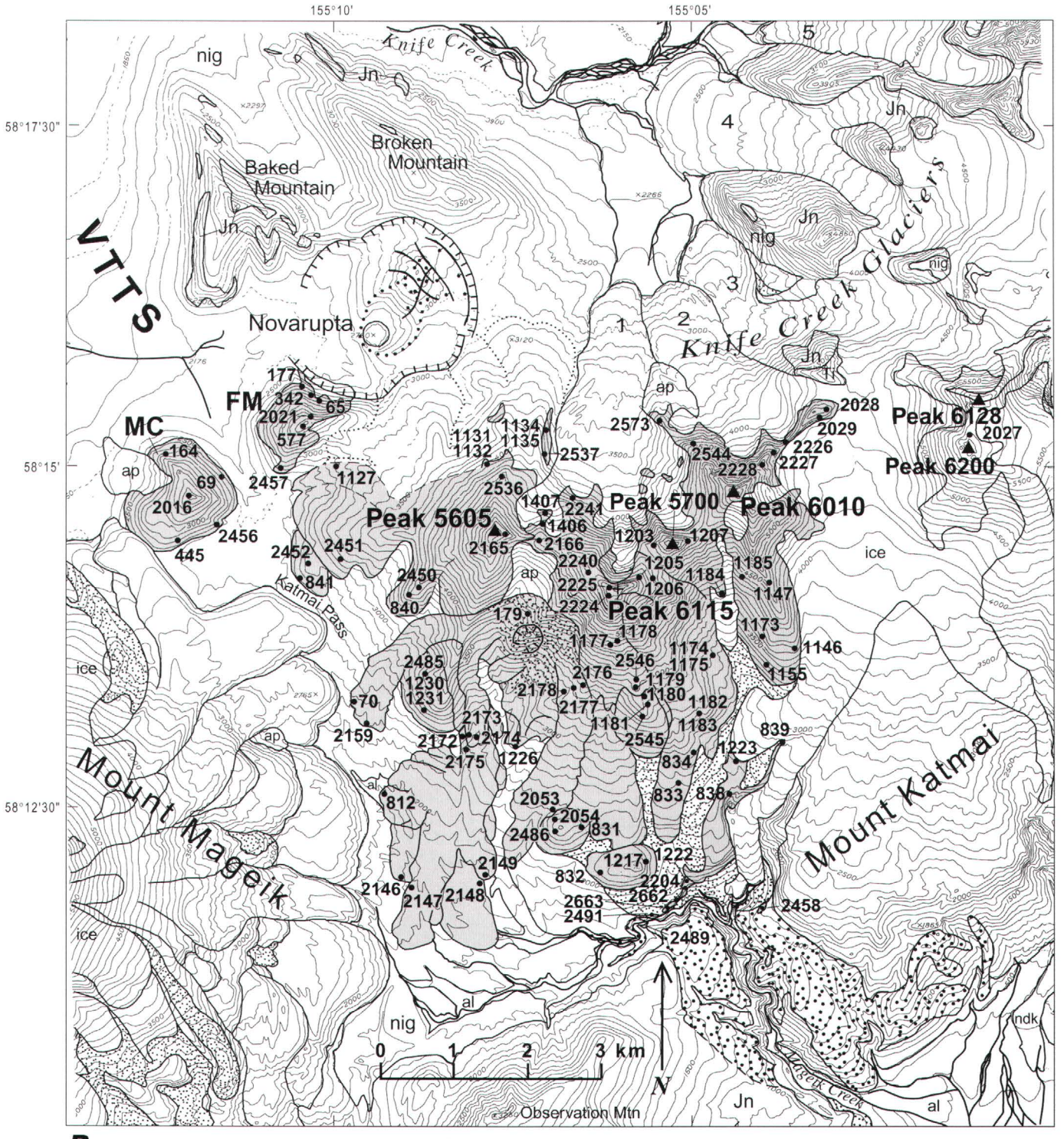

B

tic-flow deposit; both units are Trident derived. Nearby remnants (red areas) are canyon-wall exposures of late Pleistocene rhyodacitic plinian pumice fall and ignimbrite from Mount Katmai. Coarse stippling, Pleistocene till; finer stippling, Holocene till. Bold red Xs, locations of dated samples, with ages in thousands of years (ka). Red tadpoles denote clusters of warm springs. Jn, Jurassic basement rocks of the Naknek Formation; ndk, Katmai River debris-flow deposit of 1912 (Hildreth, 1983); Ti, Tertiary granitoid intrusion. Surficial deposits (pale yellow): al, stream alluvium; ap, pumiceous alluvium reworked from 1912 deposits; df, debris-flow deposits of remobilized ejecta from Southwest Trident cone; ls, landslide and rockfall rubble. *B*, Topographic map of Trident group, showing locations of samples listed in tables 1 and 2 (with K– prefixes omitted) and a few key elevations (in feet). Topographic base for both panels from U.S. Geological Survey 1:63,360-scale Mount Katmai A–4 and B–4 quadrangles (1951); contour interval, 100 ft.

1912 pyroclastic deposits completely obscure any Trident-basement contacts, the subvolcanic basement configuration is poorly known, although it might be as high as 2,500 ft (760 m) in Katmai Pass where thoroughly concealed by 1912 material. Remnants of Tertiary or early Quaternary andesite-dacite volcanic rocks are common just east of Mount Katmai (Riehle and others, 1993), but none are exposed near the Trident group, the products of which are observed (fig. 4) or inferred (fig. 3) to lie directly on the Naknek Formation.

Although Permian to Jurassic sedimentary rocks that regionally underlie the Naknek Formation (itself more than 2 km thick) do not crop out in the Katmai area, the stratigraphic framework of the Alaska Peninsula (Detterman and others, 1996) suggests that such rocks are as much as 3.5 km thick beneath the Katmai volcanoes.

The Mesozoic basement rocks upon which the volcanic centers are built belong to a tectonostratigraphic package commonly called the Peninsular terrane, which is widely thought to have originated far to the south and to have been added to southern Alaska during the middle and late Mesozoic (Plafker and others, 1994). Since then, several additional terranes and subduction-related accretionary complexes were added along Alaska's southern margin, such that the Aleutian Trench (5–6 km below sea level) now lies 350 km southeast of the volcanic line. Eocene sea floor is currently being subducted here, nearly orthogonally, at a convergence rate of about 6 cm/yr. The inclined seismic zone is well defined and 20 to 30 km thick (Kienle and others, 1983). It dips only about 10° NNW. for some 300 km, then steepens to about 45° beneath the present-day arc, and persists to depths as great as 200 km; its top lies about 100 km beneath the Katmai volcanic cluster. Although the arc alignment shifted modestly during the Tertiary (Wilson, 1985; Riehle and others, 1993), the Aleutian Arc was well established along the Alaska Peninsula by the middle Eocene, soon after the onset of northwestward motion of the Pacific Plate beneath southern Alaska (Plafker and others, 1994). The present-day volcanic front trends rather linearly N. 65° E. along the Katmai segment of the arc (fig. 1).

Although the crust beneath the modern volcanic chain remains immature and is probably only 30 km thick, it can be considered at least quasi-continental because many Tertiary

Figure 4. Trident group from the south, with gorge of Mageik Creek in foreground (figs. 1, 3). Stratified rocks on canyon walls are marine siltstone and sandstone of the Jurassic Naknek Formation, dipping 10° ESE. (to right). On skyline at left is black cone of Southwest Trident (1953–74), which largely conceals West Trident edifice, top of which is visible through the adjacent saddle. High central edifice is Trident I (peak 6115), summit lava of which yields an age of 73±12 ka. Two skyline peaks at right are both parts of East Trident edifice, altered core of which has been excavated into a large cirque, still partly occupied by ice. Dark ledge at center is pumice-covered andesitic lava flow from Trident I, forming canyon rim. Steep scree at right descends from buttress of andesitic lava flows erupted at Mount Katmai. Lavas of both Trident and Katmai rest directly on strata of the Naknek Formation. View northward.

granitoid plutons have invaded the Peninsular terrane basement. Crustal earthquakes, generally shallower than 10 km, are abundant beneath the Katmai volcanoes (except Mount Griggs). As many as 1,000 local earthquakes each year have recently been recorded here by the Alaska Volcano Observatory, nearly all of them of $M<2.5$ (Ward and others, 1991; Jolly and McNutt, 1999; Power and others, 2001).

East Trident

The two eastern peaks of the Trident group (figs. 2–4) are both remnants of East Trident Volcano (unit teo, fig. 3), a small andesite-dacite stratocone (58–65 weight percent SiO_2) almost contiguous with Mount Katmai. The rugged edifice is exposed over a 3- by 4-km area, but its lower flanks are concealed beneath glaciers. The hydrothermally altered core of East Trident is gutted by five glacial cirques excavated into the edifice, exposing on steep glacial headwalls windows of stratified ejecta deep in the interior of the skeletal cone. The ridges between cirques reveal structurally simple stacks of 10 to 25 radially dipping lava flows and breccia sheets (fig. 5), mostly silicic andesite, 8 to 30 m thick, but the 100-m-thick lava flows that support the southwest ridge and part of the northeast ridge are dacite (63–65 weight percent SiO_2). The northeast-ridge dacite, which is stratigraphically high in the pile and extends nearly to the summit (peak 6010), yields a K-Ar age of 142±15 ka. An analytically indistinguishable age of 143±8 ka for a near-basal andesitic lava flow low on the northwest ridge suggests, however, that activity at the small East Trident cone was short lived, late in the middle Pleistocene. These ages also indicate that East Trident is the oldest edifice of the Trident group and is, indeed, older than neighboring Katmai and Mageik Volcanoes, as well. Peak 5700+, central prong of the "Trident" as seen from the south or southeast (fig. 4)—the aspect that inspired the name—is not a separate cone but a west-dipping remnant of the ruggedly eroded southwest flank of East Trident. Reconstruction suggests that the cone may once have exceeded 6,600 ft (2,010 m) in elevation (fig. 2), probably making it the highest of the Trident summits.

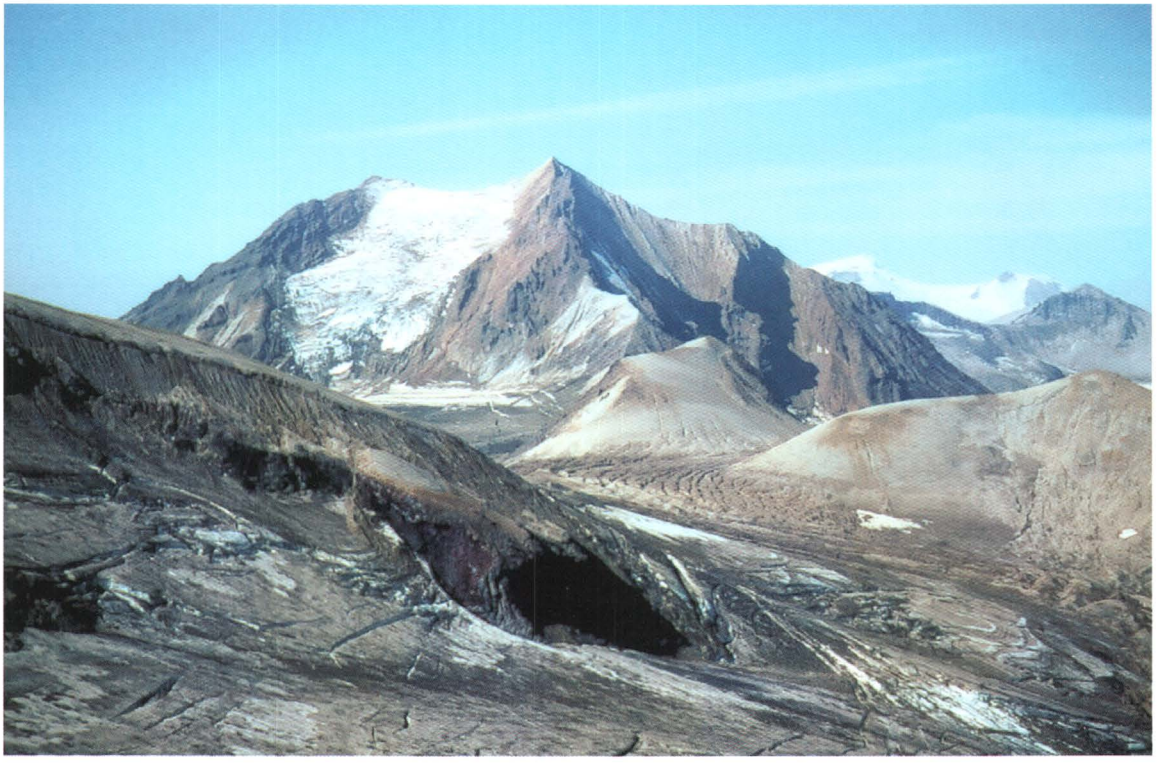

Figure 5. East Trident Volcano, with upper Glacier 3 and northwest buttress of Mount Katmai in foreground (figs. 1, 3). Radial stacks of thin rubbly andesitic lava flows and breccias that dip east (to left) and northwest (to right) support skyline ridges. Central ridge descending from sharp summit (peak 6010) is likewise a stack of andesitic-dacitic lavas, which dip northeast (toward observer) and end in pumice-mantled buttress at center. Adjacent to top of steep glacier on east face, pale-colored acid-altered rocks on skyline form rim of volcano's glacially gutted core, which is occupied by another cirque on far side of edifice (see fig. 4). Pumice-covered ridge at right consists of nonvolcanic basement rocks; ice-fringed ridge in left foreground consists of andesitic lava flows from Mount Katmai. On right skyline, snowy Mount Mageik forms backdrop 8 km beyond saddle separating West Trident (far right) from Trident I (largely hidden). View southwestward.

Trident I

Likewise sculptured glacially, Trident I (peak 6115) is a discrete andesitic cone (53–63 weight percent SiO_2) that forms the central and highest edifice (6,115 ft [1,864 m]) of the Trident group. Its lavas apparently bank against East Trident at their (poorly exposed) mutual saddle, but some overlap of their active lifetimes is not excluded by our present data. Buttressed by East Trident on its northeast, the Trident I edifice (units tcs, tca, fig. 3) grew asymmetrically toward the other sectors. The core of the Trident I edifice is eviscerated by a north-face cirque (fig. 6), the sheer headwall of which reveals the base of the vertically jointed 150-m-thick summit lava (63 weight percent SiO_2), which rests on more than 200 m of crudely stratified coarse breccia. This dacitic lava may be a dome remnant that overlies crater fill and dome breccia on its north side. On its southwest side, the summit dacite rests on a coherent andesitic lava flow (61.7 weight percent SiO_2) that yields a K-Ar age of 73±12 ka. The northwest ridge of the edifice consists mostly of a glaciated stack of thinner lava flows and breccias, but low on steep northern spurs of the ridge are two massive andesitic lavas (60 weight percent SiO_2), each 100 to 200 m thick, which are probably glacially truncated coulees but, alternatively, might be older domes.

The smoother, less dissected south slope of Trident I (fig. 4) consists largely of summit-derived andesitic lava flows (58–62 weight percent SiO_2) and poorly exposed block-and-ash flows that descend to elevations as low as 1,500 ft (450 m) at Mageik Creek. In contrast, the southwest slope (fig. 7) is made up of steeply dipping (25°–35°) sheets, 0.1 to 3 m thick, of agglutinated mafic fallout rich in accidental lithic fragments, subordinate thin pyroclastic-flow deposits, and associated avalanche rubble. Derived from the central vent of Trident I, these deposits (unit tca, fig. 3) are generally gray brown to brick red, but parts were altered ocherous yellow or orange brown, probably while still hot. Fresh juvenile scoriae and spatter in these deposits are olivine-rich andesite, the most mafic material (53–55 weight percent SiO_2) known to have been erupted from the Trident group. A dense spatter blob from agglutinate on the south slope gave a $^{40}Ar/^{39}Ar$ plateau age of 58±15 ka (Hildreth and others, 2003). The strata also contain abundant accidental clasts of the pyroxene andesite that makes up most of the edifice.

Although the edifice of Trident I is glacially ravaged and has had no Holocene eruptions, its lower southeast flank is marked at 3,600- to 4,000-ft (1,100–1,220 m) elevation by a field of sulfur-depositing fumaroles, first recorded in 1916 by Griggs (1922, p. 98) and still vigorous. Another fumarole,

Figure 6. Cirque headwall forming north face of Trident I (peak 6115, figs. 1, 3). Relief framed is 450 m (1,500 ft). Craggy dacitic lava on summit, probably a dome remnant, rests on andesitic lava that yields an age of 73±12 ka and overlies massive and stratified breccia that dips 20°–30° NW., forming cliff at right, which is northeast face of northwest ridge of edifice. Andesite knob (elev, 5,700 ft) on right skyline is draped by buff 1912 pumice-fall deposit. View southward from helicopter.

visible on 1951 aerial photographs as a 100-m-wide steaming pit at 3,850-ft (1,175 m) elevation on the southwest ridge of Trident I, became the vent site for the new volcanic cone that began to grow in 1953 (see section below entitled "Southwest Trident").

West Trident

West Trident (peak 5605) is the smallest and youngest of the prehistoric Trident edifices, as well as the one closest to Novarupta (fig. 2). Heavily mantled by 1912 fallout, its lavas (unit twt, fig. 3) are poorly exposed except near the summit (fig. 8) and along the west wall of Glacier 1. All lavas exposed are silicic andesite or dacite (58–64.4 weight percent SiO_2), and many are unusually rich in chilled enclaves (1–20-cm diam) of phenocryst-poor, relatively mafic andesite (54–58 weight percent SiO_2). The summit lava (61 weight percent SiO_2), which is nearly 100 m thick, may be part of a dome (fig. 8). Adjacent lava flows dip 20° down the north ridgeline (fig. 8), and the top one thickens downslope to 70 m. Other summit-derived lavas and breccia sheets dip east against Trident I at their mutual saddle. Although the contact is obscured by 1912 and 1953 pyroclastic deposits, the contrast between these east-dipping silicic andesite flows and the steeply southwest-dipping sheets of mafic agglutinate that make up the nearby southwest face of Trident I supports the inference (based on physiography and attitudes of lavas) that West Trident is truly a discrete cone rather than a shoulder of Trident I isolated by erosion. The K-Ar age of 44±12 ka measured for the thick andesitic lava flow that forms the crest of the north ridge (fig. 8) supports our stratigraphic and morphologic inference that West Trident is the youngest of the prehistoric centers in the Trident group.

Mostly ice free today, West Trident was formerly ice covered and is everywhere glacially modified. On its flanks, poorly exposed glaciated lavas form an array of seven sharp-crested ridges that descend radially from the summit. Four northerly spurs and the southwest ridge all appear to be lava flows, but the west and south ridges may include lava domes abutted by lava flows from West Trident and later jointly sculptured glacially and blanketed by 1912 pumice falls. Some of the northerly lava flows bank against Falling Mountain dome (70±8 ka), and just east of there the distal parts of adjacent lavas were destroyed on June 6, 1912, by collapse into the

Figure 7. Southwest face of Trident I edifice (figs. 1, 3). Entire left slope, as well as dark buttress to right of pumice scree chute, is composed of steeply dipping sheets of agglutinate, scoria, and breccia (58±15 ka) that largely consist of olivine-rich andesite (53–55 weight percent SiO_2), most mafic material identified in Trident group. Much of mafic material is altered, especially on orange-brown to ocher lower slopes. Pumice-mantled knob on left skyline (elev, 5,700 ft; also visible in fig. 6) is a stratigraphically higher andesitic lava flow (60.4 weight percent SiO_2) that dips 20° NW. down northwest ridgeline, away from observer. Craggy skyline unit at right is dacite dome on summit of Trident I (see figs. 4, 6). View northward from helicopter.

Novarupta vent, thereby providing most of the andesitic lithic clasts among the Episode I ejecta (Fierstein and Hildreth, 1992).

Trident Domes

At least five (and as many as eight) pyroxene-dacite lava domes (62–65 weight percent SiO_2) line the lower west and south flanks of the Trident group (unit tdd, fig. 3). Three ambiguous candidates along Katmai Pass are steep blunt-nosed buttresses of West Trident that were abutted or overrun by younger lava flows, sculptured glacially, and so heavily mantled by 1912 pyroclastic deposits that their distinction as domes or thick flow lobes from West Trident remains uncertain. These eight domes do not include the four domes (or thick proximal flows) already mentioned high on the adjacent edifices of Trident I and West Trident. All 12 domes lie within 7 km of each other in a compact zone that includes the site of the new cone built in 1953–74.

The two largest domes (fig. 9), 425-m-high Falling Mountain and 365-m-high Mount Cerberus (each 0.3–0.4-km^3 volume), are compositionally similar to the smaller (unnamed) domes, which range in volume from 0.015 to 0.12 km^3. Like West Trident, all the domes contain chilled enclaves (1–15-cm diam) of phenocryst-poor andesite (54–58 weight percent SiO_2), although such enclaves are uncommon in the dacite of Mount Cerberus. All the domes are glacially scoured, and several are severely eroded. Mount Cerberus and Falling Mountain, however, are stout domes that are morphologically little modified by ice and were suspected of being very young (Hildreth, 1983, 1987). Repeated search has nonetheless turned up few remnants of glassy carapace, and K-Ar data now give late Pleistocene ages for both domes—Falling Mountain 70±8 ka and Mount Cerberus 114±46 ka. The superficiality of glacial erosion may reflect their compact profiles and positions close to the Alaska Peninsula drainage divide. Flanking the entrance to Katmai Pass at the northwest foot of West Trident (fig. 9), both domes (63–65 weight percent SiO_2) have a compositional affinity (low K, Zr) with the Trident group. A lava flow from the East Summit subedifice of Mount Mageik banks against Mount Cerberus, and lavas from the West Trident cone bank against Falling Mountain (fig. 3). The northeast face of Falling Mountain was destroyed during the great eruption at Novarupta (fig. 2), providing some of the accidental lithic clasts in 1912 pyroclastic deposits (Fierstein and Hildreth, 1992).

Two low domes (2460 and 2600+) on the north side of Mageik Creek are glacially subdued, abutted by lava flows from Trident I and Southwest Trident, and heavily mantled by 1912 fallout (fig. 10). Each has only 150 m relief and a volume of 0.030 to 0.035 km^3, in contrast to dome 3900+ (2 km farther north, fig. 10), which has twice the relief and 3 times the volume. All the domes have clear compositional affinity (low K, Zr) with the Trident group and are chemically and

Figure 8. Northeast face of West Trident Volcano (peak 5605, figs. 1, 3). Steep face provides only large exposure on edifice, which is elsewhere blanketed by thick 1912 fallout from nearby Novarupta. Three andesitic lava flows dip to right, down north ridge; top flow yields K-Ar age of 44±12 ka. Face-forming lava, 70 to 100 m thick, which dips toward observer and into saddle separating West Trident from Trident I, may be a thick lobe of an otherwise-concealed summit dome. In foreground, andesitic lava flow capping northwest ridge of Trident I edifice dips northwest beneath West Trident edifice. View westward.

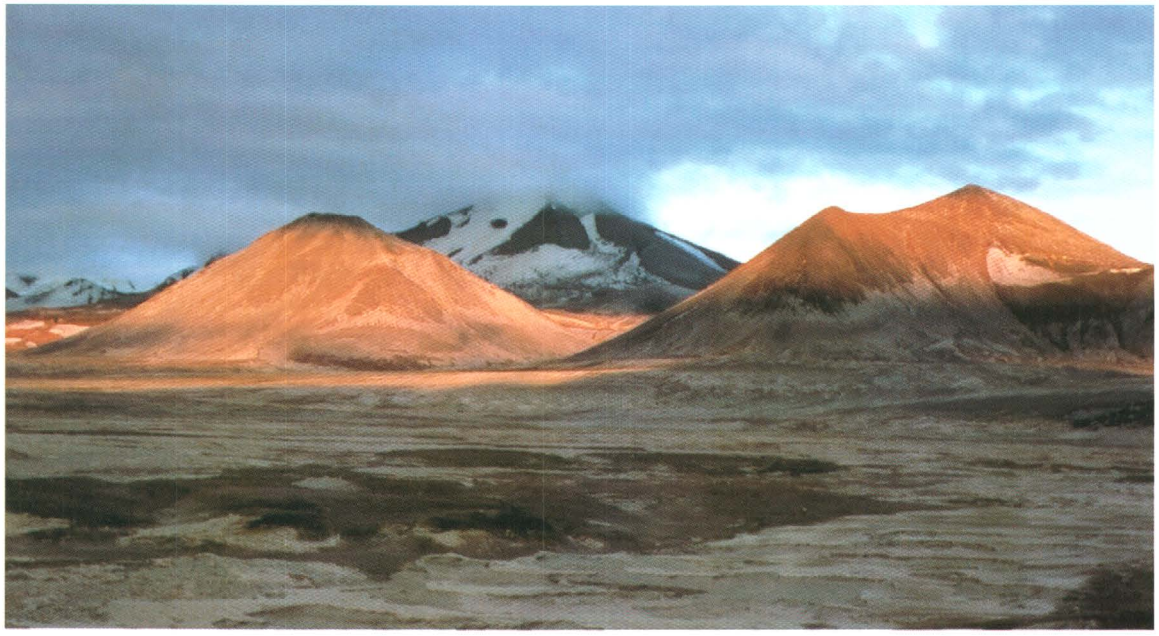

Figure 9. Falling Mountain and Mount Cerberus dacite domes, from the River Lethe on floor of the Valley of Ten Thousand Smokes (figs. 1, 3). In background, summit of snow-streaked West Trident (peak 5605) is in cloud. At left, Falling Mountain rises 430 m above valley floor, and at right, Mount Cerberus rises 365 m. Together they frame the entrance to Katmai Pass. Both domes are heavily mantled with 1912 pyroclastic deposits from Novarupta, which lies out of view, just left of Falling Mountain (see fig. 2). View southeastward.

Figure 10. Three glacially eroded dacite domes south of Trident I (snow-streaked summit edifice) and Southwest Trident (1953–74 black cone at upper left), with Mageik Creek at foot of Observation Mountain in foreground (figs. 1, 3). Saddle-shaped dome 2460 (62–63 weight percent SiO_2) in right foreground and, to its left, dome 2600+ (64–65 weight percent SiO_2) are heavily blanketed by 1912 pumice-fall deposits. At right center, dome 3900 (63.5 weight percent SiO_2) forms black triangular spur on midslope of Trident I. View northward.

petrographically similar to summit domes and thick coulees on West Trident and Trident I. Except for Falling Mountain and Mount Cerberus, none of the domes has been dated, but all are glacially eroded, and each is older than one or more contiguous lava flows from West Trident or Trident I. Attempts to date one of the domes failed twice, probably because it is too young to have accumulated measurable radiogenic Ar. The likelihood is that all the peripheral domes were extruded during the late Pleistocene, evidently contemporaneously with growth of the adjoining composite cones, Trident I and West Trident.

Pyroclastic-Flow Deposits

The many domes and thick lava flows of dacite and silicic andesite that typify activity at Trident I and West Trident suggest that numerous block-and-ash flows (hot pyroclastic flows that carry mostly nonpumiceous juvenile clasts) would have been shed during construction of those edifices. However, glaciers have removed most pre-Holocene unconsolidated material around the base of the Trident group, and thick 1912 pyroclastic deposits cover the entire apron except along the canyon of Mageik Creek. There, in several protected alcoves along the winding gorge, which is cut as deeply as 150 m into Jurassic basement rocks (fig. 4), remnants of pyroclastic deposits from both Trident and Mount Katmai are interbedded with glacial and proglacial deposits.

A nonwelded dacitic ignimbrite (pumiceous pyroclastic-flow deposit) crops out on the south wall at the upper end of the gorge of Mageik Creek, due south of Trident I (unit tig, fig. 3). The greenish-gray massive remnant, 7 m thick and only 35 m long, rests on Jurassic strata a few meters above stream level (fig. 11). The lithic-poor unconsolidated deposit is rich in 1- to 5-cm-diameter pumice clasts and has a median grain size of 1.3 mm, and its sandy matrix is relatively poor in fine ash (only 6 weight percent finer than 63 μm). Although the deposit is a single massive emplacement unit, slight size sorting of pumice clasts imparts a hint of vague layering that etches out on weathered surfaces. The dominant greenish-gray to black pumice is dacitic (63–64 weight percent SiO_2), but subordi-

Figure 11. Nonwelded dacitic ignimbrite remnant (unit tig, fig. 3*A*) on south wall of upper end of Mageik Creek gorge, due south of Trident I and dome 2460 (figs. 1, 3, 10). Single greenish-gray massive outcrop, 7 m thick and 35 m long (at center, behind 1.625-m geologist), rests on and banks against Jurassic basement rocks (lower left) a few meters above stream level. Lithic-poor tuff is rich in small (1–5-cm diam) pumice clasts. Predominant greenish-gray to black pumice is dacitic (63–64 weight percent SiO_2), but subordinate white pumice is rhyodacitic (70–71 weight percent SiO_2). Compositional affinity of all pumice types is clearly with Trident group (relatively low K and Zr contents), not with Mount Mageik or Mount Katmai, but composition fails to distinguish among Trident I, West Trident, and Trident domes as likely source of these pumiceous pyroclastic flows. Deposit is overlain directly by 3 m of boulder-rich till, capped by about 10 m of 1912 pumice falls and fines-rich ignimbrite, which provides tan mud dribbling down wall.

nate white pumice is rhyodacitic (70–71 weight percent SiO_2). Compositional affinity of all pumice types is clearly with the Trident group (low K, Zr), not with Mount Mageik or Mount Katmai, but composition fails to distinguish among Trident I, West Trident, or Trident domes as the likely source. Because the ignimbrite is directly overlain by a single sheet of bouldery till only a few meters thick (fig. 11), which is, in turn, capped only by 1912 deposits, we infer that it was emplaced very late in the Pleistocene. Because the ash flow was funneled along the gorge at a level 30 m lower than the base of lithic pyroclastic-flow unit tpf, described next, this ash flow is almost certainly younger.

A block-and-ash-flow deposit (fig. 12) is preserved as inset remnants in four alcoves high on the north wall of Mageik Creek gorge at the south foot of Trident I (unit tpf, fig. 3). Its gray sandy matrix encloses black to medium-gray, dense glassy juvenile clasts, mostly 1 to 10 cm but as much as 50 cm across, as well as abundant nonjuvenile clasts of varied andesite and dacite. Disregarding clasts coarser than 16 mm, sieve analysis shows the matrix to have a median grain size of 5 mm, with only 1.5 weight percent finer than 63 μm. The four main exposures range in thickness from 10 to 30 m, but the deposit is largely eroded away between adjacent alcoves. The alcove farthest downstream contains the coarsest and thickest deposit, which consists of several flow units and could represent more than one eruptive event. All four remnants are overlain by thin layers of till and fluvial gravel, probably representing only the last Pleistocene glacial advance, and all rest on Jurassic basement rocks or on fluvial deposits that overlie the basement rocks. The deposit is cut by numerous clastic dikes, possibly induced by the stress of overriding ice. A total of 12 glassy clasts analyzed range in SiO_2 content from 57.6 to 71.8 weight percent, a strikingly wide compositional variation that constitutes a notable anomaly, because no other sample from the Trident group has yielded more than 65.5 weight percent SiO_2 (except the white pumice in unit tig). The compositional affinity of all blocks analyzed, however, is clearly with the Trident group (low K, Zr), not with Mount Mageik or Mount Katmai. Composition does not distinguish among Trident I, West Trident, or the Trident domes as a likely source of the pyroclastic flows.

Figure 12. Block-and-ash-flow deposit preserved as inset remnants high on north wall of Mageik Creek gorge (unit tpf, fig. 3*A*), just southeast of dome 2460. Dark-gray deposit, here 20 m thick, consists of several flow units defined by zones of coarse clasts. At lower right, deposit rests on Jurassic strata, which dip gently southeast (to right). Dark-gray sandy matrix encloses black to medium-gray, dense glassy clasts as much as 50 cm across (but mostly 1–10-cm diam), as well as varied nonjuvenile andesite-dacite clasts (rarely as large as 1-m diam). Although glassy clasts vary widely in composition (63–72 weight percent SiO_2), compositional affinity of all blocks analyzed is unequivocally with the Trident group (relatively low K and Zr), not with Mount Mageik or Mount Katmai. White and tan slopes in background are covered by scree of 1912 pumice, which conceals till, talus, and fluvial gravel that overlie pyroclastic-flow deposit. View eastward, downstream along north rim of gorge.

Also preserved locally along the gorge of Mageik Creek are remnants of a major rhyodacitic plinian pumice-fall and nonwelded ignimbrite deposit (71–72 weight percent SiO_2). Its compositional affinity is with Mount Katmai, not Trident. Organic material at the base of the fallout yields a radiocarbon age of 19,240±70 ^{14}C yr B.P., equivalent to a calibrated calendar age of 22.8 ka (Hildreth and Fierstein, 2000). Pertinent here is that mutual canyon-filling relations along Mageik Creek indicate (but do not conclusively prove) that the Katmai-derived deposit predates both Trident-derived pyroclastic-flow deposits just described (units tig, tpf, fig. 3). If so, both Trident-derived units are constrained to have been emplaced during the long interval of fitful glacial retreat—between the Last Glacial Maximum (approx 21 ka) and final withdrawal to typical Holocene termini (by approx 8 ka).

Finally, on the south apron of Trident I, a sharp south-flowing gully just southeast of dome 3900+ cuts through thick 1912 fallout and 2 m deeper into a subjacent block-and-ash-flow deposit containing enclave-rich andesite blocks, as much as 50 cm across. The uniformly oxidized, purplish-brown, sandy matrix of the deposit encloses abundant dense clasts of plagioclase-rich pyroxene andesite (61.4 weight percent SiO_2), either segregated into lenses or fully matrix supported. Clearly derived from Trident I, the flow was probably not associated with extrusion of the summit dome, which is dacitic (63.4 weight percent SiO_2), but rather with one of the contiguous near-summit lavas, several of which consist of silicic andesite (60.4–62.2 weight percent SiO_2). Because it lacks the rhyodacite clasts present in the block-and-ash-flow deposit only 1.5 km farther south at Mageik Creek (unit tpf, fig. 3), this poorly exposed flow unequivocally represents a separate eruption.

Southwest Trident

Beginning in February 1953, a new andesite-dacite edifice (0.7-km^3 volume) was built at the southwestern margin of the Trident group (unit tsw, fig. 3). Though sometimes referred to informally as "New Trident," we have called it Southwest Trident (Hildreth and others, 2000), in anticipation of the day it ceases to be Trident's youngest component. During 2 decades of sporadic explosive activity (Vulcanian type and effusive), a new composite cone covering about 3-km^2 area was constructed of block-and-ash deposits, scoria, agglutinate, stubby lava lobes, and the intercalated proximal parts of the main lava flows that spread as an apron beyond the cone. The cone grew to an elevation of 4,970 ft (1,515 m) (Global Positioning System measurement by Coombs and others, 2000) on the former site of a 100-m-wide fumarolic pit at about 3,840-ft (1,170 m) elevation on the steep southwest flank of

Figure 13. Southwest Trident in July 1979 (5 years after cessation of eruptive activity), from Mount Mageik (figs. 1, 3). Dark-gray-brown pyroclastic cone, disposed asymmetrically on slope of glaciated Trident lavas, rises 750 m above Katmai Pass in foreground. Shallow summit crater is 350 m wide. Leveed 1959–60 lava flow is visible at left, and overlapping flows of 1953 and 1958 at lower right (see fig. 3); just beyond them, snow-filled trough marks western margin of 1957 flow, which extends past right edge of photograph. Rounded tan knob wrapped by young flows at lower center is snout of glaciated ridge of West Trident lava (visible in fig. 15*A* before it was overrun). Summits of West Trident and Trident I edifices are in cloud at upper left. Upper Katmai River and Shelikof Strait are visible at upper right. View eastward.

Trident I. Although relief on its south slope exceeds 700 m (fig. 13), the new cone thus has a central thickness of only 345 m and a volume of about 0.3 km^3. At successive stages of cone construction, four blocky leveed lava flows effused from its central vent, in 1953, 1957, and 1958 and during the winter of 1959–60 (figs. 3, 13). Each flow is 25 to 60 m thick and 2.5 to 4 km long, and altogether they add about 0.35 km^3 to the eruptive volume. The cone's summit is today marked by a shallow crater, 350 m wide (fig. 14), that was the site of several small ephemeral plugs, which were emplaced after the final lava flow and were repeatedly destroyed by intermittent explosive activity (1960–74).

Black, rapidly expanding, cauliflower ash clouds rose 6 to 9 km at least 10 times between 1953 and 1974 and possibly 12 km once or twice. Several times during the first month of activity, light ashfall dusted areas as far as 30 to 50 km from the vent, in all sectors. By far the most voluminous fallout appears to have resulted from the initial outburst of February 15, 1953 (Snyder, 1954), which may have been sub-Plinian. A single nongraded scoria-fall layer (5–17 cm thick) deposited during that event is preserved at a few protected sites as far away as Mount Katmai and upper Knife Creek. Sieve data for bulk samples of this layer yield median and maximum particle sizes, respectively, of 6.5 and 100 mm in the saddle 1 km north of the vent, and 2.1 and 20 mm in the saddle 7 km northeast of the vent—between the twin western summits of Mount Katmai. Thin sheets of finer ash that fell during the many smaller subsequent outbursts have been almost entirely removed or reworked by wind and runoff. Abundant ballistic blocks, variously bread-crusted, densely vitrophyric, or scoriaceous, that are scattered as far as 3 km from vent are products of many discrete explosive episodes (none of which were closely observed) distributed over 2 decades. Liberal estimates of total fallout volume yield no more than 0.05 km^3, contributing less than 10 percent of the total eruptive volume of 0.7±0.1 km^3.

The period of most frequent observation was from February to September 1953, principally by military reconnaissance aircraft during the early months (Snyder, 1954) and by a U.S. Geological Survey (USGS) party that camped at Knife Creek during the summer (Muller and others, 1954). When the vent was first seen through the cloud layer on the fourth day of activity (Feb. 18, 1953), an effusive lava flow (then already

Figure 14. East to northeast face of Southwest Trident cone in July 1997, from near summit of Trident I (figs. 3, 4). Visible cone material includes agglutinate sheets and unconsolidated stratified ejecta, covered downslope by apron of blocky scree. Primary deposits are mostly coarse but poorly sorted; blocks range in texture from dense to scoriaceous. Lava flows visible in figure 13 emerge from other side of cone. Few remaining fumaroles and little alteration mark interior of 350-m-wide crater, which was site of several plugs of dense lava, repeatedly destroyed. On outer slopes just below rim, however, hundreds of sulfurous fumaroles emerge through permeable ejecta, promoting alteration of 100-m-wide light-colored zone. In the 1960s, many of these fumaroles were still superheated, but the hottest measured in 1997 was only 95°C. In background, Holocene lava flows from Mount Mageik are overlain by pale-gray 1912 pumice-fall deposit. View southwestward.

250 m wide) was upwelling centrally and spreading radially (fig. 15*A*). Although a fumarolic pit, as much as 40 m deep, was conspicuous at the impending ventsite on aerial photographs taken in 1951 (and had probably been further excavated by the explosive outburst of Feb. 15), any such crater was soon filled and buried by the effusive lava (fig. 15*A*), which continued to be extruded and spread slowly throughout the seven months of intermittent observation in 1953. At various times, lava lobes emerged laterally through the chilled carapace at the foot of the pile, or the pile itself "expanded like a balloon" and extruded lobes by overflow from the vent, or small slumps and slide masses detached from the steep flow margins (Snyder, 1954). By June 1953, the main southerly tongue of lava, ultimately 4.2 km long, had advanced only 1,250 m from the vent. Snyder (1954) estimated the volume of fallout and lava produced by June 17, 1953, at 0.23 to 0.3 km^3, about a third of the eventual output. During the summer, steady steaming and continued spreading of the lava was punctuated sporadically by steam bursts (fig. 15*B*) or occasional "smoke columns" that rose 1 to 3 km and dusted various proximal sectors with minor additional ashfall (Muller and others, 1954).

Observations after September 1953 were sporadic and few. A general chronology of major events was compiled by Decker (1963) and augmented by Ray (1967), largely from intermittent National Park Service reports. The 1953 lava flow may not have attained its final dimensions (fig. 3) until early 1954 or later. Apparently, no observations were made

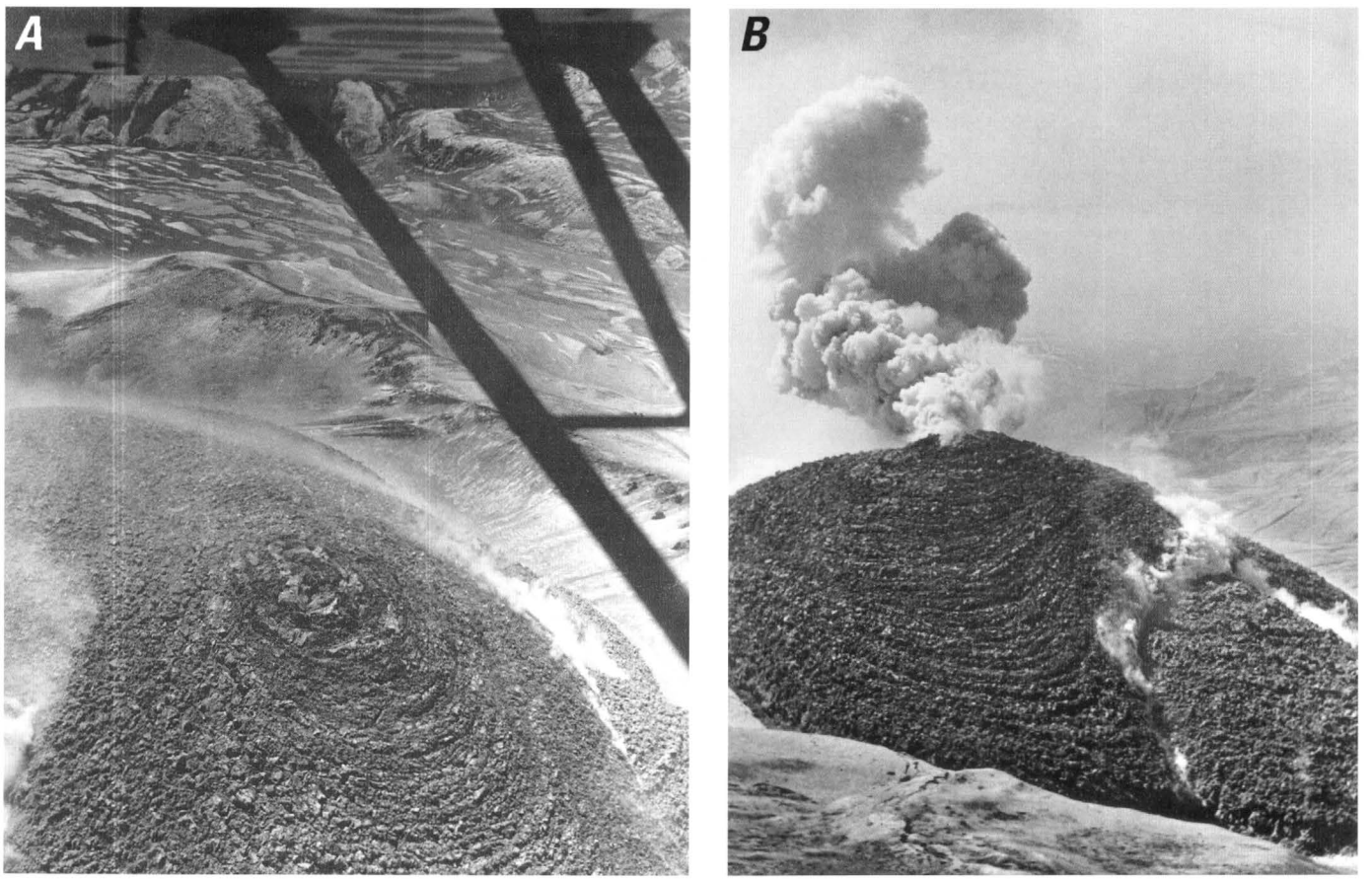

Figure 15. Transient vent configurations at Southwest Trident in June 1953 (figs. 1, 3). *A*, Concentric corrugations around orifice of initial andesite lava flow from Southwest Trident, about 4 months after initiation of 1953 eruption. Note absence of crater at focus of upwelling. Asymmetric outflow of effusive lava is partly toward observer but principally southward (to upper left). In background, streaks and patches of thin black ash that overlie light-colored 1912 pumice falls and ignimbrite were deposited as fallout, mostly during initial explosive events of February 1953. By June 1953, much of the black ash had already been reworked by wind and runoff, and by the time of our first visit in August 1976, nearly all of it had been removed. Lava visible here was completely covered by subsequent 1953–60 lava flows and by growth of a pyroclastic cone over vent. Ridge of glaciated lava crossing middle of photograph was also largely covered later, except that its rounded terminus remains exposed as a dome-shaped hump wrapped by younger flows (figs. 3, 13). Andesite-dacite coulees from Mount Mageik are visible in distance. View southwestward; National Park Service photograph taken by Garniss H. Curtis, June 1953. *B*, Same concentrically corrugated pile of effusive andesite surrounding vent in figure 15*A*, showing a small burst of steam and ash and a fissure-bounded lateral effusion on northwest flank. View southward from saddle north of vent; National Park Service photograph, taken by Garniss H. Curtis, June 1953.

during eruption and outflow of the lava flows of 1957, 1958, and 1959–60 (fig. 3), merely aerial snapshots taken in the summer seasons after the emplacement of each flow. The time of emplacement of the lava flow attributed to the winter of 1959–60 is the least well known, because no photographs are known to have been taken between September 1958 and August 1960. The 1958 lava flow partly overran the 1953 flow (fig. 3) and impounded a small lake on upper Mageik Creek that soon filled in with pumiceous alluvium, becoming a mudflat (Ferruginous Flat, fig. 3) now marked by numerous iron-precipitating warm springs.

Growth of the fragmental cone (figs. 13, 14) began only after much or all of the 1953 lava flow (fig. 15) had been emplaced. The cone accumulated progressively during the later 1950s, as shown by emergence of the successive lava flows at different levels of the fragmental edifice. National Park Service photographs show that the cone had attained nearly its full height by 1960, although explosive showers of blocks continued to augment the cone until 1974. In addition to the four main lava flows, cone construction included emplacement of several stubby lava lobes limited to its proximal southwest slope (fig. 3). The southeast side of the cone completely buried a 1-km^2-area cirque glacier, with no recognized effects on eruptive behavior or edifice structure, although enhanced steaming may have contributed to the stronger fumarolic emission and alteration on that side of the cone (fig. 14). Explosive ejections of tephra, some involving blowout of plugs and at least one spine, took place from 1960 to 1974, but volumetrically significant eruptions were over by 1963. Numerous sulfurous fumaroles, superheated in the 1960s but below and at the boiling point today, persist on the upper parts of the cone (fig. 14). Dark-gray bouldery debris flows reworked from the pyroclastic deposits have built a proximal fan and thin distal sheets (1–4 m thick) that cap stream terraces for 3 km downstream along Mageik Creek. Some debris flows resulted from the initial February 1953 fallout over snow, and others from avalanching of rubble from the steep slopes of the cone.

The lava flows and ejecta are olivine-poor two-pyroxene andesite and dacite that span a compositional continuum from 56 to 65.5 weight percent SiO_2. All products are plagioclase rich and contain 33 to 45 volume percent phenocrysts, many of them complexly zoned, resorbed, and overgrown (Ray, 1967; Kosco, 1981; Coombs and others, 2000). The least evolved bulk material identified is the initial scoria fall of February 1953 (56–57 weight percent SiO_2). Andesitic enclaves are abundant, relatively mafic (56–59 weight percent SiO_2), contain the same phenocryst species as the host material, and fall mostly in the size range 1–30 cm (Coombs and others, 2000). No evidence of contamination by leftover 1912 magma (such as quartz phenocrysts) has been found, and small but consistent compositional differences (Hildreth and Fierstein, 2000) indicate that the andesitic-dacitic magmas erupted in 1912 and in 1953–74 were different batches. For the Southwest Trident batch, Coombs and others (2000) presented experimental and analytical evidence for mixing between resident dacitic magma stored at 890°C at about 3-km depth and a newly arrived batch of 1,000°C andesitic magma; they interpreted diffusion profiles in phenocrysts to suggest that thorough mixing could have produced the linear compositional array within about a month before the eruption began.

Geochronology

K-Ar ages were determined on whole-rock samples from some of the lava domes and from each of the three main glaciated edifices of the Trident group (table 1); sample-selection criteria and analytical methods were described by Hildreth and Lanphere (1994) and Lanphere (2000). Seeking high-precision ages for late Pleistocene rocks, we used the multiple-collector mass spectrometer (Stacey and others, 1981) at the USGS laboratory in Menlo Park, Calif.

On stratigraphic grounds, the three glaciated cones of the Trident group appear to young westward, because each cone is buttressed by its eastern neighbor. This observation is borne out by the K-Ar data because the East Trident edifice yields the oldest ages and West Trident the youngest.

For East Trident, a near-basal andesitic lava flow resting on oxidized breccia at glacier level on the nose of the northwest prong (which separates Glaciers 1 and 2, fig. 3) yields a weighted mean age of 143±8 ka, analytically indistinguishable from an age of 142±15 ka on a 100-m-thick dacitic lava flow that caps part of the northeast ridge of the edifice. These samples appear to bracket most of the dozens of lava flows that make up the edifice, suggesting that eruptive activity at the small East Trident cone was short lived. The ages indicate not only that East Trident is the oldest member of the Trident group but also that it predates the oldest recognized eruptive products of neighboring Katmai and Mageik Volcanoes (Hildreth and Fierstein, 2000; Hildreth and others, 2000).

An andesitic lava flow that directly underlies the summit dome of Trident I, about 100 m southwest of peak 6115, yields an age of 73±12 ka. Most of the edifice appears to lie stratigraphically beneath this lava, except for the mafic pyroclastic assemblage (unit tca, fig. 3), which apparently drapes many of the andesites and yields a $^{40}Ar/^{39}Ar$ age of 58±15 ka (Hildreth and others, 2003). Because much of the Trident I pile is banked against its eastern neighbor (dated at 143±8 ka), the active lifetime of Trident I appears to be reasonably well bracketed.

For West Trident, which banks against Trident I, a 70-m-thick andesitic lava flow capping the north ridge gave a K-Ar age of 44±12 ka. An attempt to date the summit lava of West Trident (fig. 8) failed to yield sufficient radiogenic Ar to provide a meaningful age, supporting our field inference that it is still younger than the dated lava flow.

Falling Mountain dacite dome, the northeast face of which was sheared off (fig. 2) during the 1912 eruption at adjacent Novarupta, yields an age of 70±8 ka. Adjacent Mount Cerberus, a compositionally similar dacite dome (fig. 9), yields a less precise age of 114±46 ka, which (in view of the

Table 1. Whole-rock K-Ar ages and analytical data for Trident Volcano.

[Analysts: K by D.F. Siems; Ar by F.S. McFarland and J.Y. Saburomaru. Constants: $\lambda=0.581\times10^{-10}$ y^{-1}, $\lambda_\beta=4.962\times10^{-10}$ y^{-1}, $^{40}K/K=1.167\times10^{-4}$ mol/mol]

Sample (table 2)	Location (fig. 3)	SiO_2 (wt pct)	K_2O (wt pct)	Radiogenic ^{40}Ar		Calculated age (ka)
				(10^{-13} mol/g)	(pct)	
K–2573	East Trident: near-basal lava flow on nose of NW. ridge.	60.0	1.069±0.001	2.144	7.2	139±12
				2.279	8.7	148±12
				weighted	**mean---**	**143±8**
K–2029	East Trident: 100-m-thick dacitic lava flow capping NE. ridge.	65.1	1.657±0.006	3.380	3.9	142±15
K–2224	Trident I: thick lava flow at 6,000 ft; 100 m SW. of summit 6115.	61.7	1.348±0.008	1.960	6.4	73±12
K–2536	West Trident: thick lava flow capping north ridge at 4,500 ft.	62.1	1.403±0.003	.891	1.8	44±12
K–65	Falling Mountain: north spur.	65.0	1.759±0.004	1.763	8.0	70±8
K–69	Mount Cerberus: east face.	63.0	1.300±0.002	2.130	2.1	114±46

respective analytical errors) need not differ significantly from that of Falling Mountain.

Eruptive Volumes

The glaciated East Trident edifice today covers an area of about 7 km^2, Trident I about 15.2 km^2, and West Trident about 12.6 km^2. The eastern and northern aprons of East Trident, however, have been covered and largely removed by glaciers, and its original summit, crater, and altered core have been glacially gutted. The same is true for the core and northern apron of Trident I. The southern apron of Trident I is glacially scoured but not incised, thus relatively intact, although any former intracanyon flows along Mageik Creek have been stripped. West Trident has not been excavated so severely, but its summit and radial ridges are everywhere ice scoured, and its apron lavas were truncated distally by ice that flowed across Katmai Pass. Moreover, its northern lava-flow apron was truncated by the 1912 Novarupta vent depression, and the rest largely concealed by 1912 pyroclastic deposits, more than 10 m thick. Attempting to estimate original volumes of the edifices is therefore a difficult and uncertain exercise.

Although the summits of all three Pleistocene cones were at times ice covered, the observation that remnants of summit domes seem to have survived on Trident I and West Trident suggests that neither cone has been reduced in elevation by more than 100 m. From the attitudes of stratified ejecta and lavas that compose the radial arêtes of East Trident, however, we infer that its summit has been lowered by about 200 m (fig. 2).

Reconstructions based on the observations and assumptions just outlined yield preerosion edifice volumes of 6 to 8 km^3 for East Trident, 7 to 9 km^3 for Trident I, and 3 to 4 km^3 for West Trident, to which can be added 0.7 km^3 for the 1953–74 products of Southwest Trident and about 1 km^3 for the peripheral lava domes. The pyroclastic-flow deposits preserved along the gorge of Mageik Creek are unlikely to have contributed as much as another 1 km^3, but the remnants are in any case too few to allow meaningful reconstructions. With the possible exception of these pyroclastic-flow deposits, no eruptive unit has been observed in the Trident group that is likely to have been accompanied by a cubic-kilometer-scale explosive pyroclastic deposit subsequently lost to erosion. Regional fallout ejected during explosive phases of andesitic or low-silica dacitic eruptive episodes like those at Trident seldom amount to more than a few tenths of a cubic kilometer, as observed during the 1953–74 activity, which produced less than 0.1 km^3 of such fallout. We thus arrive at a total eruptive-volume estimate for the Trident group of about 21±4 km^3, which can be compared to 30 km^3 each for nearby Mageik and Griggs Volcanoes and to 45 km^3 for the compound edifice of Mount Katmai (excluding its far-flung tephra deposits).

Because the oldest eruptive products exposed in the (still active) Trident group yield an age of 143±8 ka, the reconstructed volume of 21±4 km^3 yields a long-term average eruption rate in the range 0.11–0.18 km^3/k.y.—greater than that of

nearby Snowy Mountain, similar to that of Mount Griggs, only a third that of Mount Mageik, and barely a tenth that of Mount Katmai (Hildreth and others, 2000, 2001, 2002, 2003; Hildreth and Fierstein, 2000, 2003).

Composition of Eruptive Products

Chemical analyses of 116 samples representing all components of the Trident group are plotted in figure 16 and listed in table 2. Sample suites for all volcanoes in the Katmai cluster, including Trident, show broadly similar, low-Ti, medium-K calc-alkaline arc trends (Gill, 1981) that are mutually distinguishable on variation diagrams by only a few element pairs. For example, the variation trends of Al, Ti, Ca, Na, Rb, Ba, Mg, and Fe plotted against SiO_2 substantially overlap for all main-chain volcanoes from Mount Martin to Snowy Mountain (fig. 1). A fair separation of several of the suites is provided, however, by variation patterns of K_2O, Zr, and Sr against SiO_2, as shown in figures 8 through 10 of Hildreth and Fierstein (2000). The key compositional differences (K_2O, Zr) that distinguish magmatic products of the Trident group from those erupted at adjacent Novarupta are plotted in figures 16*A* and 16*C*.

Alkali-lime intersections for Trident data arrays fall at 63.5 weight percent SiO_2 (fig. 16*B*), defining calcic suites by the index of Peacock (1931). The 1912 Novarupta suite and products of all the Katmai centers on the main volcanic line are likewise calcic, in contrast to the calc-alkalic suite erupted at Mount Griggs (Hildreth, 1983; Hildreth and others, 1999, 2001, 2002). By the Fe-enrichment criterion of Miyashiro (1974), however, all the compositional arrays in the Katmai cluster (including those of Trident and Mount Griggs) are strongly calc-alkaline (non-tholeiitic).

Primitive magmas have not erupted at any of the Katmai volcanoes. Although mafic magmatic inclusions (enclaves) in andesitic lavas throughout the cluster contain as little as 54 to 57 weight percent SiO_2, only at Trident I (table 2) and Snowy Mountain (Hildreth and others, 2001) have mafic products been identified that contain more than 7 weight percent MgO. At Trident, such Mg-rich compositions are restricted to the sheeted agglutinate that makes up the upper southwest slope of Trident I. Apart from a few enclaves that contain 5.0 to 5.35 weight percent MgO, no other Trident lavas or ejecta have been found to contain as much as 5 weight percent MgO.

We previously showed that the continuously zoned andesite-dacite suite erupted at Novarupta in 1912 was withdrawn from beneath Mount Katmai (Hildreth, 1991) and that the suite has a closer compositional affinity to the eruptive products of Mount Katmai than to those of other volcanoes in the cluster (Hildreth and Fierstein, 2000). Eruptive products of East Trident, oldest edifice in the Trident group and close neighbor of Mount Katmai, are distinguishable from those of Novarupta and Mount Katmai in their relatively lower contents of both Zr and K_2O (fig. 16). Trident I, West Trident, and the peripheral domes are likewise consistently deficient in Zr and K_2O relative to the Katmai-Novarupta array, and higher Sr contents distinguish them from East Trident (Hildreth and Fierstein, 2000). The data thus indicate that all pre-1953 constituents of the Trident group were supplied by magma reservoirs physically separate from those that fed Mount Katmai and Novarupta. The compositional similarity of Falling Mountain and Mount Cerberus to West Trident and the other Trident domes likewise confirms that the magmatic affinity of those dacite domes lies with the prehistoric Trident group, not with adjacent Novarupta.

Uniquely among the several components of Trident, the 1953–74 products of Southwest Trident are close to being compositionally collinear with those of Katmai and Novarupta on most variation diagrams (fig. 16). The Southwest Trident suite is nonetheless distinguishable by its slightly lower K_2O and Fe and slightly higher Na and Sr contents relative to the 1912 array (Hildreth and Fierstein, 2000). The most evolved 1953–74 material analyzed contains 65.5 weight percent SiO_2 (Coombs and others, 2000), and only a few samples contain more than 63 weight percent SiO_2 (table 2; Ray 1967; Kosco, 1980). In contrast, the 4.5 km^3 of dacite that erupted in 1912 was zoned to 68 weight percent SiO_2, and most of it contained more than 65 weight percent SiO_2 (fig. 16). No xenocrystic evidence has been observed in 1953–74 material for contamination by leftover (quartz bearing) 1912 rhyolite, and there is no hint in the 1953–74 andesite-dacite array of a mixing trend toward the (Zr deficient) 1912 rhyolite (Hildreth and Fierstein, 2000).

We conclude that the andesitic-dacitic magma that built Southwest Trident was similar, but not identical, to the 1912 andesitic-dacitic magma that drained from beneath Mount Katmai to the Novarupta vent at the toe of West Trident (figs. 2, 3). The 1953–74 dacite probably occupied a shallow reservoir near Katmai Pass, physically remote from that of 1912. The dacitic reservoir may have been disturbed by andesitic replenishment during the decade or so preceding 1951, the year when fumaroles were first observed on the subsequent site of Southwest Trident. Major andesitic replenishment may not have stimulated thorough convective mixing with the resident dacitic magma until a month or so before the eruption began in February 1953, as suggested by the mixing and diffusion-profile data of Coombs and others (2000). Compositional similarities are consistent, however, with the interpretation that the andesitic batches involved in the 1912 and 1953 eruptions were ultimately supplied by the same deep-crustal reservoir.

The Pleistocene pyroclastic-flow remnants south of the Trident group (figs. 11, 12, 16) require additional comment. All 16 samples from three different eruptive units (table 2) fall well below the 1912 Novarupta arrays on the K_2O and Zr panels (fig. 16). As illustrated in Hildreth and Fierstein (2000), these compositional constraints unequivocally eliminate nearby Mageik and Katmai Volcanoes as the sources of the pyroclastic flows, leaving the Trident group as the only possible source. The data (fig. 16; table 2) show that the block-and-ash-flow deposit (sample K–833) poorly exposed on the south flank of Trident I is compositionally similar to several lava flows high on that edifice. However, juvenile

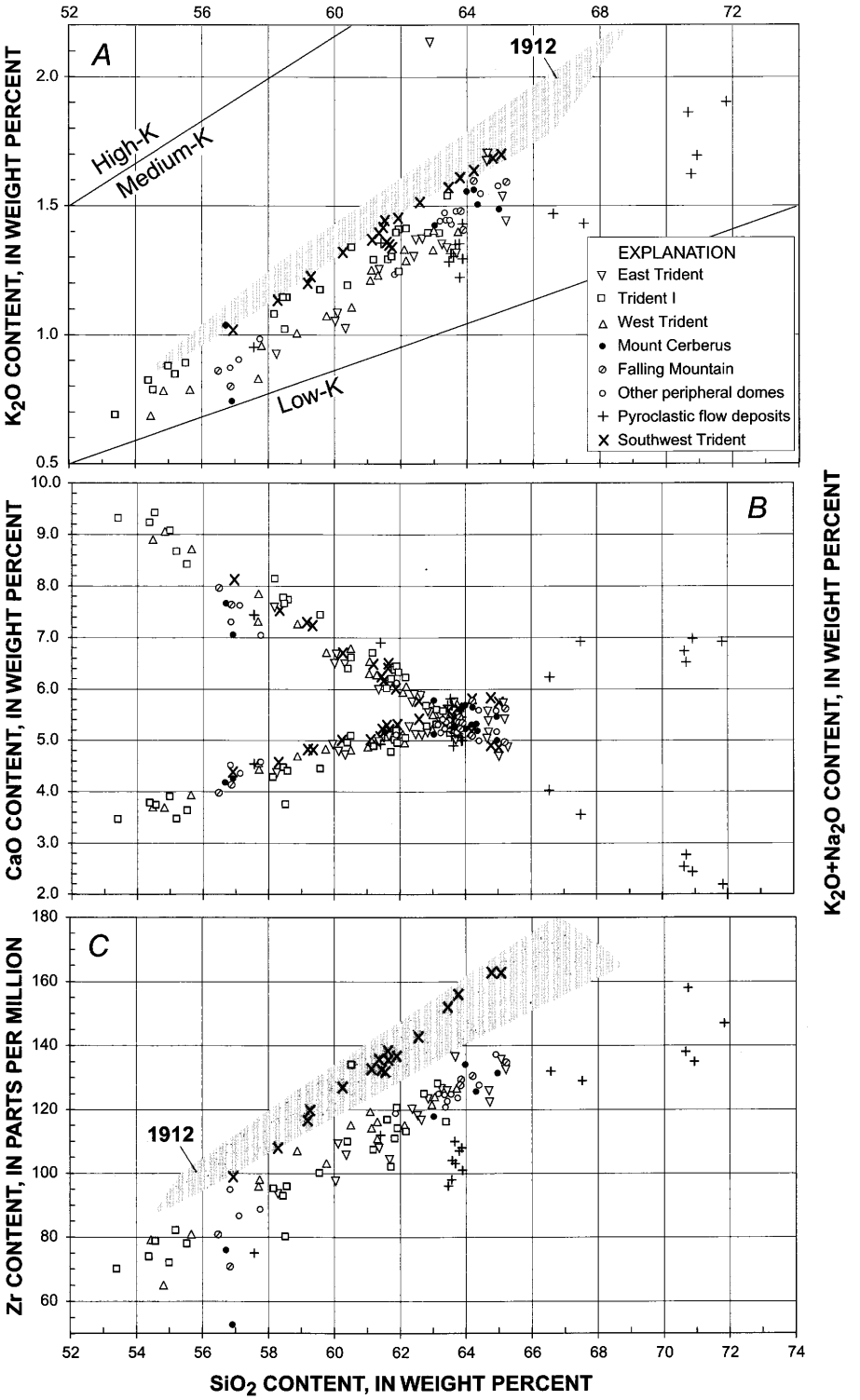

Figure 16. Whole-rock compositional data for 116 samples from Trident group, subdivided as in inset. Sample sites are shown in figure 3*B*, and data are listed in table 2. *A*, K_2O versus SiO_2 contents. *B*, CaO (upper trend) and total alkalies (lower trend) versus SiO_2 contents. C, Zr versus SiO_2 contents. For comparison, shaded fields show continuous compositional arrays for about 200 samples of zoned andesite-dacite suite erupted from Novarupta in June 1912 (Hildreth and Fierstein, 2000). Suite erupted in 1953–74 at Southwest Trident is compositionally closer to 1912 array than is any older component of Trident group. Anomalously high-Zr Trident I sample is from 200-m-thick lava, lowest unit exposed at base of north face. Anomalously high-K East Trident sample is from window of flow breccia beneath wasting ice tongue that separates south ridge of edifice from southeastern fumarole field. Note that most samples of pyroclastic flows plot below main arrays in figures 16*A* and 16*C*.

Table 2. Chemical analyses of eruptive products from Trident Volcano.

[Wavelength-dispersive X-ray-fluorescence analyses of major-element oxides in weight percent, normalized to H_2O-free totals of 99.6 weight percent (allowing 0.4 weight percent for trace-element oxides and halogens); energy-dispersive X-ray-fluorescence analyses of minor elements (Rb, Sr, Zr) in parts per million. Analyst, D.F. Siems, U.S. Geological Survey laboratory, Lakewood, Colorado. Precision and accuracy of these measurements were discussed by Baedecker (1987) and Bacon and Druitt (1988). FeO*, total Fe calculated as FeO; LOI, percentage of sample weight lost on ignition at 900°C; original total, volatile-free sum of major-element-oxide contents before normalization, with total Fe content calculated as Fe_2O_3. Suffix "–i" on sample number denotes magmatic enclave included in a host lava. See figure 3 for sample locations and lithologic units]

Sample (fig. 3)	SiO_2	TiO_2	Al_2O_3	FeO*	MnO	MgO	CaO	Na_2O	K_2O	P_2O_5	LOI	Original total	Rb	Sr	Zr
East Trident															
K–1146	60.32	0.75	16.82	7.23	0.14	2.96	6.51	3.72	1.03	0.14	0.50	98.90	22	309	106
K–1147	63.22	.76	15.98	6.27	.14	2.20	5.47	4.05	1.36	.15	1.01	98.46	25	257	127
K–1155	62.45	.65	16.37	6.08	.12	2.75	5.90	3.78	1.38	.13	.24	99.20	30	271	119
K–1173	62.63	.65	16.39	6.02	.12	2.62	5.89	3.75	1.38	.14	.54	99.07	29	273	117
K–1184	62.86	.71	16.27	6.22	.13	2.44	5.60	3.06	2.14	.18	2.09	97.33	27	273	124
K–1185	61.35	.74	16.53	6.99	.10	2.71	6.02	3.75	1.26	.14	2.58	96.43	22	275	109
K–1203	60.09	.77	16.82	7.07	.15	3.00	6.70	3.76	1.09	.14	<.01	99.45	21	293	110
K–1207a	63.39	.65	16.39	5.77	.10	2.34	5.47	3.99	1.34	.15	2.19	96.63	25	280	125
K–1207b	58.25	.71	17.21	7.36	.14	3.82	7.59	3.46	.93	.13	<.01	99.52	16	294	94
K–2028	63.65	.81	16.52	5.50	.13	1.99	5.04	4.44	1.32	.21	.37	98.90	22	291	137
K–2029	65.06	.66	15.86	5.21	.12	1.98	4.80	4.20	1.55	.16	<.01	99.20	31	265	136
K–2226	61.67	.70	16.36	6.42	.13	2.89	6.13	3.77	1.36	.18	1.04	98.03	19	291	105
K–2227	64.68	.61	15.88	5.20	.12	2.25	5.09	3.88	1.70	.19	1.81	96.93	30	258	126
K–2227r	64.68	.61	15.85	5.27	.12	2.34	5.16	3.72	1.69	.16	1.92	97.13	29	251	123
K–2228	65.17	.60	15.87	5.10	.12	2.20	4.95	4.00	1.45	.16	1.25	97.75	30	256	133
K–2573	60.00	.78	16.65	7.25	.14	3.12	6.52	3.87	1.06	.21	.38	98.82	18	306	98
K–2574	62.39	.69	16.22	6.28	.13	2.61	5.78	3.97	1.31	.22	.00	99.17	24	297	120
Trident I															
K–834	59.57	0.67	16.78	6.46	0.12	3.97	7.44	3.28	1.18	0.13	0.51	99.14	25	338	100
K–834–i	54.39	.78	17.86	7.93	.14	5.35	9.24	2.95	.82	.14	.96	99.26	18	400	74
K–838	58.18	.65	16.92	6.64	.13	4.53	8.13	3.20	1.08	.13	.18	99.46	21	357	95
K–839	61.90	.60	17.38	5.44	.11	2.41	6.45	3.92	1.25	.13	.50	99.11	28	310	121
K–1174	61.93	.65	16.52	6.06	.11	2.92	6.33	3.54	1.41	.12	.40	98.91	28	308	114
K–1175–i	54.99	.78	18.20	8.05	.15	4.33	9.07	3.03	.88	.12	.68	98.52	16	393	72
K–1177	58.50	.87	17.83	6.08	.15	4.58	7.71	2.73	1.02	.14	3.92	95.51	18	372	80
K–1178	53.41	.91	18.69	8.86	.17	4.57	9.33	2.78	0.69	.19	1.32	98.04	10	417	70
K–1179	55.20	.64	16.42	7.58	.14	7.34	8.67	2.63	0.85	.14	.85	98.60	15	241	82
K–1182	61.85	.64	16.60	5.92	.12	2.95	6.38	3.62	1.40	.12	0.87	98.39	27	309	111
K–1183–i	54.53	.79	18.24	8.00	.14	4.60	9.43	2.95	.79	.13	.65	98.82	19	409	79
K–1205	61.18	.64	16.62	6.14	.12	3.16	6.71	3.60	1.29	.13	<.01	99.47	30	309	107
K–1206	62.17	.63	16.44	5.94	.12	2.90	6.24	3.63	1.41	.12	.01	99.33	25	302	113
K–1223	58.57	.70	16.65	6.78	.13	4.47	7.73	3.26	1.15	.17	.01	99.50	19	340	96
K–1406	63.11	.65	16.45	5.63	.12	2.58	5.61	3.91	1.39	.15	.03	99.26	25	321	128
K–1407	62.81	.68	16.32	5.91	.13	2.68	5.64	3.88	1.40	.15	−.02	99.14	22	320	125
K–2166	61.61	.69	16.71	6.15	.13	3.03	6.03	3.77	1.29	.18	.07	98.98	23	332	117
K–2224	61.72	.68	16.65	6.16	.13	3.09	6.21	3.47	1.30	.18	2.28	96.71	19	294	102
K–2225	63.41	.62	16.21	5.55	.11	2.62	5.58	3.80	1.54	.16	.34	98.62	29	295	116
K–2240	60.39	.72	16.87	6.54	.13	3.39	6.41	3.75	1.19	.20	.00	98.87	21	341	110
K–2241	60.52	.74	16.70	6.39	.13	3.22	6.62	3.75	1.34	.19	−.09	99.30	28	311	134
K–2458	58.46	.69	16.64	6.71	.13	4.53	7.78	3.33	1.15	.19	−.01	99.22	20	360	93
K–2546	55.52	.63	16.35	7.54	.15	7.18	8.43	2.74	.89	.17	.83	98.12	17	237	78

Table 2. Chemical analyses of eruptive products from Trident Volcano—Continued

Sample (fig. 3)	SiO_2	TiO_2	Al_2O_3	FeO*	MnO	MgO	CaO	Na_2O	K_2O	P_2O_5	LOI	Original total	Rb	Sr	Zr
West Trident															
K–840	63.72	0.57	16.53	5.15	0.10	2.36	5.74	3.87	1.40	0.15	<0.01	99.41	28	320	127
K–840–i	57.69	.80	17.67	7.55	.17	3.68	7.32	3.73	.83	.17	<.01	99.79	15	393	96
K–841	58.88	.68	17.83	6.48	.13	3.48	7.27	3.69	1.01	.16	<.01	99.98	22	387	107
K–1127	61.30	.69	16.70	6.29	.13	3.05	6.30	3.74	1.23	.17	.09	99.38	23	332	116
K–1131	61.08	.66	16.70	6.24	.12	3.23	6.54	3.68	1.21	.15	.22	99.63	25	328	119
K–1132–i	55.64	.71	17.88	7.70	.14	4.74	8.71	3.15	.79	.14	.16	99.70	15	374	81
K–1134–i	57.71	.73	17.54	6.95	.13	4.09	7.85	3.49	.96	.16	<.01	99.93	20	398	98
K–1135	60.50	.68	17.00	6.19	.12	3.34	6.79	3.71	1.11	.15	<.01	99.59	24	346	115
K–2165	61.12	.68	16.76	6.33	.13	3.15	6.30	3.72	1.25	.17	.26	98.75	20	329	114
K–2450	62.96	.65	16.44	5.54	.12	2.75	5.73	3.88	1.33	.21	.01	99.23	22	312	122
K–2451	61.30	.68	16.55	6.25	.13	3.18	6.29	3.76	1.23	.22	–.04	99.21	22	320	111
K–2452	62.15	.67	16.52	6.00	.13	2.97	6.04	3.67	1.29	.17	.04	99.37	24	318	115
K–2452–i	54.84	.70	18.24	7.75	.15	5.04	9.05	2.91	.78	.14	.10	98.79	12	365	65
K–2536	62.09	.66	16.34	6.10	.13	3.00	5.97	3.77	1.33	.21	.02	99.47	22	338	115
K–2537	59.77	.74	17.14	6.51	.13	3.54	6.69	3.76	1.07	.24	–.11	98.87	15	374	103
Mount Cerberus															
K–69	63.02	0.65	16.14	5.82	0.12	2.73	5.78	3.74	1.43	0.17	0.15	99.48	26	281	118
K–164	63.98	.62	16.23	5.27	.10	2.34	5.23	4.13	1.56	.14	.18	99.12	31	297	134
K–164s	64.20	.63	16.29	4.96	.10	2.35	5.24	4.13	1.56	.13	– –	98.77	– –	– –	– –
K–445	64.95	.60	15.99	5.20	.11	2.11	5.01	4.02	1.49	.12	.13	99.06	29	285	132
K–2016	64.32	.64	16.01	5.42	.12	2.40	5.19	3.82	1.51	.18	.38	99.13	26	268	126
K–2456A–i	56.90	.85	17.52	8.58	.19	4.08	7.06	3.60	.74	.08	.10	98.97	13	353	53
K–2456B–i	56.72	.78	17.84	7.97	.16	4.14	7.67	3.14	1.04	.15	1.46	97.66	19	294	76
Falling Mountain															
K–177	64.19	0.62	16.22	5.20	0.10	2.20	5.15	4.19	1.60	0.13	0.31	98.59	30	299	131
K–372	63.83	.62	16.28	5.60	.12	2.31	5.47	3.82	1.41	.14	.00	99.09	25	321	129
K–577	65.17	.58	15.81	5.04	.11	2.13	4.98	4.05	1.59	.14	<.01	98.89	30	287	135
K–2021	63.79	.65	16.16	5.60	.12	2.38	5.35	3.88	1.48	.19	.00	99.54	23	311	128
K–2457A–i	56.48	.78	17.79	7.83	.16	4.45	7.96	3.13	.86	.17	.35	98.44	18	388	81
K–2457B–i	56.85	.84	17.92	7.78	.18	4.07	7.64	3.35	.80	.18	.25	98.38	16	378	71
Other peripheral domes															
K–831	64.93	0.54	16.58	4.61	0.10	1.93	5.17	4.00	1.58	0.16	0.36	99.10	22	298	137
K–832	61.87	.64	17.32	5.57	.11	2.66	6.14	3.88	1.24	.16	.15	99.48	31	352	119
K–832–i	56.85	.88	18.25	7.72	.14	3.79	7.31	3.61	.87	.18	.44	99.34	16	416	95
K–1180	63.52	.64	16.21	5.69	.12	2.55	5.40	3.91	1.43	.13	.04	98.93	33	293	125
K–1181–i	57.12	.76	17.67	7.74	.16	4.04	7.63	3.45	.90	.13	.10	99.22	18	360	87
K–1217	63.18	.69	16.29	5.79	.12	2.69	5.32	3.89	1.44	.18	.15	99.28	23	304	125
K–1230	62.99	.65	16.30	5.91	.13	2.71	5.51	3.83	1.41	.14	.31	98.98	25	280	124
K–1231–i	54.46	.77	18.26	8.20	.15	5.05	8.90	3.01	.69	.12	.64	98.75	15	379	79
K–2054	63.73	.66	16.36	5.51	.12	2.47	5.17	3.94	1.48	.17	.27	98.73	25	289	124
K–2054–i	57.74	.80	17.77	7.40	.13	3.94	7.05	3.61	.98	.18	.51	98.67	13	369	89
K–2485	64.40	.63	16.08	5.29	.12	2.27	5.01	4.05	1.55	.21	.17	98.57	30	279	128
K–2485A	63.36	.66	16.45	5.63	.12	2.53	5.24	3.93	1.45	.22	.88	98.44	24	282	121
K–2486	63.32	.67	16.34	5.64	.12	2.65	5.21	3.97	1.47	.22	.36	98.90	23	294	125
K–2545	63.42	.66	16.18	5.66	.13	2.55	5.38	3.97	1.44	.22	.11	98.78	24	293	123

Table 2. Chemical analyses of eruptive products from Trident Volcano—Continued

Sample (fig. 3)	SiO_2	TiO_2	Al_2O_3	FeO*	MnO	MgO	CaO	Na_2O	K_2O	P_2O_5	LOI	Original total	Rb	Sr	Zr
Pyroclastic-flow deposits															
Block-and-ash flow, Trident I:															
K–833	61.41	0.60	16.95	5.72	0.11	2.86	6.90	3.57	1.36	0.13	0.03	99.91	33	334	112
Pumiceous pyroclastic flow, Mageik Creek (unit tig):															
K–2489A	70.66	0.52	15.34	2.70	0.14	0.77	2.53	4.87	1.86	0.21	4.64	94.52	28	249	138
K–2489B	63.58	.82	16.46	5.33	.15	2.02	5.24	4.37	1.31	.31	2.41	96.57	21	313	104
K–2489C	63.89	.81	16.45	5.36	.16	1.99	5.00	4.34	1.29	.31	3.19	95.75	22	318	101
Lithic pyroclastic flows, Mageik Creek (unit tpf):															
K–1222	63.47	0.82	16.28	5.73	0.16	2.05	5.16	4.39	1.29	0.25	2.28	96.58	18	302	96
K–2204	63.56	.82	16.26	5.64	.16	1.99	5.09	4.50	1.31	.28	2.04	96.88	22	300	98
K–2204A	66.57	.73	15.88	4.43	.14	1.32	4.03	4.76	1.47	.26	.33	98.98	23	310	132
K–2204B	70.92	.50	15.08	2.67	.14	.73	2.44	5.28	1.69	.14	.34	98.84	26	246	135
K–2491A	67.52	.76	16.27	3.35	.09	.81	3.55	5.50	1.43	.31	.31	98.73	18	320	129
K–2491B	57.57	.99	16.75	8.57	.18	3.38	7.43	3.59	.95	.18	.70	98.44	15	334	75
K–2491C	71.83	.42	15.02	2.36	.14	.60	2.19	5.02	1.91	.13	1.52	97.34	32	239	147
K–2662A	70.73	.52	15.21	2.78	.12	.78	2.76	4.90	1.62	.17	1.12	98.85	26	232	158
K–2662B	63.68	.82	16.41	5.67	.15	2.02	5.14	4.11	1.34	.26	2.23	97.12	22	317	103
K–2662C	63.87	.83	16.28	5.67	.16	2.03	5.04	4.02	1.43	.26	2.52	96.68	22	317	108
K–2663A	63.79	.81	16.27	5.59	.16	2.01	5.12	4.35	1.23	.26	.35	99.14	22	322	107
K–2663B	63.66	.83	16.67	5.82	.16	2.03	4.94	3.93	1.34	.24	2.93	96.22	26	313	110
Southwest Trident (1953–74)															
K–70	61.64	0.68	16.74	5.81	0.11	2.81	6.47	3.85	1.35	0.14	<0.01	99.37	26	299	138
K–179	59.21	.75	17.00	6.68	.13	3.58	7.27	3.63	1.20	.14	<.01	99.58	23	343	116
K–812	61.61	.63	17.22	5.53	.11	2.61	6.44	3.95	1.35	.15	<.01	100.06	20	309	136
K–1226	59.28	.73	17.15	6.58	.13	3.51	7.25	3.59	1.22	.14	<.01	99.29	27	323	120
K–2027	56.94	.78	17.31	7.42	.14	4.31	8.12	3.39	1.02	.17	–.01	99.37	17	332	99
K–2053	64.77	.68	15.75	5.25	.12	2.12	4.91	4.15	1.69	.17	.01	99.49	33	252	163
K–2146	64.21	.66	16.01	5.24	.12	2.24	5.19	4.13	1.64	.16	.26	99.15	30	269	153
K–2147	63.77	.68	16.01	5.51	.12	2.39	5.31	4.03	1.61	.17	–.03	99.35	30	261	156
K–2148	63.46	.70	15.96	5.69	.12	2.53	5.40	4.00	1.57	.16	–.01	99.25	29	257	152
K–2149	62.58	.72	16.14	5.89	.12	2.74	5.78	3.92	1.51	.21	–.01	99.28	25	265	143
K–2159	61.50	.72	16.35	6.17	.13	3.10	6.20	3.80	1.42	.20	–.06	99.25	26	294	132
K–2172	61.47	.73	16.43	6.14	.13	3.00	6.28	3.82	1.42	.19	–.08	99.48	25	300	133
K–2173	61.40	.72	16.39	6.19	.13	3.20	6.31	3.69	1.40	.17	.02	98.90	27	292	136
K–2174	60.26	.75	16.56	6.53	.13	3.44	6.71	3.70	1.32	.20	–.10	99.75	24	302	127
K–2175	61.12	.73	16.66	6.19	.13	3.08	6.48	3.66	1.37	.17	–.04	98.99	26	301	133
K–2176	58.28	.77	17.01	7.03	.14	4.01	7.55	3.45	1.14	.23	–.14	99.37	21	350	108
K–2177	65.02	.66	15.79	5.16	.11	2.07	4.87	4.05	1.70	.16	.00	99.18	34	271	163
K–2178	61.90	.72	16.32	6.02	.13	2.97	6.07	3.82	1.46	.20	–.04	99.39	31	288	137

clasts in both the pumiceous (unit tig; sample K–2489) and dense-clast (unit tpf; 12 samples, table 2) pyroclastic-flow deposits at Mageik Creek include material more evolved (66.5–71.8 weight percent SiO_2) than any eruptive unit identified elsewhere in the whole Trident group. Moreover, for both units, most samples plot below the main data arrays of the Trident group in the K_2O and Zr panels (figs. 16*A*, 16*C*), suggesting that the magmas which produced the pyroclastic flows either fractionated zircon and a K-bearing phase (neither of which has been recognized elsewhere in the Trident group) or mixed with extraneous rhyolitic melt relatively deficient in K_2O and Zr.

Because these late Pleistocene pyroclastic-flow units are so anomalous compositionally, we infer that their vents have been buried by younger deposits or, alternatively, that any equivalent proximal material was stripped, buried, or never deposited. Potential vents include Trident I, West Trident, and any of the peripheral lava domes (fig. 3).

Warm Springs

Thermal springs south of Trident Volcano were mentioned by Spurr (1900) but not well located on his sketch map. The National Geographic Society expeditions that explored the Katmai Pass area in 1916–19 noted them as well, and their fine topographic map (Griggs, 1922), which was triangulated in the field, located the springs between Mageik Creek and dome 2600+, just east of the main present-day cluster of warm springs (fig. 3). During our own fieldwork in that area (1976–2001), the cluster has been limited to several shallow arroyos cut into 1912 pyroclastic deposits (fig. 17) just beneath the termini of the 1953 and 1958 lava flows from Southwest Trident. Bicarbonate-sulfate waters emerge from dozens of orifices at individual discharge rates of about 5 to 30 L/min (Keith and others, 1992). Most orifice temperatures (measured in July or August of various years, 1976–92) are only 9–28°C, but Keith and others (1992) measured a few at 40–42°C in 1982–84, and Johnston (1979) recorded one spring as hot as 50°C in 1978. About 2 km downstream, several springs of much greater discharge issue from the bedrock walls of Mageik Creek just south of dome 2460 (fig. 3); these measured only 15–20°C in the summers of 1997–98 but were fringed by extensive reddish-orange Fe-rich precipitates.

Another cluster of thermal springs lies 2.5 km south of Katmai Pass, at Ferruginous Flat (fig. 3), where lateral lobes of the 1958 lava flow blocked Mageik Creek, impounding a shallow lake that soon filled with alluvium and became a mudflat. Bicarbonate-sulfate waters discharge at numerous small Fe-precipitating springs that issue at about 15°C from

Figure 17. Warm spring discharging from rhyolitic pumice-fall deposit (not exposed) beneath 1912 ignimbrite, with snout of 1958 andesitic lava flow from Southwest Trident in background (figs. 1, 3). About 10 m of buff nonwelded ignimbrite is separated by 1-m-thick section of 1912 dacite pumice fall from conformably overlying lava flow, which here is 25 to 30 m thick. About 20 such warm springs, typically 25–42°C in summer, discharge near andesite flow fronts and drain along similarly vegetated gullies to Mageik Creek. View northwestward.

the alluvium and along gullies cut in 1912 pyroclastic deposits adjacent to the steep margin of the 1958 lava flow. Total discharge for the whole cluster was estimated by Keith and others (1992) at 100 to 300 L/min in the summers of 1982 and 1984.

On the basis of chemical and isotopic data, Keith and others (1992) reasoned that both sets of spring waters are products of shallow mixing between near-surface waters and a vapor-brine aureole beneath Southwest Trident. The Ferruginous Flat cluster may be influenced by the young cone and its shallow conduit, whereas the southern cluster must tap a deeper-circulating, longer-lived hydrothermal system, possibly heated by the pre-1953 dacitic magma reservoir, which Coombs and others (2000) reckoned to lie at only 3-km depth. Both sets of spring waters contain about 1 ppm As.

Fumaroles

Fumaroles at Trident Volcano likewise form two groups: those on the new composite cone of Southwest Trident and a long-lived fumarole field on the southeast flank of Trident I (fig. 3). The second group contains dozens of fumaroles distributed across a 300-m-wide patch of acid-altered ground that extends about 600 m upslope from 3,600-ft (1,100 m) to as high as 4,500-ft (1,370 m) elevation. First noted in 1916 by Griggs (1922, p. 98–99), in some places the cluster coalesces into a single conspicuous plume, and it always produces a strong odor of H_2S, which can be troublesome for those of us foolish enough to have camped downwind. In 1994–97, Bob Symonds of the USGS Cascades Volcano Observatory took several gas samples here and measured numerous near-boiling temperatures as high as 94°C. Analysis showed that the steam-dominated gas contains abundant CO_2, SO_2, H_2S, H_2, CH_4, and NH_3. Symonds' samples yielded He-isotopic ratios 7.5 times the atmospheric ratio, characteristic of magmatic gas at arc volcanoes, and $\delta^{13}C$ values of CO_2 close to −10 permil, which probably indicate a mixture of magmatic CO_2 and CO_2 derived by thermal breakdown of sedimentary rocks below the volcano.

At the site of Southwest Trident, the first evidence of a fumarole is provided by the set of aerial photographs taken by the Navy in August 1951, in which a conspicuous white plume is seen rising from a 100-m-wide pit on the southwest ridge of Trident I, at precisely the site of the magmatic outbreak that began in February 1953. Because no fumarole had previously been reported at this site, which lay in full view of the trail through Katmai Pass crossed by many parties between the 1890s and the 1930s (Spurr, 1900; Beach, 1909; Griggs, 1922; Hubbard, 1932, 1935), it can be inferred that the fumarolic vent developed during the decade or two before 1951. We are aware of no observational record for the 1940s.

During the main eruptive interval (1953–63), many fumaroles at Southwest Trident were, of course, strongly superheated, but no data are known to have been recorded. When the cone was climbed in August 1963 (by Pete Ward and Bob Decker, then of Dartmouth College), the crater interior was obscured by thick fumarolic cloud, and hundreds of fumarolic orifices lined with molten and crystalline sulfur dotted the entire crater rim (Decker, 1963); most orifices measured were hotter than 200°C, the upper limit of their thermometer. In 1978–79, we observed hundreds of fumaroles still active on and outside the crater rim (especially on the east and south slopes; fig. 14), but all measured were at or below the boiling temperature, 97°C (Johnston, 1979; Sheppard and others, 1992). Some of Johnston's 1978–79 gas samples were analyzed, showing them to be steam dominated but to contain significant concentrations of CO_2 and sulfur (Sheppard and others, 1992). In July 1990, from a fine perspective on the upper slope of Trident I less than 1 km from the steaming cone (but able to see only its east half), we counted 20 fumaroles on a lava bench low on the south flank of the cone, only 10 on lower slopes of the fragmental cone, and at least 100 high on the cone (as in fig. 14). During the 1990s, Bob Symonds measured fumarole temperatures only near or below boiling, the maximum value he recorded declining from 97°C in 1993 to 95°C in 1997. Although hundreds of orifices remain active, the odor of H_2S has abated, from strong in 1979 to barely perceptible in 1997. The H_2S output of Southwest Trident is now insignificant in comparison with that of the fumarole field southeast of Trident I.

Present-Day Seismicity and Deformation

Gravity and seismic data that identify a low-density, low-velocity region centered near Katmai Pass were summarized by Ward and others (1991). A southeasterly gravity traverse that crossed the volcanic axis by way of Katmai Pass showed the cross-axial width of the anomalous region to be about 15 km, but the data are insufficient to know how far it extends along the axis. Of the several seismic stations in Ward's 1987–91 array, only the one in Katmai Pass (central to the gravity anomaly) consistently showed traveltime delays for deep local and regional earthquakes. The delays require great thickness for the low-velocity domain, which may well extend below 20-km depth (Ward and others, 1991), thus involving most or all of the crust. Although their seismic data also indicated significant attenuation of *P* and *S* waves, they observed no screening of *S* waves (in contrast to interpretations of seismic reconnaissance studies 25 years earlier). To explain the data, they invoked present-day crustal magma storage, favoring scattered small magma bodies rather than a large chamber. One such body, of course, erupted to build the Southwest Trident volcano only a few decades ago.

The high rate of shallow microseismicity recognized by Ward and others (1991) has persisted. The Alaska Volcano Observatory expanded the Katmai seismometer network to 18 stations during the 1990s and continues to locate 40 to130 earthquakes each month along and near the volcanic axis (Jolly and McNutt, 1999; Power and others, 2001). Most of the earthquakes fall into three persistent clusters: (1) beneath Martin and Mageik Volcanoes, (2) beneath Katmai Pass and

the northwest slope of the Trident group, and (3) beneath the northwest half of Mount Katmai. Nearly all the earthquakes are of $M<2.5$; most are shallower than 5 km, and nearly all are shallower than 10 km. Such dense shallow microseismicity seems inconsistent with present-day upper-crustal storage of voluminous magma bodies and more likely reflects fluid flow, volume changes, and hydraulic microfracturing in the hydrothermal systems beneath the long-steaming volcanoes, along with slip-threshold reduction in the hydrothermally altered rocks. Nonetheless, in such an environment, dikes and sills or modest pods of magma are by no means excluded, as even a 0.7-km^3-volume pod like that erupted in 1953–74 would be hard to detect by routine seismic methods.

By comparing satellite images taken in 1993 and 1995, Lu and others (1997) used synthetic-aperture-radar interferometry to detect at least 7 cm of uplift beneath Southwest Trident. They interpreted the apparent ground deformation to reflect inflation of a pressure source at only 0.8- to 2-km depth, which they attributed to either magma intrusion or pressurization of the hydrothermal system. Considering the drastic decline in temperature and sulfur output of Southwest Trident fumaroles during the past 25 years, and in light of the field of warm springs conspicuous in the area since at least 1898, a hydrothermal explanation of the various geophysical anomalies is certainly plausible.

Behavior of Glaciers

Trident received a thicker blanket of 1912 fallout from adjacent Novarupta than did any of the other glacier-supporting volcanoes in the Katmai cluster. Moreover, the Knife Creek Glaciers north of Trident were also covered by thin pyroclastic-flow deposits, which ran up the ice and feathered out in the saddles between summits (Fierstein and Hildreth, 1992). We previously described the post-1951 behavior of the shrinking glaciers on nearby Mount Mageik (Hildreth and others, 2000) and the inconsistent patterns of retreat, advance, or stagnation for the several glaciers on Snowy Mountain (Hildreth and others, 2001) and Mount Griggs (Hildreth and others, 2002). Inspection of aerial photographs taken in 1951 and 1987 (respectively, the earliest and most recent sets available) indicates inconsistent behavior for the glaciers on Trident as well. We have observed no measurable changes in terminal positions since 1987, although small ones could have escaped detection.

Glacier 1, westernmost of the Knife Creek Glaciers, is fed largely from cirques below the north face of Trident I and the northwest face of East Trident (figs. 2, 3). Within and below each cirque, the most proximal 800 m or so of the steep and heavily crevassed ice surface has been largely cleared of 1912 pyroclastic deposits, by a combination of outflow and new ice formation. Medial and distal parts of the 4-km-long glacier are still covered, however, by as much as 12 m of 1912 material and locally by more recent avalanche deposits. The glacier terminus, which is steep and active, advanced 250 m between 1951 and 1987, edging out on top of welded 1912 ignimbrite on the floor of uppermost Knife Creek.

Contiguous to the east, Glacier 2 is fed from cirques below the north face and northeast ridge of East Trident. Only 3 km long, it terminates alongside neighboring Glacier 1 at 2,450-ft (750 m) elevation on the floor of Knife Creek (figs. 2, 3). Like its neighbor, only its steep proximal surfaces have been cleared of the thick cover of 1912 pyroclastic debris, of which most (but not all) has been disrupted by ice movement. The glacier terminus advanced more than 300 m between 1951 and 1987, and like its neighbors Glacier 1 and Glacier 3 (which is fed from Mount Katmai), it has overrun the margin of the 1912 ignimbrite.

A pair of small cirque glaciers below the north face of the arête connecting Trident I and West Trident are confluent into an icefall that joins Glacier 1 (fig. 3). Comparison of 1951 and 1987 photographs reveals little change except advanced removal of 1912 fallout from the ice surface.

A small steep slope glacier just below the summit of West Trident, on its northwest face, is only 350 m long but conspicuously crevassed. Although the glacier's margins appear to have changed little, the ice may have thickened substantially between 1951 and 1987. Adjoining snow slopes that cover much of the northwest side of West Trident (fig. 2) have accumulated atop the 1912 fallout, and by surviving summer ablation in most years, they have transformed into substantial fields of névé.

Another small cirque-floor glacier, formerly fed by avalanching of snow from the steep southwest face of Trident I, was 700 m long and still largely mantled by 1912 fallout when it was completely buried by the Southwest Trident cone and 1957 lava flow.

South of the Trident group, the west fork of Wishbone Glacier extends 7 km from the Trident-Katmai saddle to the gorge of Mageik Creek (fig. 3). From the saddle at 4,500 ft (1,370 m) to the terminus at 1,300 ft (400 m), virtually the entire glacier remains blanketed by 1912 fallout. Although the steep debris-covered terminus receded no more than 30 m between 1951 and 1987, the distal 2 km, which is canyon confined, appears to have thinned by about 10 m. Moreover, during that 36-year interval, a supraglacial stream cut an ice-confined channel, 10 to 20 m deep, down the axis of the lower 2 km of the glacier, suggesting virtual stagnation. About 3 km above the terminus, a 1-km-long lateral lobe branches off onto a plateau to the west (fig. 3). Although its pumice-mantled surface has hardly changed, the moderately sloping terminus of the lobe actually advanced about 110 m between 1951 and 1987.

Finally, a south-trending glacier flooring the narrow valley between Trident I and the south ridge of East Trident has wasted drastically. Already largely stagnant in 1951 and melting away beneath the thick blanket of 1912 pumice, the then-2-km-long glacier has since split into two segments, each 600 m long, separated by an 800-m-long gap now occupied by till, reworked pumice, and windows of andesitic lava (fig. 3). The upper segment is a crevassed slope glacier, its surface free of pumice, that drapes steeply down from the summit saddle

of East Trident. The distal segment is a wasting tongue of dead ice wholly buried by the ablation-disturbed pumice.

Acknowledgments

The purple passage quoted as our introductory epigraph typifies the overwrought mythology long attached to Katmai Pass, the only easy route around the Trident group. It recalls memorable days when we cached our packs and fled, but there were also brilliant placid nights when we slept there under the stars, enjoying the gentle seismicity and the airy whiff of brimstone. For cheerful comradeship and strong backs, we thank our Katmai Pass companions down the years, Larry Jager, Dave Johnston, Anita Grunder, Terry Keith, Mike Thompson, and Michelle Coombs. We are grateful to James Saburomaru and Forrest McFarland for K-Ar dating, and to Joel Robinson, who digitally prepared our Katmai geologic map, of which figure 3 is a localized adaptation. Most of the fieldwork was done on foot, but latter-day additions were accomplished with the help of helicopter pilots Paul Walters and Bill Springer. For encouraging completion of this study, we are particularly grateful to Terry Keith, who successively led the Alaska Volcano Observatory and the USGS Volcano Hazards Team.

References Cited

Bacon, C.R., and Druitt, T.H., 1988, Compositional evolution of the zoned calcalkaline magma chamber of Mount Mazama, Crater Lake, Oregon: Contributions to Mineralogy and Petrology, v. 98, no. 2, p. 224–256.

Baedecker, P.A., ed., 1987, Methods for geochemical analysis: U.S. Geological Survey Bulletin 1770.

Beach, Rex, 1909, The Silver Horde; a novel: New York, Harper & Brothers, 390 p. [Relates a crossing of Katmai Pass before the 1912 eruption modified the landscape].

Coombs, M.L., Eichelberger, J.C., and Rutherford, M.J., 2000, Magma storage and mixing conditions for the 1953–1974 eruptions of Southwest Trident volcano, Katmai National Park, Alaska: Contributions to Mineralogy and Petrology, v. 140, no. 1, p. 99–118.

Decker, R.W., 1963, Proposed volcano observatory at Katmai National Monument; a preliminary study: Hanover, N.H., Dartmouth College, report submitted to U.S. National Park Service, 54 p.

Detterman, R.L., Case, J.E., Miller, J.W., Wilson, F.H., and Yount, M.E., 1996, Stratigraphic framework of the Alaska Peninsula: U.S. Geological Survey Bulletin 1969–A, 74 p.

Fierstein, Judy, and Hildreth, Wes, 1992, The plinian eruptions of 1912 at Novarupta, Katmai National Park, Alaska: Bulletin of Volcanology, v. 54, no. 8, p. 646–684.

Fierstein, Judy, and Hildreth, Wes, 2000, Preliminary volcano-hazard assessment for Katmai Volcanic Cluster, Alaska: U.S. Geological Survey Open-File Report 00–489, 50 p.

Gill, J.B., 1981, Orogenic andesites and plate tectonics: Berlin, Springer-Verlag, 390 p.

Griggs, R.F., 1922, The Valley of Ten Thousand Smokes: Washington, D.C., National Geographic Society, 340 p.

Hildreth, Wes, 1983, The compositionally zoned eruption of 1912 in the Valley of Ten Thousand Smokes, Katmai National Park, Alaska: Journal of Volcanology and Geothermal Research, v. 18, no. 1–4, p. 1–56.

———1987, New perspectives on the eruption of 1912 in the Valley of Ten Thousand Smokes, Katmai National Park, Alaska: Bulletin of Volcanology, v. 49, no. 5, p. 680–693.

———1990, Trident, Alaska Peninsula, in Wood, C.A., and Kienle, Jürgen, eds., Volcanoes of North America; United States and Canada: New York, Cambridge University Press, p. 68–69.

———1991, The timing of caldera collapse at Mount Katmai in response to magma withdrawal toward Novarupta: Geophysical Research Letters, v. 18, no. 8, p. 1541–1544.

Hildreth, Wes, and Fierstein, Judy, 2000, Katmai volcanic cluster and the great eruption of 1912: Geological Society of America Bulletin, v. 112, no. 10, p. 1594–1620.

———2003, Geologic map of the Katmai volcanic cluster, Katmai National Park, Alaska: U.S. Geological Survey Miscellaneous Investigations Series Map I–2778, scale 1: 63,360.

Hildreth, Wes, Fierstein, Judy, Lanphere, M.A., and Siems, D.F., 1999, Alagogshak volcano; a Pleistocene andesite-dacite stratovolcano in Katmai National Park, *in* Kelley, K.D., ed., Geologic studies in Alaska by the U.S. Geological Survey, 1997: U.S. Geological Survey Professional Paper 1614, p. 105–113.

———2000, Mount Mageik: A compound stratovolcano in Katmai National Park, *in* Kelley, K.D., and Gough, L.P., eds., Geologic studies in Alaska by the U.S. Geological Survey, 1998: U.S. Geological Survey Professional Paper 1615, p. 23–41.

———2001, Snowy Mountain; a pair of small andesite-dacite stratovolcanoes in Katmai National Park, *in* Gough, L.P., and Wilson, F.H., eds., Geologic studies in Alaska by the U.S. Geological Survey, 1999: U.S. Geological Survey Professional Paper 1633, p. 13–34.

———2002, Mount Griggs: A compositionally distinctive Quaternary stratovolcano behind the main volcanic line in Katmai National Park, *in* Wilson, F.H., and Galloway, J.P., eds., Geologic Studies in Alaska by the U.S. Geological Survey, 2000: U.S. Geological Survey Professional Paper 1662, p. 87–112.

Hildreth, Wes, and Lanphere, M.A., 1994, Potassium-argon geochronology of a basalt-andesite-dacite arc system; the Mount Adams volcanic field, Cascade Range of southern Washington: Geological Society of America Bulletin, v. 106, no. 11, p. 1413–1429.

Hildreth, Wes, Lanphere, M.A., and Fierstein, Judy, 2003, Geochronology and eruptive history of the Katmai volcanic cluster, Alaska Peninsula: Earth and Planetary Science Letters, v. 214, p. 93–114.

Hubbard, B.R., 1932, Mush, you malemutes!: New York, America Press, 179 p.

———1935, Cradle of the storms: New York, Dodd, Mead & Co., 285 p.

Johnston, D.A., 1979, Volcanic gas studies at Alaskan volcanoes, *in* Johnson, K.M., and Williams, J.R., eds., The United States Geological Survey in Alaska; accomplishments during 1978: U.S. Geological Survey Circular 804–B, p. B83–B84.

Jolly, A.D., and McNutt, S.R., 1999, Seismicity at the volcanoes of Katmai National Park, Alaska; July 1995–December 1997: Journal of Volcanology and Geothermal Research, v. 93, no. 3–4, p. 173–190.

Keith, T.E.C., Thompson, J.N., Hutchinson, R.A., and White, L.D., 1992, Geochemistry of waters in the Valley of Ten Thousand Smokes region, Alaska: Journal of Volcanology and Geothermal Research, v. 49, no. 3–4, p. 209–231.

Kienle, Jürgen, Swanson, S.E., and Pulpan, Hans, 1983, Magmatism and subduction in the eastern Aleutian arc, *in* Shimozuru, Daisuke, and Yokoyama, Izumi, eds., Arc volcanism—physics and tectonics: Tokyo, Terra Scientific, p. 191–224.

Kosco, D.G., 1981, Characteristics of andesitic to dacitic volcanism at Katmai National Park, Alaska: Berkeley, University of California, Ph.D. thesis, 249 p.

Lanphere, M.A., 2000, Comparison of conventional K-Ar and $^{40}Ar/^{39}Ar$ dating of young mafic volcanic rocks: Quaternary Research, v. 53, no. 3, p. 294–301.

Lu, Zhong, Fatland, D.R., Wyss, Max, Eichelberger, J.C., Dean, Kenneson, and Freymueller, J.T., 1997, Deformation of New Trident volcano measured by ERS–1 SAR interferometry, Katmai National Park, Alaska: Geophysical Research Letters, v. 24, no. 6, p. 695–698.

Miyashiro, Akiho, 1974, Volcanic rock series in island arcs and active continental margins: American Journal of Science, v. 274, no. 4, p. 321–355.

Muller, E.H., Juhle, R.W., and Coulter, H.W., 1954, Current volcanic activity in Katmai National Monument: Science, v. 119, no. 3088, p. 319–321.

Peacock, M.A., 1931, Classification of igneous rock series: Journal of Geology, v. 39, no. 1, p. 54–67.

Plafker, George, Moore, J.C., and Winkler, G.R., 1994, Geology of the southern Alaska margin, chapter 12 *of* Plafker, George, and Berg, H.C., eds., The geology of Alaska, v. G–1 of The geology of North America: Boulder, Colo., Geological Society of America, p. 389–449.

Power, J.A., Moran, S.C., McNutt, S.R., Stihler, S.D., and Sanchez, J.J., 2001, Seismic response of the Katmai volcanoes to the 6 December 1999 magnitude 7.0 Karluk Lake earthquake, Alaska: Seismological Society of America Bulletin, v. 91, no. 1, p. 57–63.

Ray, D.K., 1967, Geochemistry and petrology of the Mt. Trident andesites, Katmai National Monument, Alaska: Fairbanks, University of Alaska, Ph.D. thesis, 198 p.

Riehle, J.R., Detterman, R.L., Yount, M.E., and Miller, J.W., 1993, Geologic map of the Mount Katmai quadrangle and adjacent parts of the Naknek and Afognak quadrangles, Alaska: U.S. Geological Survey Miscellaneous Investigations Series Map I–2204, scale 1:250,000.

Sheppard, D.S., Janik, C.J., and Keith, T.E.C., 1992, A comparison of gas geochemistry of fumaroles in the 1912 ash-flow sheet and on active stratovolcanoes, Katmai National Park, Alaska: Journal of Volcanology and Geothermal Research, v. 53, no. 1–4, p. 185–197.

Simkin, Tom, and Siebert, Lee, 1994, Volcanoes of the world; a regional directory, gazetteer, and chronology of volcanism during the last 10,000 years (2d ed.): Tucson, Geoscience Press, 349 p.

Snyder, G.L., 1954, Eruption of Trident volcano, Katmai National Monument, Alaska: U.S. Geological Survey Circular 318, 7 p.

Spurr, J.E., 1900, A reconnaissance in southwestern Alaska in 1898, *in* Explorations in Alaska in 1898: U.S. Geological Survey Annual Report 1898–1899, pt. 7, p. 31–264.

Stacey, J.S., Sherrill, N.D., Dalrymple, G.B., Lanphere, M.A., and Carpenter, N.V., 1981, A five-collector system for the simultaneous measurement of argon isotope ratios in a static mass spectrometer: International Journal of Mass Spectrometry & Ion Physics, v. 39, p. 167–180.

Ward, P.L., and Matumoto, Tosimatu, 1967, A summary of volcanic and seismic activity in Katmai National Monument, Alaska: Bulletin Volcanologique, v. 31, p. 107–129.

Ward, P.L., Pitt, A.M., and Endo, Elliot, 1991, Seismic evidence for magma in the vicinity of Mt. Katmai, Alaska: Geophysical Research Letters, v. 18, no. 8, p. 1537–1540.

Wilson, F.H., 1985, The Meshik arc—an Eocene to earliest Miocene magmatic arc on the Alaska Peninsula: Alaska Division of Geological and Geophysical Surveys Professional Report 88, 14 p.

Studies by the U.S. Geological Survey in Alaska, 2001
U.S. Geological Survey Professional Paper 1678

Geology and Late Quaternary Eruptive History of Kanaga Volcano, a Calc-Alkaline Stratovolcano in the Western Aleutian Islands, Alaska

By Christopher F. Waythomas, Thomas P. Miller, and Christopher J. Nye

Abstract

Recent studies of the geology and eruptive history of Kanaga Volcano in the western Aleutian Islands of Alaska have yielded new information about the timing of Holocene eruptions and an improved understanding of the evolution of the volcano. Previous studies indicated that Kanaton Ridge, a major topographic feature on the northern part of Kanaga Island, was the rim of a collapse caldera. Our studies indicate that the caldera structure more likely formed as the result of a northward-directed flank collapse that was not necessarily associated with a major eruption. Dacitic lapilli tephra deposits began accumulating on Kanaga Island about 11 ka, and we infer that most of the modern volcanic cone developed in Holocene time. At least 11 major tephra-producing eruptions of Kanaga Volcano have been documented since about 11 ka, in addition to known historical eruptions in 1763, 1768, 1786, 1790, 1791, 1827, 1829, 1904, 1906, and 1993–95. Tephra deposits on nearby Adak Island were believed to have been erupted from Kanaga Volcano throughout the Holocene. Our tephrostratigraphic and chronologic data indicate that only a few of these tephra deposits can be directly correlated with eruptions of Kanaga Volcano, and so the source of the major pumiceous tephra deposits on Adak Island is uncertain. Holocene eruptions of Mount Moffett, a broad composite cone on the northern part of Adak Island, now appears to be a possible source volcano for many of the tephra deposits on Adak Island.

Introduction

Since 1996, the Alaska Volcano Observatory has been systematically expanding its volcano-monitoring program and, at the same time, initiating new studies of the geology, eruptive history, and hazards of several active volcanoes in the Aleutian Arc of Alaska. Many volcanoes in this region have never been studied in detail; geologic maps are preliminary at best, and information about Holocene eruptions is generally unknown. Although the Aleutian Islands are a remote area inhabited by few people, eruptions from this region pose substantial hazards to overflying jet aircraft traveling North Pacific air routes between North America and the Far East. Projected increases in air travel over this region have heightened concern about the potential hazard to jet aircraft from explosively generated plumes of volcanic ash. Recent studies by the Alaska Volcano Observatory have been focused on addressing this concern by studying the geology and eruptive history of historically active volcanoes in the Aleutian Arc to better understand the characteristics of future explosive eruptions. Here, we report results from our study of Kanaga Volcano, an active calc-alkaline stratovolcano in the western Aleutian Islands of Alaska (fig. 1).

Kanaga Volcano is a 1,300-m-high, cone-shaped andesitic stratovolcano on the north end of Kanaga Island (lat 51°55′ N., long 177°10′ W.) in the Andreanof Islands Group of the western Aleutian Islands (fig. 1). The volcano is about 30 km west of Adak Island and the community of Adak, the site of a former U.S. Naval installation that still supports a major airfield and serves as an alternative landing site for trans-Pacific aircraft. Kanaga Volcano has erupted numerous times in the past 10 k.y., including at least 10 Strombolian-type to sub-Plinian eruptions in the past 250 years (Miller and others, 1998). The most recent eruption, in 1993–95, produced several aa lava flows that descended the northwest flank of the volcano to the sea (fig. 2), and several small-volume, low-altitude plumes of volcanic ash that at least once drifted eastward over Adak Island and deposited a few millimeters of fine ash on the northern part of Adak Island.

Kanaga Volcano is undissected, symmetrical in profile, and characterized by numerous blocky lava flows, with well-developed levees and steep flow fronts, that descend radially from or near the 200-m-wide summit vent crater (fig. 2). The flanks of the cone are steep (25°–30°) and consist of blocky aa lava flows, talus, spatter, coarse tephra, and clast-rich lahar deposits. The volcano does not support glaciers but is snow covered almost year round. The cone itself shows little evidence of dissection by streams or glaciers and so could have been entirely constructed in postglacial Holocene time. The volcano is one of the more active Aleutian volcanoes, and historical eruptions were reported in 1791, 1827, 1829, 1904,

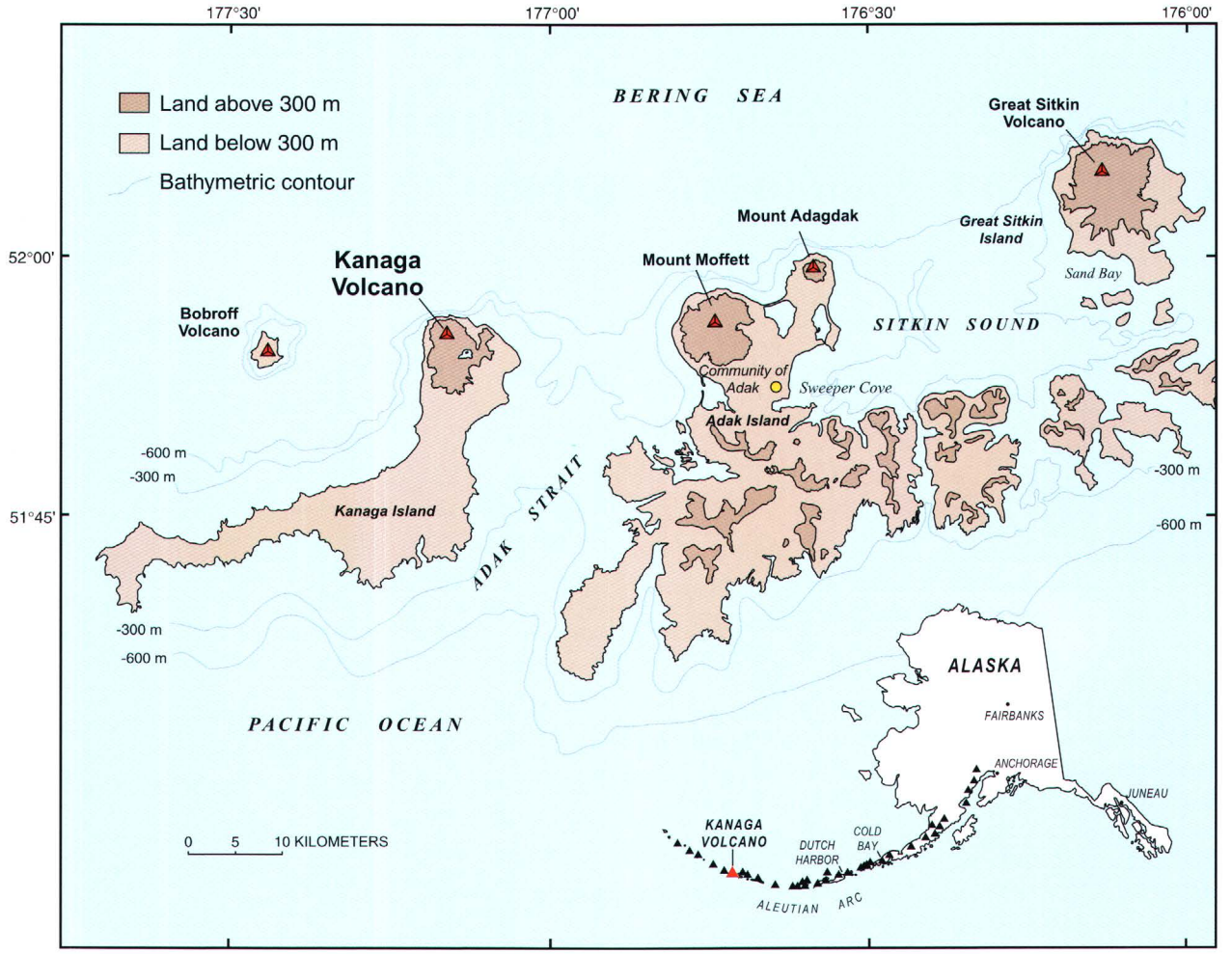

Figure 1. Western part of the Aleutian Islands, Alaska, showing location of Kanaga Volcano.

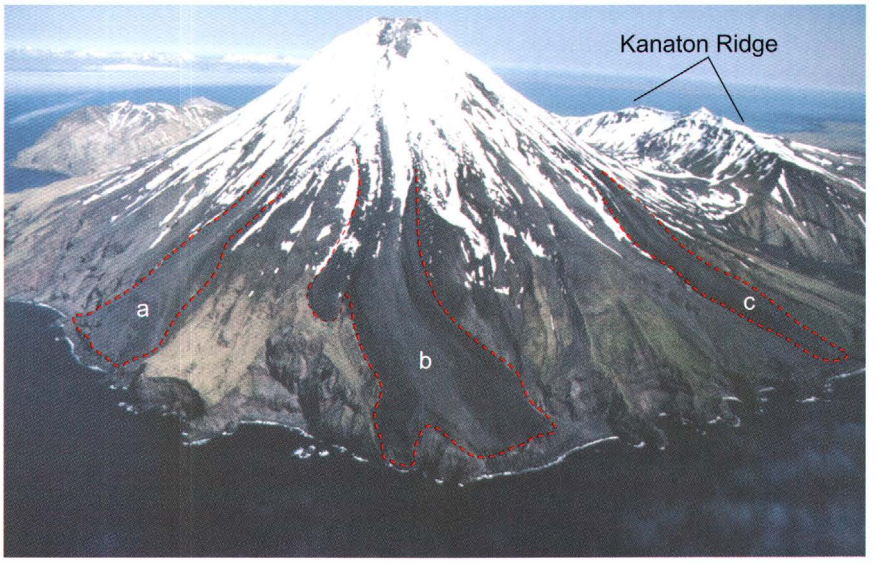

Figure 2. Kanaga Volcano. Areas a through e (outlined with red dashed line), blocky aa lava flow erupted during 1993–95. Kanaton Ridge is in background. Summit altitude, 1,307 m. View southeastward; photograph by C.J. Nye, Alaska Division of Geological and Geophysical Surveys, taken July 2000.

and 1993–95 (Miller and others, 1998); less well documented eruptions also were reported in 1763, 1768, 1786, 1790, and 1933.

The geology of the northern part of Kanaga Island was studied briefly in 1946 by R.R. Coats, who produced the first known geologic map of Kanaga Volcano based on about 10 days of fieldwork on foot (Coats, 1956). Coats described most of the major lithologic units on the northern part of Kanaga Island and made several important observations about the geology of Kanaga Volcano. He recognized Mount Kanaton, an ancestral volcano part surrounding the modern Kanaga cone, and inferred that Mount Kanaton was destroyed by structural collapse which he believed during a caldera-forming eruption. Coats also identified several older eruptive centers on the flanks of ancestral Mount Kanaton (Coats, 1956).

More recent investigations of the geology of the northern part of Kanaga Island have been petrologic studies of basaltic lava flows on Kanaton Ridge (Brophy, 1989, 1990) and at Round Head (Whittington, 1996). We visited Kanaga Island during June and July 1999 and 2000 and refined the geologic map of the volcano, sampled major lithologic units and other deposits, and evaluated the hazards posed by future eruptions. We also investigated the record of Holocene eruptive activity by studying and sampling tephra deposits in shallow stratigraphic exposures on the flanks of Mount Kanaton and Kanaga Volcano. Previous work on nearby Adak Island (Black, 1980; Romick and others, 1992; Kiriyanov and Miller, 1997), where multiple beds of pumiceous lapilli tephra of Holocene age are preserved, attributed several of these tephra deposits to eruptions of Kanaga Volcano. We thus sought to evaluate the origin of the tephra deposits on Adak Island to determine whether Kanaga Volcano was indeed the source.

Geology of the Volcano

The focus of our studies was the modern cone of Kanaga Volcano and its associated deposits. We spent little time mapping and sampling the older rocks and deposits that were described by Coats (1956). To give a better overall synopsis of the volcano, we include a brief summary of the geology of these older volcanic rocks.

Older Volcanic Cones

Kanaga Volcano is partly surrounded by, and in fault contact with, at least three overlapping volcanic cones older than the present edifice, including two small composite cones on the northeast coast of the island and a shield like edifice called Mount Kanaton by Coats (1956). The oldest of the three cones, which is exposed along the northeast coast of the island immediately east of Kanaga Volcano (fig. 3; Coats, 1956; Brophy, 1990), consists mainly of thick-bedded to massive basaltic and andesitic lava flows and includes a few beds of volcanic breccia and tuff. Most of the rocks in the cone are hydrothermally altered, and as a result, small debris-avalanche and landslide deposits are common on the flanking slopes.

The second cone is a small satellite eruptive center on the northeast side of Kanaga Island at Round Head, just north of Weed Bight (fig. 3). This cone is truncated by a seacliff that exposes a 50- to 70-m-thick sequence of olivine basalt lava flows. These rocks underlie and thus predate the volcanic rocks that make up Mount Kanaton.

Volcanic Rocks of Mount Kanaton

"Mount Kanaton" is the name that Coats (1956) used to describe a large ancestral shieldlike cone that surrounds the south flank of modern Kanaga Volcano (fig. 2). The volcanic rocks of ancestral Mount Kanaton include a 400- to 500-m-thick sequence of lava flows of basaltic andesite and andesite, volcanic breccia, and pyroclastic deposits that form most of Kanaton Ridge, a prominent scarplike feature sculpted into the side of Mount Kanaton (Coats, 1956). The lava flows exposed in the scarp of Kanaton Ridge dip gently (approx 15°) south, suggesting that the ancestral edifice was in about the same position as the modern cone of Kanaga Volcano. K-Ar ages of lavas from Kanaton Ridge indicate that Mount Kanaton was active in middle and late Quaternary time (Bradley Singer, unpub. data, 2001). Scattered deposits of till, striated and ice-molded bedrock, and U-shaped glacial valleys indicate that the south slopes of Mount Kanaton were formerly overrun by glacier ice. This area is mantled by peat and tephra deposits that began accumulating about 11 ka, suggesting that the edifice of Mount Kanaton was high enough to support glacier ice possibly associated with the latest worldwide glaciation, which peaked about 18 ka (Imbrie and others, 1983). Thus, the bulk of ancestral Mount Kanaton could have been constructed by at least Pleistocene time.

Modern Cone of Kanaga Volcano

The modern cone of Kanaga Volcano is a composite stratocone composed of interbedded andesitic lava flows and pyroclastic debris. Typical lava flows on the cone have blocky aa surface morphology, well-defined marginal levees, and distinct lobate flow fronts (figs. 2, 3). All of the major flows appear to have been erupted from the central vent and several fresh-appearing, unvegetated lava flows and flow fields (Ql_{94}, Ql_{06}, Qlh, fig. 3) are identifiable on the east-northeast, south, southwest, west-southwest, and northwest flanks of the volcano. Lava flows on the southwest, west-southwest, north, and northwest flanks of the volcano extend to the ocean. Older lava flows and flow fields (Qlcb, fig. 3) are vegetated to varying degrees and locally mantled with tephra but still retain fresh-appearing surface features. Most of the lava flows that make up the edifice of Kanaga Volcano are medium-K and calc-alkaline in composition (fig. 4) and composed primarily of porphyritic two-pyroxene andesite and basaltic andesite;

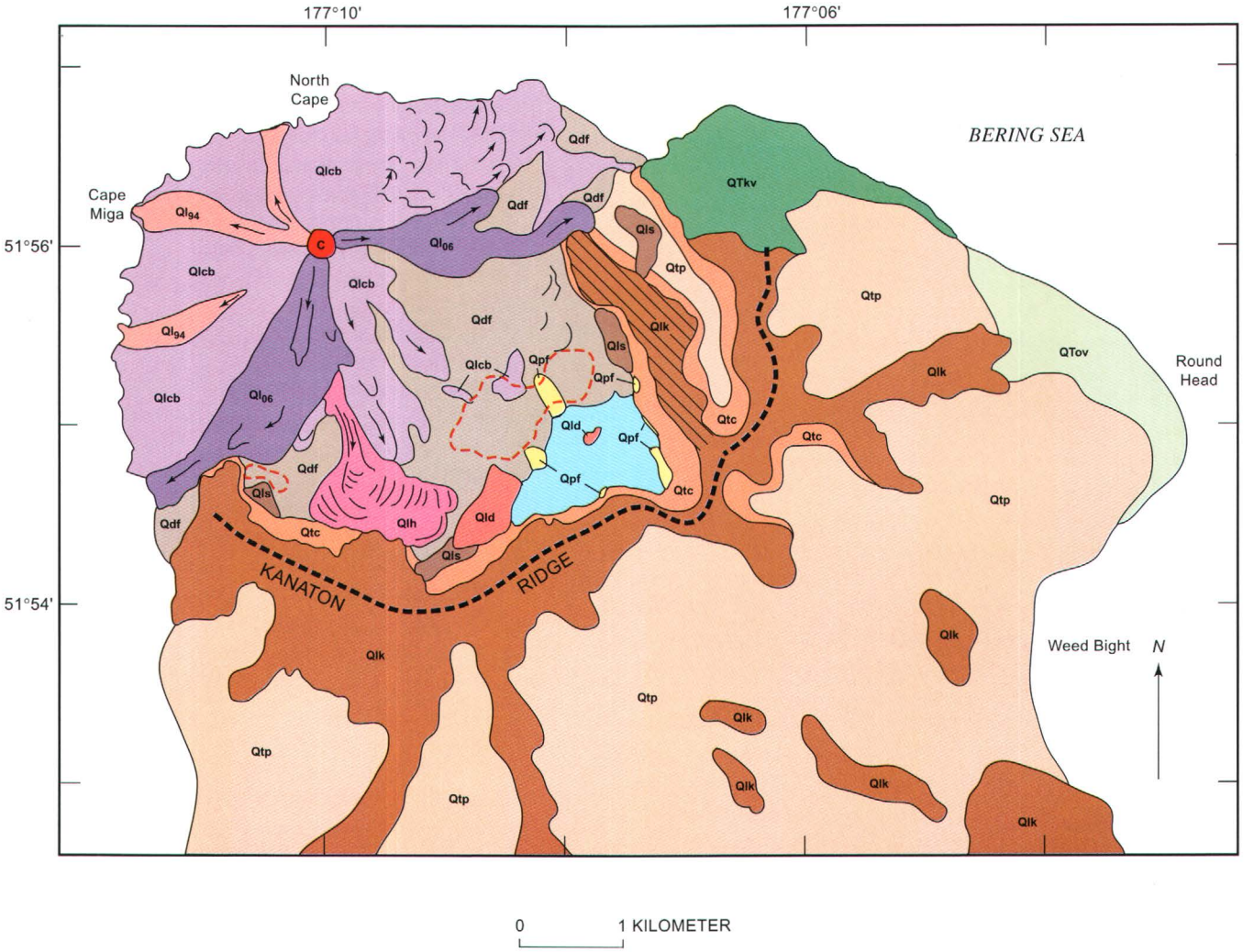

EXPLANATION

Lava flows of historical eruptions

- Ql94 — Andesite flows erupted in 1994.
- Ql06 — Andesite flows erupted in 1906.

Qlh — **Lava flow (Holocene)**—Andesite aa lava flow produced by historical(?) eruption of Kanaga Volcano

Qlcb — **Lava flows (Holocene)**—Lava flows produced by prehistorical and older eruptions of Kanaga Volcano; may include areas of blocky talus and avalanche debris

Qpf — **Pyroclastic-flow deposits (Holocene)**—Pumiceous pyroclastic-flow deposits associated with eruptions from vents on the southeast flank of Kanaga Volcano

Qdf — **Lahar and lahar run-out deposits (Holocene)**—Poorly sorted, fan-shaped deposits of boulders, gravel, sand, and silt deposited by water-saturated mixtures of volcaniclastic debris during eruptions; may contain juvenile clasts of dacite and andesite

Qtp — **Tephra, soil, and peat deposits (Holocene)**—Blanketing mantle of airfall tephra, buried soils, and peat, 1-3 m thick; may include colluvial deposits

Qls — **Landslide deposits (age uncertain)**—Intact to partially dissaggregated blocks of andesitic lava derived from the rim of Kanaton Caldera

Qtc — **Talus and other colluvial deposits (Holocene)**—Rock rubble, solifluction deposits, and rockfall debris on slopes

Qld — **Lava domes (Holocene?)**—Andesitic lava domes on the southeast flank of Kanaga Volcano

Qlk — **Lava flows erupted from Mount Kanaton (Pleistocene and Pliocene?)**—Andesitic cone-building lava flows of ancient Kanaton Volcano. Ruled pattern indicates slump block associated with caldera collapse

QTkv — **Lava flows older than Kanaton volcano (Quaternary or Tertiary)**—Basaltic lava flows erupted from vents on or near the north coast of Kanaga Island

QTov — **Lava flows erupted from vents offshore of Kanaga Island (Quaternary or Tertiary)**—Basaltic lava flows and breccia associated with no-longer-active vents offshore of Kanaga Island

C — **Crater of Kanaga Volcano**

Flow margins of lava flows

Flow path of lava flows

Collapse-caldera margin

Field of ballistic-impact craters

Figure 3. Generalized geologic map of Kanaga Volcano (fig. 1).

phenocrysts are chiefly plagioclase, clinopyroxene, orthopyroxene, and Fe oxide minerals, with traces of olivine and hornblende. The groundmass is typically a pale- to light-brown glass containing microlites of plagioclase and pyroxene. Systematic variations in mineralogy or whole-rock chemistry are not apparent, suggesting that the composition of the Kanaga lava flows has changed little over time.

Pumice-Bearing Deposits

Pumice-bearing pyroclastic-fall, pyroclastic-flow, and lahar deposits are preserved on the south flanks of Kanaga Volcano (fig. 3), and pumice lapilli tephra deposits are common on the south slopes of Kanaton Ridge. The pyroclastic-flow and lahar deposits, which are fresh, unvegetated, and little modified, are the eruptive products of relatively recent explosive eruptions. Pumice from the pyroclastic-flow, lahar, and tephra deposits is more silicic (63–66 weight percent SiO_2) than the predominant andesite of Kanaga Volcano (fig. 4), and eruptions involving dome collapse are the most likely origin for these deposits; however, lava domes of dacitic composition have not been identified at Kanaga Volcano. The position and pumice clast size (granule to cobble) of the pyroclastic deposits suggests that their parent domes may have been buried by younger lava flows erupted from the summit vent.

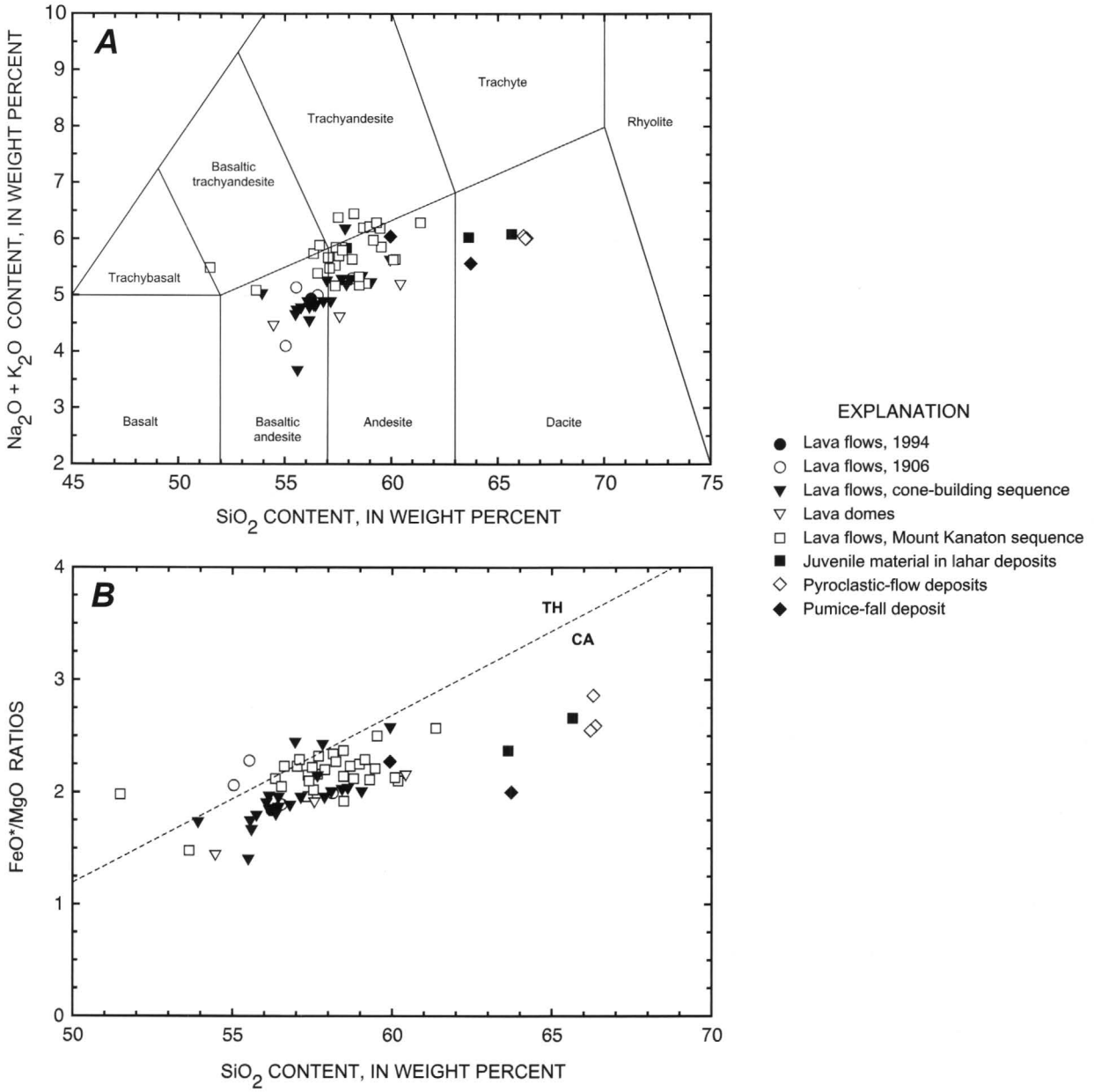

Figure 4. Compositional plots for lava flows and pyroclastic deposits from northern Kanaga Island (fig. 1). *A*, Na_2O+K_2O versus SiO_2 contents. Discriminant lines from Le Bas and others (1986). *B*, FeO^*/MgO ratio versus SiO_2 content. plot for lava flows and pyroclastic deposits from northern part of Kanaga Island. Tholeiite/calk-alkaline discriminant line from Miyashiro (1974).

Lava Domes

Andesitic lava domes are exposed in the southern part of the caldera in and adjacent to the intracaldera lake (fig. 5). These domes, which are compositionally different from the silicic pumice in tephra deposits on the flanks of the volcano (fig. 4), are believed to have been emplaced during an earlier eruptive phase more closely related to the modern andesite edifice. The age of the domes is not known, but they appear little weathered and are overlain by pyroclastic-flow deposits erupted 1.3–0.9 ka.

Eruptive History

Edifice Collapse

The modern cone of Kanaga Volcano is partly surrounded by Kanaton Ridge, a prominent semicircular scarp cut into the side of ancestral Mount Kanaton (fig. 3). The scarp is either the remnant of a typical island-arc collapse caldera now breached to the northwest, or the scarp of an avalanche caldera resulting from a northwestward-directed edifice failure. Our reconstruction of ancestral Mount Kanaton indicates a volcano with a basal diameter of about 13 km, an estimated elevation of about 2.3 km above sea level, and a volume of at least 75 km^3. We estimate that at least a third (approx 25 km^3) of Mount Kanaton has been removed by structural collapse. Typical collapse calderas in the Aleutian Arc are surrounded by voluminous pyroclastic-flow and tephra deposits emplaced during catastrophic caldera-forming eruptions (Miller and Smith, 1987). Such deposits form sheetlike accumulations of pumiceous pyroclastic debris that are tens of meters thick and extend radially from the caldera for many tens of kilometers. The geologic map of the northern part of Kanaga Island by Coats (1956) shows an extensive area of andesite tuff south and east of Kanaga Volcano. Before our work, we assumed that the andesite tuff mapped by Coats (1956) was likely the pyroclastic flow sheet generated by the caldera-forming eruption which formed Kanaton Ridge. To the contrary, we discovered that pyroclastic-flow deposits are rare on Kanaga Island and that the andesite tuff of Coats (1956) consists mostly of interbedded peat and felsic tephra deposits. These tephra deposits, though abundant, are insufficiently thick or coarse to represent a caldera-forming eruption and are absent in some areas where deposition would be expected. Deposits of pumice-rich, crossbedded alluvium that were discovered in the central part of Kanaga Island indicate that periods of explosive silicic volcanism have occurred in the past. Pumice in these deposits is reworked and may have been generated by explosive eruptions of Mount Kanaton, but we are uncertain whether the pumice was initially emplaced during a caldera-forming eruption.

These observations may be explainable if the formation of Kanaton Ridge occurred in Pleistocene time. Glaciation of the northern part of Kanaga Island could have removed some of the deposits generated by a caldera-forming eruption; however, it is unlikely that all such deposits would have been removed by glaciers and deposits of till which we did observe to contain no pumiceous material. The absence of voluminous pyroclastic-flow deposits on the flanking slopes of Mount Kanaton does not necessarily mean that a caldera-forming eruption did not occur, because elsewhere in the Aleutian Arc where Pleistocene calderas have been identified (for example, Emmons Lake and Ugashik Caldera on the Alaska Peninsula), pyroclastic-flow deposits are somewhat sparse and have limited aerial distribution. However, radiocarbon dating of buried soils and peat associated with conspicuous tephra deposits on Kanaga Island yields no evidence of major caldera-forming eruptions of Holocene age. Thus, if Kanaton Ridge is the scarp of a collapse caldera, it must have formed before the Holocene. Kanaton Ridge could be

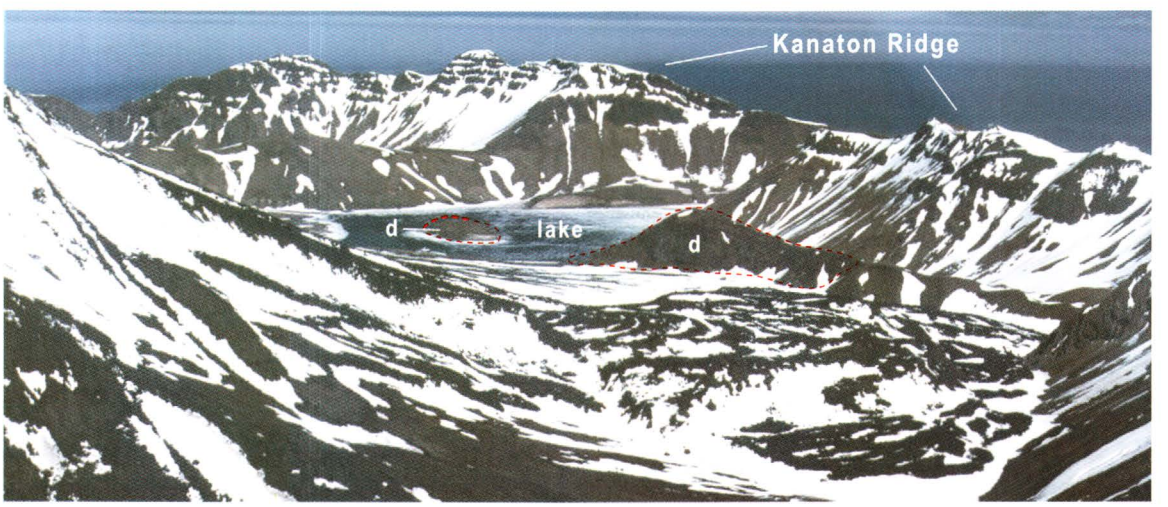

Figure 5. South flank of Kanaga Volcano, showing intracaldera lake (fig. 1), and Kanaton Ridge. Area d (outlined with red dashed line), lava domes of andesitic composition. These domes are not dated but are overlain by pyroclastic-flow deposits erupted about 1,000 yr B.P. View southeastward; photograph by C.F. Waythomas, taken July 2000.

a somma-like feature representing the headscarp of a northward-directed edifice failure. This failure may not have been associated with a major eruption and thus could have occurred without leaving extensive pyroclastic-flow deposits on Kanaga Island.

Images of the sea floor in the southern Bering Sea near Kanaga Island made during the GLORIA project (EEZ-Scan scientific staff, 1991) show an area of irregular, hummocky topography extending northwestward from Kanaga Island (fig. 6). This feature could be a debris-avalanche deposit that formed when the northwest sector of ancestral Mount Kanaton foundered into the sea. The length (L) of the feature is 38 km, measured from the presumed headscarp at Kanaton Ridge to its terminus, and the average width is 12 km, giving an area of about 460 km^2. We estimated the height (H) of ancestral Mount Kanaton at about 2,300 m, giving an H/L ratio of 0.06, a low value consistent with the long runout expected for submarine landslides (Holcomb and Searle, 1991). The width of the initial slide block is about 10 km, as estimated from the scarp width, and the minimum height of the scarp, as determined from a topographic profile (fig. 7), is about 500 m.

The tectonic architecture of the western Aleutian Arc is characterized by a series of rhomb-shaped crustal blocks of various sizes, from tens to hundreds of kilometers long (Geist and others, 1988). Subduction along the Aleutian Trench during late Cenozoic time has caused clockwise rotation of these blocks. Block rotation leads to the formation of many throughgoing strike-slip faults within the rotated massifs. However, late Cenozoic volcanic centers apparently occur in areas of unrotated crust and are beyond the limit of deformation associated with block rotation (Geist and others, 1988), suggesting that structural controls on volcanic-edifice stability may be less important than if the volcanoes were situated on structurally complex blocks of rotated crust. We did not observe any major faults on or near ancestral Mount Kanaton, nor did Coats (1956), who mapped several small faults around Kanaton Ridge. Reactivation of structures in the subvolcanic basement has been proposed as a mechanism for volcanic-edifice collapse (van Wyk de Vries and Francis, 1997; Vidal and Merle, 2000), but given the tectonic setting of Kanaga Volcano described above, this mechanism seems unlikely to have caused the collapse of ancestral Mount Kanaton.

Oceanic volcanoes, especially those in active volcanic arcs, commonly show evidence of former flank failures (Holcomb and Searle, 1991). Collapse processes are complex and commonly interrelated but almost always involve some type of magmatic activity (McGuire, 1996; Voight and Elsworth, 1997; Keating and McGuire, 2000). During our studies of Kanaga Volcano, we discovered several lava domes near the base of the scarp that defines Kanaton Ridge (fig. 3). Although the dome rocks have not been dated, they are chemically distinct from tephra deposits of Holocene age on the island and may have been emplaced during a period of magmatic activity that predates the formation of the modern volcanic edifice. The oldest dated tephra was erupted about 11 ka, suggesting that the domes may be pre-Holocene. Although it is difficult to determine the mechanism(s) that initiated failure of ancestral Mount Kanaton, the presence of a lava-dome complex at the base of Kanaton Ridge may be more than coincidental. Intrusion of the dome complex could have destabilized the north flank of Mount Kanaton through a combination of mechanical, thermal, and, possibly, seismic processes associated with the ascending magma. Hydrous magma that intrudes colder host rocks and begins to cool and crystallize will release volatile materials. At shallow depths, the volume increase associated with magma degassing can be significant and may generate substantial water pressures (Burnham, 1979; Voight and Elsworth, 1997). Such pressures can theoretically exceed 100

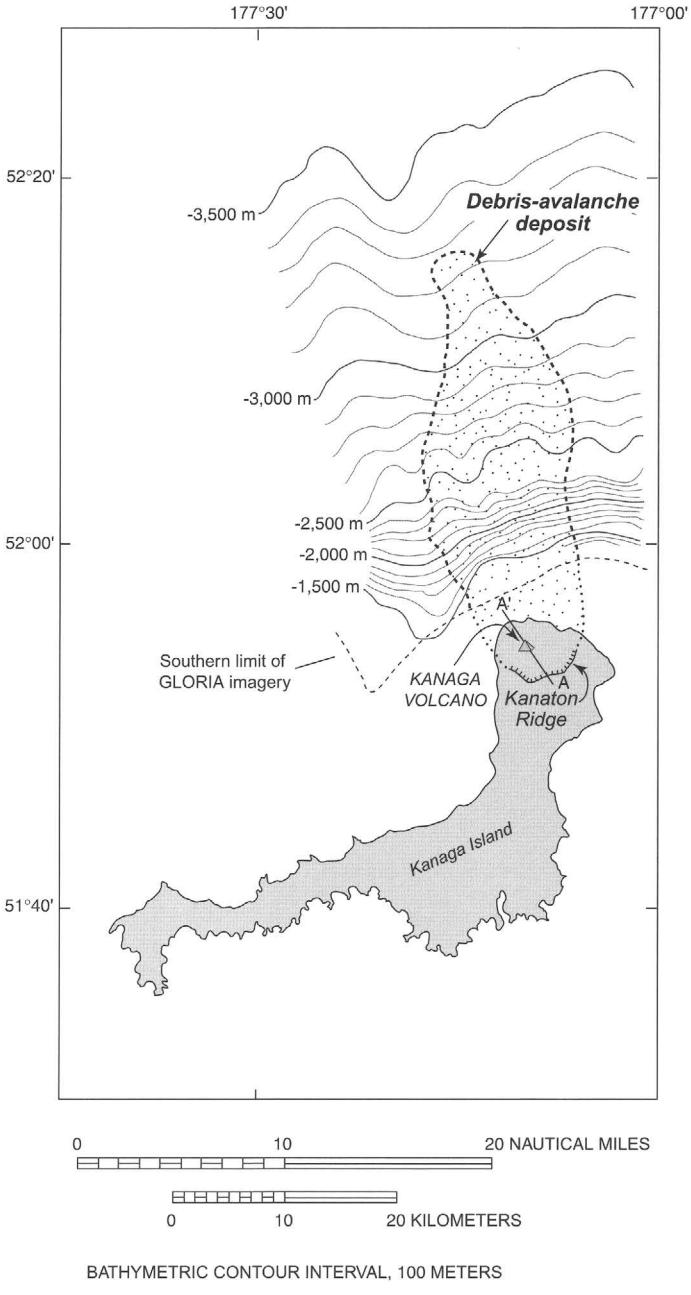

Figure 6. Bathymetry and approximate extent of debris-avalanche deposit north of Kanaga Island (fig. 1). Bathymetric data from Bering Sea (EEZ-Scan scientific staff, 1991).

MPa, whereas typical wallrock strength is less than about 20 MPa (Voight and Elsworth, 1997). Thus, a magmatic intrusion can initiate fractures that may become potential failure surfaces. A likely area for the formation of such fractures and potential planes of failure is the zone above the intrusion. Another effect of the intruding magma is to elevate pore pressures along the potential failure surface. A theoretical analysis of this effect (Elsworth and Voight, 1995; Voight and Elsworth, 1997; Voight, 2000) indicates that thermally induced pore-pressure changes could be sufficient to destabilize an oceanic volcano flank with the dimensions and geometry we estimate for ancestral Mount Kanaton. This scenario would require some rather extreme conditions, and the thermal forcing and diffusivity parameters associated with thermally driven ground-water flow would have to be maximums (Voight and Elsworth, 1997). However, the combined effects of mechanical, thermal, and seismically induced changes in pore pressure associated with magma emplacement could be sufficient to destabilize the edifice and initiate failure, as they have for other volcanoes, such as Mount St. Helens (Voight and others, 1983). In the absence of strong evidence for a collapse caldera, we suggest that Kanaton Ridge is the headscarp of an avalanche caldera which formed when the north flank of ancestral Mount Kanaton was displaced seaward by a shallow magmatic intrusion.

Tephrostratigraphy

Tephra deposits of Holocene age are common on Kanaga Island, and most of the area south of Kanaton Ridge (fig. 3) is covered by several meters of interbedded tephra, peat, and soil (fig. 8). Samples of the soil organic matter associated with many of the more conspicuous tephra beds were collected from various stratigraphic profiles around the island (fig. 9) and dated by conventional radiocarbon techniques (table 1).

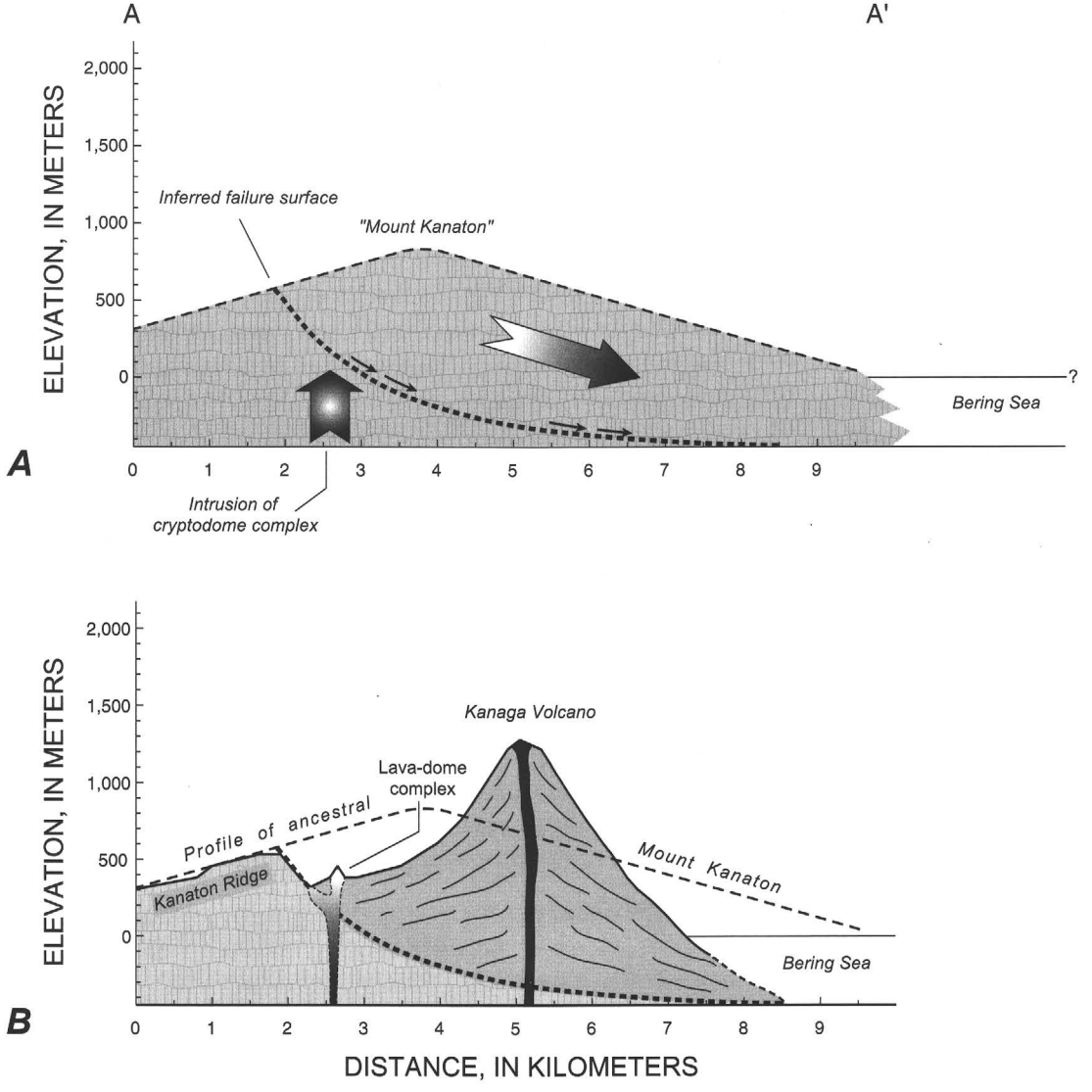

Figure 7. Simplified geologic cross sections of Mount Kanaton and Kanaga Volcano (fig. 1). *A*, Ancestral Mount Kanaton, showing inferred failure surface and location of cryptodome complex. *B*, Modern Kanaga Volcano. Line of cross section *A–A'* for both cross sections is shown in figure 6.

Table 1. Radiocarbon ages on samples from Kanaga Island.

[All ages in ^{14}C years before present (=A.D. 1950). Radiocarbon ages obtained from humic acid fraction of soil organic matter (except for sample 98CW68–7, which was obtained from peat), calibrated by the method of Stuiver and Reimer (1993). Calibrated ages listed in bold, flanked by 2σ error-limit ages]

Sample	Laboratory No.	Location (lat N., long W.)	Reported age (yr B.P.)	$\delta^{13}C$ value (permil)	Calibrated age (yr B.P.)
99CW68–7	GX–26011–LS	51°53′, 177°05′	Modern (102.98±0.73% present ^{14}C activity)	–27.3	– – –
99CW68–6	GX–26010–LS	51°53′, 177°05′	475±60	–26.2	623, 514, 337
00CW21–2	GX–27881	51°53′, 177°07′	500±60	–28.8	640, 524, 467
99CW76–2	GX–26021	51°52′, 177°03′	590±80	–27.0	672, 621, 607, 555, 505
00CW21–4	GX–27889	51°53′, 177°07′	890±60	–30.7	931, 789, 674
00CW08–2	GX–27886	51°53′, 177°07′	1,180±100	–28.1	1,293, 1,065, 925
99CW68–2	GX–26008	51°53′, 177°07′	1,390±110	–25.8	1,523, 1,294, 1,062
00CW21–6	GX–27882	51°53′, 177°07′	1,800±60	–27.6	1,873, 1,721, 1,559
00CW14–1	GX–27884	51°54′, 177°07′	1,850±120	–27.6	2,045, 1,817, 1,522
00CW21–8	GX–27888	51°53′, 177°07′	2,680±90	–28.4	2,956, 2,775, 2,512
99CW75–1	GX–26018	51°52′, 177°11′	3,100±90	–27.0	3,474, 3,342, 3,276, 3,273, 3,076
99CW83–5	GX–26029–LS	51°41′, 177°17′	3,310±60	–28.2	3,690, 3,551, 3,508, 3,483, 3,390
99CW75–3	GX–26019	51°52′, 177°11′	3,420±170	–24.6	4,146, 3,686, 3,660, 3,642, 3,271
99CW68–4	GX–26009–LS	51°53′, 177°05′	3,490±110	–26.1	4,085, 3,813, 3,792, 3,757, 3,751, 3,723, 3,472
99CW54–4	GX–25997	51°49′, 177°09′	3,630±140	–25.6	4,408, 3,961, 3,949, 3,927, 3,578
99CW82–1	GX–26027–LS	51°41′, 177°17′	3,720±70	–25.4	4,725, 4,086, 4,025, 4,020, 3,868
99CW77–4	GX–26022–LS	51°52′, 177°05′	3,790±70	–25.1	4,413, 4,151, 3,931
99CW83–4	GX–26028–LS	51°41′, 177°17′	3,850±60	–29.0	4,420, 4,244, 4,088
00CW22–5	GX–27890	51°51′, 177°07′	3,940±140	–26.5	4,829, 4,413, 3,934
00CW23–4	GX–27891	51°52′, 177°07′	3,910±200	–27.3	4,856, 4,406, 4,365, 4,363, 3,731
00CW06–4	GX–27879	51°57′, 177°06′	4,940±150	–26.7	5,989, 5,655, 5,322
99CW77–5	GX–26023–LS	51°52′, 177°05′	5,760±70	–25.9	6,728, 6,548, 6,406
99CW54–3	GX–25996	51°49′, 177°09′	5,740±170	–25.4	6,910, 6,499, 6,200
99CW75–7	GX–26020	51°52′, 177°11′	6,120±110	–25.3	7,267, 6,990, 6,684
99CW55–2	GX–25998–LS	51°48′, 177°12′	6,740±90	–25.1	7,745, 7,606, 7,602, 7,587, 7,432
00CW23–1	GX–27878	51°52′, 177°07′	8,310±210	–26.1	9,700, 9,398, 9,372, 9,358, 9,349, 9,342, 9,300, 8,641
99CW52–1	GX–25995	51°50′, 177°08′	8,470±330	–25.4	10,240, 9,490, 8,592
99CW77–10	GX–26025	51°52′, 177°05′	9,140±130	–26.0	10,668, 10,240, 9,919
00CW22–1	GX–27880	51°51′, 177°07′	9,270±500	–26.8	12,104, 10,482, 10,442, 10,428, 9,163
99CW77–9	GX–26024	51°52′, 177°05′	9,760±140	–25.6	11,553, 11,181, 10,694

Figure 8. · Typical exposure of pyroclastic-fall deposits and buried soils on Kanaga Island (fig. 1). Most light-colored beds are tephra deposits from Kanaga Volcano; dark layers are buried A soil horizons.

Radiocarbon dating of A soil horizons immediately below a tephra bed yields information about the timing of tephra deposition and allows us to outline a preliminary chronology of Holocene tephra-producing eruptions for Kanaga Volcano. Although we have not yet completed our analysis of the glass chemistry of the tephra deposits as a correlation aid, we can correlate various tephra deposits on the basis of their associated radiocarbon ages and field characteristics (fig. 11). Groups of tephra deposits so defined indicate that at least 11 eruptions of Kanaga Volcano have occurred since about 11 ka. Most of these eruptions were probably sub-Plinian to Plinian, producing moderately vesicular dacitic pumice lapilli tephra deposits ranging in thickness from a few centimeters to more than 1 m (table 2).

Studies of tephra deposits on nearby Adak Island (fig. 9) have yielded information on the age and chemistry of most of the major tephra deposits (fig. 12), many of which are believed to have been erupted from Kanaga Volcano (Black, 1980; Romick and others 1992; Kirianov and Miller, 1997). Correlation of the tephra records from Adak and Kanaga Islands based on the radiocarbon ages of the major tephra deposits indicates that only two of the major Adak tephras (the basal pink ash of Kiriyanov and Miller, 1997, and the Yellow-Brown-Olive Ash of Black, 1980) have age-equivalent tephra deposits on Kanaga Island (fig. 13). These results imply that the three thickest tephra deposits on Adak Island—the Main, Intermediate, and Sandwich Ashes of Black (1980)—are not readily identifiable as eruptive products from Kanaga Volcano and could record substantial Holocene eruptions from other volcanoes, including Mount Moffett on the northern part of Adak Island. The most conspicuous tephra deposit on Adak Island, the Main Ash, has long been regarded as the pyroclastic-fall deposit associated with the caldera-forming eruption that destroyed ancestral Mount Kanaton (Coats, 1956; Black, 1980). However, none of the dated tephra deposits on Kanaga Island matches the radiocarbon ages associated with the Main Ash (fig. 13). A thick lapilli tephra deposit about the same age as the Intermediate Ash is present at locality 00CW06 northeast of Kanaga Volcano (fig. 9) but is not recognized elsewhere on Kanaga Island. Radiocarbon ages associated with Kanaga Island tephra T7 match those of the Sandwich Ash (fig. 13); however, the T7 deposits consist of massive sand-size felsic tephra with granule-size juvenile lapilli at the base (sec. 99CW75, fig. 9) or a single thin lapilli bed (sec. 99CW83, fig. 9) and do not exhibit the sequence massive gray fine ash/

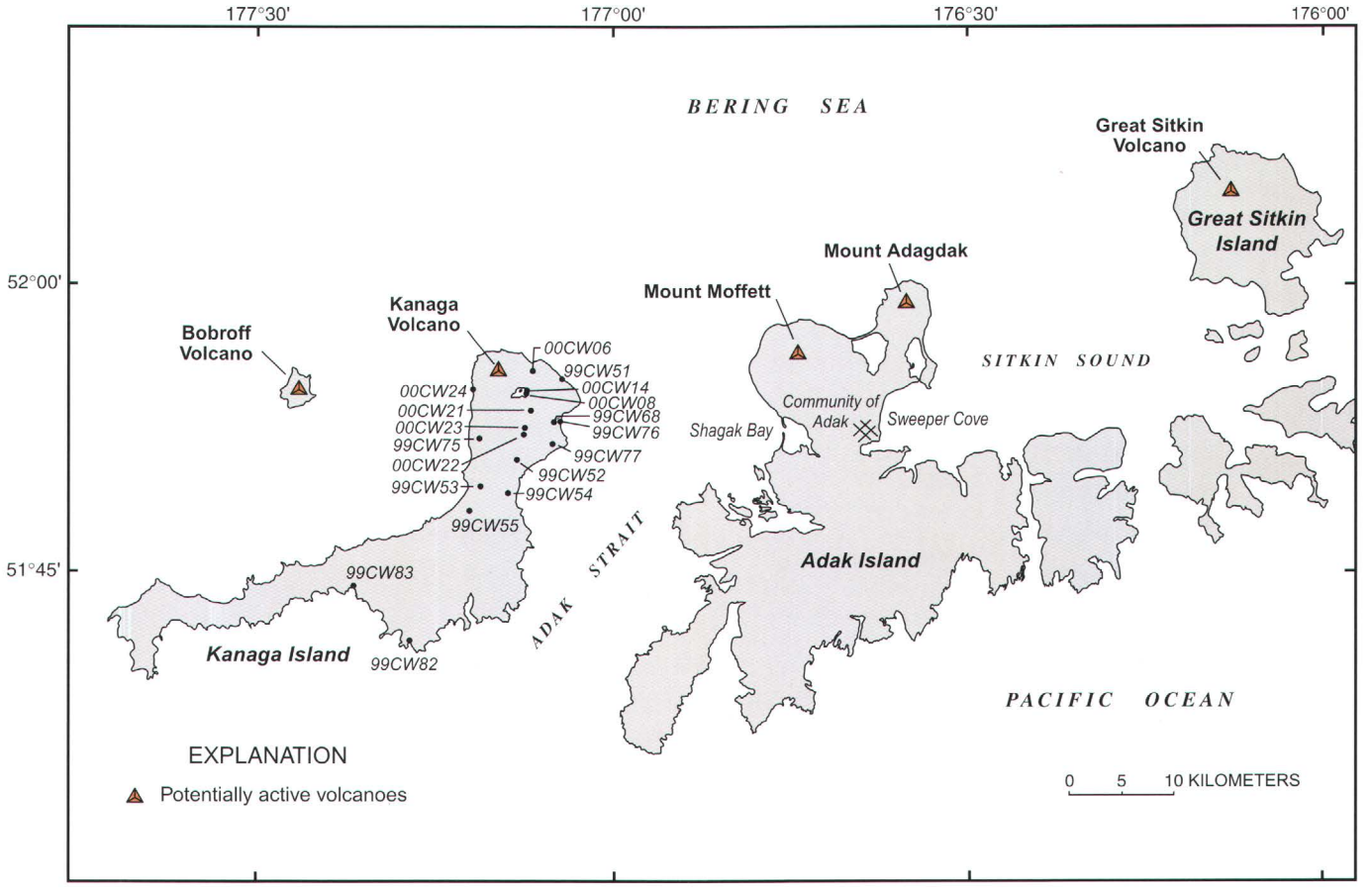

Figure 9. Western part of the Aleutian Islands, Alaska (fig. 1), showing locations of measured stratigraphic sections on Kanaga Island and other islands and of local volcanoes. Station numbers refer to stratigraphic profiles shown in figure 10.

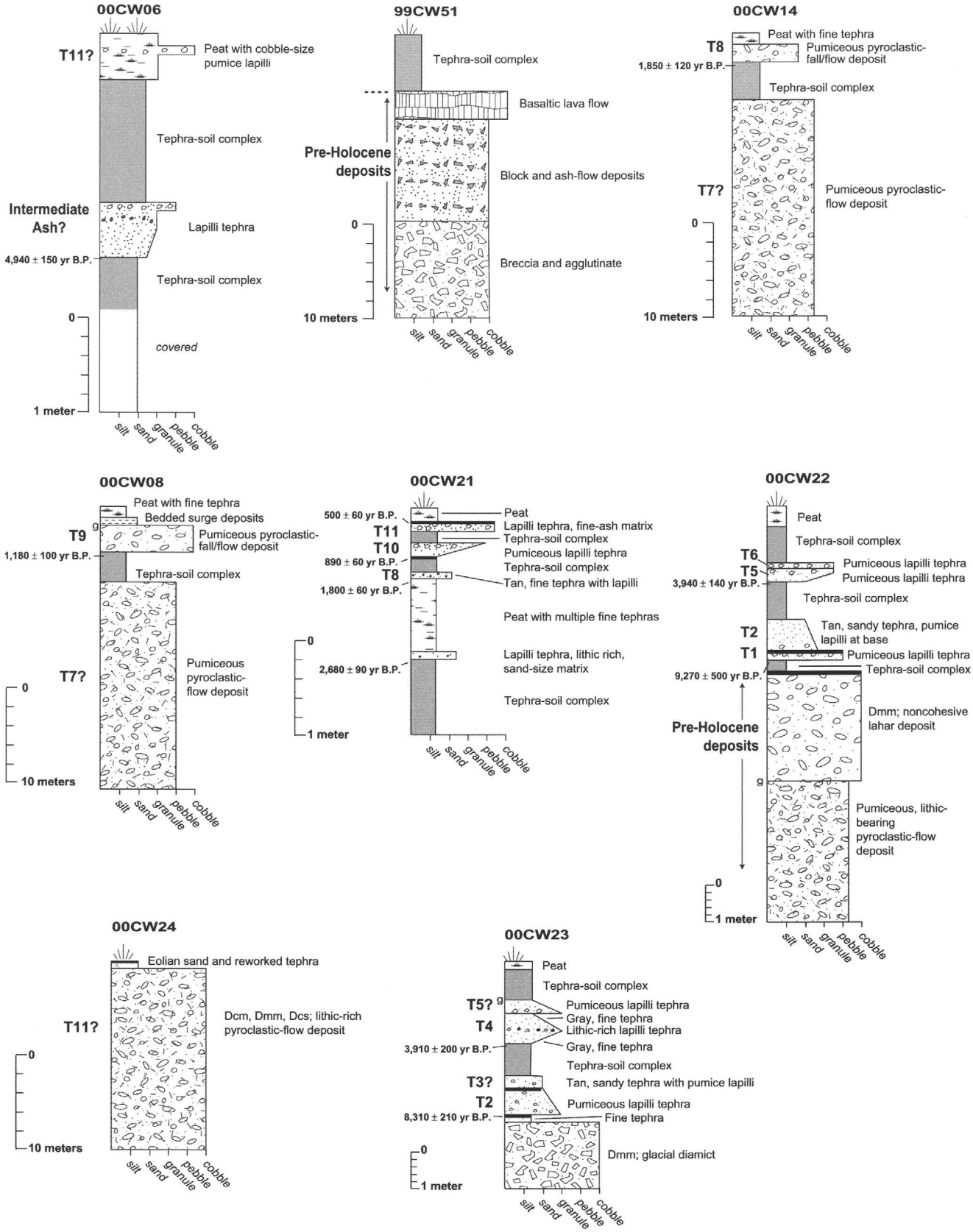

Figure 10. Stratigraphic profiles of surficial deposits on Kanaga Island (fig. 1), showing major tephra deposits, buried soils, and uncalibrated radiocarbon ages. Width of units is proportional to average particle size, as indicated by scale along base of each section. Locations of sections are shown in figure 9.

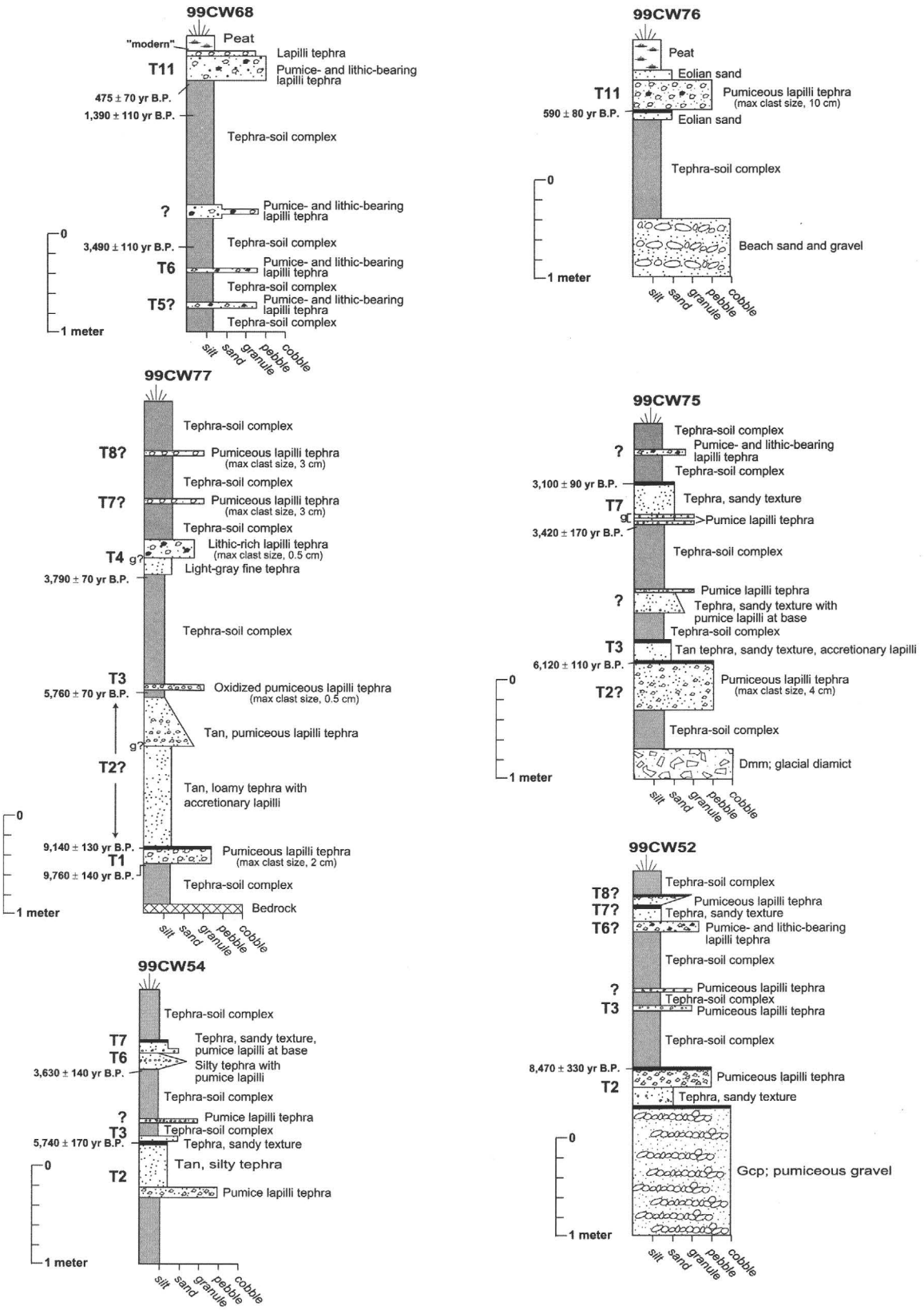

Figure 10.—Continued

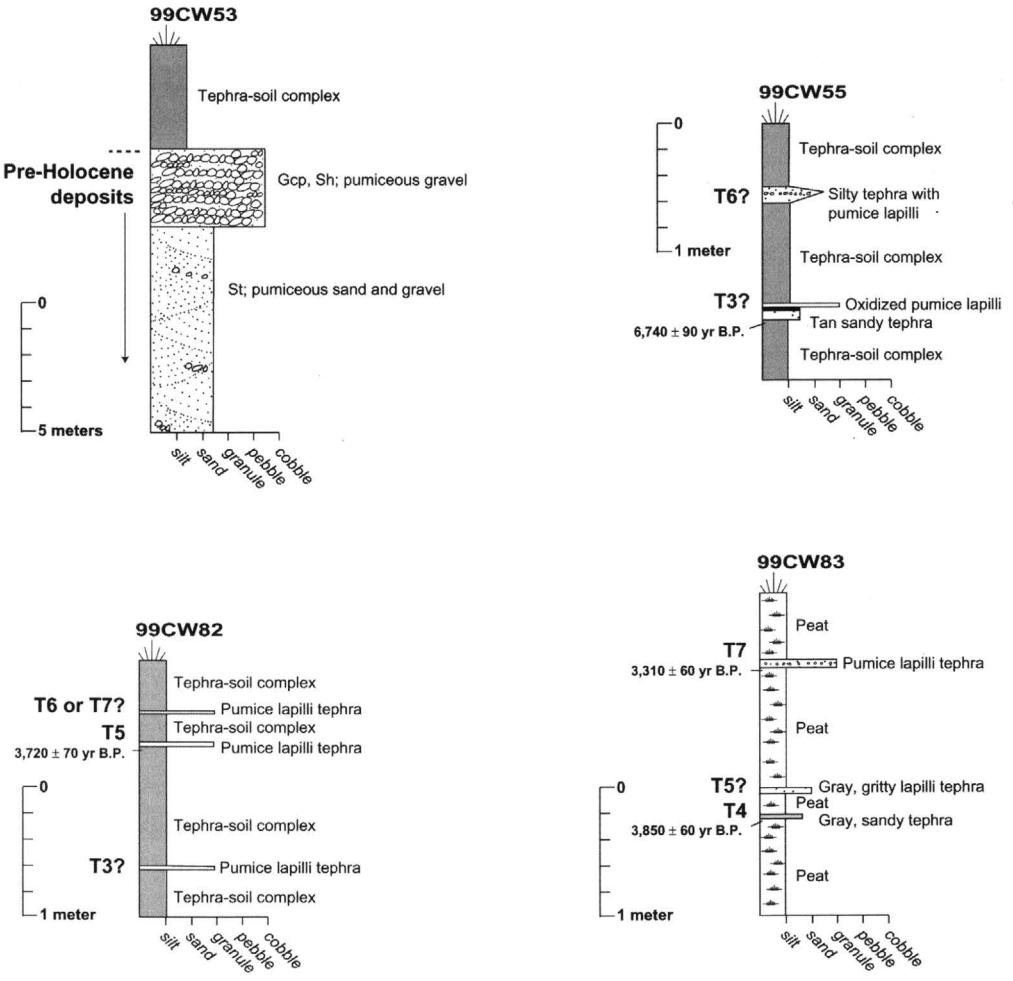

EXPLANATION

Pumice lapilli	
Lithic lapilli	
Tephra-soil complex. Multiple, fine thin tephras with A-Cox soils	
g	Gradational contact
A-Cox soil	
T	Tephra sample
C	Radiocarbon sample
R	Clast/rock sample
M	Matrix sample

Dcm	Diamict, clast-supported, massive
Dmm	Diamict, matrix-supported, massive
Dcs	Diamict, clast-supported, stratified
Gcp	Gravel, clast-supported, planar-bedded
Sh	Sand, horizontally bedded
St	Sand, trough-crossbedded

Figure 10.—Continued

Table 2. Characteristics of major tephra deposits erupted from Kanaga Volcano.

Tephra deposit	Thickness (cm)	Maximum particle size (mm)	Distance of known deposits from present vent (km)	Estimated age (yr B.P.)
T1	15–20	30	5–10	10,300–11,100
T2	10–150	40	5–10	8,800–9,700
T3	4–30	5	5–15	6,500–6,800
T4	30–90	5	5–>15	4,100–4,400
T5	2–10	5	5–>15	3,900–4,300
T6	5–10	4	5–15	3,600–4,100
T7	2–40	5	5–>15	3,400–3,600
T8	8–100	50	0–5	1,600–1,900
T9	150	100	0–5	900–1,300
T10	7	15	0–5	700–900
T11	10–30	100	0–10	500–600

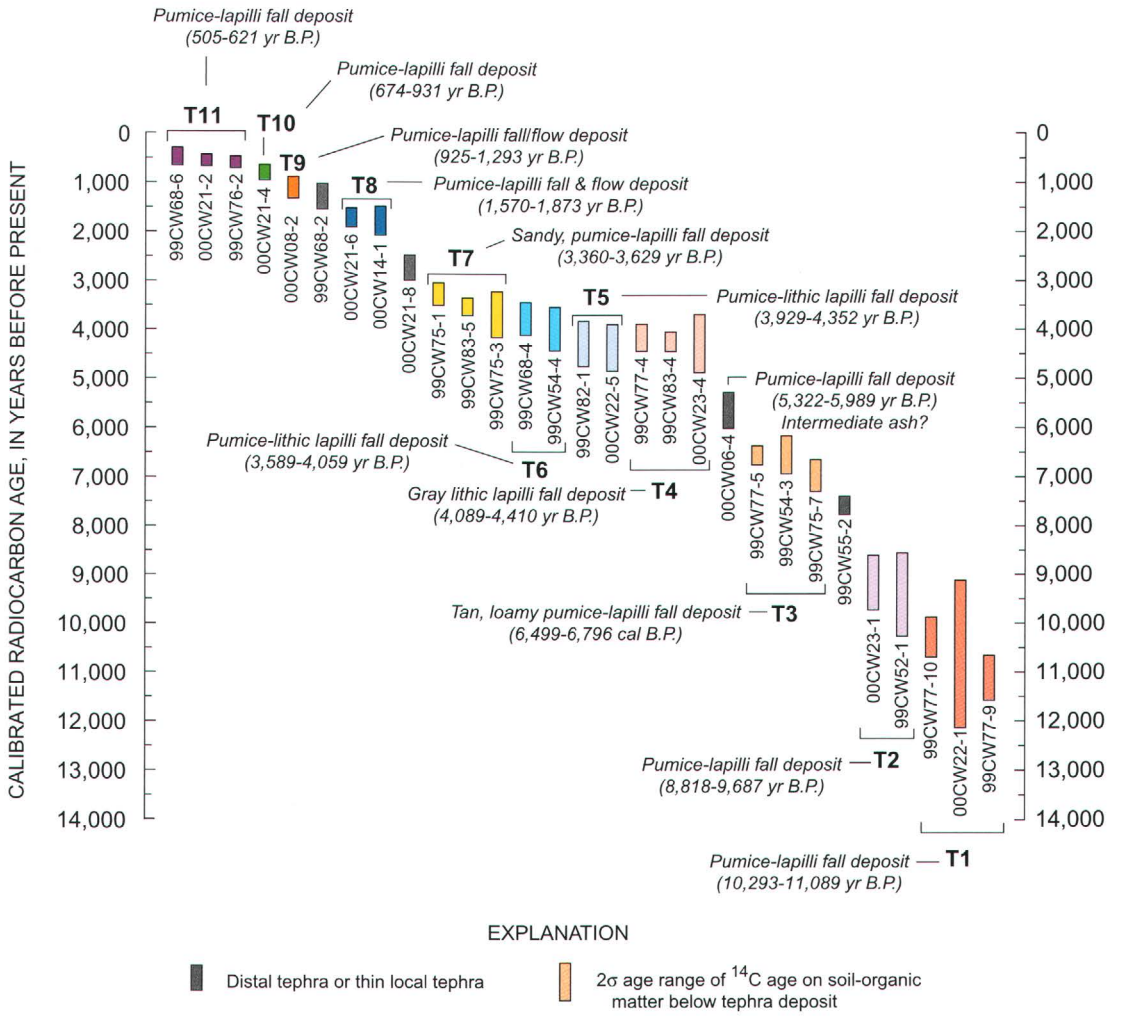

Figure 11. Correlation of tephra deposits on Kanaga Island (fig. 1), based on radiocarbon ages of buried soils. Vertical bars indicate 2σ age range for calibrated radiocarbon ages of buried soils associated with particular tephra deposit; numbers below bars denote radiocarbon samples listed in table 1. T1 through T11, preliminary groupings of tephra deposits based on radiocarbon ages and field characteristics of tephra deposits.

oxidized granule lapilli/massive gray fine ash that characterizes the Sandwich Ash on Adak Island. Thus, we are uncertain whether tephra T7 and the Sandwich ash are the same tephra deposit. The radiocarbon ages associated with tephra T8 on Kanaga Island and the Yellow-Brown-Olive Ash on Adak Island indicate that these two tephra deposits are temporally equivalent and are likely the same. The T8 deposits on Kanaga Island are coarser and thicker than deposits of the Yellow-Brown-Olive Ash on Adak, indicating that Kanaga Volcano was the likely source.

Conclusions

Our study of Kanaga Volcano reveals considerable new information about the history of the volcano as determined from stratigraphic studies of tephra deposits, radiocarbon dating of buried soils, and geologic mapping and chemical analysis of volcanic deposits. We have failed to locate credible evidence to support the hypothesis that Kanaton Ridge is the rim of a collapse caldera associated with a major pyroclastic eruption of Kanaga Volcano, as suggested by previous studies (Coats, 1956; Black, 1980). An area of hummocky topography observed in sea-floor imagery north of Kanaga Volcano appears to be a debris-avalanche deposit produced by a northward-directed edifice collapse of ancestral Mount Kanaton before the construction of the modern cone of Kanaga Volcano. Shallow magmatic intrusion of a cryptodome-like complex beneath ancestral Mount Kanaton is a plausible mechanism for destabilization of the edifice and subsequent flank collapse.

Our studies also indicate that Kanaga Volcano formed in the avalanche scar defined by Kanaton Ridge and was largely constructed in Holocene time. Tephra deposits erupted from Kanaga Volcano consist mainly of dense, moderately vesicular, coarse pumice lapilli of dacitic composition produced during explosive sub-Plinian to Plinian eruptions beginning about 11 ka. Correlation of tephra records on Kanaga and Adak Islands based on radiocarbon ages associated with major tephra beds indicates that few of the tephra deposits on Adak Island were produced by eruptions of Kanaga Volcano, as concluded by previous studies (Coats, 1956; Black, 1980; Romick and others, 1992; Kirianov and Miller, 1997). The source volcanoes for the three major middle Holocene tephra units on Adak Island (Main, Intermediate, and Sandwich Ashes) is uncertain, although Mount Moffett on the northern part of Adak Island now appears to be a likely source volcano.

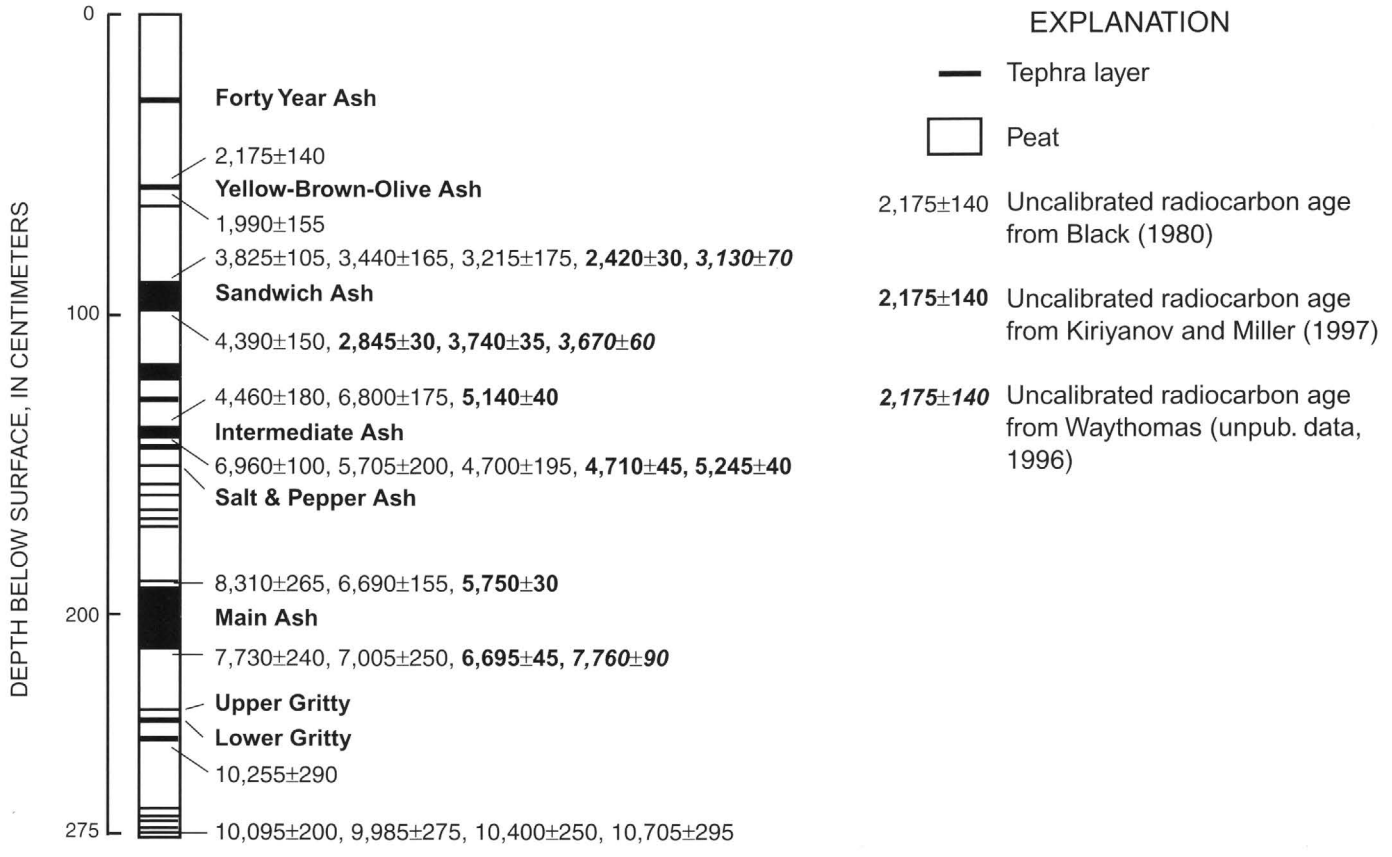

Figure 12. Tephrostratigraphic record from Adak Island (fig. 1). Modified from Black (1980).

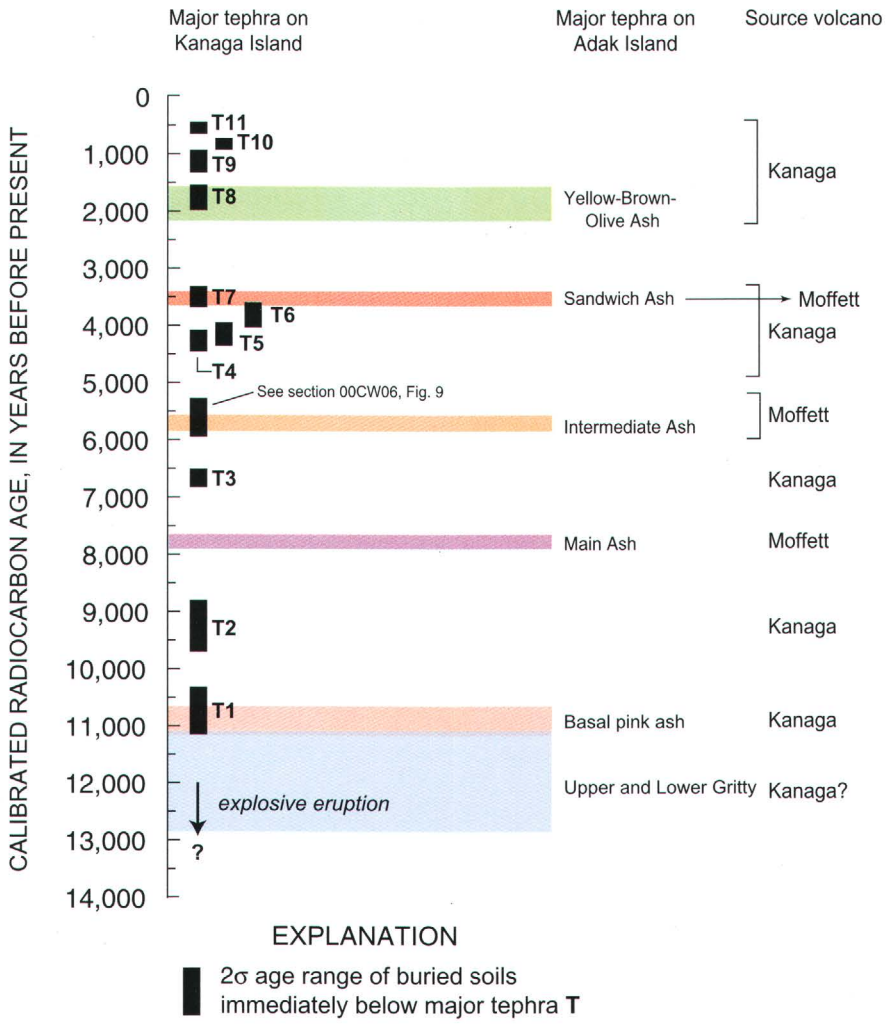

Figure 13. Correlation of tephra records from Kanaga and Adak Islands (fig. 1). Black vertical bars indicate calibrated 2σ age ranges of buried soils associated with major tephra deposits on Kanaga Island; colored bars indicate 2σ age ranges of buried soils associated with major tephra deposits on Adak Island.

References Cited

Black, R.F., 1980, Isostatic, tectonic, and eustatic movements of sea level in the Aleutian Islands, Alaska, *in* Morner, N.-A., ed., Earth rheology, isostasy, and eustasy: New York, John Wiley and Sons, p. 231–248.

Brophy, J.G., 1989, Can high-alumina arc basalt be derived from low-alumina arc basalt? Evidence from Kanaga Island, Aleutian Arc, Alaska: Geology, v. 17, no. 4, p. 333–336.

Brophy, J.G., 1990, Andesites from northeastern Kanaga Island, Aleutians—implications for calc-alkaline fractionation mechanisms and magma chamber development: Contributions to Mineralogy and Petrology, v. 104, no. 5, p. 568–581.

Burnham, C.W., 1979, Magmas and hydrothermal fluids, *in* Barnes, H.L., ed., Geochemistry of hydrothermal ore deposits (2d ed.): New York, John Wiley and Sons, p. 71–136.

Coats, R.R., 1956, Geology of northern Kanaga Island, Alaska: U.S. Geological Survey Bulletin 1028–D, p. 69–81.

EEZ-Scan scientific staff, 1991, Atlas of the U.S. Exclusive Economic Zone, Bering Sea: U.S. Geological Survey Miscellaneous Investigations Series Map I–2053.

Elsworth, Derek, and Voight, Barry, 1995, Dike intrusion as a trigger for large earthquakes and the failure of volcano flanks: Journal of Geophysical Research, v. 100, no. B4, p. 6005–6024.

Geist, E.L., Childs, J.R., and Scholl, D.W., 1988, The origin of summit basins of the Aleutian Ridge—implications for block rotation of an arc massif: Tectonics, v. 7, no. 2, p. 327–341.

Holcomb, R.T., and Searle, R.C., 1991, Large landslides from oceanic volcanoes: Marine Geotechnology, v. 10, no. 1–2, p. 19–32.

Imbrie, John, McIntyre, Andrew, and Moore, T.D., Jr., 1983, The ocean around North America at the last glacial maximum, *in* Porter, S.C., ed., The late Quaternary, v. 1 *of* Late Quaternary environments of the United States: Minneapolis, University of Minnesota Press, p. 230–236.

Keating, B.H., and McGuire, W.J., 2000, Island edifice failures and associated tsunami hazards: Pure and Applied Geophysics, v. 157, no. 6–8, p. 899–955.

Kiriyanov, V.Y., and Miller, T.P., 1997, Volcanic ashes of Adak Island, Aleutian Islands, Alaska: Volcanic Seismology, v. 19, no. 1, p. 65–78.

Le Bas, M.J., Le Maitre, R.W., Streckeisen, A.L., and Zanettin, B.A., 1986, Chemical classification of volcanic rocks based on the total alkali-silica diagram: Journal of Petrology, v. 27, no. 3, p. 745–750.

McGuire, W.J., 1996, Volcano instability—a review of contemporary themes, *in* McGuire, W.J., Jones, A.P., and Neuberg, Juergen, eds., Volcano instability on Earth and other planets: Geological Society of London Special Publication 10, p. 1–23.

Miller, T.P., and Smith, R.L., 1987, Late Quaternary caldera-forming eruptions in the eastern Aleutian arc, Alaska: Geology, v. 15, no. 5, p. 434–438.

Miller, T.P., McGimsey, R.G., Richter, D.H., Riehle, J.R., Nye, C.J., Yount, M.E., and Dumoulin, J.A., 1998, Catalog of the historically active volcanoes of Alaska: U.S. Geological Survey Open-File Report 98–582, 104 p.

Miyashiro, Akiho, 1974, Volcanic rock series in island arcs and active continental margins: American Journal of Science, v. 274, no. 4, p. 321–355.

Romick, J.D., Kay, S.M., and Kay, R.W., 1992, The influence of amphibole fractionation on the evolution of calc-alkaline andesite and dacite tephra from the central Aleutians, Alaska: Contributions to Mineralogy and Petrology, v. 112, no. 1, p. 101–118.

Stuiver, Minze, and Reimer, P.J., 1993, Extended ^{14}C data base and revised CALIB 3.0 ^{14}C age calibration program: Radiocarbon, v. 35, no. 1, p. 215–230.

van Wyk de Vries, Benjamin, and Francis, P.W., 1997, Catastrophic collapse at stratovolcanoes induced by gradual volcano spreading: Nature, v. 387, no. 6631, p. 387–390.

Vidal, Nathalie, and Merle, Oliver, 2000, Reactivation of basement faults beneath volcanoes—a new model of flank collapse: Journal of Volcanology and Geothermal Research, v. 99, no. 1–4, p. 9–26.

Voight, Barry, 2000, Structural stability of andesite volcanoes and lava domes: Royal Society of London Philosophical Transactions, v. 358, no. 1770, p. 1663–1703.

Voight, Barry, and Elsworth, Derek, 1997, Failure of volcano slopes: Geotechnique, v. 47, no. 1, p. 1–31.

Voight, Barry, Janda, R.J., Glicken, H.X., and Douglass, P.M., 1983, Nature and mechanics of the Mount St. Helens rockslide-avalanche of 18 May, 1980: Geotechnique, v. 33, no. 1, p. 243–273.

Whittington, C.M., 1996, The petrogenesis of the basalts of Round Head volcano, Kanaga Island, Aleutians: Bloomington, Indiana University, M.Sc. thesis, 79 p.

U.S. Geological Survey Reports on Alaska Released in 2001

Compiled by John P. Galloway

[Some reports dated 2000 did not become available until 2001; they are included in this listing]

Agena, W.F., Lee, M.W., and Hart, P.E., 2001, Reprocessing of multi-channel seismic-reflection data collected in the Chukchi Sea: U.S. Geological Survey Open-File Report 01–330, 2 CD–ROMS.

Agena, W.F., Lee, M.W., and Hart, P.E., 2000, Reprocessing of multi-channel seismic-reflection data collected in the Beaufort Sea: U.S. Geological Survey Open-File Report 00–460 [CD–ROM].

Ager, T.A., 2001, Holocene vegetation history of the northern Kenai Mountains, south-central Alaska, *in* Gough, L.P., and Wilson, F.H., eds., Geologic studies in Alaska by the U.S. Geological Survey, 1999: U.S. Geological Survey Professional Paper 1633, p. 91–108.

Blodgett, R.B., and Wilson, F.H., 2001, Reconnaissance geology north of the Hoholitna River, Taylor Mountains D–1 1:64,360-scale quadrangle, southwestern Alaska, *in* Gough, L.P., and Wilson, F.H., eds., Geologic studies in Alaska by the U.S. Geological Survey, 1999: U.S. Geological Survey Professional Paper 1633, p. 73–82.

Brew, D.A., 2001, The Insular-Intermontane suture zone (IISZ) of the western Coast Mountains of southeastern Alaska and British Columbia and the Adria-Europe suture zone (AESZ) of southern Europe—general description and comparison of global-scale tectonic features, *in* Gough, L.P., and Wilson, F.H., eds., Geologic studies in Alaska by the U.S. Geological Survey, 1999: U.S. Geological Survey Professional Paper 1633, p. 35–50.

Brosgé, W.P., Reiser, H.N., Dutro, J.T., Jr., Detterman, R.L., and Tailleur, I.L., 2001, Geologic map of the Arctic quadrangle, Alaska: U.S. Geological Survey Geologic Investigations Series Map I–2673, 38 p., 2 sheets, scale 1:250,000.

Brumbaugh, W.G., Krabbenhoft, D.P., Helsel, D.R., Wiener, J.G., and Echols, K.R., 2001, A national pilot study of mercury contamination of aquatic ecosystems along multiple gradients—bioaccumulation in fish: U.S. Geological Survey Biological Science Report BSR–2001–0009, 25 p.

Burrows, R.L., Langley, D.E., and Evetts, D.M., 2000, Preliminary hydraulic analysis and implications for restorations of Noyes Slough, Fairbanks, Alaska: U.S. Geological Survey Water-Resources Investigations Report 00–4227, 32 p.

Drummond, K.J., Corvalán D., José, Inoue, Eiji, Palfreyman, W.D., Doutch, H.F., Craddock, Campbell, Sato, Tadashi, McCoy, F.M., Moore, G.W., Richards, P.W., Swint-Iki, T.R., and Gartner, A.L., 2000, Geologic map of the Circum-Pacific region, Pacific Basin sheet, *with* Explanatory notes for geologic map of the Circum-Pacific region, Pacific Basin sheet, by K.J. Drummond, José Corvalán D., Eiji Inoue, H.F. Doutch, R.H. Needham, Tamotsu Nozawa, Yoji Teraoka, Takakhi Yoshida, Tadashi Sato, Campbell Craddock, F.W. McCoy, G.W. Moore, A.L. Gartner, T.R. Swint-Iki, and George Gryc: U.S. Geological Survey Circum-Pacific Series Map CP–49, 81 p., scale 1:10,000,000.

Drummond, K.J., Moore, G.W., Sumii, Tomoaki, Natori, Hiro'o, Kato, Masakazu, Wood, G.H., Richards, P.W., Bour, W.V., III, Fujii, Keizo, Inoue, Eiji, Sogabe, Masatoshi, Matsubayashi, Osamu, Teraoka, Yoji, and Swint-Iki, T.R., 2000, Energy-resources map of the Circum-Pacific region, Arctic sheet, *with* Explanatory notes for energy-resources map of the Circum-Pacific region, Arctic sheet, by K.J. Drummond, G.W. Moore, and T.R. Swint-Iki: U.S. Geological Survey Circum-Pacific Series Map CP–51, 27 p., scale 1:10,000,000.

Drummond, K.J., Salas, G.P., Yrigoyan, M.R., Sumii, Tomoaki, Natori, Hiro'o, Kato, Masakazu, Palfreyman, W.D., Fujii, Keizo, Inoue, Eiji, Sogabe, Masatoshi, Wood, G.H., Richards, P.W., Bour, W.V., III, Swint-Iki, T.R., Matsubayashi, Osamu, Wakita, Koji, Corvalán D., José, and Doutch, F.D., 2000, Energy-resource map of the Circum-Pacific region, Pacific Basin sheet, *with* Exploratory notes for energy-resource map of the Circum-Pacific region, Pacific Basin sheet, by K.J. Drummond, Tomoaki Sumii, Koji Wakita, Osammu Matsubayashi, Keizo Fujii, Tomoyuki Moritani, W.D. Palfreyman, M.R. Yrigoyan, and José Corvalán D.: U.S. Geological Survey Map Circum-Pacific Series CP–50, 109 p., scale 1,10,000,000.

Frederiksen, N.O., and McIntyre, D.J., 2000, Palynomorph biostratigraphy of mid(?)-Campanian to upper Maastrichtian strata along the Colville River, North Slope of Alaska: U.S. Geological Survey Open-File Report 00–493, 36 p.

Galloway, J.P., 2001, Reports about Alaska in non-USGS publications released in 1999 that include USGS authors, *in* Gough, L.P., and Wilson, F.H., eds., Geologic studies in Alaska by the U.S. Geological Survey, 1999: U.S. Geological Survey Professional Paper 1633, p. 139–141.

Galloway, J.P., 2001, U.S. Geological Survey reports on Alaska released in 1999, *in* Gough, L.P., and Wilson, F.H.,

eds., Geologic studies in Alaska by the U.S. Geological Survey, 1999: U.S. Geological Survey Professional Paper 1633, p. 135–138.

Gamble, B.A., Day, W.C., and Henning, M.W., 2001, Geochemistry of lithologic units, Fortymile River study area, east-central Alaska, *in* Gough, L.P., and Wilson, F.H., eds., Geologic studies in Alaska by the U.S. Geological Survey, 1999: U.S. Geological Survey Professional Paper 1633, p. 127–134.

Glass, R.L., 2001, Ground-water quality in the Cook Inlet Basin, Alaska, 1999: U.S. Geological Survey Water-Resources Investigations Report 01–4208, 58 p.

Gough, L.P., Crock, J.C., Day, W.C., and Vohden, Jim, 2001, Biogeochemistry of arsenic and cadmium, Fortymile River watershed, east-central Alaska, *in* Gough, L.P., and Wilson, F.H., eds., Geologic studies in Alaska by the U.S. Geological Survey, 1999: U.S. Geological Survey Professional Paper 1633, p. 109–126.

Gough, L.P., and Wilson, F.H., 2001, Introduction, *in* Gough, L.P., and Wilson, F.H., eds., Geologic studies in Alaska by the U.S. Geological Survey, 1999: U.S. Geological Survey Professional Paper 1633, p. 1–3.

Guffanti, Marianne, Brantley, S.R., and McClelland, Lindsay, eds., 2001, Volcanism in National Parks—summary of the workshop convened by the U.S. Geological Survey and National Park Service, 26–29 September 2000, Redding, California: U.S. Geological Survey Open-File Report 01–435, 43 p.

Heinrichs, T.A., Kennedy, B.W., Langley, D.E., and Burrows, R.L., 2001, Methodology and estimates of scour at selected bridge sites in Alaska: U.S. Geological Survey Water-Resource Investigations Report 00–4151, 44 p.

Hildreth, Wes, Fierstein, Judy, Lanphere, M.A., and Siems, D.F., 2001, Snowy Mountain—a pair of small andesite-dacite stratovolcanoes in Katmai National Park, *in* Gough, L.P., and Wilson, F.H., eds., Geologic studies in Alaska by the U.S. Geological Survey, 1999: U.S. Geological Survey Professional Paper 1633, p. 13–34.

Koch, R.D., [2000], Reconnaissance geologic map of the Bradfield Canal quadrangle, southeastern Alaska, *with an* Introduction, by H.C. Berg: U.S. Geological Survey Open-File Report 81–728–A, 35 p., scale 1:250,000.

Krimmel, R.M., 2001, Photogrammetric data set, 1957–2000, and bathymetric measurements for Columbia Glacier, Alaska: U.S. Geological Survey Water-Resources Investigations Report 01–4089, 40 p.

Kyle, R.E., and Brabets, T.P., 2001, Water temperature of streams in the Cook Inlet Basin, Alaska, and implications of climate change: U.S. Geological Survey Water-Resources Investigations Report 01–4109, 24 p.

Labay, K.A., Wilson, F.H., and Burleigh, K.A., 2001, Use of Landsat MSS and TM imagery to improve reconnaissance geologic mapping in the Ruby quadrangle, west-central Alaska, *in* Gough, L.P., and Wilson, F.H., eds., Geologic studies in Alaska by the U.S. Geological Survey, 1999: U.S. Geological Survey Professional Paper 1633, p. 83–90.

McGimsey, Game, 2001, Redoubt Volcano and the Alaska Volcano Observatory, 10 years later, *in* Gough, L.P., and Wilson, F.H., eds., Geologic studies in Alaska by the U.S. Geological Survey, 1999: U.S. Geological Survey Professional Paper 1633, p. 5–12.

Moore, G.W., Drummond, K.J., Teraoka; Yoji, Okulitch, A.V., Gramberg, I.S., Pogrebitsky, Y.E., Musatov, E.E., Parfenov, L.M., Natal'in, B.A., Jóhannesson, Haukur, McCoy, F.W., Simkin, Tom, Siebert, Lee, Swint-Iki, T.R., and Gartner, A.L., 2000, Geologic map of the Circum-Pacific region, Arctic sheet: U.S. Geological Survey Circum-Pacific Series Map CP–48, 21 p., scale 1:10,000,000.

Mueller, Seth, Verplanck, Philip, and Goldfarb, Richard, 2001, Ground-water studies in Fairbanks, Alaska—a better understanding of some of the United States' highest natural arsenic concentrations: U.S. Geological Survey Fact Sheet FS–01–111, 2 p.

Neal, C.A., McGimsey, R.G., Miller, T.P., Riehle, J.R., and Waythomas, C.F., 2001, Preliminary volcano-hazard assessment for Aniakchak Volcano, Alaska: U.S. Geological Survey Open-File Report 00–519, 35 p.

Nokleberg, W.J., Parfenov, L.M., Monger, J.W.H., Norton, I.O., Khanchuk, A.I., Stone, D.B., Scotese, C.R., Scholl, D.W., and Fujita, Kazuya, 2001, Phanerozoic tectonic evolution of the Circum-North Pacific: U.S. Geological Survey Professional Paper 1626, 122 p.

Pauk, B.A., Power, J.A., Lisowski, Mike, Dzurisin, Dan, Iwatsubo, E.Y., and Melbourne, Tim, 2001, Global positioning system (GPS) survey of Augustine Volcano, Alaska, August 3–8, 2000—data processing, geodetic coordinates and comparison with prior geodetic surveys: U.S. Geological Survey Open File Report 01–99, 20 p.

U.S. Geological Survey, 2000, 1998 Assessment of undiscovered deposits of gold, silver, copper, lead, and zinc in the United States: U.S. Geological Survey Circular 1178, 21 p.

U.S. Geological Survey, 2001, Distribution of arsenic in water and streambed sediments, Cook Inlet Basin, Alaska: U.S. Geological Survey Fact Sheet FS–01–83, 4 p.

U.S. Geological Survey, 2001, Natural gas hydrates—vast resource, uncertain future: U.S. Geological Survey Fact Sheet FS–01–21, 2 p.

U.S. Geological Survey, 2001, The National Petroleum Reserve-Alaska (NPRA) data archive: U.S. Geological Survey Fact Sheet FS–01–24, 2 p.

U.S. Geological Survey, 2001, USGS Mineral Resources Program—national maps and datasets for research and land planning: U.S. Geological Survey Fact Sheet FS–01–79, 2 p.

Wilson, F.H., and Weber, F.R., 2001, Quaternary geology, Cold Bay and False Pass quadrangle, Alaska Peninsula, *in* Gough, L.P., and Wilson, F.H., eds., Geologic studies in Alaska by the U.S. Geological Survey, 1999: U.S. Geological Survey Professional Paper 1633, p. 51–72.

Reports on Alaska in Non-USGS Publications Released in 2001 That Include USGS Authors

Compiled by John P. Galloway

[USGS authors are marked with asterisks (*), Some reports dated 1995, 1999, and 2000 did not become available until 2001; they are included in this listing]

Allewalt, Jessica, *Forester, R.M., *Ager, T.A., Strasser, J.C., and Ensminger, S.L., 2001, A postglacial history of the Matanuska valley [abs.]: Geological Society of America Abstracts with Programs, v. 33, no. 4, p. 4.

Amato, J.M., Bogar, M.J., and *Calvert, A.T., 2001, Metamorphism in the Tlikakila Complex Lake Clark National Park, Alaska—does it record the collision of the Peninsular terrane with Alaska? [abs.]: Eos (American Geophysical Union Transactions), v. 82, no. 47, p. 1238.

*Atwater, B.F., Yamaguchi, D.K., Bondevik, Stein, *Barnhardt, W.A., Amidon, L.J., Benson, B.E., Skjerdal, Gudrun, Shulene, J.A., and Nanayama, Futoshi, 2001, Rapid resetting of an estuarine recorder of the 1964 Alaska earthquake: Geological Society of America Bulletin, v. 113, no. 9, p. 1193–1204.

*Bailey, E.A., *Gray, J.E., and Hines, M.E., 2001, Mercury methylation and demethylation in soils near abandoned mercury mines in Alaska, USA [abs.]: Geological Society of America Abstracts with Programs, v. 33, no. 6, p. 361.

*Bird, K.J., 2000, Potential oil and gas resources of the Arctic National Wildlife Refuge in Alaska—1002 area: Polar Geography, v. 24, no. 1, p. 13–34.

Bruhn, R.L., Pavlis, T.L., *Plafker, George, Serpa, Lora, and Picornell, Carlos, 2001, Structure and tectonics of the Saint Elias Orogen [abs.]: Eos (American Geophysical Union Transactions), v. 82, no. 47, p. 857–858.

*Carlson, P.R., *Hooge, P.N., and *Stevenson, Andrew, 2001, Multibeam imagery shows extensive iceberg reworking of the lower Glacier Bay, Alaska fjord [abs.]: Eos (American Geophysical Union Transactions), v. 82, no. 47, p. 165.

Clautice, K.H., Newberry, R.J., Blodgett, R.B., Bundtzen, T.K., Gage, B.G., Harris, E.E., Liss, S.A., *Miller, M.L., Reifenstuhl, R.R., Clough, J.G., and Pinney, D.S., 2001, Bedrock geologic map of the Chulitna region, southcentral Alaska: Alaska Division of Geological and Geophysical Surveys Report of Investigations 2001–1A, 31 p., scale 1:63,360.

Clautice, K.H., Newberry, R.J., Pinney, D.S., Blodgett, R.B., Bundtzen, T.K., Gage, B.G., Harris, E.E., Liss, S.A., *Miller, M.L., Reifenstuhl, R.R., and Clough, J.G., 2001, Geologic map of the Chulitna region, southcentral Alaska: Alaska Division of Geological and Geophysical Surveys Report of Investigations 2001–1B, 32 p., scale 1:63,360.

*Coombs, M.L., and Gardner, J.E., 2001, Shallow-storage conditions for the rhyolite of the 1912 eruption at Novarupta, Alaska: Geology, v. 29, no. 9, p. 775–778.

Cunico, M.L., Walder, J.S., Fountain, A.G., and *Trabant, D.C., 2001, Localized glacier deformation associated with filling and draining of a glacier-dammed lake and implications for outburst flood hydraulics [abs.]: Eos (American Geophysical Union Transactions), v. 82, no. 47, p. 522.

*Detweiler, Shane, *Catchings, R.D., *Goldman, M.R., *Gandhok, Gini, Kiger, Lora, *Nelson, G.L., and *Moran, Edward, 2001, Preliminary results of a high-resolution seismic imaging investigation on St. Paul Island, Pribilof Islands, Alaska [abs.]: Eos (American Geophysical Union Transactions), v. 82, no. 47, p. 1204.

Drake, Jeff, Layer, P.W., *Mangan, M.T., *Miller, T.P., and *Waythomas, C.F., 2001, $^{40}Ar/^{39}Ar$ age constraints on caldera formation of the Emmons Lake volcanic center, Alaska Peninsula, Alaska [abs.]: Eos (American Geophysical Union Transactions), v. 82, no. 47, p. 1405.

Duk-Rodkin, Alejandra, Barendregt, R.W., and *Weber, Florence, 2001, Traces of old glaciations in east-central Alaska [abs.]: Eos (American Geophysical Union Transactions), v. 82, no. 47, p. 320.

*Dumoulin, J.A., *Harris, A.G., Young, L.E., and *Blome, C.D., 2001, Sedimentologic and paleontologic constraints on setting and age of the Red Dog Zn-Pb-Ag massive sulfide deposit, western Brooks Range, Alaska [abs.]: Geological Society of America Abstracts with Programs, v. 33, no. 6, p. 272.

*Dusel-Bacon, Cynthia, and Murphy, J.M., 2001, Apatite fission-track evidence of widespread Eocene heating and exhumation in the Yukon-Tanana Upland, interior Alaska: Canadian Journal of Earth Science, v. 39, no. 8, p. 1191–1204.

*Dusel-Bacon, Cynthia, *Wooden, J.L., and Bressler, J.R., 2001, New U-Pb zircon and geochemical evidence for bimodal Mid-Paleozoic magmatism and syngenetic base

metal mineralization in the Yukon-Tanana terrane, Alaska [abs.]: Geological Society of America Abstracts with Programs, v. 33, no. 6, p. 185–186.

*Emsbo, Paul, 2001, Gold in sedex deposits, *in* Hagemann, S.G., and Brown, P.E., eds., 2001, Gold in 2000: Reviews in Economic Geology, v. 13, p. 427–427.

Farris, D.W., *Haeussler, P.J., and Rieser, Michael, 2001, Formation of the Kodiak batholith—a consequence of spreading ridge subduction [abs.]: Eos (American Geophysical Union Transactions), v. 82, no. 47, p. 1354.

George, Rhiannon, Turner, Simon, Hawkesworth, Chris, Nye, Chris, *Bacon, Charles, Stelling, Peter, and Dreher, Scott, 2001, Chemical versus temporal controls on evolution of tholeiitic and calc-alkaline volcanoes in the Aleutian arc [abs.]: Eos (American Geophysical Union Transactions), v. 82, no. 47, p. 1200.

Ghent, E.D., Roeske, Sarah, Stout, M.Z., *Bradshaw, J.Y., and *Snee, Larry, 2001, Mesozoic granulite facies metamorphism of the Pitka mafic-ultramafic complex, northern Alaska [abs.]: Geological Society of America Abstracts with Programs, v. 33, no. 6, p. 249–250.

*Glen, J.M.G., 2001, Regional faulting associated with the southern Alaska orocline [abs.]: Eos (American Geophysical Union Transactions), v. 82, no. 47, p. 1203.

*Gray, J.E., 2001, Mercury methylation and environmental effects of inactive mercury mines in the Circum-Pacific region [abs]: Eos (American Geophysical Union Transactions), v. 82, no. 20, p. 93.

Gu, Yingxin, Rose, W.I., and *Schneider, D.J., 2001, Advantageous GOES IR results for volcanic ash mapping at high latitudes—Cleveland eruptions 2001 [abs.]: Eos (American Geophysical Union Transactions), v. 82, no. 47, p. 1360.

*Haeussler, P.J., *Bradley, D.C., *Wells, Ray, Rowley, D.B., *Miller, Marti, *Otteman, Aaron, and *Labay, Keith, 2001, Life and death of the Resurrection Plate—evidence for an additional plate in the NE Pacific in Paleocene-Eocene time [abs.]: Eos (American Geophysical Union Transactions), v. 82, no. 47, p. 1118.

*Hamilton, T.D., 2001, Quaternary glacial, lacustrine, and fluvial interactions in the western Noatak basin, northwest Alaska: Quaternary Science Reviews, v. 20, no. 1–3, p. 371–391.

Hancock, J.R., Werner, Al, *Waythomas, C.F., and Kaufman, D.S., 2001, Reconstructing the ashfall history of the Anchorage Alaska area [abs.]: Geological Society of America Abstracts with Programs, v. 33, no. 1, p. 66.

*Houseknecht, D.W., and *Bird, K.J., 2001, From boundaries to barrels—sequences stratigraphy and petroleum resource assessment of federal land in northern Alaska [abs.]: Geological Society of America Abstracts with Programs, v. 33, no. 6, p. 354.

*Josberger, E.G., Meadows, G.A., Shuchman, R.A., and Payne, John, 2001, Sediment control of convection in glacier dammed lakes [abs.]: Eos (American Geophysical Union Transactions), v. 82, no. 47, p. 556.

*Kelley, K.D., *Leach, D.L., *Slack, J.F., *Anderson, V.M., Clark, J.L., *Ayuso, R.A., and *Ridley, W.I., 2001, Evolution of trace element compositions in sphalerite and pyrite through time in the Zn-Pb-Ag shale-hosted Red Dog deposits, western Brooks Range, Alaska [abs.]: Geological Society of America Abstracts with Programs, v. 33, no. 6, p. 272.

Kerrich, Robert, *Goldfarb, Richard, Groves, David, and Garwin, Steven, 2001, The geodynamics of world-class gold deposits: characteristics, space-time distribution, and origins, *in* Hagemann, S.G., and Brown, P.E., eds., 2001, Gold in 2000: Reviews in Economic Geology, v. 13, p. 501–551.

LePain, D.L., *Adams, K.E., and Mull, C.G., 1999, Measured section and interpretation of the Tingmerkpuk sandstone (Neocomian), northwestern DeLong Mountains, western Arctic Slope Alaska, *in* Pinney, D.S., and Davis, P.K., eds., Short notes on Alaska geology, 1999: Alaska Division of Geological and Geophysical Surveys Professional Report 229, p. 45–62.

Lewchuk, M.T., *Leach, David, Symons, David, and Elmore, R.D., 2001, Paleomagnetic dating of mineralization at Red Dog and the Mesozoic tectonic history of the Brooks Range, Alaska [abs.]: Geological Society of America Abstracts with Programs, v. 33, no. 6, p. 272.

*Lu, Zhong, *Power, J.A., McConnell, V.S., *Wicks, Charles, and *Dzurisin, Daniel, 2001, Eruptive activity and ground deformation revealed by satellite radar interferometry at Makushin volcano, Alaska—1993–2000 [abs.]: Eos (American Geophysical Union Transactions), v. 82, no. 47, p. 273.

*Manies, K.L., *Harden, J.W., and *King, S.L., 2001, The role of woody debris in boreal forest recovery after fire [abs.]: Eos (American Geophysical Union Transactions), v. 82, no. 47, p. 184.

Mankowski, L.C., Riley, C.M., Rose, W.I., and *McGimsey, R.G., 2001, Mapping ash grain-size distribution from the August 18, 1992, eruption of Mt. Spurr [abs.]: Eos (American Geophysical Union Transactions), v. 82, no. 47, p. 1379.

*Marsh, Erin, *Goldfarb, Richard, Hart, Craig, and *Johnson, Craig, 2001, The Clear Creek intrusion-related gold deposit, Tintina Gold Belt, Yukon Canada [abs.]: Geological Society of America Abstracts with Programs, v. 33, no. 6, p. 420.

*McNamara, D.E., and *Benz, Harley, 2001, Three-dimensional P and S wave velocity structure of the Alaskan subduction zone [abs.]: Eos (American Geophysical Union Transactions), v. 82, no. 47, p. 1203.

McNutt, S.R., Marzocchi, Warner, and *Power, J.A., 2001, Simultaneous earthquake swarms and eruptions in Alaska, fall 1996 [abs.]: Eos (American Geophysical Union Transactions), v. 82, no. 47, p. 811.

Meier, M.F., Cohn, John, *Krimmel, R.M., and, Pfeffer, W.T., 2001, The past and future dynamics of Columbia Glacier, Alaska [abs.]: Eos (American Geophysical Union Transactions), v. 82, no. 47, p. 535.

*Molnia, B.F., 2001, Assessing the response of Alaskas glaciers to Post-Little Ice Age climate change [abs.]: Eos (American Geophysical Union Transactions), v. 82, no. 47, p. 541.

*Moran, S.C., *Power, J.A., and Stihler, S.D., 2001, Volcanic earthquake triggered by dynamic stresses associated with nearby tectonic earthquakes—constraints from theKatmai Group volcanoes, Alaska [abs.]: Eos (American Geophysical Union Transactions), v. 82, no. 47, p. 837–838.

*Muhs, D.R., *Ager, T.A., and Begét, J.E., 2001, Vegetation and paleoclimate of the Last Interglacial period, central Alaska: Quaternary Science Reviews, v. 20, no. 1–3, p. 41–61.

*Nokleberg, W.J., Bundtzen, T.K., *Brew, D.A., and *Plafker, George, 1995, Metallogenesis and tectonics of porphyry copper, molybdenum (gold, silver), and granitoid-hosted gold deposits of Alaska, *in* Schroeter, T.G., ed., Porphyry deposits of the northwest Cordillera of North America: Canadian Institute of Mining, Metallurgy and Petroleum Special Volume 46, p. 103–141.

Pfeffer, W.T., *Krimmel, R.M., and Meier, M.F., 2001, Heterogeneity of strain rate and the location of fracture events leading to iceberg calving, Columbia Glacier, Alaska [abs.]: Eos (American Geophysical Union Transactions), v. 82, no. 47, p. 529.

*Phillips, R.L., *Ager, T.A., *Barron, J.A., and *Starratt, Scott, 2001, Diamictite from the Chukchi Sea—evidence of northern glaciation during the Late Miocene and Early Pliocene [abs.]: Eos (American Geophysical Union Transactions), v. 82, no. 47, p. 798–799.

*Plafker, George, Synolakis, C.E., and Okal, E.A., 2001, New near-source tsunami field data for the April 1, 1946 Aleutian earthquake, Alaska [abs.]: Eos (American Geophysical Union Transactions), v. 82, no. 47, p. 819.

*Potter, C.J., and *Moore, T.E., 2001, Application of regional structural interpretations to oil and gas assessments of federal lands in the frontal Brookian deformed belt of Alaska's North Slope [abs.]: Geological Society of America Abstracts with Programs, v. 33, no. 6, p. 353–354.

Rioux, M.E., Mehl, Luc, Hacker, B.R., Mattinson, J.M., Gans, Phillip, and *Wooden, J.L., 2001, Understanding island arc evolution through U/Pb and $^{40}Ar/^{39}Ar$ geochronology of the Talkeetna Arc, south-central Alaska [abs.]: Eos (American Geophysical Union Transactions), v. 82, no. 47, p. 1200.

Rioux, Matthew, Mehl, Luc, Hacker, Bradley, Mattinson, James, and *Wooden, J.L., 2001, Understanding island arc thermal structure through U-Pb and ^{40}Ar-^{39}Ar geochronology of the Talkeetna arc section, south-central Alaska [abs.]: Geological Society of America Abstracts with Programs, v. 33, no. 6, p. 256–257.

Roeske, S.M., Ghent, E.D., Stout, M.Z., and *Bradshaw, J.Y., 2001, Thickened ocean crust or basal island arc origin for the Pitka Mafic-ultramafic Complex, northern Alaska [abs.]: Eos (American Geophysical Union Transactions), v. 82, no. 47, p. 1237.

Roman, D.C., *Power, J.A., and *Moran, S.C., Cashman, K.V., and Stihler, S.D., 2001, Unrest at Iliamna volcano, Alaska in 1996—evidence for a magmatic intrusion? [abs.]: Eos (American Geophysical Union Transactions), v. 82, no. 47, p. 1329.

Rose, W.I., Bluth, G.J.S., *Schneider, D.J., Ernst, G.J., Riley, C.M., Henderson, L.J., and *McGimsey, R.G., 2001, Observations of volcanic clouds in their first few day of atmospheric residence—the 1992 eruptions of Crater Peak, Mount Spurr volcano, Alaska: Journal of Geology, v. 109, no. 6, p. 677–694.

*Saltus, R.W., *Haeussler, P.J., and *Phillips, J.D., 2001, Geophysical mapping of subsurface structures in the Upper Cook Inlet basin, Alaska [abs.]: Geological Society of America Abstracts with Programs, v. 33, no. 6, p. 345.

*Saltus, R.W., Hudson, T.L., and *Phillips, J.D., 2001, Basement geophysical interpretation of the National Petroleum Reserve Alaska (NPRA), northern Alaska [abs.]: Geological Society of America Abstracts with Programs, v. 33, no. 3, p. 45.

*Schneider, D.J., Prata, F.J., Gu, Yingzin, Watson, Matthew, and Rose, W.I., 2001, Use of MODIS for volcanic eruption cloud detection, tracking, and measurement—examples from the 2001 eruption of Cleveland volcano, Alaska [abs.]: Eos (American Geophysical Union Transactions), v. 82, no. 47, p. 1356.

*Slack, J.F., *Kelley, K.D., *Anderson, V.M., Clark, J.L., and *Ayuso, R.A., 2001, Geochemistry of silicified rocks in the Red Dog Zn-Pb-Ag district, western Brooks Range, Alaska—evidence for multistage diagenetic and hydrothermal fluid flow and fluid-rock reactions [abs.]: Geological Society of America Abstracts with Programs, v. 33, no. 6, p. 272.

*Stephens, C.D., and *Chouet, B.A., 2001, Evolution of the December 14, 1989 precursory long-period event swarm at Redoubt volcano, Alaska: Journal of Volcanology and Geothermal Research, v. 109, no. 1–3, p. 133–148.

*Stottlemyer, Robert, 2001, Biogeochemistry of a treeline watershed, northwestern, Alaska: Journal of Environmental Quality, v. 30, no. 6, p. 1990–1998.

*Trabant, D.C., and *Krimmel, R.M., 2001, Hubbard Glacier will block the entrance to Russell Fiord, Alaska [abs.]: Eos (American Geophysical Union Transactions), v. 82, no. 47, p. 531–532.

*Verplanck, P.L., *Mueller, S.H., *Nordstrom, K.K., *Goldfarb, R.J., *Sanzolone, R.F., Youcha, E.K., and Roller, Michelle, 2001, Arsenic variability in ground water, Ester Dome, Alaska [abs.]: Geological Society of America Abstracts with Programs, v. 33, no. 6, p. 54.

*Waythomas, C.F., 2001, Formation and failure of volcanic debris dams in the Chakachatna River valley associated with eruptions of the Spurr volcanic complex, Alaska: Geomorphology v. 39, no. 3–4, p. 111–129.

*Waythomas, C.F., *Mangan, M.T., *Miller, T.P., Layer, P.L., and *Trusdell, F.A., 2001, Caldera-forming eruptions of the Emmons Lake volcanic center, Alaska Peninsula, Alaska—probable source of the Dawson Creek tephra in Yukon Territory, Canada [abs.]: Eos (American Geophysical Union Transactions), v. 82, no. 47, p. 1405.

*Waythomas, C.F., *Miller, T.P., and Begét, J.E., 2000, Record of Late Holocene debris avalanches and lahars at Iliamna

Volcano, Alaska: Journal of Volcanology and Geothermal Research, v. 104, no. 1–4, p. 97–130.

*Woodruff, L.G., *Harden, J.W., *Cannon, W.F., and *Gough, L.P., 2001, Mercury loss from the forest floor during wildland fire [abs.]: Eos (American Geophysical Union Transactions), v. 82, no. 47, p. 199.

Zhuang, Qianiai, Clein, J.S., *McGuire, D.A., Dargaville, R.J., Kicklighter, D.W., Melillo, J.M., Hobbie, J.E., and Rastetter, E.B., 2001, Modeling the effects of soil thermal dynamics on the seasonality of carbon fluxes across northern temperate and high latitude regions [abs.]: Eos (American Geophysical Union Transactions), v. 82, no. 47, p. 181.